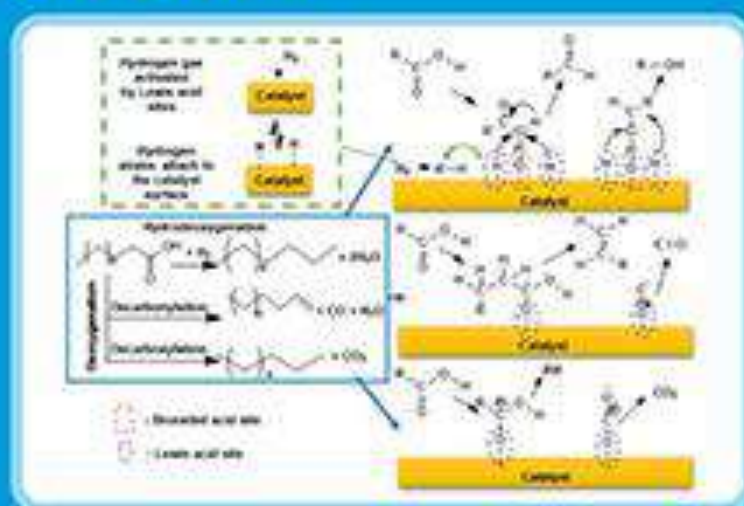


# Indonesian Journal of Chemistry

Vol. 23, No. 2, April 2023



Accredited by RISTEK/BRIN  
No. 80/SK/MPT/2023

## Activity and Selectivity of Mesoporous Silica Catalyst for Hydrocracking Process of Used Palm Oil into Biogasoline

Ahmad Suseno<sup>1</sup>, Karna Wijaya<sup>2\*</sup>, Edy Herald<sup>3</sup>, Lukman Hakim<sup>4</sup>,  
Wahyu Dita Saputri<sup>5</sup>, and Gunawan Gunawan<sup>1</sup>

<sup>1</sup>Department of Chemistry, Faculty of Sciences and Mathematics, Diponegoro University,  
Jl. Prof. H. Soedarto, S.H., Tembalang, Semarang 50275, Indonesia

<sup>2</sup>Department of Chemistry, Faculty of Mathematics and Natural Sciences, Universitas Gadjah Mada,  
Sekip Utara, Yogyakarta 55281, Indonesia

<sup>3</sup>Department of Chemistry, Faculty of Mathematics and Natural Sciences, Universitas Sebelas Maret,  
Jl. Ir. Sutami 36A, Surakarta 57126, Indonesia

<sup>4</sup>Department of Chemistry, Faculty of Mathematics and Natural Sciences, Brawijaya University,  
Jl. Veteran, Malang 65145, Indonesia

<sup>5</sup>Research Center for Quantum Physics, National Research and Innovation Agency (BRIN),  
Habibie Science and Technology Complex (Puspiptek), Serpong 15314, South Tangerang, Indonesia

\* **Corresponding author:**

email: karnawijaya@ugm.ac.id

Received: November 15, 2021

Accepted: February 22, 2023

DOI: 10.22146/ijc.70460

**Abstract:** Research on the synthesis of mesoporous silica catalyst, as well as its activity and selectivity in the hydrocracking of used palm oil, has been carried out. The research involved the preparation of mesoporous silica catalyst by varying the volume ratio of TEOS:CTAB at 2:1, 4:1, and 8:1, then calcined at 500 °C. Synthesis success was confirmed by FTIR, XRD, SEM-EDX, GSA, and hydrocracking selectivity by GC-MS analysis. The results showed that the more TEOS added, the silica bond composition, crystallinity, pore size, and product selectivity increased. The best catalyst performance was obtained from a TEOS:CTAB ratio of 8:1 at a calcination temperature of 500 °C (MCT81-500), which indicated the presence of Si-OH and Si-O-Si groups with a Si percentage of 45.31%, pore size diameter of 31.912 nm, and a total pore volume of 0.040 cc/g. In addition, the application of MCT81-500 in the hydrocracking process of used palm oil can produce a bio-gasoline (C5-C12) and kerosene (C12-C15) of 92.24 and 7.76 wt.%, respectively. This study shows that mesoporous silica has good potential for catalytic activity to convert used cooking oil waste into an environmentally friendly energy source.

**Keywords:** mesoporous silica; hydrocracking; palm oil; biogasoline

### ■ INTRODUCTION

For several years, fossil fuels have been widely used in various aspects of life. However, this fuel is non-renewable and will eventually run out. Various studies on alternative fuel sources to overcome the problem of fossil fuels have been carried out [1]. Biogasoline is like fossil fuels in terms of functionality and clean combustion [2-3]. Used palm oil is an alternative source of biogasoline. Used palm oil is produced mostly by households, the food industry, and fast-food restaurants. Used palm oil consists

of long hydrocarbon chains, such as fatty acids, triglycerides, and their derivatives which can be converted into biogasoline. Therefore, the hydrocracking process is very necessary for converting used palm oil into fuel [4-5].

Mesoporous silica nanoparticles have attracted attention in various applications such as separation [6], catalysis [7], chemical sensing [8], and biomedicine [9]. Mesoporous silica has been synthesized in many previous studies showing various shapes or

morphologies, including monoliths, spheres, rods, films, and fibers [10-18]. They display promising functions for catalytic, electronic, separation, electrochemical, and optical applications [19-20]. In addition, the development of nanostructured materials is increasingly attracting interest in various application fields, including catalysis and adsorption. Thermal and hydrothermal stabilities are also important parameters to be considered when designing materials for heterogeneous catalytic reaction applications. The type of heterogeneous catalyst currently being studied is a silica-based catalyst. This type of catalyst has some advantages, namely surface reactivity, good chemical and thermal resistance and acidity, which is easily modified by the hydrocracking process [21].

Hydrocracking is one of the important processes in petroleum processing. In the hydrocracking process, hydrocarbon compounds break down into small-chain hydrocarbons such as gasoline, diesel, and kerosene fractions [22-23]. Development with the addition of a catalyst can speed up the hydrocracking process. Based on previous studies, it is known that hydrocracking catalysts with mesoporous dimension silica can increase the liquid yield [24]. Silica-based catalysts have surface reactive properties, good thermal, chemical, and acid resistance, and are easy to modify [25]. The nature of the silica catalyst is determined by several synthesis parameters, such as calcination temperature, solution pH, method of preparation, and precursor concentration [26]. In addition, a modification that can be made to increase the reactivity of silica is by forming mesopores. A pore is considered a mesopore when it has a pore size of 2 to 50 nm [27]. Mesoporous materials are very encouraging for hydrocracking processes due to their large surface area, thermal, chemical, and mechanical stability, regular pore distribution, and high adsorption capacity [24,28]. So, the development of mesoporous silica synthesis becomes important.

Mesoporous silica synthesis requires a silica source and a template. The most used silica sources are tetraethyl orthosilicate (TEOS) or sodium silicate, while cationic organic compounds such as cetyltrimethylammonium bromide (CTAB) are used as molds [29-30]. The type of template and the ratio of precursors used determine the

size and distribution of mesoporous silica materials [24,31] as catalysts for hydrocracking [32-36]. Therefore, this study observed the activity and selectivity of mesoporous silica catalysts for the hydrocracking process of used palm oil into biogasoline. The effect of TEOS:CTAB composition variations were observed by characterization with FTIR, XRD, SEM-EDX, GSA, and hydrocracking selectivity with GC-MS to obtain the optimum catalyst performance ratio. In addition, this research is also expected to be a solution to the potential use of used cooking oil that is not utilized as an environmentally friendly energy source.

## ■ EXPERIMENTAL SECTION

### Materials

The materials used in this study consisted of CTAB, TEOS, ammonium hydroxide (NH<sub>4</sub>OH), and sodium hydroxide (NaOH) obtained from E. Merck. Palm oil was purchased from a traditional market in Semarang, Central Java. Hydrogen and nitrogen gases were obtained from PT. Samator Gas (Semarang, Central Java).

### Instrumentation

The equipment and instruments used in this study included laboratory glassware, magnetic stirrers, ovens (Kirin), filter paper (Whatman no. 42), Gas Sorption Analyzers (GSA, Quantachrome Nova 1200e), Scanning Electron Microscope (SEM, Phenom ProX G6 desktop), X-ray Diffractometer (XRD, X'Pert3 Powder), Fourier Transform Infra-Red Spectrometer (FTIR, PerkinElmer Spectrum 100), and Gas Chromatography-Mass Spectrometry (GC-MS, GC-2010 Shimadzu).

### Procedure

#### Preparation

An outline of the production scheme for mesoporous silica (MCT) as a catalyst for hydrocracking palm oil is shown in Fig. 1. Synthesis of mesoporous silica was performed by mixing 0.8018 g CTAB and 2, 4 and 8 mL TEOS separately. Then, the synthesis results are labeled as MCT21-500, MCT41-500, and MCT81-500. The mixture was stirred for 15 min. Then 5 mL of 2 M NaOH solution was added dropwise and continued

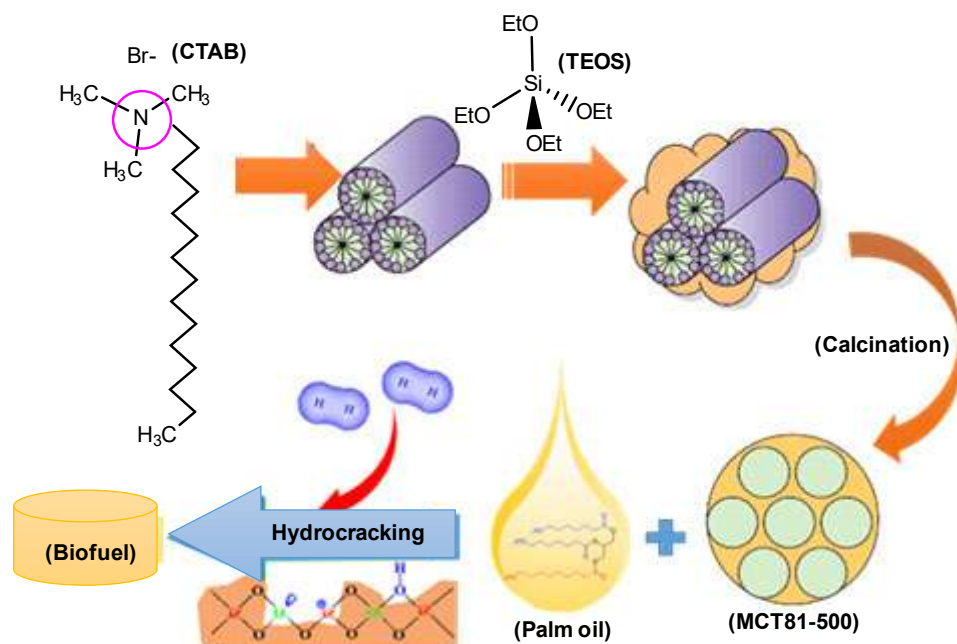


**Fig 1.** Schematic illustration for the synthesis of MCT catalyst for hydrocracking palm oil

with stirring for 3 h at 80 °C. The solids obtained were filtered and washed with distilled water at neutral pH conditions. After that, drying was done at 150 °C for 2 h and followed by grinding and sifting at a size of 200 mesh. The final step was the calcination process in an open stainless reactor at 500 °C for 4 h in an inert N<sub>2</sub> atmosphere at 2 °C/min and then let it cool down to reach room temperature.

### Characterization

The synthesis success of the mesoporous silica catalyst was analyzed by FTIR to confirm the functional groups, and the diffraction patterns were measured using the X'Pert3 Powder XRD in continuous scanning mode with a scan range of 1–10° and a scanning interval of 0.02°. In addition, morphology and pore size observations were carried out by using SEM and gas sorption analyzers while GC-MS was used to determine the effectiveness and composition of hydrocracking products.

### Catalytic activity

The catalytic activity was observed in the hydrocracking process of used palm oil samples in a flex-bed microreactor system, as shown in Fig. 2. The catalyst was fed into the microreactor system with a weight ratio of catalyst/used palm oil of 1:100 (w/w). The used oil sample

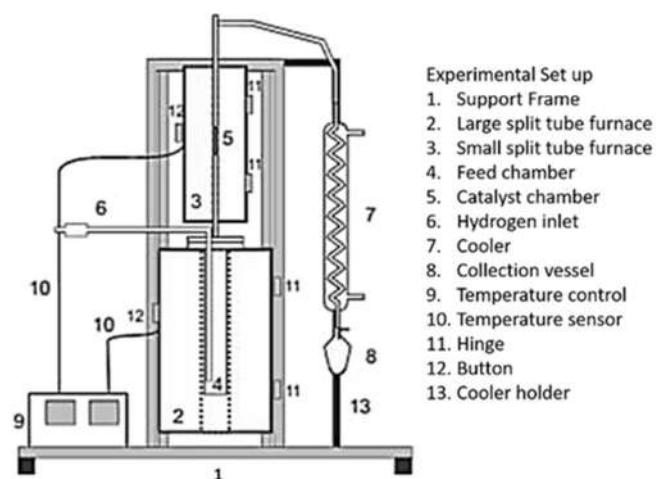


**Fig 2.** Schematic of a hydrocracking microreactor

was put into the chamber feed and then heated until it evaporated. Simultaneously, the catalyst reactor was heated at 500 °C. Then H<sub>2</sub> gas was flowed into the feed chamber at a speed of 20 mL/min. Oil vapor entered the catalyst reactor containing mesoporous silica catalyst (MCT21-500, MCT41-500, and MCT81-500), and a hydrocracking reaction occurred. Furthermore, the product was cooled in a cool trap and collected in a container. Finally, the products obtained were analyzed using GC-MS. The chromatogram showed the relative percentage for each compound contained in the liquid

product. The selectivity of the catalyst in the hydrocracking reaction was measured from the peak area of the GC-MS chromatogram of each fraction. The conversion of feed to yield was calculated by using the following equations [32]:

$$\text{Liquid yield (wt.\%)} = \frac{W_{LP}}{W_F} \times 100\%$$

$$\text{Solid yield (wt.\%)} = \frac{W_R + (W_{UC} - W_{FC})}{W_F} \times 100\%$$

$$\text{Gas product (wt.\%)} = 100\% - \text{wt.\% (liquid - solid)}$$

Selectivity of liquid yield

$$= \frac{\% \text{ area GCMS fraction } C_x - C_y}{\% \text{ total area GCMS}} \times 100\%$$

where,  $W_{LP}$ : weight of liquid product,  $W_F$ : weight of feed,  $W_R$ : weight of residue,  $W_{FC}$ : weight of fresh catalyst, and  $W_{UC}$ : weight of used catalyst

## ■ RESULTS AND DISCUSSION

The results of the infrared analysis of mesoporous silica material (MCT81-500) are shown in the spectra of Fig. 3. This analysis was carried out to determine the absorption resulted by the synthesized mesoporous silica and to observe changes in absorption after the adsorption of ammonia by mesoporous silica catalysts with a volume ratio of TEOS:CTAB = 8:1. Fig. 3(a) shows the initial spectra consisting of absorption of functional groups from Si-O-Si bending vibrations, symmetric Si-O-Si stretching vibrations, Si-OH stretching vibrations, asymmetric Si-O-Si stretching vibrations, H-O-H bending vibrations, Brønsted acid sites, and O-H stretching vibrations were observed to occur at wavenumbers 455, 794–802, 956–964, 1082–1087, 1635–1640 and 3465–3434  $\text{cm}^{-1}$ , respectively. Then in Fig. 3(b) a new absorption peak appears at 1388  $\text{cm}^{-1}$ , which shows an ammonia adsorption vibration band indicating the presence of Lewis acid and a combination of all acid sites. Ammonia is adsorbed on top of the sample at Lewis acid sites forming ammonium ions in the silica structure. The results of this study indicate that the adsorption of ammonia by MCT81-500 was carried out successfully through the acidic active site.

MCT catalyst crystallinity was analyzed by XRD to produce a diffractogram as shown in Fig. 4. The analysis

was carried out at  $2\theta = 2-15^\circ$  with MCT samples of CTAB:TEOS variations (2:1; 4:1; and 8:1). The diffractograms of all samples after calcination showed indexable peaks at 100, at angles  $2\theta$  2.61°, 3.02°, and 2.67° for MCT21-500, MCT41-500, and MCT81-500 materials, respectively.

The results showed that the CTAB:TEOS ratio variation produced a different crystallinity from the MCT81-500 sample, which resulted the highest crystallinity degree. Peak intensity increases with increasing silica content or TEOS/matrix ratio. The results

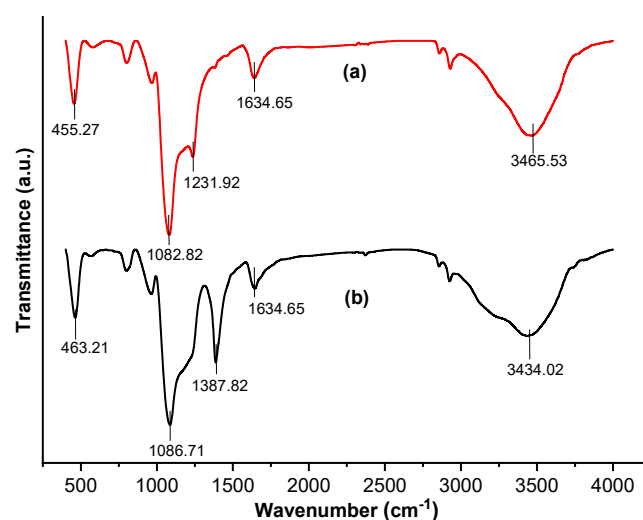


**Fig 3.** FTIR spectra of MCT81-500: (a) before and (b) after adsorption of ammonia

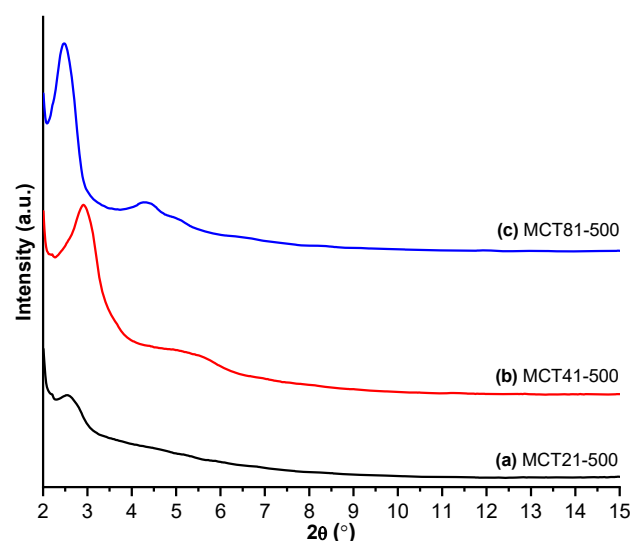


**Fig 4.** XRD patterns of the mesoporous silica materials: (a) MCT21-500, (b) MCT41-500, and (c) MCT81-500

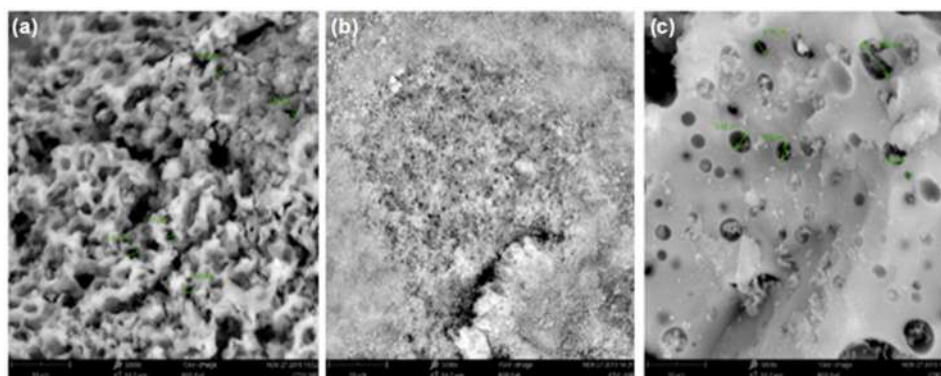


**Fig 5.** SEM images of (a) MCT21-500, (b) MCT41-500, and (c) MCT81-500

reflect that the composition of the precursor and surfactant significantly affects the morphology and crystallinity of the resulting mesoporous silica. These results also show whether the addition of a suitable matrix can improve the intensity of silica crystallinity based on SEM analysis.

Characterization of the catalyst morphology to determine the surface topography was carried out by SEM while the elemental composition on the surface of the catalyst was carried out by EDX. The SEM results in Fig. 5 illustrate that the variations in the TEOS:CTAB ratio affect many properties, such as pore size, surface area, and morphology. SEM images of the samples also show non-uniform particle sizes. This shows that CTAB as a mesoporous matrix agent has a wide range of molecular weight distribution. As shown in Fig. 5(a), (b), and (c), the surface morphology of the silica samples tends to be round and most of the particles tend to form bonds or large spherical particle pieces which are commonly known as clustering.

The results of the EDX analysis showed that the elemental content in Table 1 concluded that higher crystallinity was associated with an increase in silicate content. These results also conclude that higher crystallinity is consistent with higher silica

concentrations. Where in this result, the highest crystallinity structure was obtained from the synthesis of hierarchical mesoporous silica with a ratio of 8:1.

In the EDX analysis, the elements silica (Si), oxygen (O), carbon (C), and nitrogen (N) appear. Specifically, O and Si elements show the formation of silanol (Si–OH) and siloxane (Si–O–Si) groups. In addition, the appearance of certain carbon content in the MCT81-500 material confirms the XRD peak ( $2\theta = 2.61^\circ$ ) shown in Fig. 4.

Analysis of catalyst properties such as average diameter, pore distribution, total pore volume, and specific surface area was carried out by GSA. The results of the porous properties of the mesoporous silica catalyst are presented in Table 2.

The GSA analysis showed that the largest average pore radius was obtained with the MCT81-500 sample. This indicates that a larger radius of porous silica can be

**Table 1.** Elemental analysis results measured using EDX

Sample	Content (%)			
	Si	O	N	C
MCT21-500	27.50	64.24	8.26	-
MCT41-500	35.76	55.83	8.41	-
MCT81-500	45.31	41.11	6.02	7.75

**Table 2.** Pore properties of the mesoporous silica catalysts

Sample	Specific surface area (m <sup>2</sup> /g)	Total pore volume (cc/g)	Average pore diameter (nm)
MCT21-500	324.254	0.109	31.484
MCT41-500	382.514	0.199	31.892
MCT81-500	292.294	0.040	31.912

achieved by adding a minimal proportion of CTAB, especially in TEOS (silicon) precursors with a mold ratio of 8:1. However, other parameters such as specific surface area and total pore volume of MCT81-500 catalyst were the lowest. The increase and decrease in surface area are followed by the pore diameter. The pore diameter shows the highest pore distribution. The increased pore size does not slow down the process of diffusion of triglycerides into the catalyst. This ensures an optimal cracking process.

The adsorption isotherm of mesoporous silica is shown in Fig. 6. The isotherm pattern of mesoporous silica follows the type IV adsorption pattern. The type IV isotherm diagram shows four types of hysteresis loops which describe the mesoporous character of the intrinsic pore dimensions of the material [37-38]. To see the pore state more accurately, it is necessary to analyze the pore distribution curve in the material. The pore radius distribution data is shown in Fig. 7. The data shows the pore distribution according to mesoporous materials which have a sensitivity range of 2 to 50 nm.

The catalytic activity of MCT21-500, MCT41-500, and MCT81-500 was observed in the hydrocracking process of used palm oil. The product composition was analyzed by GC-MS to obtain a chromatogram like the example shown in Fig. 8. Fig. 8 shows the chromatogram of hydrocracking products with MCT81-500 catalyst, which produces different peaks according to their respective retention times. Hydrocracking products are differentiated due to differences in boiling points based

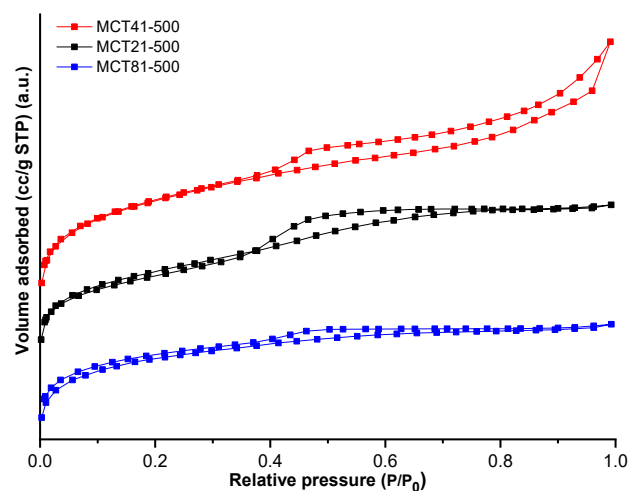


Fig 6. Adsorption-desorption isotherm curves of the mesoporous silica materials

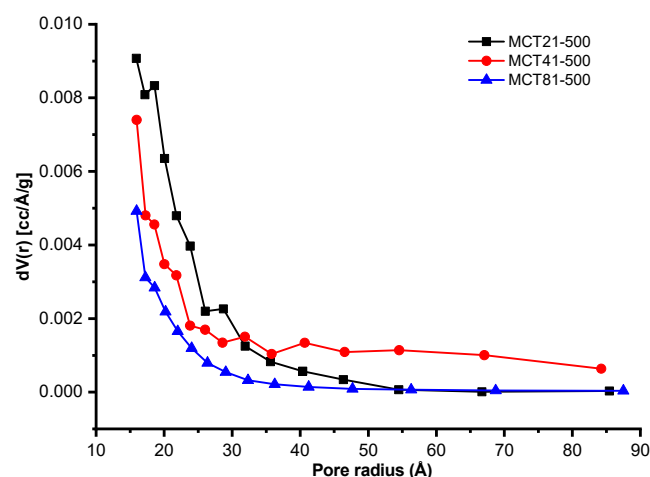


Fig 7. Pore radius size distribution of the mesoporous silica materials

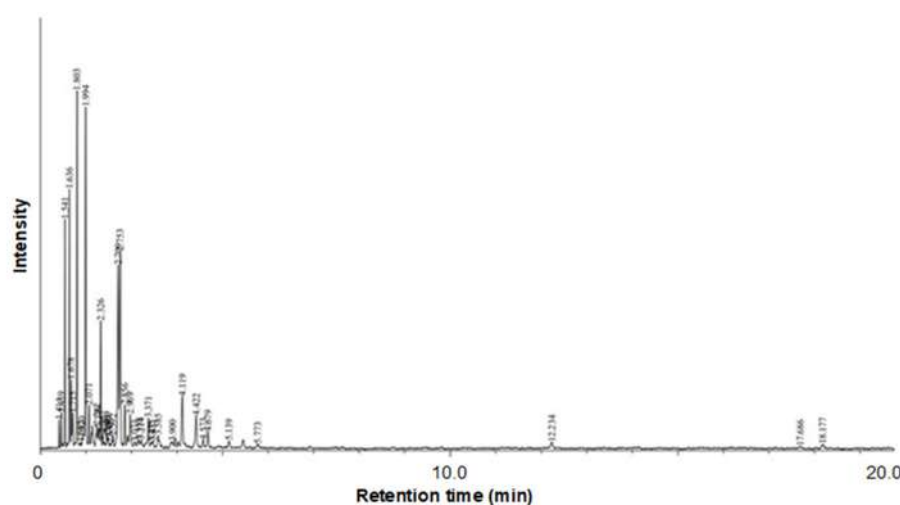


Fig 8. GC-MS chromatogram of hydrocracking product with MCT81-500

on differences in the content of carbon chains, as summarized in Table 3.

GC-MS data for liquid products from the cracking

process are divided into several fractions, including biogasoline (C<sub>5</sub>-C<sub>12</sub>), kerosene (C<sub>12</sub>-C<sub>15</sub>), diesel (C<sub>16</sub>-C<sub>18</sub>), and wax fractions (> C<sub>18</sub>). The percentage of each product

**Table 3.** Chemical composition of hydrocracking product with MCT81-500

Chemical compound	Fraction	R. Time	Area (%)	Height (%)	A/H
<i>n</i> -Heptane	C <sub>7</sub>	1.41	0.66	1.20	0.71
1- <i>n</i> -Heptene	C <sub>7</sub>	1.46	0.99	1.50	0.85
<i>n</i> -Octane	C <sub>8</sub>	1.54	6.37	9.89	0.84
1-Octene (CAS) Caprylene	C <sub>8</sub>	1.64	7.50	11.18	0.87
2-Octene, (Z)- (CAS) (Z)-2-Octene	C <sub>8</sub>	1.68	2.41	2.96	1.06
2-Octene (CAS) Oct-2-ene	C <sub>8</sub>	1.72	1.34	1.50	1.15
<i>n</i> -Nonane	C <sub>9</sub>	1.80	12.01	15.44	1.01
3-Propylcyclopentene,	C <sub>5</sub>	1.88	0.50	0.25	2.61
(Z)-Cycloheptene	C <sub>7</sub>	1.92	0.38	0.43	1.16
<i>n</i> -Non-1-ene	C <sub>9</sub>	1.99	13.40	14.74	1.18
2-Nonene	C <sub>9</sub>	2.07	1.92	1.86	1.34
Propylcyclohexane	C <sub>6</sub>	2.24	1.61	0.98	2.14
1-Ethylcyclohexene	C <sub>6</sub>	2.28	1.13	0.86	1.69
Decane	C <sub>10</sub>	2.33	4.98	5.49	1.18
7-Methyl-bicyclo[2,2,1]heptane	C <sub>8</sub>	2.37	0.80	0.66	1.57
9,12,15-Octadecatrienal	C <sub>20</sub>	2.40	0.28	0.28	1.31
Bis(cyclopent-2-enyl)	C <sub>11</sub>	2.47	0.68	0.63	1.40
3,10-Dioxa-tricyclo	C <sub>12</sub>	2.49	0.44	0.44	1.31
<i>trans</i> -1-Ethenyl-2-methylcyclohexane	C <sub>6</sub>	2.53	0.28	0.20	1.82
Cyclopentane	C <sub>5</sub>	2.59	0.95	0.53	2.32
1-Decene	C <sub>10</sub>	2.71	10.16	7.91	1.66
Cyclooctene	C <sub>8</sub>	2.75	10.14	8.52	1.54
<i>cis</i> -3-Decene	C <sub>10</sub>	2.86	2.04	1.87	1.42
Pentalene	C <sub>8</sub>	2.97	2.49	1.46	2.22
4,5-Nonadiene	C <sub>9</sub>	3.07	0.63	0.27	3.02
<i>n</i> -Butylcyclohexane	C <sub>6</sub>	3.16	0.79	0.37	2.77
Hexanal	C <sub>6</sub>	3.21	0.77	0.37	2.71
Undecane	C <sub>11</sub>	3.37	1.77	1.31	1.75
Cyclodecene	C <sub>10</sub>	3.44	0.43	0.26	2.16
4-Cyclopropylcyclohexene	C <sub>9</sub>	3.47	0.47	0.32	1.88
6-Methyl-bicyclo[4.2.0]octan-7-ol	C <sub>9</sub>	3.59	1.10	0.55	2.58
Ethylbenzene	C <sub>6</sub>	3.90	0.79	0.26	3.93
1-Dodecene	C <sub>12</sub>	4.12	3.48	2.19	2.06
2-Undecene	C <sub>11</sub>	4.42	2.69	1.40	2.50
1-Butylcyclohexane	C <sub>6</sub>	4.57	0.67	0.35	2.48
1-Undecene	C <sub>11</sub>	4.68	1.16	0.69	2.20
1,2-Dimethylbenzene, (CAS) <i>o</i> -Xylene	C <sub>6</sub>	5.14	0.55	0.29	2.45
Propylbenzene (CAS) <i>n</i> -Propylbenzene	C <sub>6</sub>	5.77	0.27	0.14	2.39
3-Methylcyclohex-3-en-1-one	C <sub>7</sub>	12.23	0.57	0.25	2.93
Pentadecane	C <sub>15</sub>	17.69	0.18	0.08	2.86
Benzaldehyde	C <sub>7</sub>	18.18	0.24	0.12	2.49



fraction is calculated from the resulting peak area to obtain the data summarized in Fig. 9.

Based on Fig. 9, the percentage of the product fraction from the thermal and hydrocracking processes with a catalyst shows significantly different results. The thermal cracking performed showed that the biogasoline and kerosene fractions obtained were relatively low. On the other hand, the selectivity of catalysts MCT21-500, MCT41-500, and MCT81-500 in hydrocracking palm oil resulted in a dominant gasoline fraction of 76.81, 83.54, and 92.24 wt.%, respectively. This is indicated that mesoporous silica catalysts can capture the free fatty acid (FFA) as well as it can make cracking into shorter hydrocarbons, as shown in Fig. 10. Based on GC-MS analysis, the resulting molecules are hydrocarbons and oxygenated compounds containing fatty acids and alcohols. This fact confirms that the mechanism of the cracking reaction of palm oil includes the hydrogenation of triglycerides into fatty acids, hydrogenation of fatty acids into aldehydes and alcohols, and deoxygenation of fatty acids through decarbonylation, decarboxylation, and hydrodeoxygenation reactions [35,39-40].

Hydrocarbon molecules can be formed directly

from fatty acids through decarboxylation by releasing carbon dioxide molecules ( $\text{CO}_2$ ) to produce alkanes (saturated hydrocarbons) and decarbonylation by releasing carbon monoxide ( $\text{CO}$ ) and water ( $\text{H}_2\text{O}$ ) to produce alkenes (unsaturated hydrocarbons). Both of these reactions mostly occur in Lewis acid sites [41],

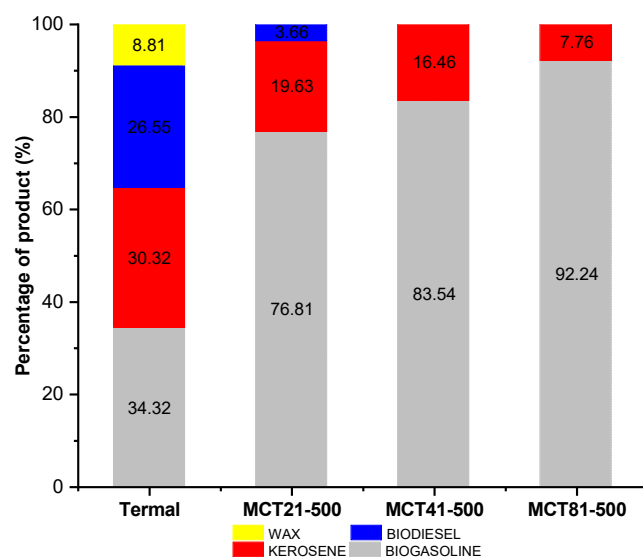


Fig 9. Product fraction percentages produced from the hydrocracking process using various catalysts

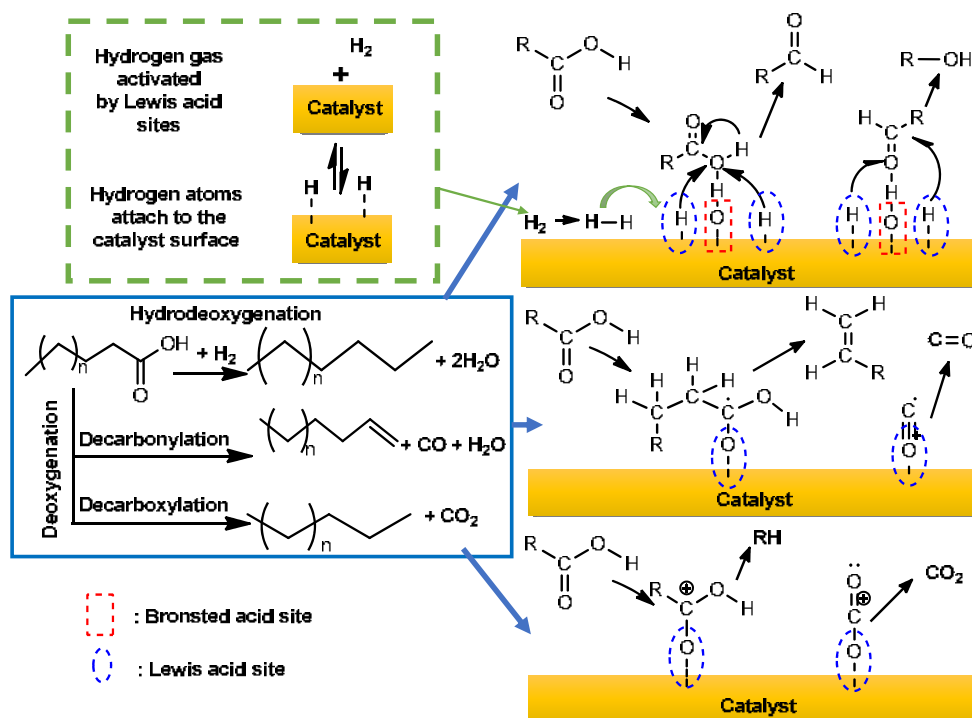


Fig 10. Mechanism of hydrocracking of palm oil with MCT catalyst

with the hydrocarbons formed being  $C_{15}$  (kerosene group) and  $C_{17}$  (diesel group).

On the other hand, hydrocarbons below  $C_{15}$  and oxygenated compounds are formed by hydrocracking reactions with the hydrogenation of hydrogen gas activated by Lewis acid sites [42]. The reactions mostly take place at Brønsted acid sites. In this study, this hydrogenation mechanism dominates the reaction as evidenced by the GC-MS results produced in Fig. 8. It is suggested that alcohol molecules are formed through the hydrogenation of fatty acids into aldehydes and then converted into alcohols through further hydrogenation of aldehydes. In addition, the hydrogenation reaction is more detailed theoretically, as shown in Fig. 11 [43]. In heterogeneous catalysts, the hydrogen forms surface hydrides (M-H) from which the hydrogen can be transferred to the chemically adsorbed substrate.  $H_2$  undergoes heterolytic association to form  $H^+H^-$  [44]. In heterogeneous catalysts, hydrogen forms surface hydrides (M-H) from which hydrogens can be transferred to the chemisorbed substrate. Hydrogen gas is activated by Lewis acid sites to produce alkanes (or hydrogen) and carbenium ions  $n-C_iH_{2i}$  [42]. While Brønsted acid plays a role in cracking carbon chains so that a reaction mechanism occurs, forming the hydrocarbons below  $C_{15}$  and oxygenated compounds by hydrocracking reactions, protonated to the secondary alkyl carbenium ions ( $n-C_iH_{2i+1}^+$ ) [43]. The mesoporous silica catalyst protonates the alkane chains to produce a transition state of

carbonium ions which collapse to give alkanes (or hydrogen) and the carbenium ions  $n-C_iH_{2i}$  dissociate from the Lewis acid site and diffuse to the Brønsted acid site where they are protonated into secondary alkyl carbenium ions,  $n-C_iH_{2i+1}^+$ . Carbenium ion is a reactive intermediate that can undergo several conversions, such as rearrangement of the framework and breaking of the C-C bond. The  $\beta$ -scission fragment is a smaller alkyl carbenium ion and an alkene. In the case of  $\beta$ -scission  $n-C_iH_{2i+1}^+$ , a primary carbenium ion is formed, which is energetically unfavorable. Therefore, the  $n$ -alkyl carbenium ion undergoes an exclusively skeletal rearrangement, in which a single branched alkyl carbenium ion,  $iso-C_iH_{2i+1}^+$ , is formed. If there is an efficient desorption mechanism from the acid site, single-branched alkenes,  $iso-C_iH_{2i}$ , are released and diffuse to the Lewis acid site where they are hydrogenated to become single-branched alkanes,  $iso-C_iH_{2i+2}$ . These are prime products that are observed with low conversions [43].

Thus, the type of catalyst in the hydrocracking of used palm oil can affect the selectivity of liquid products to the gasoline fraction that is produced. The results showed that the use of mesoporous silica in the catalytic activity test increased the amount of product from the gasoline fraction ( $C_5-C_{12}$ ). The percentage of product using mesoporous silica catalyst MCT81-500 showed an increase in the product of the gasoline fraction associated with an increase in crystallinity and a decrease

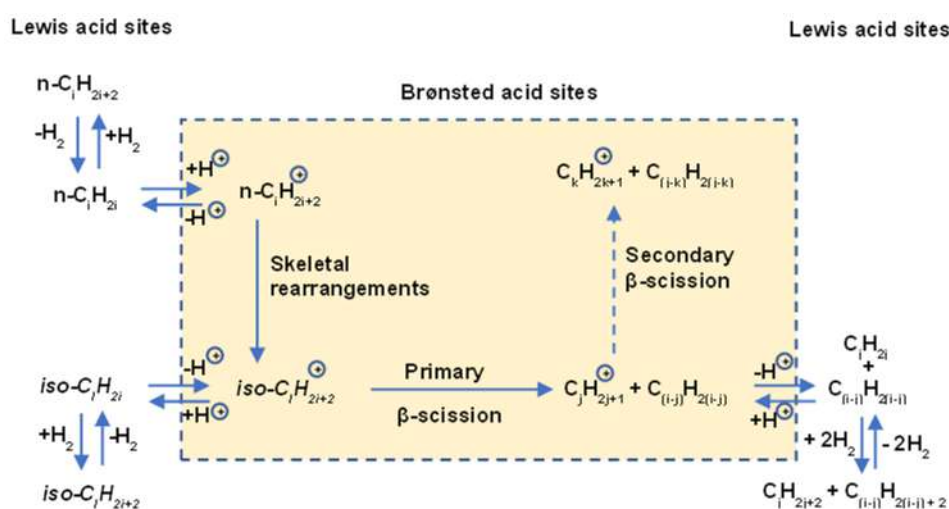


Fig 11. Mechanism of hydrogenation reaction on hydrocracking by MCT catalyst

in matrix content in the synthesis of this material. Based on this description, MCT81-500 with an H<sub>2</sub> gas flow rate of 20 mL/min, a catalyst/feed ratio of 1:100, and a time of 1 h was found to be the most optimal to produce the best gasoline fraction. MCT81-500 material has been successfully used as a catalyst for the process of hydrocracking palm oil into biogasoline.

The concentration of TEOS used affects the amount of silica yield obtained. The greater the amount of TEOS used, the greater the silica product obtained. This result is in accordance with reference [45], where TEOS concentration strongly influences the formation of a mesoporous material network. A higher amount of TEOS showed an irregular mesostructured, while a lower amount was insufficient to form a mesoporous structure [46]. The particle size increased with an increasing number of TEOS. Table 2 shows an increase in the pore diameter of the MCT81-500 sample, thereby increasing the availability of the active surface, allowing an increase in the ability of mesoporous silica for hydrocracking used palm oil into the biogasoline. This is shown by the catalyst with a larger average pore diameter in Table 2, which has a higher absorbed volume intensity in Fig. 6. This results in an increasing number of active catalyst surface sites that play a role in the hydrogenation process in hydrocracking. The more hydrogenation processes in hydrocracking that occur, as shown in Fig. 10 and 11, the more gasoline products will be produced compared to other products. This is because of the reasons explained in the reaction mechanism that products with molecules below C<sub>15</sub>, especially gasoline and oxygenated compounds, are formed more in the hydrogenation process through the Lewis acid site and Brønsted acid site. In addition, the larger pore volume does not impede the diffusion process, so the hydrogenation reaction runs faster. Thus, the gasoline product will be dominant with a large porous catalyst and more surface-active sites in the hydrogenation reaction.

In addition, by looking at the hydrocracking mechanism involving Lewis acid sites and Brønsted acid sites on the catalyst, further studies related to acidity and the effect of pH on the optimal performance of hydrocracking reactions become important parameter

studies. Higher catalyst acidity will show better potential for use as a catalyst that requires an acidic site, such as hydrocracking [35]. The presence of H<sup>+</sup> will help the process of protonation of *n*-alkanes to become the secondary alkyl carbenium ions (*n*-C<sub>i</sub>H<sub>2i+1</sub><sup>+</sup>) so that more product conversions can be produced.

## ■ CONCLUSION

Synthesis of mesoporous silica catalyst and its activity and selectivity in the hydrocracking of used palm oil has been carried out. The use of CTAB as a matrix in the production of mesoporous silica has been successfully achieved, as evidenced by the crystallinity, and increase in the pore size distribution of silica in the meso dimension. This study showed that the highest selectivity for the biogasoline fraction (92.24 wt.%) was produced by the MCT81-500 catalyst at an H<sub>2</sub> gas flow rate of 20 mL/min with a catalyst/feed ratio of 1:100 (w/w) for 1 h. Material MCT81-500 was successfully used as a catalyst in the process of hydrocracking palm oil into hydrocarbons (biogasoline).

## ■ ACKNOWLEDGMENTS

The author expresses his gratitude for research funding support to the Diponegoro University Citation Improvement Program with contract number 205-02/UN7.P4.3/PP/2019, as well as collaborators from Indonesia-10 from PTNBH, UGM, UB, and UNS (PPKI Project 2019).

## ■ AUTHOR CONTRIBUTIONS

All authors have contributed equally.

## ■ REFERENCES

- [1] Yaqoob, H., Teoh, Y.H., Goraya, T.S., Sher, F., Jamil, M.A., Rashid, T., and Yar, K.A., 2021, Energy evaluation and environmental impact assessment of transportation fuels in Pakistan, *Case Stud. Chem. Environ. Eng.*, 3, 100081.
- [2] Altarazi, Y.S.M., Abu Talib, A.R., Yu, J., Gires, E., Abdul Ghafir, M.F., Lucas, J., and Yusaf, T., 2022, Effects of biofuel on engines performance and emission characteristics: A review, *Energy*, 238, 121910.

- [3] Kabeyi, M.J.B., and Olanrewaju, O.A., 2022, Biogas production and applications in the sustainable energy transition, *J. Energy*, 2022, 8750221.
- [4] Hanafi, S.A., Elmelawy, M.S., El-Syed, H.A., and Shalaby, N.H., 2015, Hydrocracking of waste cooking oil as renewable fuel on NiW/SiO<sub>2</sub>-Al<sub>2</sub>O<sub>3</sub> catalyst, *J. Adv. Catal. Sci. Technol.*, 2 (1), 27–37.
- [5] Dik, P.P., Danilova, I.G., Golubev, I.S., Kazakov, M.O., Nadeina, K.A., Budukva, S.V., Pereyma, V.Y., Klimov, O.V., Prosvirin, I.P., Gerasimov, E.Y., Bok, T.O., Dobryakova, I.V., Knyazeva, E.E., Ivanova, I.I., and Noskov, A.S., 2019, Hydrocracking of vacuum gas oil over NiMo/zeolite-Al<sub>2</sub>O<sub>3</sub>: Influence of zeolite properties, *Fuel*, 237, 178–190.
- [6] Sarvi, M.N., Budianto Bee, T., Gooi, C.K., Woonton, B.W., Gee, M.L., and O'Connor, A.J., 2014, Development of functionalized mesoporous silica for adsorption and separation of dairy proteins, *Chem. Eng. J.*, 235, 244–251.
- [7] Tao, Y., Ju, E., Ren, J., and Qu, X., 2015, Bifunctionalized mesoporous silica-supported gold nanoparticles: Intrinsic oxidase and peroxidase catalytic activities for antibacterial applications, *Adv. Mater.*, 27 (6), 1097–1104.
- [8] Lee, Y.C., Dutta, S., and Wu, K.C.W., 2014, Integrated, cascading enzyme-/chemocatalytic cellulose conversion using catalysts based on mesoporous silica nanoparticles, *ChemSusChem*, 7 (12), 3241–3246.
- [9] Gao, W., Hu, Y., Xu, L., Liu, M., Wu, H., and He, B., 2018, Dual pH and glucose sensitive gel gated mesoporous silica nanoparticles for drug delivery, *Chin. Chem. Lett.*, 29 (12), 1795–1798.
- [10] Lai, S.M., Lai, H.Y., and Chou, M.Y., 2014, A facile approach for the tunable wormlike or ordered pore morphology of mesoporous silica: Effect of catalyst types and polyethylene glycol, *Microporous Mesoporous Mater.*, 196, 31–40.
- [11] Hikosaka, R., Nagata, F., Tomita, M., and Kato, K., 2016, Adsorption and desorption characteristics of DNA onto the surface of amino functional mesoporous silica with various particle morphologies, *Colloids Surf., B*, 140, 262–268.
- [12] Ng, T.N., Chen, X.Q., and Yeung, K.L., 2015, Direct manipulation of particle size and morphology of ordered mesoporous silica by flow synthesis, *RSC Adv.*, 5 (18), 13331–13340.
- [13] Knežević, N., and Durand, J.O., 2015, Large pore mesoporous silica nanomaterials for application in delivery of biomolecules, *Nanoscale*, 7 (6), 2199–2209.
- [14] Wei, J., Sun, Z., Luo, W., Li, Y., Elzatahry, A.A., Al-Enizi, A.M., Deng, Y., and Zhao, D., 2017, New insight into the synthesis of large-pore ordered mesoporous materials, *J. Am. Chem. Soc.*, 139 (5), 1706–1713.
- [15] Wang, X., Zhang, Y., Luo, W., Elzatahry, A.A., Cheng, X., Alghamdi, A., Abdullah, A.M., Deng, Y., and Zhao, D., 2016, Synthesis of ordered mesoporous silica with tunable morphologies and pore sizes via a nonpolar solvent-assisted Stöber method, *Chem. Mater.*, 28 (7), 2356–2362.
- [16] Zhang, W., Zuo, H., Cheng, Z., Shi, Y., Guo, Z., Meng, N., Thomas, A., and Liao, Y., 2022, Macroscale conjugated microporous polymers: controlling versatile functionalities over several dimensions, *Adv. Mater.*, 34 (18), 2104952.
- [17] Luo, W., Zhao, T., Li, Y., Wei, J., Xu, P., Li, X., Wang, Y., Zhang, W., Elzatahry, A.A., Alghamdi, A., Deng, Y., Wang, L., Jiang, W., Liu, Y., Kong, B., and Zhao, D., 2016, A micelle fusion-aggregation assembly approach to mesoporous carbon materials with rich active sites for ultrasensitive ammonia sensing, *J. Am. Chem. Soc.*, 138 (38), 12586–12595.
- [18] Yuan, K., Che, R., Cao, Q., Sun, Z., Yue, Q., and Deng, Y., 2015, Designed fabrication and characterization of three-dimensionally ordered arrays of core-shell magnetic mesoporous carbon microspheres, *ACS Appl. Mater. Interfaces*, 7 (9), 5312–5319.
- [19] Gao, M., Zeng, J., Liang, K., Zhao, D., and Kong, B., 2020, Interfacial assembly of mesoporous silica-based optical heterostructures for sensing applications, *Adv. Funct. Mater.*, 30 (9), 1906950.
- [20] Nasir, T., Herzog, G., Hébrant, M., Despas, C., Liu, L., and Walcarius, A., 2018, Mesoporous silica thin

- films for improved electrochemical detection of paraquat, *ACS Sens.*, 3 (2), 484–493.
- [21] Liu, Y., Shen, D., Chen, G., Elzatahry, A.A., Pal, M., Zhu, H., Wu, L., Lin, J., Al-Dahyan, D., Li, W., and Zhao, D., 2017, Mesoporous silica thin membranes with large vertical mesochannels for nanosize-based separation, *Adv. Mater.*, 29 (35), 1702274.
- [22] Upare, D.P., Park, S., Kim, M.S., Kim, J., Lee, D., Lee, J., Chang, H., Choi, W., Choi, S., Jeon, Y.P., Park, Y.K., and Lee, C.W., 2016, Cobalt promoted Mo/beta zeolite for selective hydrocracking of tetralin and pyrolysis fuel oil into monocyclic aromatic hydrocarbons, *J. Ind. Eng. Chem.*, 35, 99–107.
- [23] Upare, D.P., Park, S., Kim, M.S., Jeon, Y.P., Kim, J., Lee, D., Lee, J., Chang, H., Choi, S., Choi, W., Park, Y.K., and Lee, C.W., 2017, Selective hydrocracking of pyrolysis fuel oil into benzene, toluene and xylene over CoMo/beta zeolite catalyst, *J. Ind. Eng. Chem.*, 46, 356–363.
- [24] Munir, D., and Usman, M.R., 2016, Synthesis and characterization of mesoporous hydrocracking catalysts, *IOP Conf. Ser.: Mater. Sci. Eng.*, 146, 012007.
- [25] Williams, S., Neumann, A., Bremer, I., Su, Y., Dräger, G., Kasper, C., and Behrens, P., 2015, Nanoporous silica nanoparticles as biomaterials: Evaluation of different strategies for the functionalization with polysialic acid by step-by-step cytocompatibility testin, *J. Mater. Sci.: Mater. Med.*, 26 (3), 125.
- [26] Porrang, S., Davaran, S., Rahemi, N., Allahyari, S., and Mostafavi, E., 2022, How advancing are mesoporous silica nanoparticles? A comprehensive review of the literature, *Int. J. Nanomed.*, 17, 1803–1827.
- [27] Huo, Q., Margolese, D.I., and Stucky, G.D., 1996, Surfactant control of phases in the synthesis of mesoporous silica-based materials, *Chem. Mater.*, 8 (5), 1147–1160.
- [28] Lai, C.Y., 2014, Mesoporous silica nanomaterials applications in catalysis, *J. Thermodyn. Catal.*, 5 (1), 1000e124.
- [29] Lu, M., Liu, X., Li, Y., Nie, Y., Lu, X., Deng, D., Xie, Q., and Ji, J., 2016, Hydrocracking of bio-alkanes over Pt/Al-MCM-41 mesoporous molecular sieves for bio-jet fuel production, *J. Renewable Sustainable Energy*, 8 (5), 053103.
- [30] Nurmalasari, N., Trisunaryanti, W., Sutarno, S., and Falah, I., 2016, Mesoporous silica impregnated by Ni and NiMo as catalysts for hydrocracking of waste lubricant, *Int. J. ChemTech Res.*, 9 (9), 607–614.
- [31] Yang, L., Wu, H., Jia, J., Ma, B., and Li, J., 2017, Synthesis of bimodal mesoporous silica with coexisting phases by co-hydrothermal aging route with P123 containing gel and F127 containing gel, *Microporous Mesoporous Mater.*, 253, 151–159.
- [32] Wijaya, K., Saputri, W.D., Aziz, I.T.A., Wangsa, W., Heraldly, E., Hakim, L., Suseno, A., and Utami, M., 2021, Mesoporous silica preparation using sodium bicarbonate as template and application of the silica for hydrocracking of used cooking oil into biofuel, *Silicon*, 14 (4), 1583–1591.
- [33] Sirajudin, N., Jusoff, K., Yani, S., Ifa, L., and Roesyady, A., 2013, Biofuel production from catalytic cracking of palm oil, *World Appl. Sci. J.*, 26 (26), 67–71.
- [34] Tambun, R., Gusti, O.N., Nasution, M.A., and Saptawaldi, R.P., 2017, Biofuel production from palm olein by catalytic cracking process using ZSM-5 catalyst, *JBAT*, 6 (1), 50–55.
- [35] Salamah, S., Trisunaryanti, W., Kartini, I., and Purwono, S., 2021, Hydrocracking of waste cooking oil into biofuel using mesoporous silica from Parangtritis beach sand synthesized with sonochemistry, *Silicon*, 14 (7), 3583–3590.
- [36] Liang, J., Liang, Z., Zou, R., and Zhao, Y., 2017, Heterogeneous catalysis in zeolites, mesoporous silica, and metal–organic frameworks, *Adv. Mater.*, 29 (30), 1701139
- [37] Guillet-Nicolas, R., Bérubé, F., Thommes, M., Janicke, M.T., and Kleitz, F., 2017, Selectively tuned pore condensation and hysteresis behavior in mesoporous SBA-15 silica: Correlating material synthesis to advanced gas adsorption analysis, *J. Phys. Chem. C*, 121 (44), 24505–24526.
- [38] Trisunaryanti, W., Triyono, T., Falah, I.I., Siagian, A.D., and Marsuki, M.F., 2018, Synthesis of Ce-mesoporous silica catalyst and its lifetime

- determination for the hydrocracking of waste lubricant, *Indones. J. Chem.*, 18 (3), 441–447.
- [39] Schreiber, M.W., Rodriguez-Nino, D., Gutiérrez, O.Y., and Lercher, J.A., 2016, Hydrodeoxygenation of fatty acid esters catalyzed by Ni on nano-sized MFI type zeolites, *Catal. Sci. Technol.*, 6 (22), 7976–7984.
- [40] Istadi, I., Riyanto, T., Khofiyandita, E., Buchori, L., Anggoro, D.D., Sumantri, I., Putro, B.H.S., and Firnanda, A.S., 2021, Low-oxygenated biofuels production from palm oil through hydrocracking process using the enhanced Spent RFCC catalysts, *Bioresour. Technol. Rep.*, 14, 100677.
- [41] Istadi, I., Riyanto, T., Buchori, L., Anggoro, D.D., Gilbert, G., Meiranti, K.A., and Khofiyandita, E., 2020, Enhancing Brønsted and Lewis acid sites of the utilized spent RFCC catalyst waste for the continuous cracking process of palm oil to biofuels, *Ind. Eng. Chem. Res.*, 59 (20), 9459–9468.
- [42] Li, Y., Hou, C., Jiang, J., Zhang, Z., Zhao, C., Page, A.J., and Ke, Z., 2016, General H<sub>2</sub> activation modes for Lewis acid-transition metal bifunctional catalysts, *ACS Catal.*, 6 (3), 1655–1662.
- [43] Weitkamp, J., 2012, Catalytic hydrocracking—Mechanisms and versatility of the process, *ChemCatChem*, 4 (3), 292–306.
- [44] Aireddy, D.R., and Ding, K., 2022, Heterolytic dissociation of H<sub>2</sub> in heterogeneous catalysis, *ACS Catal.*, 12 (8), 4707–4723.
- [45] Wang, D.K., and da Costa, J.C.D., 2018, "Silica, Template Silica and Metal Oxide Silica Membranes for High Temperature Gas Separation" in *Advanced Materials for Membrane Fabrication and Modification*, Eds. Gray, S., Tsuru, T., Cohen, Y., and Lau, W.J., CRC Press, Boca Raton, Florida, 231–274.
- [46] Chiang, Y.D., Lian, H.Y., Leo, S.Y., Wang, S.G., Yamauchi, Y., and Wu, K.C.W., 2011, Controlling particle size and structural properties of mesoporous silica nanoparticles using the Taguchi method, *J. Phys. Chem. C*, 115 (27), 13158–13165.

### Supplementary Data

This supplementary data is a part of a paper entitled “Effect of Acetic Acid and/or Sodium Hydroxide Treatment towards Characters of Wonosari Natural Zeolite for Hydrotreatment of Castor Oil into Biofuel”.

**Table S1.** Products distribution based on GC-MS in Fig.S1

Fraction	Ret. Time (min.)	Predicted compound	Molecular mass (g/mol)
Gasoline (C <sub>4</sub> -C <sub>12</sub> )	2.28	Butane (C <sub>4</sub> )	58.12
	2.72	Hexene (C <sub>6</sub> )	84.16
	2.79	Hexane (C <sub>6</sub> )	86.18
	3.90	Heptene (C <sub>7</sub> )	98.18
	4.05	Heptane (C <sub>7</sub> )	100.20
	6.90	Octane (C <sub>8</sub> )	114.23
	14.14	Octadiene (C <sub>8</sub> )	110.20
	10.42	Undecene (C <sub>11</sub> )	156.31
	14.30	Nonene (C <sub>9</sub> )	126.24
	34.35	Dodecene (C <sub>12</sub> )	168.20
34.49	Dodecane (C <sub>12</sub> )	170.30	
Diesel (C <sub>13</sub> -C <sub>22</sub> )	40.79	Undecenoic acid (C <sub>19</sub> )	184.20
	36.58	Octadecanoic acid (C <sub>18</sub> )	248.50
Others	2.93	Cyclopropane	42.08
	3.07	Acetic acid	60.05
	3.49	Benzene	78.11
	5.85	Toluene	92.14
	10.75	Cyanic acid	43.02
	11.29	Heptanal	116.80
	24.43	Hydroperoxide	34.01
	24.51	Naphthalene	128.10
	27.05	Silane	32.12
	27.17	Heptanoic acid	130.10
	27.40	Cyclopentaneundecanoic acid	254.40
	28.71	Bromo heptane	179.10
	29.40	Pentanoyl chloride	120.50
	29.60	2-Nonenal	140.20
	31.81	1,2,5,6-Diepoxyoctane	140.80
	35.49	Cyclopropanepentanoic acid	310.00
	35.94	13-Docosenoic acid	352.00
	36.58	1-Nitro-2-octanone	173.00
41.87	Oleic acid	282.20	

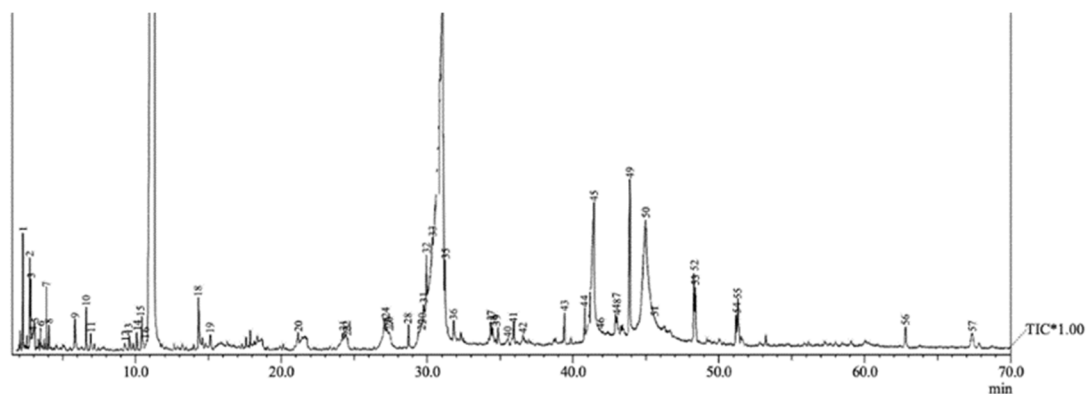


Fig S1. GC-MS chromatogram of liquid product of hydrotreatment of castor oil using ZAA catalyst



## Effect of Acetic Acid and/or Sodium Hydroxide Treatment towards Characters of Wonosari Natural Zeolite for Hydrotreatment of Castor Oil into Biofuel

Triyono Triyono, Wega Trisunaryanti\*, Iip Izul Falah, and Lailatul Rahmi

Department of Chemistry, Faculty of Mathematics and Natural Sciences, Universitas Gadjah Mada, Sekip Utara, Yogyakarta 55281, Indonesia

\* Corresponding author:

tel: +62-811256055

email: wegats@ugm.ac.id

Received: March 24, 2022

Accepted: February 22, 2023

DOI: 10.22146/ijc.73746

**Abstract:** Natural zeolite (ZA) obtained from Wonosari, Indonesia, was treated with acetic acid (ZAA) or NaOH (ZAB), and the combination of both treatments (ZAAB) in order to increase the Si/Al ratio and catalytic performance on hydrotreatment of castor oil. The Si/Al ratio of ZA increased after the combination of acetic acid and NaOH treatment. The change of the Si/Al ratio was observed in the FTIR spectra as the shifting of internal asymmetric stretching vibration of T–O–T at 1032-1100  $\text{cm}^{-1}$ . The XRD profile of ZA was maintained after being subjected to treatments, and ZAB exhibited the lowest crystallinity. The surface area of the ZA after treatment is in the order ZAA < ZA < ZAAB < ZAB. The ZAB catalyst having the highest surface area (19.144  $\text{m}^2 \text{g}^{-1}$ ) showed the highest catalytic activity on the hydrotreatment of castor oil with a liquid fraction of 55.1 wt.% and selectivity towards the hydrocarbon compounds of 22.40 wt.%.

**Keywords:** acetic acid; natural zeolite; sodium hydroxide; hydrotreatment

### ■ INTRODUCTION

The usage of fossil fuels presents two significant difficulties. The first is its quick decline in value and rising prices. The second is its environmental impact due to the toxic gases ( $\text{CO}_x$ ,  $\text{SO}_x$ , and  $\text{NO}_x$ ) created during the combustion of conventional fuels and other air pollutants. These led to various negative environmental, ecosystem, human health consequences, and their significant contribution to the greenhouse effect [1]. As a result, numerous researchers have begun investigating alternative energy sources with manageable environmental implications. Biofuel was once regarded as one of the considerable substitutes for conventional diesel fuel [2]. Biofuel is a non-toxic, environmentally benign, and biodegradable fuel [3]. Furthermore, it is compatible with current engines without modification [4].

Non-edible biofuel feedstocks are receiving global attention due to their widespread distribution. Additionally, they can alleviate food competition, are environmentally friendly, provide valuable products (glycerol), and are more cost-effective as a feedstock than edible oils [5]. Second-generation biodiesel is considered

to be oil derived from non-edible plants. Some of the potential non-edible oil-producing plants are *Jatropha curcas* L. (jatropha), *Thespesia populnea* L. (milo), *Pongamia pinnata* (Karanja or honge), *Moringa oleifera* (drumstick tree), *Calophyllum inophyllum* L. (undi), *Croton megalocarpus* (croton), and *Ricinus communis* L. (castor) [6].

Natural zeolites are utilized in a variety of processes that result in the production of chemicals, fuels, and other commodities. Designing zeolite catalysts with better selectivity, lower operating temperatures, and increased stability is vital. Optimizing the porosity structure in enhanced zeolite catalysts enhances mass transfer and active site design. Sites that are unattractive and take away from the benefits of active sites must be eliminated or prohibited [7]. On the other hand, natural zeolite requires a precise acid and alkali treatment to maintain the silicon-aluminum ratio and specific surface area [8].

Acid treatments, in general, can remove impurities such as  $\text{SiO}_2$ ,  $\text{Al}_2\text{O}_3$ , and  $\text{Fe}_2\text{O}_3$  from the zeolite's surface and pores. Simultaneously, the acid solution dissolves amorphous materials within the pores and exchanges

large cations for small protons via ion exchange, increasing the pore size, specific surface area, and adsorption capacity. Additionally, acid treatment modifies the surface properties of the zeolite molecular sieve, optimizing the mordenite material's qualities. Meanwhile, alkali treatment is a widely used technique for partially dissolving the zeolite structure due to silicon extraction. At a somewhat higher reaction temperature, catalytic cracking might be employed to get a high yield of hydrocarbon biofuel from vegetable oil [9-10]. Catalytic cracking is a simple and cost-effective method of converting vegetable oil to hydrocarbon biofuel [11].

One option to use the higher biofuel content in diesel fuel is to use hydrotreated vegetable oils. This would provide another way to accomplish our CO<sub>2</sub> reduction goal in the future [12]. There may be economic implications associated with efforts to reduce environmental pollution. Economic growth and carbon emissions are positively related, which indicates that reducing emissions could hinder economic growth. Additionally, pollution control measures may require increased production costs, which could also slow economic growth. Biofuels are renewable in comparison to fossil fuels. The topic of biofuels is still in its early stages in terms of technological progress [13].

Hydrotreating and hydrotreatment are both examples of hydroprocessing. Because it eliminates heteroatoms and saturates C–C bonds while retaining carbon atom count, hydrotreating is preferred for diesel range fuel. Hydrocracking (a severe form of hydroprocessing) induces the breakdown of C–C bonds to produce gasoline-range fuels [14]. Hydroprocessing is a procedure that is frequently used in refineries and vegetable oil upgrading to remove oxygen via the addition of H<sub>2</sub> [15]. The choice of a hydrotreating catalyst is essential in determining the yield and quality of hydrotreating products. Hydrotreating catalysts are often composed of essential metals such as Mo, Co, and Ni as active metals and are supported by alumina or silica-alumina [16]. Kristiani et al. [17] reported converting ethanol to gasoline utilizing a natural catalyst supported by different transition metals, including Ni, Co, Cu, and Zn. Their catalytic activity was evaluated for ethanol to

gasoline conversion and demonstrated a high conversion rate of up to 80–90%. The addition of Ni, Ni-Mo, Co, and Co-Mo metals was loaded into the activated natural zeolite to increase the activity and selectivity for the hydrocracking process [18]. As Sun et al. [19] stated, the development of zeolite-supported metal catalysts has promoted the progress of heterogeneous catalysis, which exhibited excellent performance in much catalytic activity.

Numerous studies have employed catalysts impregnated with metals. However, these metals can be wasteful and expensive. Additionally, impregnation of the metal might result in blockage (closing of pores), resulting in lower catalytic activity. Typically for zeolite treatment by employing a strong acid such as (HCl, HNO<sub>3</sub>, and H<sub>2</sub>SO<sub>4</sub>), as performed by Trisunaryanti et al. [20], mordenite's Si/Al ratio increased as a result of HNO<sub>3</sub> acid treatment, and the treatments did not cause damage to the crystalline structure of the mordenite.

Another study by Anggoro et al. [21] employed the strong acid H<sub>2</sub>SO<sub>4</sub> to treat zeolite Y. However, the treatment using strong acid is not environmentally friendly. As a result, this research employs acetic acid, a more environmentally friendly organic acid, as previously done by Chung [22]. In this research, the natural zeolite was treated with acetic acid and sodium hydroxide to improve the natural zeolite character.

Base treatment with NaOH is the common method applied to zeolite treatment [23]. Base treatment of zeolites with intermediate Al contents involves the selective extraction of silicon atoms resulting in a decrease of the Si/Al ratio or increase (case of low Si/Al ratio) and a significant loss of material at high base concentration [24]. Numerous investigations have demonstrated that activating natural zeolites with NaOH can increase crystallinity and the Si/Al ratio in catalysts at low concentrations such as 0.2 M [25]. The presence of the weak, medium and strong acid sites in zeolite altered the Si/Al ratio, which depends on the NaOH solution concentration and the zeolite composition [26]. The originality of this research is the treatment of natural zeolite with a weak organic acid (acetic acid) and base treatments (sodium hydroxide),

which has not been conducted previously and extensively. The catalyst activity in hydrotreatment with castor oil was then determined.

## ■ EXPERIMENTAL SECTION

### Materials

Natural zeolite was obtained from Wonosari, Yogyakarta Special Region, Indonesia. The glacial acetic acid (CH<sub>3</sub>COOH), sodium hydroxide (NaOH), Whatman filter paper No. 42, and universal pH paper were acquired from Merck. Co. Castor oil was purchased from CV Fruitanol Yogyakarta. The distilled and demineralized water was supplied by CV. Progo Mulyo. While the H<sub>2</sub>, and N<sub>2</sub> gas were supplied from PT. Samator Gas Industri.

### Instrumentation

The metal contents in the zeolite samples were characterized using X-Ray Fluorescence (XRF, RIGAKU-NEXQC+QuanTEZ). The change in the Si-O-Al functional group was determined using Fourier-Transform Infrared spectrometer (FTIR, Thermo Nicolet Avatar 360 IR) at the wavenumber range of 400–4000 cm<sup>-1</sup> using KBr pellet. X-Ray Diffraction (XRD, D2 Phaser diffractometer) using monochromatic Cu Kα source with a 2θ scan range of 3–80° and a scan speed of 3°/min. A surface Area Analyzer (SAA, JWGB meso 112) was conducted to obtain the porosity properties of the samples. The liquid product was analyzed using Gas Chromatography-Mass Spectrometry (GC-MS, Shimadzu QP2010S).

### Procedure

#### Acetic acid treatment on natural zeolite (ZA)

Natural zeolite (denoted as ZA) was heated under stirring in 6 M CH<sub>3</sub>COOH solution (ZA: acetic acid ratio of 1:5 (w/v)) for 10 h at 75–80 °C. Afterward, the mixture was filtered and washed using aquadest until pH neutral was achieved and dried at 110 °C for overnight to obtain ZAA. The ZA and ZAA were characterized using XRF, XRD, FTIR, and SAA.

#### Sodium hydroxide treatment on ZA and ZAA

ZA was heated under stirring in 0.1 M NaOH solution with ZA volume ratio towards sodium hydroxide of 1:5 at 75 °C for 30 min, continued with aging for 30 min.

The mixture was then washed by aquadest until neutral and dried at 110 °C for 24 h, to produce ZAB. The ZAA was also treated using the same procedure as mentioned to obtain ZAAB. The ZAB and ZAAB were characterized using XRF, XRD, FTIR, and SAA.

### Catalytic activity test of catalysts

The catalytic activity of catalysts (ZA, ZAA, ZAB, and ZAAB) was tested on the hydrotreatment process of castor oil. A sufficient amount of catalyst and feed was put into a bed in a stainless steel reactor (i.d = 2.0 cm, o.d = 2.2 cm, l = 30 cm). The catalyst/feed weight ratio was 1/100 wt.%. The hydrotreatment process was carried out at 450 °C for 2 h under H<sub>2</sub> gas with a flow rate of 10 mL/min. The product obtained from the reaction was flown into a condenser, where it was allowed to cool down using an ice bath in a flask. The percentage (%) of each product yield was determined gravimetrically using Eq. (1-3).

$$\text{Liquid product (wt.\%)} = \frac{\text{weight of liquid product}}{\text{weight of initial feed}} \times 100\% \quad (1)$$

$$\text{Coke (\%)} = \frac{\text{Catalyst weight differences before and after reaction}}{\text{weight of initial feed}} \times 100\% \quad (2)$$

$$\text{Residue (wt.\%)} = \frac{\text{Weight of remained feed}^*}{\text{weight of initial feed}} \times 100\% \quad (3)$$

$$^* = W_1 - W_0$$

where, W<sub>0</sub> = the weight of empty feed part, W<sub>1</sub> = the weight of the feed part after the catalytic process.

$$\text{Total conversion (wt.\%)} = 100 - \text{residue (wt.\%)} \quad (4)$$

The liquid products were analyzed by using GC-MS to determine gasoline and diesel fraction. Gasoline fraction was hydrocarbon compounds consisting of carbon numbers between C<sub>4</sub> to C<sub>12</sub>, while diesel fraction consisted of those with hydrocarbon chains between C<sub>13</sub> to C<sub>22</sub>. The selectivity of these products was calculated by using Eq. (5-7).

$$\text{Gasoline fraction (wt.\%)} = \frac{\text{Area GC of C}_4 \text{ to C}_{12} \text{ compounds}}{\text{Total area GC}} \times \text{Liquid product (wt.\%)} \quad (5)$$

$$\text{Diesel fraction (wt.\%)} = \frac{\text{Area GC of C}_{13} \text{ to C}_{22} \text{ compounds}}{\text{Total area GC}} \times \text{Liquid product (wt.\%)} \quad (6)$$

$$\text{Other compounds (wt.\%)} = \frac{\text{Area GC of nonhydrocarbon compounds}}{\text{Total area GC}} \times \text{Liquid product (wt.\%)} \quad (7)$$

## ■ RESULTS AND DISCUSSION

### The Effect of Acetic Acid and NaOH Treatment towards Characters of Zeolite

Table 1 shows the results of the XRF analysis, which revealed that the ZA contains metal impurities such as Ca 5.80% and Fe 5.01%. Following acetic acid treatment, contaminants were still present and slightly increased; this could have occurred as a result of the dealumination process, which also removed some of the contaminants. The dealumination process removed metal contaminants such as Ca and Fe and removed Al, which was further proved by the slight increase in the Si/Al ratio from 7.30 to 7.85 for the ZA and ZAA, respectively. This result confirmed that the acetic acid successfully removed aluminum atoms, as previously reported by others [22,27]. The breakage of Al caused the removal of Al–O bonds which were more accessible than the Si–O bonds, whereas the dissociation energy of the Al–O bond (116 kcal/mol) is lower than the Si–O bond (190 kcal/mol). Notably, the Si/Al ratio change after acetic acid treatment was insignificant because acetic acid is weak. The strength of acetic acid can be seen from its dissociation constant, which has a  $K_a$  value of  $1.7 \times 10^{-5}$ . The greater the  $K_a$  value, the easier  $\text{CH}_3\text{COO}^-$  and  $\text{H}^+$  to dissociate. In this case, the  $\text{CH}_3\text{COO}^-$ 's ability to bind to  $\text{Al}^{3+}$  was not strong, which caused the removal of non-framework aluminum atoms rather than the Al framework (FAL). When aluminum is removed, the zeolite structure is frequently disrupted, resulting in octahedral coordinated extra framework aluminum (EFAL) within the pores [28]. The dealumination process begins with the cleavage of O–Al–O bonds, then the atoms leave atomic gaps, and silanol nests and refills empty spaces by Si atoms.

The ZA and ZAB have the content of silicon which slightly decreased from 77.41 to 68.56, and for ZAA and ZAAB, 77.09 to 74.64. This result proved that NaOH treatment successfully removed the silicon content from the framework. However, it is noticeable that Si/Al ratio slightly changes even after the NaOH treatment (ZAB and ZAAB samples), and the result is not greater than 25. This finding suggests that some aluminum content might also

**Table 1.** Metal compositions and Si/Al ratio of zeolite

Compositions (%)	ZA	ZAA	ZAB	ZAAB
Al	10.5	9.82	9.43	9.79
Si	77.4	77.0	68.5	74.6
Ca	5.80	6.58	8.95	8.29
Fe	5.01	5.27	7.60	5.74
Ni	0.07	0.09	0.13	0.11
Cu	0.04	0.04	0.06	0.06
Zn	0.03	0.04	0.07	0.06
Si/Al Ratio	7.30	7.85	7.26	7.61

remove from the framework during NaOH treatment. The silicon and aluminum are close when the Si/Al ratio is low. Aluminum is removed along with silicon due to aluminum's amphoteric properties [29].

### FTIR Characterization

Zeolite materials incorporate the network between tetrahedral  $[\text{SiO}_4]^{2-}$  and  $[\text{AlO}_4]^{5-}$ , which are detectable in the FTIR characterization's energy range. Moreover, the FTIR characterization could be employed to identify the Brønsted and Lewis acid sites that arise from the natural zeolite and its modification. Overall, the bands observed in the range of  $445\text{--}464\text{ cm}^{-1}$  indicate the bending vibration of T–O–T groups (T = Si or Al atoms) in the zeolite. The vibration of T–O–T groups also appears at a wavenumber of  $794\text{ cm}^{-1}$  attributing to the symmetric stretching vibration. The bands around  $1032\text{--}1100\text{ cm}^{-1}$  assigned to the internal asymmetric stretching vibration of T–O–T groups could be used to observe the change in the Si/Al ratio of zeolite due to the continued removal of aluminum and silicon's removal [30]. Additionally, the bands assigned to the OH groups attached to the Al or Si observe at  $3451\text{--}3457$  and  $3600\text{--}3650\text{ cm}^{-1}$ .

Fig. 1 presents the FTIR spectra of the natural zeolite before and after being subjected to the acid and NaOH treatment. The significant change after both treatments is the Si/Al ratio of zeolites observed in the FTIR as the shifting of the internal asymmetric stretching vibration of T–O–T. Fig. 1 observed that the bands at  $1032\text{--}1100\text{ cm}^{-1}$  shifted, indicating the change in the Si/Al ratio of ZA after the acid and NaOH treatment. The acid treatment caused the bands to change

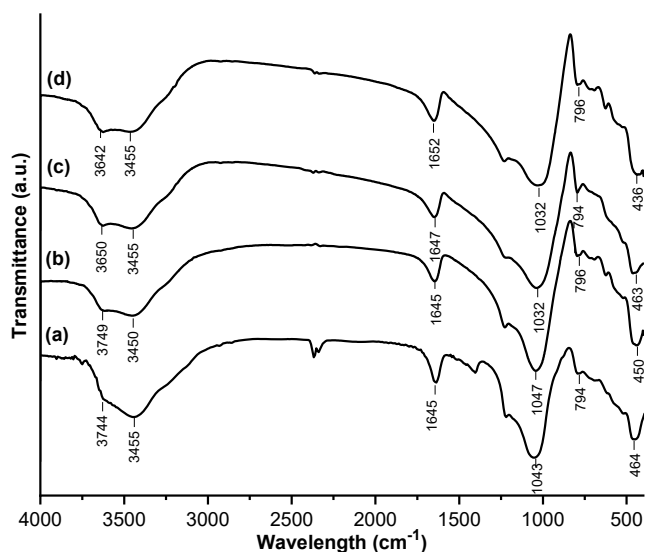


**Fig 1.** FTIR spectra of natural zeolite after the acid and NaOH treatment: (a) ZA, (b) ZAA, (c) ZAB, and (d) ZAAB

to a higher wavenumber from 1043 to 1047  $\text{cm}^{-1}$ , contributing to the increasing Si/Al ratio. On the other hand, the NaOH treatment on both ZA and ZAA induced the shifting of internal asymmetric stretching vibration of T–O–T to lower wavenumber from 1043 to 1032  $\text{cm}^{-1}$  and from 1047 to 1032  $\text{cm}^{-1}$ , respectively. This result further validated that the NaOH treatment decreased the Si/Al ratio of zeolite.

### The Effect of Acetic Acid and NaOH on Crystallinity

Natural zeolite usually contains many natural zeolites, such as Analcime, Clinoptilolite, Faujasite, Mordenite, and many more, which are greatly influenced

by zeolite's origin. Therefore, XRD characterization is needed to determine the kind of zeolite presented in the natural zeolite. Fig. 2(a) depicts the XRD profile of natural zeolite (ZA) obtained from Wonosari, Special Region of Yogyakarta, Indonesia. The XRD profile of the ZA indicated that it consists of mordenite and clinoptilolite as its primary structure. The mordenite peaks appeared at  $2\theta$  of 13.48°, 19.62°, 22.26°, 25.68°, 26.24°, 27.62°, and 30.9° (JCPDS: 068448) and clinoptilolite profile presented at  $2\theta$  of 11.14°, 14.92°, 20.41°, 23.16°, and 32.15° (JCPDS: 251349). This result is in good agreement with the previous report on the use of zeolite obtained from the Special Region of Yogyakarta and the surrounding area [31-32]. Table 1 provides the chemical analysis by using XRF. It is noticed that ZA contains impurities atoms such as Fe, Ni, Cu, and Zn with a total of 5.15%. These atoms originated from the impurities mineral in ZA, such as pyrite ( $\text{FeS}_2$ ). Other impurities compound found in the ZA is Albite ( $\text{NaAlSi}_3\text{O}_8$ ), quartz ( $\text{SiO}_2$ ), gibbsite ( $\text{Al}(\text{OH})_3$ ), and muscovite ( $\text{KAl}_2\text{Si}_3\text{O}_{10}(\text{OH})_2$ ) with a total composition of less than 20%.

Employing acetic acid in the dealumination preserve the crystallinity of the treated zeolite [22,27]. It can be clearly observed that after the treatment using acetic acid, the intensity of some peaks in the ZAA (Fig. 1(b)) increased, explaining that acetic acid treatment not only eliminates the aluminum atoms but also eliminates some impurities. On the other hand, NaOH treatment on

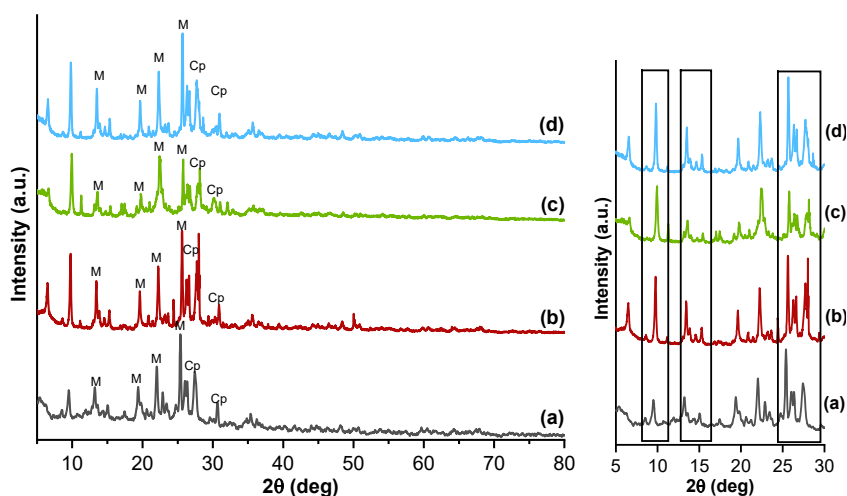


**Fig 2.** XRD spectra of (a) ZA, (b) ZAA, (c) ZAB, and (d) ZAAB (M = Mordenite, Cp = Clinoptilolite)

the ZA to obtain ZAB (Fig. 1(c)) caused a decrease in the crystallinity of Zeolite. It assumed that NaOH not only removes the silicon atoms but also aluminum atoms from the zeolite framework. It was proved by the ZAB's Si/Al ratio, which did not change much after the alkaline treatment (Table 1). The combination of the acid-alkaline treatment on the ZA (ZAAB) did not cause a significant decrease in the crystallinity of zeolite (Fig. 1(d)).

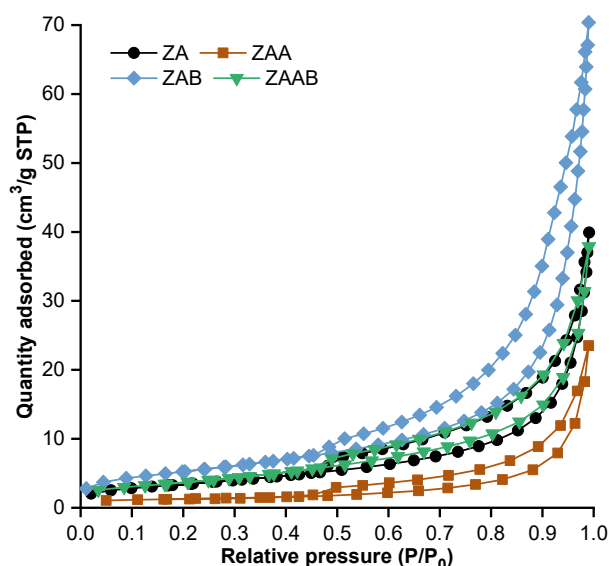
### Adsorption Isotherm Curve

Fig. 3 shows the adsorption isotherm plot of the ZA before and after acid-alkaline treatment (ZAA, ZAB, and ZAAB). This type of plot can be considered a type IV isotherm typical for mesoporous materials, which have flat slits between two crystalline planes. The ZA is naturally a mesoporous material based on the isotherm plot and porous properties listed in Table 2. As shown in Fig. 3, even after the acid-alkaline treatment on ZA, the hysteresis type of treated ZA did not change. As indicated by the Si/Al ratio of the treated ZA (see Table 1), it suggested that the treatment condition is suitable for modifying the Si/Al ratio while maintaining the other properties. These phenomena are also supported by the XRD profile of ZAA, ZAB, and ZAAB, which have not significantly changed. Notably, from Fig. 3, the ZAA has low-pressure hysteresis while maintaining the hysteresis type. It may indicate the increased complexity of zeolite channels after acid treatment.

Fig. 4 present the range of pore distribution of zeolites between 2–20 nm, indicating that the pore ranges from the material were mesoporous. The specific surface area was determined on a sorption analyzer using the BET method. The specific surface area was determined to see the improved character of the catalysts after the zeolite was treated by acid and alkaline as well as metals impregnation, the sizes of pores can influence the order and the energy of activation of the catalytic reaction, and so it is essential to know the total specific surface area and the total pore volume are distributed in pores of the catalysts [33].

Table 2 lists zeolites' surface area, pore volume, and diameter change after acid-alkaline treatment. Interestingly, the surface area and total pore volume of ZA

after acid treatment (ZAA) decreased greatly from 12.542 to 4.058  $\text{m}^2 \text{g}^{-1}$  and 0.06 to 0.04  $\text{cm}^3 \text{g}^{-1}$ , respectively. During the acetic acid treatment, the acetic acid disrupts the Al atoms and some impurities in the ZA, as shown in Table 1. As a result, ZAA exhibited the highest Si/Al ratio and lowest surface area. On the contrary, the alkaline treatment on the ZA caused an increase in the surface area. Eventually, the ZAB possessed the lowest average pore diameter among others. NaOH treatment might eliminate the impurities in the zeolite channel while preserving the zeolite network, as indicated by the slight modification in the Si/Al ratio (see Table 1). It can also be explained that both aluminum and silicon atoms are extracted during the NaOH treatment [34].



**Fig 3.** Nitrogen adsorption/desorption isotherms of natural zeolite (ZA) after being subjected to acetic acid and alkaline treatment

**Table 2.** Surface parameters of catalysts

Catalyst	Surface area ( $\text{m}^2 \text{g}^{-1}$ )	Total pore volume ( $\text{cm}^3 \text{g}^{-1}$ ) <sup>b</sup>	D (nm) <sup>b</sup>
ZA	12.542	0.06	19.24
ZAA	4.058	0.04	35.71
ZAB	19.144	0.11	17.02
ZAAB	13.144	0.06	22.70

<sup>a</sup>Surface area determined by using BET theory. <sup>b</sup>Total pore volume (at  $P/P_0 = 0.99$ ), and average pore volume determined by using BJH theory

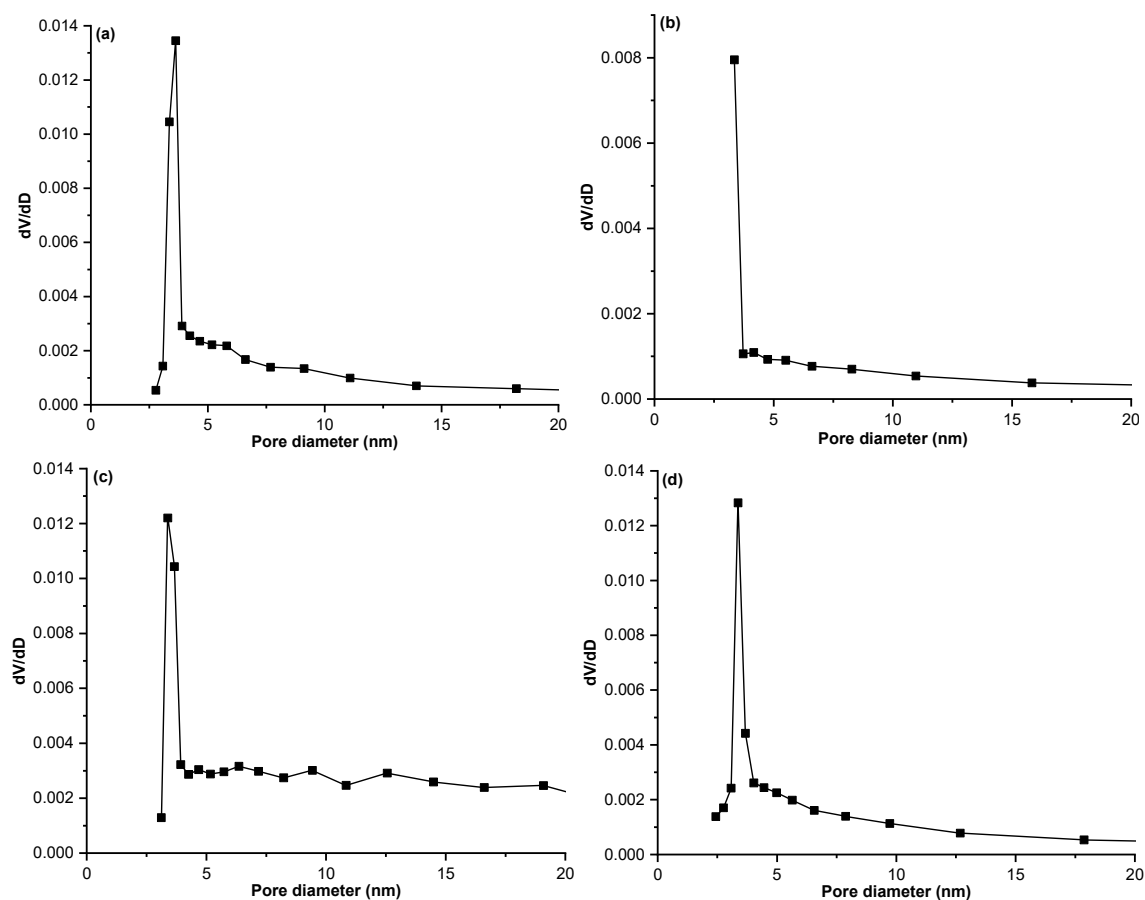


Fig 4. Pore size distribution of (a) ZA, (b) ZAB, (c) ZAA, and (d) ZAAB

It is well known that a catalyst possessing a high surface area is desirable to obtain high catalytic activity due to the accessibility of the active catalytic site. There is a limited number of reports on the application of acetic acid in acid treatment. Chung [22] reported that acetic acid treatment on the Mordenite increased the surface area and the alkylation reaction of cumene and 2-propanol. Moreover, it also overcomes the diffusion limitation of the Mordenite as a catalyst. Yusniyanti et al. [35] revealed that a combination of acetic acid and NaOH treatment on Mordenite caused the increment of its catalytic activity towards the hydrotreatment of bio-oil obtained from cellulose. Both report the positive effect on the application of zeolite catalyst after the acid or acid-alkaline treatment. As revealed in Table 1 and 2, the Si/Al ratio and surface area of zeolite changed upon the acid and the combination of acid-alkaline treatment. Therefore, treated zeolite is expected to exhibit better catalytic performance than natural zeolite.

#### Catalytic Activity and Selectivity of ZA, ZAA, ZAB, and ZAAB Catalysts in Hydrotreatment of Castor Oil

Castor oil has high linoleic acid content and the potential to be used as feed to obtain biofuel. The hydrotreatment process is needed to turn castor oil into valuable biofuel. Here, the prepared catalysts (ZA, ZAA, ZAB, and ZAAB) were tested on the hydrotreatment of castor oil to evaluate the effect of the acetic acid, and NaOH treatment on the ZA and the results are shown in Table 3. The liquid product from the hydrocracking process was analyzed using GC-MS to determine the plausible compound (Fig. S1 and Table S1). The GC-MS results showed a small distribution of hydrocarbons from the radical cracking mechanism, and the liquid product still contained a lot of oxygenated compounds. Table 3 shows that all the catalysts exhibit high conversion of castor oil, around 98–99%. The aspect of choosing the best catalyst is the liquid production percentage.

**Table 3.** Products distribution of hydrotreatment of castor oil

Catalyst	Conv. (wt.%)	Gas (wt.%)	Liquid fraction (wt.%)				Coke (wt.%)	Residue (wt.%)
			Gasoline	Diesel	Others	Total		
ZA	99.7	45.0	11.6	1.5	40.7	53.9	0.8	0.3
ZAB	97.8	41.4	19.5	2.9	32.6	55.1	1.3	2.2
ZAA	99.8	58.0	13.1	6.8	21.6	41.6	0.2	0.2
ZAAB	98.6	42.0	18.6	1.0	35.1	54.8	1.8	1.4

As presented in Table 3, the catalysts show different performances in terms of liquid production. The acetic acid treatment on ZA (ZAA) caused a decrease in catalytic activity, which exhibited the most inadequate liquid production (41.6%), suggesting due to a decrease in the surface area after the acid treatment. Although the ZAA catalyst that only underwent acid treatment exhibited the lowest catalytic activity due to the low surface area, the ZAA catalyst produces the least amount of coke and high selectivity to the diesel fraction contributing to its big pore diameter. It indicated that acid treatment on the ZA has a positive effect on lowering the coke production in the catalyst, which could slow down the deactivation of the catalyst. Further treatment of the ZAA with the NaOH (ZAAB) recovers the surface area and catalytic activity. The liquid production increased from 41.6 to 54.8%, with 18.6% selectivity towards the gasoline fraction.

Interestingly, the ZAB catalyst, which resulted from the NaOH treatment on ZA, showed the highest liquid production (55.1%) with 19.5% selectivity towards the gasoline fraction, contributing to increased catalyst surface area. Because active sites were created on the surface of the catalysts, increasing the surface area of the catalysts increases the availability of active sites, resulting in increased catalytic activity. As shown in Table 2, the ZAB exhibits the highest surface among others. The surface area of the catalyst is in the order (from the lowest to the highest): ZAA < ZAAB < ZA < ZAB, and the catalytic activity is in the order: ZAA < ZA < ZAAB < ZAB.

### Correlation between Specific Surface Area towards the Activity of the Catalysts

The correlation between the specific surface area of catalysts and the number of liquid products produced is shown in Fig. 5. The amount of liquid product made was also used to determine the catalyst's activity. Fig. 5 offered

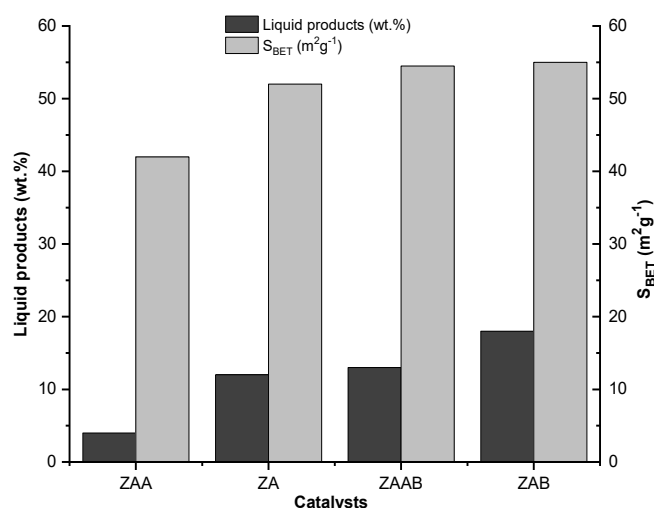


**Fig 5.** Correlation between the specific surface area of catalysts and the amount of liquid product

that the number of liquid products produced increases as the specific surface area of the catalyst increases. Increases in a catalyst's specific surface area can improve active sites' availability. Catalytic reactions rely heavily on active sites [36]. The ZAB exhibited the highest catalytic activity, attributed to its large specific surface area. Due to its low specific surface area, the ZAA showed the most insufficient catalytic activity. This conclusion is consistent with the research from [37], which indicates that a catalyst with a high specific surface area has a greater chance of exhibiting good catalytic activity during the hydrocracking process.

### CONCLUSION

In this study, the preparation of heterogeneous catalysts has successfully been carried out. The acetic acid and sodium hydroxide treatment was treated on Wonosari natural zeolite and denoted as ZAA, ZAB, and ZAAB. The acid treatment towards zeolite increased Si/Al ratio from 7.30 to 7.85, respectively. Sodium



hydroxide treatment decreased Si/Al ratio from 7.30 to 7.26 and after acid-sodium hydroxide treatment from 7.85 to 7.61, respectively. The ZA, ZAB, ZAA, and ZAAB catalysts produced liquid products of 53.9, 55.1, 41.6, and 54.8 wt.%, respectively. The ZAB had the highest liquid product with selectivity towards hydrocarbon compounds of 22.4 wt.%. The higher specific surface area increased the activity and selectivity of the catalyst towards liquid production and hydrocarbon compounds in the hydrotreatment process of castor oil. The ZAB catalyst showed the highest surface area.

### ■ ACKNOWLEDGMENTS

This research was conducted under the research grant of PTUPT 2022 Universitas Gadjah Mada (Contract No: 018/E5/PG.02.00.PT/2022 with the serial contract No: 1681/UN1/DITLIT/DIT-LIT/PT.01.03/2022). Therefore, the authors would like to thank The Ministry of Research, Technology and Higher Education, the Republic of Indonesia, for the financial support.

### ■ AUTHOR CONTRIBUTIONS

Lailatul Rahmi conducted the research and wrote the manuscript, Wega Trisunaryanti proposed the research topic and revised the manuscript, Triyono and Iip Izul Falah revised the manuscript.

### ■ REFERENCES

- [1] Anuar, M.R., and Abdullah, A.Z., 2016, Challenges in biodiesel industry with regards to feedstock, environmental, social and sustainability issues: A critical review, *Renewable Sustainable Energy Rev.*, 58, 208–223.
- [2] Rabie, A.M., Shaban, M., Abukhadra, M.R., Hosny, R., Ahmed, S.A., and Negm, N.A., 2019, Diatomite supported by CaO/MgO nanocomposite as heterogeneous catalyst for biodiesel production from waste cooking oil, *J. Mol. Liq.*, 279, 224–231.
- [3] Ajala, O.E., Aberuagba, F., and Odetoeye, T.E., 2015, Biodiesel: Sustainable energy replacement to petroleum-based diesel fuel – A review, *ChemBioEng Rev.*, 2 (3), 145–156.
- [4] Zhang, Q., Wang, T., Xu, T., Zhang, Q., and Ma, L., 2014, Production of liquid alkanes by controlling reactivity of sorbitol hydrogenation with a Ni/HZSM-5 catalyst in water, *Energy Convers. Manage.*, 77, 262–268.
- [5] Atabani, A.E., Silitonga, A.S., Ong, H.C., Mahlia, T.M.I., Masjuki, H.H., Badruddin, I.A., and Fayaz, H., 2013, Non-edible vegetable oils: A critical evaluation of oil extraction fatty acid compositions, biodiesel productions, characteristic, engine performance, and emissions production and refining technologies, *Renewable Sustainable Energy Rev.*, 18, 211–245.
- [6] Kamel, D.A., Farag, H.A., Amin, N.K., Zatout, A.A., and Ali, R.M., 2018, Smart utilization of jatropha (*Jatropha curcas* Linnaeus) seeds for biodiesel production: Optimization and mechanism, *Ind. Crops Prod.*, 111, 407–413.
- [7] Vorontsov, A.V., Valdés, H., and Smirniotis, P.G., 2019, Design of active sites in zeolite catalysts using modern semiempirical methods: The case of mordenite, *Comput. Theor. Chem.*, 1166, 112572.
- [8] Alver, B.E., and Esenli, F., 2017, Acid treated mordenites as adsorbents of C<sub>2</sub>H<sub>4</sub> and H<sub>2</sub> gases, *Microporous Mesoporous Mater.*, 244, 67–73.
- [9] Sousa, L.V., Silva, A.O.S., Silva, B.J.B., Quintela, P.H.L., Barbosa, C.B.M., Fréty, R., and Pacheco, J.G.A., 2018, Preparation of zeolite P by desilication and recrystallization of zeolites ZSM-22 and ZSM-35, *Mater. Lett.*, 217, 259–262.
- [10] Ahmad, M., Farhana, R., Raman, A.A.A., and Bhargava, S.K., 2016, Synthesis and activity evaluation of heterometallic nano oxides integrated ZSM-5 catalysts for palm oil cracking to produce biogasoline, *Energy Convers. Manage.*, 119, 352–360.
- [11] Zhao, X., Wei, L., Julson, J., Gu, Z., and Cao, Y., 2015, Catalytic cracking of inedible camelina oils to hydrocarbon fuels over bifunctional Zn/ZSM-5 catalysts, *Korean J. Chem. Eng.*, 32 (8), 1528–1541.
- [12] Žibert, J., Cedilnik, J., and Pražnikar, J., 2016, Particulate matter (PM<sub>10</sub>) patterns in Europe: An exploratory data analysis using non-negative matrix factorization, *Atmos. Environ.*, 132, 217–228.

- [13] Procházka, P., and Hönic, V., 2018, Economic analysis of diesel-fuel replacement by crude palm oil in Indonesian power plants, *Energies*, 11 (3), 504.
- [14] De, S., and Luque, R., 2014, Upgrading of waste oils into transportation fuels using hydrotreating technologies, *Biofuel Res. J.*, 1 (4), 107–109.
- [15] Zarchin, R., Rabaev, M., Vidruk-Nehemya, R., Landau, M.V., and Herskowitz, M., 2015, Hydroprocessing of soybean oil on nickel-phosphide supported catalysts, *Fuel*, 139, 684–691.
- [16] Bezergianni, S., Dimitriadis, A., and Meletidis, G., 2014, Effectiveness of CoMo and NiMo catalysts on co-hydroprocessing of heavy atmospheric gas oil-waste cooking oil mixtures, *Fuel*, 125, 129–136.
- [17] Kristiani, A., Sudiarmanto, S., Aulia, F., Hidayati, L.N., and Abimanyu, H., 2017, Metal supported on natural zeolite as catalysts for conversion of ethanol to gasoline, *MATEC Web Conf.*, 101, 01001.
- [18] Sriningsih, W., Saerodji, M.G., Trisunaryanti, W., Triyono, T., Armunanto, R., and Falah, I.I., 2014, Fuel production from LDPE plastic waste over natural zeolite supported Ni, Ni-Mo, Co and Co-Mo Metals, *Procedia Environ. Sci.*, 20, 215–224.
- [19] Sun, Q., Wang, N., and Yu, J., 2021, Advances in catalytic of zeolite-supported metal catalysts, *Adv. Matter.*, 33 (51), 2104442.
- [20] Trisunaryanti, W., Wijaya, K., Suryani, D., and Chasanah, U., 2021, “The Effect of HNO<sub>3</sub> and/or NaOH Treatments on Characteristics of Mordeinite” in *Advances in Geopolymer-Zeolite Composites - Synthesis and Characterization*, Eds. Vizureanu, P., and Krivenko, P., IntechOpen, Rijeka, 83–89.
- [21] Anggoro, D.D., Oktavianty, H., Sasongko, S.B., and Buchori, L., 2020, Effect of dealumination on the acidity of zeolite Y and the yield of glycerol mono stearate (GMS), *Chemosphere*, 257, 127012.
- [22] Chung, K.H., 2008, Dealumination of mordenites with acetic acid and their catalytic activity in the alkylation of cumene, *Microporous Mesoporous Mater.*, 111 (1-3), 544–550.
- [23] Muttaqii, M., Birawidha, C.D., Isnugroho, K., Amin, M., Hendro, Y., Istiqomah, A., and Dewangga, D., 2019, Pengaruh aktivasi secara kimia menggunakan larutan asam dan basa terhadap karakteristik zeolit alam, *JRTI*, 13 (2), 266–271.
- [24] Bertrand-Drira, C., Cheng, X.W., Cacciaguerra, T., Trens, P., Melinte, G., Ersen, O., Minoux, D., Finiels, A., Fajula, F., and Gerardin, C., 2015, Mesoporous mordenites obtained by desilication: Mechanistic considerations and evaluation in catalytic oligomerization of pentene, *Microporous Mesoporous Mater.*, 213, 142–149.
- [25] Gea, S., Haryono, A., Andriyani, A., Sihombing, J.L., Pulungan, A.N., Nasution, T., Rahayu, R., and Hutapea, A.Y., 2020, The effect of chemical activation using base solution with various concentrations towards sarulla natural zeolite, *Elkawanie*, 6 (1), 85–95.
- [26] Ates, A., 2018, Effect of alkali-treatment on the characteristics of natural zeolites with different compositions, *J. Colloid Interface Sci.*, 523, 266–281.
- [27] Triyono, T., Trisunaryanti, W., and Yusniyanti, F., 2020, Sonicated-assisted acid treatment of mordenite using acetic acid, *Key Eng. Mater.*, 840, 520–525.
- [28] Tišler, Z., Hrachovcová, K., Svobodová, E., Šafář, J., and Pelíšková, L., 2019, Acid and thermal treatment of alkali-activated zeolite foams, *Minerals*, 9 (12), 719.
- [29] Wei, Y., Parmenrier, T.E., de Jong, K.P., and Zečević, J., 2015, Tailoring and visualizing the pore architecture of hierarchical zeolites, *Chem. Soc. Rev.*, 44 (20), 7234–7235.
- [30] Wijaya, K., Baobalabuana, G., Trisunaryanti, W., and Syoufian, A., 2013, Hydrotreatment of palm oil into biogasoline catalyzed by Cr/natural zeolite, *Asian J. Chem.*, 25 (16), 8981–8986.
- [31] Trisunaryanti, W., Triyono, T., Falah, I.I., Widyawati, D., and Yusniyanti, F., 2022, The effect of oxalic acid and NaOH treatments on the character of Wonosari natural zeolite as Ni, Cu, and Zn metal support catalyst for hydrocracking of castor oil, *Biomass Convers. Biorefin.*, 2022, s13399-022-02779-5.
- [32] Kurniawan, T., Muraza, O., Bakare, I.A., Sanhoob, M.A., and Al-Amer, A.M., 2018, Isomerization of

- n*-butane over cost-effective mordenite catalyst fabricated via recrystallization of natural zeolite, *Ind. Eng. Chem. Res.*, 57 (6), 1894–1902.
- [33] Ramesh, K., Reddy, K.S., Rashmi, I., and Biswas, A.K., 2014, Porosity distribution, surface area and morphology of synthetic potassium zeolites: A SEM and N<sub>2</sub> adsorption study, *Commun. Soil Sci. Plant Anal.*, 45 (16), 2171–2181.
- [34] Nurliati, G., Krisnandi, Y.K., Sihombing, R., and Salimin, Z., 2015, Studies of modification of zeolite by tandem acid-base treatments and its adsorptions performance towards thorium, *Atom Indonesia*, 41 (2), 87–95.
- [35] Yusniyanti, F., Trisunaryanti, W., and Triyono, T., 2021, Acid-alkaline treatment of mordenite and its catalytic activity in the hydrotreatment of bio-oil, *Indones. J. Chem.*, 21 (1), 37–45.
- [36] Bernard, P., Stelmachowski, P., Broś, P., Makowski, W., and Kotarba, A., 2021, Demonstration of the influence of specific surface area on reaction rate in heterogeneous catalysis, *J. Chem. Educ.*, 98 (3), 935–940.
- [37] Trisunaryanti, W., Triyono, T., Purwono, S., Purwanti, S.A., and Sumbogo, S.D., 2021, Synthesis of mesoporous carbon from merbau sawdust as a nickel metal catalyst support for castor oil hydrocracking, *Bull. Chem. React. Eng. Catal.*, 17 (1), 216–224.

# New Heterocyclic Organo-Chalcogenide Compounds: Synthesis, Physicochemical Characterization, and Evaluation of Anticancer Activity against Breast Cancer Cells

Hayat Hamza Abbas<sup>1\*</sup>, Majeed Yacoob Al-Luaibi<sup>1</sup>, and Mohammed Jassem Al-Assadi<sup>2</sup>

<sup>1</sup>Department of Chemistry, College of Science, University of Basrah, Basrah, 61004, Iraq

<sup>2</sup>Department of Laboratory Techniques, Faculty of Health and Medical Techniques, University of Almaaqaal, Basrah, Iraq

\* **Corresponding author:**

email: hayat.hamza@uobasrah.edu.iq

Received: June 20, 2022

Accepted: December 23, 2022

DOI: 10.22146/ijc.75582

**Abstract:** This work aimed to synthesize, characterize and evaluate the thermal stability of new sulfur and selenium organochalcogenide derivatives and to test the cytotoxic activity against breast adenocarcinoma cell line (MCF-7) through conducting MTT assay and AO/EB dual staining-technique. Two series of ten organo-chalcogen compounds: 4-(substituted)phenylthiomorpholine-3,5-dione and 4-(substituted)phenylselenomorpholine-3,5-dione were prepared by the reaction of  $\text{Na}_2\text{S}\cdot 3\text{H}_2\text{O}$  and  $\text{NaHSe}$  with N-(substituted)phenyl-2-chloro-N-(2-chloroacetyl)acetamide, respectively, under nitrogen atmosphere to give the corresponding cyclic chalcogenide ligands. All new compounds were characterized by melting point, FTIR, elemental analysis, UV-Visible, <sup>1</sup>H-NMR and <sup>13</sup>C-NMR. Meanwhile, TG/DTA analysis of some of these ligands was conducted to evaluate the thermal stability, kinetic, and characteristic thermodynamic parameters. Absorption spectroscopy was used to investigate these compounds with human DNA. The experimental results investigated a hypochromic effect via intercalation binding mode. The role of the prepared ligands in breast cell lines has been investigated by conducting MTT assay via spectroscopic techniques on HBL100 and MCF-7, normal and cancer breast cell lines, respectively. Cell death was seen after AO/EB dye staining method employing the fluorescence microscopy technique. The results revealed that these compounds possess cytotoxic activity on the MCF-7 and HBL-100 cell lines at a fixed concentration.

**Keywords:** chalcogenide; phenylacetamide; seleno-morpholine; heterocyclic chalcogenide; thio-morpholine

## ■ INTRODUCTION

Materials containing organochalcogens or coordination compounds with chalcogen bond(s) have been extensively investigated due to their unique properties, such as electric and thermal conductivities, molecular self-assemblies, nanotube formation, ion exchange capacity, non-linear optics, photoelectro-chemical behavior, and drug delivery [1-2].

Sulfur (S) and selenium (Se) compounds present several applications in a great variety of fields. The anticancer activity of these compounds was considered the most important application due to the burden, costs, and mortality rates caused by cancer disease [3-4].

Se is a crucial trace element [5-6] that is naturally occurring with both nutritional and toxicological properties. Se is non-toxic to humans in low concentrations, but it plays a significant role in human's health in addition to regulating many critical functions involving cells; therefore, an adduct that releases selenium to the biological system at a steady rate act as an effective pharmaceutical agent [7-10]. This is mediated by incorporating it into selenoproteins. Apparently, the effectiveness of Se adducts as an anti-infective or antioxidant agent depends on the bioavailability of Se at the site of action [11]. The use of Se in medicinal chemistry is helpful to care for many kinds of illness due to compatibility with the biological

system either directly or indirectly [7] e.g., Se supplements are given to repay its deficiency, while selenium sulfide is used in shampoos for the treatment of dandruff [12-13]. Moreover, through extensive experimental evidence *in vitro*, animal, and prospective studies, it emerged that the supplementation of Se reduces the incidence of different cancer types [14].

Natural heterocyclic five-membered ring compounds thiazolin-4-carboxylic acid (a derivative of formyl-cysteine), thiazolidine-4-carboxylic acid (thioprolin), 2-amino-2-thiazoline-4-carboxylic acid (ATCA), and 2-amino-3-methyl-5-sulfanylimidazol-4-yl propanoic acid (ovothiol A) [15]. All these compounds demonstrated to possess different and, in some cases convergent biological activities such as oxygen and nitrogen-free radical scavenging capacity, detoxification of cyanide, and antioxidant activity [16].

Morpholine and thiomorpholine are organic heterocyclic compounds which have several practical applications as they are the most favorable organic solvent due to their low cost and can be considered good bases [17]. A large number of heterocyclic bases, such as thiomorpholine and their derivatives, have been reported [18] due to their thermal stability and bioinorganic applications such as antimalarial and antioxidant.

Our interest in this area is focused on the investigation of the thermal stability of the newly chalcogen ligands and on preparing compounds that may have an ability of cell-growth inhibition or have a selective or directed action on cancerous cells and to study the compound-DNA interactions of these chalcogen ligands by various techniques.

## ■ EXPERIMENTAL SECTION

### Materials

All chemicals and solvents used were of analytical grade supplied by Sigma-Aldrich, Fluka, Merck, BDH, and SCH companies and were used as such without further purifications. Sodium carbonate, chloroacetyl chloride, sodium borohydride, and MTT stain were obtained from Sigma-Aldrich company. Dichloromethane was obtained from Fluka, USA. Dimethyl sulfoxide, sodium chloride, sodium hydroxide, and potassium

hydroxide were obtained from Merck company. Selenium powder and chloroform were obtained from BDH. Absolute ethanol, acetone, and ethyl acetate were obtained from SCH. Normal (HBL-100) and cancer cell lines (MCF-7) were obtained from the IRAQ Biotech Cell Bank Unit in Basra and maintained in RPMI-1640 supplemented with 10% Fetal bovine, 100 units/mL penicillin, and 100 µg/mL streptomycin. Cells were passaged using Trypsin-EDTA reseeded at 70% confluence twice to third a week and incubated at 37 °C and 5% CO<sub>2</sub>; the CO<sub>2</sub> incubator was obtained from Cypress Diagnostics (Belgium).

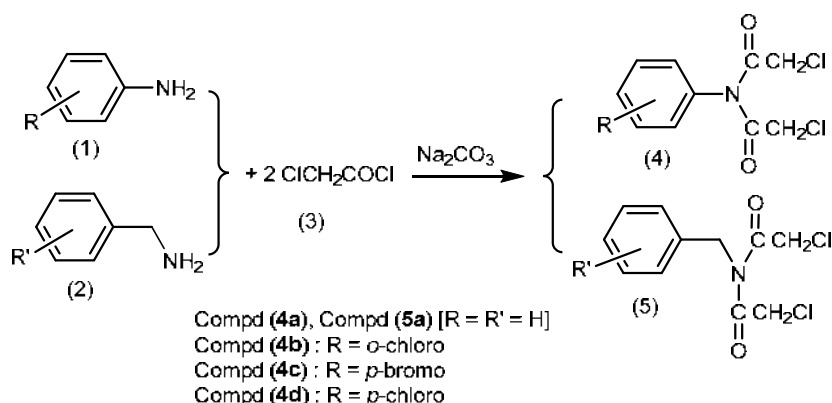
### Instrumentation

The melting points of all prepared compounds were determined by a Buchi 510 melting point apparatus. FTIR (Fourier transform Infrared) spectra were recorded using an FTIR-8400S Shimadzu Spectrophotometer in the range (4000–400) cm<sup>-1</sup> in KBr disk. Elemental analysis (C, H, N, S) was performed by using the EuroFA-Vector-EA-3000 Elemental Analyzer Apparatus. <sup>1</sup>H and <sup>13</sup>C-NMR spectra were recorded on a Bruker DRX 500 MHz and 125 MHz, respectively, using CD<sub>3</sub>OD and DMSO-*d*<sub>6</sub> as internal standards (Central Laboratory, University of Tehran, Iran). UV-Vis spectra for ligands were measured on a Shimadzu 1800 UV-Vis spectrophotometer. The thermal analysis was carried out by NETZSCH STA449 F3 Jupiterg-Thermal analyzer.

### Procedure

**General procedure for the synthesis of compound (4) 2-Chloro-(substituted)phenyl acetamide.** A mixture of aryl amine compounds (4 mmol) and sodium carbonate (4.24 g; 4 mmol) in 70 mL of acetone was stirred for 30 min. Then, chloroacetyl chloride (6.5 mL; 8 mmol) was added dropwise. The reaction was stirred at room temperature for 2 h, filtered, and then the excess solvent was removed under a vacuum. To the filtrate, 30 mL of distilled water was added, and then the resulting solid was filtered, dried, and crystallized from ethanol/water (ratio 80:20) mixture [18-19] (see Scheme 1).

**N-phenyl-2-chloro-N-(2-chloroacetyl) acetamide as compound (4a).** Follow the general procedure of 2-chloro-(substituted)phenyl acetamide(4) using aniline(1)



**Scheme 1.** Synthesis of *N*-aryl-2-chloro-*N*-(2-chloroacetyl)acetamide and their derivatives

(3.72 g; 4 mmol), sodium carbonate (4.24 g; 4 mmol) in 70 mL of acetone and chloroacetyl chloride (6.5 mL; 8 mmol). The silvery precipitate was obtained in 80% yield, m.p. 127–129 °C, IR  $\text{vcm}^{-1}$  (KBr): 1674 (C=O amide), 559 (C-Cl).

***N*-*o*-chlorophenyl-2-chloro-*N*-(2-chloroacetyl)acetamide as compound (4b).** Follow the general procedure of 2-chloro-(substituted)phenyl acetamide (4) using *o*-chloroaniline (5.14 g; 4 mmol), sodium carbonate (4.24 g; 4 mmol) in 70 mL of acetone and chloroacetyl chloride (6.5 mL; 8 mmol). The white precipitate was obtained in 78% yield, m.p. 71–73 °C, IR  $\text{vcm}^{-1}$  (KBr): 1674 (C=O amide), 570 (C-Cl).

***N*-*p*-bromophenyl-2-chloro-*N*-(2-chloroacetyl)acetamide as compound (4c).** Follow the general procedure of 2-chloro-(substituted)phenyl acetamide (4) using *p*-bromoaniline (6.88 g; 4 mmol), sodium carbonate (4.24 g; 4 mmol) in 70 mL of acetone and chloroacetyl chloride (6.5 mL; 8 mmol). A chalky white precipitate was obtained in 75% yield, m.p. 191–193 °C, IR  $\text{vcm}^{-1}$  (KBr): 1670 (C=O amide), 567 (C-Cl).

***N*-*p*-chlorophenyl-2-chloro-*N*-(2-chloroacetyl)acetamide as compound (4d).** Follow the general procedure of 2-chloro-(substituted)phenyl acetamide (4) using *p*-chloroaniline (5.14 g; 4 mmol), sodium carbonate (4.24 g; 4 mmol) in 70 mL of acetone and chloroacetyl chloride (6.5 mL; 8 mmol). The white cotton precipitate was obtained in 82% yield, m.p. 177–179 °C, IR  $\text{vcm}^{-1}$  (KBr): 1670 (C=O amide), 567 (C-Cl).

***N*-benzyl-2-chloro-*N*-(2-chloroacetyl)acetamide as compound (5a).** Follow the general procedure of 2-

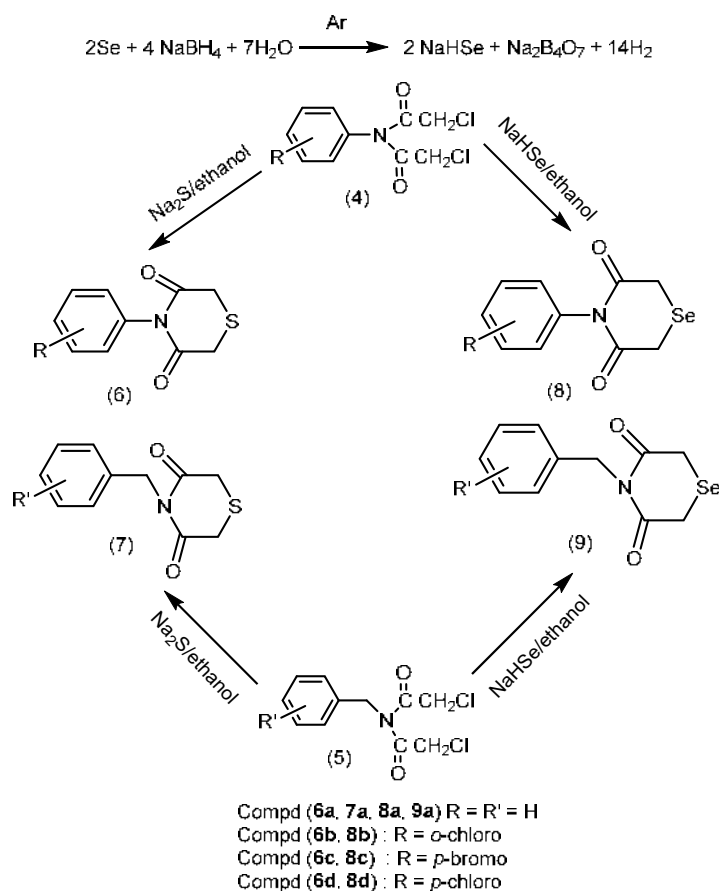
chloro-(substituted)phenyl acetamide (4) using benzylamine (2) (3.55 g; 3.3 mmol), sodium carbonate (4.24 g; 4 mmol) in 70 mL of acetone and chloroacetyl chloride (6.5 mL; 8 mmol). The white transparent precipitate was obtained in 85% yield m.p. 99–102 °C, IR  $\text{vcm}^{-1}$  (KBr): 1651 (C=O amide), 590 (C-Cl).

#### **General procedure for the synthesis of compound (6) 4-(Substituted)phenylthiomorpholine-3,5-dione.**

An aqueous solution of  $\text{Na}_2\text{S}\cdot 3\text{H}_2\text{O}$  (0.32 g; 2.00 mmol) was added to a solution of compound 4 (2.00 mmol) in 20 mL of ethanol under a nitrogen atmosphere. After about 30 min, a pale-yellow solution formed and filtered, then 50 mL of distilled  $\text{H}_2\text{O}$  was added, and the resulting solution was extracted with  $\text{CH}_2\text{Cl}_2$  (30 mL) three times. The solvent was evaporated to a minimum amount; a pale-yellow precipitate was collected, then dried and recrystallized from ethanol (see Scheme 2).

**4-Phenylthiomorpholine-3,5-dione as compound (6a).** Follow the general procedure of 4-(substituted)phenylthiomorpholine-3,5-dione (6) using an aqueous solution of  $\text{Na}_2\text{S}\cdot 3\text{H}_2\text{O}$  (0.32 g; 2.00 mmol) and compound 4a (0.49 g; 2.00 mmol). White, yield: 83%, m.p. 172–174 °C, IR  $\text{vcm}^{-1}$  (KBr): 1651 (C=O amide), 752 (C-S), 1554 (C=C), 2914 (C-H<sub>al</sub>), 3198 (C-H<sub>ar</sub>), 3479 (C-OH), UV-Vis  $\lambda$  nm: 216 band I, 240 band II, 252 band III, Anal. Calculated for  $\text{C}_{10}\text{H}_9\text{NO}_2\text{S}$ : C, 57.95; H, 4.34; N, 6.76. Found: C, 56.79; H, 4.32; N, 6.74.

**4-*o*-Chlorophenylthiomorpholine-3,5-dione as compound (6b).** Follow the general procedure of 4-(substituted)phenylthiomorpholine-3,5-dione (6) using



**Scheme 2.** Synthesis of chalcogenides (6a-8d and 9) derivatives from *N*-aryl-2-chloro-*N*-(2-chloroacetyl) acetamide

an aqueous solution of  $\text{Na}_2\text{S}\cdot 3\text{H}_2\text{O}$  (0.32 g; 2.00 mmol) and compound 4b (0.56 g; 2.00 mmol). White, yield: 68%, m.p. 135–137 °C, IR  $\text{vcm}^{-1}$  (KBr): 1651 (C=O amide), 756 (C-S), 1531 (C=C), 2947 (C-H<sub>al</sub>), 3036 (C-H<sub>ar</sub>), 3452 (C-OH),  $^1\text{H}$ -NMR spectra (ppm) DMSO- $d_6$  solvent: 2.55 (1H<sub>3</sub>, s); 3.60 (4H<sub>1</sub>, s); 7.19–7.15 (1H<sub>7</sub>, t, Ar); 7.32–7.29 (1H<sub>8</sub>, t, Ar); 7.49–7.47 (1H<sub>9</sub>, d, Ar); 7.79–7.77 (1H<sub>6</sub>, d, Ar), UV-Vis  $\lambda$  nm: 216 band I, 240 band II, 257 band III, Anal. Calculated for *o*-ClC<sub>10</sub>H<sub>8</sub>NO<sub>2</sub>S: C, 49.48; H, 3.29; N, 5.77. Found: C, 49.50; H, 3.21; N, 5.78.

**4-*p*-Bromophenylthiomorpholine-3,5-dione as compound (6c).** Follow the general procedure of 4-(substituted)phenylthiomorpholine-3,5-dione (6) using an aqueous solution of  $\text{Na}_2\text{S}\cdot 3\text{H}_2\text{O}$  (0.32 g; 2.00 mmol) and compound 4c (0.65 g; 2.00 mmol). White, yield: 82%, m.p. 212–215 °C, IR  $\text{vcm}^{-1}$  (KBr): 1662 (C=O amide), 732 (C-S), 1543 (C=C), 2928 (C-H<sub>al</sub>), 3037 (C-H<sub>ar</sub>), 3502 (C-OH),  $^1\text{H}$  and  $^{13}\text{C}$ -NMR spectra (ppm) DMSO- $d_6$  solvent: 2.51 (1H<sub>3</sub>, s); 3.37 (4H<sub>1</sub>, s); 7.49–7.46 (1H<sub>6</sub> 1H<sub>8</sub>, d, Ar);

7.58–7.55 (1H<sub>5</sub> 1H<sub>9</sub>, d, Ar); 10.32 (OH, s) and 36.57 (2C<sub>1</sub>); 155.41 (C<sub>7</sub>); 121.57 (C<sub>6</sub>, C<sub>8</sub>); 132.00 (C<sub>5</sub>, C<sub>9</sub>); 138.83 (C<sub>4</sub>); 168.18 (C<sub>2</sub>, C<sub>3</sub>), respectively, UV-Vis  $\lambda$  nm: 227 band I, 240 band II, 258 band III, Anal. Calculated for *p*-BrC<sub>10</sub>H<sub>8</sub>NO<sub>2</sub>S: C, 41.81; H, 2.78; N, 4.87. Found: C, 41.77; H, 2.80; N, 4.85.

**4-*p*-Chlorophenylthiomorpholine-3,5-dione as compound (6d).** Follow the general procedure of 4-(substituted)phenylthiomorpholine-3,5-dione (6) using an aqueous solution of  $\text{Na}_2\text{S}\cdot 3\text{H}_2\text{O}$  (0.32 g; 2.00 mmol) and compound 4d (0.56 g; 2.00 mmol). White, yield: 80%, m.p. 183–185 °C, IR  $\text{vcm}^{-1}$  (KBr): 1662 (C=O amide), 740 (C-S), 1546 (C=C), 2935 (C-H<sub>al</sub>), 3063 (C-H<sub>ar</sub>), 3479 (C-OH),  $^1\text{H}$  and  $^{13}\text{C}$ -NMR spectra (ppm) DMSO- $d_6$  solvent: 2.44 (1H<sub>3</sub>, s); 3.52 (4H<sub>1</sub>, s); 7.38–7.35 (1H<sub>5</sub> 1H<sub>9</sub>, d, Ar); 7.64–7.61 (1H<sub>6</sub> 1H<sub>8</sub>, d, Ar); 10.36 (OH, s) and 38.71 (2C<sub>1</sub>); 123.36 (C<sub>6</sub>, C<sub>8</sub>); 129.58 (C<sub>4</sub>); 131.28 (C<sub>5</sub>, C<sub>9</sub>); 140.58 (C<sub>7</sub>); 170.34 (C<sub>2</sub>, C<sub>3</sub>), respectively, UV-Vis  $\lambda$  nm: 227 band I, 240 band II, 258 band III, Anal. Calculated

for *p*-BrC<sub>10</sub>H<sub>8</sub>NO<sub>2</sub>S: C, 49.48; H, 3.29; N, 5.77. Found: C, 49.51; H, 3.81; N, 5.76.

**4-Benzylthiomorpholine-3,5-dione as compound (7a).** Follow the general procedure of 4-(substituted) phenylthiomorpholine-3,5-dione (6) using an aqueous solution of Na<sub>2</sub>S·3H<sub>2</sub>O (0.32 g; 2.00 mmol) and compound 5a (0.52 g; 2.00 mmol). Pale-yellow, yield: 79%, m.p. 155–158 °C, IR vcm<sup>-1</sup> (KBr): 1647 (C=O amide), 736 (C-S), 1535 (C=C), 2916 (C-H<sub>al</sub>), 3032 (C-H<sub>ar</sub>), 3425 (C-OH), UV-Vis λ nm: 227 band I, 237 band II, 251 band III, Anal. Calculated for C<sub>11</sub>H<sub>11</sub>NO<sub>2</sub>S: C, 59.71; H, 5.01; N, 6.33. Found: C, 59.73; H, 5.11; N, 6.28.

**General procedure for the synthesis of compound (8) 4-(Substituted)phenylselenomorpholine-3,5-dione.**

To a suspended solution of Se powder (0.14 g; 1.8 mmol) in 25 mL of H<sub>2</sub>O has added a solution of NaBH<sub>4</sub> (0.118 g; 3.1 mmol) in 25 mL of H<sub>2</sub>O under an argon atmosphere. A vigorous reaction occurs with the evolution of hydrogen gas. Se powder was consumed in less than 10 min, and a colorless solution of sodium hydrogen selenide NaHSe was formed [7]. To the resulting solution was added a solution of compound 4 (1.8 mmol) in 20 mL of ethanol under an argon atmosphere. After about 30 min, a colored precipitate was formed, collected by filtration and washed several times with ethanol, dried, and then Recrystallized from ethanol [20] (Scheme 2).

**4-Phenylselenomorpholine-3,5-dione as compound (8a).** Follow the general procedure of 4-(substituted) phenylselenomorpholine-3,5-dione (8) using a colorless solution of sodium hydrogen selenide NaHSe (prepared from the reduction of selenium with sodium borohydride) and a solution of compound 4a (0.48 g; 1.8 mmol) under argon atmosphere. Violet, yield: 83%, m.p. 172–174 °C, IR vcm<sup>-1</sup> (KBr): 1647 (C=O amide), 497 (C-Se), 1554 (C=C), 2943 (C-H<sub>al</sub>), 3144 (C-H<sub>ar</sub>), 3290 (C-OH), UV-Vis λ nm: 216 band I, 240 band II, 252 band III, Anal. Calculated for C<sub>10</sub>H<sub>9</sub>NO<sub>2</sub>Se: C, 47.25; H, 3.54; N, 5.51. Found: C, 47.22; H, 3.59; N, 5.49.

**4-*o*-Chlorophenylselenomorpholine-3,5-dione as compound (8b).** Follow the general procedure of 4-(substituted)phenylselenomorpholine-3,5-dione (8) using a colorless solution of sodium hydrogen selenide NaHSe (prepared from the reduction of selenium with sodium

borohydride) and a solution of compound 4b (0.50 g; 1.8 mmol) under argon atmosphere. Pale gray, yield: 80%, m.p. 121–123 °C, IR vcm<sup>-1</sup> (KBr): 1654 (C=O amide), 486 (C-Se), 1531 (C=C), 2952 (C-H<sub>al</sub>), 3252 (C-H<sub>ar</sub>), 3448 (C-OH), <sup>1</sup>H-NMR spectra (ppm) DMSO-*d*<sub>6</sub> solvent: 3.31 (1H<sub>3</sub>, s); 3.63 (4H<sub>1</sub>, s); 7.21–7.17 (1H<sub>7</sub>, t, Ar); 7.34–7.31 (1H<sub>8</sub>, t, Ar); 7.51–7.49 (1H<sub>9</sub>, d, Ar); 7.81–7.79 (1H<sub>6</sub>, d, Ar); 9.70 (OH, s), UV-Vis λ nm: 216 band I, 240 band II, 257 band III, Anal. Calculated for *o*-ClC<sub>10</sub>H<sub>8</sub>NO<sub>2</sub>Se: C, 41.46; H, 2.76; N, 4.83. Found: C, 41.44; H, 2.75; N, 4.80.

**4-*p*-Bromophenylselenomorpholine-3,5-dione as compound (8c).** Follow the general procedure of 4-(substituted)phenylselenomorpholine-3,5-dione (8) using a colorless solution of sodium hydrogen selenide NaHSe (prepared from the reduction of selenium with sodium borohydride) and a solution of compound 4c (0.58 g; 1.8 mmol) under argon atmosphere. Pale gray, yield: 80%, m.p. 201–203 °C, IR vcm<sup>-1</sup> (KBr): 1658 (C=O amide), 501 (C-Se), 1539 (C=C), 2939 (C-H<sub>al</sub>), 3117 (C-H<sub>ar</sub>), 3275 (C-OH), <sup>1</sup>H and <sup>13</sup>C-NMR spectra (ppm) DMSO-*d*<sub>6</sub> solvent: 2.51 (1H<sub>3</sub>, s); 3.37 (4H<sub>1</sub>, s); 7.49–7.46 (1H<sub>6</sub> 1H<sub>8</sub>, d, Ar); 7.58–7.55 (1H<sub>5</sub> 1H<sub>9</sub>, d, Ar); 10.32 (OH, s) and 3.33 (1H<sub>3</sub>, s); 4.26 (4H<sub>1</sub>, s); 7.52–7.47 (1H<sub>6</sub> 1H<sub>8</sub>, d, Ar); 7.57–7.53 (1H<sub>5</sub> 1H<sub>9</sub>, d, Ar); 10.27 (OH, s), respectively, UV-Vis λ nm: 240 band I, 258 band II, 271 band III, Anal. Calculated for *p*-BrC<sub>10</sub>H<sub>8</sub>NO<sub>2</sub>Se: C, 35.94; H, 2.39; N, 4.19. Found: C, 35.89; H, 2.37; N, 4.21.

**4-*p*-Chlorophenylselenomorpholine-3,5-dione as compound (8d).** Follow the general procedure of 4-(substituted)phenylselenomorpholine-3,5-dione (8) using a colorless solution of sodium hydrogen selenide NaHSe (prepared from a reduction of selenium with sodium borohydride) and a solution of compound 4d (0.50 g; 1.8 mmol) under argon atmosphere. Pale pink, yield: 79%, m.p. 197–198 °C, IR vcm<sup>-1</sup> (KBr): 1658 (C=O amide), 505 (C-Se), 1543 (C=C), 2939 (C-H<sub>al</sub>), 3190 (C-H<sub>ar</sub>), 3279 (C-OH), <sup>1</sup>H and <sup>13</sup>C-NMR spectra (ppm) DMSO-*d*<sub>6</sub> solvent: 3.55 (1H<sub>3</sub>, s); 4.27 (4H<sub>1</sub>, s); 7.39–7.35 (1H<sub>5</sub> 1H<sub>9</sub>, d, t, Ar); 7.62–7.59 (1H<sub>6</sub> 1H<sub>8</sub>, d, Ar); 10.28 (OH, s) and 29.57 (2C<sub>1</sub>); 121.10 (C<sub>7</sub>); 127.13 (C<sub>6</sub>, C<sub>8</sub>); 129.13 (C<sub>5</sub>, C<sub>9</sub>); 138.46 (C<sub>4</sub>); 169.23 (C<sub>2</sub>, C<sub>3</sub>), respectively, UV-Vis λ nm: 216 band I, 240 band II, 258 band III,



Anal. Calculated for *p*-ClC<sub>10</sub>H<sub>8</sub>NO<sub>2</sub>Se: C, 41.46; H, 2.76; N, 4.83. Found: C, 41.40; H, 2.66; N, 4.83.

**4-Benzylselenomorpholine-3,5-dione as compound (9a).** Follow the general procedure of 4-(substituted) phenylselenomorpholine-3,5-dione (8) using a colorless solution of sodium hydrogen selenide NaHSe (prepared from a reduction of selenium with sodium borohydride) and a solution of compound 5a (0.46 g; 1.8 mmol) under argon atmosphere. Pale violet, yield: 83%, m.p. 132–134 °C, IR  $\nu_{\text{cm}^{-1}}$  (KBr): 1647 (C=O amide), 493 (C-Se), 1550 (C=C), 2920 (C-H<sub>al</sub>), 3059 (C-H<sub>ar</sub>), 3271 (C-OH), UV-Vis  $\lambda$  nm: 216 band I, 240 band II, 252 band III, Anal. Calculated for C<sub>11</sub>H<sub>11</sub>NO<sub>2</sub>Se: C, 47.25; H, 3.54; N, 5.51. Found: C, 47.22; H, 3.59; N, 5.49.

### Biological evaluation

Cytotoxicity is one of the most important indicators of biological evaluation test that use tissue cells (normal and cancer cell line); HBL-100 and MCF-7, respectively. The MTT assay is typically performed after the insoluble formazan produced is then solubilized by organic solvent such as DMSO (positive control), while serum-free media is considered as negative control.

### Cytotoxicity measurement

To determine the cytotoxic effect of organo-chalcogen compounds; 4-(substituted)phenylthiomorpholine-3,5-dione (**6a–6d**, **7a**) and 4-(substituted)phenylselenomorpholine-3,5-dione (**8a–8d**, **9a**), the 3-(4,5-dimethylthiazole)-2,5-diphenyltetrazolium bromide (MTT) assay was used by reseeded [20] and then incubated at 37 °C and 5% CO<sub>2</sub>. Cells were placed in 96-well micro assay culture plates (1 × 10<sup>4</sup>) cells/well. After 24 h or a confluent monolayer was achieved, cells were treated with the tested compounds (I–X) (**6a–8d**, **9a**), which dissolved in DMSO at a concentration of 1000 µg/mL. Suspended cell with complete media 10% reseeded in 96-well plate 100 µL (1 × 10<sup>4</sup>) cells/well, incubated at 37 °C and 100% humidity 5% CO<sub>2</sub>. Untreated cells serve as a control group.

Cell viability was measured after 72 h of treatment by removing the medium, adding 28 µL of 2 mg/mL solution of MTT, and incubating the cells for 2 h at 37 °C. After removing the MTT solution, the crystals remaining

in the wells were solubilized by the addition of 100 µL of DMSO and followed by 37 °C incubation for 15 min with shaking [21]. The optical density of each well was measured on a microplate reader at 620 nm (test wavelength). The assay was performed in triplicate to obtain mean values and the inhibition rate of cell growth. The percentage of cytotoxicity was calculated according to Eq. (1)

$$PR = \frac{B}{A \times 100} \quad (1)$$

where PR represents the proliferation rate, B represents the absorbance of compound-treated wells and A represents absorbance for a non-treated control group. Therefore, the inhibition rate (IR) was calculated using Eq. (2) [22].

$$IR = 100 - PR \quad (2)$$

### Apoptosis studies with AO/EB staining method

Dual acridine orange/ethidium bromide (AO/EB) fluorescent staining, visualized under a fluorescent microscope, was employed to identify apoptosis-associated changes in cells during the process of apoptosis [23]. Dual fluorescent staining solution (1 µL) containing (5 mg/mL) acridine orange (AO) and (1 µL) containing (3 mg/mL) ethidium bromide (EB) was added to each 1 mL of phosphate buffer saline (PBS) and mixed well, then stored at room temperature and make fresh every few weeks before using. AO/EB stained MCF-7 cells. Cell death can occur in several modes when the cells are exposed to cytotoxic agents.

### DNA binding experiments

The human-DNA interactive studies of compound **8a** were carried out in 5 mmol/L Tris-HCl and 5 mmol/L NaCl buffer (10 mM, pH = 7.2) which was prepared in deionized water. The 50 µM DNA stock in the buffer gave a ratio of UV absorbance at 260 and 280 nm of about > 1.86 indicating that the human DNA that was used for absorption titration was sufficiently free from protein [24].

The concentration of DNA per nucleotide was determined by using the molar absorption coefficient  $\epsilon_{260} = 6600 \text{ M}^{-1} \text{ cm}^{-1}$ . The resulting DNA stock solution was kept at 4 °C and used within 24 h. A solution of 4-phenylselenomorpholine-3,5-dione (ligand **8a**) with

constant concentration  $5 \times 10^{-5}$  M, was prepared in 10% DMSO with 90% Tris-HCl buffer. Upon addition of varying concentrations of DNA stock solution (20–120  $\mu$ M over 20  $\mu$ M increments the resultant solutions) were incubated at 25 °C for 15 min before recording UV spectra [25]. The intrinsic binding constant ( $k_b$ ) was determined by fitting the titration data into the following Eq. (3) [26]

$$\frac{[\text{DNA}]}{\varepsilon_a - \varepsilon_f} = \frac{[\text{DNA}]}{\varepsilon_b - \varepsilon_f} + \frac{1}{k_b(\varepsilon_b - \varepsilon_f)} \quad (3)$$

where  $\varepsilon_a$ ,  $\varepsilon_f$  and  $\varepsilon_b$  are apparent, free, and bound ligand extinction coefficients, respectively. The  $\varepsilon_f$  was determined from a calibration curve of an isolated ligand following Beer's law. The  $\varepsilon_a$  matches the extinction coefficient of the particular absorption band at the specified DNA concentration (corresponding to  $A_{\text{obs}}/[\text{complex}]$ ),  $\varepsilon_b$  is equated to the extinction coefficient of a fully bound ligand to DNA. The plot of  $([\text{DNA}])/(\varepsilon_a - \varepsilon_b)$  versus  $[\text{DNA}]$ , produces a slope  $1/(\varepsilon_a - \varepsilon_f)$  and a Y-intercept of  $1/k_b(\varepsilon_b - \varepsilon_f)$ . The ratio of slope to the Y-intercept is expected to be the intrinsic binding constant ( $k_b$ ).

## ■ RESULTS AND DISCUSSION

### Thermogravimetric Study

The thermo-analytical methods (TG/DTA) were used in this work to evaluate the thermal stability, kinetic, and thermodynamic characteristic parameters. The thermal decomposition of some prepared ligands was done from ambient temperature to 800 °C under an argon atmosphere using  $\alpha\text{-Al}_2\text{O}_3$  as a reference. Kinetic parameters like frequency factor; Z; and activation energy,  $E_a$  of four chalcogen ligands were calculated from the Arrhenius plot of the rate of decomposition; Eq. (4-6)  $\ln k$  versus  $1/T_s$ .  $E_a$  was calculated from the slope and Z defined from the obtained intercept. The low value of Z indicates that the

decomposition process was slow in nature [27]. The temperature of half weight loss ( $T_{50\%}$ ), which represents the temperature at which the sample loses half of its total weight, has been appointed. The thermodynamic parameters (entropy  $\Delta S^\ddagger$ , enthalpy  $\Delta H^\ddagger$  and free energy  $\Delta G^\ddagger$ ) of the decomposing process were calculated by analyzing the TG curves mathematically using the Freeman-Carroll equation [28]. These calculations are dependent on the peak temperature  $T_s$  in order to get the highest rate of process Table 1. The negative value of  $\Delta S^\ddagger$  indicates that the decomposition reactions proceed spontaneously and indicates that the activated ligands have more ordered structures than the reactants [29]. The thermal decomposition process of some of these ligands has one decomposition temperature (7a), while the others have two (8d, 6d) or three (6a) decomposition temperatures (Fig. 2). The thermogram results show that the order of relative thermal stability of these ligands is 7a > 8d > 6d > 6a according to the decomposition temperature, while according to the crucial kinetic standards, the  $E_a$  values of these ligands take the order of 7a < 6d < 8d < 6a, which mostly differ from those defined by the thermal stability.

$$\Delta S^\ddagger = 2.303 \log \left( \frac{Z h}{k_b T_s} \right) R \quad (4)$$

$$\Delta H^\ddagger = E_a - RT_s \quad (5)$$

$$\Delta G^\ddagger = \Delta H^\ddagger - T \Delta S^\ddagger \quad (6)$$

### In Vitro Cytotoxicity MTT Test

To assess the cytotoxic activity of the ten ligands (6a–8d), the cell viability was determined by the MTT test, a colorimetric assay determined by the mitochondrial-dependent reduction of soluble yellow tetrazolium salt to blue formazan crystals [30-31]. The data received from

**Table 1.** Thermal stability and thermodynamic parameters of prepared compounds

Compd	$W_t$	$T_s$ [K]	Temp. of 50 wt.% loss (°C)	Rate of decomp.	Char. content 800 °C, (%)	Activation energy ( $E_a$ )	Temp. range (°C)	Z	$\Delta H^\ddagger$ (KJ/mol)	$\Delta S^\ddagger$ (J/mol k)	$\Delta G^\ddagger$ (KJ/mol)
6a	1.069	538.99	381.25	2.8	5.80	15.83	69–244	0.0012	11.35	–9.490	026.8
7a	2.163	578.33	246.00	3.4	15.0	14.07	67–172	0.0080	09.27	–275.7	168.7
6d	3.634	544.37	306.25	2.7	24.6	15.04	56–231	0.0003	10.51	–163.5	099.5
8d	1.568	550.91	321.50	3.4	8.20	15.63	125–250	0.0010	11.05	–324.6	289.5

this assay was analyzed by subtraction of the blank control absorbance value from all the other values. The DMSO-solvent control value is set to 100% viability, as no growth-inhibiting compound was added [32]. Fig. 3 shows the vitality of the cell line MCF-7 and normal breast cell line (HBL-100) when exposed to one concentration 1000  $\mu\text{g}/\text{mL}$  for each one of the ten ligands (**6a–8d**) prepared. This concentration causes growth inhibition of normal and human MCF-7 breast cancer cells. The highest rate of vital percentage was 72.4% of *p*-chlorophenylthiomorpholine-3,5-dione (**6d**) ligand, while the lowest rate of vital percentage was 32% of 4-phenylselenomorpholine-3,5-dione (**8a**) ligand. While the normal cell line HBL-100, exposed to 4-phenylselenomorpholine-3,5-dione (**8a**) ligand and benzylselenomorpholine-3,5-dione (**9a**) ligand at the same concentration 1000  $\mu\text{g}/\text{mL}$  for 72 h. The results showed that the vitality of the normal breast cell line was affected by these two ligands, **8a** and **9a**, and the rate of vital percentage was 30.9 and 39.3%, respectively. The percentage of cell viability was plotted against the concentration of compound added to the medium (Fig. 1).

#### AO/EB Staining and Programmed Cell Death

The AO/EB dye was employed to stain MCF-7 breast cancer cells that examine by fluorescence microscopic before and after treatment with compounds

**8a** and **8c**. Thus, this assay was conducted to diagnose stages of programmed cell death. Cells that have undergone apoptosis are non-viable and emit red fluorescence upon binding of AO/EB to ssDNA or RNA, as the red blocks indicate the advanced stages of cell death. The viable cells colored green refer to the combined dye to dsDNA, while lumpy chromatin formed in yellow indicates the early stages of nucleus fragmentation and the appearance of cell death bodies [17].

Fig. 2 explores the microscopic fluorescence images of MCF-7 breast cancer cell line untreated (Fig. 2(a)) and treated AO/EB stained cells with compounds (**8a**) and (**8c**), Fig. 2(b) and 2(c), respectively. The untreated cells appear unaffected, showing a single integral monolayer of healthy and highly organized structure as they emit green fluorescence with AO/EB at magnification 10 $\times$ . The MCF-7 cell line grill with AO/EB dye treated with compounds (**8a**), Fig. 2(b), and (**8c**), Fig. 2(c) appeared affected as they lost their normal characteristics. Thus, the appearance of the yellow-colored nucleus fragments indicates the early stages of programmed cell death showing large areas lacking cells at magnification 40 $\times$  (Fig. 2(d) and 2(e)). The emergence of the large spaces devoid of cells in Fig. 2(e) reveals clearly that (**8c**) is more effective than compound (**8a**).

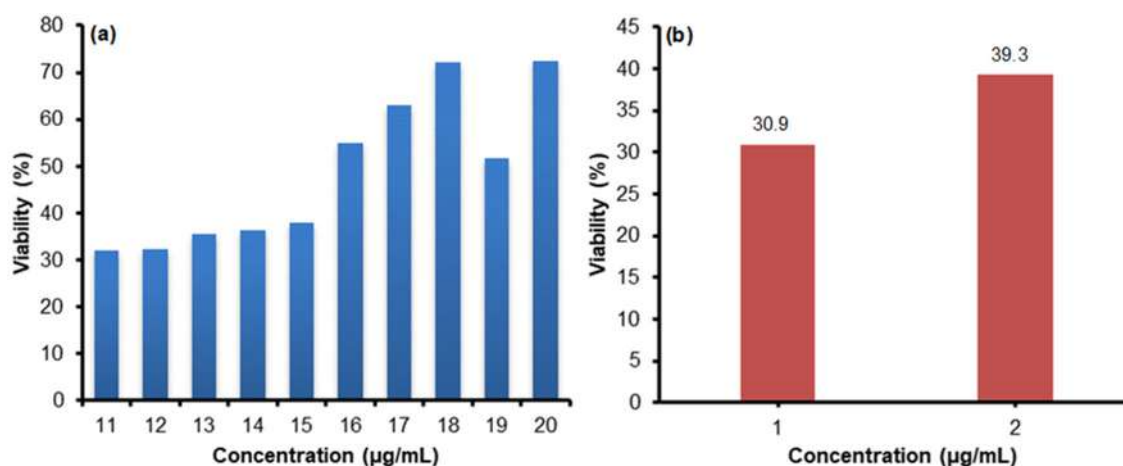


**Fig 1.** Percentage of cell viability in the cell line of (a) Breast cancer type (MCF-7) vs one concentration 1000  $\mu\text{g}/\text{mL}$  for each one of the five (11–15) 4-(substituted)phenylselenomorpholine ligands (**8a–8d**), and of another five (16–20) 4-(substituted)phenylthiomorpholine ligands (**6a–6d**), (b) Normal breast cell line (HBL-100) vs one concentration 1000  $\mu\text{g}/\text{mL}$  for each one of the two ligands (1 and 2) 4-phenylselenomorpholine ligand (**8a**) and 4-benzylselenomorpholine ligand (**9a**), respectively added to the medium

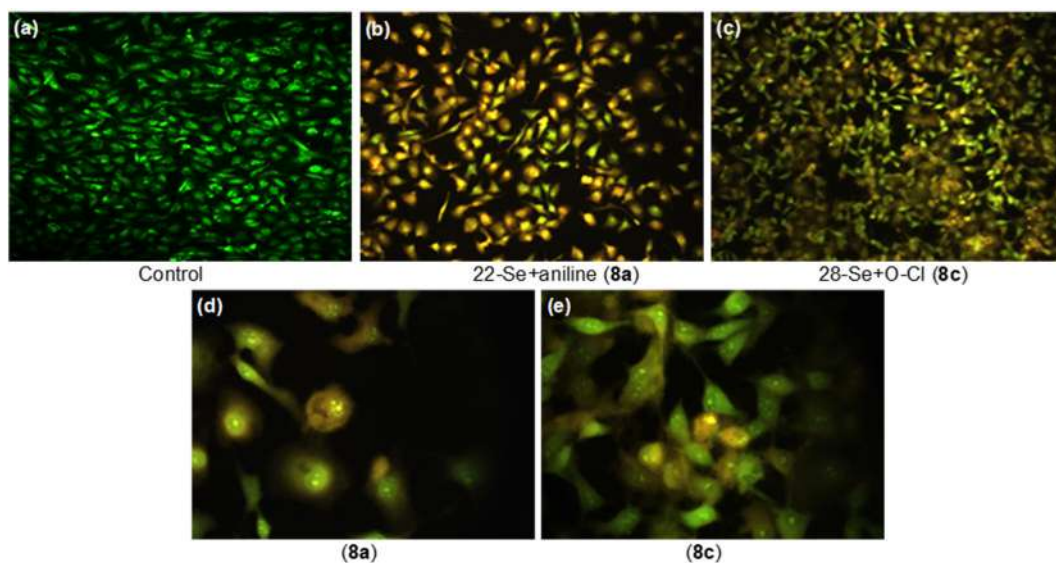


**Fig 2.** MCF-7 cell line dye AO/EB stain, (a) Untreated cells look unaffected, forming a monolayer strain green with AO/EB at magnification 10 $\times$ , (b) Cells treated with compound (**8a**) appear affected as colored in yellow AO/EB at magnification 10 $\times$ , (c) Cells treated with compound (**8c**); losing of normal characteristics refers to one of the early stages of cell death, AO/EB at magnification 10 $\times$ . (d) and (e) images of (**8a**) and (**8c**) at magnification 40 $\times$

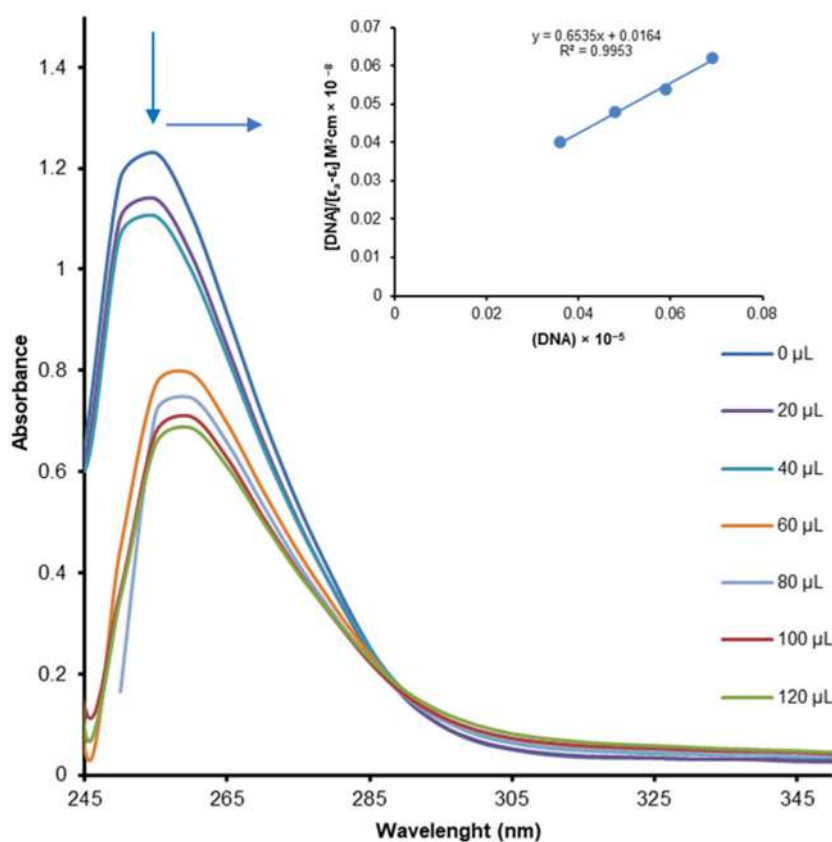


**Fig 3.** Overlay UV-Vis spectra of 4-phenylselenomorpholine, ligand (**8a**), in the absence and presence of increasing amounts of human-DNA. Arrow indicates that absorbance changes upon increasing DNA concentrations. Inset: Plot of  $[DNA]/(\epsilon_a - \epsilon_f) \times 10^8$  vs  $[DNA] \times 10^5$  and the linear fit for the titration

## DNA-Binding

Absorption studies: the binding of prepared ligands to the helix has been characterized through the measurement of absorbance and the significant shift of maxima as a function of an added amount of DNA (20–120  $\mu\text{M}$ ) to a fixed ligands concentration ( $3.0 \times 10^{-4} \mu\text{M}$ ). For ligand **8a** (Fig. 3), the broadband at 260 nm was monitored as it has been noticed that an increase in the amount of DNA led to decreasing in molar absorptivity beside an 8–10 nm red shift i.e., a hypochromic shift indicating intercalative interaction of compound **8a** with DNA. The intrinsic binding constant was found to be  $k_b = 3.60 \times 10^6 \text{ M}^{-1}$  suggesting moderate intercalative interaction, compared to classical intercalators ( $k_b \sim 10^6$ ) function of added DNA. The isosbestic point at 290 nm confirms the bonding of ligands with DNA [33–34].

## CONCLUSION

According to the decomposition temperature of the newly chalcogen ligands in the current study, the thermogram results show that the relative thermal stability of these ligands takes this order **7a** > **8d** > **6d** > **6a** while their activation energies  $E_a$  take another order **7a** < **6d** < **8d** < **6a** differs completely from that sequence. The results of absorption studies show that the absorption intensity decreased (hypochromic) evidently after the addition of DNA, which indicates that the interaction between DNA and ligand **8a** occurred. The intrinsic binding constant ( $k_b = 3.42 \times 10^6 \text{ M}^{-1}$ ) is roughly comparable to other intercalators' interactions. According to the toxicity by new ligands through the MTT-assay to both normal and cancerous lines, they have no selective or directed action on cancerous cells. Nevertheless, this method does not provide any information regarding the cell death mechanism, the phase in the cell cycle that is affected by the drug and its possible biological target. AO/EB assay and cell cycle analysis were conducted to diagnose stages of programmed cell death. It can be concluded that the low viability percentage of compounds **8a** and **8c** (Fig. 3), besides the cytofluorimetric inconclusive results, may indicate that these prepared compounds may have the ability of cell-growth inhibition. More studies need to be

subjected to confirm this conclusion, such as the employment of variable concentrations of these compounds and increasing the time of exposure.

## ACKNOWLEDGMENTS

The authors would like to acknowledge the University of Basrah, Faculty of Science, Department of Chemistry for supporting this work and Professor Ali Abd Allateef Abd Alhassan Al-Ali, Biological Department, College of Education for Basic Science, University of Basrah, for analyzing the cytotoxic effects.

## AUTHOR CONTRIBUTIONS

Hayat Hamza Abbas who is a PhD student at the Chemistry Department at College of Science has done all the experiments with supervisors. All authors have read and approved the manuscript.

## REFERENCES

- [1] Garrett, G.E., Gibson, G.L., Straus, R.N., Seferos, D.S., and Taylor, M.S., 2015, Chalcogen bonding in solution: Interactions of benzotelluradiazoles with anionic and uncharged Lewis bases, *J. Am. Chem. Soc.*, 137 (12), 4126–4133.
- [2] Alcolea, V., Garnica, P., Palop, J.A., Sanmartín, C., González-Peñas, E., Durán, A., and Lizarraga, E., 2017, Antitumoural sulphur and selenium heteroaryl compounds: Thermal characterization and stability evaluation, *Molecules*, 22 (8), 1314.
- [3] Uivarosi, V., Badea, M., Aldea, V., Chirigiu, L., and Olar, R., 2013, Thermal and spectral studies of palladium(II) and platinum(IV) complexes with dithiocarbamate derivatives, *J. Therm. Anal. Calorim.*, 111 (2), 1177–1182.
- [4] Zhou, G., Deng, X., Pan, C., Goh, E.T.L., Lakshminarayanan, R., and Srinivasan, R., 2020, SLAP reagents for the photocatalytic synthesis of C3/C5-substituted, *N*-unprotected selenomorpholines and 1,4-selenazepanes, *Chem. Commun.*, 56 (83), 12546–12549.
- [5] Li, Q., Zhang, Y., Chen, Z., Pan, X., Zhang, Z., Zhu, J., and Zhu, X., 2020, Organoselenium chemistry-based polymer synthesis, *Org. Chem. Front.*, 7 (18), 2815–2841.

- [6] Mamgain, R., Kostic, M., and Singh, F.V., 2023, Synthesis and antioxidant properties of organoselenium compounds, *Curr. Med. Chem.*, 29, 0929867329666220801165849.
- [7] Rother, M., and Quitzke, V., 2018, Selenoprotein synthesis and regulation in *Archaea*, *Biochim. Biophys. Acta, Gen. Subj.*, 1862 (11), 2451–2462.
- [8] Solovyev, N.D., 2015, Importance of selenium and selenoprotein for brain function: From antioxidant protection to neuronal signalling, *J. Inorg. Biochem.*, 153, 1–12.
- [9] Liu, T., Yang, T., Xu, Z., Tan, S., Pan, T., Wan, N., and Li, S., 2018, MicroRNA-193b-3p regulates hepatocyte apoptosis in selenium-deficient broilers by targeting MAML1, *J. Inorg. Biochem.*, 186, 235–245.
- [10] Rangraz, Y., Nemati, F., and Elhampour, A., 2020, Selenium-doped graphitic carbon nitride decorated with Ag NPs as a practical and recyclable nanocatalyst for the hydrogenation of nitro compounds in aqueous media, *Appl. Surf. Sci.*, 507, 145–164.
- [11] Du, P., Viswanathan, U.M., Xu, Z., Ebrahimnejad, H., Hanf, B., Burkholz, T., Schneider, M., Bernhardt, I., Kirsch, G., and Jacob, C., 2014, Synthesis of amphiphilic seleninic acid derivatives with considerable activity against cellular membranes and certain pathogenic microbes, *J. Hazard. Mater.*, 269, 74–82.
- [12] Kamal, A., Nazari, M., Yaseen, M., Iqbal, M.A., Ahamed, M.B.K., Majid, A.S.A., and Bhatti, H.N., 2019, Green synthesis of selenium-*N*-heterocyclic carbene compounds: Evaluation of antimicrobial and anticancer potential, *Bioorg. Chem.*, 90, 103042.
- [13] Khalifa, M.E., Abdel-Hafez, S.H., Gobouri, A.A., and Kobeasy, M.I., 2015, Synthesis and biological activity of novel arylazothiazole disperse dyes containing selenium for dyeing polyester fibers, *Phosphorus, Sulfur Silicon Relat. Elem.*, 190 (4), 461–476.
- [14] Cisnetti, F., and Gautier, A., 2013, Metal/*N*-heterocyclic carbene complexes: Opportunities for the development of anticancer metallodrugs, *Angew. Chem., Int. Ed.*, 52 (46), 11976–11978.
- [15] Francioso, A., Conrado, A.B., Mosca, L., and Fontana, M., 2020, Chemistry and biochemistry of sulfur natural compounds: Key intermediates of metabolism and redox biology, *Oxid. Med. Cell. Longevity*, 2020, 8294158.
- [16] Castellano, I., and Seebeck, F.P., 2018, On ovothiols biosynthesis and biological roles: From life in the ocean to therapeutic potential, *Nat. Prod. Rep.*, 35 (12), 1241–1250.
- [17] Al-Harbi, S.A., Al-Saidi, H.M., Debbabi, K.F., Allehyani, E.S., Alqorashi, A.A., and Emara, A.A.A., 2020, Design and anti-tumor evaluation of new platinum(II) and copper(II) complexes of nitrogen compounds containing selenium moieties, *J. Saudi Chem. Soc.*, 24 (12), 982–995.
- [18] Khalib, A.A.K., Al-Hazam, H.A.J., and Hassan, A.F., 2022, Inhibition of carbon steel corrosion by some new organic 2-hydroselenoacetamide derivatives in HCl medium, *Indones. J. Chem.*, 22 (5), 1269–1281.
- [19] Hassan, A.F., Abdalwahed, A.T., Al-Luaibi, M.Y., and Aljadaan, S.A., 2021, Synthesis, characterization and thermal study of some new organochalcogenide compounds containing arylamide group, *Egypt. J. Chem.*, 64 (9), 5009–5015.
- [20] Al-Ali, A.A.A., and Jawad, R.K., 2021, Cerium oxide nanoparticles CeO<sub>2</sub>NP and retinoic acid trigger cytotoxicity and apoptosis pathway in human breast cell lines, *Ann. Rom. Soc. Cell Biol.*, 35 (4), 8448–8477.
- [21] Al-Shammari, A.M., Al-Esmaeel, W.N., Al-Ali, A.A.A., Hassan, A.A., and Ahmed, A.A., 2019, Enhancement of oncolytic activity of Newcastle disease virus through combination with retinoic acid against digestive system malignancies, *Mol. Ther.*, 27 (4S1), 126–127.
- [22] Freshney, R.I., 2015, *Culture of Animal Cells: A Manual of Basic Technique and Specialized Applications*, John Wiley & Sons, Hoboken, New Jersey.
- [23] He, M., Du, F., Zhang, W.Y., Yi, Q.Y., Wang, Y.J., Yin, H., Bai, L., Gu, Y.Y., and Liu, Y.J., 2019,

- Photoinduced anticancer effect evaluation of ruthenium(II) polypyridyl complexes toward human lung cancer A549 cells, *Polyhedron*, 165, 97–110.
- [24] Abdel-Rahman, L.H., El-Khatib, R.M., Nassr, L.A.E., and Abu-Dief, A.M., 2017, DNA binding ability mode, spectroscopic studies, hydrophobicity, and *in vitro* antibacterial evaluation of some new Fe(II) complexes bearing ONO donors amino acid Schiff bases, *Arabian J. Chem.*, 10, S1835–S1846.
- [25] Kaplanis, M., Stamatakis, G., Papakonstantinou, V.D., Paravatou-Petsotas, M., Demopoulos, C.A., and Mitsopoulou, C.A., 2014, Re(I) tricarbonyl complex of 1,10-phenanthroline-5,6-dione: DNA binding, cytotoxicity, anti-inflammatory and anti-coagulant effects towards platelet activating factor, *J. Inorg. Biochem.*, 135, 1–9.
- [26] Bondi, R., Biver, T., Dalla Via, L., Guarra, F., Hyeraci, M., Sissi, C., Labella, L., Marchetti, F., and Samaritani, S., 2020, DNA interaction of a fluorescent, cytotoxic pyridinimino platinum(II) complex, *J. Inorg. Biochem.*, 202, 110874.
- [27] Hsu, S.Y., Murphy, M.C., Smolensky, N.T., Vogels, C.M., Lebel, A.A., Masuda, J.D., Boudreau, L.H., Morin, P., and Westcott, S.A., 2023, Iminophosphine platinum(II) complexes containing long chain aniline derivatives: Synthesis, characterization, and anticancer properties, *Polyhedron*, 230, 116236.
- [28] Gul, H., Shah, A.H.A., Gul, S., Arjomandi, J., and Bilal, S., 2018, Study on the thermal decomposition kinetics and calculation of activation energy of degradation of poly(*o*-toluidine) using thermogravimetric analysis, *Iran. J. Chem. Chem. Eng.*, 37 (1), 193–204.
- [29] Song, M.Y., and Kwak, Y.J., 2022, Three methods for application of data from a volumetric method to the Kissinger equation to obtain activation energy, *Micromachines*, 13 (11), 1809.
- [30] Patnaik, S., Panda, A.K., and Kumar, S., 2020, Thermal degradation of corn starch based biodegradable plastic plates and determination of kinetic parameters by isoconversional methods using thermogravimetric analyzer, *J. Energy Inst.*, 93 (4), 1449–1459.
- [31] da Silva, M.M., de Camargo, M.S., Castelli, S., de Grandis, R.A., Castellano, E.E., Deflon, V.M., Cominetti, M.R., Desideri, A., and Batista, A.A., 2020, Ruthenium(II)-mercapto complexes with anticancer activity interact with topoisomerase IB, *J. Braz. Chem. Soc.*, 31 (3), 536–549.
- [32] Ganot, N., Meker, S., Reytman, L., Tzuber, A., and Tshuva, E.Y., 2013, Anticancer metal complexes: Synthesis and cytotoxicity evaluation by the MTT assay, *J. Visualized Exp.*, 81, e50767.
- [33] Swathy, S., Chandran, H., Reshma, G., Nakul, S., Kumar, M., Krishnan, M.A., Kulkarni, N.V., and Arakera, S.B., 2022, First row transition metal complexes of bis(3,5-dimethyl pyrazolyl)methane: Synthesis, molecular structure and antibacterial properties, *J. Mol. Struct.*, 1251, 132018.
- [34] Tarai, S.K., Mandal, S., Bhaduri, R., Pan, A., Biswas, P., Bhattacharjee, A., and Moi, S.C., 2023, Bioactivity, molecular docking and anticancer behavior of pyrrolidine based Pt(II) complexes: Their kinetics, DNA and BSA binding study by spectroscopic methods, *Spectrochim. Acta, Part A*, 287, 122059.

## Microencapsulation of *Ruellia tuberosa* L. Extracts Using Alginate: Preparation, Biological Activities, and Release

Andriana Kusuma Pertiwi<sup>1</sup>, Choirin Annisa<sup>1</sup>, Zubaidah Ningsih<sup>1</sup>, and Anna Safitri<sup>1,2\*</sup>

<sup>1</sup>Department of Chemistry, Faculty of Mathematics and Natural Sciences, Brawijaya University, Jl. Veteran, Malang 65145, Indonesia

<sup>2</sup>Research Centre of SMONAGENES (Smart Molecules of Natural Genetic Resources), Brawijaya University, Jl. Veteran, Malang 65145, Indonesia

\* **Corresponding author:**

email: a.safitri@ub.ac.id

Received: August 3, 2022

Accepted: November 1, 2022

DOI: 10.22146/ijc.76821

**Abstract:** The bioactive compounds naturally present in plants have great importance due to their biological characteristics. These substances could lose their active characteristics since they are highly unstable. Microencapsulation is one of the techniques to improve stability and protect these compounds. In this work, *Ruellia tuberosa* L. ethanolic extracts microcapsules were prepared using a freeze-drying method by varying pH, alginate concentration, and stirring time. The encapsulation efficiency (EE), characteristics, alpha-amylase inhibition activity, and release behavior of the microcapsules were investigated. The results highlighted that the highest encapsulation efficiency for the microcapsules was obtained at pH 6, alginate concentration of 1% (w/v), and 30 min of stirring time (51.63% EE). The microcapsules mostly had spherical shapes with a mean diameter of 197.53  $\mu\text{m}$ . The alpha-amylase inhibition assay from microcapsules resulted in the  $\text{IC}_{50}$  value of  $46.66 \pm 0.13 \mu\text{g/mL}$ , demonstrating high biological activity. The bioactive substances from microcapsules were released during intervals of 30–120 min at pH values of 1.2 and 7.4. Only 3.51% of the bioactive substances were released at pH 1.2 after 120 min, compared to 55.78% at pH 7.4. Overall, this work confirms the possibility of developing plant extracts with preserved biological activity using the produced microcapsules.

**Keywords:** alginate; alpha-amylase; freeze drying; microencapsulation; *Ruellia tuberosa* L.

### ■ INTRODUCTION

Discovering bioactive compounds in natural materials can support the expansion of their functional value in both disease prevention and treatment. Indonesia has a wide variety of plants and has been represented as one of the best producers of medicinal plants. Along with the times, the use of medicinal plants in the treatment of disease increased due to their fewer side effects [1-2]. *Ruellia tuberosa* Linn is a herbaceous plant of the *Acanthaceae* family from Central America and has widely spread in Southeast Asia countries, such as Indonesia. Based on the previous study, the leaves of this plant had anti-inflammatory activity; the roots and stems can be used as a disinfectant; the flower parts were used in the

treatment of wounds [3]. This plant had also been proven to have antioxidant, anti-microbial, anti-cancer, and antidiabetic activities [4].

Several previous studies stated that the hydroethanolic extract of *R. tuberosa* L. contained several secondary metabolites compounds, such as flavonoids, phenolic compounds, ascorbic acid, and steroids [3-5]. Flavonoids can demonstrate antidiabetic activity through their function as antioxidants. The presence of hydroxyl groups (O-H) and conjugated double bonds in the structure of flavonoids produced antioxidant activity [6]. However, bioactive compounds like flavonoids are sensitive to environmental conditions such as pH or temperature and have low bioavailability



[7]. The poor bioavailability may affect the number of bioactive compounds that can attain the circulatory system. Hence, the microencapsulation method was required to protect these compounds [8]. Microencapsulation is the shielding process of small particles using a polymer. This method resulted in microcapsules with a size range of 2–2000  $\mu\text{m}$  [9-10]. The primary purpose of microencapsulation is to avoid the degradation or inactivation of the active compounds due to the unstable environmental conditions [9].

Ionic gelation is one of the techniques in the encapsulating process based on the electrostatic interaction between two ionic species, where one of them is a polymer. The bioactive compounds from natural materials may be trapped between the polymer chains and form microcapsule beads [11-12]. A common polymer used in the microencapsulation process is sodium alginate due to its ability to form a very versatile, biocompatible, and non-toxic matrix to encapsulate the compounds [13]. Furthermore, the calcium chloride addition as a cross-linker plays a role in forming alginate beads due to the exchange of sodium ions with calcium cations. The resulting cross-linked beads were beneficial for the controlled release of bioactive molecules [14]. Drying is a necessary process to obtain microcapsules. One of the drying techniques that are generally used is freeze-drying. This technique may prevent the substances inside the dried microcapsules from degradation due to high temperatures [15-16]. Numerous factors, including pH of medium, coating material concentration, and stirring time contribute to the properties of microcapsules. Carboxylate groups in sodium alginate structure can be readily dissociated and form ionic bonds in an acid solution. The coating materials concentration and stirring time may affect the size of the microcapsules. In addition, smaller microcapsules may generate greater efficiency [17-18].

Due to the antidiabetic activity of *R. tuberosa* L. extracts, the inhibition against alpha-amylase can be conducted to determine their biological activities. Alpha-amylase is one of the targeted enzymes for type 2 diabetes mellitus (DM) treatment. The alpha-amylase enzyme (E.C.3.2.1.1) is a hydrolase class enzyme catalyzing the

hydrolysis of  $\alpha$ -1,4-glycosidic bonds of amylose to produce glucose and maltose [19]. Theoretically, inhibition of the alpha-amylase is expected to slow down the hydrolysis of carbohydrates and the formation of glucose, so this may automatically reduce the post-prandial glucose levels [20]. Moreover, the resistance of microcapsules in carrying the bioactive compound must be done through a microcapsule release test [21]. The release of microcapsules is carried out by evaluating the amount of released active compounds at very acidic (pH 1–3) and physiological conditions (pH 7.4) [22]. In this analysis, the zero-order release kinetic model is used to determine the relationship between the release time and percentage of microcapsules. The zero-order kinetic model is effectively considered for the sustained released samples [23-24].

This study was aimed to examine the process of microencapsulation using the freeze-drying technique. Calcium chloride, which serves as a cross-linker, and sodium alginate polymer constructed the shielding components. In order to find the ideal microcapsule conditions, a number of variables were examined, including pH, sodium alginate content, and stirring time. Additionally, an alpha-amylase inhibition experiment was performed on microcapsules under the optimum conditions to determine their effectiveness in treating type 2 diabetes mellitus.

## ■ EXPERIMENTAL SECTION

### Materials

The materials were acquired from Merck: sodium alginate ( $\geq 99\%$ , molecular biology grade), calcium chloride ( $\text{CaCl}_2$ ), aluminum chloride ( $\text{AlCl}_3$ ), alpha-amylase enzyme originated from *Aspergillus oryzae* ( $\geq 150$  units/mg protein), D-(+) glucose (analytical standard), glacial acetic acid (pharmaceutical primary standard), soluble starch (from potato, ACS grade), sodium hydroxide ( $\geq 98\%$ , pellets, anhydrous), potassium sodium tartrate tetrahydrate ( $\geq 99\%$ ), sodium acetate (anhydrous,  $\geq 99\%$ ), 3,5-dinitrosalicylic acid (DNS) reagent ( $\geq 98\%$ , HPLC grade), acarbose ( $\geq 95\%$ ), release mediums (simulated gastric fluid (SGF) and simulated intestinal fluid (SIF)). The *R. tuberosa* L. root

powder was purchased with a letter confirming the species from UPT Materia Medica Batu in East Java.

### Instrumentation

The instrumentations used in this study were UV-Vis spectrophotometer (Shimadzu), Fourier transform infrared spectrometer (FTIR, Shimadzu Prestige 21), particle size analyzer (PSA, CILAS 1090), and scanning electron microscope (SEM, TM 3000 Hitachi).

### Procedure

#### Preparation of *R. tuberosa* L. extract

A total of 250 g of *R. tuberosa* L. root powder was macerated using 96% ethyl alcohol for 3 × 24 h, in the volume ratio of 4:1 with the dried weight. The resulting extracts were filtrated and evaporated using a rotary evaporator (120 rpm; 50 °C) to acquire the concentrated extracts. For subsequent analysis, the concentrated extracts were stored at a low temperature of 4 °C.

#### Microencapsulation of *R. tuberosa* L. extracts

The 2% sodium alginate (w/v) solution was prepared in 10 mL of 1% acetate buffer (v/v, pH variations of 4, 5, 6, and 7). Then, 0.5 g extracts of *R. tuberosa* L. were dissolved with 1 mL of 96% ethyl alcohol. The mixture was gradually added to the sodium alginate solution. The mixture was stirred using a magnetic stirrer at a speed of 300 rpm until. After that, the mixture was added dropwise using a syringe to 40 mL of calcium chloride solution (0.1 M) and stirred again with a magnetic stirrer for 30 min. The forming alginate beads were washed using distilled water to remove unreacted calcium chloride (CaCl<sub>2</sub>) from the surface of the beads. Then, the beads were freeze-dried for 6 h with a temperature of -55 °C and air pressure of -60 mmHg until they changed to microcapsules powder.

The same process was repeated under different conditions with the following sodium alginate concentration of 1; 1.5; 2; and 2.5% (w/v). The initial pH contributing to the optimum percentage of encapsulation efficiency was used, which was also conducted in other conditions. Lastly, the influence of stirring time was established using the same steps with different stirring times at 15, 30, 45, and 60 min. The highest percentage of

encapsulation efficiency (%EE) was used to estimate the optimum conditions of microcapsules.

#### Encapsulation efficiency

The encapsulation efficiency expressed the percentage of encapsulated active ingredients in the polymer solution. This value denoted the effectiveness of shielding materials in trapping the extract [24]. The encapsulation efficiency was determined using the Eq. (1).

$$\text{Encapsulation efficiency(\%)} = \frac{\text{Total flavonoid content in microcapsules}}{\text{Total flavonoid content in extracts}} \times 100\% \quad (1)$$

The colorimetric technique with aluminum chloride reagent was used to determine the total flavonoid content in samples. The extract and microcapsule of *R. tuberosa* L. were prepared by dissolving 5 mg samples in 3 mL methanol, incubating at 40 °C for 45 min, and centrifuging at 1,000 rpm for 2 min. An amount of 0.6 mL of prepared solution was combined with 0.6 mL of 2% of AlCl<sub>3</sub>. The combined solution was then incubated for 23 min at room temperature. UV-Vis spectrophotometer was used to measure the absorbance of solution at a wavelength of 420 nm. According to the quercetin standard curve plot ( $y = 0.0469x + 0.0138$ ,  $R^2 = 0.9977$ ), the amount of total flavonoid content in each sample was determined and reported as mg quercetin equivalent (QE)/g. All the determinations were completed in triplicate.

#### Alpha-amylase inhibition assay

All samples, including extracts and microcapsules of *R. tuberosa* L., and the positive control acarbose, were made in numerous concentrations (20–100 µg/mL). Then, 250 µL of each sample was added to 250 µL alpha-amylase enzyme solution (10 U/mL), which was then incubated for 30 min at 37 °C. The mixture was then mixed with 250 µL of 1% soluble starch solution (w/v) and incubated at 25 °C for 10 min. Furthermore, 500 µL of DNS reagent was included, and the entire mixture was heated to a temperature of boiling water and incubated for 5 min until the color changed into reddish brown. The solution was then mixed with 5 mL of distilled water after the solution had been cooled down under running

water. Lastly, a UV-Vis spectrophotometer operating at a wavelength of 480 nm was used to test the absorbance of solution. The assays were carried out in triplicates. Eq. (2) was used to determine the alpha-amylase inhibitory activity:

$$\text{Percentage of enzyme inhibition (\%)} = \frac{\text{Absorbance of control} - \text{Absorbance of sample}}{\text{Absorbance of control}} \times 100\% \quad (2)$$

The results were represented by the IC<sub>50</sub> value, which can be defined as the level of inhibition needed to block 50% of the activity of the alpha-amylase enzyme. Plotting a linear regression equation between sample concentration and enzyme percent inhibition was carried out to determine the IC<sub>50</sub> value.

### In vitro release study

The *in vitro* release of extracts from microcapsules matrix was performed in the release medium consisting of simulated gastric fluid (SGF) and simulated intestinal fluid (SIF) with pH of 1.2 and 7.4, respectively. The release medium was prepared, and the microcapsules were added. Next, the mixture was constantly stirred at 100 rpm and placed in the water bath at 37 °C. A total of 10 mL of the solution was sampled at the intervals of 30, 60, 90, and 120 min, and then analyzed using a UV-Vis spectrophotometer at the wavelength of 420 nm. By using the quercetin standard curve, the concentration of the substance released from the microcapsules was determined as a total flavonoid content. Eq. (3) was used to express the outcome as a percentage of release (%).

$$\text{Percentage of release (\%)} = \frac{\text{Total flavonoid content release from microcapsules}}{\text{Total flavonoid content of microcapsules in optimum condition}} \times 100\% \quad (3)$$

### FTIR, particle size distribution, and SEM analyses

A dried sample that had been compressed into a KBr pellet was used for the FTIR measurement, which was conducted in the 4000–400 cm<sup>-1</sup> wavenumber region using an FTIR Shimadzu Type IR Prestige-21. A CILAS 1090 PSA was used to analyze the distribution and size of microcapsules. An SEM TM 3000 Hitachi was used to examine the microcapsule's surface morphology and form at magnifications ranging from 4,000× to 12,000×.

### Data analysis

The mean ± standard deviation was used to express the results. A software, Statistical Package for The Social Science (SPSS) v.26, was used to conduct the statistical analysis. The one-way analysis of variance (ANOVA) and Tukey's HSD test was then used to assess the true difference from each variation. The differences were deemed statistically significant at  $p < 0.05$ .

## RESULTS AND DISCUSSION

The dried microcapsules from *R. tuberosa* L. extracts were prepared using the freeze-drying technique. The optimization was carried out to determine the best conditions leading to the formation of microcapsules with a high percentage of encapsulation efficiency. Table 1–3 expresses the percentage of encapsulation efficiency from microcapsules set up at diverse pH, sodium alginate concentrations, and stirring times. The highest encapsulation efficiency has resulted in *R. tuberosa* L.

**Table 1.** Effect of pH on the encapsulation efficiency of *R. tuberosa* L.

pH*	Encapsulation efficiency (%)**
4	33.72 ± 0.26 <sup>b</sup>
5	41.73 ± 0.25 <sup>c</sup>
6	46.21 ± 0.32 <sup>d</sup>
7	30.56 ± 0.24 <sup>a</sup>

\*Microcapsules were prepared using 2% (w/v) of sodium alginates for 30 min stirring time; \*\*Different notations, using the One-Way ANOVA test with a level of confidence  $\alpha = 5\%$ , indicate significant differences between conditions

**Table 2.** Effect of sodium alginate concentration on the encapsulation efficiency of *R. tuberosa* L.

Concentration of sodium alginate (%w/v)*	Encapsulation efficiency (%)**
1	51.53 ± 0.15 <sup>d</sup>
1.5	44.93 ± 0.18 <sup>c</sup>
2	37.84 ± 0.12 <sup>b</sup>
2.5	32.46 ± 0.26 <sup>a</sup>

\*Microcapsules were prepared at optimum pH 6 for 30 min stirring time; \*\*Different notations, using the One-Way ANOVA test with a level of confidence  $\alpha = 5\%$ , indicate significant differences between conditions

**Table 3.** Effect of stirring time on the encapsulation efficiency of *R. tuberosa* L.

Stirring time (min)*	Encapsulation efficiency (%)**
15	50.92 ± 0.15 <sup>c</sup>
30	51.63 ± 0.09 <sup>d</sup>
45	49.79 ± 0.09 <sup>b</sup>
60	42.17 ± 0.2 <sup>a</sup>

\*Microcapsules were prepared at optimum pH 6 using the optimum concentration of sodium alginate of 1% (w/v);

\*\*Different notations, using the One-Way ANOVA test with a level of confidence  $\alpha = 5\%$ , indicate significant differences between conditions

microcapsules set in pH 6, 1% (w/v) sodium alginate, and 30 min stirring time, with 51.63% encapsulation efficiency.

The microcapsules prepared at pH 6 showed the highest encapsulation efficiency. Sodium alginate can dissolve in acidic pH due to the pKa values of mannuronic and guluronic acid residues around 3.38–3.65 [25]. Moreover, in acidic solutions, the repulsion force among groups in sodium alginate decreased, so the gel strength tended to increase [26]. At weaker acidic pH (~6), sodium alginate dissociates easier and breaks the bond between the sodium (Na<sup>+</sup>) ion and carboxylate ion (COO<sup>-</sup>) of mannuronic or guluronic acid. As a result, the divalent ion Ca<sup>2+</sup> of cross-linker CaCl<sub>2</sub> displaces Na<sup>+</sup> ions and forms ionic bonds with carboxylate ions. Thus, the increasing ionic bonds might strengthen the matrix, escalate the amount of encapsulated bioactive ingredients, and result in the greatest encapsulation efficiency [26-27]. The results agreed with previous research [28], which stated that a higher pH solution would produce less protonated forms. The protonation of the carboxylate anions can interrupt the coordination with calcium cations and reduce the existing sites for cross-linking.

In this research, the optimum condition of microcapsules was acquired at a sodium alginate

concentration of 1% (w/v). The higher sodium alginate concentration produced a lower encapsulation efficiency, as shown in Table 2. Similar results were informed by Wibowo et al. [29], in which encapsulation efficiency decreased with the enhancement of sodium alginate concentration. A lower concentration of sodium alginate generated a larger pore size of the beads. In contrast, the pore size of the beads decreased with the increase in sodium alginate concentration. Therefore, enhancing sodium alginate concentration might inhibit the entrance of bioactive compounds into the beads and lead to lower encapsulation efficiency.

The stirring time was also a parameter investigated in this study. The short stirring time resulted in particle aggregates and less discreet microcapsules, whereas the longer time resulted in particles with fragile and breakable properties [30-31]. Table 3 shows that the stirring time of 30 min gave the maximum encapsulation efficiency. This results were similar to earlier research [30], which explained that smaller microcapsules formed at a stirring time of 30 min with the increased size distribution. As a result, the larger particle surface area was developed and facilitated the adsorption of extracts into the polymer matrix.

The antidiabetic activity of a sample can be determined by an alpha-amylase inhibition assay. The samples used in this assay were the ethanolic extract of *R. tuberosa* L., microcapsules prepared under the optimum conditions, and acarbose. Based on Table 4, all samples displayed a high alpha-amylase enzyme inhibition, as seen from the low IC<sub>50</sub> values. The microcapsules had a higher IC<sub>50</sub> value (46.66 ± 0.13 µg/mL) than *R. tuberosa* L. ethanolic extract (33.77 ± 0.87 µg/mL). A higher IC<sub>50</sub> value corresponds to weaker inhibition activity against the

**Table 4.** The IC<sub>50</sub> value of *R. tuberosa* L. ethanolic extracts, microcapsules, and acarbose on alpha-amylase inhibition assay

Sample	IC <sub>50</sub> values (µg/mL)*
<i>R. tuberosa</i> L. ethanolic extract	33.77 ± 0.87 <sup>b</sup>
Microcapsules prepared at the optimum conditions	46.66 ± 0.13 <sup>c</sup>
Acarbose	24.31 ± 0.40 <sup>a</sup>

\*Different notations, using the One-Way ANOVA test with a level of confidence  $\alpha = 5\%$ , indicate significant differences between conditions

alpha-amylase enzyme. In the microcapsule sample, the bioactive compounds cannot be entirely released. Some compounds were still restrained in a polymer matrix, resulting in a lower ability to inhibit enzyme activity [32]. The fundamental goal of microencapsulation is not to increase the antidiabetic activity of the sample but to enhance the protection and avoid the degradation of bioactive ingredients. Besides, the encapsulating samples can manage the release of bioactive compounds [33]. Hence, the microcapsule of *R. tuberosa* L. extracts had the potential role of an antidiabetic source due to the presence of flavonoid compounds [11]. Flavonoids can form a covalent bond with the alpha-amylase enzyme and change their activity due to the capability to establish quinones or lactones that react with nucleophilic groups on the enzyme [34].

Acarbose, as a positive control, had the lowest  $IC_{50}$  value of  $24.31 \pm 0.40 \mu\text{g/mL}$ , which denoted the most vigorous inhibitory activity against the alpha-amylase. Acarbose is a synthetic drug for DM type 2 treatment. This drug has a similar structure to oligosaccharides and acts as a competitive inhibitor of the alpha-amylase [35]. According to [34], acarbose produced maximum inhibition against alpha-amylase by suspending the digestion of carbohydrates and delaying glucose absorption. Moreover, although the ethanolic extract of *R. tuberosa* L. contains various bioactive compounds [3-5], not all of these compounds could inhibit alpha-amylase [36].

Among all the *in vitro* assays for microparticles, the release study is one of the essential parameters. Through this assay, the assessment of the safety, efficiency, and

quality of the microcapsules can be found [37]. In this study, the microcapsules were dissolved in two mediums, SGF at pH 1.2 and SIF at pH 7.4. The dissolution was carried out continuously in different time variations [38].

The whole drug release process was affected by both the physical and mechanical properties of the gel shielding around the microcapsules [39]. Based on the release profile in Fig. 1, the release of microcapsules at pH 1.2 was lower than that at pH 7.4. At pH 1.2, the curve gradually increased at a 30–90 min of release time with a release value of around 1.1 to 3.2%, but then it reached a plateau of about 3.2 to 3.5% in the remaining time. The sodium alginate comprises mannuronic and guluronic acid with  $pK_a$  values of 3.38 and 3.65, respectively. An intermolecular hydrogen bonding system could stabilize alginate beads in the medium with a pH below these  $pK_a$  values. As a consequence, the swelling ratio of the alginate particles reduces in the gastric environment, so the encapsulated drug will be difficult to reach out from the network [25,40].

The low-release profile of microcapsules in pH 1.2 is also proven by the SEM image in Fig. 2(c). The image of released microcapsules in an acidic medium produced ruptured and folded spherical shapes. The shapes indicating that the coating matrix experienced erosion, and the microcapsules were partially bursting, resulting in a low percentage of drug release [41].

In contrast, at pH 7.4, the release value significantly increased and reached the maximum value of 55.8% at 120 min. This was due to the increase of negatively charged of carboxylate ions because of a higher level of

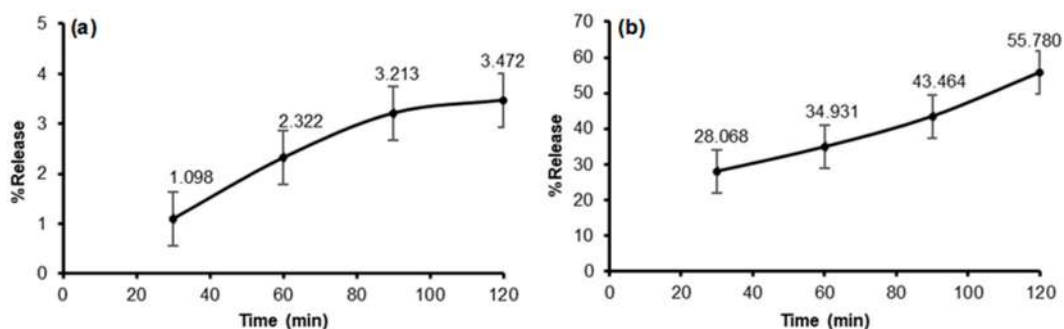


**Fig 1.** The released profile of microcapsules of *R. tuberosa* L. extract prepared in pH 6, 1% (w/v) sodium alginate, and 30 min stirring time at: (a) pH 1.2; (b) 7.4

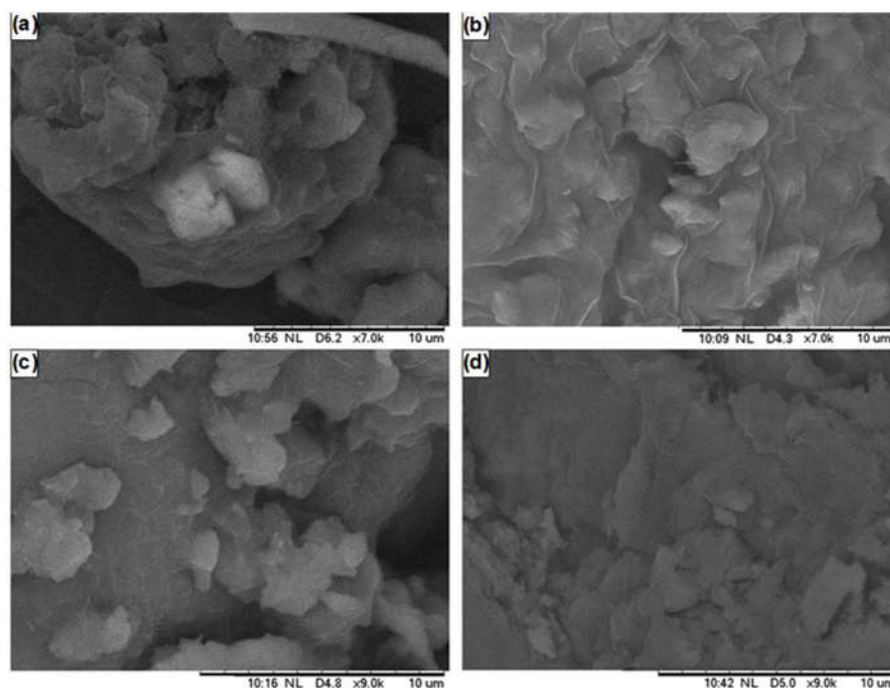


**Fig 2.** The SEM images of (a) *R. tuberosa* L. ethanolic extract; (b) microcapsules of *R. tuberosa* L. prepared in pH 6, 1% (m/v) sodium alginate concentration, and 30 min stirring time; (c) microcapsules released in pH 1.2; (d) microcapsules released in pH 7.4. The magnifications were 7,000 $\times$  for (a) and (b), and 9,000 $\times$  for (c) and (d)

ionization. These carboxylate ions might repel each other and cause the disaggregating of the alginate-CaCl<sub>2</sub> matrix structure, then lead to swollen microcapsules [42]. This result was also supported by the SEM image in Fig. 2(d) showing a flatter morphological surface than the previous one. The more released compounds might increase the intensity of matrix erosion, and the microcapsules might break more easily. The similar results have also been informed that bioactive ingredients were released more easily in the alkaline condition than in acidic pH [25].

Characterization with SEM was carried out to confirm the surface morphology of the samples. According to Fig. 2(a-b), there were difference between SEM images of extracts and microcapsules. The microcapsules showed an irregular shape with a few spherical, followed by the uniform distribution of wrinkled surfaces. This result was in agreement with a previous study that reported freeze-dried samples did not have a specific shape [43]. The irregularities of the surface and the existence of wrinkles might be allied with the low drying temperatures. The forming ice crystals during the freeze-drying step also established the cavities [43-44].

The FTIR analysis identified functional groups in *R. tuberosa* L. extracts and microcapsules. Fig. 3 shows the FTIR spectra, while the assignments of the absorption functional groups are listed in Table 5. Based on Fig. 3(a), the extract of *R. tuberosa* L. denoted the stretching vibrations of the hydroxyl (O-H) group at 3354 cm<sup>-1</sup>. Then, the characteristic peaks of methine C-H stretching were observed at 2926 and 2855 cm<sup>-1</sup>. Moreover, the absorption at 1608 cm<sup>-1</sup> was interpreted as ketone C=O stretching, whereas peaks at 1450 and 1168 cm<sup>-1</sup> showed the stretching vibrations of aromatic C=C and vinyl ether C-O-C, respectively [45]. These absorptions suggested that *R. tuberosa* L. contained flavonoid compounds [46-47].

The FTIR spectra of microcapsules of *R. tuberosa* L. (Fig. 3(b)) showed broader and higher intensity band at 3448 cm<sup>-1</sup> coming the stretching vibrations of the O-H group. This peak corresponded to the sum of the peaks from coating materials, namely sodium alginate and CaCl<sub>2</sub> [48]. Then, the same absorption from the vibration of C-H methine, C=O ketone, C=C aromatic, and C-O-C vinyl ether groups also resulted in peaks 2-6 [45]. In addition,

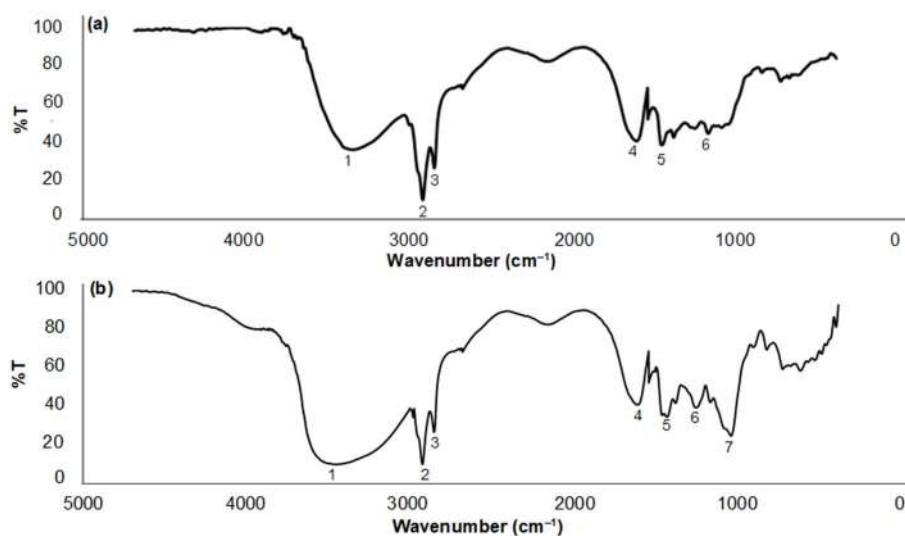


**Fig 3.** FTIR spectra of (a) *R. tuberosa* L. extract; (b) microcapsules of *R. tuberosa* L. extracts prepared in pH 6, 1% (w/v) sodium alginate, and 30 min stirring time

**Table 5.** Assignment of FTIR spectra

Peak number	Wavelength (cm <sup>-1</sup> )		Functional groups
	<i>R. tuberosa</i> L. extracts [43-45]	Microcapsules of <i>R. tuberosa</i> L. extracts [43-46]	
1	3354	3448	O-H alcohol
2	2926	2925	C-H methine
3	2855	2853	C-H methine
4	1608	1609	C=O ketone
5	1450	1429	C=C aromatic
6	1168	1252	C-O-C vinyl ether
7		1036	C-O-C aliphatic ether

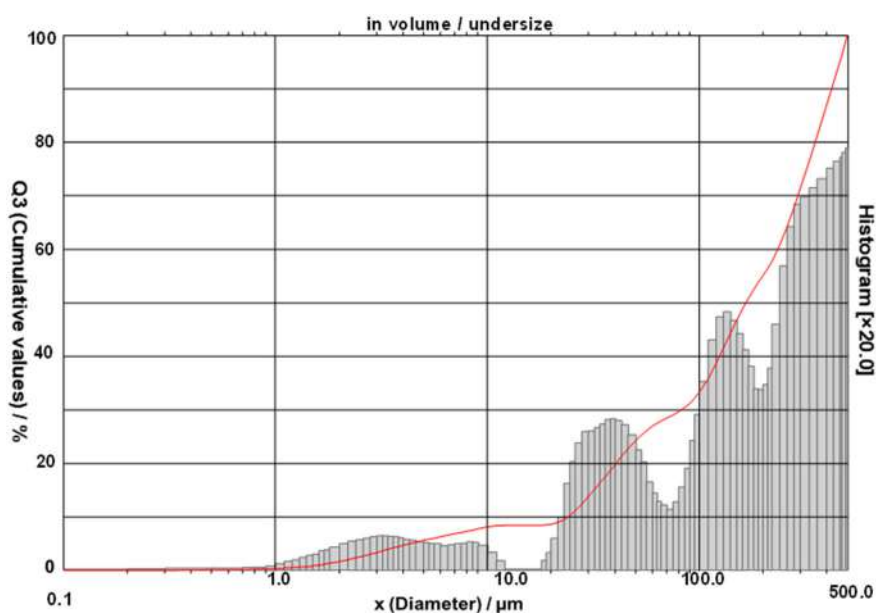


**Fig 4.** Particle size distribution from microcapsules of *R. tuberosa* L. extracts set in pH 6, 1% (w/v) sodium alginate, and 30 min stirring time. The mean diameter was 197.53 μm

the new absorption (peak 7) at 1036  $\text{cm}^{-1}$  represented the presence of C-O-C aliphatic ether coming from sodium alginate [48].

In this work, the size of the microcapsules was also evaluated. The properties of powder samples majorly depend on the sizes of the particles. The PSA is the standard instrument in the sizing test. This instrument was objected to determine particle size and hydrodynamic diameter of the microcapsules [49]. The microcapsules formed in this study had a mean diameter of 197.53  $\mu\text{m}$ , which was in the range of microparticle size, as shown in Fig. 4. This outcome satisfied the criteria for extrusion and freeze-drying-produced particles with a size range of 15–3500  $\mu\text{m}$ . Extrusion is a technique that relies on the interaction of a multivalent ion with a polysaccharide gel [50-51].

## ■ CONCLUSION

This study has carried out the microencapsulation of *R. tuberosa* L. extracts using the freeze-drying method with sodium alginate and  $\text{CaCl}_2$  as shielding materials. The optimum conditions of microcapsules were pH 6, sodium alginate concentration of 1% (w/v), and 30 min of stirring time. The alpha-amylase was inhibited by the microcapsules with an  $\text{IC}_{50}$  value of  $46.66 \pm 0.13 \mu\text{g/mL}$ . The *in vitro* release assay presented that the microcapsule of *R. tuberosa* L. extract was released more readily at pH 7.4 than at pH 1.2. The morphological surface analysis by SEM indicated an irregular shape with a few spherical followed by the uniform distribution of wrinkling; hence the PSA result stated that the microcapsules had micro-sized particles with a mean diameter of 197.53  $\mu\text{m}$ . Moreover, the FTIR analysis demonstrated that the cross-linking between sodium alginate and  $\text{CaCl}_2$  has been obtained. Microencapsulation of plant extracts can be one of the strategies for natural product enhancement with preserved biological functions.

## ■ ACKNOWLEDGMENTS

This work was supported by Hibah Penelitian Doktor grant, contract number 3110.1/UN10.F09/PN/2022, and was part of Penelitian Tesis Magister grant, year of 2022.

## ■ AUTHOR CONTRIBUTIONS

Andriana Kusuma Pertiwi conducted the experiment, Choirin Annisa analyzed the data, Andriana Kusuma Pertiwi, Anna Safitri, and Zubaidah Ningsih wrote and revised the manuscript. All authors agreed to the final version of this manuscript.

## ■ REFERENCES

- [1] Sholikhah, E.N., 2016, Indonesian medicinal plants as sources of secondary metabolites for pharmaceutical industry, *JMedSci*, 48 (4), 226–239.
- [2] Batubara, I., and Prastya, M.E., 2020, Potential use of Indonesian medicinal plants for cosmetic and oral health: A review, *J. Kim. Valensi*, 6 (1), 118–132.
- [3] Khan, I., Jan, S., Shinwari, Z.K., Ali, M., Khan, Y., and Kumar, T., 2017, Ethnobotany and medicinal uses of folklore medicinal plants belonging to family acanthaceae: An updated review, *MOJ Biol. Med.*, 1 (2), 34–38.
- [4] Ramadhan, M., Sabarudin, A., and Safitri, A., 2019, *In vitro* anti-microbial activity of hydroethanolic extracts of *Ruellia tuberosa* L.: Eco-friendly based-product against selected pathogenic bacteria, *IOP Conf. Ser.: Earth Environ. Sci.*, 239, 012028.
- [5] Safitri, A., Roosdiana, A., Rosyada, I., Evindasari, C.A., Muzayyana, Z., and Rachmawanti, R., 2019, Phytochemicals screening and anti-oxidant activity of hydroethanolic extracts of *Ruellia tuberosa* L, *IOP Conf. Ser.: Mater. Sci. Eng.*, 509, 012017.
- [6] Roosdiana, A., Permata, F.S., Fitriani, R.I., Umam, K., and Safitri A., 2020, *Ruellia tuberosa* L. extract improves histopathology and lowers malondialdehyde levels and TNF alpha expression in the kidney of streptozotocin-induced diabetic rats, *Vet. Med. Int.*, 2020, 8812758.
- [7] Lucas, J., Ralaivao, M., Estevinho, B.N., and Rocha, F., 2020, A new approach for the microencapsulation of curcumin by a spray drying method, in order to value food products, *Powder Technol.*, 362, 428–435.
- [8] Rahayu, I., Zainuddin, A., and Hendrana, S., 2020, Improved maleic anhydride grafting to linear low



- density polyethylene by microencapsulation method, *Indones. J. Chem.*, 20 (5), 1110–1118.
- [9] Safitri, A., Roosdiana, A., Kurnianingsih, N., Fatchiyah, F., Mayasari, E., and Rachmawati, R., 2022, Microencapsulation of *Ruellia tuberosa* L. aqueous root extracts using chitosan-sodium tripolyphosphate and their *in vitro* biological activities, *Scientifica*, 2022, 9522463.
- [10] Chaemsawang, W., Prasongchean, W., Papadopoulos, K.I., Sukrong, S., Kao, W.J., and Wattanaarsakit, P., 2018, Emulsion cross-linking technique for human fibroblast encapsulation, *Int. J. Biomater.*, 2018, 9317878.
- [11] Pedroso-Santana, S., and Fleitas-Salazar, N., 2020, Ionotropic gelation method in the synthesis of nanoparticles/microparticles for biomedical purposes, *Polym. Int.*, 69 (5), 443–447.
- [12] He, L., Shang, Z., Liu, H., and Yuan, Z.X., 2020, Alginate-based platforms for cancer-targeted drug delivery, *Biomed Res. Int.*, 2020, 1487259.
- [13] Alvarez-Berrios, M.P., Aponte-Reyes, L.M., Diaz-Figueroa, L., Vivero-Escoto, J., Johnston, A., and Sanchez-Rodriguez, D., 2020, Preparation and *in vitro* evaluation of alginate microparticles containing amphotericin B for the treatment of *Candida* infections, *Int. J. Biomater.*, 2020, 2514387.
- [14] Abasalizadeh, F., Moghaddam, S.V., Alizadeh, E., Akbari, E., Kashani, E., Fazljou, S.M.B., Torbati, M., and Akbarzadeh, A., 2020, Alginate-based hydrogels as drug delivery vehicles in cancer treatment and their applications in wound dressing and 3D bioprinting, *J. Biol. Eng.*, 14 (1), 8.
- [15] Pudziuvelyte, L., Marksa, M., Sosnowska, K., Winnicka, K., Morkuniene, R., and Bernatoniene, J., 2020, Freeze-drying technique for microencapsulation of *Elsholtzia ciliata* ethanolic extract using different coating materials, *Molecules*, 25 (9), 2237.
- [16] Zhao, L., Duan, X., Cao, W., Ren, X., Ren, G., Liu, P., and Chen, J., 2021, Effects of different drying methods on the characterization, dissolution rate and antioxidant activity of ursolic acid-loaded chitosan nanoparticles, *Foods*, 10 (10), 2470.
- [17] Cáceres, L.M., Velasco, G.A., Dagnino, E.P., and Chamorro, E.R., 2020, Microencapsulation of grapefruit oil with sodium alginate by gelation and ionic extrusion: Optimization and modeling of crosslinking and study of controlled release kinetics, *Rev. Tecnol. Cienc.*, 39, 41–61.
- [18] Bennacef, C., Desobry-Banon, S., Probst, L., and Desobry, S., 2021, Advances on alginate use for spherification to encapsulate biomolecules, *Food Hydrocolloids*, 118, 106782.
- [19] Farooq, M.A., Ali, S., Hassan, A., Tahir, H.M., Mumtaz, S., and Muntaz, S., 2021, Biosynthesis and industrial applications of  $\alpha$ -amylase: A review, *Arch. Microbiol.*, 203 (4), 1281–1292.
- [20] Mphahlele, M.J., Agbo, E.N., and Choong, Y.S., 2021, Synthesis, structure, carbohydrate enzyme inhibition, antioxidant activity, *in silico* drug-receptor interactions and drug-like profiling of the 5-styryl-2-aminochalcone hybrids, *Molecules*, 26 (9), 2692.
- [21] Parhizkar, A., and Asgary, S., 2021, Local drug delivery systems for vital pulp therapy: A new hope, *Int. J. Biomater.*, 2021, 5584268.
- [22] Braim, S., Śpiewak, K., Brindell, M., Heeg, D., Alexander, C., and Monaghan, T., 2019, Lactoferrin-loaded alginate microparticles to target *Clostridioides difficile* infection, *J. Pharm. Sci.*, 108 (7), 2438–2446.
- [23] Fauzi, M.A.R.D., Hendradi, E., Pudjiastuti, P., and Widodo, R.T., 2021, Analysis of dissolution of salicylamide from carrageenan based hard-shell capsules: A study of the drug-matrix interaction, *Indones. J. Chem.*, 21 (1), 148–156.
- [24] Witzler, M., Vermeeren, S., Kolevatov, R.O., Haddad, R., Gericke, M., Heinze, T., and Schulze, M., 2021, Evaluating release kinetics from alginate beads coated with polyelectrolyte layers for sustained drug delivery, *ACS Appl. Bio Mater.*, 4 (9), 6719–6731.
- [25] Chuang, J.J., Huang, Y.Y., Lo, S.H., Hsu, T.F., Huang, W.Y., Huang, S.L., and Lin, Y.S., 2017, Effects of pH on the shape of alginate particles and its release behavior, *Int. J. Polym. Sci.*, 2017, 3902704.

- [26] Ramdhan, T., Ching, S.H., Prakash, S., and Bhandari, B., 2019, Time dependent gelling properties of cuboid alginate gels made by external gelation method: Effects of alginate-CaCl<sub>2</sub> solution ratios and pH, *Food Hydrocolloids*, 90, 232–240.
- [27] Perkasa, D.P., Erizal, E., Purwanti, T., and Tontowi, A.E., 2018, Characterization of semi-interpenetrated network alginate/gelatin wound dressing crosslinked at Sol Phase, *Indones. J. Chem.*, 18 (2), 367–375.
- [28] dos Santos de Macedo, B., de Almeida, T., da Costa Cruz, R., Netto, A.D.P., da Silva, L., Berret, J.F., and Vitorazi, L., 2020, Effect of pH on the complex coacervation and on the formation of layers of sodium alginate and PDADMAC, *Langmuir*, 36 (10), 2510–2523.
- [29] Wibowo, A.A., Suryandari, A.S., Naryono, E., Pratiwi, V.M., Suharto, M., and Adiba, N., 2021, Encapsulation of clove oil within Ca-alginate-gelatine complex: Effect of process variables on encapsulation efficiency, *JTKL*, 5 (1), 71–77.
- [30] Ningsih, Z., Lestari, M.L.A.D., and Maharin, S.A.R., 2021, Preparation and characterization of curcumin nanoemulsion in olive oil-tween 80 system using wet ball milling method, *ICS Phys. Chem.*, 1 (1), 16–19.
- [31] Panigrahi, D., Sahu, P.K., Swain, S., and Verma, R.K., 2021, Quality by design prospects of pharmaceuticals application of double emulsion method for PLGA loaded nanoparticles, *SN Appl. Sci.*, 3 (6), 638.
- [32] Safitri, A., Roosdiana, A., Hitdatania, E., and Damayanti, S.A., 2022, *In vitro* alpha-amylase inhibitory activity of microencapsulated *Cosmos caudatus* Kunth extracts, *Indones. J. Chem.*, 22 (1), 212–222.
- [33] Suratman, A., Purwaningsih, D.R., Kunarti, E.S., and Kuncaka, A., 2020, Controlled release fertilizer encapsulated by glutaraldehyde-crosslinked chitosan using freeze-drying method, *Indones. J. Chem.*, 20 (6), 1414–1421.
- [34] Oyedemi, S.O., Oyedemi, B.O., Ijeh, I.I., Ohanyerem, P.E., Cooposamy, R.M., and Aiyegoro, O.A., 2017, Alpha-amylase inhibition and antioxidative capacity of some antidiabetic plants used by the traditional healers in southeastern Nigeria, *Sci. World J.*, 2017, 3592491.
- [35] Hsu, P.F., Sung, S.H., Cheng, H.M., Shin, S.J., Lin, K.D., Chong, K., Yen, F.S., Yu, B.H., Huang, C.T., and Hsu, C.C., 2018, Cardiovascular benefits of acarbose vs sulfonylureas in patients with type 2 diabetes treated with metformin, *J. Clin. Endocrinol. Metab.*, 103 (10), 3611–3619.
- [36] Chelladurai, G.R.M., and Chinnachamy, C., 2018, Alpha amylase and alpha glucosidase inhibitory effects of aqueous stem extract of *Salacia oblonga* and its GC-MS analysis, *Braz. J. Pharm. Sci.*, 54 (1), e17151.
- [37] Weng, J., Tong, H.H.Y., and Chow, S.F., 2020, *In vitro* release study of the polymeric drug nanoparticles: Development and validation of a novel method, *Pharmaceutics*, 12 (8), 732.
- [38] Li, L., Li, J., Si, S., Wang, L., Shi, C., Sun, Y., Liang, Z., and Mao, S., 2015, Effect of formulation variables on *in vitro* release of a water-soluble drug from chitosan–sodium alginate matrix tablets, *Asian J. Pharm. Sci.*, 10 (4), 314–321.
- [39] Abbasnezhad, N., Zirak, N., Shirinbayan, M., Tcharkhtchi, A., and Bakir, F., 2021, On the importance of physical and mechanical properties of PLGA films during drug release, *J. Drug Delivery Sci. Technol.*, 63, 102446.
- [40] Sreekanth Reddy, O., Subha, M.C.S., Jithendra, T., Madhavi, C., and Chowdoji Rao, K., 2021, Curcumin encapsulated dual cross linked sodium alginate/montmorillonite polymeric composite beads for controlled drug delivery, *J. Pharm. Anal.*, 11 (2), 191–199.
- [41] Lengyel, M., Kállai-Szabó, N., Antal, V., Laki, A.J., and Antal, I., 2019, Microparticles, microspheres, and microcapsules for advanced drug delivery, *Sci. Pharm.*, 87 (3), 20.
- [42] Thomas, D., Latha, M.S., and Kurienthomas, K., 2018, Zinc-alginate beads for the controlled release of rifampicin, *Orient. J. Chem.*, 34 (1), 428–433.
- [43] Moayyedi, M., Eskandari, M.H., Rad, A., Ziaee, E., and Khodaparast, M., 2018, Effect of drying methods (electrospraying, freeze drying and spray drying) on survival and viability of microencapsulated

- Lactobacillus rhamnosus* ATCC 7469, *J. Funct. Foods*, 40, 391–399.
- [44] Makouie, S., Alizadeh, M., Maleki, O., and Khosrowshahi, A., 2019, Optimization of wall components for encapsulation of *Nigella sativa* seed oil by freeze-drying, *IFSTJ*, 3 (1), 1–9.
- [45] Nandiyanto, A.B.D., Oktiani, R., and Ragadhita, R., 2019, How to read and interpret FTIR spectroscopy of organic material, *IJoST*, 4 (1), 97–118.
- [46] Abbas, O., Compère, G., Larondelle, Y., Pompeu, D., Rogez, H., and Baeten, V., 2017, Phenolic compound explorer: A mid-infrared spectroscopy database, *Vib. Spectrosc.*, 92, 111–118.
- [47] Kartini, K., Putri, L.A.D., and Hadiyat, M.A., 2020, FTIR-based fingerprinting and discriminant analysis of *Apium graveolens* from different locations, *J. Appl. Pharm. Sci.*, 10 (12), 62–67.
- [48] Nastaj, J., Przewłocka, A., and Rajkowska-Myśliwiec, M., 2016, Biosorption of Ni(II), Pb(II) and Zn(II) on calcium alginate beads: Equilibrium, kinetic and mechanism studies, *Polish J. Chem. Technol.*, 18 (3), 81–87.
- [49] Gerasimov, A.M., Eremina, O.V., Cherkasova, M.V., and Dmitriev, S.V., 2021, Application of particle-size analysis in various industries, *J. Phys.: Conf. Ser.*, 1728, 012003.
- [50] Pech-Canul, Á.C., Ortega, D., García-Triana, A., González-Silva, N., and Solis-Oviedo, R.L., 2020, A brief review of edible coating materials for the micro encapsulation of probiotics, *Coatings*, 10 (3), 197.
- [51] de Freitas Santos, P.D., Rubio, F.T.B., da Silva, M.P., Pinho, L.S., and Favaro-Trindade, C.S., 2021, Microencapsulation of carotenoid-rich materials: A review, *Food Res. Int.*, 147, 110571.

## Anticancer Activity of Synthesized ZnO and ZnO/AgCl Nanocomposites against Five Human Cancer Cells

Fattima Al-Zahra Gabar Gassim<sup>1\*</sup> and Ali Jabbar Jasim Makkawi<sup>2</sup>

<sup>1</sup>Department of Pharmaceuticals, College of Pharmacy, University of Babylon, Hilla 51002, Iraq

<sup>2</sup>Department of Chemistry, College of Science, University of Babylon, Ministry of Education, Hilla 51002, Iraq

\* **Corresponding author:**

tel: +964-07725741416

email: alzahraafatema6@gmail.com

Received: August 5, 2022

Accepted: December 12, 2022

DOI: 10.22146/ijc.76872

**Abstract:** In this work, a refluxing method is used to prepare nanoparticles of zinc oxide (ZnO NPS) and zinc oxide /silver chloride nanocomposites (ZnO/AgCl NCS). The structural properties of nanocrystals are studied by Atomic Force Microscope (AFM), X-Ray Diffraction (XRD), and Field Emission Scanning Electron Microscopy (FE-SEM) to determine the average crystal size, morphology, particle size and average grain size of nanocrystals. The results of anticancer efficiency of ZnO NPs and ZnO/AgCl NCs show cytotoxic activity against five human cancer cells, namely hepatocellular carcinoma, rhabdomyosarcoma (RD), colorectal carcinoma (HCT116), mammary gland (MCF-7), and epidermoid carcinoma (Hep2) compared against doxorubicin. The anticancer mechanism of pure and nanocomposites ZnO are suggested according to the release of  $Zn^{+2}$  and the production of reactive oxidation species (ROS) and the effect of these species on cancer inhibition.

**Keywords:** ZnO nanoparticles; the anticancer activity of nanoparticles; ZnO/AgCl nanocomposites

### ■ INTRODUCTION

Doxorubicin is one of the most important anticancer (cytotoxic or antineoplastic) drugs used in high doses, but these drugs have had severe side effects. So, another drug with the same high activity and safety should be used. Nano-medicine techniques have paved the way for new targeted cancer therapies by allowing therapeutic compounds to be encapsulated in nanomaterials and selectively delivered to cancers by active uptake mechanisms and passive permeation. Resistance, to treatment, is one of the most important obstacles to conventional treatment [1]. Nanomedicine is the most important application of nanotechnology in medical problems because nanostructures of different shapes exhibit new and greatly enhanced physical, biological and chemical properties as well as distinct phenomena and functions [2-3]. Nano-systems were used to treat cancer by different nanotechnologies as shown in Fig. 1.

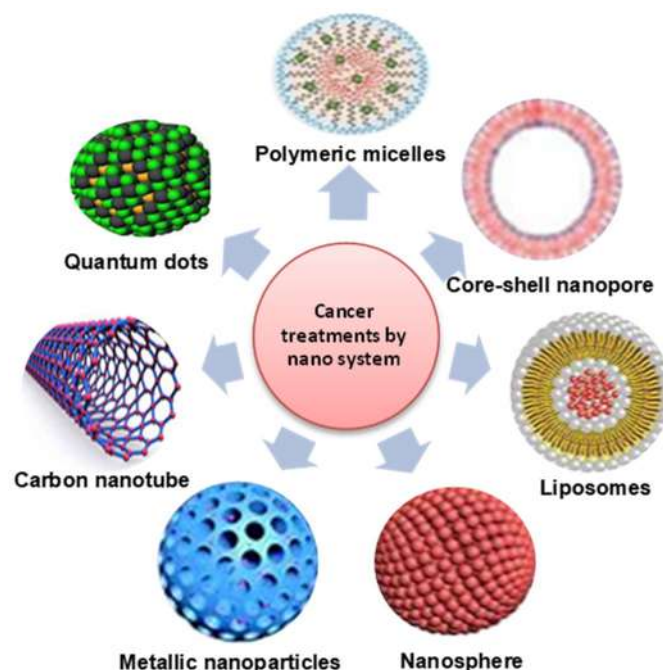


**Fig 1.** The schematic diagram represents various nanotechnologies that use nano-systems to treat cancer

Zinc oxide nanoparticles (ZnO NPs) have remarkable properties due to their ability the treatment of different kinds of cancers because of their biodegradability, biocompatibility [4], and unique physical and chemical features [5-6]. ZnO NPs have been exploited in preclinical and biomedical research, including drug delivery and cellular imaging [7-8]. ZnO absorbs UV rays at wavelengths ranging between 350–380 nm to produce reactive oxidation species (ROS) [9-10] so this semiconductor was modified by loading noble metals such as Ag on the surface of ZnO nanostructures to improve the image stability, it promotes efficiency in separating electron and hole pairs for photo-generation and expands light absorption of the visible region [11]. ROS plays an important role mechanism of ZnO NPs cytotoxicity through oxidative stress [12].

The aim of this study is to use pure and loaded ZnO NPs as anticancer materials as a new biomedical drug [4] instead of doxorubicin to decrease the dangerous side effect of this drug on the human body.

## ■ EXPERIMENTAL SECTION

### Materials

The materials used in this study were zinc acetate dihydrate ( $\text{Zn}(\text{CH}_3\text{COO})_2 \cdot 2\text{H}_2\text{O}$ ) (99% purity, Sigma Aldrich (USA), silver nitrate ( $\text{AgNO}_3$ ), zinc nitrate tetrahydrate ( $\text{Zn}(\text{NO}_3)_2 \cdot 4\text{H}_2\text{O}$ ) (98% purity HANNOVER), and sodium chloride are produced from HANNOVER. While high-quality absolute ethanol and sodium hydroxide (99% purity Merck) is obtained from Germany.

### Instrumentation

The instrumentations used in this study were X-Ray Diffraction Spectroscopy (D5000 XRD6000, Shimadzu, Japan), Filed Emission Scanning Electron Microscopy (INSPECT S50 FEL (USA)), and Atomic Force Microscopy (Sartorius Arium 611).

### Procedure

#### ZnO NPs preparation

One pot refluxing method was used in the preparation of ZnO NPs. A 22 g of zinc acetate was dissolved in 600 mL of absolute ethanol. The solution was

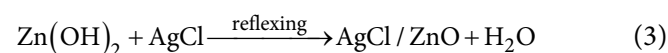
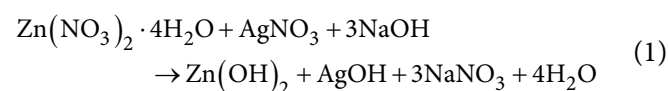
heated it to 60 °C for 30 min. The second solution was prepared by dissolving 25.2 g of oxalic acid in 400 mL of absolute ethanol then heated to 50 °C and then mixed with the above solution under constant stirring for 4 h. After that, the thick solution was dried at 80 °C overnight to produce a white powder of ZnO NPs [13].

#### Modification of ZnO NPs

Oleic acid was used as a coupling agent to modify the surface of nanoparticles to make the surface of ZnO NPs more hydrophobic dispersed in the organic area. This modification consists of dissolving 9 mL of oleic acid in 300 mL *o*-xylene to produce a solution of oleic acid. Then, recently 6 g of synthesized nanoparticles were added to the oleic acid solution. Then the reaction was allowed under stirring at 50 °C for 1 h. Then, nanoparticles were centrifuged for 15 min at 15000 rpm and washed with toluene, to remove un-reacted coupling agents. Finally, ZnO NPs were dried for one night at room temperature [14].

#### ZnO/AgCl nanocomposites preparation

ZnO/AgCl NCs were prepared by dissolving 2.110 g of  $\text{AgNO}_3$  and 5.220 g of  $\text{Zn}(\text{NO}_3)_2 \cdot 4\text{H}_2\text{O}$  in 50 mL of deionized water under constant stirring at room temperature. After that, an aqueous solution of NaOH (5 M) was added dropwise until the pH of the solution reached 10. After that, 1.450 g of NaCl was dissolved in 20 mL of deionized water. An aqueous solution of NaCl was added to the above solution. The suspension was refluxed for 3 h at about 90 °C. The solution was centrifuged to separate the grey precipitate. This precipitate was washed twice with deionized water and absolute ethanol. After that, the grey precipitate was dried at 600 °C overnight. Then ceramic slurry was used for crushing nanocomposites powder. The final nanocomposites were produced by calcination of the grey powder at 2000 °C for 1 h [15] (see Fig. 2). The reactions to obtain ZnO/AgCl NCs are written as follows:



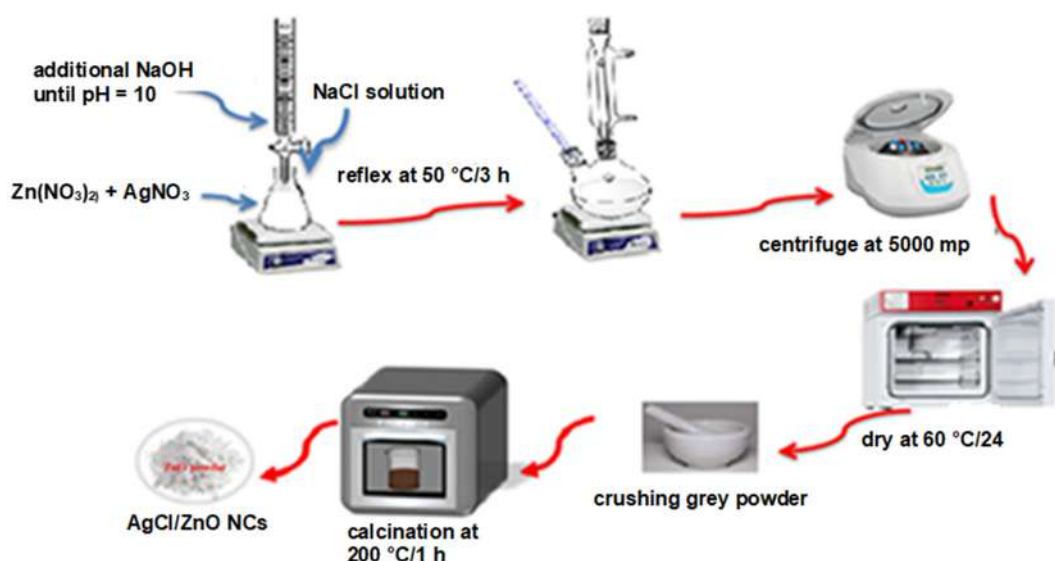


Fig 2. The schematic diagram for the steps for synthesizing AgCl/ZnO nanocomposites

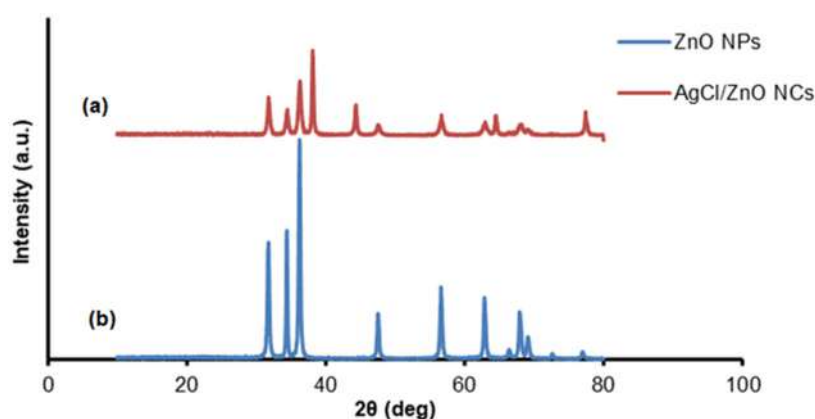


Fig 3. XRD patterns for ZnO NPs and AgCl/ZnO nanocomposites

### Antioxidant assays by ABTS

ABTS method was used to determine antioxidant efficiency. This method consisted of adding 2 mL of ABTS solution (60  $\mu$ M) to 3 mL  $\text{MnO}_2$  suspension (25 mg/mL), in a phosphate buffer solution of (pH 7, 0.1 M). The mixture solution was shaken and filtered. Then the absorbance of the ABTS radical solution was measured at 734 nm. After that, spectroscopic grade MeOH:phosphate buffer (1:1) was added to 50  $\mu$ L of 2  $\mu$ M solutions of the AgCl/ZnO NCs. The absorbance was adjusted, and the inhibition percentage was determined by the reduction in color intensity [16]. A blank sample consists of MeOH/phosphate buffer (1:1) instead of tested nanocomposites. ABTS inhibition of each sample was estimated by the following equation.

$$\text{ABTS (\% inhibition)} = \frac{\text{Abs}_{\text{control}} - \text{Abs}_{\text{test}}}{\text{Abs}_{\text{control}}} \times 100 \quad (4)$$

## RESULTS AND DISCUSSION

### XRD Analysis

Fig. 3(a) appears diffraction peaks of naked ZnO at  $2\theta$  values 31.83°, 34.48°, 36.30°, 47.80°, 56.66°, 63.38°, and 68.48° which indicated hexagonal wurtzite structure of ZnO crystalline [17] (JCPDS 36-1451). Fig. 3(b) illustrated additional peaks at  $2\theta$  of 27.6°, 46.32°, 54.95°, 57.55°, 66.92°, 74.51°, and 76.71° indicating the presence of  $\text{Ag}_2\text{Cl}$  NPs on the surface of ZnO nanoparticles [18]. Average size crystal (L) in nm were estimated by Scherrer's formula [19]

$$L = \frac{k\lambda}{\beta \cos \theta} \quad (5)$$

where  $k$  is the Scherrer's constant (0.94),  $\lambda$  is the wavelength of the X-ray radiation (0.15406 nm for  $\text{CuK}\alpha$ ),  $\beta$  is the full width of half-maximum (FWHM) intensity expressed in radians, and  $\theta$  is a diffraction (Bragg) angle. The average crystallite sizes were estimated to be about 30.164 and 33.077 nm for pure ZnO NPs and ZnO/AgCl NCs, respectively.

### FE-SEM

FE-SEM was applied to observe the morphological properties and particle size of the prepared nanoparticles [20]. Fig. 4 shows FE-SEM images of the ZnO NPs and ZnO/AgCl NCs. The results of FE-SEM analysis show ZnO NPs have an individual sheets structure with particle size ranging between 18–41 nm. As shown in Fig. 4(a), SEM images of ZnO/AgCl NCs show a nanorod structure and the nanorods' diameter was ranged from 15–52 nm as appeared in Fig. 4(b).

### AFM

Fig. 5 and 6 illustrate the average diameters for both prepared samples are bigger than the values present for the size of the crystals indicating that each particle consists of several crystals (multi crystals) [21].

### Anticancer Activity

Cytotoxic efficiency of ZnO-NPs and ZnO/AgCl NCs was evaluated and compared against doxorubicin. The results of the cytotoxicity assessment of ZnO NPs and ZnO/AgCl NCs, against five human cancer cells Mammary gland (MCF-7), Hepatocellular carcinoma (HepG2), Colorectal carcinoma (HCT116),

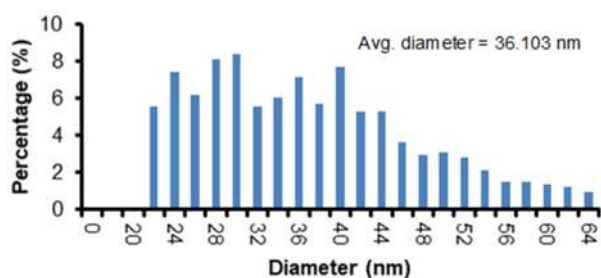


Fig 5. AFM cross-section analysis of ZnO NRs

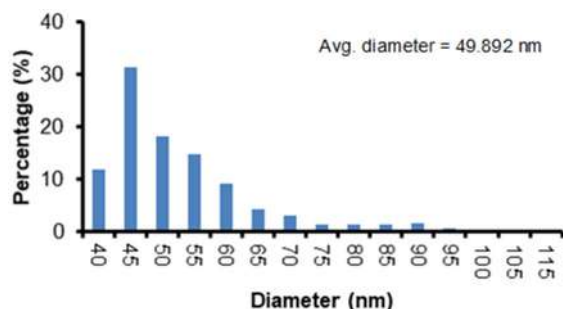


Fig 6. AFM cross-section analysis of ZnO/AgCl NCs

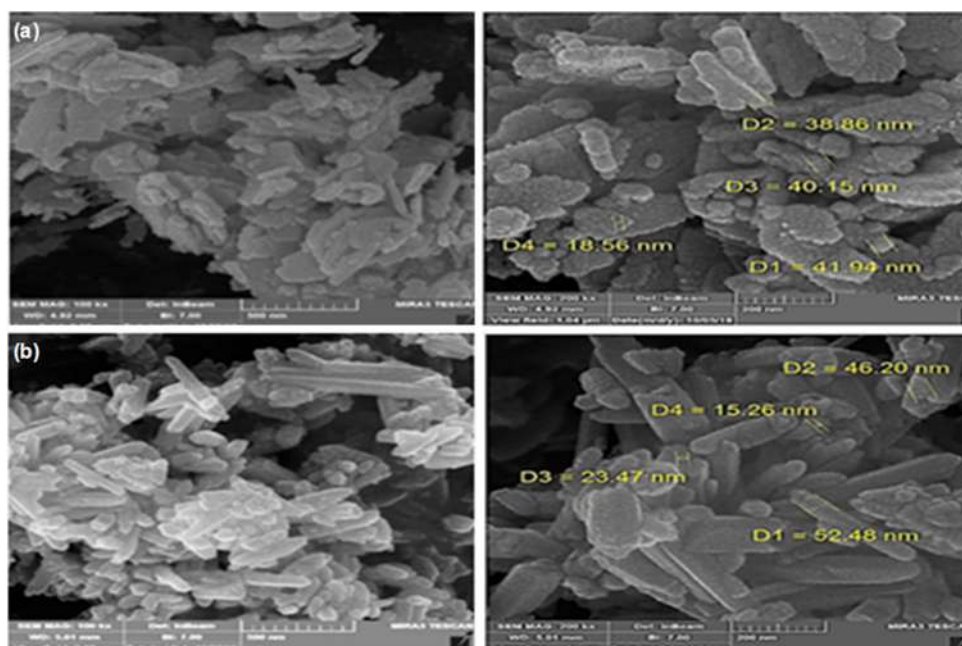


Fig 4. SEM images of (a) ZnO NPs and (b) ZnO-AgCl NCs nanocomposites

Epidermoid Carcinoma (Hep2), and Rhabdomyosarcoma (RD) are summarized in Table 1.

The results indicate that the *in vitro* cytotoxicity of IC<sub>50</sub> (μg) to all kinds of human cancer cells was moderate for pure ZnO NPs, while in the presence of ZnO/AgCl NCs the *in vitro* cytotoxicity of IC<sub>50</sub> (μg) to HCT116, Hep2, MCF-7, and HepG2 were strong, and RD was moderate. Fig. 7–9 explain the relative viability of cancer cells percentage (%) with various concentrations of doxorubicin, pure ZnO NPs, and ZnO/AgCl NCs. The

results indicate that these percentages decreased with increasing of nanoparticles as a result of increasing interaction between prepared nanoparticles and cancer cells [22].

The mechanism of cytotoxicity from ZnO NPs and ZnO/AgCl NCs was based on the reactive oxidation species ROS (O<sub>2</sub><sup>•-</sup>, OH<sup>•</sup>, H<sub>2</sub>O<sub>2</sub>) generation through oxidative stress [23]. It is believed that intracellular oxidation species can connect the chain of mitochondrial electron transport, and it is suggested that

**Table 1.** *In vitro* IC<sub>50</sub> of ZnO NPs and ZnO/AgCl NCs against human tumor cells HepG2, HCT116, MCF-7, RD, and Hep2 compared to doxorubicin

Compounds	<i>In vitro</i> cytotoxicity IC <sub>50</sub> (μg)				
	HepG2	HCT116	MCF-7	RD	Hep2
DOX	4.50 ± 0.2	5.23 ± 0.3	4.17 ± 0.2	6.10 ± 0.4	8.54 ± 0.6
ZnO	33.23 ± 3.2	37.09 ± 3.8	29.50 ± 2.7	47.08 ± 4.1	20.53 ± 2.3
ZnO/AgCl#	10.92 ± 1.3	11.15 ± 1.2	19.25 ± 1.9	24.93 ± 2.5	17.38 ± 1.4

IC<sub>50</sub> (μg): 1–10 (very strong), 11–20 (strong), 21–50 (moderate), 51–100 (weak) and above 100 (non-cytotoxic)

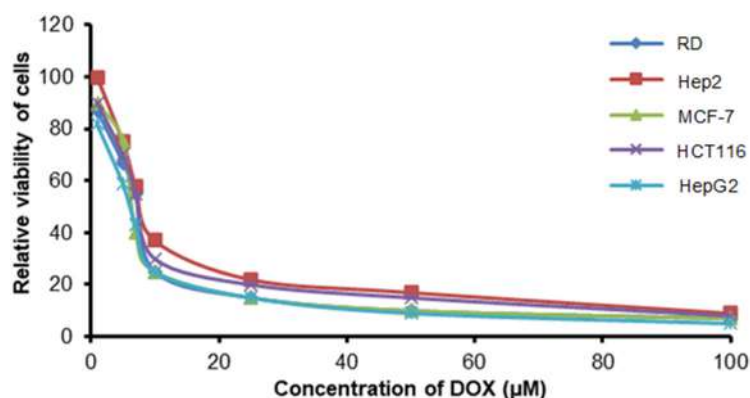


**Fig 7.** Relative viability of cells cancer (%) against the doxorubicin concentration (μM)

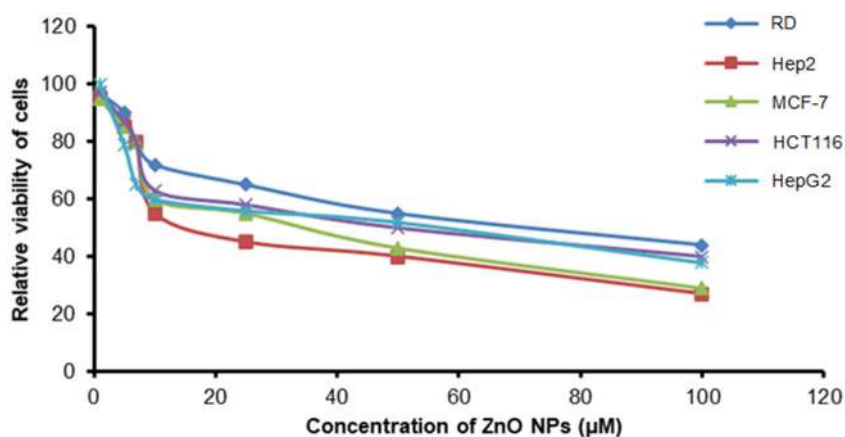


**Fig 8.** Relative viability of cells cancer (%) against the ZnO oxide nanoparticles concentration (μM)



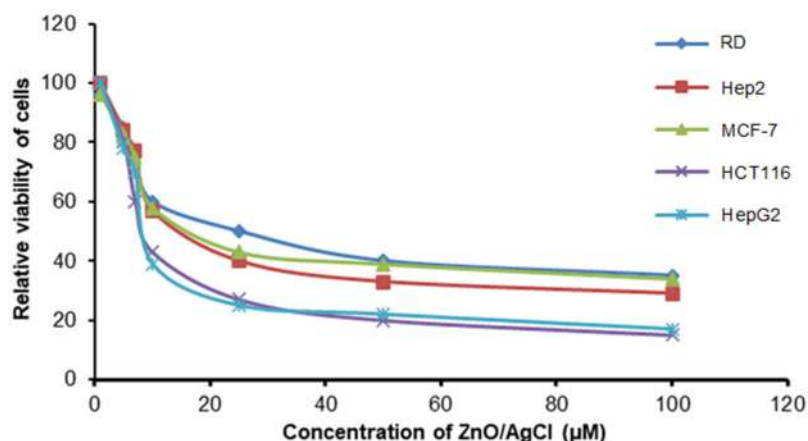


Fig 9. Relative viability of cells cancer (%) against the ZnO/AgCl nanocomposites concentration (μM)

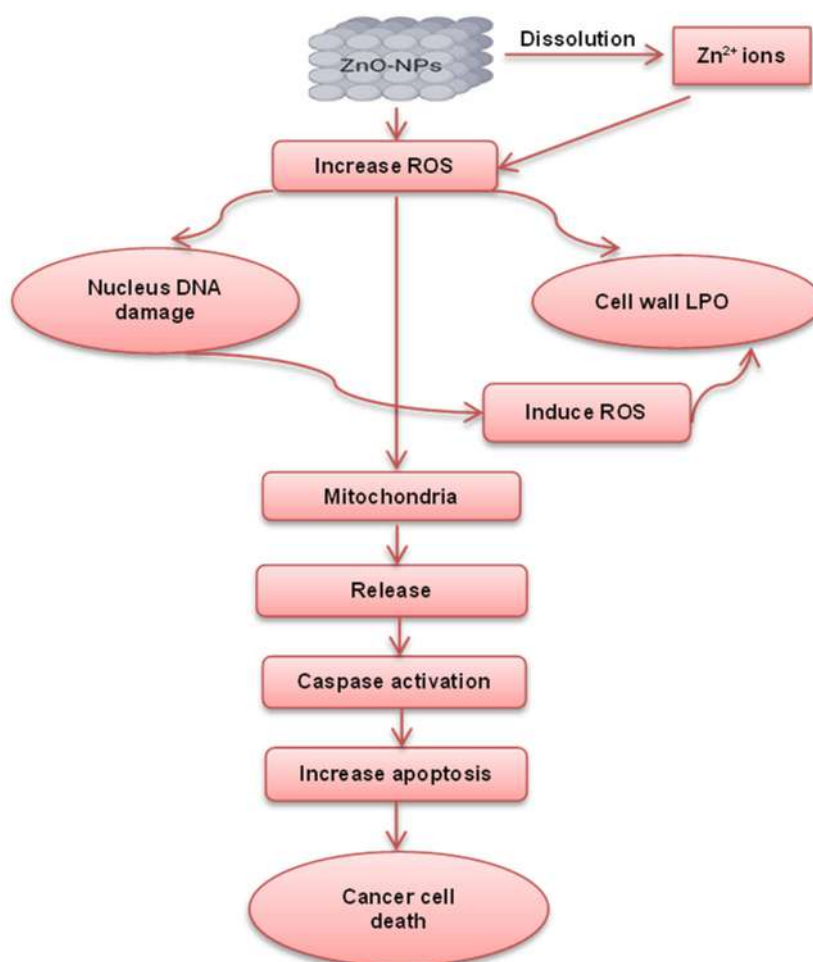


Fig 10. Schematic diagram of the possible mechanism for anticancer activity of ZnO NPs

the anticancer agents can attack cancer cells and damage the chain of electron transport due to the release of ROS intracellular [24]. Mitochondrial was damaged due to elevated levels of ROS then the balance of protein

activities was lost, ultimately leading to apoptosis [25]. Dissolution of ZnO NPs causes increasing in intracellular levels of dissolved  $Zn^{2+}$  and enhancing ROS production. These ROS disrupted the mitochondrial

membrane and caused the death of cancer cells via an apoptotic signaling pathway [26].

The results of Table 1 show increasing in anticancer activity by using ZnO/AgCl NCs as compared to pure ZnO NPs. This remark can be interpreted as the coupling of ZnO NPs with AgCl can reduce the band gap energy of ZnO (3.2 eV) and extend the excitation process from UV to the visible region [27]. Reducing the energy of band gap nanoparticles causes enhances the ability of these nanoparticles to generate oxidation species which leads to harm to the components of cancer cells [28]. A possible mechanism of ZnO NPs anticancer activity was illustrated in Fig. 10.

## ■ CONCLUSION

Pure ZnO NPs and ZnO/AgCl NCs were prepared. The structural properties of nanoparticles were investigated through XRD, FE-SEM, and AFM. Five human cancer cells (HCT116, HepG2, Hep-2, RD, and MCF-7) were used to examine anticancer activity for prepared samples. The previous studies were increasing anticancer potential by using ZnO/AgCl NCs as compared to pure ZnO NRs due to decreasing band gap energy of nanocomposites which lead to elevated levels of ROS and oxidative stress. Elevated ROS causes harm to the mitochondrial membrane and the destruction of cellular components such as DNA, lipids, proteins, and damage cells. The results show the anticancer activity of ZnO/AgCl NCs was increased as compared to naked ZnO NRs of cytotoxicity. The main mechanism of ZnO NPs and ZnO/AgCl NCs cytotoxicity results from ROS generation and release of  $Zn^{2+}$  and  $Ag^{1+}$  ions. Another mechanism suggested the formation of electrostatic forces on the surface of nanoparticles and the layered membrane of the cancer cell.

## ■ REFERENCES

- [1] Ratan, Z.A., Haidere, M. F., Nurunnabi, M., Shahriar, S.M., Ahammad, A.J.S., Shim, Y.Y., Reaney, M.J.T., and Cho, J.Y., 2020, Green chemistry synthesis of silver nanoparticles and their potential anticancer effects, *Cancers*, 12 (4), 855.
- [2] Abdolmaleki, A., Asadi, A., Gurushankar, K., Shayan, T.K., and Sarvestani, F.A., 2021, Importance of nano medicine and new drug therapies for cancer, *Adv. Pharm. Bull.*, 11 (3), 450–457.
- [3] Hussain, A., Oves, M., Alajmi, M.F., Hussain, I., Amir, S., Ahmed, J., Rehman, M.T., El-Seedi, H.R., and Ali, I., 2019, Biogenesis of ZnO nanoparticles using *Pandanus odorifer* leaf extract: Anticancer and antimicrobial activities, *RSC Adv.*, 9 (27), 15357–15369.
- [4] Anjum, S., Hashim, M., Malik, S.A., Khan, M., Lorenzo, J.M., Abbasi, B.H., and Hano, C., 2021, Recent advances in zinc oxide nanoparticles (ZnO NPs) for cancer diagnosis, target drug delivery, and treatment, *Cancers*, 13 (18), 4570.
- [5] Wang, J., Gao, S., Wang, S., Xu, Z., and Wei, L., 2018, Zinc oxide nanoparticles induce toxicity in CAL 27 oral cancer cell lines by activating PINK1/Parkin-mediated mitophagy, *Int. J. Nanomed.*, 13, 3441.
- [6] Makkawi, A.J.J., Aysa, N.H., and Gassim, F.A.G., 2019, Anticancer activity of zinc oxide and zinc oxide/cadmium sulfide nanocomposites, *Asian J. Pharm. Clin. Res.*, 12 (2), 535–539.
- [7] Sawant, V.J., and Bamane, S.R., 2018, PEG-beta-cyclodextrin functionalized zinc oxide nanoparticles show cell imaging with high drug payload and sustained pH responsive delivery of curcumin in to MCF-7 cells, *J. Drug Delivery Sci. Technol.*, 43, 397–408.
- [8] Safdar Ali, R., Meng, H., and Li, Z., 2022, Zinc-based metal-organic frameworks in drug delivery, cell imaging, and sensing, *Molecules*, 27 (1), 100.
- [9] Xiong, H.M., 2013, ZnO nanoparticles are applied to bioimaging and drug delivery, *Adv. Mater.*, 25 (37), 5329–5335.
- [10] Hashimoto, H., Tanino, R., Nakamura, M., and Fujita, Y., 2015, Surface treatment of zinc oxide nanoparticles by silica coating and evaluation of their dispersibility and photoluminescent properties, *e-J. Surf. Sci. Nanotechnol.*, 13, 451–454.

- [11] Khatami, M., Varma, R.S., Zafarnia, N., Yaghoobi, H., Sarani, M., and Kumar, V.G., 2018, Applications of green synthesized Ag, ZnO and Ag/ZnO nanoparticles for making clinical antimicrobial wound-healing bandages, *Sustainable Chem. Pharm.*, 10, 9–15.
- [12] Ng, C.T., Yong, L.Q., Hande, M.P., Ong, C.N., Yu, L.E., Bay, B.H., and Baeg, G.H., 2017, Zinc oxide nanoparticles exhibit cytotoxicity and genotoxicity through oxidative stress responses in human lung fibroblasts and *Drosophila melanogaster*, *Int. J. Nanomed.*, 12, 1621–1637.
- [13] Chica, A., Gatti, G., Moden, B., Marchese, L., and Iglesia, E., 2006, Selective catalytic oxidation of organosulfur compounds with *tert*-butyl hydroperoxide, *Chem. - Eur. J.*, 12 (7), 1960–1967.
- [14] Aysa, N.H., Al-Maamori, M.H., and Al-Maamori, N.A.A., 2017, Preparation and surface modification of zinc oxide nanoparticles, *J. Univ. Babylon Pure Appl. Sci.*, 25 (2), 497–503.
- [15] Pirhashemi, M., and Habibi-Yangjeh, A., 2014, Preparation of AgCl–ZnO nanocomposites as highly efficient visible-light photocatalysts in water by a one-pot refluxing method, *J. Alloys Compd.*, 601, 1–8.
- [16] Xiao, F., Xu, T., Lu, B., and Liu, R., 2020, Guidelines for antioxidant assays for food components, *Food Front.*, 1 (1), 60–69.
- [17] Kavitha, R., 2018, Antidiabetic and enzymatic antioxidant potential from ethanolic extracts of leaf and fruit of *Trichosanthes dioica* and leaf of *Clitoria ternatea* on diabetic rats induced by streptozotocin, *Asian J. Pharm. Clin. Res.*, 11 (5), 233–239.
- [18] Bazant, P., Kuritka, I., Munster, L., and Kalina, L., 2015, Microwave solvothermal decoration of the cellulose surface by nanostructured hybrid Ag/ZnO particles: A joint XPS, XRD and SEM study, *Cellulose*, 22 (2), 1275–1293.
- [19] Ai, L., Zhang, C., and Jiang, J., 2013, Hierarchical porous AgCl@Ag hollow architectures: Self-templating synthesis and highly enhanced visible light photocatalytic activity, *Appl. Catal., B*, 142–143, 744–751.
- [20] Gabar Gassim, F.A.Z., Makkaw, A.J., and Aysa, N.H., 2021, Removal of mercury(II) in aqueous solution by using ZnO and ZnO/CdS nanoparticles as photocatalysts, *Iran. J. Catal.*, 11 (4), 397–403.
- [21] Savaloni, H., and Savari, R., 2018, Nano-structural variations of ZnO:N thin films as a function of deposition angle and annealing conditions: XRD, AFM, FESEM and EDS analyses, *Mater. Chem. Phys.*, 214, 402–420.
- [22] Weiss, C., McLoughlin, P., and Cathcart, H., 2015, Characterisation of dry powder inhaler formulations using atomic force microscopy, *Int. J. Pharm.*, 494 (1), 393–407.
- [23] Fan, M., Han, Y., Gao, S., Yan, H., Cao, L., Li, Z., Liang, X.J., and Zhang, J., 2020, Ultrasmall gold nanoparticles in cancer diagnosis and therapy, *Theranostics*, 10 (11), 4944–4957.
- [24] Diebold, L., and Chandel, N.S., 2016, Mitochondrial ROS regulation of proliferating cells, *Free Radical Biol. Med.*, 100, 86–93.
- [25] Moghimipour, E., Rezaei, M., Ramezani, Z., Kouchak, M., Amini, M., Angali, K.A., Dorkoosh, F.A., and Handali, S., 2018, Transferrin targeted liposomal 5-fluorouracil induced apoptosis via mitochondria signaling pathway in cancer cells, *Life Sci.*, 194, 104–110.
- [26] Guo, C., Sun, L., Chen, X., and Zhang, D., 2013, Oxidative stress, mitochondrial damage, and neurodegenerative diseases, *Neural Regener. Res.*, 8 (21), 2003–2014.
- [27] Jiang, J., Pi, J., and Cai, J., 2018, The advancing of zinc oxide nanoparticles for biomedical applications, *Bioinorg. Chem. Appl.*, 2018, 1062562.
- [28] Pimpliskar, P.V., Motekar, S.C., Umarji, G.G., Lee, W., and Arbuj, S.S., 2019, Synthesis of silver-loaded ZnO nanorods and their enhanced photocatalytic activity and photoconductivity study, *Photochem. Photobiol. Sci.*, 18 (6), 1503–1511.

### Supplementary Data

This supplementary data is a part of a paper entitled “Synthesis and Biological Activity Study of Co and Cr Complexes with  $\alpha$ -(2-Salsayl)-*N*-phenyl Nitron and Oxide Nanoparticles”.

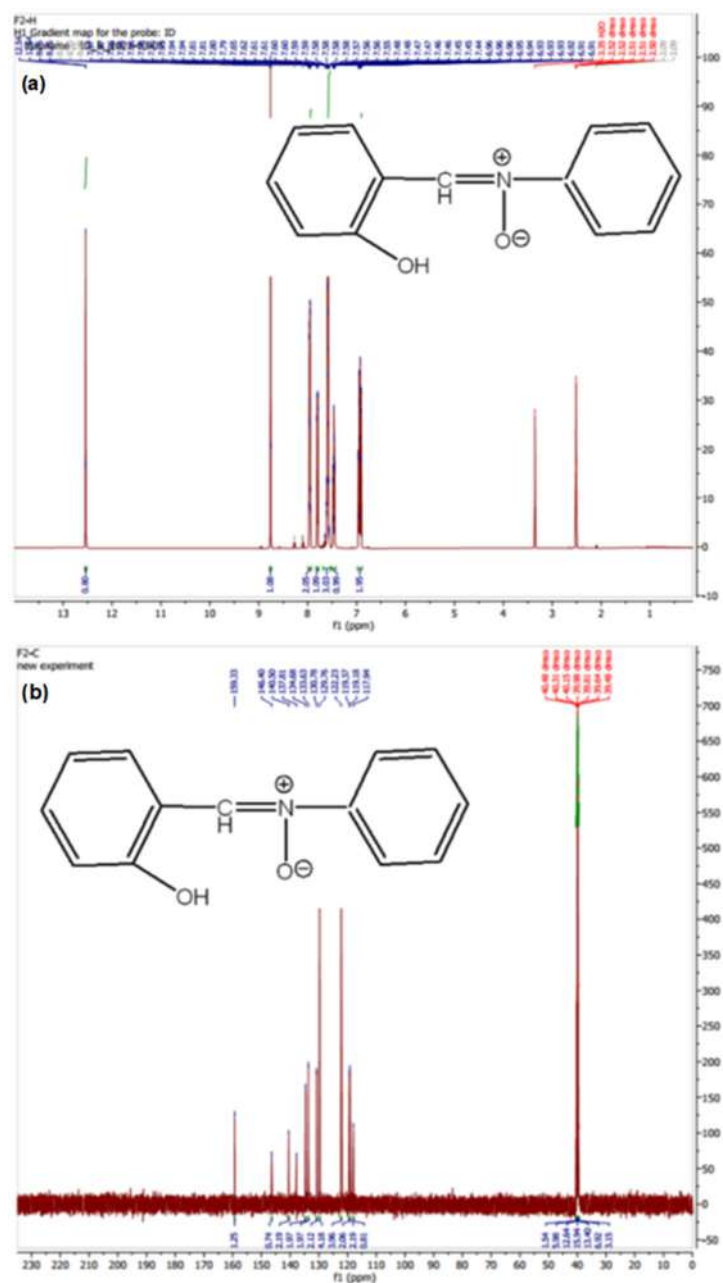


**Fig S1.** (a)  $^1\text{H-NMR}$  spectra of  $\alpha$ -(2-Salsayl)-*N*-phenyl Nitron (L), (b)  $^{13}\text{C-NMR}$  spectra of  $\alpha$ -(2-Salsayl)-*N*-phenyl Nitron (L)

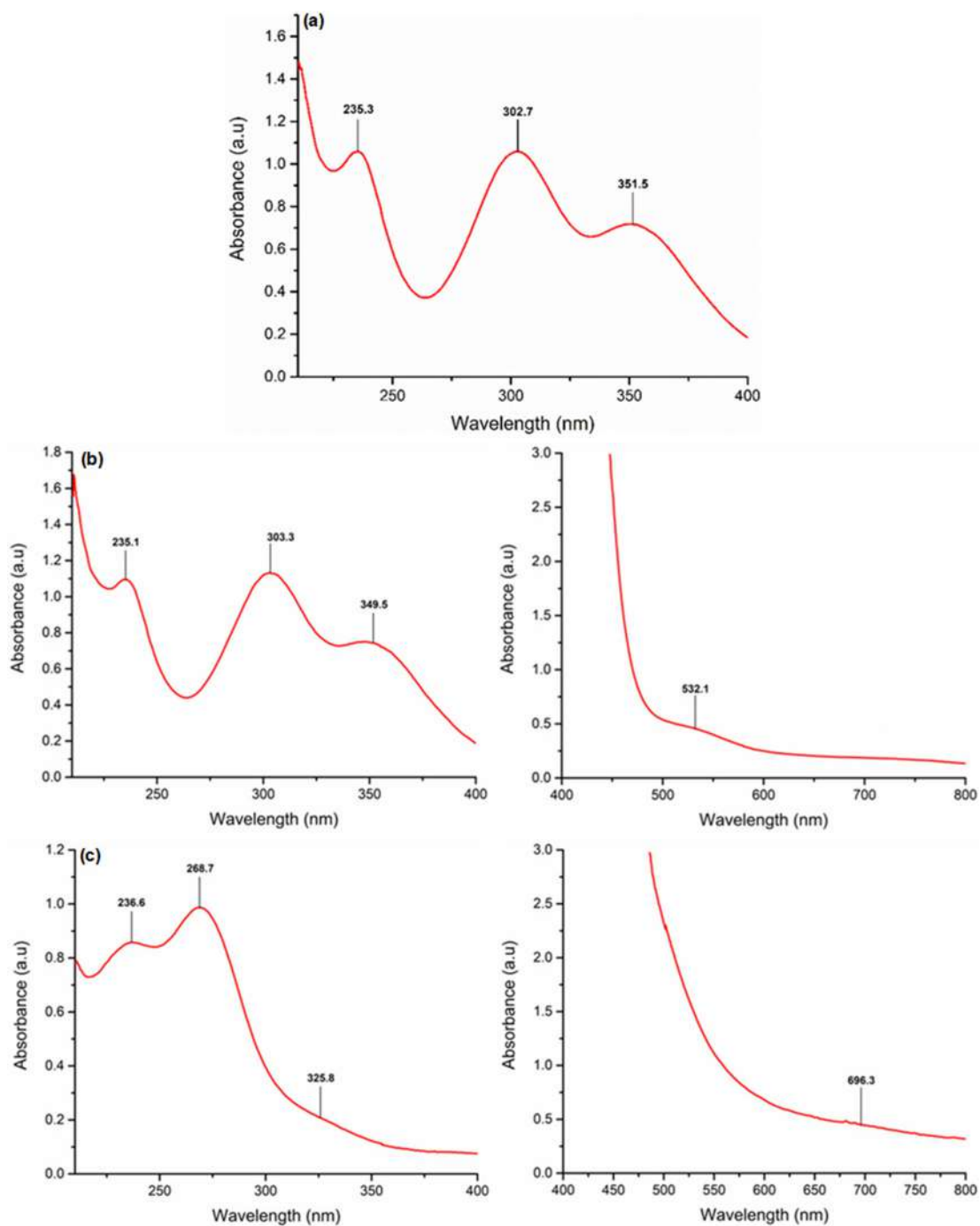


Fig S2. UV-Vis spectra of (a) L, (b) Complex 1, and (c) Complex 2

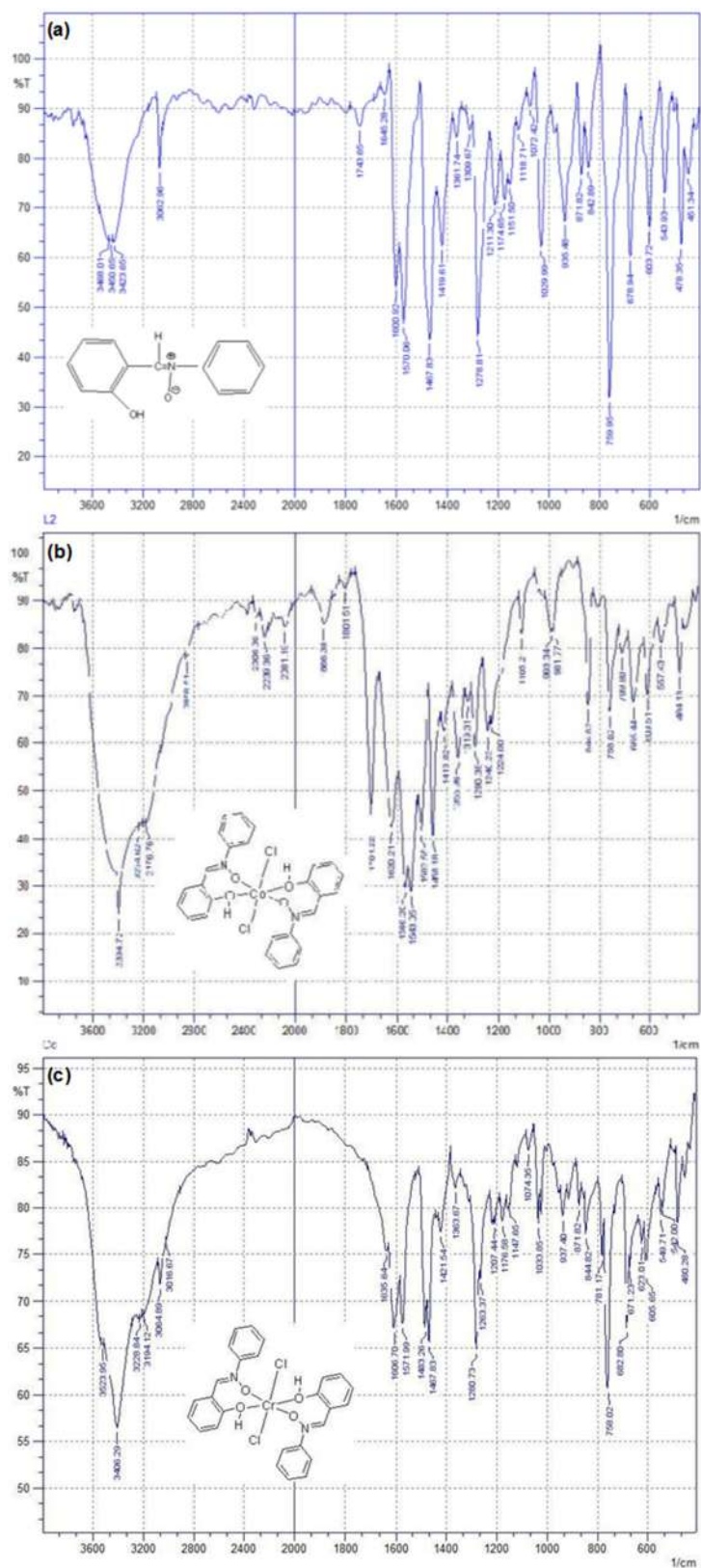


Fig S3. Infrared spectrum of (a) L, (b) Complex 1, and (c) Complex 2

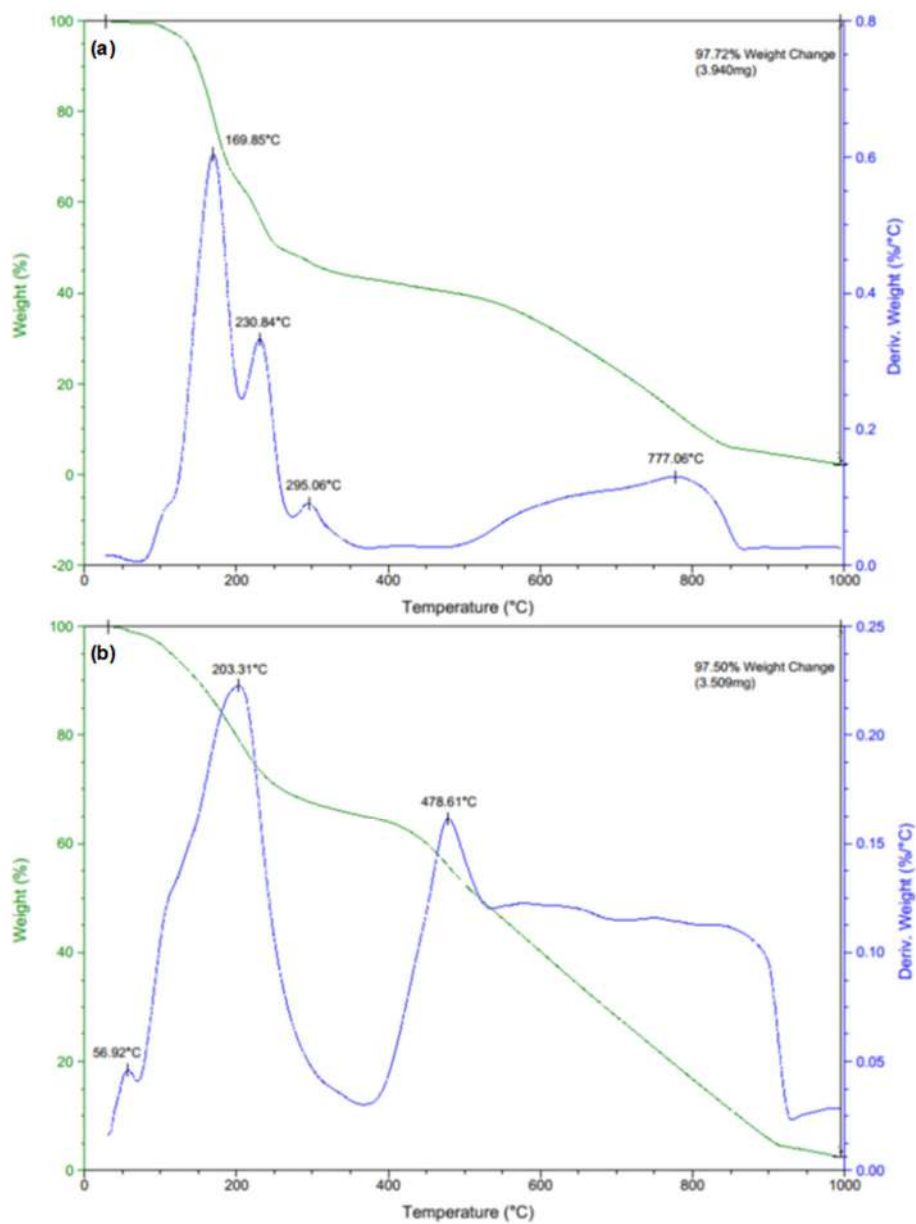


Fig S4. TGA/DTG of (a) Complex 1 and (b) Complex 2

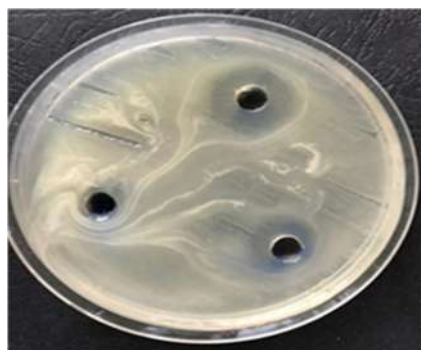


Fig S5. Antibacterial activity of 100  $\mu\text{g}/\text{mL}$  concentration of L on *E. coli*

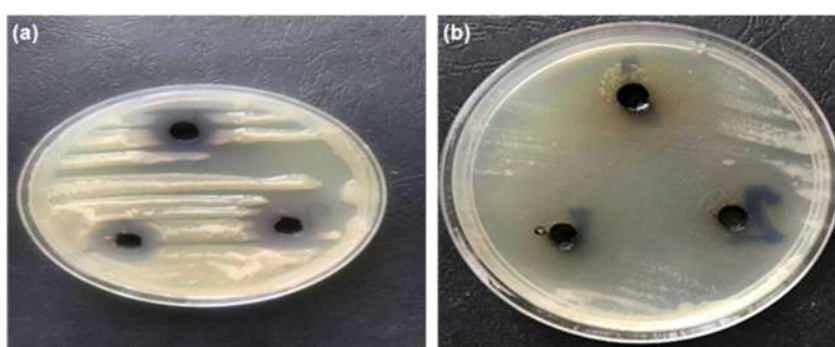


Fig S6. Antibacterial activity of 100  $\mu\text{g}/\text{mL}$  concentration of (a) Co(III) and (b) Cr(III) complexes on *E. coli*

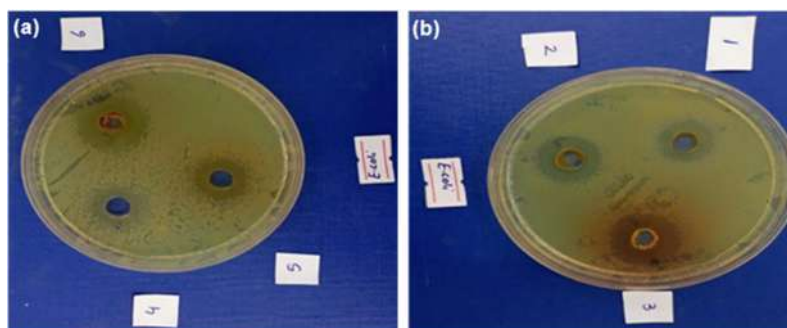
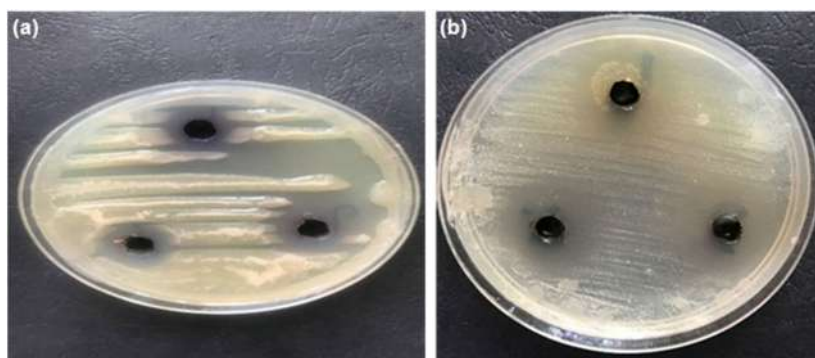


Fig S7. Antibacterial activity of 100  $\mu\text{g}/\text{mL}$  concentration of (a) Co(III) and (b) Cr(III) complexes by sonochemical on *E. coli*





**Fig S8.** Antibacterial activity of 100  $\mu\text{g}/\text{mL}$  concentration of L on *S. epidermis*



**Fig S9.** Antibacterial activity of 100  $\mu\text{g}/\text{mL}$  concentration of (a) Co(III) and (b) Cr(III) complexes on *S. epidermis*

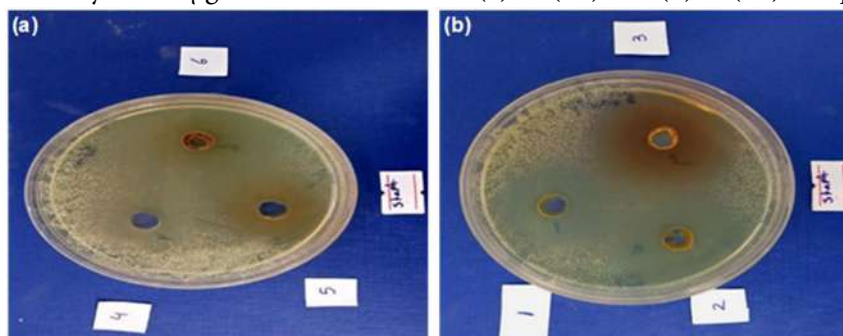


**Fig S10.** Antibacterial activity of 100  $\mu\text{g}/\text{mL}$  concentration of (a) Co(III) and (b) Cr(III) complexes by sonochemical on *S. epidermis*

## Synthesis and Biological Activity Study of Co and Cr Complexes with $\alpha$ -(2-Salsayl)-N-phenyl Nitron and Oxide Nanoparticles

Dhamiaa Abdul-Shaheed Issa, Hayder Baqer Abdullah, and Faeza Abdulkareem Al-Mashal\*

Department of Chemistry, College of Education for Pure Science, University of Basrah, 61004 Basrah, Iraq

\* Corresponding author:

email: faeza.nasser@uobasrah.edu.iq

Received: August 25, 2022

Accepted: January 13, 2023

DOI: 10.22146/ijc.77276

**Abstract:** This paper describes the synthesis of two complexes from the ligand  $\alpha$ -(2-Salsayl)-N-phenyl nitron with  $\text{CoCl}_2$  and  $\text{CrCl}_2$ . The ligand was characterized by several spectroscopic techniques (ultraviolet/visible (UV/Vis), nuclear magnetic resonance ( $^1\text{H-NMR}$  and  $^{13}\text{C-NMR}$ ), Fourier-transform infrared spectroscopy (FTIR), and mass spectrometry (MS). While infrared, ultraviolet-visible (UV-Vis), thermal analysis, and job method studies were used to reveal the structure of the complexes. The synthesized complexes were then synthesized by the sonochemical method, and the copper and chromium oxide nanoparticles were produced using the thermal decomposition method. Scanning electron microscopy (SEM), Energy dispersive X-ray spectroscopy (EDX), and X-ray diffraction (XRD) characterization confirmed the formation of  $\text{Co}_3\text{O}_4$  and  $\text{Cr}_2\text{O}_3$  nanoparticles. Antimicrobial studies of the complexes against some microorganisms, such as *Staphylococcus epidermis* and *Escherichia coli*, utilizing the disk diffusion method, revealed the antibacterial activity of the complexes.

**Keywords:** nitrones; complex; nanoparticles; biological activity

### ■ INTRODUCTION

Nitron is an amine that contains N-oxide. Nitron derivatives preserve biological activity and are useful in pharmaceutical applications in which they are used as anti-microbial [1], electron spin spin-trapping [2-3], antioxidant [4-5], blood-brain barrier opening [6], and anti-cancer agents [7]. The nitron group forms the electron density on the oxygen atom that assists the process of coordination bonding with metals to form a stable coordination complex [8]. Major factors affecting the coordination are the metal ion and its charge, radius, and position in the periodic table, the ligands, and the mole ratio of metal-ligand; these factors affect the stability of the complex [9-10]. Many studies have reported the formation of coordination complexes that include nitron compounds as ligands. These ligands react with metals from transition elements, such as Zn(II), Cu(II), Ni(II), Cd(II), Co(II), and Cr(III) to form complexes that reveal high biological activity against inflammation and fungi [8,11-12]. Recently, several papers have reported exploiting compounds as capping agents for the synthesis of metal

oxide nanoparticles via numerous approaches [13]. This research presents ways to control sizes and shapes using different methods, such as microwave and hydrothermal synthesis [14], thermal decomposition methods [15], and chemical precipitation [16]. The thermal decomposition of transition metal complexes is fast, practicable, economical, and solvent- and surfactant-free, resulting in precise particle size, purity, and precise process conditions [17]. This work describes the reflex and sonochemical synthesis of two new complexes of Cr(III) and Co(III) in coordination with  $\alpha$ -(2-Salsayl)-N-phenyl nitron as the ligand after which the prepared metal oxide nanoparticles were prepared using the thermal decomposition method, physical properties were studied. Furthermore, the study of the ligand and the complexes' biological activity against *Staphylococcus epidermis* and *Escherichia coli* were examined (Fig. 1).

### ■ EXPERIMENTAL SECTION

#### Materials

Reagents and solvents were obtained from Fluka or

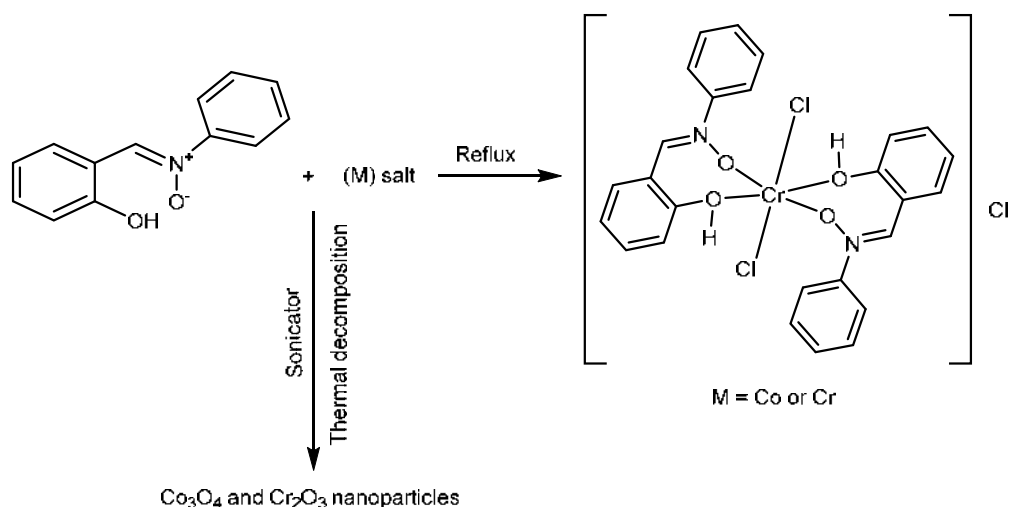


Fig 1. Schematic template of complexes and nanoparticles

Aldrich and were used as supplied. They included *N*-phenylhydroxylamine (95%), salicylaldehyde (98%), Cobalt chloride ( $\text{CoCl}_2 \cdot 6\text{H}_2\text{O}$ ) (97%), Chromium chloride ( $\text{CrCl}_2 \cdot 6\text{H}_2\text{O}$ ) (98%), ethanol (95%), chloroform (99%), and *n*-hexane (95%).

### Instrumentation

Ultraviolet/visible (UV/Vis) spectra were characterized using PD-303 UV-Vis Spectrophotometer, and infrared (IR) spectra were recorded on a Fourier transform infrared spectrometer (FTIR-8400S, Shimadzu) at wavelengths ranging from 600 to  $3800\text{ cm}^{-1}$ . Thermo Scientific™ FD1530M Muffle for furnace, Thermal analyses were performed using TG 209 F1 Libra. Nuclear magnetic resonance ( $^1\text{H}$  and  $^{13}\text{C}$ -NMR) spectra were analyzed on a BRUCKER-400 MHz  $\text{DMSO}-d_6$  solution using tetramethylsilane (TMS) as a reference. X-ray diffraction (XRD) characterization was achieved using a Philips PW 1730/10 X-Ray Diffractometer. Scanning electron microscopy (SEM) was done with a Nova NanoSEM 230.

### Procedure

#### Synthesis of $\alpha$ -(2-salsalyl)-*N*-phenyl nitron (L) [18]

A hot solution of 0.098 g (0.09 mmol) *N*-phenylhydroxylamine in 5 mL ethanol was added to a hot solution of 0.099 g (0.09 mmol) salicylaldehyde with continuous stirring, after which the solution was refluxed for 1 h until the disappearance of reactants as verified by thin layer chromatography. The yellow crystals were

recrystallized using a mixture of 3:7 ratio chloroform to *n*-hexane, and the yield was 88% with a melting point (m.p.) of  $116\text{ }^\circ\text{C}$ .

#### Synthesis of dichlorobis(2-hydroxyphenyl)-*N*-phenylmethanimine oxide)cobalt(III) (1)

A solution containing 0.0426 g (2.00 mmol) of L in 20 mL methanol was added to 0.230 g (1.00 mmol)  $\text{CoCl}_2 \cdot 6\text{H}_2\text{O}$  in methanol (20 mL), after which the mixture was refluxed with a stirrer until the disappearance of reactants as verified by thin layer chromatography for 3 h. After cooling, a yellowish-green precipitate was washed with cyclohexane three times. The yield was 93%, and the m.p. was  $265\text{ }^\circ\text{C}$ .

#### Synthesis of dichlorobis(2-hydroxyphenyl)-*N*-phenylmethanimine oxide)chromium(III) (2)

A solution containing 0.0426 g (2.00 mmol) of L in 20 mL methanol was added into 0.0237 g (1.00 mmol)  $\text{CrCl}_2 \cdot 6\text{H}_2\text{O}$  in methanol (20 mL), after which the mixture was refluxed with a stirrer until the disappearance of reactants as verified by thin-layer chromatography for 3 h. After cooling, the dark yellowish-green precipitate was washed with cyclohexane three times. The yield was 80%, and the m.p. of  $250\text{ }^\circ\text{C}$ .

#### Synthesis of complexes (1) and (2) via the sonochemical method

Solutions (1 L each) containing 0.170 g (0.01 mmol) in methanol (10 mL) were added to  $\text{CoCl}_2 \cdot 6\text{H}_2\text{O}$  0.090 g

(0.04 mmol) or  $\text{CrCl}_2 \cdot 6\text{H}_2\text{O}$  0.106 g (0.04 mmol). A methanol solution was added dropwise for 1 h in a 480 W (60 kHz) sonicator. The precipitate was filtered and washed with ethanol, followed by diethyl ether, dried, and saved under a vacuum desiccator.

### Synthesis of metal oxide nanoparticles

$\text{Cr}_2\text{O}_3$  and  $\text{Co}_3\text{O}_4$  nanoparticles were prepared via the thermal decomposition method [17]. The sonochemical method was applied to synthesize the complexes and was grounded to acquire a homogeneous powder, and afterward, the Cr(III) complex was heated at 530 °C, and the Co(III) complex was heated at 750 °C for 2 h in a muffle furnace. The resulting compound was washed with methanol 5 mL three times to remove any contamination.

## RESULTS AND DISCUSSION

The  $^1\text{H-NMR}$  spectra of **L** exhibited a singlet signal at 12.5 ppm that could be attributed to the hydroxide group proton (OH). A single signal for all spectra appeared at 8.95 ppm related to the proton of the nitrone group ( $-\text{HC}=\text{NO}$ ). Moreover, the **L** exhibited multiple signals ranging from 7.9 to 6.9 ppm, ascribed to the phenyl ring's protons. Depending on integration and position, they could be explained as; 6.9 ppm related to the  $\text{H}^3$  and  $\text{H}^5$  due to the electron donating group ( $-\text{OH}$ ), 7.5 ppm to the  $\text{H}^6$ , 7.58 ppm to the  $\text{H}^4$ ,  $\text{H}^{10}$  and  $\text{H}^{12}$ , 7.6 ppm to the  $\text{H}^{11}$ , and 7.9 ppm attributed to the  $\text{H}^9$  and  $\text{H}^{13}$ , (Fig. S1(a)).

The  $^{13}\text{C-NMR}$  spectral data were recorded to provide additional confirmation for the ligand and exhibited a band at 146.40 ppm that was attributed to the C-OH group; in addition, a band at 159.33 ppm related to the carbon resonance of the C=NO group and another band at 117 to 137 ppm, which was attributed to the aromatic carbon resonance (Ar-C). Moreover, the

spectrum shows an exceptional band for the carbon resonance of the C-NO group at 140.50 ppm (Fig. S1(b)).

The electronic spectrum of a methanol solution of **L** exhibits three bands at 335 nm (visible region) that could be ascribed to the  $\pi \rightarrow \pi^*$  transitions of the nitrone group, and at 302 nm and 351 nm, the bands were ascribed to the  $\pi \rightarrow \pi^*$  electronic transitions of the aromatic system. The electronic spectrum of a methanol solution of complex **1** displayed a hypsochromic shift at 349 nm and an electronic band at 532 nm that could be attributed to a  $d-d$  transition. Comparable results appear for complex **2**, hypsochromic shift at 325 nm for both complexes with a decrease in intensity. Moreover, complexes **2** and **3** exhibited  $d-d$  electronic transitions at 696 and 541 nm, respectively, verifying the coordination of the complex (Fig. S2).

IR spectra ( $400-4000\text{ cm}^{-1}$ ) of **L** and complexes **1** and **2** were recorded, and a character assessment of the infrared spectra bands of the synthesized parent ligand with that of complexes is presented. The ligand exhibited significant spectra in the regions 1570, 1600, and  $1174\text{ cm}^{-1}$  that could be ascribed to the  $\nu(\text{C}=\text{C})$ ,  $\nu(\text{C}=\text{N})$ , and  $\nu(\text{N} \rightarrow \text{O})$ , respectively [19]. Moreover, a strong band at  $3450\text{ cm}^{-1}$  was assigned to  $\nu(\text{O}-\text{H})$ .

The ( $\text{N} \rightarrow \text{O}$ ) and  $\nu(\text{C}=\text{N})$  bands of the complexes were found to be shifted to higher values compared with that of the parent ligand, recommending the involvement of the oxygen of the nitrone group in the complex [8]. Table 1 summarizes the most important spectra of the **L** and its complexity (Fig. S3).

Thermogravimetric analysis (TGA) curves and the consistent differential thermogravimetric analysis (DTG) curves for the synthesized complex in an atmosphere of nitrogen are presented in Fig. S4. A small weight loss occurred at 56.9 °C and 98.1 °C for Cr(III) and Co(III) complexes, respectively. These peaks could

**Table 1.** Infrared (IR) spectra for the ligand and the complexes

Compound	Ar(C-H)	Al(C-H)	C=N	C=C	N-O	O-H
<b>L</b>	3082	2950	1600	1570	1174	3450
<b>L-Co</b>	3234	2858	1620	1601	1240	3394
<b>L-Cr</b>	3064	2956	1606	1571	1176	3405

be attributed to the dehydration of water adsorbed by the complexes, whereas no indication of peaks in DTG at a range around 105–145 °C, which are related to coordinated water molecules, could be found; thus, the complexes are not coordinated with water [20]. The complexes then undergo the decomposition of related ligands in two or three stages. Furthermore, the complexes show high stability reaching up to ≈800 °C, and the total weight loss and the residue for the Co(III) and Cr(III) complexes were 97.72%/3.94 mg and 97.5%/3.50 mg, respectively. The residue can be explained by considering that the weight was either metal or metal oxide, which is an indication of complex formation.

To determine the mole ratio of the ligand to the metal, the method of continuous variation method was selected. A series of solutions were prepared in which the total mole fraction amount of the metal ions and the ligand were equal for all solutions. The absorbance of the solutions was then measured against methanol as a blank. When the difference between the observed absorbance was plotted against the mole fraction of solutions, a complex containing two moles of L to one mole of metal for Co(III) and Cr(III) was detected.

The synthesized Co<sub>3</sub>O<sub>4</sub> and Cr<sub>2</sub>O<sub>3</sub> nanoparticles' crystal phases and crystallinity were studied. The XRD patterns displayed the reflection planes as exhibited in Fig. 2 and Table 3, a highly ordered cubic Co<sub>3</sub>O<sub>4</sub> NPs was formed after calcination at 750 °C. This result proves the

purity of phase formation and the crystal structure of the nano-metal oxide products. The annealed sample shows well-resolved Bragg peaks of the XRD pattern, which are in good correspondence with the cubic structure of the Co<sub>3</sub>O<sub>4</sub> NPs. (Eq. (1)) estimated the Debye–Scherrer approximation of the average crystalline size assessment of the samples.

$$D = \frac{K\lambda}{\beta \cos\theta} \quad (1)$$

for which D represents the crystalline size,  $\theta$  represents the Bragg diffraction angle, K is the Scherrer constant,  $\lambda$  is the wavelength (0.15406 nm), and  $\beta$  represents the width of the XRD peak at half maximum height. The

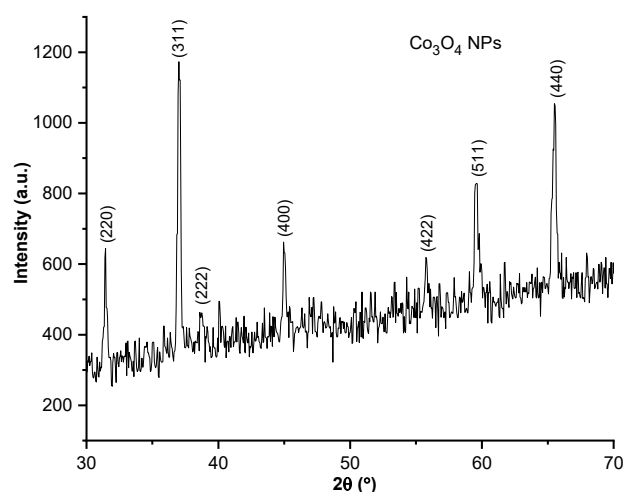


**Fig 2.** X-ray diffraction (XRD) patterns of the cubic Co<sub>3</sub>O<sub>4</sub> nanoparticles

**Table 2.** The absorbance of the metal complex solutions with L using the continuous variation method

	Vm/Vt	1/10	2/10	3/10	4/10	5/10
Co(III) complex	Xvm	0.10	0.20	0.30	0.40	0.50
	ABS	0.94	0.81	0.73	0.55	0.35
Cr(III) complex	Xvm	0.1	0.2	0.3	0.4	0.5
	ABS	0.55	0.48	0.45	0.33	0.24

**Table 3.** X-ray diffraction analysis of Co<sub>3</sub>O<sub>4</sub> nanoparticles shows estimated crystalline size for five intense peaks

Position 2θ (°)	Height (cts)	FWHM left 2θ (°)	d-spacing (Å)	Relative intensity (%)	Tip width	Crystalline size (D) value
31.4560	331.60	0.1968	2.84404	42.28	0.2362	41.26
37.0465	784.32	0.2460	2.42670	100.00	0.2952	35.37
44.9908	236.31	0.2952	2.01495	30.13	0.3542	27.70
59.5440	338.98	0.1968	1.55259	43.22	0.2362	41.26
65.5217	548.48	0.1968	1.42467	69.93	0.2362	41.26

Co<sub>3</sub>O<sub>4</sub> NPs' average crystalline size was found to be 36.89 nm.

Fig. 3 shows the X-ray diffraction of prepared Cr<sub>2</sub>O<sub>3</sub>. Table 4 shows the reflection plane patterns, which imply the existence of the rhombohedral structure. In addition, no peaks could be detected due to any other material or phase, thus proving a high degree of purity of the synthesized sample after calcination at 750 °C. The broadening of the XRD lines, as seen in Fig. 3, reflects the nano-particle nature of the sample.

The sharpness of the peaks indicates good crystal growth of the oxide nanoparticles. The average particle size (D) of the particles was calculated from the intensity peaks operating the Debye–Scherrer equation, as depicted in Table 4. The calculated average crystalline size for Cr<sub>2</sub>O<sub>3</sub> NPs is 30.55 nm.

Fig. 4 illustrates a scanning electron microscopy (SEM) image of prepared Co(III) and Cr(III) complexes utilizing the sonochemical method. The graph indicates a high degree of agglomeration among fine particles, mostly of nanoscale size, the diameter of the Co(III) complex was

mostly between 50 and 80 nm, and the size of the Cr(III) complex was close to 112–27 nm.

Fig. 5(a) exhibits an SEM image of the Co<sub>3</sub>O<sub>4</sub> NPs. The Co<sub>3</sub>O<sub>4</sub> NPs crystallinity was determined, and grains of the Co<sub>3</sub>O<sub>4</sub> NPs presented a closely consistent morphology with approximately 80 nm average diameter.

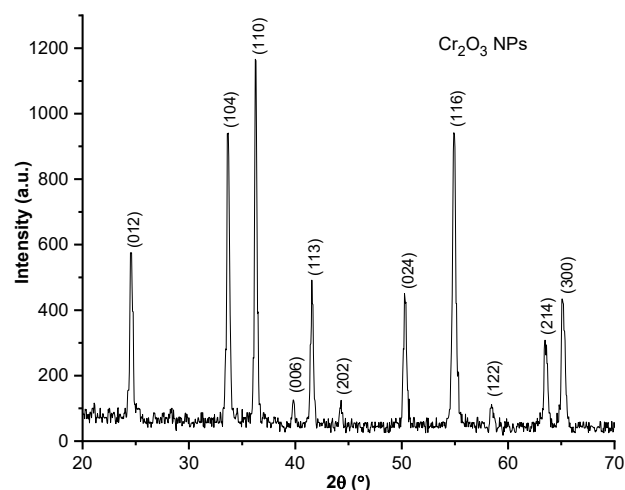


**Fig 3.** XRD patterns of the rhombohedral Cr<sub>2</sub>O<sub>3</sub> nanoparticles

**Table 4.** The XRD analysis of Cr<sub>2</sub>O<sub>3</sub> nanoparticles shows the estimated crystalline size for six intense peaks

Position 2θ (°)	Height (cts)	FWHM left 2θ (°)	d-spacing (Å)	Relative intensity (%)	Tip width	Crystalline size (D) value
24.5397	501.62	0.1968	3.62767	43.72	0.2362	41.26
33.6627	882.13	0.2952	2.66249	76.89	0.3542	27.70
36.2684	1147.27	0.2460	2.47696	100.00	0.2952	35.37
41.6022	369.99	0.2952	2.17089	32.25	0.3542	23.58
50.3359	379.96	0.3444	1.81280	33.12	0.4133	14.14
63.4590	269.07	0.1968	1.46591	23.45	0.2362	41.26

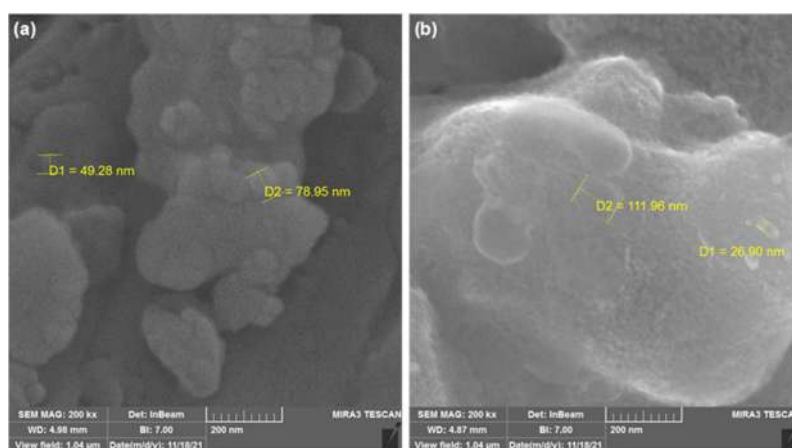


**Fig 4.** SEM micrograph of (a) Co(III) and (b) Cr(III) complexes prepared via the sonochemical method

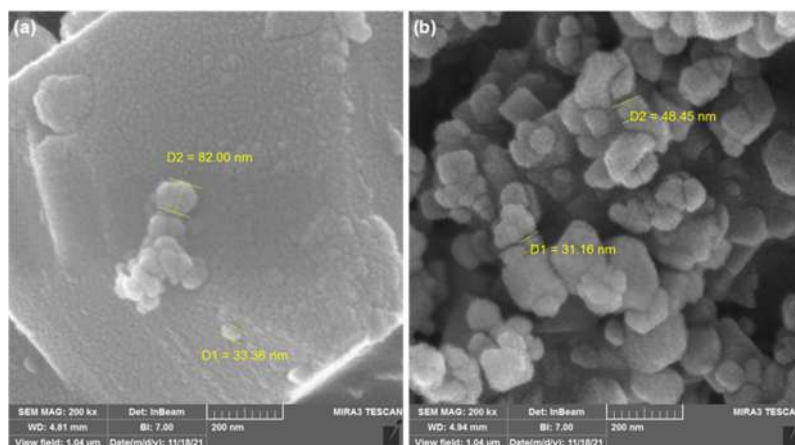


**Fig 5.** SEM micrograph of (a)  $\text{Co}_3\text{O}_4$  and (b)  $\text{Cr}_2\text{O}_3$  nanoparticles

**Table 5.** Antibacterial activity of different concentrations against *Escherichia coli* and *Staphylococcus epidermis*

No.	Compound	Concentration (mg/mL)	Inhibition zone (mm)	
			<i>S. epidermis</i>	<i>E. coli</i>
1	Ampicillin	10	29	21
2	Gentamycin	10	19	18
3	$L_1$	50	22	18
		25	21	12
		10	13	0
4	Co(III) CR	50	16	25
		25	15	20
		10	14	19
5	Cr(III) CR	50	25	22
		25	22	20
		10	21	18
	Co(III) NC	50	36	21
		25	24	15
		10	16	14
	Cr(III) NC	50	35	18
		25	20	18
		10	22	15

CR: complex made by reflux, NC: complex made by sonochemical

In addition, Fig. 5(b) illustrates an SEM image of the  $\text{Cr}_2\text{O}_3$  nanoparticles. The grains of  $\text{Cr}_2\text{O}_3$  NPs consisted of an average diameter of approximately 50 nm, indicating a uniform morphology.

The crystalline size differs from the particle size in this work since the particle characterized by XRD was a crystallized size, a crystal particle termed a primary particle, while the particles analyzed by SEM are typically particles consisting of more than primary particles.

*In vitro*, antibacterial activity for the Nitrotrone base ligand and complexes against *E. coli* and *S. epidermis* using the diffusion method were studied. This test was assessed depending on inhibition formed around the paper disks on the seeded agar plates by calculating the size basis of the zone appearing. Ampicillin and gentamycin were used as standards, Fig. S5–S10 shows the inhibition zone diameter of *E. coli* and *S. epidermis* by the ligand and complexes.

The results are embedded in Table 5. Evaluating the biological activity of the complex with the standard, the biological activity of the metal complexes was imminent to that of the standard. Besides, Co(III) and Cr(III) complexes synthesized by the sonochemical method affected the *E. coli* and *S. epidermis* to inhibit to the greatest degree.

## ■ CONCLUSION

In this paper, cobalt(III) and chromium(III) complexes from  $\alpha$ -(2-Salsayl)-*N*-phenyl Nitron were synthesized using the reflux and sonochemical methods and then characterized. Pure  $\text{Co}_3\text{O}_4$  and  $\text{Cr}_2\text{O}_3$  nanoparticles with cubic and rhombohedral structures, respectively, were well prepared via the decomposition of the complex under a muffle furnace. The thermal decomposition method is simple, practicable, and appropriate for producing high-purity products for metal oxide nanoparticles. The complexes synthesized via the two methods were selected for antibacterial activity against *E. coli* and *S. epidermis*, which are considered clinically important bacteria, and the complexes demonstrated high antibacterial activity against these types of bacteria.

## ■ ACKNOWLEDGMENTS

The authors gratefully acknowledge the Department of Chemistry, College of Education for Pure Sciences, University of Basrah, for the support.

## ■ AUTHOR CONTRIBUTIONS

Dhamiaa Abdul-Shaheed Issa conducted the experiment, Hayder Baqer Abdullah writing the original Draft and Editing, Faeza Abdulkareem Al-Mashal Supervision and revised the manuscript. All authors agreed to the final version of this manuscript.

## ■ REFERENCES

- [1] Ferraz, M.C., Mano, R.A., Oliveira, D.H., Maia, D.S.V., Silva, W.P., Savegnago, L., Lenardão, E.J., and Jacob, R.G., 2017, Synthesis, antimicrobial, and antioxidant activities of chalcogen-containing nitron derivatives from (*R*)-citronellal, *Medicines*, 4 (2), 39.
- [2] Scott, M.J., Billiar, T.R., and Stoyanovsky, D.A., 2016, *N*-*tert*-butylmethanimine *N*-oxide is an efficient spin-trapping probe for EPR analysis of glutathione thiy radical, *Sci. Rep.*, 6 (1), 38773.
- [3] Pinheiro, A.C., Fazzi, R.B., Esteves, L.C., Machado, C.O., Dörr, F.A., Pinto, E., Hattori, Y., Sa, J., da Costa Ferreira, A.M., and Bastos, E.L., 2021, A bioinspired nitron precursor to a stabilized nitroxide radical, *Free Radical Biol. Med.*, 168, 110–116.
- [4] Lo Celso, F., Barone, G., Maiuolo, L., Algieri, V., Cretu, C., and Calandra, P., 2022, Dissolution of nitrones in alkylphosphates: A structural study, *J. Mol. Liq.*, 367, 120517.
- [5] Chamorro, B., Diez-Iriepa, D., Merás-Sáiz, B., Chioua, M., García-Vieira, D., Iriepa, I., Hadjipavlou-Litina, D., López-Muñoz, F., Martínez-Murillo, R., González-Nieto, D., Fernández, I., Marco-Contelles, J., and Oset-Gasque, M.J., 2020, Synthesis, antioxidant properties and neuroprotection of  $\alpha$ -phenyl-*tert*-butylnitron derived *HomoBisNitrones* in *in vitro* and *in vivo* ischemia models, *Sci. Rep.*, 10 (1), 14150.
- [6] Towner, R.A., Saunders, D., Lerner, M., Silasi Mansat, R., Yuan, T., Barber, D., Faakye, J., Nyul-Toth, A., Csiszar, A., Greenwood-Van Meerveld, B., and Smith, N., 2021, Temporary opening of the blood-brain barrier with the nitron compound OKN-007, *Am. J. Nucl. Med. Mol. Imaging*, 11 (5), 363–373.
- [7] Haddad, B.S., and Al-Shawi, A.A.A., 2020, Cytotoxicity of new selenimine, selenonitron and nitron derivatives against human breast cancer MDA-MB231 cells, *Egypt. J. Chem.*, 63 (11), 4607–4613.
- [8] Raspertova, I.V., Doroschuk, R.O., Khomenko, D.M., and Lampeka, R.D., 2017, Synthesis, spectroscopic, structural characterization of Cd(II) and Zn(II) complexes based on the *N*-methyl-*C*-(2-pyridyl)nitron, *J. Coord. Chem.*, 70 (16), 2888–2899.
- [9] Sorriso, S., 1982, “Structural Chemistry” in *The Chemistry of Amino, Nitroso and Nitro Compounds*



- and Their Derivatives, Eds. Patai, S., John Wiley & Sons, Hoboken, New Jersey, 1–51.
- [10] Hussein, K.A., and Shaalan, N., 2022, Synthesis, characterization, and antibacterial activity of lanthanide metal complexes with Schiff base ligand produced from reaction of 4,4-methylene diantipyrine with ethylenediamine, *Indones. J. Chem.*, 22 (5), 1365–1375.
- [11] Thirumalaikumar, M., Sivakolunthu, S., Muthusubramanian, S., Mohan, P., and Sivasubramanian, S., 1999, Synthesis, characterization and antimicrobial studies of metal(II) bis-chelates and mixed-ligand complexes of alpha-(2-hydroxyphenyl)-N-(1-phenyl-2-nitroethyl)nitron, *Boll. Chim. Farm.*, 138 (5), 207–210.
- [12] Petkova, E.G., Domasevitch, K.V., Gorichko, M.V., Zub, V.Y., and Lampeka, R.D., 2001, New coordination compounds derived from nitron ligands: Copper(II) complexes with 8-hydroxyquinoline-2-carbaldehyde- and pyridine-2-carbaldehyde-N-methylnitrones, *Z. Naturforsch., B: Chem. Sci.*, 56 (12), 1264–1270.
- [13] Subhi, H.M., Bader, A.T., and Al-Gubury, H.Y., 2022, Synthesis and characterization of ZnO nanoparticles via thermal decomposition for Zn(II) Schiff base complex, *Indones. J. Chem.*, 22 (5), 1396–1406.
- [14] Onwudiwe, D.C., 2019, Microwave-assisted synthesis of PbS nanostructures, *Heliyon*, 5 (3), e01413.
- [15] Abdel-Monem, Y.K., Emam, S.M., and Okda, H.M.Y., 2017, Solid state thermal decomposition synthesis of CuO nanoparticles from coordinated pyrazolopyridine as novel precursors, *J. Mater. Sci.: Mater. Electron.*, 28 (3), 2923–2934.
- [16] Bekele, B., Degefa, A., Tesgera, F., Jule, L.T., Shanmugam, R., Priyanka Dwarampudi, L., Nagaprasad, N., and Ramasamy, K., 2021, Green versus chemical precipitation methods of preparing zinc oxide nanoparticles and investigation of antimicrobial properties, *J. Nanomater.*, 2021, 9210817.
- [17] Kafi-Ahmadi, L., and Shirmohammadzadeh, L., 2017, Synthesis of Co(II) and Cr(III) salicylidenic Schiff base complexes derived from thiourea as precursors for nano-sized Co<sub>3</sub>O<sub>4</sub> and Cr<sub>2</sub>O<sub>3</sub> and their catalytic, antibacterial properties, *J. Nanostruct. Chem.*, 7 (2), 179–190.
- [18] Chen, S., Zhao, K., and Chen, G., 2015, Synthesis and application of phenyl nitron derivatives as acidic and microbial corrosion inhibitors, *J. Chem.*, 2015, 201259.
- [19] Lin-Vien, D., Colthup, N.B., Fateley, W.G., and Grasselli, J.G., 1991, “Double Bonds Containing Nitrogen Atoms” in *The Handbook of Infrared and Raman Characteristic Frequencies of Organic Molecules*, Academic Press, San Diego, 191–211.
- [20] Kavitha, N., and Anantha Lakshmi, P.V., 2017, Synthesis, characterization and thermogravimetric analysis of Co(II), Ni(II), Cu(II) and Zn(II) complexes supported by ONNO tetradentate Schiff base ligand derived from hydrazino benzoxazine, *J. Saudi Chem. Soc.*, 21, S457–S466.

## Solubility Enhancement of Carvedilol by Solid Dispersion Technique Using Sodium Alginate, Guar Gum, Xanthan Gum, and Locust Bean Gum as Polymers

Iyan Sopyan<sup>1\*</sup>, Nurdiani Adiningsih<sup>1</sup>, Sandra Megantara<sup>2</sup>, and Siska Sari Marvita<sup>1</sup>

<sup>1</sup>Department Pharmaceutics and Pharmaceutical Technology, Faculty of Pharmacy, Padjadjaran University, Jl. Bandung-Sumedang KM 21, Sumedang 45363, West Java, Indonesia

<sup>2</sup>Department Pharmaceutical Analysis and Medicinal Chemistry, Faculty of Pharmacy, Padjadjaran University, Jl. Bandung-Sumedang KM 21, Sumedang 45363, West Java, Indonesia

\* Corresponding author:

email: i.sopyan@unpad.ac.id

Received: September 13, 2022

Accepted: December 15, 2022

DOI: 10.22146/ijc.77698

**Abstract:** Carvedilol (CVD) is a non-selective  $\beta$ -blocker. CVD is included in BCS class II. It has low water solubility. In this research, solid dispersion was used to increase the solubility and dissolution profile of CVD. In silico study using the ligand-ligand docking method. The preparation of solid dispersion using the kneading method with a weight ratio of 1:1, 1:2, 1:3, and 1:4, evaluation of solid dispersion includes solubility and dissolution. The best solid dispersion was characterized using FTIR, DSC, and PXRD. In silico study showed complexes CVD-SA, CVD-GG, CVD-XG and CVD-LBG have a hydrogen interaction. SA and XG were chosen as carriers in solid dispersion. CVD solid dispersion showed increased solubility in all samples, with the highest increase at 90.63 times at CVD: XG (1:4). The results of the dissolution profile obtained at 60 min are  $64.95 \pm 0.45\%$  at pure CVD,  $83.32 \pm 1.19\%$  at CVD:SA (1:4), and  $72.56 \pm 3.62\%$  at CVD: XG (1:4). The FTIR spectrum indicates an interaction between CVD and SA. The thermogram indicated the amorphous drug, and the diffractogram showed a decrease in crystallinity. Solid dispersion is proven to increase the solubility and dissolution profile of CVD. Solid dispersion CVD: SA (1:4) showed the highest solubility and dissolution profile.

**Keywords:** carvedilol; BCS class II; solid dispersion

### INTRODUCTION

Oral administration is the most common and convenient method of drug administration. The drug concentration in the blood must be reached for oral drugs to work effectively. The drug concentration depends on its bioavailability, which is strongly influenced by the rate and extent of drug absorption [1-2]. More than 70% of active pharmaceutical ingredients in formulation development have solid hydrophobic characteristics. As a result, inadequate bioavailability is a significant difficulty in the design of oral dosage forms. When it comes to poorly soluble drugs in water, substantial doses are frequently required to achieve therapeutic plasma concentrations following oral administration [3].

Cardiovascular disease is the leading cause of death globally. In 2019, an estimated 17.9 million individuals died

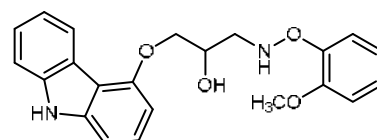


**Fig 1.** Chemical structure of carvedilol (CVD) [5]

from cardiovascular disease. And it is estimated that around 1.28 billion adults aged 30–79 years worldwide suffer from hypertension. Carvedilol (CVD) is a non-selective beta blocker with alpha-1 receptor blocking activity commonly used to treat cardiovascular diseases such as hypertension, ischemic heart disease, post-myocardial infarction, left ventricular dysfunction, and congestive heart failure [4]. The carvedilol structure (Fig. 1) shows various functional groups as donor and acceptor proton. With such a structure, CVD has several issues with its pharmaceutical formulations.

CVD has a minimal bioavailability of about 25–30% due to its practically insoluble solubility in water (10.42 mg/L) and exhibits a pH-dependent solubility and its dissolution limits absorption from the gastrointestinal tract. CVD undergoes extensive first-line metabolism, contributing to its low bioavailability [2]. CVD is classified as BCS class II by the Biopharmaceutics Classification System (BCS) because it has a high membrane permeability but poor solubility [6].

There have been several studies conducted to increase the solubility and bioavailability of CVD, some of which are micronization techniques, complex inclusion techniques [7–8], carbon dioxide supercritical techniques [9], hydrotropic techniques [10], nanotechnology [11], but these techniques are still inefficient in overcoming the problem of CVD solubility so that other efforts need to be made, including the solid dispersion approach. Solid dispersions are solid products in which the hydrophobic drug is dispersed in a hydrophilic polymer, which might be in an amorphous and molecularly microcrystalline form. The characteristics of the solid dispersion formulation are influenced by these hydrophilic polymers, also known as carriers. Due to the ease of preparation, optimization, and reproducibility of the production procedure, the solid dispersion technique is an excellent way to enhance solubility [7].

Determination of polymers as carriers in solid dispersions can be done by conducting in-silico studies. This computational technique is used to see the interactions between the drug and each candidate polymer. Using natural polymers as carriers in solid dispersions is an excellent choice to increase solubility because natural polymers are low in toxicity, biocompatible, biodegradable, and widely available. Natural polymers that can be used are sodium alginate (SA), guar gum (GG), xanthan gum (XG), and locust bean gum (LBG) [11–13].

SA is a hydrophilic polymer extracted from brown seaweed cell walls. As a hydrophilic polysaccharide, SA can improve the wettability of poorly soluble pharmaceuticals in water, reducing agglomeration and increasing surface area [14]. It has been demonstrated

that SA, a carrier of telmisartan's solid dispersion (an antihypertensive and member of BCS class II), can boost solubility up to 16.7 times more than pure telmisartan. Additionally, SA works well as an anti-plasticizer to avoid the recrystallization of drugs [11].

GG and XG have been shown to increase the dissolution of solid dispersion of valsartan (antihypertensive and belongs to BCS class II) up to 4.62 times compared to pure valsartan [15]. The solid dispersion of domperidone (an antiemetic and belongs to BCS class II drugs) using modified locust bean gum (MLBG) as a carrier showed an increase in solubility up to 12.62 times compared to pure drugs. The ability of MLBG to increase drug wettability and reduce drug particle size in solid dispersion leads to increased drug dissolution and results in increased drug bioavailability [16]. Therefore, SA, GG, XG, and LBG polymers allow an increase in the solubility of CVD through the solid dispersion method. Although it has been reported to increase the solubility of CVD using some of the techniques previously mentioned, it is still not efficient to increase the solubility of CVD, so in this study, an increase in the solubility of CVD was carried out utilizing the solid dispersion techniques with selected polymers based on the results of in silico studies. So far, there have not been many developed.

## ■ EXPERIMENTAL SECTION

### Materials

The materials used in this study were Hydrochloric acid (Merck), potassium bromide (Merck), carvedilol (Kalbe), ethanol (Merck), sodium alginate (Kimica), and xanthan gum (Qingdao ICD Biochemistry).

### Instrumentation

The instrumentations used in this study were UV-Vis spectrophotometer (Specord 205 Analytical Jena), USP dissolution apparatus type 2 (SotaX AT7 Smart dissolution tester), Fourier-Transformed Infrared Spectrophotometer (FTIR) (Specord 100), Differential Scanning Calorimetry (DSC) (Linseis PTA ST 1600), and X-ray diffractometer (PanAnalytical).

## Procedure

### *In silico simulation*

2D structures of CVD and polymer were drawn using ChemDraw. Ligand preparation was performed using AutoDockTools, and ligand-ligand docking was performed using the Vina Wizard on PyRX. Observation of interactions formed between drugs and polymers was carried out using AutoDockTools [17].

### *Solid dispersion preparation*

The solid dispersion was prepared by kneading method with the ratio of drug and polymer w/w 1:1, 1:2, 1:3, and 1:4. The drug and polymer are mixed with a sufficient amount of methanol to form a paste. The mixture was dried at 40 °C in an oven, then ground into a fine powder and sieved using a mesh no. 80. A physical mixture of CVD and polymer was also prepared in a ratio of 1:4 [15].

### *Saturated solubility test*

Pure CVD and solid dispersion in excess were each dissolved in 10 mL of distilled water and stirred for 24 h at room temperature (25 °C). Then, filtered using Whatman paper No. 42 and analyzed using a UV-Vis spectrophotometer at 286 nm [18].

### *Dissolution test*

The dissolution test was carried out using USP apparatus II (paddle method) using HCl pH 1.45 (900 mL), a speed of 50 rpm at 37 °C. Pure CVD and solid dispersion were weighed as much as 25 mg or the equivalent amount of solid dispersion. The test sample was put into the media, and 10 ml of the sample solution was taken at certain time intervals, 10, 20, 30, 40, 50, and 60 min and was refilled with the same amount using new media. The samples were then analyzed using a UV-Vis spectrophotometer at a wavelength of 286 nm [19].

### *Fourier transform infrared (FTIR)*

The readings of the FTIR spectra on samples of pure CVD, polymer, physical mixture, and CVD solid dispersion were carried out separately using an FTIR spectrophotometer. FTIR spectrum readings are seen in the 4000–400  $\text{cm}^{-1}$  at a resolution of 4  $\text{cm}^{-1}$  [20].

### *Differential scanning calorimetry (DSC)*

The phase transitions of pure CVD, physical mixture,

and CVD solid dispersion were analyzed using the DSC method. Approximately 2 mg of the sample is heated over a temperature range of 25–180 °C at a rate of 10 °C /min under a nitrogen atmosphere (50 mL/min) [21-22].

### *Powder X-ray diffraction (PXRD)*

The diffractogram pattern of pure CVD, physical mixture and solid dispersion of CVD was performed using an X-ray diffractometer with copper K $\alpha$  radiation (wavelength = 1.54060), a voltage of 40 kV and a current of 20 mA. 100-200 mg samples were scanned in the range of 5–60° (2 $\theta$ ) at a speed of 0.02°/sec [20].

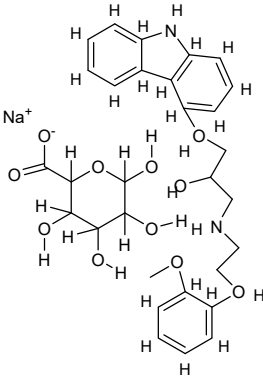
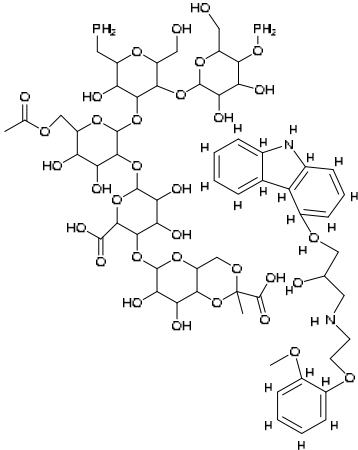
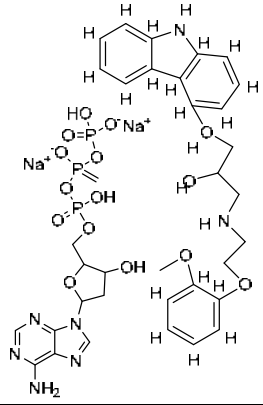
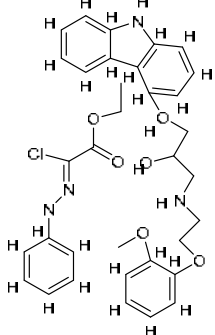
## ■ RESULTS AND DISCUSSION

### *In Silico Simulation*

*In silico* studies between drugs and polymers were conducted to examine possible interactions. The polymers used include sodium alginate (SA), Xanthan Gum (XG), Guar Gum (GG), and Locust Bean Gum (LBG). These polymers have a hydroxyl group (-O-H) in their chemical structure, making it possible to form hydrogen bonds with CVDs having hydroxyl (-O-H) and amine (-N-H) groups. The results of the in-silico study can be seen in Table 1. Hydrogen bonding has an essential role in influencing the physicochemical properties of an active pharmaceutical ingredient, one of which is solubility and dissolution rate [23]. The binding energy or also known as binding affinity indicates the ability of the drug to bind to the receptor (in this case, the drug and the polymer). The bond affinity between the drug and the polymer increases when the bond energy value decreases and vice versa [24].

Hydrogen bonds are included in polar interactions, so they have a high water-attracting ability. Therefore, it is expected that the presence of hydrogen bonds can increase the contact between the drug and water, increasing the solubility of the drug. Two polymers were selected for solid dispersion; considering the convenience and availability of resources, the polymer chosen was the one that formed the most and the fewest hydrogen bonds. For the creation of CVD solid dispersions, SA and XG were chosen as the polymers.

**Table 1.** Results of in silico studies of drugs and polymers

Compound	Complex structure	Interaction	Binding energy (kcal/mol)
Carvedilol-Sodium Alginate (CVD-SA)		2 hydrogen bonds, 5 hydrophobic interactions	-2.4
Carvedilol-Xanthan Gum (CVD-XG)		1 hydrogen bond, 2 hydrophobic interactions, $\pi$ - $\pi$ interactions	-2.6
Carvedilol-Guar Gum (CVD-GG)		2 hydrogen bonds, 4 hydrophobic interactions, $\pi$ - $\pi$ interactions	-2.9
Carvedilol-Locust Bean Gum (CVD-LBG)		1 hydrogen bond, 2 hydrophobic interactions, $\pi$ - $\pi$ interactions	-2.9

### Saturated Solubility Test Results

The solubility test was carried out in aqueous media for 24 h at room temperature to reach saturation, and the solubility results can be seen in Fig. 2. The saturated solubility of CVD in water was  $2.46 \pm 0.03$  mg/L. An increase in the saturated solubility of CVD was observed in all variations of solid dispersion with both SA and XG polymers. The solid dispersion with SA polymer showed an increase in saturated solubility from the highest at CVD:SA (1:4) of  $27.48 \pm 1.59$  mg/L (11.17 times), CVD:SA (1:3) of  $25.40 \pm 0.34$  mg/L (10.32 times), CVD:SA (1:2) of  $17.39 \pm 0.13$  mg/L (7.07 times), and CVD:SA (1:1) of  $12.34 \pm 0.14$  mg/L (5.01 times). This finding shows that the greater the number of polymers used, the higher the solubility increase. This fact can be related to the hydrogen bonds formed between CVD and polymer caused by the addition of polymer ratio. The tendency of increasing solubility, which increases with the high ratio between drug and polymer, has also occurred in several previous studies [25-26].

The solid dispersion with XG polymer showed an increase in saturated solubility from the highest at CVD:XG (1:4) of  $222.95 \pm 3.53$  mg/L (90.63 times), CVD:XG (1:1) of  $168.40 \pm 5.69$  mg/L (68.46 times), CVD:XG (1:3) of  $165.48 \pm 5.62$  mg/L (67.27 times), and CVD:XG (1:2) of  $150.11 \pm 0.70$  mg/L (61.02 times).

The increase in solubility of the solid dispersion can occur because the drug is dispersed molecularly in the

hydrophilic polymer. The decrease in particle size also facilitates the formation of new surfaces, thereby causing an increase in the effective surface area. This new surface allows for an increase in wettability so that the solubility of the drug increases [24,27].

Statistical tests were also carried out and showed a significance value of 0.000 ( $p < 0.05$ ), so it can be said that there was a significant difference between the solubility of pure CVD and CVD solid dispersion. Two solid dispersions with the highest increase in solubility of each polymer were then continued for dissolution test, solid dispersion CVD:SA (1:3), CVD:SA (1:4), CVD-XG (1:1), and CVD-XG (1:4).

### Dissolution Test Results

The dissolution test results can be seen in Fig. 3. At 60 min, the pure CVD that can be dissolved is  $64.95 \pm 0.45\%$ . The solid dispersion CVD:SA (1:4) and CVD:XG (1:4) showed an increase in the dissolution profile at 60 min, respectively, which was  $83.32 \pm 1.19\%$  and  $72.56 \pm 3.62\%$ . Several mechanisms can cause the increase in the dissolution profile in the solid dispersion system due to a decrease in the particle size of the drug, the drug being in an amorphous state, the particles in the solid dispersion having high porosity, and particles with increased wettability.

The statistical test results showed a significance value of 0.448 ( $p > 0.05$ ), so it can be said that there was no significant difference between pure CVD dissolution

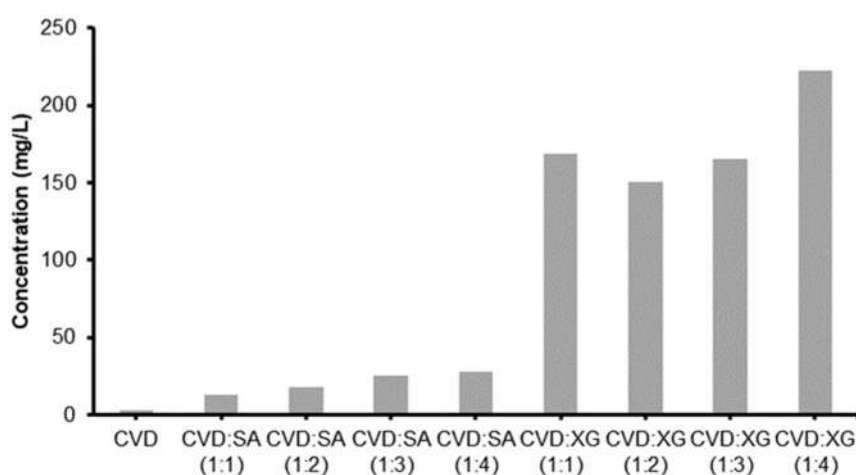


Fig 2. Graph of pure CVD and CVD solid dispersion saturated solubility test

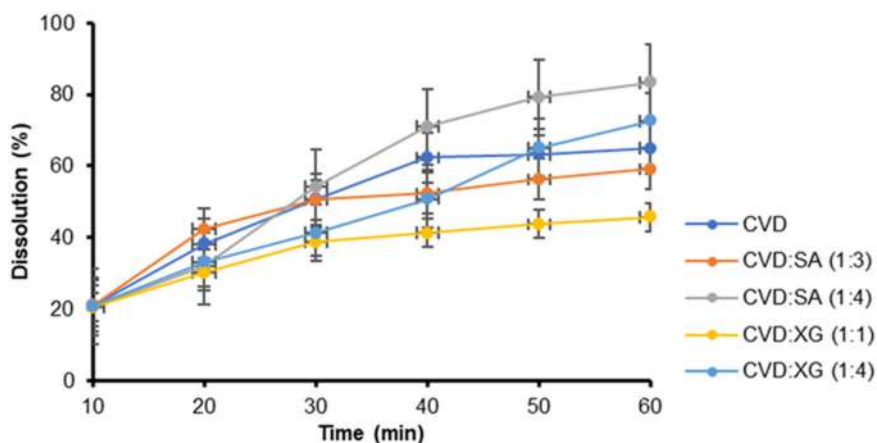


Fig 3. Graph of pure CVD and CVD solid dissolution test results

and CVD solid dispersion. Therefore, one solid dispersion variation with the highest dissolution profile at 60 min was selected for the characterization, namely CVD:SA (1:4) solid dispersion.

#### Fourier Transform Infrared (FTIR)

The results of the characterization using FTIR can be seen in Fig. 4. In the pure CVD IR spectrum, it can be seen that there are two N-H groups with stretching vibrations at  $3342$  and  $3305$   $\text{cm}^{-1}$  and stretching vibration of an O-H group at  $3343$   $\text{cm}^{-1}$ . Other peaks were also observed at wavenumbers  $2923$   $\text{cm}^{-1}$  (C-H stretch),  $1214$   $\text{cm}^{-1}$  and  $1257$   $\text{cm}^{-1}$  (C-O), and  $1592$   $\text{cm}^{-1}$  (C=C) [28].

The FTIR results on the SA polymer showed a peak at a wavenumber of  $1419$   $\text{cm}^{-1}$  caused by the presence of a carboxylate group. The absence of a peak associated with the COOH group at  $1700$   $\text{cm}^{-1}$  indicates that the carboxylic acid is converted to a carboxylic acid in the presence of sodium (COO-Na). The broad peak at wave number  $3415$   $\text{cm}^{-1}$  indicates the presence of an O-H stretch. The peak formed at  $1363$   $\text{cm}^{-1}$  indicates the presence of carbonyl (-C=O) stretching [21,29].

The FTIR spectra of the physical mixture (PM) and CVD:SA (1:4) solid dispersion (SD) present overlapping characteristics of the drug and carrier at a lower intensity, indicating an interaction between CVD and SA and showing that the drug is evenly dispersed in the polymer [23,28]. Peaks of SA dominated the spectrum of the physical mixture and solid dispersion, but peaks of pure CVD were still found. A shift in the wavenumber of the

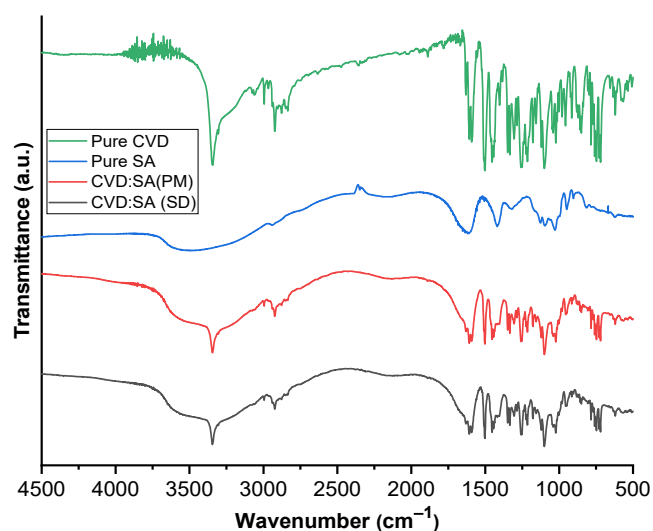


Fig 4. FTIR spectrum overlay of pure CVD, SA, CVD:SA physical mixture (PM), and CVD:SA solid dispersion (SD)

C-O functional group in solid dispersion was also observed, namely from  $1257$  (pure CVD) to  $1251$   $\text{cm}^{-1}$ ; this is following the results of in silico studies where there is the formation of hydrogen bonds on the O atom in fragment 2-methoxyphenyl of CVD.

#### Differential Scanning Calorimetry (DSC)

Characterization with DSC aims to assess the physical state of the drug and see the phase transition of CVD, physical mixture, and solid dispersion of CVD. The thermogram of each sample can be seen in Fig. 5.

The thermogram results of CVD showed a single and sharp maximum endothermic peak at a temperature

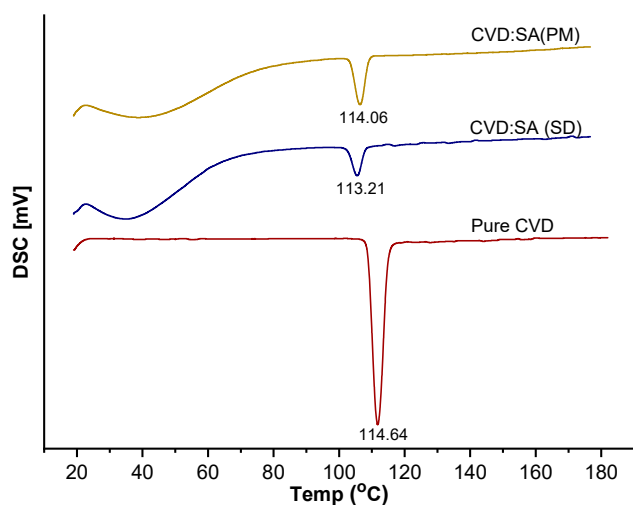


**Fig 5.** Thermogram overlay of pure CVD, CVD:SA physical mixture (PM), and CVD:SA solid dispersion (SD)

of 111.76 °C, which is close to the melting point of CVD form II, which is at 114 °C, indicates that CVD is crystalline [29]. In the thermogram of the physical mixture and solid dispersion CVD:SA (1:4), sharp endothermic peaks of the pure drug were still observed. However, the reduced intensity of the endothermic peak on the thermogram of the physical mixture and solid dispersion indicates the amorphous state of the drug [2,7].

Melting point and enthalpy decreases also occur in pure CVD, physical mixtures and solid dispersions of CVD:SA (1:4) (Table 2). The shift in the relative energy needed to break bonds between solute molecules can be linked to this decreasing trend, meaning that the higher the solubility, the less energy is needed to break the solute bonds as the enthalpy value decreases.

### Powder X-Ray Diffraction (PXRD)

Characterization with PXRD aims to identify the crystalline phase and see changes in the state of drug molecules. The diffractogram of pure CVD, physical mixture, and solid dispersion of CVD:SA (1:4) can be seen

in Fig. 6. The characterization results show that the pure CVD used in the test has a degree of crystallinity of 90.7%. The  $2\theta$  characteristics observed in the pure CVD diffractogram pattern are 5.77°, 11.59°, 12.94°, 14.74°, 16.42°, 17.47°, 18.37°, 24.25°, 26.15°, 29.37° according to the CVD diffractogram pattern form II [29].

The diffractogram of the physical mixture and solid dispersion shows the formation of a diffractogram halo. However, the  $2\theta$  characteristic of CVD can still be observed as less than pure CVD. A decrease in the intensity of the diffractogram was also observed, both of which indicate that the crystallinity of the pure drug has decreased and shows the amorphous nature of the drug [11]. The formation of the amorphous phase is also supported by the calculation results, which show the degree of crystallinity in the CVD:SA (1:4) physical mixture is 37.5% and the CVD:SA (1:4) solid dispersion is 34.8%.

Compared to crystalline compounds, which tend to be more rigid in structure, amorphous compounds have

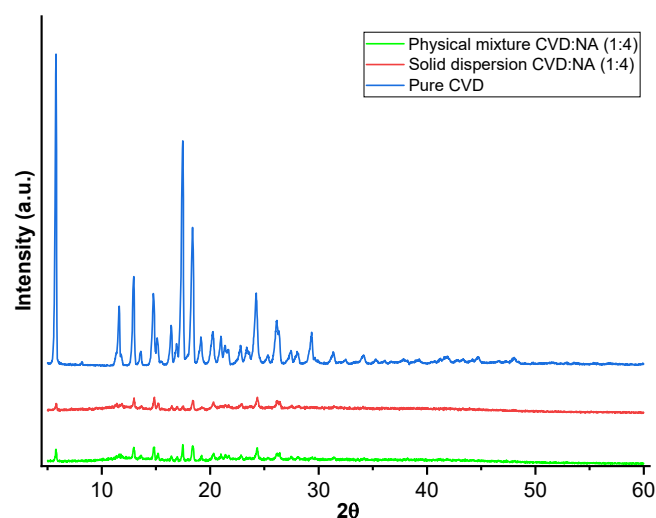


**Fig 6.** Diffractogram overlay of pure CVD, CVD:SA physical mixture (PM) and CVD:SA solid dispersion (SD)

**Table 2.** DSC characterization results

No	Sample	Melting point (°C)			Enthalpy (J/g)
		Onset	Endset	Maximum peak	
1	Pure CVD	108.91	114.64	111.76	-60.69
2	CVD:SA (1:4) physical mixture	108.82	114.06	111.52	-14.89
3	CVD:SA (1:4) solid dispersion	108.25	113.21	110.87	-8.35



a more irregular molecular arrangement and more excellent intermolecular interactions, resulting in faster solubility and dissolution rates. Furthermore, this amorphous state has the benefit of improved wettability and smaller particle size, which can increase solubility.

## ■ CONCLUSION

Based on the *in silico* study results, there was an interaction between CVD and each candidate polymer. Sodium alginate (SA) and xanthan gum (XG) were selected as carriers in solid dispersion. The results of the *in silico* study showed that there were two hydrogen bonds and five hydrophobic interactions in the CVD-SA complex, and one hydrogen bond, two hydrophobic interactions, and  $\pi$ - $\pi$  interactions in the CVD-XG complex. The results of the saturation solubility test and the dissolution rate of CVD increased; solid dispersion CVD:SA (1:4) showed the best results, namely an increase of 11.17 times in the saturated solubility test and an increase in the dissolution profile from 64.95 to 83.32%. Changes in the physicochemical properties of the CVD:SA (1:4) solid dispersion also occurred, which can be seen from the characterization results. The decrease in intensity and shift in wavenumber in the FTIR spectrum indicates an interaction between CVD and SA. The reduced intensity of the endothermic peak on the DSC thermogram indicates the amorphous state of the drug, and this is also supported by the PXRD results, which show a decrease in the crystallinity of the drug.

## ■ ACKNOWLEDGMENTS

We gratefully acknowledges Financial support from a RKDU grant of DRPM UNPAD (No: 2203/UN6.3.1/PT.00/2022).

## ■ REFERENCES

- [1] Holford, N., 2016, Absorption and half-life, *Transl. Clin. Pharmacol.*, 24 (4), 157–160.
- [2] Arregui, J.R., Kovvasu, S.P., Kunamaneni, P., and Betageri, G.V., 2019, Carvedilol solid dispersion for enhanced oral bioavailability using rat model, *J. Appl. Pharm. Sci.*, 9 (12), 042–050.
- [3] Krstić, M., Manić, L., Martić, N., Vasiljević, D., Mračević, S.Đ., Vukmirović, S., and Rašković, A., 2020, Binary polymeric amorphous carvedilol solid dispersions: *In vitro* and *in vivo* characterization, *Eur. J. Pharm. Sci.*, 150, 105343.
- [4] Lee, S.N., Poudel, B.K., Tran, T.H., Marasini, N., Pradhan, R., Lee, Y.I., Lee, D.W., Woo, J.S., Choi, H.G., Yong, C.S., and Kim, J.O., 2013, A novel surface-attached carvedilol solid dispersion with enhanced solubility and dissolution, *Arch. Pharmacol Res.*, 36 (1), 79–85.
- [5] Liu, D., Xu, H., Tian, B., Yuan, K., Pan, H., Ma, S., Yang, X., and Pan, W., 2012, Fabrication of carvedilol nanosuspensions through the anti-solvent precipitation-ultrasonication method for the improvement of dissolution rate and oral bioavailability, *AAPS PharmSciTech*, 13 (1), 295–304.
- [6] Hirlekar, R., and Kadam, V., 2009, Preparation and characterization of inclusion complexes of carvedilol with methyl- $\beta$ -cyclodextrin, *J. Inclusion Phenom. Macrocyclic Chem.*, 63 (3-4), 219–224.
- [7] Zoghbi, A., Geng, T., and Wang, B., 2017, Dual activity of hydroxypropyl- $\beta$ -cyclodextrin and water-soluble carriers on the solubility of carvedilol, *AAPS PharmSciTech*, 18 (8), 2927–2935.
- [8] Shojaee, S.A., Rajaei, H., Hezave, A.Z., Lashkarbolooki, M., and Esmaeilzadeh, F., 2013, Experimental investigation and modeling of the solubility of carvedilol in supercritical carbon dioxide, *J. Supercrit. Fluids*, 81, 42–47.
- [9] Fernandes, G.J., Kumar, L., Sharma, K., Tunge, R., and Rathnanand, M., 2018, A review on solubility enhancement of carvedilol—A BCS class II drug, *J. Pharm. Innovation*, 13 (3), 197–212.
- [10] Sadr, M.H., and Nabipour, H., 2013, Synthesis and identification of carvedilol nanoparticles by ultrasound method, *J. Nanostruct. Chem.*, 3 (1), 26.
- [11] Shejul, A.A., Deshmahe, S., and Biyani, K., 2014, Modified natural carrier in solid dispersion for enhancement of solubility of poorly water soluble drugs, *J. Drug Delivery Ther.*, 4 (1), 111–116.
- [12] Borba, P.A.A., Pinotti, M., de Campos, C.E.M., Pezzini, B.R., and Stulzer, H.K., 2016, Sodium alginate as a potential carrier in solid dispersion formulations to enhance dissolution rate and

- apparent water solubility of BCS II drugs, *Carbohydr. Polym.*, 137, 350–359.
- [13] Siraj, N.S., Athar, S.H., Khan, G.J., Raza, S., and Ansari, M.A., 2019, Review on solid dispersion of poor water soluble drug by using natural polymers, *Pharma Innovation J.*, 8 (1), 631–636.
- [14] Guan, J., Liu, Q., Zhang, X., Zhang, Y., Chokshi, R., Wu, H., and Mao, S., 2018, Alginate as a potential diphase solid dispersion carrier with enhanced drug dissolution and improved storage stability, *Eur. J. Pharm. Sci.*, 114, 346–355.
- [15] Kaza, R., Raju, Y.P., and Nagaraju, R., 2013, Dissolution enhancement of valsartan using natural polymers by solid dispersion technique, *Pharm. Lett.*, 5 (2), 126–134.
- [16] Nagpal, M., Kaur, L., Chander, J., and Sharma, P., 2016, Dissolution enhancement of domperidone fast disintegrating tablet using modified locust bean gum by solid dispersion technique, *J. Pharm. Technol. Res. Manage.*, 4 (1), 1–11.
- [17] Siswandi, S., Rusdiana, T., and Levita, J., 2015, Virtual screening of co-formers for ketoprofen co-crystallization and the molecular properties of the co-crystal, *J. Appl. Pharm. Sci.*, 5 (6), 078–082.
- [18] Yuvaraja, K., and Khanam, J., 2014, Enhancement of carvedilol solubility by solid dispersion technique using cyclodextrins, water soluble polymers and hydroxyl acid, *J. Pharm. Biomed. Anal.*, 96, 10–20.
- [19] Prado, L.D., Rocha, H.V.A., Resende, J.A.L.C., Ferreira, G.B., and de Figueiredo Teixeira, A.M.R., 2014, An insight into carvedilol solid forms: Effect of the supramolecular interactions on the dissolution profiles, *CrystEngComm*, 16 (15), 3168–3179.
- [20] Eesam, S., Bhandaru, J.S., Naliganti, C., Bobbala, R.K., and Akkinapally, R.R., 2020, Solubility enhancement of carvedilol using drug–drug cocrystallization with hydrochlorothiazide, *Future J. Pharm. Sci.*, 6 (1), 77.
- [21] Fernandes, G.J., Rathnanand, M., and Kulkarni, V., 2019, Mechanochemical synthesis of carvedilol cocrystals utilizing hot melt extrusion technology, *J. Pharm. Innovation*, 14 (4), 373–381.
- [22] Thenge, R., Patel, R., Kayande, N., and Mahajan, N., 2020, Co-crystals of carvedilol: Preparation, characterization and evaluation, *Int. J. Appl. Pharm.*, 12 (1), 42–49.
- [23] Sathisaran, I., and Dalvi, S.V., 2018, Engineering cocrystals of poorlywater-soluble drugs to enhance dissolution in aqueous medium, *Pharmaceutics*, 10 (3), 108.
- [24] Saputri, K.E., Fakhmi, N., Kusumaningtyas, E., Priyatama, D., and Santoso, B., 2016, Docking molekular potensi anti diabetes melitus tipe 2 turunan zerumbon sebagai inhibitor aldosa reduktase dengan Autodock-Vina, *Chim. Nat. Acta*, 4 (1), 16–20.
- [25] Sharma, A., Jain, C.P., and Tanwar, Y.S., 2013, Preparation and characterization of solid dispersions of carvedilol with poloxamer 188, *J. Chil. Chem. Soc.*, 58 (1), 1553–1557.
- [26] Sharma, U., Joshi, A., Vyas, N., Malviya, S., and Kharia, A., 2017, Solubility enhancement of clopidogrel bisulfate by solid dispersion technique using carboxymethylcellulose sodium and xanthan gum, *J. Drug Delivery Ther.*, 7 (7), 35–37.
- [27] Rajeswari, S., Bhanu, K., Panda, S., Swain, R.P., Murthy, K.V.R., and Kudamala, S., 2016, Solid dispersions: An evergreen solubility enhancement technique for hydrophobic drugs, *J. Chem. Pharm. Res.*, 8 (4), 1218–1228.
- [28] Luo, C., Wu, W., Lou, S., Zhao, S., and Yang, K., 2020, Improving the *in vivo* bioavailability and *in vitro* anti-inflammatory activity of tanshinone IIA by alginate solid dispersion, *J. Drug Delivery Sci. Technol.*, 60, 101966.
- [29] Beattie, K., Phadke, G., and Novakovic, J., 2013, Carvedilol, *Profiles Drug Subst., Excipients, Relat. Methodol.*, 38, 113–157.

## Characterization and Antibacterial Activity Assessment of Hydroxyapatite-Betel Leaf Extract Formulation against *Streptococcus mutans* *In Vitro* and *In Vivo*

Fitriari Izzatunnisa Muhaimin<sup>1\*</sup>, Sari Edi Cahyaningrum<sup>2</sup>,  
Riska Amalia Lawarti<sup>2</sup>, and Dina Kartika Maharani<sup>2</sup>

<sup>1</sup>Department of Biology, Faculty of Science and Mathematics, Universitas Negeri Surabaya,  
Jl. Ketintang, Surabaya 60231, Indonesia

<sup>2</sup>Department of Chemistry, Faculty of Science and Mathematics, Universitas Negeri Surabaya,  
Jl. Ketintang, Surabaya 60231, Indonesia

\* **Corresponding author:**

email: fitriarimuhaimin@unesa.ac.id

Received: September 19, 2022

Accepted: December 15, 2022

DOI: 10.22146/ijc.77853

**Abstract:** Hydroxyapatite is an inorganic material that is commonly used as a remineralizing agent. Adding natural ingredients such as green betel leaf can increase the antibacterial properties due to the presence of phenolic compounds, flavonoids, and tannins. This study aims to determine the physical and chemical characteristics of the formulation of hydroxyapatite-betel leaf extract and the antibacterial activity against *Streptococcus mutans*. To characterize the combination of hydroxyapatite-betel leaf extract, XRD, PSA and FTIR analyses were performed. Particle size analysis showed the smallest results in the variation of betel 0.3 g, which is 690.08 nm. FTIR characterization showed the presence of OH, PO<sub>4</sub><sup>3-</sup> and CO<sub>3</sub><sup>2-</sup> functional groups from hydroxyapatite and C=O derived from betel leaf extract. In addition, *in vitro* and *in vivo* analyses were performed to assess the antibacterial activity of this formulation. The *in vitro* antibacterial activity test against *S. mutans* showed strong inhibitory activity. Our finding suggests that the formulation has the potential to be used as a medication or prevention agent for dental caries.

**Keywords:** hydroxyapatite; betel leaf; *Streptococcus mutans*

### ■ INTRODUCTION

Dental caries is one of the most common oral health problems in society which is caused by the interaction between teeth, microbial biofilms, and acids from food residues [1]. Another cause of dental caries is the formation of plaque on the teeth, a structured and organized multi-species biofilm caused by the presence of complex microbes that grow, survive, and colonize the tooth surface, such as *Streptococcus mutans* [2-5]. *S. mutans* bacteria play a role in synthesizing extracellular polymers of glucan from glucose by releasing glucosyltransferase to produce glucan from sucrose [6]. Glucans can promote the development of tooth surface biofilms by acting as binding intermediaries for other oral bacteria [7]. One of the factors that can increase the glucan synthesis ability of *S. mutans* is the sucrose-

dependent adhesion which causes the formation of plaque ecology and triggers dental caries [8]. Caries prevention can be done in various ways, one of which is the application of hydroxyapatite (HAp) as a remineralization agent [9].

HAp is the main inorganic mineral of bones and teeth with the shape of calcium phosphate crystals [10]. HAp is widely used in the medical field because of its biocompatibility, bioactivity, osteoconductivity, non-toxic, and non-immunogenic properties [11-12]. HAp can assist in the remineralization process of teeth, especially in dental caries caused by *S. mutans* bacteria, by acting as a source of calcium and phosphate ions [13]. Precursors that can be used to synthesize HAp include eggshells, clamshells, limestone, and beef bones [14-17].

Betel leaves (*Piper betle* L.) is a glabrous climbing vine that belongs to the *Piperaceae* family and can be

found in countries throughout Asia. It has been used for thousands of years in traditional medicine as a stimulant, antifungal, antioxidant, and antimicrobial agent due to its high phytochemical concentration [18]. Furthermore, it has bioactivity potential due to metabolite compounds such as phenols, flavonoids, and tannins that act as antibacterial agents [19]. A previous study has shown that betel leaf extract can inhibit gram-positive bacteria *Staphylococcus aureus* and gram-negative bacteria *Pseudomonas aeruginosa* [20]. Combining HAp with betel leaf extract can significantly increase antibacterial and antimicrobial properties against *S. aureus* [21].

In this study, we aim to determine the physical and chemical characteristics of the HAp-betel leaf extract formulation and its antibacterial activity against *S. mutans in vitro*. To address this, a formulation of HAp-betel leaf extract in liquid and gel preparations was carried out, which is expected to prevent tooth decay without any toxic effects.

## ■ EXPERIMENTAL SECTION

### Materials

Green betel leaves (*Piper betle* L.) were obtained from the Jombang area. Phosphoric acid (85%  $H_3PO_4$ ) and aquadest were purchased from PT. Brataco. Hydroxyapatite was synthesized from beef bone, according to [22]. Propylene glycol, NA, and NB medium were purchased from Merck, while gentamicin, saline, and Na-CMC were from PT. Gunacipta Multirasa. *Streptococcus mutans* (ATCC 35668) bacteria used in *in vitro* study were performed from the Microbiology Lab, Faculty of Medicine, Airlangga University. Winstar rats (*Rattus norvegicus*) used in *in vivo* study were performed by the Faculty of Veterinary, Airlangga University.

### Instrumentation

The functional groups of liquid and gel samples were analyzed using a Perkin-Elmer Spectrum Two™ IR spectrometer for frequencies ranging from 400 to 4000  $cm^{-1}$ . The particle size analysis of the formulations was analyzed using the Zetasizer Malvern series particle size analyzer. The diameter of the inhibition zone for the antibacterial activity test was measured using a digital

caliper with the Sigmat Vernier Caliper with an accuracy of  $\pm 0.2$  mm.

### Procedure

#### Hydroxyapatite synthesis-green betel leaf extract

The thick extract of green betel leaf obtained from the maceration of fresh green betel leaf with distilled water was weighed as much as 0.1; 0.3; 0.5; 0.7; and 1 g. Then put into a beaker, added 2 mL of 1% HAp solution made of 0.2 g of HAp dissolved in 20 mL of  $H_3PO_4$  and stirred until homogeneous [22]. The functional groups of liquid and gel samples were analyzed using a IR spectrometer.

#### Hydroxyapatite gel-green betel leaf extract

A total of 30 mL of distilled water was put into a beaker and then heated at 100 °C on a stirrer until it boiled. Then, 5 mL of propylene glycol and 50 mL mixture of HAp-green betel leaf extract were then added while stirring with a magnetic stirrer. In order to form gel consistency, 0.4 g of Na-CMC was stirred with a magnetic stirrer while heated [23]. X-Ray Diffraction (XRD) analysis was performed using the XRD Phillips PW-1170 Diffractometer ( $Cu-K\alpha = 1.5404 \text{ \AA}$ ). Next, particle size analysis of the formulations was analyzed using the Zetasizer Malvern series particle size analyzer. The material in the form of powder is weighed approximately 0.01 g then put into the beaker and mixed with 1 mL dispersant (Tween 20) while stirring thoroughly. Aquadest was added up to 10 mL and stirred until dissolved. Next, the sample was ultrasonicated for 5 s, put into a 1 mL cuvette then measured in diameter distribution using PSA.

#### Anti-bacterial activity test

Antibacterial activity was tested by the disc diffusion method. NA medium (Merck) was heated by autoclaving for 15 min at 120 °C. Next, 1 mL of suspension of *S. mutans* bacteria was taken, which had been inoculated on NB media (Merck) under sterile conditions and put into a petri dish. Solid media were made by pouring 5 mL of NA medium under slightly hot conditions into the petri dish. Furthermore, the petri dish is shaken slowly until the suspension of *S. mutans* bacteria, and NA media is homogeneous. Liquid and gel

formulation of HAp-green betel leaf extract with variations in the composition of green betel leaf extract 0.1; 0.3; 0.5; 0.7; and 1 g, positive control, negative control and blank dish was prepared. Next, the blank dish is dipped into the sample to be tested. Then put 3 blank dishes that had been dipped in samples into a petri dish containing NA media and *S. mutans* bacteria which started to solidify. Samples were then incubated at 37 °C for 24 h. After incubation, the petri dish was removed from the incubator, and the clear zone around the blank dish was measured using a digital caliper (Sigmat Vernier Caliper) [24]. The diameter of the inhibition zone for the antibacterial activity test was measured using a digital caliper with the Sigmat Vernier Caliper with an accuracy of  $\pm 0.2$  mm.

#### **Spreadability test**

A total of 0.5 g of HAp gel formulation-betel leaf extract was placed in the center of the glass and then covered with another glass. The measurement of dispersion is based on the diameter of the distribution of the preparation horizontally and vertically, with the addition of a load of 50 g to a total weight of 150 g [25].

#### **Adhesion test**

A total of 0.25 g of the HAp-betel leaf extract gel formulation was placed on a glass slide and then covered with another glass slide until it was completely covered. Next, a load weighing 1000 g is placed on top of the slide for 5 min. To remove the glass object from the gel attachment, a load weighing 80 g is used. The time needed for two glass slides is separated [26].

#### **In vivo testing on rats**

**Rats.** Male Wistar rats aged 10 weeks with an average weight of 150–200 g were used as experimental animals. The rats have received an animal certificate from the Animal Husbandry Service and were handled in accordance with the care guidelines of an *in vivo* ethical clearance research issued by the Faculty of Medicine, Universitas Airlangga (Decision no: 262/EC/KEPK/FKUA/2021). Rats were placed in polypropylene cages at a controlled temperature of  $25 \pm 5$  °C and were acclimatized for 7 days before the experiment was carried out [27].

#### **Test animal treatment**

A total of 9 male Wistar rats were divided into 3 groups, each consisting of 3 rats. Each group of Wistar rats was infected with 0.1 mL ( $10^6$  cfu/mL) of *S. mutans* suspension intraperitoneally. After 24 h, rats were injected with the positive control, negative control, and formulation of HAp gel-green betel leaf extract in each group. The positive control group was injected with 0.1 mL of gentamicin, while the negative control group was injected with 0.4 mL of saline solution. The treatment group was injected with 1 mL of HAp-green betel leaf extract via intraperitoneal. The injection was done intraperitoneally for 3 d. After 24 h, the specimen was removed from the intraperitoneal fluid. Then the intraperitoneal was diluted using NaCl to  $10^4$  cfu/mL to be tested for its antibacterial activity [28]. Next, 1 mL of diluted intraperitoneal fluid was cultured on NA media with the pouring agar method into a sterile petri dish and then added 15 mL of NA agar medium at 40–45 °C. After it solidified, plates were incubated at 37 °C for 24 h. Then, bacterial colonies were counted using the total plate count (TPC) method [24,29].

## **RESULTS AND DISCUSSION**

### **Hydroxyapatite-Betel Leaf Extract Formulation Characterization**

HAp-betel leaf extract formulation is characterized by conducting several analyses, such as XRD, PSA, and FTIR. To determine the physical characteristics, including chemical composition, crystallographic structure, and physical properties, XRD was performed. The results analysis shows that HAp calcined from bovine bones has similarities with HAp from the Tissue Bank, which has been applied in the medical field at Dr. Soetomo Hospital. Both HAp are dominated by the HAp phase, with the highest peak being at an angle of  $2\theta = 31.8023^\circ$ , which corresponds to JCPDS data number 09-0432. HAp ( $\text{Ca}_{10}(\text{PO}_4)_6(\text{OH})_2$ ) appears with a relative intensity of 100% (Fig. 1). Other phases formed in the two HAp are A-type carbonate apatite (AKA) and B-type carbonate apatite (AKB). AKA ( $\text{Ca}_{10}(\text{PO}_4)_6\text{CO}_3$ ) is formed because carbonate ions replace  $\text{OH}^-$  ions in the HAp structure, while AKB

(Ca<sub>10</sub>(PO<sub>4</sub>)<sub>3</sub>(CO<sub>3</sub>)(OH)<sub>2</sub>) is formed because carbonate ions replace PO<sub>4</sub><sup>3-</sup> ions in the HAp structure. AKA appears at an angle of 2θ = 26.0214° and 32.2708° corresponding to JCPDS data number 35-0180. AKA appeared with relative intensities of 40.69 and 63.24%, respectively. AKB appears at 2θ = 28.234°; this corresponds to JCPDS data number 19-0272. AKB appeared with a relative intensity of 7.54%. In this study, the AKA phase is more dominant when compared to the AKB phase because HAp compounds are produced from the calcination process at high temperatures, namely 900 °C. However, if the synthesis of HAp is carried out at low temperatures (60–100 °C), the AKB phase will dominate more. A combination of carbonates is not harmful because it is also found in human bones as carbonate apatite [30].

To determine the particle size and distribution of liquid and gel formulations of HAp-green betel leaf extract samples, PSA was conducted. The results show the average particle size in the variation of the addition of betel extract are 0.1; 0.3; 0.5; 0.7; and 1 g are 5956.00; 690.08; 306300; 5042.40; and 5832.20 nm, respectively (Fig. 2).

Based on the results, the formulation of HAp and green betel leaf extract with 0.3 g of betel can be categorized in the nanoparticle group, while the variation of betel extract is 0.1, 0.5, 0.7, and 1 g is excluded. Nanoparticles are materials with a particle size of less than 1 μm [31]. Variations that have not been optimal in nano size are probably due to particle agglomeration. Thus, the particles grow bigger and easily detached. The larger the particle size, the greater the polarity and affinity [32]. The smaller the particle size, the larger the surface area, allowing for higher contact with microorganisms' cell walls [33]. Therefore, based on our results, further optimization is needed to prevent the agglomeration of HAp.

The determination of the functional groups in the sample was qualitatively analyzed using FTIR. Previously, we analyzed HAp calcined from bovine bones compared to HAp from the Tissue Bank. It can be seen that HAp calcined from bovine bones is similar to HAp from the Tissue Bank; this is evidenced by the typical functional

groups belonging to HAp that appear at almost the same wavenumber (Fig. 3(a1)). HAp from the analyzed bovine bone showed an absorption band of the OH<sup>-</sup> group at wavenumber 3572.68; 1993.09; and 602.51 cm<sup>-1</sup>, while HAp from the Network Bank showed absorption bands from the OH<sup>-</sup> group at wavenumber 3570.76; 2016.24; and 604.44 cm<sup>-1</sup>. It can be seen that the spectra of the OH<sup>-</sup> group look uncharacteristically pointed, which is seen to be this ramp because the OH<sup>-</sup> group of HAp binds to the metal Ca<sup>2+</sup> (Fig. 3(a2)). The PO<sub>4</sub><sup>3-</sup> the group

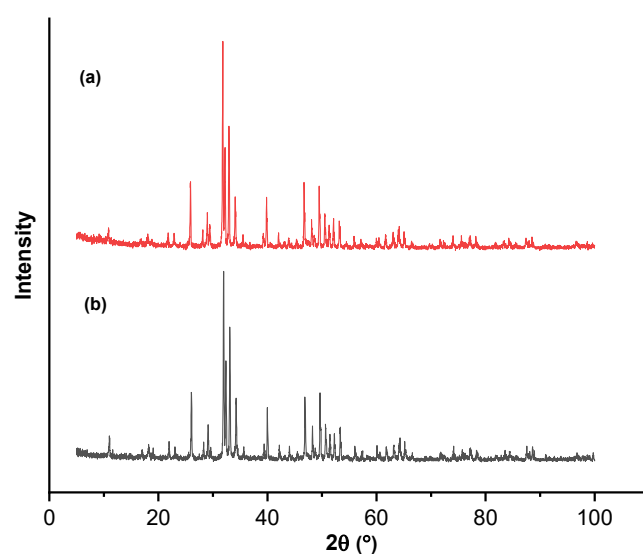


**Fig 1.** Results of the XRD spectrum (a) beef bone hydroxyapatite; (b) standard hydroxyapatite from the Tissue Bank (Dr. Soetomo Hospital)

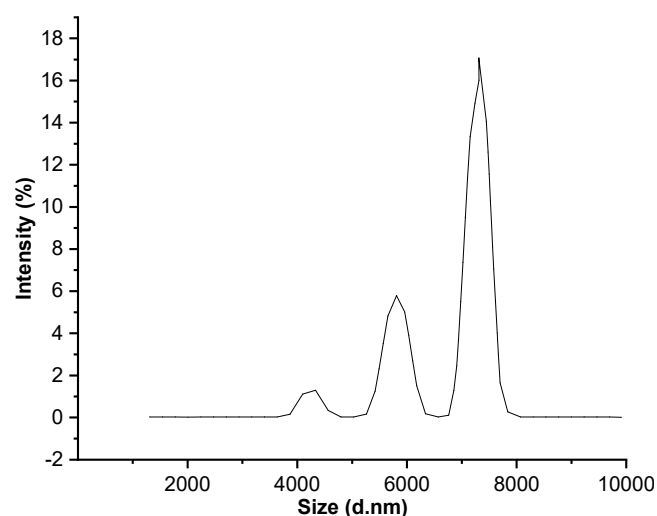


**Fig 2.** Graph of PSA analysis of the formulation of HAp-betel leaf extract

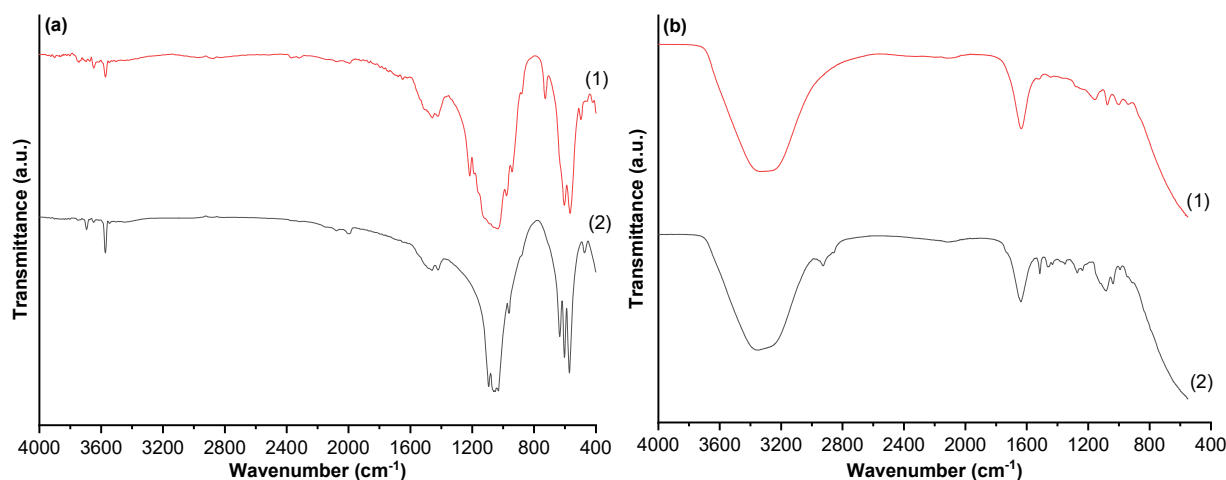


**Fig 3.** Results of the FTIR spectrum. (a) hydroxyapatite from beef bone (1) and Tissue bank (2); (b) HAp-betel leaf extract formulation in gel (1) and liquid sample (2)

has 4 vibration modes, namely stretching symmetry vibration ( $\nu_1$ ) with a wavenumber of about  $956\text{ cm}^{-1}$ , bending symmetry vibration ( $\nu_2$ ) with a wavenumber of about  $430\text{--}460\text{ cm}^{-1}$ , stretching asymmetry vibration ( $\nu_3$ ) with a wavenumber of about  $1040\text{--}1090\text{ cm}^{-1}$ , bending asymmetric vibration ( $\nu_4$ ) with a wavenumber of about  $571\text{--}610\text{ cm}^{-1}$ . Calcined HAp from bovine bones showed an absorption band of the carbonate group ( $\text{CO}_3^{2-}$ ) at a wavenumber of about  $1400\text{ cm}^{-1}$ . The presence of a carbonate group in the resulting HAp is caused by direct contact between HAp samples and carbon dioxide ( $\text{CO}_2$ ) in the air.

Meanwhile, the results of the FTIR analysis for the liquid sample (Fig. 3(b2)) showed peaks at a wavenumber of  $3325.44$ ,  $1634.72$ ,  $1156.81$ , and  $1075.29\text{ cm}^{-1}$  indicating the presence of a hydroxyl group (OH), a carbonyl group (C=O) and a carbonate group ( $\text{CO}_3^{2-}$ ) and a phosphate group ( $\text{PO}_4^{3-}$ ), respectively.

In the gel sample (Fig. 3(b1)), the hydroxyl (OH) group was detected at a wavenumber of  $3279.84\text{ cm}^{-1}$ , which was also previously observed by Liu et al. [34]. The carbonyl group (C=O) was seen at a wave of  $1639.49\text{ cm}^{-1}$ , indicating the presence of one of the functional groups of the metabolite compounds contained in the betel leaf. The carbonate group ( $\text{CO}_3^{2-}$ ) was detected at a wavenumber of  $1136.83\text{ cm}^{-1}$ . This finding is in line with the previous finding, which states that the carbonate group in human bone is detected at a wavenumber of  $\sim 1100.00\text{ cm}^{-1}$  [35].

The detected carbonate group comes from  $\text{CO}_2$  in the air, which reacts with calcium to form a bond so that a calcium carbonate phase appears during synthesis [36]. Furthermore, the phosphate group ( $\text{PO}_4^{3-}$ ) was detected at a wave of  $1078.69\text{ cm}^{-1}$ . Mondal et al. support the detection of phosphate groups, which states that wavenumbers between  $1000\text{--}1100\text{ cm}^{-1}$  indicate the presence of a phosphate group with a stretching vibration pattern [37].

The OH,  $\text{PO}_4^{3-}$  and  $\text{CO}_3^{2-}$  functional groups are functional groups derived from HAp, but the C=O group is a functional group derived from green betel leaf extract [38]. The existence of a shifting wavenumber indicates that there has been a bond between HAp and the metabolite compounds present in the green betel leaf extract (Table 1).

Next, the gel preparation spreadability test was carried out to determine the ability of the formulation of HAp-green betel leaf extract gel to spread when applied to the teeth (Table 2). Dispersibility is an important characteristic in formulations, as it affects the transfer of the active ingredient to the target area at the correct dose, ease of use, the pressure required to exit the package, and acceptance by the consumer. The dispersion is related to water; the more water content, the wider the dispersion [39]. The results of the tests showed that the increase in the spreading area was accompanied by adding a given load (Table 3). The formula found the best

**Table 1.** Wavenumber data from FTIR

Functional groups	HAp wavenumber (cm <sup>-1</sup> )			
	Beef bone	Tissue bank	Liquid sample	Gel sample
OH	604.44	602.51	3325.44	3279.84
	2016.24	1993.09	-	
	3570.76	3572.68	-	
C=O	-	-	1634.72	1639.49
CO <sub>3</sub> <sup>2-</sup>	1414.49	1420.27	1156.81	1136.83
	1462.70	1460.78		
PO <sub>4</sub> <sup>3-</sup>	961.25	961.25	1075.29	1078.69
	471.36	473.29		
	1048.04	1049.97		
	1090.47	1092.40		
	571.65	571.65		
	961.25	961.25		

**Table 2.** Test results of HAp gel-betel leaf extract spreadability

Sample	Horizontal (cm)	Vertical (cm)	Average
Betel 0.1 g	7.77	8.23	8.00
Betel 0.3 g	8.54	8.28	8.41
Betel 0.5 g	8.82	9.12	8.97
Betel 0.7 g	8.53	8.67	8.60
Betel 1 g	8.84	8.82	8.83

**Table 3.** The results of the stickiness test of the HAp gel-betel leaf extract

Sample	Adhesion (s)
Betel 0.1 g	1.83
Betel 0.3 g	1.03
Betel 0.5 g	0.78
Betel 0.7 g	1.07
Betel 1 g	0.88

results by adding 0.1 g of betel leaf because it has a spreading power close to the dispersion scale that meets the standards. Good dispersion will provide the speed of contact between the gel and the teeth. The viscosity value of the preparation influences the difference in dispersion. It has a low viscosity value (watery) which results in the dispersion diameter becoming large because it is easier to flow. While for preparations that have a high viscosity value, the resulting dispersion diameter is small [40]. Preparations that are too spread or difficult to spread will reduce the comfort and effectiveness of use, while

preparations that are too dilute will cause reduced adhesion. Therefore, the contact time of active substances with the application site will reduce [41]. Many factors affect the dispersion, one of which is the amount and strength of the gel matrix. The dispersion will decrease along with the more and the strength of the gel matrix. In this case, what affects the formation of the gel matrix is the gelling agent, therefore, the concentration of the gelling agent can increase and strengthen the gel matrix [42].

To determine the adhesion time of the hydroxyapatite gel formulation-green betel leaf extract to the tooth surface adhesive test was performed. Hence, it will suggest whether the active substances in the preparation were absorbed. The general characteristic of gel preparations is the ability to adhere to the surface of the application for a long time. The longer the preparation time can be attached, and the additive can be in contact with the application, the antibacterial effect is expected to be optimal [43]. The data suggest that the differences in the stickiness of each formulation are due to differences in the composition of the green betel leaf extract, which affects the viscosity and spreadability (Table 4). Adhesion to toothpaste is related to the absorption of the active substance into the teeth. Based on the tested samples, the formula with the addition of 0.1; 0.3; and 0.7 betel leaf extract meet the standard of adhesion test, which is above 1 s. Adhesion of semi-solid



**Table 4.** Inhibition zone of HAp-betel leaf extract formulation

Sample	Clear zone diameter (mm)			Average
Liquid betel 0.1 g	22.6	22.5	20.1	21.73 ± 9.58
Liquid betel 0.3 g	17.3	16.1	16.6	16.67 ± 14.27
Liquid betel 0.5 g	18.4	18.9	18.2	18.50 ± 8.39
Liquid betel 0.7 g	20.0	20.6	17.8	19.47 ± 11.22
Liquid betel 1 g	18.4	18.9	20.5	19.27 ± 2.19
Gel betel 0.1 g	12.7	12.6	11.2	12.17 ± 20.07
Gel betel 0.3 g	13.6	14.8	13.9	14.10 ± 14.59
Gel betel 0.5 g	9.2	7.7	10.6	9.17 ± 10.48
Gel betel 0.7 g	12.8	13.3	14.5	13.53 ± 20.58
Gel betel 1 g	12.7	13.6	12.6	12.97 ± 13.13
Hydroxyapatite	14.7	11.2	9.1	11.67 ± 19.53
Aquadest	0	0	0	0

preparations should be more than 1 s [42]. In addition, the addition of Na CMC in the gel system in excess can interfere with the ionization process of the carboxyl group.

#### **In Vitro Antibacterial Activity Test**

HAp is widely studied as an excellent candidate for bone repair and substitution. Recently, studies conducted by Seyedmajidi et al. [44] have shown that HAp has an antibacterial activity by killing *S. mutans* in different concentrations. In addition, another study has shown that the antimicrobial effect of piper betel leaf extract against *S. mutans* formulation can inhibit the growth of *S. mutans* [45]. To determine the antibacterial activity of HAp-betel leaf extract in liquid and gel formulation antibacterial activity test was conducted by disc diffusion method *in vitro*. The results showed the ability to inhibit the growth of *S. mutans*, as indicated by forming a clear zone around the colony (Fig. 4). The data obtained were analyzed by statistical tests, including a normality test, one-way ANOVA and a follow-up test using Duncan. One way ANOVA test with a confidence level of 5% obtained results with a significant level of 0.000 ( $p < 0.05$ ) so that it can be seen that there is a significant difference between one data and another. The normality test received a significant value of 0.200 ( $p > 0.05$ ), which indicates that the variety of inhibition zones in the HAp-green betel leaf extract formulation was normally distributed. Furthermore, Duncan's test was carried out as a follow-up test, which showed that the formulation of

HAp-green betel leaf extract had an inhibitory effect on *S. mutans*. The clear zone was categorized based on its diameter with a range below 5 mm as weak inhibition, 5–10 mm as moderate inhibition, 10–20 mm as strong inhibition, and above 20 mm have very strong resistance [38]. In liquid form, betel extract of 0.1 g has the most

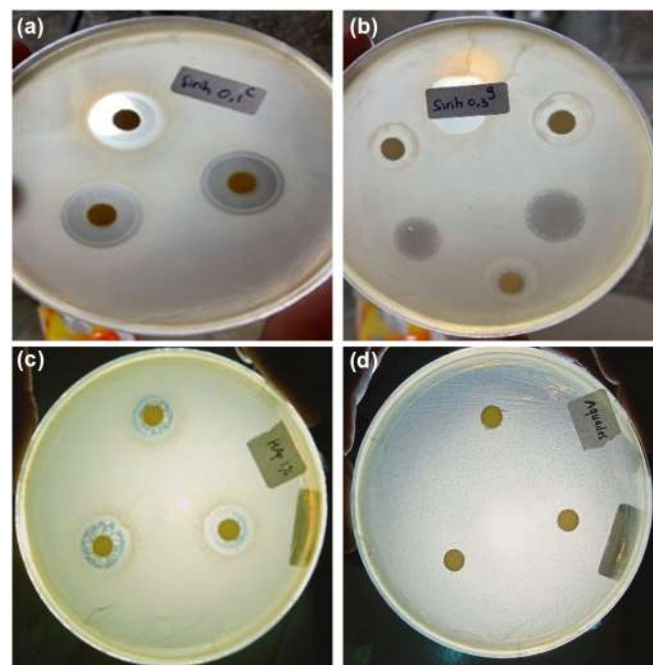


**Fig 4.** Clear zone formation of HAp-green betel extract against the growth of *S. mutans* in (a) Liquid formulation, (b) gel formulation, (c) 1% hydroxyapatite was used as a positive control, and (d) aquadest was used as a negative control

expansive clear zone with around 21.73 mm, while in gel form is 14.10 mm (Table 4). This observation indicates that the increasing concentration of betel leaf did not dictate the size of clear zone formation. The data suggests that there may be an optimum concentration of betel leaf that will give the best effects in the growth inhibition of *S. mutans*.

Overall, the formulation of HAp-green betel leaf extract has strong inhibition against *S. mutans* bacteria. It is caused by secondary metabolites activity of green betel leaves, such as phenols, flavonoids, and tannins that damage the bacterial cell membrane. Phenol compounds can denature bacterial cells by disrupting the covalent structure of gram-positive bacteria [46-47]. The presence of carboxyl groups in aromatic hydrocarbons will form complexes with extracellular proteins, which result in the loss of the infection ability of bacteria. Flavonoid compounds act as antibacterial agents that interfere with the potassium concentration of gram-positive bacteria, cause the malfunction of the cytoplasmic membrane and inhibit the adhesion and biofilm formation [48]. In addition, flavonoid compounds can cause damage to the phospholipid bilayer and inhibit the respiratory chain or ATP synthesis in gram-positive bacteria [49]. Tannins work by destroying bacterial cell membranes by inactivating the function of genetic material and inactivating enzymes. It will inhibit the growth of bacteria and inactivate the ability to stick to bacteria [50-51].

### In Vivo Antibacterial Activity Test

*In vivo* test was conducted to determine the antibacterial activity of the HAp formulation of green betel leaf extract against rats infected with *S. mutans*

bacteria. In this test, gentamicin was used as a positive control, saline as a negative control, and the sample was in the form of a gel formulation of HAp-betel leaf extract with variations in the addition of 0.3 g of betel leaf extract.

The results have shown that the number of colonies in the gel formulation was greater than that of the positive control and negative control (Fig. 5 and Table 5). This could be due to the long storage of the formulation and dilution needs to be conducted in order to get a better analysis of the colony counts. However, there were no toxic side effects to the rats after testing, and the rats were in good health.

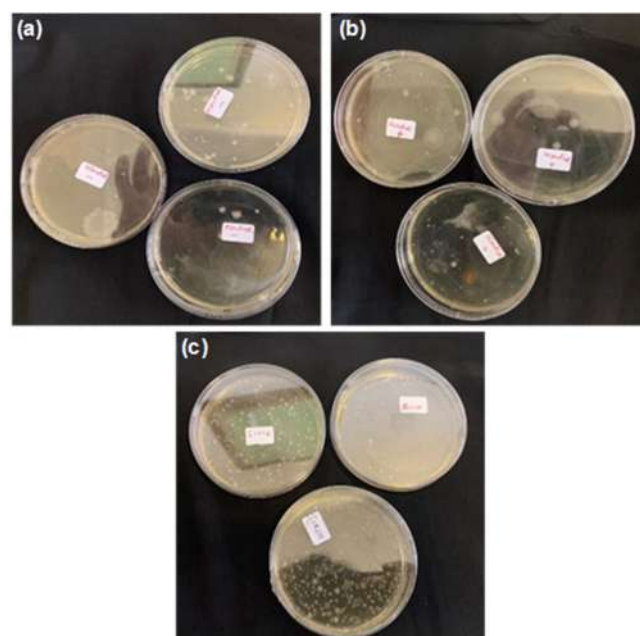


**Fig 5.** Colony test results (a) saline as negative controls; (b) gentamicin as positive controls; (c) hydroxyapatite gel formulation-green betel leaf extract

**Table 5.** Number of colonies after treatment on rats

Group	Number of colonies			Average
	Rat 1	Rat 2	Rat 3	
Saline (-)	167	96	70	111.00 ± 50.21
Gentamicin (+)	193	218	75	162.00 ± 76.37
Betel 0.3 g	313	421	260	331.33 ± 82.05

\*The data were normally distributed with a significant value of 0.200 ( $p > 0.05$ ). Then a one-way ANOVA test was performed with a significant level of 5%, and a significant value of 0.021 ( $p < 0.05$ ) was performed, which indicated that there was a difference from one data to another

## ■ CONCLUSION

Hydroxyapatite-betel leaf extract formulation characterization has shown there is a bond between hydroxyapatite and the metabolite compounds present in the green betel leaf extract. In addition, the spreadability of the formulation also already meets the standard of toothpaste. Antibacterial *in vitro* test suggests that a combination of hydroxyapatite and betel leaf extract gives high antibacterial activity against *S. mutans*. Unfortunately, our *in vivo* study failed to validate this due to the possibility of improper storage of the formulation. However, it was shown that there were no toxic effects of the formulation on the test animal, which indicates the safe formulation for caries prevention or treatment. Based on our results, the hydroxyapatite-betel leaf extract formulation has shown its high potential as an ingredient to prevent tooth decay and the observed concentration already meets the standard even though *in vivo* study needs to be repeated. Furthermore, the potential of this formulation can be explored further, especially in the demineralization potential with its hydroxyapatite composition.

## ■ ACKNOWLEDGMENTS

The authors would like to thank DIKTI for the financial support through research funding *Hibah Penelitian Terapan Unggulan Perguruan Tinggi* (PTUPT) program 2022 No. contract: B/29531/UN38.9/LK.0400/2022.

## ■ REFERENCES

- [1] Cho, G.J., Kim, S.Y., Lee, H.C., Kim, H.Y., Lee, K.M., Han, S.W., and Oh, M.J., 2020, Association between dental caries and adverse pregnancy outcomes, *Sci. Rep.*, 10 (1), 5309.
- [2] Gutiérrez-Venegas, G., Gómez-Mora, J.A., Meraz-Rodríguez, M.A., Flores-Sánchez, M.A., and Ortiz-Miranda, L.F., 2019, Effect of flavonoids on antimicrobial activity of microorganisms present in dental plaque, *Heliyon*, 5 (12), e03013.
- [3] Pitts, N.B., Twetman, S., Fisher, J., and Marsh, P.D., 2021, Understanding dental caries as a non-communicable disease, *Br. Dent. J.*, 231 (12), 749–753.
- [4] Gholibegloo, E., Karbasi, A., Pourhajibagher, M., Chiniforush, N., Ramazani, A., Akbari, T., Bahador, A., and Khoobi, M., 2018, Carnosine-graphene oxide conjugates decorated with hydroxyapatite as promising nanocarrier for ICG loading with enhanced antibacterial effects in photodynamic therapy against *Streptococcus mutans*, *J. Photochem. Photobiol., B*, 181, 14–22.
- [5] Chen, X., Daliri, E.B.M., Kim, N., Kim, J.R., Yoo, D., and Oh, D.H., 2020, Microbial etiology and prevention of dental caries: Exploiting natural products to inhibit cariogenic biofilms, *Pathogens*, 9 (7), 569.
- [6] Mallya, P.S., and Mallya, S., 2020, Microbiology and clinical implications of dental caries – A review, *J. Evol. Med. Dent. Sci.*, 9 (48), 3670–3675.
- [7] Watanabe, A., Kawada-Matsuo, M., Le, M.N.T., Hisatsune, J., Oogai, Y., Nakano, Y., Nakata, M., Miyawaki, S., Sugai, M., and Komatsuzawa, H., 2021, Comprehensive analysis of bacteriocins in *Streptococcus mutans*, *Sci. Rep.*, 11 (1), 12963.
- [8] Lemos, J.A., Palmer, S.R., Zeng, L., Wen, Z.T., Kajfasz, J.K., Freires, I.A., Abranches, J., and Brady, L.J., 2019, The Biology of *Streptococcus mutans*, *Microbiol. Spectrum*, 7 (1), 7.1.03.
- [9] Amaechi, B.T., Phillips, T.S., Evans, V., Ugwokaegbe, C.P., Luong, M.N., Okoye, L.O., Meyer, F., and Enax, J., 2021, The potential of hydroxyapatite toothpaste to prevent root caries: A pH-cycling study, *Clin., Cosmet. Invest. Dent.*, 13, 315–324.
- [10] Sawada, M., Sridhar, K., Kanda, Y., and Yamanaka, S., 2021, Pure hydroxyapatite synthesis originating from amorphous calcium carbonate, *Sci. Rep.*, 11 (1), 11546.
- [11] Suresh Kumar, C., Dhanaraj, K., Vimalathithan, R.M., Ilaiyaraja, P., and Suresh, G., 2020, Hydroxyapatite for bone related applications derived from sea shell waste by simple precipitation method, *J. Asian Ceram. Soc.*, 8 (2), 416–429.
- [12] Siddiqui, H.A., Pickering, K.L., and Mucalo, M.R., 2018, A review on the use of hydroxyapatite-carbonaceous structure composites in bone

- replacement materials for strengthening purposes, *Materials*, 11 (10), 1813.
- [13] Nozari, A., Ajami, S., Rafiei, A., and Niazi, E., 2017, Impact of nano hydroxyapatite, nano silver fluoride and sodium fluoride varnish on primary enamel remineralization: An *in vitro* study, *J. Clin. Diagn. Res.*, 11 (9), ZC97–ZC100.
- [14] Wu, S.C., Hsu, H.C., Hsu, S.K., Chang, Y.C., and Ho, W.F., 2016, Synthesis of hydroxyapatite from eggshell powders through ball milling and heat treatment, *J. Asian Ceram. Soc.*, 4 (1), 85–90.
- [15] Mtavangu, S.G., Mahene, W., Machunda, R.L., van der Bruggen, B., and Njau, K.N., 2022, Cockle (*Anadara granosa*) shells-based hydroxyapatite and its potential for defluoridation of drinking water, *Results Eng.*, 13, 100379.
- [16] Sinulingga, K., Sirait, M., Siregar, N., and Abdullah, H., 2021, Synthesis and characterizations of natural limestone-derived nano-hydroxyapatite (HAP): A comparison study of different metals doped HAPs on antibacterial activity, *RSC Adv.*, 11 (26), 15896–15904.
- [17] Manalu, J.L., Soegijono, B., and Indrani, D.J., 2015, Characterization of hydroxyapatite derived from bovine bone, *Asian J. Appl. Sci.*, 3 (4), 758–765.
- [18] Nayaka, N.M.D.M.W., Sasadara, M.M.V., Sanjaya, D.A., Yuda, P.E.S.K., Dewi, N.L.K.A.A., Cahyaningsih, E., and Hartati, R., 2021, *Piper betle* (L): Recent review of antibacterial and antifungal properties, safety profiles, and commercial applications, *Molecules*, 26 (8), 2321.
- [19] Lubis, R.R., Marlisa, M., and Wahyuni, D.D., 2020, Antibacterial activity of betle leaf (*Piper betle* L.) extract on inhibiting *Staphylococcus aureus* in conjunctivitis patient, *Am. J. Clin. Exp. Immunol.*, 9 (1), 1–5.
- [20] Madhumita, M., Guha, P., and Nag, A., 2019, Extraction of betel leaves (*Piper betle* L.) essential oil and its bio-actives identification: Process optimization, GC-MS analysis and anti-microbial activity, *Ind. Crops Prod.*, 138, 111578.
- [21] Umesh, M., Choudhury, D.D., Shanmugam, S., Ganesan, S., Alsehli, M., Elfasakhany, A., and Pugazhendhi, A., 2021, Eggshells biowaste for hydroxyapatite green synthesis using extract piper betel leaf - Evaluation of antibacterial and antibiofilm activity, *Environ. Res.*, 200, 111493.
- [22] Puzanov, I., Diab, A., Abdallah, K., Bingham, C.O., Brogdon, C., Dadu, R., Hamad, L., Kim, S., Lacouture, M.E., LeBoeuf, N.R., Lenihan, D., Onofrei, C., Shannon, V., Sharma, R., Silk, A.W., Skondra, D., Suarez-Almazor, M.E., Wang, Y., Wiley, K., Kaufman, H.L., Ernstoff, M.S., and Society for Immunotherapy of Cancer Toxicity Management Working Group, 2017, Managing toxicities associated with immune checkpoint inhibitors: Consensus recommendations from the Society for Immunotherapy of Cancer (SITC) Toxicity Management Working Group, *J. ImmunoTher. Cancer*, 5 (1), 95.
- [23] Qian, G., Liu, W., Zheng, L., and Liu, L., 2017, Facile synthesis of three dimensional porous hydroxyapatite using carboxymethylcellulose as a template, *Results Phys.*, 7, 1623–1627.
- [24] Hoelzer, K., Cummings, K.J., Warnick, L.D., Schukken, Y.H., Siler, J.D., Gröhn, Y.T., Davis, M.A., Besser, T.E., and Wiedmann, M., 2011, Agar disk diffusion and automated microbroth dilution produce similar antimicrobial susceptibility testing results for *Salmonella* serotypes Newport, Typhimurium, and 4,5,12:i-, but differ in economic cost, *Foodborne Pathog. Dis.*, 8 (12), 1281–1288.
- [25] Dantas, M.G.B., Reis, S.A.G.B., Damasceno, C.M.D., Rolim, L.A., Rolim-Neto, P.J., Carvalho, F.O., Quintans-Junior, L.J., and da Silva Almeida, J.R.G., 2016, Development and evaluation of stability of a gel formulation containing the monoterpene borneol, *Sci. World J.*, 2016, 7394685.
- [26] Ariyanthini, K.S., Angelina, E., Permana, K.N.B., Thelmalina, F.J., and Prasetia, I.G.N.J.A., 2021, Antibacterial activity testing of hand sanitizer gel extract of coriander (*Coriandrum sativum* L.) Seeds against *Staphylococcus aureus*, *J. Pharm. Sci. Appl.*, 3 (2), 98–107.
- [27] Razoooki, S.M.M., and Rabee, A.M., 2019, Kinetic profile of silver and zinc oxide nanoparticles by

- intraperitoneal injection in mice, a comparative study, *Period. Eng. Nat. Sci.*, 7 (3), 1499–1511.
- [28] Iciek, M., Kotańska, M., Knutelska, J., Bednarski, M., Zygmunt, M., Kowalczyk-Pachel, D., Bilaska-Wilkosz, A., Górny, M., and Sokołowska-Jeżewicz, M., 2017, The effect of NaCl on the level of reduced sulfur compounds in rat liver. Implications for blood pressure increase, *Postepy Hig. Med. Dosw.*, 71 (1), 564–576.
- [29] Wolfvoviz-Zilberman, A., Kraitman, R., Hazan, R., Friedman, M., Hourri-Haddad, Y., and Beyth, N., 2021, Phage targeting *Streptococcus mutans in vitro* and *in vivo* as a caries-preventive modality, *Antibiotics*, 10 (8), 1015.
- [30] Kono, T., Sakae, T., Nakada, H., Kaneda, T., and Okada, H., 2022, Confusion between carbonate apatite and biological apatite (carbonated hydroxyapatite) in bone and teeth, *Minerals*, 12 (2), 170.
- [31] Jeevanandam, J., Barhoum, A., Chan, Y.S., Dufresne, A., and Danquah, M.K., 2018, Review on nanoparticles and nanostructured materials: History, sources, toxicity and regulations, *Beilstein J. Nanotechnol.*, 9, 1050–1074.
- [32] Xu, Y., Chu, Y., Feng, X., Gao, C., Wu, D., Cheng, W., Meng, L., Zhang, Y., and Tang, X., 2020, Effects of zein stabilized clove essential oil Pickering emulsion on the structure and properties of chitosan-based edible films, *Int. J. Biol. Macromol.*, 156, 111–119.
- [33] da Silva, B.L., Abuçafy, M.P., Berbel Manaia, E., Oshiro Junior, J.A., Chiari-Andréo, B.G., Pietro, R.C.L.R., and Chiavacci, L.A., 2019, Relationship between structure and antimicrobial activity of zinc oxide nanoparticles: An overview, *Int. J. Nanomedicine*, 14, 9395–9410.
- [34] Liu, X., Yu, Y., Bai, X., Li, X., Zhang, J., and Wang, D., 2023, Rapid identification of insecticide- and herbicide-tolerant genetically modified maize using mid-infrared spectroscopy, *Processes*, 11 (1), 90.
- [35] Wang, M., Qian, R., Bao, M., Gu, C., and Zhu, P., 2018, Raman, FT-IR and XRD study of bovine bone mineral and carbonated apatites with different carbonate levels, *Mater. Lett.*, 210, 203–206.
- [36] Bang, L.T., Ramesh, S., Purbolaksono, J., Ching, Y.C., Long, B.D., Chandran, H., Ramesh, S., and Othman, R., 2015, Effects of silicate and carbonate substitution on the properties of hydroxyapatite prepared by aqueous co-precipitation method, *Mater. Des.*, 87, 788–796.
- [37] Mondal, S., Mondal, B., Dey, A., and Mukhopadhyay, S.S., 2012, Studies on processing and characterization of hydroxyapatite biomaterials from different bio wastes, *J. Miner. Mater. Charact. Eng.*, 11 (1), 55–67.
- [38] Cahyaningrum, S.E., Amaria, A., Ramadhan, M.I.F., and Herdyastuti, N., 2020, Synthesis hydroxyapatite/collagen/chitosan composite as bone graft for bone fracture repair, *Proceedings of the International Joint Conference on Science and Engineering (IJCSE 2020)*, Atlantis Press, Paris, France, 337–341.
- [39] Jiménez-Martínez, J., Le Borgne, T., Tabuteau, H., and Méheust, Y., 2017, Impact of saturation on dispersion and mixing in porous media: Photobleaching pulse injection experiments and shear-enhanced mixing model, *Water Resour. Res.*, 53 (2), 1457–1472.
- [40] van Dijke, K., Kobayashi, I., Schroën, K., Uemura, K., Nakajima, M., and Boom, R., 2010, Effect of viscosities of dispersed and continuous phases in microchannel oil-in-water emulsification, *Microfluid. Nanofluid.*, 9 (1), 77–85.
- [41] Chen, M.X., Alexander, K.S., and Baki, G., 2016, Formulation and evaluation of antibacterial creams and gels containing metal ions for topical application, *J. Pharm.*, 2016, 5754349.
- [42] Nugrahaeni, F., Nining, N., and Okvianida, R., 2022, The effect of HPMC concentration as a gelling agent on color stability of copigmented blush gel extract of purple sweet (*Ipomoea batatas* (L.) Lam.), *IOP Conf. Ser.: Earth Environ. Sci.*, 1041, 012070.
- [43] Bornare, S.S., Aher, S.S., and Saudagar, R.B., 2018, A review: Film forming gel novel drug delivery system, *Int. J. Curr. Pharm. Res.*, 10 (2), 25–28.
- [44] Seyedmajidi, S., Rajabnia, R., and Seyedmajidi, M., 2018, Evaluation of antibacterial properties of

- hydroxyapatite/bioactive glass and fluorapatite/bioactive glass nanocomposite foams as a cellular scaffold of bone tissue, *J. Lab. Physicians*, 10 (3), 265–270.
- [45] Subri, L.M., Dewi, W., and Satari, M.H., 2012, The antimicrobial effect of piper betel leaves extract against *Streptococcus mutans*, *Padjadjaran J. Dent.*, 24 (3), 174–178.
- [46] Nazzaro, F., Fratianni, F., De Martino, L., Coppola, R., and De Feo, V., 2013, Effect of essential oils on pathogenic bacteria, *Pharmaceuticals*, 6 (12), 1451–1474.
- [47] Lobiuc, A., Pavál, N.E., Mangalagiu, I.I., Gheorghiuță, R., Teliban, G.C., Amăriucăi-Mantu, D., and Stoleru, V., 2023, Future antimicrobials: Natural and functionalized phenolics, *Molecules*, 28 (3), 1114.
- [48] Xie, Y., Yang, W., Tang, F., Chen, X., and Ren, L., 2014, Antibacterial activities of flavonoids: Structure-activity relationship and mechanism, *Curr. Med. Chem.*, 22 (1), 132–149.
- [49] Yuan, G., Guan, Y., Yi, H., Lai, S., Sun, Y., and Cao, S., 2021, Antibacterial activity and mechanism of plant flavonoids to gram-positive bacteria predicted from their lipophilicities, *Sci. Rep.*, 11 (1), 10471.
- [50] Štumpf, S., Hostník, G., Primožič, M., Leitgeb, M., Salminen, J.P., and Bren, U., 2020, The effect of growth medium strength on minimum inhibitory concentrations of tannins and tannin extracts against *E. coli*, *Molecules*, 25 (12), 2947.
- [51] Kaczmarek, B., 2020, Tannic acid with antiviral and antibacterial activity as a promising component of biomaterials—A minireview, *Materials*, 13 (14), 3224.

## The Stability Study of Electrochemical Aptasensor to Detect SARS-CoV-2 Spike Protein and Its Application for Clinical Samples of Nasopharyngeal Swab

Arum Kurnia Sari<sup>1</sup>, Ghina Nur Fadhilah<sup>1</sup>, Irkham Irkham<sup>1</sup>, Muhammad Yusuf<sup>2</sup>, Shabarni Gaffar<sup>1,2</sup>, and Yeni Wahyuni Hartati<sup>1,2\*</sup>

<sup>1</sup>Department of Chemistry, Faculty of Mathematics and Natural Sciences, Universitas Padjadjaran, Jl. Raya Bandung-Sumedang Km. 21, Jatinangor, Sumedang 45363, Indonesia

<sup>2</sup>Molecular Biotechnology and Bioinformatics Research Center, Universitas Padjadjaran, Jl. Singaperbangsa No. 2, Bandung 40132, Indonesia

\* **Corresponding author:**

tel: +62-8122132349

email: yeni.w.hartati@unpad.ac.id

Received: September 21, 2022

Accepted: February 18, 2023

DOI: 10.22146/ijc.77887

**Abstract:** The stability characteristics associated with the shelf life of a biosensor are rarely investigated, however, they are important factors for real applications. Stability is the variation in the detection signal over a long period of storage. This study aims to determine the effect of storage time on the stability of SARS-CoV-2 receptor binding domain (RBD) spike protein aptamers related to shelf life and the performance of an electrochemical aptasensor on clinical samples. The research method includes a stability study conducted using the accelerated stability method based on the Arrhenius equation at three variations of temperature and storage time. The electrochemical aptasensor's performance was evaluated on clinical samples of 32 nasopharyngeal swabs at biosafety level 3 and its potential on clinical saliva samples. The results indicated that the developed electrochemical aptasensor was stable for  $\pm 15$  days with a shelf life of 18, 17 and 16 days, respectively, at 25, 40 and 50 °C. This electrochemical aptasensor has the potential to be a Point of Care (POC) device for the clinical detection of SARS-CoV-2 because it can be tested on clinical samples of nasopharyngeal swabs and the results show its potential application to detect in clinical saliva samples.

**Keywords:** stability; aptasensor; SARS-CoV-2 RBD S Protein

### ■ INTRODUCTION

In late December 2019, a case caused by an unidentified pneumonia outbreak was first reported in Wuhan, Hubei Province, China. This disease outbreak originated in the Huanan seafood market, which has since grown rapidly and begun to spread throughout the world. The new coronavirus caused by severe acute respiratory syndrome coronavirus 2 (SARS-CoV-2) was later identified as the cause of the Coronavirus Disease 2019 (COVID-19) outbreak. SARS-CoV-2 is a positive single-strand RNA virus with a size of 29.9 kb. SARS-CoV-2 has four structural proteins, namely spike protein (S), membrane protein (M), envelope protein (E), and nucleocapsid protein (N) [1-2]. The S protein consists of two functional subunits, namely the S1 subunit, responsible for the

attachment of the virus to the receptor on the host cell surface via the receptor-binding domain (RBD), and S2 subunit, responsible for the fusion of the viral membrane with the host cell to facilitate the entry of the virus into the host cell [3-4]. Therefore, SARS-CoV-2 RBD S protein can be used as the main target for diagnosis, treatment, and vaccination [5].

Currently, there are several types of methods used to detect SARS-CoV-2, namely molecular tests based on the detection of viral RNA, antigen tests based on the detection of viral proteins, and antibody tests based on the detection of specific antibodies against viral proteins. Reverse Transcription Polymerase Chain Reaction (RT-PCR) is the gold standard method for the detection of SARS-CoV-2 virus RNA. The main limitations of this method are the expensive equipment requirements and

the need for highly qualified experts [6]. In the case of the molecular approach, a long sample processing time is required, which also requires sophisticated and expensive facilities. Lateral Flow Immunoassays (LFIAs) provide a faster response but it has lower sensitivity [6]. Meanwhile, detection methods targeting antibodies based on Enzyme-Linked Immunosorbent Assay (ELISA) are not suitable for early diagnosis because most patients have antibody responses around 7 to 21 days after infection [7-8].

Alternative diagnostic methods for the detection of SARS-CoV-2 can be done using a biosensor-based approach. Electrochemical biosensors have been widely used to detect several biomolecules, such as proteins as the biomarker of disease [9-11] or a marker of bacterial [12-13] or viral infection [14-15]. They have been shown to have several advantages, including portability, good sensitivity, high specificity, fast response, and ease of use [16-18]. Several bioreceptors such as antibodies, aptamers, and nucleic acids can be immobilized on the electrode surface for detection purposes [15]. Electrochemical biosensor methods have also been reported to be used for the detection of SARS-CoV-2 using various bioreceptors, such as antibodies [19-20], ssDNA [21-22], antigens [23-25], and aptamers [26-27].

In the preliminary research that has been carried out, an electrochemical aptasensor method was developed using a screen-printed carbon electrode/AuNP to detect the SARS-CoV-2 RBD S protein. In the creation of disposable electrodes for electrochemical biosensors, screen-printed carbon electrodes (SPCE), which incorporate three electrodes (WE, RE, and CE) into a single design, are frequently employed [28]. AuNPs are used to improve the performance of electrochemical biosensors by modifying the electrodes with nanomaterials, thereby increasing the electroactive surface area and increasing electron transfer between the electrodes and analytes [14]. Aptamers as bioreceptors for detecting SARS-CoV-2 have been reported by Song et al. [5] of the SELEX method that can bind to the SARS-CoV-2 RBD S protein. The RBD S protein of SARS-CoV-2 and the aptamer CoV2-RBD form hydrogen bonds with amino acids of the SARS-CoV-2 RBD S protein [5]. The

aptamer was immobilized to the electrode surface by the streptavidin-biotin system via the MPA (3-mercaptopropionic acid) linker [29]. The aptamer will then bind to the SARS-CoV-2 RBD S protein, which can be detected electrochemically using the  $K_3[Fe(CN)_6]$  solution redox system and the differential pulse voltammetry electrochemical detection technique. This electrochemical aptasensor with the streptavidin-biotin system has a low detection limit of 2.6308 ng/mL, a quantification limit of 7.9720 ng/mL, an accuracy of 99.89%, and a precision of 99.61%. Based on the results of several analytical parameters that have been obtained, this electrochemical aptasensor has the potential to be a method of detecting SARS-CoV-2 [14].

Biosensors generally consist of three basic components, namely bioreceptors, transducers, and signal processing systems [30]. Factors that affect stability are bioreceptor affinity (level of analyte binding to bioreceptors) and bioreceptor degradation over time [31]. Usually, bioreceptor limits the shelf life and stability of a biosensor [32]. Bioreceptors are quite susceptible to environmental changes, which can be characterized as a decrease in signaling over time. It is therefore very important to test the stability of a biosensor, especially for commercial purposes and because biosensors are currently being applied to more and more diverse applications. Stability characteristics related to shelf life are often under-investigated or underreported in the literature, even though they are important factors. The instability of a biosensor is referred to as a decrease in sensitivity over a certain period of time.

SARS-CoV-2 has been detected in various human body samples, including saliva, nasopharyngeal swabs, and oropharyngeal swabs [33]. A nasopharyngeal swab is a commonly used sample to detect respiratory viruses such as SARS-CoV-2. Currently, nasopharyngeal swabs are used in the RT-PCR method [34]. However, nasopharyngeal swab sampling is an invasive technique that can cause patients to cough or bleed, increasing the risk of transmitting the virus to healthcare workers. The use of saliva samples may offer a way to reduce this limitation, as sampling can be done individually, thereby



reducing the likelihood of exposure to the virus to healthcare workers. Thus, saliva samples can also be used as an alternative for the detection of SARS-CoV-2 [33-35].

Liv [36] studied the interference effect of several enzymes, compounds, and ions that can be found in saliva on electrochemical immunosensors to detect SARS-CoV-2 antibodies, namely  $\alpha$ -amylase, lipase,  $\text{Na}^+$ ,  $\text{K}^+$ ,  $\text{Ca}^{2+}$ ,  $\text{Mg}^{2+}$ ,  $\text{H}_2\text{PO}_4^-$ ,  $\text{HPO}_4^{2-}$ , urea,  $\text{HCO}_3^-$ , and  $\text{NH}_3$ . The presence of interference in saliva samples is the reason for the need for selectivity studies first before electrochemical aptasensors are applied to clinical saliva samples.

In this research, a stability study was conducted as proof of the quality of a sensor that will be developed and has the potential to become an applicable and commercial method. The stability of the biosensor was evaluated by comparing the response of peak currents measured on different days (1, 15, 30, and 60 days) in temperature variations of 25, 40 and 50 °C. The estimation of the shelf life of the biosensor can be done by the accelerated stability method using the Arrhenius equation. The performance of the electrochemical aptasensor was then tested on clinical samples of nasopharyngeal swabs and their potential against other clinical samples, namely saliva.

## ■ EXPERIMENTAL SECTION

### Materials

The materials used in this study were 1-ethyl-3-(3-dimethyl aminopropyl) carbodiimide (EDC) (Sigma Aldrich, Singapore), 3-mercaptopropionic acid (MPA) (Sigma Aldrich, Singapore), demineralized water (PT Ikapharmindo Putramas, Indonesia), biotinylated aptamer (biotin 5'- CAG CAC CGA CCT TGT GCT TTG GGA GTG CTG GTC CAA GGG CGT TAA TGG ACA-3') (Bioneer, Korea), chloroauric acid trihydrate ( $\text{HAuCl}_4 \cdot 3\text{H}_2\text{O}$ ) (synthesized by the Chemical Analysis and Separation Laboratory, 2018, Indonesia), ethanolamine (Merck, Germany), potassium ferricyanide ( $\text{K}_3[\text{Fe}(\text{CN})_6]$ ) (Sigma Aldrich, Singapore), potassium chloride (KCl) (Merck, Germany), SARS-CoV-2 RBD S protein solution (GenScript, USA), trisodium citrate dihydrate ( $\text{Na}_3\text{C}_6\text{H}_5\text{O}_7 \cdot 2\text{H}_2\text{O}$ ) (Merck, Germany), *N*-hydroxysuccinimide (NHS) (Sigma Aldrich, Singapore),

phosphate-buffered saline (PBS) pH 7.4 (Merck, Germany), and streptavidin (Promega, USA).

### Instrumentation

The SPCE (GSI Technologies, USA) and homemade SPCE were used carbon as a working and auxiliary electrode, and Ag/AgCl was used as a reference electrode for the electrochemical transducer. The electrochemistry measurements were conducted using a Zimmer & Peacock potentiostat connected to a computer using PSTRACE 5.8 software (Zeamer & Peacock, UK).

### Procedure

#### SPCE modification with AuNP

The overall schematic of the electrochemical aptasensor method is shown in Fig. 1. The SPCE surface was rinsed with demineralized water and dried at room temperature. Then, 25  $\mu\text{L}$  of colloidal AuNP solution was dropped onto the surface of the SPCE and incubated at room temperature for 24 h. The SPCE/AuNP was rinsed with demineralized water and dried at room temperature before being electrochemically characterized by differential pulse voltammetry over a potential range of  $-1.0$  to  $1.0$  V at a scan rate of  $0.008$  V/s, step potential ( $E_{\text{step}}$ )  $0.004$  V with a pulse potential ( $E_{\text{pulse}}$ ) of  $0.025$  V and the pulse time ( $t_{\text{pulse}}$ ) of  $0.05$  s.

#### Fabrication of the electrochemical aptasensor

The SPCE/AuNP was incubated with  $0.01$  M MPA for  $20$  min at  $25$  °C. After that, the SPCE/AuNP/MPA were rinsed with ethanol. Then  $0.1$  M EDC solution and  $0.1$  M NHS solution ( $1:1$  v/v) were incubated for  $60$  min at  $25$  °C, and rinsed with demineralized water. The streptavidin solution was incubated overnight at  $4$  °C on the surface of the SPCE/AuNP/MPA/EDC:NHS, and then rinsed with PBS solution  $0.01$  M. Ethanolamine was dropped onto the surface of the SPCE/AuNP/MPA/EDC:NHS/streptavidin for  $20$  min at  $25$  °C, and then rinsed with demineralized water. Furthermore, the  $0.5$   $\mu\text{g}/\text{mL}$  biotinylated aptamer was immobilized on the SPCE/AuNP surface using a streptavidin-biotin system for  $40$  min at  $25$  °C, and then rinsed with PBS solution  $0.01$  M.

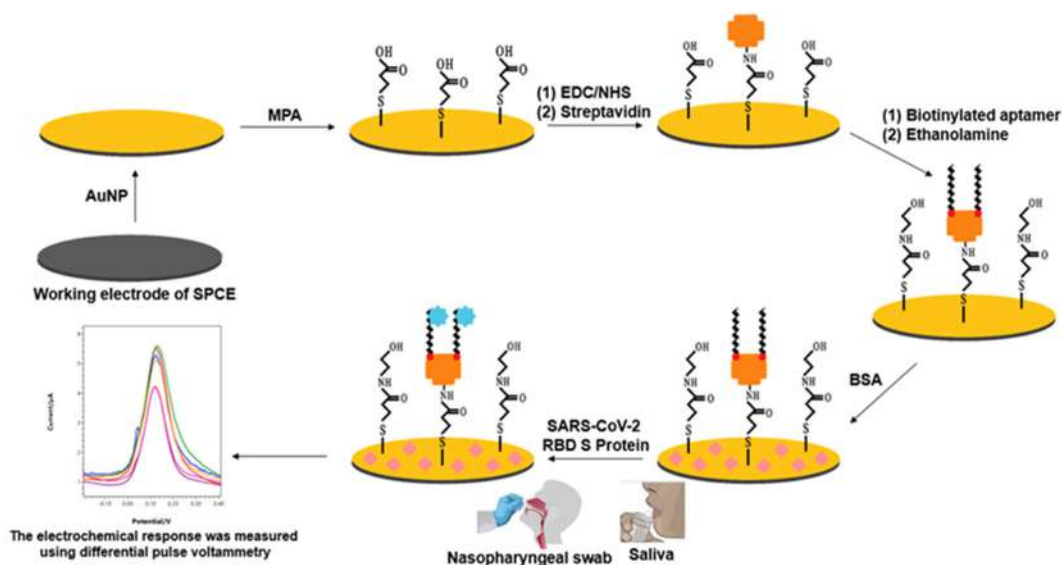


**Fig 1.** Schematic of an electrochemical aptasensor for SARS-CoV-2 RBD S protein detection

After the aptamer was successfully immobilized on the surface of the SPCE/AuNP electrode with the streptavidin-biotin system, the non-specific binding site on the electrode surface was incubated using a 1% BSA solution for 15 min at 25 °C, and then rinsed with PBS solution 0.01 M. After that, a solution of SARS-CoV-2 RBD S protein with a certain concentration was dropped on the electrode and incubated for 60 min at 25 °C. The differential pulse voltammetry was then performed using a redox system of 10 mM  $K_3[Fe(CN)_6]$  solution in 0.1 M KCl over a potential range of  $-1.0$  to  $1.0$  V at a scan rate of  $0.008$  V/s,  $E_{step}$   $0.004$  V with an  $E_{pulse}$  of  $0.025$  V and a  $t_{pulse}$  of  $0.05$  s.

### Stability

Electrochemical aptasensors were stored for 1, 15, 30, and 60 days at 25, 40 and 50 °C. After the aptasensor was stored, BSA (20  $\mu$ L 1%) was added, and then SARS-CoV-2 RBD S protein was added with a concentration of 30 ng/mL. The electrochemical response was measured using differential pulse voltammetry on a redox system containing 10 mM  $K_3[Fe(CN)_6]$  solution in 0.1 M KCl at a potential range of  $-1.0$  to  $1.0$  V at a scan rate of  $0.008$  V/s,  $E_{step}$   $0.004$  V with an  $E_{pulse}$  of  $0.025$  V and a  $t_{pulse}$  of  $0.05$  s. The stability was evaluated by looking at the peak current response at each different temperature and storage time.

### Clinical samples analysis

After the aptamer was successfully immobilized on the surface of the SPCE/AuNP electrode with the streptavidin-biotin system, the non-specific binding site on the electrode surface was incubated using 1% BSA solution and incubated for 15 min. A total of 32 clinical samples were collected from nasopharyngeal swabs and tested using aptasensors at biosafety level 3. As required by current law, clinical samples of nasopharyngeal swabs were obtained from patients after receiving the explicit agreement of the person whose material was being obtained. Next, the sample solution was dropped on the surface of the electrode and incubated for 60 min. Differential pulse voltammetry was used to measure current response in a redox system of 10 mM  $K_3[Fe(CN)_6]$  solution in 0.1 M KCl over a potential range of  $-1.0$  to  $1.0$  V at a scan rate of  $0.008$  V/s,  $E_{step}$   $0.004$  V with an  $E_{pulse}$  of  $0.025$  V and a  $t_{pulse}$  of  $0.05$  s.

### Selectivity to interference in saliva samples

Selectivity was determined by measuring the current response of the aptamer as a negative control, SARS-CoV-2 RBD S protein as a positive control, and  $Na^+$ ,  $K^+$ ,  $Ca^{2+}$ , and  $Mg^{2+}$  ions to the electrochemical aptasensor. The electrochemical response was measured using differential pulse voltammetry with a redox system of 10 mM  $K_3[Fe(CN)_6]$  solution in 0.1 M KCl at a

potential range of  $-1.0$  to  $1.0$  V at a scan rate of  $0.008$  V/s,  $E_{\text{step}}$   $0.004$  V with an  $E_{\text{pulse}}$  of  $0.025$  V and a  $t_{\text{pulse}}$  of  $0.05$  s, and the relative% response was calculated.

## RESULTS AND DISCUSSION

### Stability

Biosensor stability is an important aspect in terms of long-term application requirements. To study the stability of the aptasensor, the current response of the aptasensor to  $30$  ng/mL SARS-CoV-2 RBD S protein was recorded after 1, 15, 30, and 60 days of storage at  $25$  °C. Higher temperatures, such as  $40$  and  $50$  °C are also used for tests that allow accelerated stability prediction. Fig. 2 shows that the current response decreases with increasing storage time. Within 15 days, the current response decreased at  $25$ ,  $40$  and  $50$  °C, respectively, 6, 8 and 8% of the initial current response. Thirty days later, the sensor was re-measured and only maintained at 83, 82 and 82% of current response activity, at  $25$ ,  $40$  and  $50$  °C, respectively. Meanwhile, after 60 days, the sensor can only maintain current response activity of 60% at  $25$  °C, 56% at  $40$  °C, and 52% at  $50$  °C. These results indicate that the aptasensor is able to detect well up to  $\pm 15$  days after fabrication. The electrochemical aptasensor that was developed was able to produce  $> 90\%$  current response

activity on the 15<sup>th</sup> day compared to 100% of the current response activity on the first day, so that the aptasensor had good stability up to  $\pm 15$  days.

The determination of shelf-life stability is usually estimated by two different stability testing procedures, namely the real-time stability test and the accelerated stability test. In accelerated stability testing, the product is stored under conditions such as high temperatures. Temperature is the most commonly used acceleration factor for chemicals, pharmaceuticals, and biological products because of its relationship with the rate of degradation characterized by the Arrhenius equation [37]. The accelerated stability method is the determination of product shelf life by accelerating quality changes in critical parameters. This method uses environmental conditions that can accelerate the decline in product quality. With this method, product storage uses three temperatures that are able to predict shelf life at the desired storage temperature [38].

Based on the results of the current response in Table 1, it is made in graphic form with the x-axis being the storage time in days and the y-axis being the current response value for the linear equation and the coefficient of determination ( $R^2$ ) of order 0. The graph of the current response of the order 0 electrochemical aptasensor

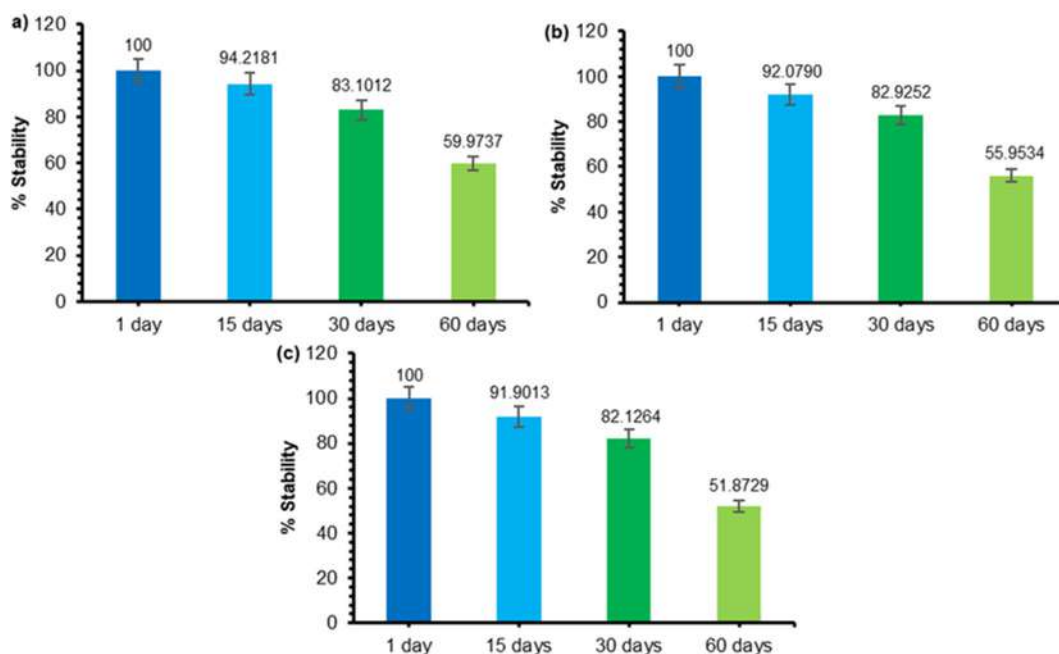


Fig 2. Stability of the aptasensor after 1, 15, 30, and 60 days of storage at (a)  $25$  °C, (b)  $40$  °C, and (c)  $50$  °C

**Table 1.** Current response of the electrochemical aptasensor to 30 ng/mL SARS-CoV-2 RBD S Protein recorded after 1, 15, 30, and 60 days of storage at 25, 40 and 50 °C

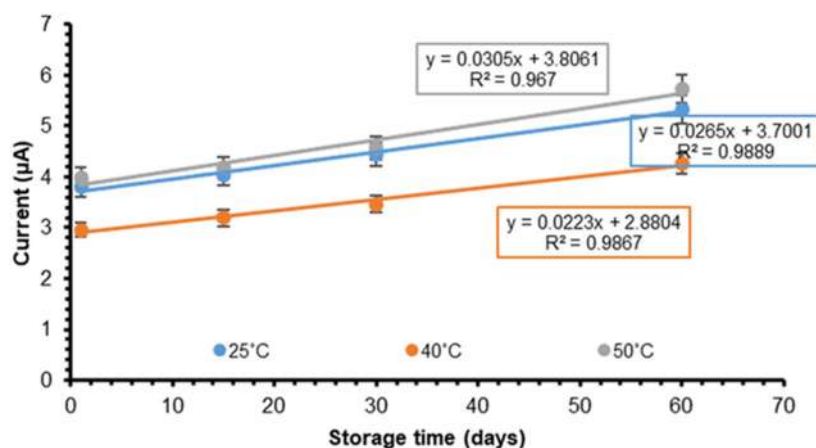
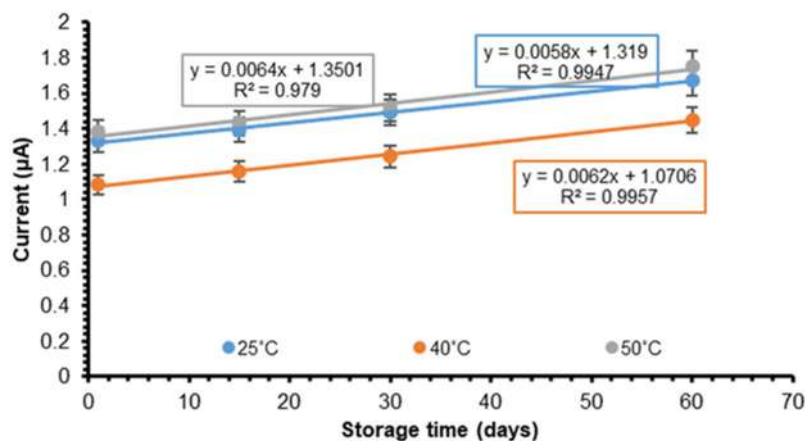
Storage time (day)	Average current response ( $\mu\text{A}$ )		
	25 °C	40 °C	50 °C
Aptamer	6.2820	4.4570	6.1540
1	3.8050	2.9605	3.9780
15	4.0250	3.1950	4.1845
30	4.4480	3.4660	4.5625
60	5.3280	4.2645	5.7340

can be seen in Fig. 3. In the first order graph, the current response value is converted to the form  $\ln$  before being made in the form of a graph with the storage time as shown in Fig. 4. From Fig. 3 and 4, it can be seen that the largest value of  $R^2$  is 0.9957, namely  $R^2$  of the current response for order 1 at a temperature of 40 °C so the estimated shelf-life calculation uses a linear equation plot of order 1. The value of  $k$  is the slope value, which is

obtained from the value of  $b$  in the equation  $y = bx + a$ . The value of  $k$  is then converted into the form  $\ln k$  and then used to create an Arrhenius graph between  $\ln k$  and  $1/T$ . The Arrhenius graph can be seen in Fig. 5. Based on the linear regression equation obtained in Fig. 5, the Arrhenius equation can be determined as follows:

$$y = -328.79x - 4.0318$$

$$\ln k = -328.79 (1/T) - 4.0318$$

**Fig 3.** Electrochemical aptasensor current response to storage time of order 0**Fig 4.** Electrochemical aptasensor current response to storage time of order 1

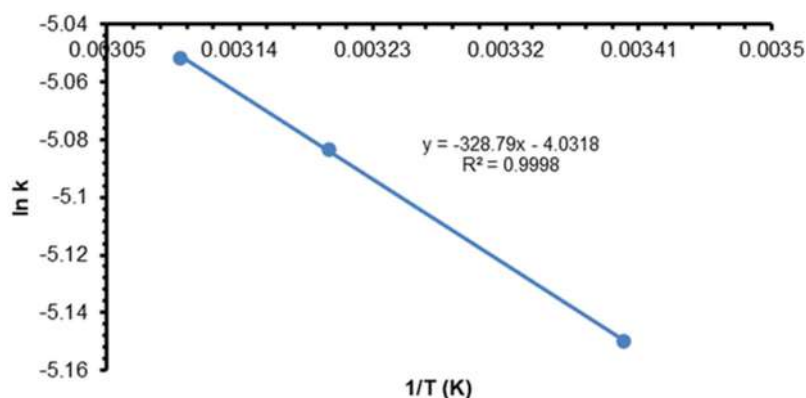


Fig 5. Correlation of  $\ln k$  to temperature in the Arrhenius equation

If the slope value of the linear regression equation for each temperature at order 1 is changed to the  $\ln$  value and plotted with  $1/T$  (units of degrees Kelvin), the Arrhenius equation is obtained as shown in Fig. 5. The value of the degradation reaction rate constant ( $k$ ) at each storage temperature can be estimated by the Arrhenius equation obtained as shown in Table 2. The results of determining the shelf life of electrochemical aptasensors can be seen in Table 2. The optimum storage of aptasensor is at 25 °C, because it has a longer shelf life than other storage temperatures.

The shelf life of the aptasensor at different temperatures can also be calculated using the Arrhenius equation. The Arrhenius equation obtained is  $\ln k = -328.79x - 4.0318$ , so the shelf life of the product if stored at a temperature of 4 °C or 277 °K will produce a value of  $\ln k = -5.2188$  or  $k = 0.3051$ . This means that there will be a decrease in the current response of 0.0054 units per day. Thus, the estimated storage time (90% activity maintained) at 4 °C can be estimated at about 20 days.

### Clinical Samples Analysis

To assess the feasibility of electrochemical aptasensors in detecting SARS-CoV-2 RBD S protein in clinical samples, the detection performance was tested using clinical samples and compared with the RT-PCR

method. A total of 32 samples (labeled S1 to S32) were collected from nasopharyngeal swabs and tested using aptasensors. In the electrochemical aptasensor method, if the peak current response is smaller than the peak current of the aptamer as a negative control or not much different from the peak current response of RBD as a positive control, then the sample is positive for COVID-19. Meanwhile, if the peak current response is greater than or equal to the peak current response of the aptamer, then the sample is negative for COVID-19. The peak current of the aptamer as a negative control is 30.124  $\mu\text{A}$ , while the peak current of RBD as a positive control is 19.857  $\mu\text{A}$ . The RT-PCR method used to diagnose COVID-19 provides an overview of the Ct value or Cycle threshold, which is the size of the viral load in the sample. A low Ct value indicates a high viral load. The Ct result is inversely proportional to the amount of viral nucleic acid present in the sample. The low Ct value indicates that the amplification cycle required to reach the threshold is shorter because the nucleic acid contained in the sample is high. Of the 32 samples tested, 3 samples were confirmed positive for SARS-CoV-2 and 29 samples were confirmed negative, as shown in Table 3. Based on the results obtained, this developed electrochemical aptasensor can be applied to detect SARS-CoV-2 RBD S protein in clinical samples of nasopharyngeal swabs.

Table 2. Determination of shelf life of electrochemical aptasensors

Temperature (°C)	k	$A_0$	$A_t$	$\ln A_0$	$\ln A_t$	t (days)
25	0.0058	100	90	4.6052	4.4998	18
40	0.0062	100	90	4.6052	4.4998	17
50	0.0064	100	90	4.6052	4.4998	16

**Table 3.** Application of electrochemical aptasensors to detect SARS-CoV-2 on clinical samples compared with RT-PCR. S# is the number of clinical samples tested

Sample of patient	Ct value			RT-PCR	Aptasensor
	ORF1ab	N gene	E gene		
S1	<b>27.50</b>	<b>22.52</b>	<b>25.55</b>	(+)	(+) <b>20.885 <math>\mu</math>A</b>
S2	<b>17.13</b>	<b>14.32</b>	<b>16.64</b>	(+)	(+) <b>20.550 <math>\mu</math>A</b>
S3	-	-	-	(-)	(-)
S4	-	-	-	(-)	(-)
S5	-	-	-	(-)	(-)
S6	-	-	-	(-)	(-)
S7	-	-	-	(-)	(-)
S8	-	-	-	(-)	(-)
S9	-	-	-	(-)	(-)
S10	-	-	-	(-)	(-)
S11	-	-	-	(-)	(-)
S12	-	-	-	(-)	(-)
S13	-	-	-	(-)	(-)
S14	-	-	-	(-)	(-)
S15	-	-	-	(-)	(-)
S16	-	-	-	(-)	(-)
S17	-	-	-	(-)	(-)
S18	-	-	-	(-)	(-)
S19	-	-	-	(-)	(-)
S20	-	-	-	(-)	(-)
S21	-	-	-	(-)	(-)
S22	<b>20.31</b>	<b>18.68</b>	<b>20.46</b>	(+)	(+) <b>20,578 <math>\mu</math>A</b>
S23	-	-	-	(-)	(-)
S24	-	-	-	(-)	(-)
S25	-	-	-	(-)	(-)
S26	-	-	-	(-)	(-)
S27	-	-	-	(-)	(-)
S28	-	-	-	(-)	(-)
S29	-	-	-	(-)	(-)
S30	-	-	-	(-)	(-)
S31	-	-	-	(-)	(-)
S32	-	-	-	(-)	(-)

### Selectivity to Interference in Saliva Samples

Selectivity is a very important characteristic, especially in clinical applications where the sample matrix, contains many molecules that are very similar to the target analyte and compete for binding to bioreceptors [39]. Salivary components can be divided into organic and inorganic components. However, this level is still low compared to the main component of saliva, which is water, which is around 99.5% [40-41].

Selectivity was determined by the interference ions present in saliva, namely  $\text{Na}^+$ ,  $\text{K}^+$ ,  $\text{Ca}^{2+}$ , and  $\text{Mg}^{2+}$ . The measured current response was compared with the RBD peak response of SARS-CoV-2 S protein as a positive (+) control and the aptamer as a negative control (-) as shown in Fig. 6. The results obtained indicate that the measured ion current response is not much different from the aptamer. This indicates that there is no binding between the aptamer and the interference ions.

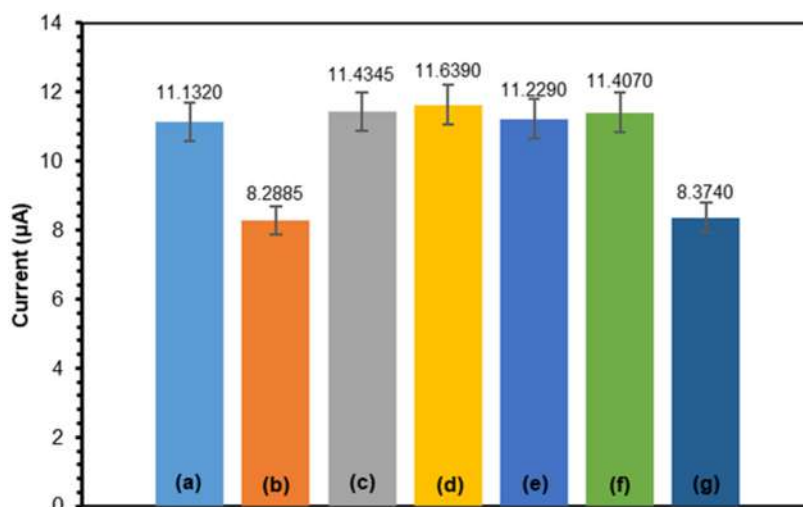


**Fig 6.** Selectivity of electrochemical aptasensor to interference in the form of ions. Current response (a) aptamer, (b) SARS-CoV-2 RBD S protein, (c) Na<sup>+</sup> ions, (d) K<sup>+</sup> ions, (e) Ca<sup>2+</sup> ions, (f) Mg<sup>2+</sup> ions, and (g) RBD + Na<sup>+</sup> + K<sup>+</sup> + Ca<sup>2+</sup> + Mg<sup>2+</sup>

As for other components in saliva, namely enzymes, such as the results of research by Liv [36]. Interferences in saliva samples are  $\alpha$ -amylase and lipase enzymes, but due to the unavailability of enzyme reagents, the alternative is to use individual saliva, because the saliva component itself contains the required enzymes. From the results of the salivary flow response obtained, when compared with the aptamer current response as a negative control (-) and SARS-CoV-2 RBD S protein as a positive control (+), the salivary flow response was not much different from the aptamer current response as shown in Fig. 7. This means

that there is no interaction between enzyme interference in saliva and the aptamer. Meanwhile, when saliva was added to SARS-CoV-2 RBD S protein and then tested on the aptasensor, the current response obtained was not much different from the current response to SARS-CoV-2 RBD S protein alone. This shows that the presence of interference or interference does not affect the activity of the aptamer against SARS-CoV-2 RBD S protein.

Aptasensor selectivity testing was also carried out on the saliva of other individuals. The results also showed

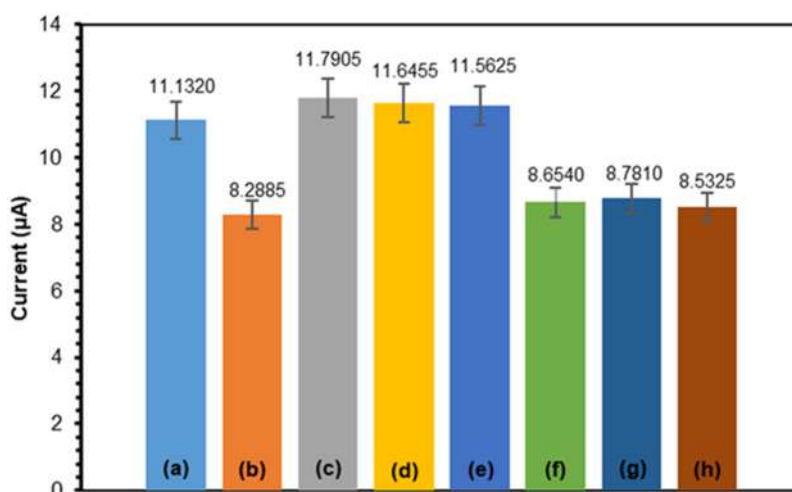


**Fig 7.** Selectivity of electrochemical aptasensors in saliva samples. Current response (a) aptamer, (b) SARS-CoV-2 RBD S protein, (c) Saliva 1, (d) Saliva 2, (e) Saliva 3, (f) Saliva 1 + RBD, (g) Saliva 1 + RBD, and (h) Saliva 3 + RBD

**Table 4.** Electrochemical aptasensor studies to detect SARS-CoV-2

Method	% Recovery	Limit of detection, ng/mL	Ref.
Two-dimensional (2D) metal-organic framework (MOF)-based photoelectrochemical (PEC) aptasensor for SARS-CoV-2 spike glycoprotein (S protein) detection	104–106%	72	[42]
Electrochemical dual-aptamer biosensor based on the metal-organic frameworks MIL-53(Al) decorated with Au@Pt nanoparticles and enzymes to determine SARS-CoV-2 nucleocapsid protein (2019-nCoV-NP) via co-catalysis of the nanomaterials, horseradish peroxidase (HRP) and G-quadruplex DNAzyme	92–110%	0.00833	[43]
CRISPR-Cas12a-mediated label-free electrochemical aptamer-based sensor for SARS-CoV-2 antigen detection	98–105%	0.077	[44]
Electrochemical aptasensor to detect SARS-CoV-2 S protein RBD as a biomarker of COVID-19 disease using a screen-printed carbon electrode/AuNP	95–99%	2.63	This research
CRISPR/Cas12a-derived electrochemical aptasensor for ultrasensitive detection of COVID-19 nucleocapsid protein	99–101%	0.0165	[45]

that interference in saliva samples did not interfere with the binding activity of the aptamer with SARS-CoV-2 RBD S protein, which means that the developed aptasensor can detect SARS-CoV-2 RBD S protein in saliva samples non-invasively. Aptamer selectively only recognized its target, namely SARS-CoV-2 RBD S protein and obtained the percentage selectivity value, which was 97% for ions, 87% for saliva 1, 82% for saliva 2, and 91% for saliva 3.

The developed aptasensor method was also used to determine the amount of SARS-CoV-2 RBD S protein in spiked-saliva samples. Saliva samples were taken from negative individuals which were then dissolved in PBS pH 7.4 0.01 M. The saliva samples were then tested on the aptasensor with 100 ng/mL of SARS-CoV-2 RBD S protein. The resulting peak current response is entered into the equation  $y = 0.0634x - 0.4449$ . The % recovery values obtained were 99.85% and 95.22%, respectively. Thus, the results show that this method also provides good accuracy. The quantitative analysis of SARS-CoV-2 RBD S protein in spiked-saliva samples for the early diagnosis of COVID-19 showed reliability and accuracy, as shown in Table 4, and the results were comparable to those of the electrochemical aptasensor studies to detect SARS-CoV-2. The results obtained with this external

standard calibration curve also illustrate that the developed method is not affected by the sample matrix.

## ■ CONCLUSION

The accelerated stability method can be used to determine the shelf-life stability of electrochemical aptasensors, namely 18 days at 25 °C, 17 days at 40 °C, and 16 days at 50 °C. Electrochemical aptasensors can be applied to detect SARS-CoV-2 RBD S protein in clinical samples of nasopharyngeal swabs. Of the 32 samples tested, 3 samples were confirmed positive and 29 samples were confirmed negative for COVID-19. This electrochemical aptasensor also shows the potential to detect SARS-CoV-2 RBD S protein in clinical saliva samples.

## ■ ETHICAL APPROVAL

The ethical approval has been given by Research Ethics Committee Universitas Padjadjaran Bandung, Molecular Biotechnology and Bioinformatics Research Center No. 860/UN6.KEP/EC/2022.

## ■ ACKNOWLEDGMENTS

This research was supported by the Ministry of Education, Culture, Research and Technology of the Republic of Indonesia, PTM No.094/E5/PG.02.00.PT/



2022, Matching Fund No./UN6.RKT/LT/2022, and the Academic Leadership Grant (ALG) Universitas Padjadjaran No.1318/UN.3.1/PT.00/2022.

#### ■ AUTHOR CONTRIBUTIONS

Yeni Wahyuni Hartati and Shabarni Gaffar designed the experiment, evaluated, and corrected the manuscript. Irkham guided the experiment. Muhammad Yusuf prepared the ethical approval and clinical samples for aptasensor. Arum Kurnia Sari and Ghina Nur Fadhillah conducted the experiment, wrote, and revised the manuscript. Yeni Wahyuni Hartati was the funding leader of the Academic Leadership Grant (ALG). All authors agreed to the final version of this manuscript.

#### ■ REFERENCES

- [1] Schoeman, D., and Fielding, B.C., 2019, Coronavirus envelope protein: Current knowledge, *Virology*, 16 (1), 69.
- [2] Jin, Y., Yang, H., Ji, W., Wu, W., Chen, S., Zhang, W., and Duan, G., 2020, Virology, epidemiology, pathogenesis, and control of COVID-19, *Viruses*, 12 (4), 372.
- [3] Walls, A.C., Park, Y.J., Tortorici, M.A., Wall, A., McGuire, A.T., and Veesler, D., 2020, Structure, function, and antigenicity of the SARS-CoV-2 spike glycoprotein, *Cell*, 180 (2), 281–292.e6.
- [4] Tai, W., He, L., Zhang, X., Pu, J., Voronin, D., Jiang, S., Zhou, Y., and Du, L., 2020, Characterization of the receptor-binding domain (RBD) of 2019 novel coronavirus: Implication for development of RBD protein as a viral attachment inhibitor and vaccine, *Cell. Mol. Immunol.*, 17 (6), 613–620.
- [5] Song, Y., Song, J., Wei, X., Huang, M., Sun, M., Zhu, L., Lin, B., Shen, H., Zhu, Z., and Yang, C., 2020, Discovery of aptamers targeting receptor-binding domain of the SARS-CoV-2 spike glycoprotein, *Anal. Chem.*, 92 (14), 9895–9900.
- [6] Drobysh, M., Ramanaviciene, A., Viter, R., and Ramanavicius, A., 2021, Affinity sensors for the diagnosis of COVID-19, *Micromachines*, 12 (4), 390.
- [7] Cui, F., and Zhou, H.S., 2020, Diagnostic methods and potential portable biosensors for coronavirus disease 2019, *Biosens. Bioelectron.*, 165, 112349.
- [8] Chen, Z., Wu, Q., Chen, J., Ni, X., and Dai, J., 2020, A DNA aptamer based method for detection of SARS-CoV-2 nucleocapsid protein, *Virology*, 35 (3), 351–354.
- [9] Hartati, Y.W., Syahrini, S., Gaffar, S., Wyantuti, S., Yusuf, M., and Subroto, T., 2021, An electrochemical aptasensor for the detection of HER2 as a breast cancer biomarker based on gold nanoparticles-aptamer bioconjugates, *Indones. J. Chem.*, 21 (6), 1526–1536.
- [10] Fazrin, E.I., Sari, A.K., Setiyono, R., Gaffar, S., Sofiatin, Y., Bahti, H.H., and Hartati, Y.W., 2022, The selectivity and stability of epithelial sodium channel (ENaC) aptamer as an electrochemical biosensor, *Anal. Bioanal. Electrochem.*, 14 (7), 715–729.
- [11] Hartati, Y.W., Nurdjanah, D., Wyantuti, S., Anggraeni, A., and Gaffar, S., 2018, Gold nanoparticles modified screen-printed immunosensor for cancer biomarker HER2 determination based on anti HER2 bioconjugates, *AIP Conf. Proc.*, 2049, 020051.
- [12] Kaya, H.O., Cetin, A.E., Azimzadeh, M., and Topkaya, S.N., 2021, Pathogen detection with electrochemical biosensors: Advantages, challenges and future perspectives, *J. Electroanal. Chem.*, 882, 114989.
- [13] Hartati, Y.W., Wyantuti, S., Firdaus, M.L., Auliany, N., Surbakti, R., and Gaffar, S., 2016, A rapid and sensitive diagnosis of typhoid fever based on nested PCR-voltammetric DNA biosensor using flagellin gene fragment, *Indones. J. Chem.*, 16 (1), 87–91.
- [14] Sari, A.K., Hartati, Y.W., Gaffar, S., Anshori, I., Hidayat, D., and Wiraswati, H.L., 2022, The optimization of an electrochemical aptasensor to detect RBD protein S SARS-CoV-2 as a biomarker of COVID-19 using screen-printed carbon electrode/AuNP, *J. Electrochem. Sci. Eng.*, 21 (1), 219–235.
- [15] Chand, R., and Neethirajan, S., 2017, Microfluidic platform integrated with graphene-gold nano-

- composite aptasensor for one-step detection of norovirus, *Biosens. Bioelectron.*, 98, 47–53.
- [16] Labib, M., Zamay, A.S., Muharemagic, D., Chechik, A.V., Bell, J.C., and Berezovski, M.V., 2012, Aptamer-based viability impedimetric sensor for viruses, *Anal. Chem.*, 84 (4), 1813–1816.
- [17] Yao, C.Y., and Fu, W. L., 2014, Biosensors for hepatitis B virus detection, *World J. Gastroenterol.*, 20 (35), 12485–12492.
- [18] Fadhilah, G.N., Yusuf, M., and Hartati, Y.W., 2020, Electrochemical immunosensor to detect hepatitis B antigen (HBsAg) and hepatitis B e antigen (HBeAg) as biomarkers of hepatitis B infection: A review, *Curr. Top. Electrochem.*, 22, 121–127.
- [19] Mahari, S., Roberts, A., Shahdeo, D., and Gandhi, S., 2020, eCovSens-ultrasensitive novel in-house built printed circuit board based electrochemical device for rapid detection of nCovid-19 antigen, a spike protein domain 1 of SARS-CoV-2, *bioRxiv*, 2020.04.24.059204.
- [20] Fabiani, L., Saroglia, M., Galatà, G., De Santis, R., Fillo, S., Luca, V., Faggioni, G., D'Amore, N., Regalbuto, E., Salvatori, P., Terova, G., Moscone, D., Lista, F., and Arduini, F., 2020, Magnetic beads combined with carbon black-based screen-printed electrodes for COVID-19: A reliable and miniaturized electrochemical immunosensor for SARS-CoV-2 detection in saliva, *Biosens. Bioelectron.*, 171, 112686.
- [21] Zhao, H., Liu, F., Xie, W., Zhou, T.C., OuYang, J., Jin, L., Li, H., Zhao, C.Y., Zhang, L., Wei, J., Zhang, Y.P., and Li, C.P., 2021, Ultrasensitive supersandwich-type electrochemical sensor for SARS-CoV-2 from the infected COVID-19 patients using a smartphone, *Sens. Actuators, B*, 327, 128899.
- [22] Tripathy, S., and Singh, S.G., 2020, Label-free electrochemical detection of DNA hybridization: A method for COVID-19 diagnosis, *Trans. Indian Natl. Acad. Eng.*, 5 (2), 205–209.
- [23] Ali, M.A., Hu, C., Jahan, S., Yuan, B., Saleh, M.S., Ju, E., Gao, S.J., and Panat, R., 2021, Sensing of COVID-19 antibodies in seconds via aerosol jet nanoprinted reduced-graphene-oxide-coated 3D electrodes, *Adv. Mater.*, 33 (7), 2006647.
- [24] Rashed, M.Z., Kopechek, J.A., Priddy, M.C., Hamorsky, K.T., Palmer, K.E., Mittal, N., Valdez, J., Flynn, J., and Williams, S.J., 2021, Rapid detection of SARS-CoV-2 antibodies using electrochemical impedance-based detector, *Biosens. Bioelectron.*, 171, 112709.
- [25] Yakoh, A., Pimpitak, U., Rengpipat, S., Hirankarn, N., Chailapakul, O., and Chaiyo, S., 2021, Paper-based electrochemical biosensor for diagnosing COVID-19: Detection of SARS-CoV-2 antibodies and antigen, *Biosens. Bioelectron.*, 176, 112912.
- [26] Idili, A., Parolo, C., Alvarez-Diduk, R., and Merkoçi, A., 2021, Rapid and efficient detection of the SARS-CoV-2 spike protein using an electrochemical aptamer-based sensor, *ACS Sens.*, 6 (8), 3093–3101.
- [27] Abrego-Martinez, J.C., Jafari, M., Chergui, S., Pavel, C., Che, D., and Siaj, M., 2022, Aptamer-based electrochemical biosensor for rapid detection of SARS-CoV-2: Nanoscale electrode-aptamer-SARS-CoV-2 imaging by photo-induced force microscopy, *Biosens. Bioelectron.*, 195, 113595.
- [28] Fadhilah, G.N., Yusuf, M., Sari, A.K., Tohari, T.R., Wiraswati, H.L., Ekawardhani, S., Faridah, L., Fauziah, N., Anshori, I., and Hartati, Y.W., 2023, An scFv-based impedimetric immunosensor using SPCE/AuNP for RBD of SARS-CoV-2 detection, *ChemistrySelect*, 8 (1), e202203928.
- [29] Sari, A.K., Gaffar, S., and Hartati, Y.W., 2022, A review on the development of aptamer immobilization techniques in aptamer-based electrochemical biosensors for viruses detection, *Anal. Bioanal. Electrochem.*, 14 (1), 127–143.
- [30] Sahoo, S., Sahu, S.N., Pattanayak, S.K., Misra, N., and Suar, M., 2020, “Biosensor and Its Implementation in Diagnosis of Infectious Diseases” in *Smart Biosensors in Medical Care*, Eds. Chaki, J., Dey, N., and Se D., Academic Press, Cambridge, Massachusetts, United States, 29–47.
- [31] Naresh, V., and Lee, N., 2021, A review on

- biosensors and recent development of nanostructured materials-enabled biosensors, *Sensors*, 21 (4), 1109.
- [32] Choi, M.M.F, 2005, Application of a long shelf-life biosensor for the analysis of L-lactate in dairy products and serum samples, *Food Chem.*, 92 (3), 575–581.
- [33] Nasiri, K., and Dimitrova, A., 2021, Comparing saliva and nasopharyngeal swab specimens in the detection of COVID-19: A systematic review and meta-analysis, *J. Dent. Sci.*, 16 (3), 799–805.
- [34] Kim, Y.G., Yun, S.G., Kim, M.Y., Park, K., Cho, C.H., Yoon, S.Y., Nam, M.H., Lee, C.K., Cho, Y.J., and Lim, C.S., 2017, Comparison between saliva and nasopharyngeal swab specimens for detection of respiratory viruses by multiplex reverse transcription-PCR, *J. Clin. Microbiol.*, 55 (1), 226–233.
- [35] Comber, L., Walsh, K.A., Jordan, K., O'Brien, K.K., Clyne, B., Teljeur, C., Drummond, L., Carty, P.G., De Gascun, C.F., Smith, S.M., Harrington, P., Ryan, M., and O'Neill, M., 2021, Alternative clinical specimens for the detection of SARS-CoV-2: A rapid review, *Rev. Med. Virol.*, 31 (4), e2185.
- [36] Liv, L., 2021, Electrochemical immunosensor platform based on gold-clusters, cysteamine and glutaraldehyde modified electrode for diagnosing COVID-19, *Microchem. J.*, 168, 106445.
- [37] Haouet, M.N., Tommasino, M., Mercuri, M.L., Benedetti, F., Di Bella, S., Framboas, M., Pelli, S., and Altissimi, M.S., 2018, Experimental accelerated shelf life determination of a ready-to-eat processed food, *Ital. J. Food. Saf.*, 7 (4), 189–192.
- [38] Arif, A.B., 2016, Metode accelerated shelf life test (ASLT) dengan pendekatan Arrhenius dalam pendugaan umur simpan sari buah nenas, pepaya dan cempedak, *Informatika Pertanian*, 25 (2), 189–198.
- [39] Tetyana, P., Shumbula, P.M., and Njengele-Tetyana, Z., 2021, “Biosensors: Design, Development and Applications” in *Nanopores*, Eds. Ameen, S., Akhtar, M.S., and Shin, H.S., IntechOpen, Rijeka, 137–144.
- [40] Rahayu, Y.C., and Kurniawati, A., 2015, *Cairan Rongga Mulut*, Pustaka Panasea, Yogyakarta, Indonesia.
- [41] Riskayanty, R., Fitriani, N.R.D., and Samad, R., 2014, Profil kandungan unsur anorganik dan organik saliva pada keadaan usia lanjut, *Dentofasial*, 13 (1), 22–27.
- [42] Jiang, Z.W., Zhao, T.T., Li, C.M., Li, Y.F., and Huang, C.Z., 2021, 2D MOF-based photoelectrochemical aptasensor for SARS-CoV-2 spike glycoprotein detection, *ACS Appl. Mater. Interfaces*, 13 (42), 49754–49761.
- [43] Tian, J., Liang, Z., Hu, O., He, Q., Sun, D., and Chen, Z., 2021, An electrochemical dual-aptamer biosensor based on metal-organic frameworks MIL-53 decorated with Au@Pt nanoparticles and enzymes for detection of COVID-19 nucleocapsid protein, *Electrochim. Acta*, 387, 138553.
- [44] Liu, N., Liu, R., and Zhang, J., 2022, CRISPR-Cas12a-mediated label-free electrochemical aptamer-based sensor for SARS-CoV-2 antigen detection, *Bioelectrochemistry*, 146, 108105.
- [45] Han, C., Li, W., Li, Q., Xing, W., Luo, H., Ji, H., Fang, X., Luo, Z., and Zhang, L., 2022, CRISPR/Cas12a-derived electrochemical aptasensor for ultrasensitive detection of COVID-19 nucleocapsid protein, *Biosens. Bioelectron.*, 200, 113922.

## Enhancement of Ozonation Reaction for Efficient Removal of Phenol from Wastewater Using a Packed Bubble Column Reactor

Saja Abdulhadi Alattar, Khalid Ajmi Sukkar\*, and May Ali Alsaffar

Department of Chemical Engineering, University of Technology-Iraq, Baghdad, Iraq

\* **Corresponding author:**

email: khalid.a.sukkar@uotechnology.edu.iq

Received: October 9, 2022

Accepted: February 18, 2023

DOI: 10.22146/ijc.78271

**Abstract:** In the ozonation process, the phenol degradation in wastewater undergoes a low mass transfer mechanism. In this study, ozonized packed bubble column reactor was designed and constructed to remove phenol. The reactor's inner diameter and height were 150 and 8 cm, respectively. The packing height was kept constant at 1 m in accordance with the reactor hydrodynamics. The gas distributor was designed with 55 holes of 0.5 mm. The phenol removal efficiency was evaluated at ozone concentrations of 10, 15, and 20 mg/L, contact times of 15, 30, 45, 60, 75, 90, 105, and 120 min, and phenol concentrations of 3, 6, 9, 12, and 15 mg/L. The results indicated that the highest phenol removal efficiency of 100% was achieved at 30 min in presence of packing. Moreover, the use of packing improved the contact between the gas and liquid, which significantly enhanced the phenol degradation. Actually, a thin film over a packing surface enhances the mass transfer. Also, it was found that the phenol is degraded into CO<sub>2</sub> and H<sub>2</sub>O through a series of reaction steps. Additionally, a kinetic study of a first-order reaction provided an efficient estimation of reaction parameters with a correlation factor of 0.997.

**Keywords:** wastewater treatment; phenol removal; advanced oxidation process; ozonation reaction; kinetics study

### ■ INTRODUCTION

Most industrial processes, including those at chemical plants, in the petrochemicals industry, and in petroleum refining processes, discharge wastewater into the environment without being treated or reused [1]. Thus, these industrial activities continuously create large amounts of wastewater at high rates with varying quantities of pollutants [2]. Wastewater from petroleum refineries contains high levels of harmful materials (grease, sulfides, cyanides, suspended solids, heavy metals, and phenols) that can be fatal to humans as well as cause other environmental problems [3-8]. Phenol and its derivatives are usually produced in petroleum refineries as a result of operating unit activities. These materials are regarded as highly toxic compounds in the petroleum industry because they cause pollution in water supplies [9-12].

The ozonation process is one of the most advanced oxidation techniques employed to remove organic

pollutants from wastewater [10,13]. In the ozonation technique, the hydroxyl group and other radicals are generated during the oxidation reaction, which provides a high removal percentage of organic materials [14-18]. Ozone gas is a strong oxidizing agent that is widely applied in wastewater treatment to remove microorganisms, organic, and inorganic compounds. Ozones are utilized in direct and indirect processes, which may produce hydroxyl radicals and other chemical by-products [19-22]. Furthermore, it is important to consider that the ozonation process is characterized by a low reaction rate. Accordingly, the chemical reaction required a long reaction time to degrade hydrocarbons. The limited reaction rate is attributed to the low mass transfer mechanism inside reactors. Then, the enhancement of the contact area between the gas phase (ozone) and the liquid phase (polluted wastewater) can improve the reaction rate of the ozonation process [6,20].

Moreover, due to the difficulty of degrading phenol compounds, many researchers have explored enhanced removal techniques depending on the phenol concentration, operating conditions, and reactor design [23-27]. The efficient removal of phenolic compounds from industrial wastewater requires a high-performance process with economic feasibility. Different reactor designs have been employed to remove phenol from wastewater, including a semi-batch reactor [28], fluidized bed reactor [29], trickle bed reactor, and bubble column reactor [30-33].

Karri et al. [34] investigated the removal of phenol using a fluidized-bed reactor and activated carbon from coconut shells. The authors noted that with a lower concentration of activated carbon and shorter contact times, about 96% phenol removal was achieved. Annisa et al. [35] evaluated the efficiency of ozonation procedures in the removal of phenolic compounds in a bubble column reactor. They found that at 60 min, the removal efficiency for 4-chlorophenol using ozonation was 62.79%, but for RB-19 dye, it was 99.70%. Yusoff et al. [36] studied the performance of a hybrid growth sequencing batch reactor under three toxicity conditions by adding phenol to activated sludge at full organic loading. The authors found that a treatment time of 30 min produced a clear reduction in the phenol and chemical oxygen demand (COD) by 61 and 52%, respectively.

Liu et al. [37] applied a fixed-bed reactor for the phenol removal process using stainless steel-graphene film as a metal-free catalyst. They noted that after a working time of 72 h, the catalyst provided full phenol removal and an impressive total organic carbon (TOC) removal of 80.7–91%. Zheng et al. [38] employed a fluidized bed reactor for the phenolic degradation process and observed that the activated carbon/lignite showed a higher rate of phenolic degradation in comparison with activated sludge reactors. The authors indicated that the adsorption capacity was 90 and 70% for fluidized and activated sludge reactors, respectively. Qin et al. [39] studied phenol removal in two stages (fixed-bed reactor and heterogeneous Fenton-reaction) using a Cu/Bi-Ce/Al<sub>2</sub>O<sub>3</sub> catalyst. They noted that the highest phenol removal was 32.6% for two-stage operations. Al Ezzi [40]

used an internal airlift loop reactor to remove phenol, with rice husk and granular activated carbon as adsorbent materials and hydrogen peroxide as an oxidant agent. After 60 min of treatment time, the phenol removal was 81 and 83% for the rice husk and activated carbon, respectively.

Hashim et al. [41] and Sang et al. [42] pointed to the importance of using packing materials to increase the contact between gas and liquid phases. The authors used packing materials in the fixed-bed reactor and micro-fixed-bed reactor, respectively. They found that the diffusion resistance was reduced efficiently when packing materials were applied inside the reactors. Furthermore, the main reason for using the packing is the low solubility of ozone in water. This low solubility leads to low mass transfer of ozone from the gas to the liquid phase and the high ozone demand for contaminants decomposition during ozonation. Then, adding packing material to the reactors is an efficient method for increasing the residence time, which causes the enhancing decomposition of ozone gas in an aqueous solution to improve ozone utilization and increase the removal efficiency of phenol degradation [10,43]. In comparison with other multiphase reactors, the bubble column reactor is characterized by having no moving parts, low maintenance, and simple operation [44] and can be applied in the ozone oxidation process with high performance [32,45]. From a reaction kinetics point of view, the ozonation reaction is dependent on the radical oxidation process. Then, species of reactive oxygen contribute significantly to minimizing the amount of pollutants in the wastewater [46-48]. According to a literature survey, the ozonation reaction operates with limited efficiency due to the low mass transfer rate between the gas and liquid in the reactor and due to the low contact surface area between these two substances. Therefore, it is desirable to develop an effective operational mechanism using a packed bubble column reactor to maximize phenol removal by enhancing ozone mass transfer in the reactor. Consequently, the ozone concentration and phenol degradation mechanism, as well as a kinetic study of packed and unpacked bubble columns, was evaluated.

## ■ EXPERIMENTAL SECTION

### Materials

In the present experimental study, phenol (99.6% purity, Gryfskand Co., Poland), potassium iodide (98.2% purity), sodium thiosulfate (99.95% purity), and sulfuric acid (99.8% purity) were purchased from Sigma-Aldrich Company, USA. Also, pure starch was used in the experimental work.

### Instrumentation

The instrumentations used in this study were TOC analyzer (TOC-L-CSH E200, Shimadzu, Japan), ozone generator type (DNA-Series Company, China), and bubble column reactor (locally designed and constructed from QF-glass).

### Procedure

For the starter, the removal of phenol from wastewater was achieved using a packed bubble column. Fig. 1 illustrates the experimental apparatus of the packed bubble column reactor. The experimental operation in this reactor was conducted under a semi-batch operational mode. The reactor was constructed from QF-glass, 150 cm in height and 8 cm in diameter. Moreover, spherical glass beads with a diameter of 1.5 cm were used as packing material over a height of 100 cm inside the reactor. Also, gas distribution was designed and constructed from stainless steel supported at the reactor bottom. The gas distributor had 51 holes, 0.5 mm in diameter. Furthermore, an ozone generator with a capacity of 3-g/h dose (DNA-Series Company, China) was used to allow ozone gas into the bubble column reactor at a supply rate of 0 to 20 mg/L. The flow rate of ozone gas was controlled with the aid of a sensitive airflow meter supported inside the ozone generation system. Also, an air compressor was used to combine the water and phenol mixing inside the reactor before any run to ensure that a uniform mixture was achieved. A calibrated gas flow meter was used to control the ozone gas flow from the bottom of the reactor. The output ozone gas was collected at the reactor top and then passed over a column of a 2% solution of potassium iodide (KI) to convert  $O_3$  into  $O_2$ . Additionally, the sampling draw zone was fitted

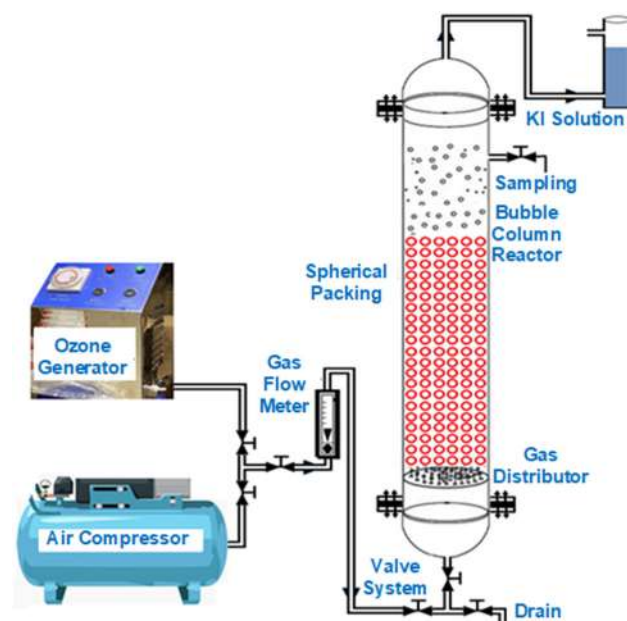


**Fig 1.** Schematic diagram of the experimental bubble column reactor apparatus

15 cm from the reactor top and sent to the TOC analyzer to measure the phenol concentration.

Simulated wastewater was prepared by mixing phenol with deionized water at different concentrations: 3, 6, 9, 12, and 15 mg/L. Dry air was fed to an ozone generator to produce ozone gas. The input ozone gas used in the treatment of phenol in the reactor ranged from 0 to 20 mg/L. The operating temperature was kept constant in the bubble column reactor at 25 °C for all experimental runs, and the treatment time for each run was 15 min. During the course of the test, a 5 mL sample of treated wastewater was collected from the sampling valve at the reactor top. Additionally, the experimental procedure was achieved using two different phenol treatment modes in bubble column reactors. The first was carried out in a bubble column reactor with ozone gas only. The second mode of treatment used ozone in the presence of packing ( $O_3$ /packing). Fig. 2 summarizes the two operating modes in the bubble column. At the end of each experiment, the phenol concentration was measured using a TOC analyzer (TOC-L-CSH E200, Shimadzu, Japan). Moreover, the reaction time (or contact time) was tested in the present experimental work of ozonation reaction at the two modes of operation. The contact time represents the accumulative

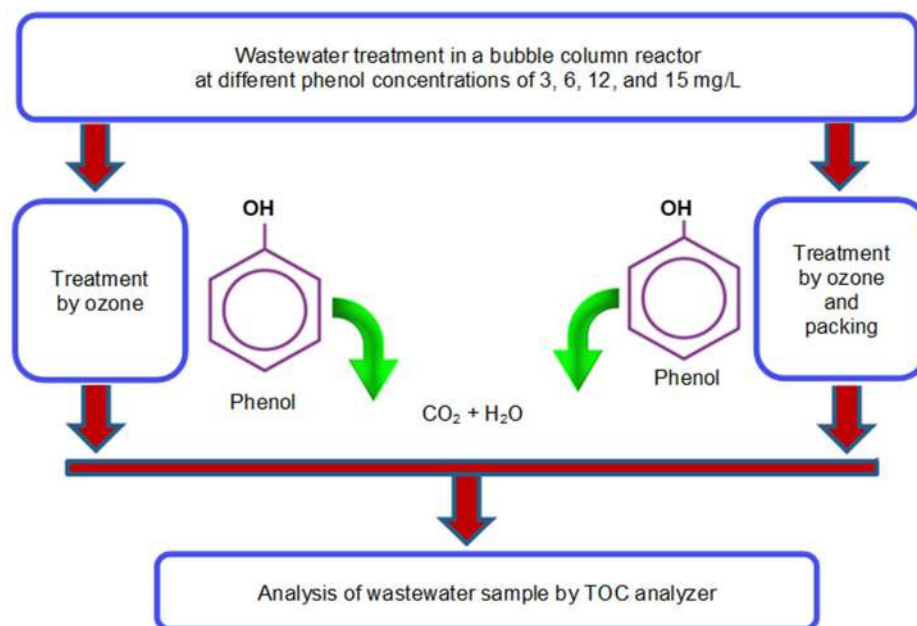
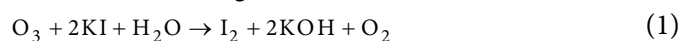


**Fig 2.** Modes of the ozonation process in the bubble column reactor in the absence and presence of packing inside the reactor

time to achieve phenol degradation. The sample was collected from the reactor every 15 min for a period of 2 h (15, 30, 45, 60, 75, 90, 105, and 120 min).

The ozone concentration in the wastewater was determined in mg/L using the indigo method [26] as a practical calibration. The following steps summarize the operating procedure of ozone gas quality evaluation. First, the generated ozone gas was passed directly into two containers containing a 2% KI solution for 10 min. Next, 10 mL of  $\text{H}_2\text{SO}_4$  of 2 N was added to 200 mL of the KI solution. Then, the solution was titrated with sodium thiosulfate ( $\text{Na}_2\text{S}_2\text{O}_3$ ) of 0.005 N till the yellow color of the iodine was no longer visible. At this point, two drops of starch were added. The titration procedure was continued until the blue color was no longer visible. The chemical reaction is presented in Eq. (1). Then, the total amount of consumed sodium thiosulfate in the titration process was estimated using Eq. (2) to calculate the generated ozone concentration in mg/L [17,26].



$$\text{Ozone concentration (mg/L)} = \frac{(A+B) \times N \times 24}{T} \quad (2)$$

where A is the amount of sodium thiosulfate used in the first container (mL); B is the amount of sodium

thiosulfate used in the second container (mL); T is the ozone period (min); and N is the sodium thiosulfate normality.

## RESULTS AND DISCUSSION

### Effect of Phenol Concentration

The use of a bubble column reactor in the phenol removal process from wastewater is challenging due to the complex hydrodynamic characteristics of such a reactor. In addition, petroleum refineries produce wastewater with many organic pollutants; the phenol effluent from various operating units in the petroleum refinery ranges from 2–15 ppm [3,6,8]. The results in Fig. 3 show the variation in the phenol removal efficiency with the phenol concentration at different treatment times, indicating that the phenol removal efficiency decreased with increasing phenol concentration. For example, at a contact time of 30 min, the phenol concentration was 3 mg/L, and the phenol removal efficiency was 65.42%. Moreover, the removal efficiency of phenol was 52.32 and 38.69% at phenol concentrations of 9 and 15 mg/L, respectively. In other words, it was found that as the concentration of phenol increased in the wastewater, it required more treatment

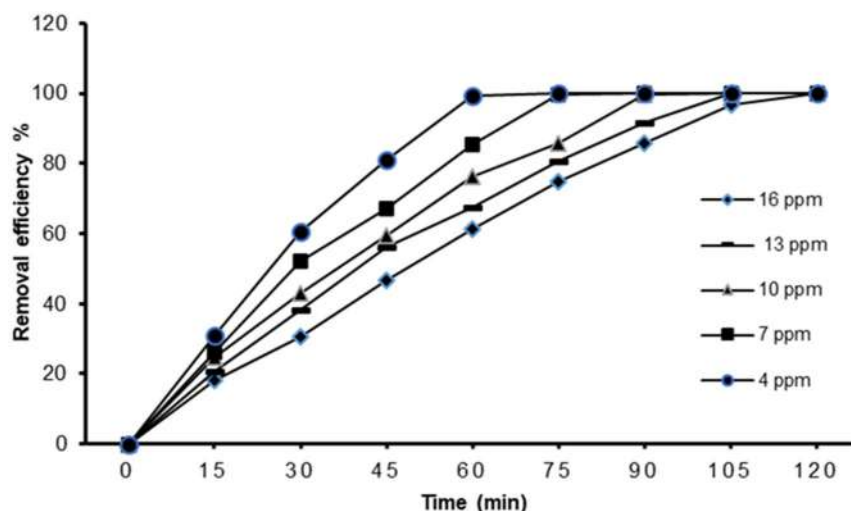


**Fig 3.** Variation in the phenol removal efficiency with the phenol concentration in the presence of ozone gas only in a bubble column reactor

time (contact time) in the reactor to obtain a high removal rate.

Furthermore, from the results in Fig. 3, it was noted that the contact time plays a major role in determining the phenol removal efficiency. As the contact time increased, the removal of phenol also increased. These results are attributed to the semi-batch operation mode in the bubble column, in which the degradation reaction of phenol continued with increasing contact time. Cheng et al. [22] and Barlak et al. [33] pointed to the importance of treatment time to produce higher rates of phenol degradation from wastewater. Also, Wang et al. [27] showed that the hydrodynamic parameters, such as

column height, column diameter, gas distributor, bubble size, bubble rise velocity, and superficial gas velocity, provided optimal operating conditions in the treatment of organic pollutants from wastewater using a bubble column reactor.

#### Effect of Packing on Ozonation Reaction

Fig. 4 illustrates the results of the phenol treatment process in the presence of ozone gas using a packed bubble column reactor at different contact times. It shows that a dramatically high activity for phenol degradation was noted for all tested phenol concentrations. For example, at a contact time of 30 min,

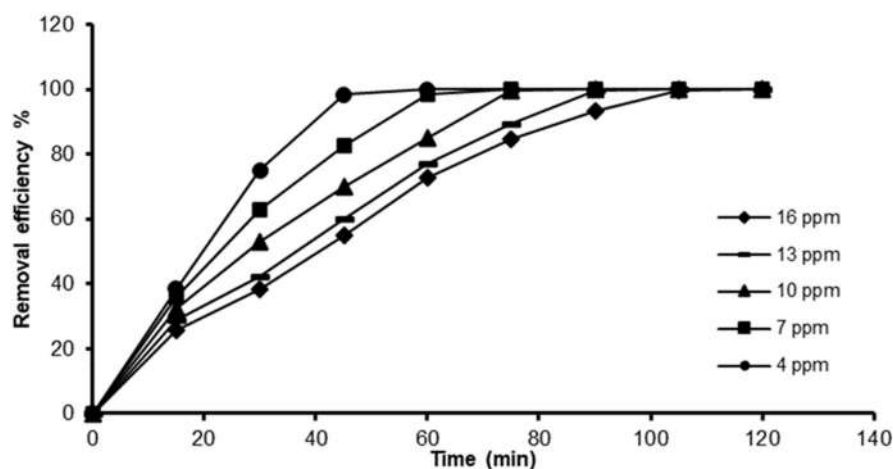


**Fig 4.** Variation in the phenol removal efficiency with the phenol concentration in the presence of ozone gas and packing in a bubble column reactor



for a phenol concentration of 3 mg/L, the phenol removal efficiency value was 74.98%. Moreover, the removal efficiency of phenol was 47.01 and 41.22% for phenol concentrations of 9 and 15 mg/L, respectively. In addition, for a reaction time of 45 min and at a phenol concentration of 3 ppm, the results showed a removal of 100%, while at the highest phenol concentration of 15 ppm, a phenol removal rate of 100% was achieved at a contact time of 105 min. The addition of spherical packing to the bubble column reactor significantly enhanced the phenol removal efficiency due to the high surface area. Accordingly, the available surface area improved the mass transfer operation between the gas and liquid contact, leading to a high phenol degradation performance.

The comparison of the results shown in Fig. 3 and 4 indicated that the best removal efficiency of phenol was achieved when the reactor used packing material (Fig. 4). Then, the use of packing material in the bubble column reactor provided a clear increase in the interfacial area with low ozone gas rising velocity. Actually, the long pathway of ozone gas along the packing height will enhance contact time and provide an efficient mass transfer mechanism. This enables the enhancement of the exposures of ozone in the aqueous solution, which improves ozone utilization efficiency and increases phenol degradation. The same result was noted by Hashim et al. [41] and Sang et al. [42].

To understand the activity of the ozonation process with a variation in the phenol dose, Fig. 5 illustrates the effectiveness of phenol removal at different phenol concentrations at a contact time of 45 min. The removal efficiency was 98.43, 77.53, 65.82, 60.207, and 55.11% at phenol dosages of 3, 6, 9, 12, and 15 mg/L, respectively. Also, it was found that when the phenol concentration increased in the wastewater mixture in the packed bubble column reactor, the removal efficiency decreased. This behavior is attributed to the need for a long contact time to provide an efficient phenol degradation process. Additionally, it was observed that the phenol dosage is a significant variable in the ozonation process performance in the presence or absence of packing in a bubble column reactor. These results agree with the reported trends [10,22,27].

#### Effect of Ozone Dosage on Phenol Degradation

The degradation of phenol in a bubble column reactor was investigated at various ozone gas concentrations (10, 15, and 20 mg/L) in the absence or presence of packing inside the reactor. Fig 6 shows the effects of the ozone concentration on the phenol removal efficiency at a phenol concentration of 3 mg/L and an operating temperature of 25 °C. The results indicated that the concentration of ozone in the aqueous phase had a significant impact on the phenol oxidation rate. As shown in Fig. 6, the experiments that used high ozone

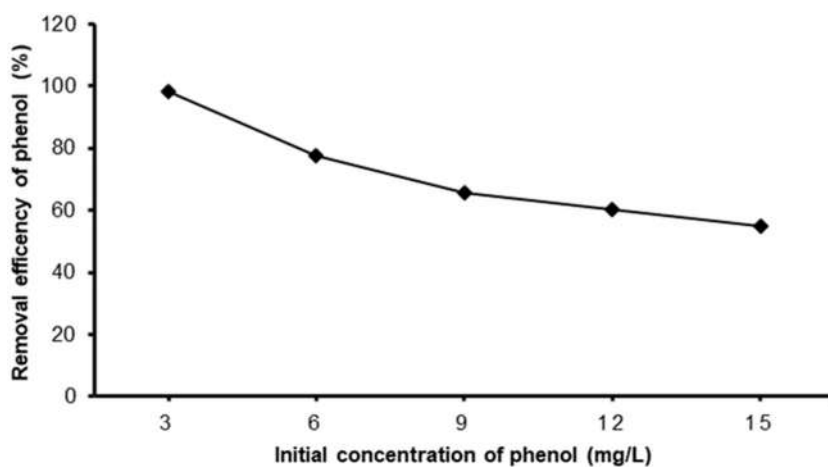


**Fig 5.** Effect of phenol dosages on the phenol removal efficiency at a contact time of 45 min using an O<sub>3</sub>/packing mode with an ozone concentration of 20.6 mg /L

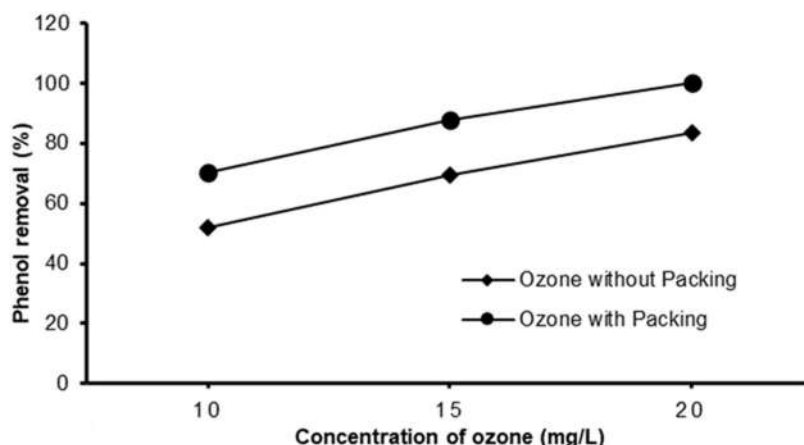


**Fig 6.** Influence of the ozone dosage on the phenol degradation process in a bubble column reactor in the presence and absence of packing (at 3 mg/L phenol concentration and 45 min of contact time)

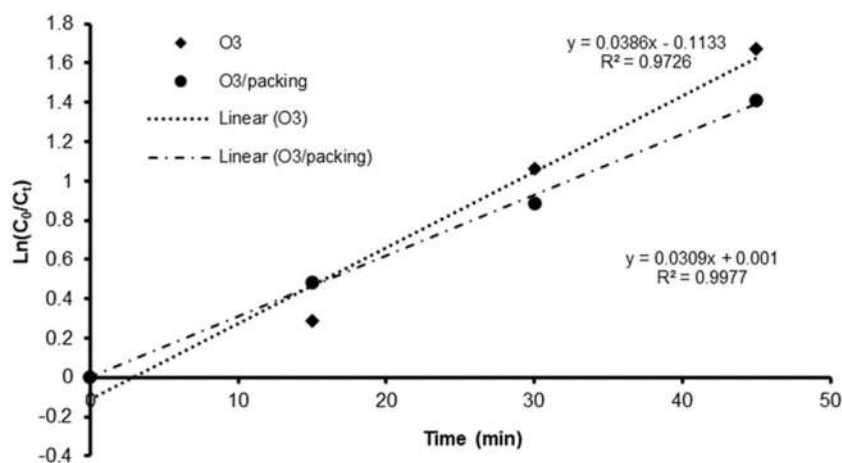


**Fig 7.** Evaluation of the first-order reaction kinetics for the ozonation process

dosage provided fast phenol removal efficiency. For example, at an ozone dosage of 10, 15, and 20 mg/L, the removal rate was 52.00, 69.30, and 83.60%, respectively, in the absence of packing inside the reactor; however, in the presence of packing, values of 70.50, 88.00, and 98.75%, respectively, were achieved. Also, in their investigations, Dehghani et al. [9] and Xiao et al. [19] showed that the increase of ozone dose increases the phenol removal efficiency.

### Reaction Kinetics Study

The present work studied the kinetics of the phenol degradation process using ozonation technology. The evaluation was achieved by applying two reaction orders (first- and second-order), depending on the phenol reaction mechanism. Accordingly, for each assumed

reaction order, the reaction rate constant was estimated depending on the various phenol concentrations [47]. Then, the mass balance equations for phenol at a given time of the first- and second-order reactions were estimated using Eq. (3) and (4), respectively.

$$\ln \frac{C_t}{C_0} = k_1 t \quad (3)$$

$$C_t = \frac{C_0}{1 + C_0 k_2 t} \quad (4)$$

where  $C_t$  is the concentration of phenol at any time ( $t$ );  $C_0$  is the initial concentration of phenol;  $k_1$  and  $k_2$  are the reaction rate constants for the first- and second-order reactions, respectively, and  $t$  is the reaction time.

Fig. 7 and 8 show the comparison between the theoretical and experimental results of the ozonation

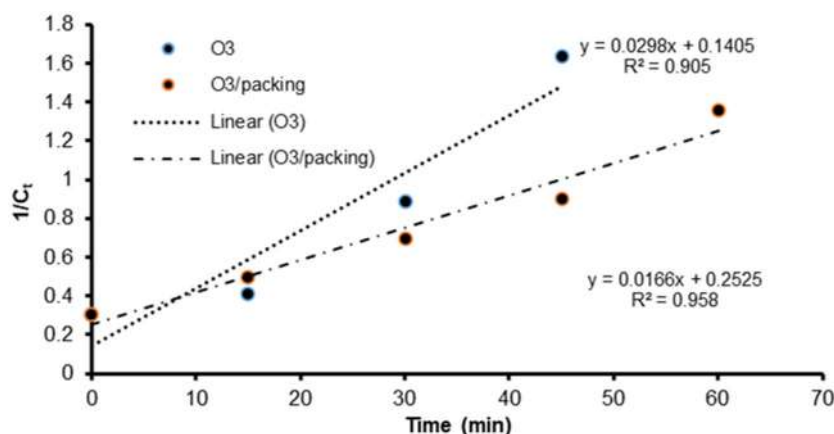


Fig 8. Evaluation of the second-order reaction kinetics for the ozonation process

process for the first- and second-order reactions, respectively. The correlation factor ( $R^2$ ) was used to validate or refute the reaction order assumption. The  $k_1$  of the first-order reaction was calculated and plotted in Fig. 7 as the slope of the best-fit line of  $\ln(C_t/C_0)$  vs. time. For the second-order reaction model, the best fit of the line plot of  $1/C_t$  vs. time provided the required slope, as shown in Fig. 8 [46]. Additionally, the use of the packed bubble column reactor provided a considerable rise in the  $k$  value for the ozonation process. These results agree with the findings of Barlak et al. [33] and Dai et al. [46].

Table 1 shows the results of the calculation process. It was found that the highest value of  $R^2$  (0.9977) was obtained for the assumption of the first-order model with a perfect fitting for the kinetic data achieved. The result indicated that the presence of packing material in the bubble column reactor showed a clear increase in the  $k_1$  value. It was noted that the  $k_1$  increased from 0.078 to 0.096 for the assumption of first-order reaction with  $R^2$  (0.9977). On the other hand, the second-order

assumption provides a low  $R^2$  value of (0.9580) in comparison with the first assumption. Then, it was concluded that the addition of packing material improves the phenol degradation in the ozonation process. This is attributed to the increased ozone concentration in the reaction mixture, which enhances the mass transfer rate, contact time, and reaction rate.

### Phenol Degradation Process Mechanism

Applying the principles of ozone treatment to wastewater in petroleum refineries requires a deep understanding because ozone gas can play several roles in the treatment process. Our understanding of the degradation mechanism of phenol allowed the reaction paths to operate clearly and safely, which is especially important as phenol presents a great danger to human health and the environment. Many authors have indicated that the degradation of phenol requires many stages, which eventually produce carbon dioxide and water. These stages depend mainly on the phenol

Table 1. Results of the experimental kinetic data of the phenol ozonation reactions for the first- and second-order assumptions

First-order Assumption			
Type of treatment	$y = \ln(C_0/C_t)$ and $x = t$	$k_1$ (1/min)	$R^2$
O <sub>3</sub> only	$y = 0.0386x - 0.1133$	0.0780	0.9726
O <sub>3</sub> in the presence of packing	$y = 0.0309x + 0.0010$	0.0960	0.9977
Second-order Assumption			
Type of Treatment	$y = 1/C_t - 1/C_0$ and $x = t$	$k_2$ (1/mg min)	$R^2$
O <sub>3</sub> only	$y = 0.0298x + 0.1405$	0.0081	0.9050
O <sub>3</sub> in the presence of packing	$y = 0.0166x + 0.2525$	0.0128	0.9580

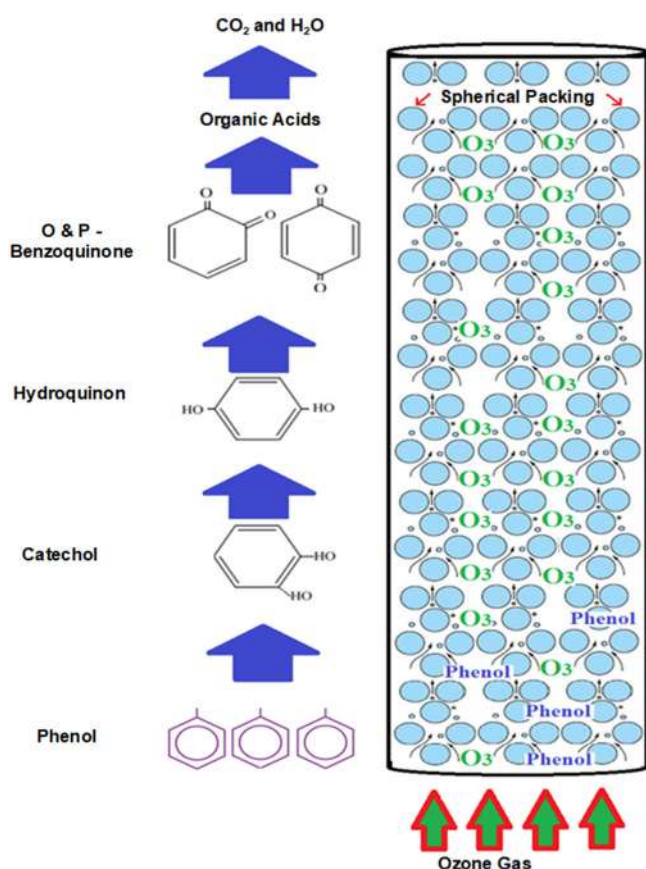


**Fig 9.** Phenol degradation mechanism by ozone in the packed bubble column

concentration in the wastewater and on the type of reactor used [5,22,28].

The current research employed a bubble column reactor, which is considered one of the most complex multiphase reactors due to the high interaction between the hydrodynamic properties that determine the reactor's performance. Therefore, the use of a packed bubble column provided an efficient contact surface area between the ozone gas and the aqueous solution, which included phenol. Thus, the mass transfer operation was enhanced by using an efficient reaction mechanism. From a diffusion point of view, the formation of a thin film over the spherical packing in the reactor plays a major role in providing efficient mass transfer operation. Actually, this thin film is characterized by low resistance to diffusion, and then a high phenol degradation process was achieved [21,27]. Water and carbon dioxide are the end products of phenol degradation via various advanced oxidation stages. Fig. 9 summarizes the chief stages in the degradation process of

phenol into different kinds of compounds. The first step in the oxidation of phenol results in the formation of catechol and hydroquinone, while the next step results in the formation of *o*-benzoquinone and *p*-benzoquinone [25,47]. Additionally, the ozone gas that rises from the reactor bottom is responsible for the breakdown of aromatic compounds into new products of organic acids. After that, *o*-benzoquinone and *p*-benzoquinone undergo decomposition, which results in the formation of oxalic acid, propionic acid, formic acid, and acetic acid. Finally, these acids undergo an oxidation process to produce CO<sub>2</sub> and H<sub>2</sub>O [10,18,36].

## ■ CONCLUSION

The packed bubble column reactor was used efficiently in the ozonation process to remove phenol from wastewater with a high rate and a low contact time. The effectiveness of the phenol and TOC removal was achieved at an ozone rate of 3 g/h and a contact time of 45 min. The results indicated that the use of packing inside the reactor greatly enhanced the amount of phenol removal and its efficiency. The phenol removal efficiency was measured at 99.45 and 81.52% in the presence and absence of packing in the reactor, respectively. Furthermore, it was found that the presence of packing inside the reactor enhanced the mass transfer process by improving the contact surface area between the gas and liquid in the reactor, increasing the phenol removal efficiency. Furthermore, from the two assumed kinetic models that describe the phenol reaction's kinetics, it was observed that the first-order assumption was optimal, with a R<sup>2</sup> of 0.9977 in relation to the experimental result. Additionally, a deep understanding of the reaction mechanism of phenol degradation was achieved, which explained the stages in the transformation of phenol into carbon dioxide and water. Finally, the use of packing in a bubble column reactor in the ozonation process was an effective method for the removal of phenol from industrial wastewater with a low cost and simple operation.

## ■ ACKNOWLEDGMENTS

The authors are grateful to the team of the Design and Industrial Production Research Unit (DIPRU) at the

Chemical Engineering Department, University of Technology, Iraq for their scientific, academic, and administrative support of this study.

## ■ REFERENCES

- [1] Saravanan, A., Senthil Kumar, P., Jeevanantham, S., Karishma, S., Tajsabreen, B., Yaashikaa, P.R., and Reshma, B., 2021, Effective water/wastewater treatment methodologies for toxic pollutants removal: Processes and applications towards sustainable development, *Chemosphere*, 280, 130595.
- [2] Singh, R., Dutta, R.K., Naik, D.V., Ray, A., and Kanaujia, P.K., 2021, High surface area *Eucalyptus* wood biochar for the removal of phenol from petroleum refinery wastewater, *Environ. Challenges*, 5, 100353.
- [3] Mao, G., Han, Y., Liu, X., Crittenden, J., Huang, N., and Ahmad, U.M., 2022, Technology status and trends of industrial wastewater treatment: A patent analysis, *Chemosphere*, 288, 132483.
- [4] Chowdhary, P., Bharagava, R.N., Mishra, S., and Khan, N., 2020, "Role of Industries in Water Scarcity and Its Adverse Effects on Environment and Human Health" in *Environmental Concerns and Sustainable Development: Volume 1: Air, Water and Energy Resources*, Eds. Shukla, V., and Kumar, N., Springer, Singapore, 235–256.
- [5] Saxena, G., Chandra, R., and Bharagava, R.N., 2017, "Environmental Pollution, Toxicity Profile and Treatment Approaches for Tannery Wastewater and Its Chemical Pollutants" in *Reviews of Environmental Contamination and Toxicology Volume 240*, Eds. de Voogt, P., Springer International Publishing, Cham, Switzerland, 31–69.
- [6] Singh, S., and Shikha S., 2019, Treatment and recycling of wastewater from oil refinery/petroleum industry, *Advances in Biological Treatment of Industrial Waste Water and their Recycling for a Sustainable Future*, Eds. Singh, R.L., and Singh, R.P., Springer, Singapore, 303–332.
- [7] Mousa, N.E., Mohammed, S.S., Shnain, Z.Y., Abid, M.F., Alwasiti, A.A., and Sukkar, K.A., 2022, Catalytic photodegradation of cyclic sulfur compounds in a model fuel using a bench-scale falling-film reactor irradiated by a visible light, *Bull. Chem. React. Eng. Catal.*, 17 (4), 755–767.
- [8] Sun, Y., Liu, Y., Chen, J., Huang, Y., Lu, H., Yuan, W., Yang, Q., Hu, J., Yu, B., Wang, D., Xu, W., and Wang, H., 2021, Physical pretreatment of petroleum refinery wastewater instead of chemicals addition for collaborative removal of oil and suspended solids, *J. Cleaner Prod.*, 278, 123821.
- [9] Dehghani, M.H., Karamitabar, Y., Changani, F., and Heidarinejad, Z., 2019, High performance degradation of phenol from aqueous media using ozonation process and zinc oxide nanoparticles as a semiconductor photocatalyst in the presence of ultraviolet radiation, *Desalin. Water Treat.*, 166, 105–114.
- [10] Alattar, S.A., Sukkar, K.A., and Alsaffar, M.A., 2023, The role of TiO<sub>2</sub> NPs catalyst and packing material in removal of phenol from wastewater using ozonized bubble column reactor, *Acta Innovations*, 46, 93–105.
- [11] Karamah, E.F., Adripratiwi, I.P., and Anindita, L., 2018, Combination of ozonation and adsorption using granular activated carbon (GAC) for tofu industry wastewater treatment, *Indones. J. Chem.*, 18 (4), 600–606.
- [12] Wang, Y., Yang, W., Yin, X., and Liu, Y., 2016, The role of Mn-doping for catalytic ozonation of phenol using Mn/ $\gamma$ -Al<sub>2</sub>O<sub>3</sub> nanocatalyst: Performance and mechanism, *J. Environ. Chem. Eng.*, 4 (3), 3415–3425.
- [13] Centurião, A.P.S.L., Baldissarelli, V.Z., Scaratti, G., de Amorim, S.M., and Moreira, R.F.P.M., 2019, Enhanced ozonation degradation of petroleum refinery wastewater in the presence of oxide nanocatalysts, *Environ. Technol.*, 40 (10), 1239–1249.
- [14] Alardhi, S.M., Albayati, T.M., and Alrubaye, J.M., 2020, Adsorption of the methyl green dye pollutant from aqueous solution using mesoporous materials MCM-41 in a fixed-bed column, *Heliyon*, 6 (1), e03253.
- [15] Rayaroth, M.P., Aravindakumar, C.T., Shah, N.S., and Boczkaj, G., 2022, Advanced oxidation processes (AOPs) based wastewater treatment-unexpected

- nitration side reactions-a serious environmental issue: A review, *Chem. Eng. J.*, 430, 133002.
- [16] Almukhtar, R., Hammoodi, S.I., Majdi, H.S., and Sukkar, K.A., 2022, Managing transport processes in thermal cracking to produce high-quality fuel from extra-heavy waste crude oil using a semi-batch reactor, *Processes*, 10 (10), 2077.
- [17] Liu, X., Su, X., Tian, S., Li, Y., and Yuan, R., 2021, Mechanisms for simultaneous ozonation of sulfamethoxazole and natural organic matters in secondary effluent from sewage treatment plant, *Front. Environ. Sci. Eng.*, 15 (4), 75.
- [18] Jiao, W., Shao, S., Yang, P., Gao, K., and Liu, Y., 2021, Kinetics and mechanism of nitrobenzene degradation by hydroxyl radicals-based ozonation process enhanced by high gravity technology, *Front. Chem. Sci. Eng.*, 15 (5), 1197–1205.
- [19] Xiao, J., Xie, Y., and Cao, H., 2015, Organic pollutants removal in wastewater by heterogeneous photocatalytic ozonation, *Chemosphere*, 121, 1–17.
- [20] Wei, C., Zhang, F., Hu, Y., Feng, C., and Wu, H., 2017, Ozonation in water treatment: The generation, basic properties of ozone and its practical application, *Rev. Chem. Eng.*, 33 (1), 49–89.
- [21] Sukkar, K.A., Al-Zuhairi, F.K., and Dawood, E.A., 2021, Evaluating the influence of temperature and flow rate on biogas production from wood waste via a packed-bed bioreactor, *Arabian J. Sci. Eng.*, 46 (7), 6167–6175.
- [22] Cheng, W., Quan, X., Li, R., Wu, J., and Zhao, Q., 2018, Ozonation of phenol-containing wastewater using  $O_3/Ca(OH)_2$  system in a micro bubble gas-liquid reactor, *Ozone: Sci. Eng.*, 40 (3), 173–182.
- [23] Temesgen, T., and Han, M., 2021, Ultrafine bubbles as an augmenting agent for ozone-based advanced oxidation, *Water Sci. Technol.*, 84 (12), 3705–3715.
- [24] Awad, A.M., Sukkar, K.A., and Jaed, D.M., 2022, Development of an extremely efficient Iraqi nano-lubricating oil (base-60) employing  $SiO_2$  and  $Al_2O_3$  nanoparticles, *AIP Conf. Proc.*, 2443, 030049.
- [25] Oputu, O.U., Fatoki, O.S., Opeolu, B.O., and Akharam, M.O., 2020, Degradation pathway of ozone oxidation of phenols and chlorophenols as followed by LC-MS-TOF, *Ozone: Sci. Eng.*, 42 (4), 294–318.
- [26] Bader, H., and Hoigné, J., 1981, Determination of ozone in water by the indigo method, *Water Res.*, 15 (4), 449–456.
- [27] Wang, Z., Guo, K., Liu, H., Liu, C., Geng, Y., Lu, Z., Jiao, B., and Chen, D., 2020, Effects of bubble size on the gas-liquid mass transfer of bubble swarms with Sauter mean diameters of 0.38–4.88 mm in a co-current upflow bubble column, *J. Chem. Technol. Biotechnol.*, 95 (11), 2853–2867.
- [28] Saputera, W.H., Putrie, A.S., Esmailpour, A.A., Sasongko, D., Suendo, V., and Mukti, R.R., 2021, Technology advances in phenol removals: Current progress and future perspectives, *Catalysts*, 11 (8), 998.
- [29] Piao, M., Zou, D., Ren, X., Gao, S., Qin, C., and Piao, Y., 2019, High efficiency biotransformation of bisphenol A in a fluidized bed reactor using stabilized laccase in porous silica, *Enzyme Microb. Technol.*, 126, 1–8.
- [30] Shnain, Z.Y., Abid, M.F., and Sukkar, K.A., 2021, Photodegradation of mefenamic acid from wastewater in a continuous flow solar falling film reactor, *Desalin. Water Treat.*, 210, 22–30.
- [31] Prasetyaningrum, A., Arum Kusumaningtyas, D., Suseno, P., Jos, B., and Ratnawati, R., 2018, Effect of pH and gas flow rate on ozone mass transfer of K-carrageenan solution in bubble column reactor, *Reaktor*, 18 (4), 177–182.
- [32] Lima, V.N., Rodrigues, C.S.D., Sampaio, E.F.S., and Madeira, L.M., 2020, Insights into real industrial wastewater treatment by Fenton's oxidation in gas bubbling reactors, *J. Environ. Manage.*, 265, 110501.
- [33] Barlak, M.S., Değermenci, N., Cengiz, I., Özel, H.U., and Yildiz, E., 2020, Comparison of phenol removal with ozonation in jet loop reactor and bubble column, *J. Environ. Chem. Eng.*, 8 (5), 104402.
- [34] Karri, R.R., Jayakumar, N.S., and Sahu, J.N., 2017, Modelling of fluidised-bed reactor by differential evolution optimization for phenol removal using coconut shells based activated carbon, *J. Mol. Liq.*, 231, 249–262.

- [35] Annisa, N., Nadisti, M.S., Karamah, E.F., and Bismo, S., 2018, Degradation of batik dye wastewater in basic condition by ozonation technique in bubble column reactor, *E3S Web Conf.*, 67, 04019.
- [36] Yusoff, N.A., Ong, S.A., Ho, L.N., Wong, Y.S., Mohd Saad, F.N., Khalik, W.F., and Lee, S.L., 2019, Performance of the hybrid growth sequencing batch reactor (HG-SBR) for biodegradation of phenol under various toxicity conditions, *J. Environ. Sci.*, 75, 64–72.
- [37] Liu, F., Zhang, H., Yan, Y., and Huang, H., 2020, Graphene as efficient and robust catalysts for catalytic wet peroxide oxidation of phenol in a continuous fixed-bed reactor, *Sci. Total Environ.*, 701, 134772.
- [38] Zheng, M., Bai, Y., Han, H., Zhang, Z., Xu, C., Ma, W., and Ma, W., 2021, Robust removal of phenolic compounds from coal pyrolysis wastewater using anoxic carbon-based fluidized bed reactor, *J. Cleaner Prod.*, 280, 124451.
- [39] Qin, W., Ren, M., Lu, Y., and Yang, S., 2022, High effective degradation of phenol with Cu/Bi-Ce/Al<sub>2</sub>O<sub>3</sub> heterogeneous Fenton-like catalyst in a two-stage fixed-bed reactor, *Sep. Purif. Technol.*, 299, 121733.
- [40] Al Ezzi, A.A.R., 2022, Removal of phenol by expanded bed airlift loop reactor, *Iran. J. Chem. Chem. Eng.*, 41 (1), 154–162.
- [41] Hashim, M.A., Kundu, A., Mukherjee, S., Ng, Y.S., Mukhopadhyay, S., Redzwan, G., and Gupta, B.S., 2019, Arsenic removal by adsorption on activated carbon in a rotating packed bed, *J. Water Process Eng.*, 30, 100591.
- [42] Sang, L., Tu, J., Cheng, H., Luo, G., and Zhang, J., 2020, Hydrodynamics and mass transfer of gas-liquid flow in micropacked bed reactors with metal foam packing, *AIChE J.*, 66 (2), e16803.
- [43] Pishgar, R., Kanda, A., Gress, G.R., Gong, H., Dominic, J.A., and Tay, J.H., 2018, Effect of aeration pattern and gas distribution during scale-up of bubble column reactor for aerobic granulation, *J. Environ. Chem. Eng.*, 6 (5), 6431–6443.
- [44] Karamah, E.F., and Nurcahyani, P.A., 2019, Degradation of blue KN-R dye in batik effluent by an advanced oxidation process using a combination of ozonation and hydrodynamic cavitation, *Indones. J. Chem.*, 19 (1), 41–47.
- [45] Ayanda, O.S., Adeleye, B.O., Aremu, O.H., Ojobola, F.B., Lawal, O.S., Amodu, O.S., Oketayo, O.O., Klink, M.J., and Nelana, S.M., 2023, Photocatalytic degradation of metronidazole using zinc oxide nanoparticles supported on acha waste, *Indones. J. Chem.*, 23 (1), 158–169.
- [46] Dai, Q., Chen, L., Chen, W., and Chen, J., 2015, Degradation and kinetics of phenoxyacetic acid in aqueous solution by ozonation, *Sep. Purif. Technol.*, 142, 287–292.
- [47] Sumegová, L., Derco, J., and Melicher, M., 2013, Influence of reaction conditions on the ozonation process, *Acta Chim. Slovaca*, 6 (2), 168–172.
- [48] Yang, P., Luo, S., Liu, H., Jiao, W., and Liu, Y., 2019, Aqueous ozone decomposition kinetics in a rotating packed bed, *J. Taiwan Inst. Chem. Eng.*, 96, 11–17.

## Fast Microwave-Assisted Green Synthesis of Silver Nanoparticles Using Low Concentration of Seminyak (*Champeria* sp.) Leaf Extract

Muhammad Bagas Ananda<sup>1</sup>, Fathan Aditya Sanjaya<sup>2</sup>, Tami Bachrurozy<sup>2</sup>, Helmi Majid Ar Rasyid<sup>3</sup>, Anggraini Barlian<sup>4</sup>, Akfiny Hasdi Aimon<sup>5</sup>, Fitriyatul Qulub<sup>6</sup>, Prihartini Widiyanti<sup>6</sup>, and Arie Wibowo<sup>2,7\*</sup>

<sup>1</sup>Department of Materials and Metallurgical Engineering, Faculty of Industrial Technology and Systems Engineering, Institut Teknologi Sepuluh Nopember, Kampus ITS Sukolilo, Surabaya 60111, Indonesia

<sup>2</sup>Materials Science and Engineering Research Group, Faculty of Mechanical and Aerospace Engineering, Institut Teknologi Bandung, Jl. Ganesha No. 10, Bandung 40132, Indonesia

<sup>3</sup>Magister Nanotechnology, Graduate School, Institut Teknologi Bandung, Jl. Ganesha No. 10, Bandung 40132, Indonesia

<sup>4</sup>School of Life Science & Technology, Institut Teknologi Bandung, Jl. Ganesha No. 10, Bandung 40132, Indonesia

<sup>5</sup>Department of Physics, Faculty of Mathematical and Natural Sciences, Institut Teknologi Bandung, Jl. Ganesha No. 10, Bandung 40132, Indonesia

<sup>6</sup>Biomedical Engineering Study Program, Department of Physics, Faculty of Science and Technology, Universitas Airlangga, Campus C, Surabaya 60115, Indonesia

<sup>7</sup>Research Center for Nanosciences and Nanotechnology, Institut Teknologi Bandung, Jl. Ganesha No. 10, Bandung 40132, Indonesia

---

\* **Corresponding author:**

email: ariewibowo@material.its.ac.id

Received: October 21, 2022

Accepted: February 22, 2023

DOI: 10.22146/ijc.78545

**Abstract:** Silver nanoparticles (AgNPs) are fascinating materials for biomedical applications thanks to their strong antibacterial activity and biocompatibility. This study applied the green synthesis method using 0.5 wt.% Seminyak leaf extract and assisted with one min microwave irradiation to enhance AgNPs formation. Extremely small sizes AgNPs with an average particle size of  $9.1 \pm 4.1$  nm and spherical shapes were obtained. The synthesized AgNPs displayed potent antibacterial activity against *Escherichia coli* and *Staphylococcus aureus* bacteria with a zone of inhibition of  $12.3 \pm 0.1$  and  $13.7 \pm 0.7$  mm, respectively. The MTT assay results demonstrated that the cells' viability of the obtained AgNPs was  $88.5 \pm 7.0$  %, implying biocompatibility for biomedical applications.

**Keywords:** antibacterial materials; green synthesis; microwave irradiation; Seminyak leaf extract; silver nanoparticles

---

### ■ INTRODUCTION

Currently, the demand for anti-infection implants has risen over time as an attractive approach to solving the implant-related infection problem during implantation. Many materials have been attempted to prevent implant-related infection, including peptides [1], chitosan [2], and silver nanoparticles [3]. Among those options, silver nanoparticles (AgNPs) emerged as one promising material as a filler for anti-infection implants, thanks to

their potent antibacterial properties and excellent biocompatibility [4]. In addition, AgNPs also possess high electrical conductivity, making them potentially utilized as a filler for electroactive scaffold fabrication [3]. However, the utilization of hazardous reducing agents such as sodium borohydride ( $\text{NaBH}_4$ ) and hydrazine ( $\text{N}_2\text{H}_4$ ) during the fabrication of AgNPs has raised concerns for biomedical applications because of their toxicity [5].



In this context, AgNPs preparation through a green synthesis approach using plant extract is an appealing strategy because it offers non-toxic, cost-effective, and environmentally friendly methods [6]. Extracts from plants contain biomolecules such as proteins, amino acids, flavonoids, and polyphenols that act as reducing agents for AgNPs formation and as capping agents to prevent agglomeration of nanoparticles [6]. Various plant extracts such as butterfly pea flower extract (*Clitoria ternatea*) [4], Cilembu sweet potato (*Ipomoea batatas* L. var. Rancing) [3], and *Ferula ovina* Boiss. [7] have been explored to produce AgNPs with excellent antibacterial activity and extremely small nanoparticle sizes below 17 nm. Although many plants are already exploited for the green synthesis of AgNPs, there are plenty of unexplored plants that might offer unique characteristics. One of them is the Seminyak (*Champeria* sp.), an endemic plant in Riau province, Indonesia. Seminyak plant, particularly the leaf part, is utilized for the local diet and as an alternative medicine for headaches and stomachaches thanks to its excellent medicinal properties. Moreover, Seminyak leaf, as one of the plants from the genus *Champeria*, contains high concentrations of secondary metabolites such as flavonoids, phenolic, lutein, phytol, and  $\beta$ -carotene, which can be potentially utilized to reduce  $\text{Ag}^+$  to produce AgNPs [8-9].

In general, water was used as a solvent in the green synthesis approach to extract useful organic compounds from plants to avoid the utilization of toxic organic solvents. However, the concentration of organic compounds in the obtained extract solution is sometimes too scarce for AgNPs formation due to its low concentration in the original plant or its low solubility in water. A higher extract concentration can be used to obtain the necessary quantity of reducing agents for AgNPs formation, but this strategy might not be sustainable. A sustainable and green strategy to combat this problem is by combining plant extract with microwave irradiation. Microwave irradiation has been studied extensively in the synthesis of AgNPs and succeeded in providing rapid initial heating, which increasing the reaction rate [10]. Francis et al. [11] successfully fabricated tiny AgNPs with robust

antibacterial properties after combining *Elephantopus scaber* leaf extract and 4 min of microwave irradiation. In addition, it requires less energy than conventional heating methods [12] and is suitable for obtaining monodispersed nanoparticles with higher crystallinity in a short reaction time [11].

In this study, AgNPs were synthesized using 0.5 wt.% of Seminyak leaf extract and 1 min of microwave irradiation time. To the best of our knowledge, the utilization of Seminyak leaf extract together with AgNPs fabrication strategy to employ low extract concentration and short microwave irradiation time has not been explored yet. Thus, we expected this work could offer a rapid, sustainable, and safe synthesis method in AgNPs preparation for biomedical applications.

## ■ EXPERIMENTAL SECTION

### Materials

Silver nitrate ( $\text{AgNO}_3$ ), sodium hydroxide (NaOH), sodium chloride (NaCl), sodium dodecyl sulfate (SDS), and methanol with p.a. grade were acquired from Merck, Germany, without further modification. Biological reagents such as culture media containing Roswell Park Memorial Institute-1640 (RPMI-1640) 89%, Pen-Strep 1%, Fetal Bovine Serum (FBS) 10%, fungizone, 3-(4,5-dimethylthiazol-2-yl)-2,5-diphenyltetrazolium bromide (MTT) reagent, phosphate buffer saline (PBS), ciprofloxacin, Mueller Hinton Agar (MHA) media, and Formazans dyes were procured from Oxoid. Alcohol 70%, sterile distilled water, and demineralized water were purchased from Brataco Chemical, Indonesia. Seminyak leaf was obtained from the market in Riau, Indonesia. *Escherichia coli* (*E. coli*, ATCC 25922), *Staphylococcus aureus* (*S. aureus*, ATCC 25923), and cell line culture BHK-21 were supplied by Tropical Diseases Diagnostic Center, Universitas Airlangga.

### Instrumentation

UV-Vis spectrophotometry (Hewlett Packard Agilent Technologies, 8453 Series) was carried out to confirm the existence of AgNPs in the sample by observing their surface plasmon resonance (SPR). The

functional groups of the extract and AgNPs were investigated by Fourier Transformation Infrared Spectroscopy (FTIR, Prestige 21 Shimadzu). X-ray diffraction (XRD, Bruker D8 Advance, using Cu K $\alpha$ ,  $\lambda$  = 1.54 Å) was performed to analyze the phase structure and crystallinity of the AgNPs. Dynamic Light Scattering (DLS, Beckman Coulter, Delsa Nano C Particle Analyser) was carried out to investigate the particle size and distribution of AgNPs. The stability of AgNPs was measured by Zeta Potential (Zetasizer Nano, Malvern Pananalytical Ltd). Morphological and particle size of the AgNPs were observed using Transmission Electron Microscopy (TEM, Hitachi HT77000 Series).

## Procedure

### Extract preparation

Seminyak leaf extract (hereinafter denoted as extract) was prepared based on the previous procedure with slight modifications [13]. Briefly, 1 g of dried leaf powders were mixed with 100 mL of demineralized water in a glass beaker, then heated and stirred at 100 °C for 30 min. The mixture was then filtered to ensure that the extract was free from any impurities. The extract was gradually added with NaOH until the pH of the solution reached 8 which is a favorable pH for AgNPs formation [3].

### Fabrication of AgNPs

Three samples were used in this study, as shown in Table 1. Sample A was fabricated by combining 200 mM AgNO<sub>3</sub> and extract solution in a 1:1 ratio without the presence of microwave irradiation. Sample B was assembled by 1 min microwave irradiation (Panasonic NN GT35 1000 W, Japan) of 100 mM AgNO<sub>3</sub> solution without the presence of extract. Sample C was synthesized by mixing extract solution with 200 mM AgNO<sub>3</sub> in a 1:1 ratio and irradiated by microwave for 1 min. Samples A and B were observed after storing the samples for one day because of their slow transformation. While sample C was observed immediately after irradiation due to its fast transformation.

### Biological characterizations of AgNPs

The antibacterial test was conducted using the disc diffusion method to evaluate the antibacterial activity of

**Table 1.** Summary of samples in this experiment

No	Sample name	AgNO <sub>3</sub>	Extract	Microwave
1	Extract	×	✓	×
2	Sample A	✓	✓	×
3	Sample B	✓	×	✓
4	Sample C	✓	✓	✓

AgNPs against *E. coli* and *S. aureus*. The bacteria were inoculated on MHA media by streaking the swab three times over the entire agar surface. The sample-impregnated disk was placed on the inoculated MHA media and incubated at 37 °C for 24 h. Zone of inhibition (ZOI) was determined by measuring the bright zone around the disk, which is an indicator of the occurrence of antibacterial inhibition, using a caliper.

The MTT assay was performed to investigate the cytotoxicity of the synthesized AgNPs against the BHK-21 cell line. This experiment was conducted by preparing BHK-21 cell culture in a 96-wells microplate with a density of  $2 \times 10^5$  in 100  $\mu$ L of culture media and splitting it in half. Each sample was repeated six times. The microplate was incubated for 20 h at 37 °C. Then, the microplate was removed from the incubation apparatus, added 5 mg/mL MTT reagent in 25  $\mu$ L of PBS for each well, and incubated again for 4 h. Afterward, 50  $\mu$ L of dimethyl sulfoxide (DMSO) solution was added to each well and incubated for another 10 min. The spectrophotometer was used to calculate the optical density value of formazan, which is the reduced form of MTT in active cells, at 540 nm [14]. The percentage of living cells was calculated using Eq. (1) as follow:

$$\text{Percentage of living cells} = \frac{\text{treatment} + \text{media}}{\text{cell} + \text{media}} \times 100$$

## RESULTS AND DISCUSSION

### Preliminary Observation of the Samples

#### Visual observation results

Early determination of AgNPs formation in the sample can be recognized from the color change of the solution to dark brown once the AgNO<sub>3</sub> solution is mixed with the extract solution [15]. Visual observation of the prepared samples can be observed in Fig. 1. The appearance of the extract (Fig. 1(a)) was transparent pale yellow. This appearance changed to brownish-yellow after

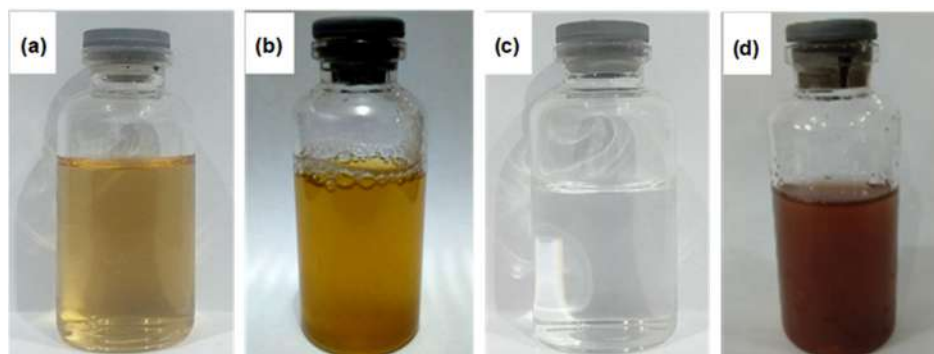


**Fig 1.** Visual observation of (a) extract, (b) sample A, (c) sample B, and (d) sample C

the addition of  $\text{AgNO}_3$  solution and storing it for one day (sample A; Fig 1(b)).

Meanwhile, the color change was not observed in sample B (Fig. 1(c)) suggesting that solely 1 min microwave irradiation might not be enough to reduce silver ions ( $\text{Ag}^+$ ). In addition, the absence of extract in sample B leads to the slower formation of AgNPs due to the lack of reducing agents in the solution. Interestingly, an immediate color transformation from pale yellow to dark brown was noticed in sample C (Fig. 1(d)). This color switch can be implied as the formation of AgNPs in the aqueous solution due to electron energy levels alteration and electrons excitation, indicating the reduction of  $\text{Ag}^+$  into  $\text{Ag}^0$  [16]. The combination between extract and quick microwave irradiation might induce the fast formation of AgNPs in the sample. Microwave irradiation offers rapid initial heating, which directs to enhanced reaction kinetics and reaction rates [17]. To confirm these findings, further characterization using UV-Vis spectrophotometry has been conducted.

#### UV-Vis spectrophotometry results

UV-Vis spectrophotometry was performed to investigate the presence of phytoconstituents in the extract and to detect the presence of AgNPs in solution due to their SPR characteristic, which typically occurred at 400 to 500 nm [18]. In Fig. 2, the extract showed two peaks at 285 and 324 nm, implying the existence of phenolic compounds which are known as active components that contributed to reducing  $\text{Ag}^+$  in AgNPs formation [19] and also one of the secondary metabolites that existed in *Champeria* family [8-9].

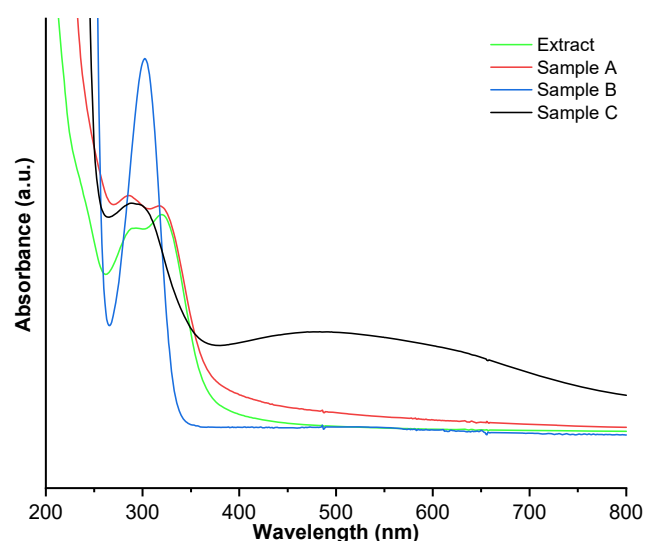


**Fig 2.** UV-Vis spectra of extract (green), sample A (red), sample B (blue), and sample C (black)

Characteristics of the AgNPs' SPR peak were not observed in sample A, suggesting  $\text{Ag}^+$  reduction using the extract and AgNPs formation might not occur even after one day. In addition, peaks observed from sample A indicate similarities with the extract peaks. This might be a suggestion that no reduction process occurred in the solution. Meanwhile, sample B spectrum only demonstrates a sharp peak at 300 nm, which is a characteristic of  $\text{AgNO}_3$  [20]. This result implies that 1 min microwave irradiation without the presence of reducing agents from the extract might not be enough to produce AgNPs. Intriguingly, sample C showed the presence of a broad peak at 400–700 nm, with the highest point at 483 nm, which is correlated with the AgNPs' SPR peak. This phenomenon suggests that the

extract can provide the necessary reducing agents while the cooperation of microwave irradiation offers uniform heating to the sample that will enhance the formation rate of AgNPs [21]. It is also noted that peak at 324 nm in sample C is not observed, indicating that the phenolic compound from the extract acted as a reducing agent and successfully reduced  $\text{Ag}^+$  into  $\text{Ag}^0$ . Further characterizations to investigate the presence of AgNPs and their biological characteristic was performed on sample C.

### Materials Characterization of Sample C

Several characterization methods, such as FTIR, XRD, TEM, DLS, and zeta potential were performed on sample C. The results of these characterizations can be seen in Fig. 3, respectively.

#### FTIR results

The comparison of FTIR spectra of sample C and extract is presented in Fig. 3(a). It was observed that both spectra have similar peaks, implying that the phytochemical compounds in the extract might be responsible as capping agents to prevent the agglomeration of AgNPs. The emergence of notable peaks at wavenumber  $3425\text{ cm}^{-1}$  can be designated as the O–H stretching group of polyphenols or flavonoids [11]. In addition, two peaks were observed at  $2918$  and  $2850\text{ cm}^{-1}$  in the extract, which is related to the C–H stretching functional group of alkane [22]. Two peaks related to the C=O stretching of the amide proteins and flavonoids were detected at  $1639$  and  $1409\text{ cm}^{-1}$  [23]. The peak at  $1159\text{ cm}^{-1}$  can be ascribed to C–O stretching functional groups and the presence of a group of flavonoids and terpenoids that are widely found in the leaves [24] and also were found in *Champeria* family [8-9].

#### XRD result

Fig. 3(b) demonstrated the XRD pattern of sample C with five peaks at  $2\theta$  values of  $38.12^\circ$ ,  $44.3^\circ$ ,  $64.44^\circ$ ,  $77.38^\circ$ , and  $81.66^\circ$  that were designated to lattice planes of (111), (200), (220), (311), and (222), respectively. This pattern indicates that the synthesized silver metal in sample C was comprised of face-centered cubic (FCC) lattice and matched with JCPDS No. 00-004-0783 [3]. From this XRD pattern, it is clear that the AgNPs formed using the extract were in the form of high crystalline [25].

Furthermore, the most intense diffraction peak in the lattice plane (111) proves that the obtained AgNPs are dominant in the (111) direction [26].

#### TEM result

The TEM image in Fig. 3(c) shows the morphology of nanoparticles with a spherical shape that is well dispersed in sample C. The particle size of AgNPs was also measured using ImageJ and followed the Gaussian trend as demonstrated in Fig. 3(d). Moreover, it was revealed that the synthesized AgNPs have an average particle size of  $9.1 \pm 4.1\text{ nm}$ , which was comparable with our previous AgNPs that were prepared by extract of Cilembu sweet potatoes ( $9.95 \pm 3.69\text{ nm}$ ) [3], and relatively smaller than the previous research using another leaf-mediated extract where the average particle size was in the range between 12 to 30 nm [27]. This phenomenon can be accredited to a high concentration of secondary metabolites such as flavonoids, phenolic, lutein, phytol, and  $\beta$ -carotene in Seminyak leaf extract, leading to rapid reaction times which correspond to extensive nucleation sites and smaller nanoparticles. The smaller particle size of AgNPs leads to higher antibacterial activity and spherical shapes have been recognized to exhibit improved antibacterial properties because they can provide a larger surface-to-volume ratio [28].

#### DLS and zeta potential results

DLS measurement was conducted to investigate the average particle size of the obtained AgNPs and their particles distribution. Fig. 3(e) displays that the average particle size of the synthesized AgNPs is  $145.5\text{ nm}$  with a moderate polydispersity index (PI; 0.469). It was notable that the DLS tends to generate bigger average particles size than the TEM because the former quantifies the hydrodynamic diameter, which is the combined diameter of the core nanoparticles and the outer capping layer [29]. The stability of AgNPs in the sample can be predicted by performing zeta potential measurement. Fig. 3(f) exhibited that the zeta potential value of the synthesized AgNPs was  $0.28\text{ mV}$ , which is more neutral than our previous AgNPs that were prepared by extract of Cilembu sweet potatoes ( $-41.0\text{ mV}$ ) [3]. Since the zeta potential value of the synthesized AgNPs was in the range

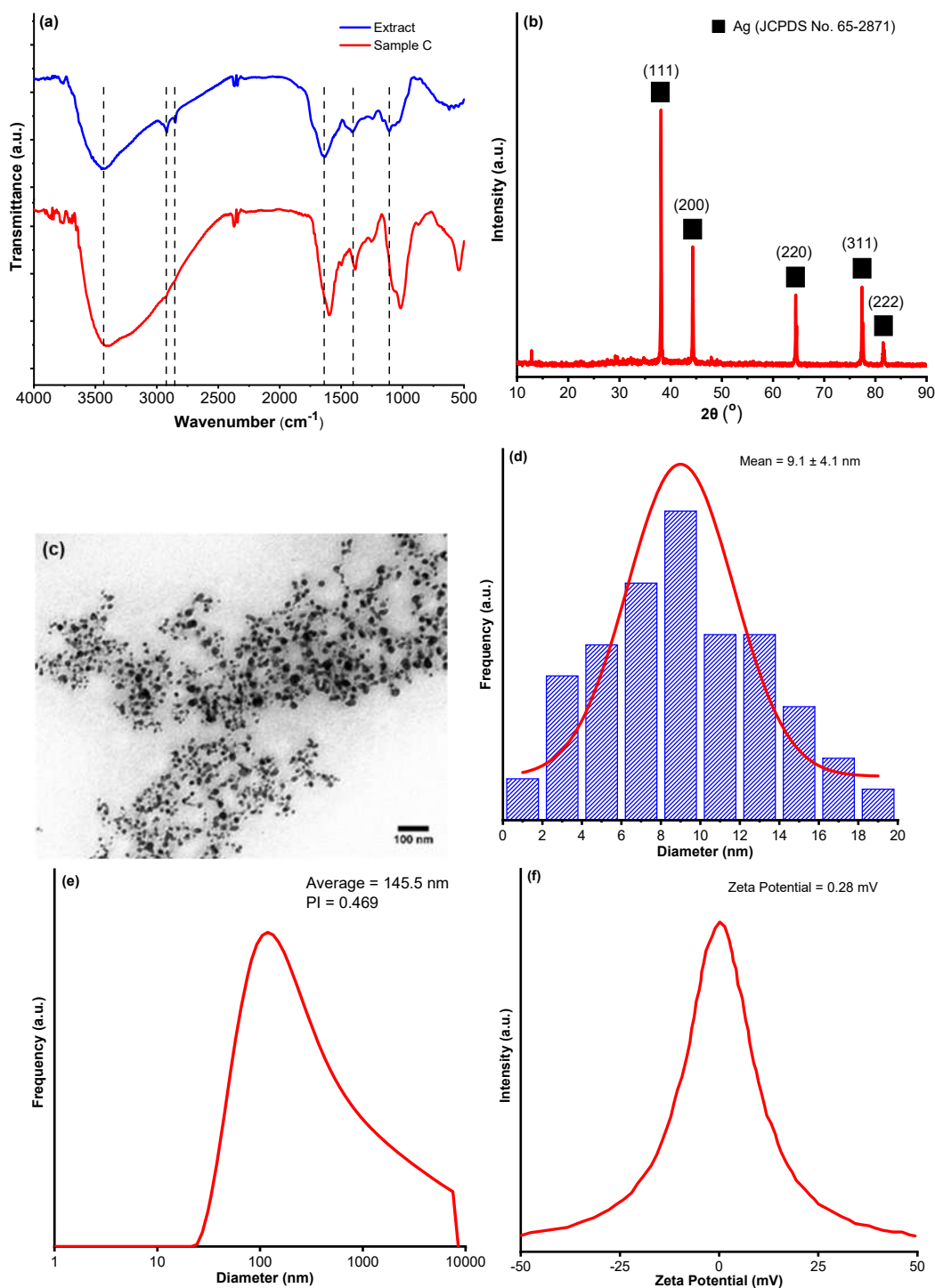


**Fig 3.** Further characterization results of sample C: (a) FTIR spectra (in comparison with extract, (b) XRD, (c) TEM, (d) particle distribution based on TEM image, (e) DLS, and (f) zeta potential results

of  $0 \pm 3$  mV, the synthesized AgNPs are susceptible to agglomeration and might form big particles after some time [26]. Therefore, it is reasonable that the DLS result

of the obtained AgNPs (145.5 nm, with PI 0.469) is relatively bigger and less uniform than the DLS result of our previous work ( $105.5 \pm 12.6$  nm, with PI 0.29 [3]).

## Biological Characterization of Sample C

### Antibacterial test results

Representative images of antibacterial test results of samples and a summary of the measured samples' ZOI were shown in Fig. 4 and Table 2 respectively. Antibacterial test results showed that ZOI of the extract was not observed against *E. coli* (Fig. 4(a)) and *S. aureus* (Fig. 4(b)), suggesting that the extract did not have any antibacterial activity against both bacteria [30]. On the other hand, sample C which contains AgNPs showed antibacterial activity against *E. coli* (Fig. 4(c)) and *S. aureus* (Fig. 4(d)) with ZOI of  $12.3 \pm 0.1$  and  $13.7 \pm 0.7$  mm, respectively (Table 2). According to the fact that the ZOI of sample C is in the range of 10–20 mm, sample C can be considered to have strong antibacterial activities against both bacteria [31].

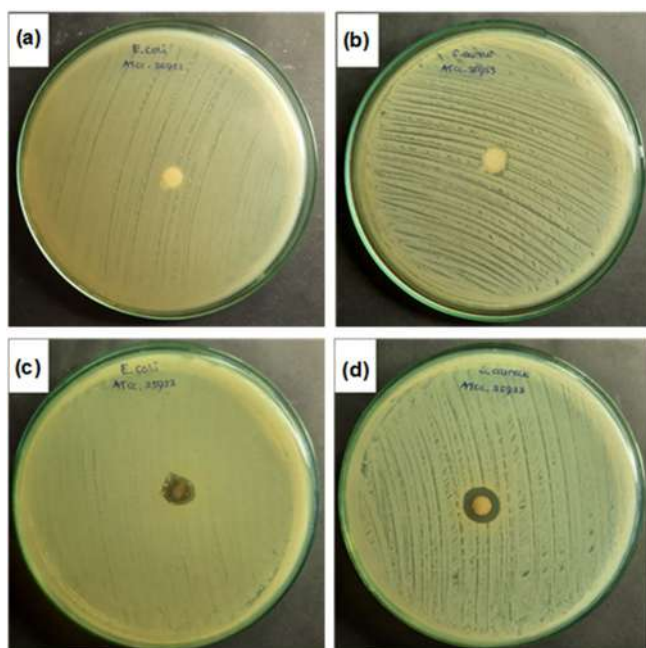


**Fig 4.** Antibacterial activity of the extract against (a) *E. coli*, (b) *S. aureus*; and sample C against (c) *E. coli*, (d) *S. aureus*

**Table 2.** Summary of the antibacterial test results from the disc diffusion method

No.	Sample name	Type of bacteria	ZOI (mm)
1	Extract	<i>E. coli</i>	0
		<i>S. aureus</i>	0
2	Sample C	<i>E. coli</i>	$12.3 \pm 0.1$
		<i>S. aureus</i>	$13.7 \pm 0.7$

**Table 3.** Cell viability of BHK-21 cells for extract and sample C

No	Sample name	Cell viability (%)
1	Control cell	$100.0 \pm 4.9$
2	Extract	$84.4 \pm 2.2$
3	Sample C	$88.5 \pm 7.0$

These strong antibacterial activities of AgNPs in sample C could be correlated with their small particle size ( $9.1 \pm 4.1$  nm), providing high numbers of silver atoms on the surface and releasing  $\text{Ag}^+$  to kill bacteria cells [28].

### MTT assay results

The cell viability of the extract and AgNPs in sample C was determined by MTT assay after 1 day in BHK-21 cells culture. Table 3 suggests that both samples were non-toxic because the percentage of cell viability is above 60% (approximately 84.4% for extract and 88.5% for sample C respectively) [32]. Cell viability of AgNPs is lower than control cells because AgNPs could induce mitochondrial dysfunction by producing reactive oxygen species (ROS), causing damage to cell membranes, proteins, and DNA leading to cell apoptosis [33]. However, in this research both extract and sample C were non-toxic. Thus, it can be concluded that the obtained AgNPs were biocompatible for biomedical applications.

## CONCLUSION

Green synthesis method in AgNPs formation using a low concentration of Seminyak leaf extract (0.5 wt.%) and incorporation with short microwave irradiation time (1 min) led to a rapid synthesis process and successfully prepared AgNPs with the extremely small size of  $9.1 \pm 4.1$  nm. The synthesized AgNPs demonstrate notable antibacterial properties against *E. coli* and *S. aureus* with ZOI of  $12.3 \pm 0.1$  and  $13.7 \pm 0.7$  mm, respectively. The cytotoxicity of AgNPs was very minimal on BHK-21 cells, resulting in high cell viability. These findings suggest the potential of microwave-Seminyak-mediated AgNPs for various biomedical applications such as drug carriers, promotion of wound repair and bone healing, biosensors, and antibacterial scaffold. In the future, the stability, and biocompatibility

of the AgNPs in the human body should be observed as these properties are critical for their prospective applications.

## ■ ACKNOWLEDGMENTS

This research was funded by The Research, Community Service and Innovation Program (P3MI) for Electronic Materials Physics Research Group, Faculty of Mathematical and Natural Sciences, Institut Teknologi Bandung, 2021.

## ■ AUTHOR CONTRIBUTIONS

Conceptualization, Arie Wibowo, and Muhammad Bagas Ananda; Methodology, Arie Wibowo, Anggraini Barlian, Prihartini Widiyanti, and Muhammad Bagas Ananda; Data acquisition, Muhammad Bagas Ananda, Tami Bachrurozy, Fathan Aditya Sanjaya, Helmi Majid Ar Rasyid, Fitriyatul Qulub, and Prihartini Widiyanti; Data analysis, Arie Wibowo, Anggraini Barlian, Prihartini Widiyanti, Tami Bachrurozy, and Muhammad Bagas Ananda; Funding acquisition, Akfiny Hasdi Aimon; Project administration, Arie Wibowo, and Akfiny Hasdi Aimon; Resources, Arie Wibowo, and Akfiny Hasdi Aimon; Supervision, Arie Wibowo, and Anggraini Barlian; Writing—original draft, Muhammad Bagas Ananda, Arie Wibowo, Fitriyatul Qulub, and Prihartini Widiyanti; Writing—review & editing, Anggraini Barlian, Akfiny Hasdi Aimon, Tami Bachrurozy, Fathan Aditya Sanjaya, and Helmi Majid Ar Rasyid. All authors have read and agreed to the published version of the manuscript.

## ■ REFERENCES

- [1] Ye, Z., Zhu, X., Mutreja, I., Boda, S.K., Fischer, N.G., Zhang, A., Lui, C., Qi, Y., and Aparicio, C., 2021, Biomimetic mineralized hybrid scaffolds with antimicrobial peptides, *Bioact. Mater.*, 6 (8), 2250–2260.
- [2] Tamayo Marín, J.A., Londoño, S.R., Delgado, J., Navia Porras, D.P., Valencia Zapata, M.E., Mina Hernandez, J.H., Valencia, C.H., and Grande Tovar, C.D., 2019, Biocompatible and antimicrobial electrospun membranes based on nanocomposites of chitosan/poly(vinyl alcohol)/graphene oxide, *Int. J. Mol. Sci.*, 20 (12), 2987.
- [3] Wibowo, A., Tajalla, G.U., Marsudi, M.A., Cooper, G., Asri, L.A., Liu, F., Ardy, H., and Bartolo, P.J., 2021, Green synthesis of silver nanoparticles using extract of Cilembu sweet potatoes (*Ipomoea batatas* L var. Rancing) as potential filler for 3D printed electroactive and anti-infection scaffolds, *Molecules*, 26 (7), 2042.
- [4] Citradewi, P.W., Hidayat, H., Purwiandono, G., Fatimah, I., and Sagadevan, S., 2021, *Clitorea ternatea*-mediated silver nanoparticle-doped hydroxyapatite derived from cockle shell as antibacterial material, *Chem. Phys. Lett.*, 769, 138412.
- [5] Garibo, D., Borbón-Nuñez, H.A., de León, J.N.D., García Mendoza, E., Estrada, I., Toledano-Magaña, Y., Tiznado, H., Ovalle-Marroquin, M., Soto-Ramos, A.G., Blanco, A., Rodríguez, J.A., Romo, O.A., Chávez-Almazán, L.A., and Susarrey-Arce, A., 2020, Green synthesis of silver nanoparticles using *Lysiloma acapulcensis* exhibit high-antimicrobial activity, *Sci. Rep.*, 10 (1), 12805.
- [6] Tarannum, N., Divya, D., and Gautam, Y.K., 2019, Facile green synthesis and applications of silver nanoparticles: A state-of-the-art review, *RSC Adv.*, 9 (60), 34926–34948.
- [7] Allafchian, A.R., Vahabi, M.R., Jalali, S.A.H., Mahdavi, S.S., Sepahvand, S., and Farhang, H.R., 2022, Design of green silver nanoparticles mediated by *Ferula ovina* Boiss. extract with enhanced antibacterial effect, *Chem. Phys. Lett.*, 791, 139392.
- [8] Ragasa, C.Y., Ng, V.A.S., Ulep, R.A., Brkljača, R., and Urban, S., 2015, Chemical constituents of *Champereia manillana* (Blume) Merrill, *Pharm. Lett.*, 7 (7), 256–261.
- [9] Abdul Wahab, N., Ahdan, R., Ahmad Aufa, Z., Kong, K.W., Johar, M.H., Shariff Mohd, Z., and Ismail, A., 2015, Nutritional values and bioactive components of under-utilised vegetables consumed by indigenous people in Malaysia, *J. Sci. Food Agric.*, 95 (13), 2704–2711.

- [10] Kaur, N., Singh, A., and Ahmad, W., 2022, Microwave assisted green synthesis of silver nanoparticles and its application: A review, *J. Inorg. Organomet. Polym. Mater.*, 2022, s10904-022-02470-2.
- [11] Francis, S., Joseph, S., Koshy, E.P., and Mathew, B., 2018, Microwave assisted green synthesis of silver nanoparticles using leaf extract of *Elephantopus scaber* and its environmental and biological applications, *Artif. Cells, Nanomed., Biotechnol.*, 46 (4), 795–804.
- [12] Hardiansyah, A., Budiman, W.J., Yudasari, N., Isnaeni, I., Kida, T., and Wibowo, A., 2021, Facile and green fabrication of microwave-assisted reduced graphene oxide/titanium dioxide nanocomposites as photocatalysts for rhodamine 6G degradation, *ACS Omega*, 6 (47), 32166–32177.
- [13] Yasir, M., Singh, J., Tripathi, M.K., Singh, P., and Shrivastava, R., 2017, Green synthesis of silver nanoparticles using leaf extract of common arrowhead houseplant and its anticandidal activity, *Pharmacogn. Mag.*, 13 (Suppl. 4), S840–S844.
- [14] Rai, Y., Pathak, R., Kumari, N., Sah, D.K., Pandey, S., Kalra, N., Soni, R., Dwarakanath, B., and Bhatt, A.N., 2018, Mitochondrial biogenesis and metabolic hyperactivation limits the application of MTT assay in the estimation of radiation induced growth inhibition, *Sci. Rep.*, 8 (1), 1531.
- [15] Chakravarty, A., Ahmad, I., Singh, P., Ud Din Sheikh, M., Aalam, G., Sagadevan, S., and Ikram, S., 2022, Green synthesis of silver nanoparticles using fruits extracts of *Syzygium cumini* and their bioactivity, *Chem. Phys. Lett.*, 795, 139493.
- [16] Melkamu, W.W., and Bitew, L.T., 2021, Green synthesis of silver nanoparticles using *Hagenia abyssinica* (Bruce) JF Gmel plant leaf extract and their antibacterial and anti-oxidant activities, *Heliyon*, 7 (11), e08459.
- [17] Nadagouda, M.N., Speth, T.F., and Varma, R.S., 2011, Microwave-assisted green synthesis of silver nanostructures, *Acc. Chem. Res.*, 44 (7), 469–478.
- [18] Ashraf, J.M., Ansari, M.A., Khan, H.M., Alzohairy, M.A., and Choi, I., 2016, Green synthesis of silver nanoparticles and characterization of their inhibitory effects on AGEs formation using biophysical techniques, *Sci. Rep.*, 6 (1), 20414.
- [19] Fatimah, I., and Aftrid, Z.H.V.I., 2019, Characteristics and antibacterial activity of green synthesized silver nanoparticles using red spinach (*Amaranthus tricolor* L.) leaf extract, *Green Chem. Lett. Rev.*, 12 (1), 25–30.
- [20] Nakamura, T., Magara, H., Herbani, Y., and Sato, S., 2011, Fabrication of silver nanoparticles by highly intense laser irradiation of aqueous solution, *Appl. Phys. A*, 104 (4), 1021–1024.
- [21] Fatimah, I., 2016, Green synthesis of silver nanoparticles using extract of *Parkia speciosa* Hassk pods assisted by microwave irradiation, *J. Adv. Res.*, 7 (6), 961–969.
- [22] Swidan, N.S., Hashem, Y.A., Elkhatib, W.F., and Yassien, M.A., 2022, Antibiofilm activity of green synthesized silver nanoparticles against biofilm associated enterococcal urinary pathogens, *Sci. Rep.*, 12 (1), 3869.
- [23] Mussin, J., Robles-Botero, V., Casañas-Pimentel, R., Rojas, F., Angiolella, L., San Martín-Martínez, E., and Giusiano, G., 2021, Antimicrobial and cytotoxic activity of green synthesis silver nanoparticles targeting skin and soft tissue infectious agents, *Sci. Rep.*, 11 (1), 14566.
- [24] Moodley, J.S., Krishna, S.B.N., Pillay, K., and Govender, P., 2018, Green synthesis of silver nanoparticles from *Moringa oleifera* leaf extracts and its antimicrobial potential, *Adv. Nat. Sci. Nanosci. Nanotechnol.*, 9, 015011.
- [25] Khalil, M.M.H., Ismail, E.H., El-Baghdady, K.Z., and Mohamed, D., 2014, Green synthesis of silver nanoparticles using olive leaf extract and its antibacterial activity, *Arabian J. Chem.*, 7 (6), 1131–1139.
- [26] Allafchian, A., Balali, F., Vahabi, M.R., and Jalali, S.A.H., 2022, Antibacterial and cytotoxic effects of silver nanoparticles fabricated by *Eryngium billardieri* Delar. extract, *Chem. Phys. Lett.*, 791, 139385.
- [27] Wang, Y., Chinnathambi, A., Nasif, O., and Alharbi, S.A., 2021, Green synthesis and chemical



- characterization of a novel anti-human pancreatic cancer supplement by silver nanoparticles containing *Zingiber officinale* leaf aqueous extract, *Arabian J. Chem.*, 14 (4), 103081.
- [28] Hong, X., Wen, J., Xiong, X., and Hu, Y., 2016, Shape effect on the antibacterial activity of silver nanoparticles synthesized via a microwave-assisted method, *Environ. Sci. Pollut. Res.*, 23 (5), 4489–4497.
- [29] Madivoli, E.S., Kareru, P.G., Gachanja, A.N., Mugo, S.M., Makhanu, D.S., Wanakai, S.I., and Gavamukulya, Y., 2020, Facile synthesis of silver nanoparticles using *Lantana trifolia* aqueous extracts and their antibacterial activity, *J. Inorg. Organomet. Polym. Mater.*, 30 (8), 2842–2850.
- [30] Davis, W.W., and Stout, T.R., 1971, Disc plate method of microbiological antibiotic assay: I. Factors influencing variability and error, *Appl. Microbiol.*, 22 (4), 659–665.
- [31] Martha, A.A., Permatasari, D.I., Dewi, E.R., Wijaya, N.A., Kunarti, E.S., Rusdiarso, B., and Nuryono, N., 2022, Natural magnetic particles/chitosan impregnated with silver nanoparticles for antibacterial agents, *Indones. J. Chem.*, 22 (3), 620–629.
- [32] International Organization for Standardization, 2009, *Biological evaluation of medical devices — Part 5: Tests for in vitro cytotoxicity*, ISO 10993-5:2009, <https://www.iso.org/standard/36406.html>.
- [33] El-Hussein, A., and Hamblin, M.R., 2017, ROS generation and DNA damage with photo-inactivation mediated by silver nanoparticles in lung cancer cell line, *IET Nanobiotechnol.*, 11 (2), 173–178.

## Oxygen Reduction Reaction (ORR) of Pt/C Standard in Different Electrolyte Solutions and Terbium(III) Monoporphyrinato Complex

Atmanto Heru Wibowo<sup>1\*</sup>, Annisa Nur Buana Wati<sup>1</sup>, Anas Santria<sup>2,3</sup>,  
Abu Masykur<sup>1</sup>, and Maulidan Firdaus<sup>1</sup>

<sup>1</sup>Department of Chemistry, Faculty of Natural Sciences and Mathematics, Universitas Sebelas Maret, Jl. Ir. Sutami 36A, Kentingan, Surakarta 57126, Indonesia

<sup>2</sup>Department of Chemistry, Graduate School of Science, Osaka University, Toyonaka, Osaka 560-0043, Japan

<sup>3</sup>Research Center for Chemistry, National Research and Innovation Agency (BRIN), Serpong 15314, Indonesia

### \* Corresponding author:

tel: +62-85878677541

email: aheruwibowo@staff.uns.ac.id

Received: November 2, 2022

Accepted: March 22, 2023

DOI: 10.22146/ijc.78807

**Abstract:** Electrocatalytic parameters of a Pt/C standard and a sample of terbium(III) monoporphyrinato were investigated in different solutions. *N* electron transfer, Tafel slope,  $E_{\text{onset}}$ , and overpotential of the catalyst of Pt/C in different solutions were calculated and analyzed using a rotating ring disk electrode (RRDE) in 0.5 M H<sub>2</sub>SO<sub>4</sub>, 0.1 M HClO<sub>4</sub> and 0.1 M NaOH. In the RRDE measurements, a bipotentiostat at a potential range of 1.03 to 0.05 V vs RHE ( $E_{\text{ring}} = 1.2$  V vs RHE) with a scan rate of 5 mV/s and rotation rates of 200, 400, 900, 1600 and 2500 rpm was used. Hereafter, the test of terbium(III) monoporphyrinato compound formulated in [Tb(TPP)(cyclen)]Cl (TPP = 5,10,15,20-tetraphenylporphyrinato; cyclen = 1,4,7,10-tetraazacyclododecane) as a candidate material for ORR electrocatalyst was also done. The results showed that the measurement of Pt/C standards was satisfactory according to the literature for all parameters with the *n* electron transfer close to 4 in all electrolytes media. [Tb(TPP)(cyclen)]Cl had an *n* electron transfer value of 2.38, suggesting that the [Tb(TPP)(cyclen)]Cl compound has less potential for ORR catalysts.

**Keywords:** oxygen reduction reaction (ORR); RRDE technique; Pt/C; monoporphyrinato

## ■ INTRODUCTION

The fuel cell is one of the options to obtain promising energy in the future. However, the kinetic sluggishness on the cathode and high overpotential is the main problem that is mostly found in the fuel cell, especially for oxygen reduction reactions (ORR). Therefore, high efficiency is required in the oxygen reduction process that occurs on the cathode and is inevitable in the polymer electrolyte membrane fuel cells (PEMFC). PEMFC affords high efficiency of the fuel cell in supplying electricity with nearly nonexistent emission [1]. For a PEMFC that uses a Pt electrode, the ORR occurred in the cathode and the hydrogen oxidation reaction (HOR) occurred in the anode [2]. Because the nature of ORR being a kinetically slow reaction with high overpotential, an efficient electrocatalyst

is necessary [3]. However, Pt is still used mostly for ORR due to its good catalytic activity compared to other materials. A significant portion of the high cost of PEMFCs was contributed due to the price of Pt-based catalysts [4]. Therefore, it is important to design an electrocatalyst that is cheap and efficient for ORR [5].

The potential candidate to replace Pt are precursors containing nitrogen, carbon, and metals [6]. Molecules of N<sub>4</sub>-metallomacrocyclic have been considered as one of the promising compounds for ORR since 1964. The advantage of using these materials for electrocatalysts is due to the more affordable price compared to Pt. Catalytic activity can be modified by changing the substitution of the metal center or by the structure modification of N<sub>4</sub>-macrocyclic ligand [7].

Porphyrin, corrole, and phthalocyanine have been studied extensively regarding the substituent effect for the catalyst of ORR [8]. The use of metals on porphyrin (henceforth called metalloporphyrin) showed some benefits from the aspect of its coordination. Porphyrin affords rigid environments and good stability with the metal center in the cavity. Metalloporphyrin is considered as a stable complex in acid or base, and is also a redox-active compound. As a consequence, metalloporphyrin can be used for redox activity materials such as in the applications for fuel cells. The porphyrin molecule can be modified with different substituents on the *meso* and  $\beta$  position to obtain various metalloporphyrin with different chemical or physico-chemical properties that can also be applied for the ORR catalyst [9]. A metalloporphyrin complex with a lanthanide ion as a metal center has also contributed to porphyrin chemistry since 1974, in which the study of this complex has been done in many aspects such as photoluminescence and molecular magnetism [10].

An electrocatalyst performance should be evaluated first before involving the fabrication of the fuel cell in the lab using a three-electrode system [11]. Evaluation can be done using a rotating disk electrode (RDE) and rotating-ring-disk electrode (RRDE) as the working electrode in the system. The Pt/C electrocatalyst has been used as a reference material for evaluating the performance of new catalysts, which is dependent on some factors [12]. Here we report the determination of the catalytic activity of platinum in different electrolyte media, together with an investigation of the catalytic performance of lanthanide(III) monoporphyrimato complex, namely [Tb(TPP)(cyclen)]Cl (Tb = terbium; TPP = 5,10,15,20-tetraphenylporphyrinato; cyclen = 1,4,7,10-tetraazacyclododecane; Cl = chloride).

## ■ EXPERIMENTAL SECTION

### Materials

[Tb(TPP)(cyclen)]Cl complex was prepared using the previously reported method [10]. The Pt/C (20 wt.% Pt), Sulfuric Acid (H<sub>2</sub>SO<sub>4</sub>, 97%), perchloric acid (HClO<sub>4</sub>, 96%), sodium hydroxide (NaOH), isopropanol (C<sub>3</sub>H<sub>8</sub>O) and Nafion 5 wt.% were purchased from commercial suppliers, E Merk and DuPont.

### Instrumentation

The RRDE measurements were carried out using bipotentiostat Corrtest CS2150 from Corrtest Instruments Corp., Ltd. with the current control range:  $\pm 2$  A. The computational chemistry calculations were done using Supercomputer System SQUID at the Cybermedia Centre, Osaka University.

### Procedure

The electrocatalytic activities of catalysts were studied using RRDE measurement in a three-electrode cell. A Pt/GC RRDE (7 mm OD, 5 mm ID Pt ring (0.189 cm<sup>2</sup>) and 4 mm diameter GC (0.126 cm<sup>2</sup>), Ag/AgCl (sat. KCl) and GC plate (10 × 15 mm, 2 mm thickness, connected with Au wire) were used as the working, reference and counter electrode, respectively. The ink catalyst was prepared by mixing 2 mg of catalyst and 1 mL stock solution (20% isopropanol, 0.02% Nafion ionomer), followed by sonification for about 60 min. About 10  $\mu$ L of dispersed ink was drop cast on the surface of the GC-electrode disk and then air-dried for about 60 min. The RRDE measurements were carried out at +1.03 to +0.05 V vs RHE ( $E_{\text{ring}} = 1.2$  V vs RHE) with the rotating rate of 200, 400, 900, 1600, and 2500 rpm and a scan rate of 10 mV s<sup>-1</sup> in the 0.1 M KOH solution.

Computational chemistry calculations was performed on the Gaussian 16 package, Rev. C.01. The geometry structure of [Tb(TPP)cyclen]<sup>+</sup> was taken from the experimental structure [10]. The Grimme's density functional theory (DFT-D3) method of B3LYP with the energy-consistent pseudopotentials of the Stuttgart (Stuttgart RSC 1997 ECP) basis set for terbium ion and 6-31G\*\* basis set for the other atoms was performed to optimize the geometry of structure [13-15].

## ■ RESULTS AND DISCUSSION

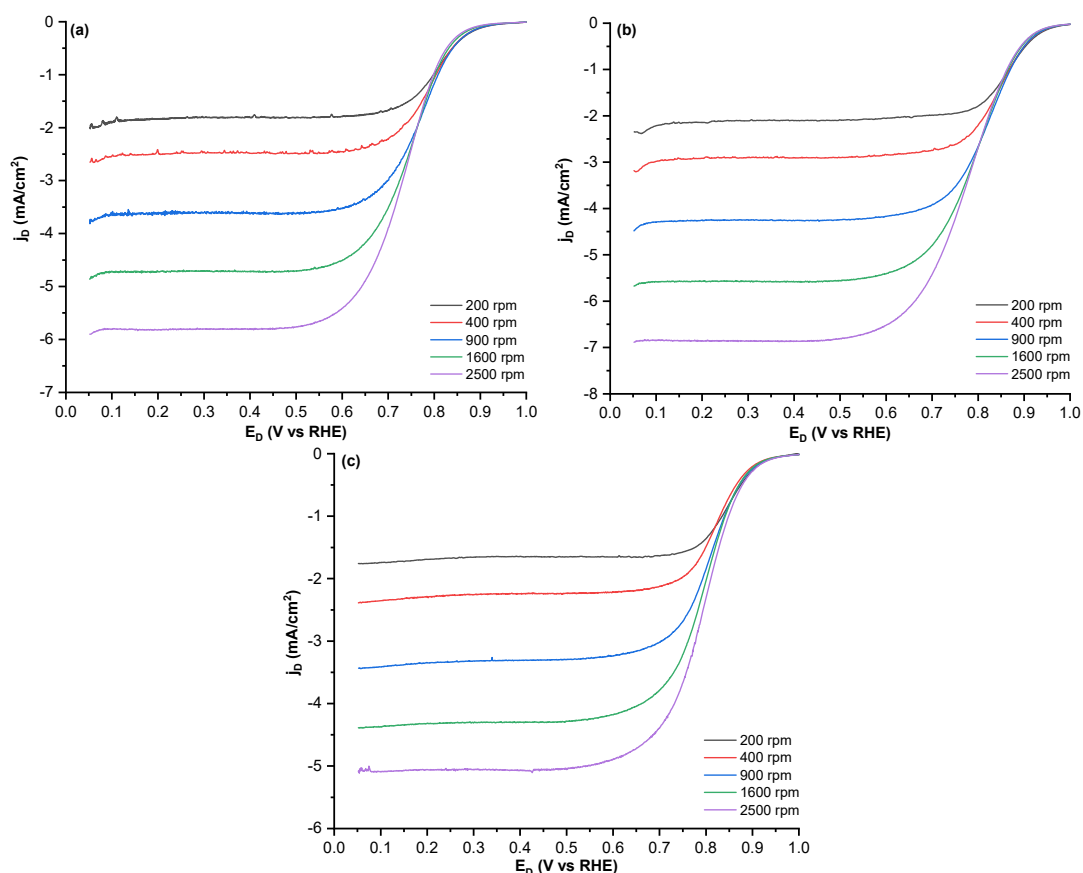
### Pt/C test in Various Electrolytes

The polarization curve was obtained with the linear sweep voltammetry (LSV) from RRDE at the range of 1.03 to 0.05 V vs RHE with scanning rates of 5 mV/s and rotation rates of 200, 400, 900, 1600 and 2500 rpm for Pt/C in various O<sub>2</sub> saturated solution of H<sub>2</sub>SO<sub>4</sub> 0.5 M, HClO<sub>4</sub> 0.1 M and NaOH 0.1 M. Current

obtained from the measurement was normalized with the disk surface ( $S_g$ ) at about  $0.126 \text{ cm}^2$ . The profile of the Pt/C voltammetry in the various  $\text{O}_2$  saturated solution (Fig. 1) showed that the current density increased with the increase of rotation rate from 200 to 2500 rpm. Table 1 shows the parameter analyzed from polarization curves at 2500 rpm. Analysis of the activation area (AR) of the polarization curve at 2500 rpm made it possible to obtain the parameter of  $E_{\text{onset}}$  value. More positive  $E_{\text{onset}}$  and  $E_{1/2}$  means that the electrocatalysis will be more active [16]. The Pt/C catalyst in the medium of  $\text{HClO}_4$  0.1 M and  $\text{NaOH}$  0.1 M showed more positive  $E_{\text{onset}}$  value than in  $\text{H}_2\text{SO}_4$  0.1 M, indicating that Pt/C was more active in both solutions. The controlled region that was measured was in the mixed region of diffusion-kinetic (KR) to obtain information about  $E_{1/2}$ . The  $E_{1/2}$  value was in the same correlation with the electrocatalytic activity of Pt/C in various electrolyte solutions of  $\text{NaOH}$  0.1 M >  $\text{HClO}_4$  0.1 M >  $\text{H}_2\text{SO}_4$  0.5 M. The theory of the overpotential ( $\eta$ ) and

real overpotential ( $\eta_{\text{exp}}$ ) was calculated from the different values of  $E_{\text{eq}(\text{exp})}$  and  $E_{\text{onset}}$  with  $E_{\text{eq}}$ . The difference of both overpotentials was used in the calculation of the sluggishness of ORR, where Pt/C in  $\text{HClO}_4$  0.1 M solution obtained the best value among other solutions.

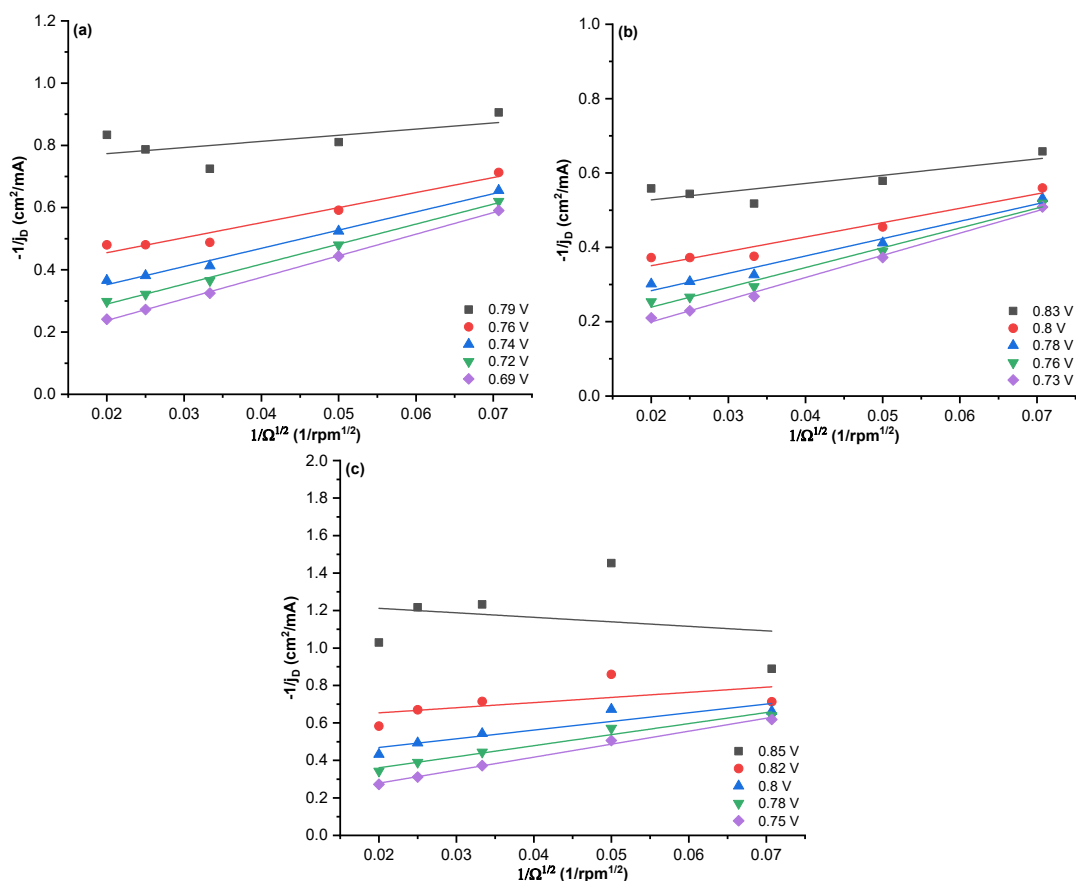
From Eq. (1), the Koutecky-Levich plot is defined as a straight line characterized by the slope  $\alpha_{\text{K-L}} = (n_{\text{ex}}B)^{-1}$  and the intercept  $\beta_{\text{K-L}} = j_{\text{k}}^{-1}$  where  $j$  is the measured current density,  $j_{\text{k}}$  is the kinetic current density,  $j_{\text{l}}^{\text{film}}$  is the diffusion-limiting current density in catalyst film,  $j_{\text{l}}^{\text{ads}}$  is the diffusion-limiting current density associated with  $\text{O}_2$  adsorption in the active site,  $j_0$  is the current exchange density,  $n_{\text{ex}}$  is the exchange number of electrons,  $\Omega$  is the rotation rate,  $\theta$  and  $\theta_{\text{eq}}$  is the degree of coverage of the catalyst surface (active sites) by oxygen at potential  $E$ , and at the equilibrium potential  $E_{\text{eq}}$ ,  $\eta$  is the overpotential and  $b$  is the Tafel slope. The plot of Koutecky-Levich for Pt/C in various electrolyte solutions at different potentials showed a good linearity of the lines (Fig. 2). Typical



**Fig 1.** Polarization curve of Pt/C in various electrolyte solutions of (a)  $\text{H}_2\text{SO}_4$  0.5 M, (b)  $\text{HClO}_4$  0.1 M and (c)  $\text{NaOH}$  0.1 M at various rotation rates

**Table 1.** Parameters of the polarization curves for Pt/C in various electrolytes

Electrolyte	$E_{\text{onset}}$ (V vs RHE)	$E_{1/2}$ (V vs RHE)	$\eta$ (mV)	$\eta_{(\text{exp})}$ (mV)	Sluggishness (mV)
0.5 M $\text{H}_2\text{SO}_4$	0.84	0.74	264	348	84
0.1 M $\text{HClO}_4$	0.89	0.78	232	291	59
0.1 M NaOH	0.89	0.80	167	296	129

**Fig 2.** Koutecky-Levich plot obtained from Fig. 1 for Pt/C in the  $\text{O}_2$  saturated solution of (a)  $\text{H}_2\text{SO}_4$  0.5 M, (b)  $\text{HClO}_4$  0.1 M and (c) NaOH 0.1 M at the different potentials

characteristics of first-order kinetics in correlation with dissolved  $\text{O}_2$  in the solution were seen with linearity and parallelism of the plots [17]. Kinetic current density ( $j_k$ ) was normalized with the mass of Pt/C, which was drop-casted on the disk surface ( $20 \mu\text{g}$ ). The value of  $j_k$  at 0.8 V vs RHE for the activation of Pt/C in various electrolytes is shown in Table 2.

$$\frac{1}{j} = \frac{1}{n_{\text{ex}} B \Omega^2} + \frac{1}{j_1^{\text{film}}} + \frac{1}{j_1^{\text{ads}}} + \frac{1}{j_0 \frac{\theta}{\theta_{\text{eq}}} e^{\frac{n}{b}}} \Rightarrow j^{-1} \quad (1)$$

$$= (n_{\text{ex}} B)^{-1} \Omega^{-\frac{1}{2}} + j_k^{-1} \quad = \frac{1}{j_L}$$

Fig. 3 shows plots based on Eq. (2), in which  $j_L$  (limiting current density) can be determined from these extrapolation plots. The  $j_L$  value for Pt/C in various electrolytes can be seen in Table 2. The  $j_L$  is always higher than  $j_0$ , independent of the solution used. This indicated that electron transfer is the determining stage for the reaction rate (rds) [18].

$$\frac{1}{j_k} = \frac{1}{j_L} + \frac{1}{j_0 \frac{\theta}{\theta_{\text{eq}}} e^{\frac{n}{b'}}} = \frac{1}{j_L} + \frac{1}{j_0 \frac{\theta}{\theta_{\text{eq}}} e^{\frac{E-E_{\text{eq}}}{b'}}} \Rightarrow \lim_{\eta \rightarrow \infty} \left( \frac{1}{j_k} \right) \quad (2)$$

$$= \frac{1}{j_L}$$

**Table 2.** ORR kinetic parameter of Pt/C in various solutions

Electrolyte	n	$j_k$ (mA/cm <sup>2</sup> mg) at 0.8 V vs RHE	$j_L$ (mA/cm <sup>2</sup> )	B (mV/dec)	$j_0$ (mA/cm <sup>2</sup> )
0.5 M H <sub>2</sub> SO <sub>4</sub>	3.95	52.74	62.35	114	$5.52 \times 10^{-4}$
0.1 M HClO <sub>4</sub>	3.99	183.02	61.57	112	$1.42 \times 10^{-3}$
0.1 M NaOH	3.98	132.79	32.03	134	$4.92 \times 10^{-3}$

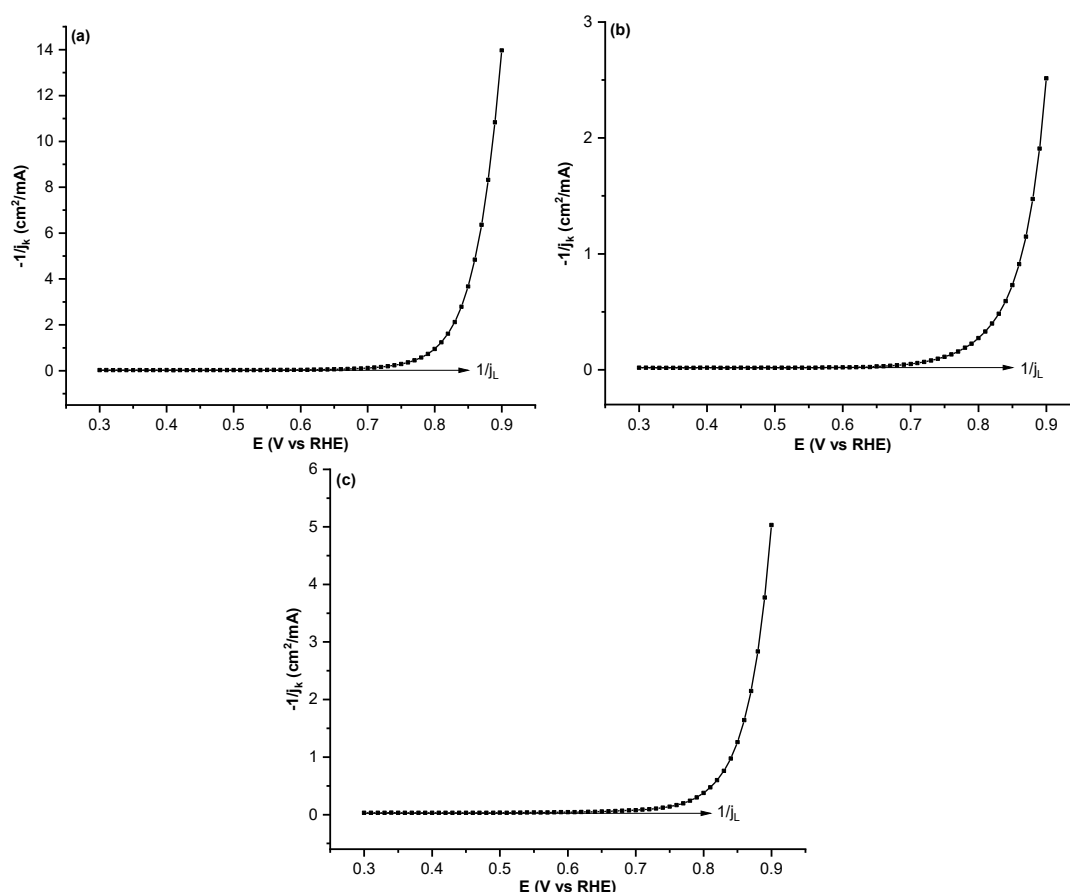
**Fig 3.** Plot “ $j_k^{-1}$  vs. E” for the determination of the limiting current density ( $j_L$ ) for Pt/C in the electrolyte solution of (a) H<sub>2</sub>SO<sub>4</sub> 0.5 M, (b) HClO<sub>4</sub> 0.1 M and (c) NaOH 0.1 M

Fig. 4 shows the relative Tafel plot of Pt/C in various electrolyte solutions. This plot can give information about the value of the Tafel slope ( $b$ ) and exchange current density ( $j_0$ ) obtained from Eq. (3) and (4), respectively, as seen in Table 2. From this calculation, the  $b$  value obtained was close to the literature with a high overpotential of about 120 mV/dec [19], indicating that the first electron reduction occurred as rds at high overpotential. Electrocatalytic material with high  $j_0$  and low  $b$  is intended for electrocatalysis of ORR. This means that with lower  $b$ , the current density increases but with

smaller overpotential, and it also means that the kinetic charge transfer occurred faster.

$$\alpha_{\text{Tafel}} = \frac{\partial \eta}{\partial \left( \log \left( \frac{j_k}{j_L - j_k} \right) \right)} = -b \quad (3)$$

$$\beta_{\text{Tafel}} = -b \log \left( \frac{j_L}{j_0} \right) \Rightarrow j_0 = j_L \times 10^{-\frac{\beta_{\text{Tafel}}}{b}} \quad (4)$$

The polarization curve of RRDE (Fig. 5) showed the currents on the disk and ring as well. The ring current ( $I_R$ ) was parallel with the number of intermediate species

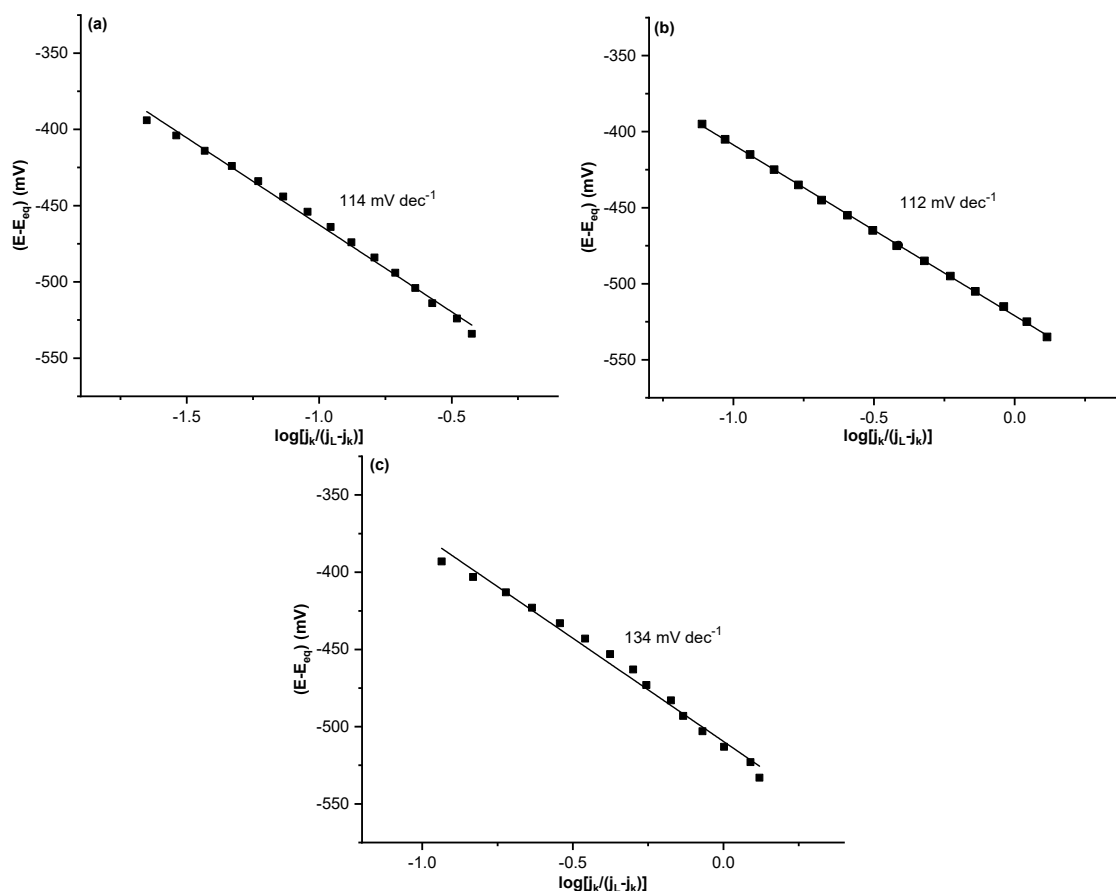


Fig 4. Relative Tafel plot for Pt/C in the solution of (a)  $\text{H}_2\text{SO}_4$  0.5 M, (b)  $\text{HClO}_4$  0.1 M, and (c)  $\text{NaOH}$  0.1 M

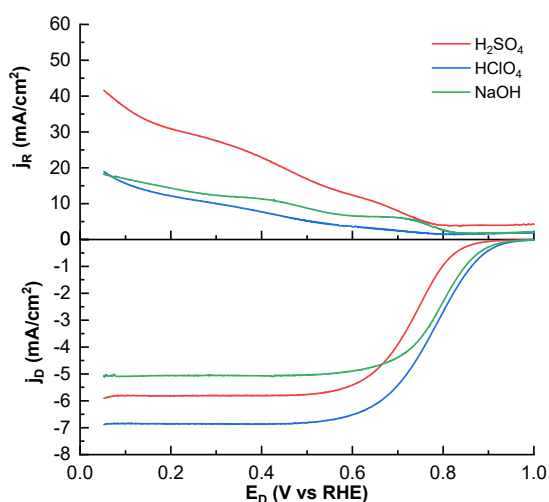


Fig 5. Polarization curves of RRDE for Pt/C in the different electrolyte solutions at 2500 rpm

yielded from the reduction of  $\text{O}_2$ . The smaller ring current means that the electron transfer is closer to 4. The polarization curve of RRDE can be used to determine the

electron transfer number (as seen in Fig. 6) at a certain potential range with Eq. (5), where  $N$  is the collection efficiency (42%),  $I_D$  and  $I_R$  are disk and ring current, respectively.

$$n = \frac{4N|I_D|}{N|I_D| + I_R} = \frac{4}{1 + \frac{I_R}{N|I_D|}} \leq 4 \quad (5)$$

The value of  $n$  electron transfer in the electrolyte of  $\text{HClO}_4$  0.1 M was the closest to 4 and also the most stable as well, followed by  $\text{NaOH}$  0.1 M and  $\text{H}_2\text{SO}_4$  0.5 M. The result was similar to what Garsany et al. [20] reported. They reported that the electrocatalytic properties of Pt in the media of  $\text{H}_2\text{SO}_4$  is sensible due to its surface in adsorbing  $\text{HSO}_4^-$  and  $\text{SO}_4^{2-}$  and the best performance of Pt/C is in the electrolyte of  $\text{HClO}_4$  0.1 M. The effect of the electrocatalyst performance was dependent on the electrolyte having interactions that occur between oxygen, salt ion, water, and the electrode. Electrolytes with

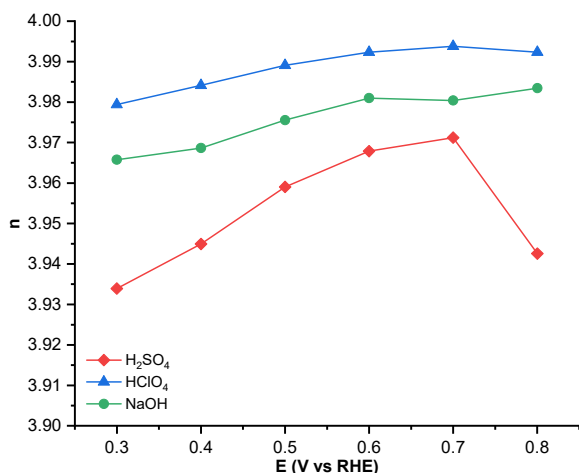


**Fig 6.** The electron transfer number for Pt/C in the different mediums at the potential range 0.8–0.3 V vs RHE

high O<sub>2</sub> saturation, lower viscosity, and weaker adsorption species increase the activity of ORR [21]. For example, the strongest adsorption is in H<sub>2</sub>SO<sub>4</sub>, and the weakest adsorption is in the solution of HClO<sub>4</sub> [22].

Tables 3 to 5 shows the result of the Pt/C test in the various electrolytes compared to the literature. The resulting test in our study was close to the literature. The slight difference between our test and the literature was due to a slightly different loading on the GC surface. In general, the test of the cell system obtained from this study was quite good. Therefore, the system we used is quite reliable with good confidence in determining unknown electrocatalysts from a sample.

### The Electrocatalytic Performance of [Tb(TPP)(cyclen)]Cl

The measurement of the sample of [Tb(TPP)(cyclen)]Cl was conducted using the RRDE method at the potential range of 1.03 to 0.05 V vs RHE with the scanning rate of 5 mV/s and rotation rate of 200, 400, 900, 1600 and 2500 rpm to obtain the polarization curve in the O<sub>2</sub> saturated solution of NaOH 0.1 M. This choice of solution was considered due to the best stability of the sample in the alkaline media. Besides, in the alkaline media, the rate of the oxygen reduction reaction is faster [17]. The current obtained from the measurement was normalized with a surface ( $S_g$ ) of about 0.126 cm<sup>2</sup>. Fig. 7 shows the voltammetry profile of [Tb(TPP)(cyclen)]Cl in O<sub>2</sub> saturated electrolyte solution, in which the current density increases with the increase of rotation rate from 200 to 2500 rpm, similar to the Pt/C standard. Table 6 shows the  $E_{onset}$ ,  $E_{1/2}$ ,  $\eta$ ,  $\eta$  (exp), and sluggishness of the polarization curve at 2500 rpm of the drop casted sample of [Tb(TPP)(cyclen)]Cl. [Tb(TPP)(cyclen)]Cl showed lower  $E_{onset}$  and  $E_{1/2}$  values than Pt/C in the electrolyte solution. This indicated that [Tb(TPP)(cyclen)]Cl had less catalytic activity than Pt/C. Theoretically, the  $E_{onset}$  and  $E_{1/2}$  that represent the electrocatalysis activity showed that [Tb(TPP)(cyclen)]Cl was 2.16 times slower than Pt/C.

The linearity of the Koutecky-Levich plot was quite good for [Tb(TPP)(cyclen)]Cl (see Fig. 8). Kinetic current

**Table 3.** The comparison of the test of Pt/C standard in H<sub>2</sub>SO<sub>4</sub> 0.5 M and the literature

Electrolyte of	Pt loading	$E_{onset}$	$E_{1/2}$
0.5 M H <sub>2</sub> SO <sub>4</sub>	( $\mu\text{g}_{\text{Pt}}/\text{cm}^2$ )	(V vs RHE)	(V vs RHE)
In this study	31.8	0.84	0.74
Sun et al. [23]	19.4	0.95	0.78

**Table 4.** The comparison of the test of Pt/C standard in HClO<sub>4</sub> 0.1 M and the literature

Electrolyte of	Pt loading	$E_{onset}$	$E_{1/2}$	$n$ , 0.5 V	$j_l^{\text{diff}}$ (mA/cm <sup>2</sup> ),
0.1 M HClO <sub>4</sub>	( $\mu\text{g}_{\text{Pt}}/\text{cm}^2$ )	(V vs RHE)	(V vs RHE)	vs RHE	1600 rpm
In this study	31.8	0.89	0.78	3.99	5.68
Wu et al. [24]	30	0.86	0.78	3.96	5.37

**Table 5.** The comparison of the test of Pt/C standard in NaOH 0.1 M and in the literature

Electrolyte of	Pt loading	$E_{onset}$	$E_{1/2}$	$n$ , 0.7 V	$j_l^{\text{diff}}$ (mA/cm <sup>2</sup> ),
0.1 M NaOH	( $\mu\text{g}_{\text{Pt}}/\text{cm}^2$ )	(V vs RHE)	(V vs RHE)	vs RHE	1600 rpm
In this study	31.8	0.89	0.8	3.98	4.39
Holade et al. [25]	26	1.005	0.85	4	4.7



density ( $j_k$ ) was normalized with the mass of [Tb(TPP)(cyclen)]Cl that was drop-casted on the surface disk (20  $\mu\text{g}$ ). The value of  $j_k$  at 0.8 V vs RHE for the catalytic activity of [Tb(TPP)(cyclen)]Cl was about 0.06  $\text{mA}/\text{cm}^2 \text{ mg}$ .

The plot was based on Eq (2) as shown in Fig. 9, in which the value of  $j_L$  was determined from the plot extrapolation. The value of  $j_L$  for [Tb(TPP)(cyclen)]Cl was about 0.52  $\text{mA}/\text{cm}^2$ .

The Relative Tafel plot for [Tb(TPP)(cyclen)]Cl is shown in Fig. 10. Information about the value of the Tafel slope ( $b$ ) and exchange current density ( $j_0$ ) could be obtained from this plot. The  $b$  value obtained was about 117  $\text{mV}/\text{dec}$ , close to 120  $\text{mV}/\text{dec}$ , and the  $j_0$  was about  $4.30 \times 10^{-7} \text{ mA}/\text{cm}^2$ . The value of  $j_0$  [Tb(TPP)(cyclen)]Cl was lower than Pt/C ( $4.92 \times 10^{-3}$ ). This means that with a similar overpotential, the increase of the current density of [Tb(TPP)(cyclen)]Cl was much lower, and the kinetic charge exchange occurred very slowly.

The polarization curve of RRDE (Fig. 11) showed the current on the disk and the ring. The electron number at a certain potential range was obtained from the data

of the polarization curve of RRDE using Eq. (5). The result of the  $n$  electron transfer number is shown in Fig. 12. [Tb(TPP)(cyclen)]Cl showed a fairly stable  $n$  electron transfer curve at a certain range of potentials. The  $n$  electron transfer increased with the decrease of the average potential at about 2.38. This result was still an inferior value compared to the  $n$ -transfer electron ideal, such as Pt at about 4. This result also indicated that

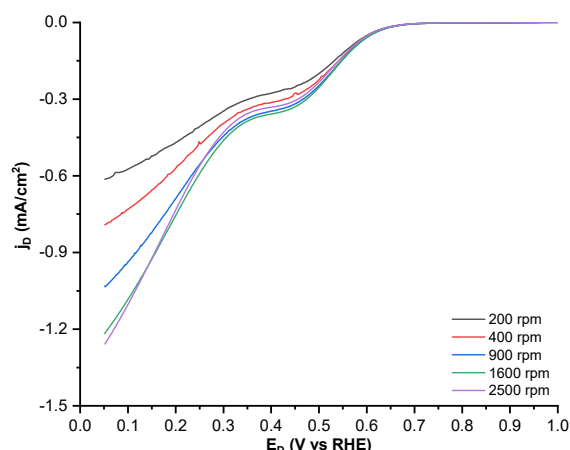


Fig 7. Polarization curve of [Tb(TPP)(cyclen)]Cl in the electrolyte of NaOH 0.1 M in the different rotation rates

Table 6. Parameter of polarization curve for [Tb(TPP)(cyclen)]Cl and comparison with Pt/C

Electrocatalyst	$E_{\text{onset}}$ (V vs RHE)	$E_{1/2}$ (V vs RHE)	$\eta$ (mV)	$\eta_{(\text{exp})}$ (mV)	Sluggishness (mV)
[Tb(TPP)(cyclen)]Cl	0.62	0.53	283	558	275
Pt/C 20%	0.89	0.80	167	296	129

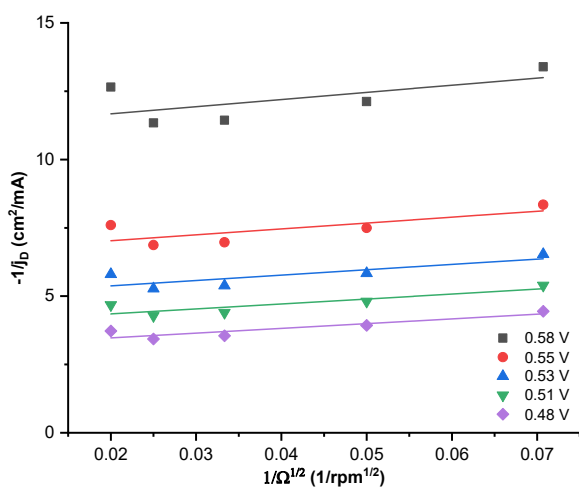


Fig 8. Koutecky-Levich plot determined from Fig. 7 for [Tb(TPP)(cyclen)]Cl in NaOH 0.1 M solution

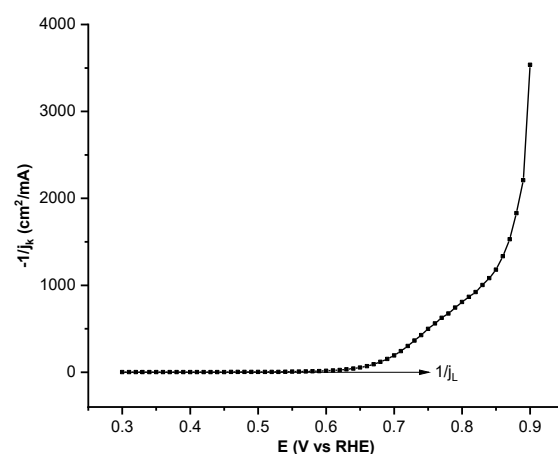


Fig 9. The plot of " $j_k^{-1}$  vs.  $E$ " for the determination of limiting current density ( $j_L$ ) for [Tb(TPP)(cyclen)]Cl in NaOH 0.1 M solution.

the ORR mechanism of [Tb(TPP)(cyclen)]Cl was via the (2 + 2) mechanism, where O<sub>2</sub> was first reduced to H<sub>2</sub>O<sub>2</sub>, followed by the reduction of H<sub>2</sub>O<sub>2</sub> to H<sub>2</sub>O.

The resume test result of [Tb(TPP)(cyclen)]Cl in the NaOH 0.1 M solution is shown in Table 7. The kinetic parameter of [Tb(TPP)(cyclen)]Cl was not ideal compared to Pt/C. This indicated that [Tb(TPP)(cyclen)]Cl was inappropriate material for the electrocatalysis of ORR. Some literature reported that this compound was mostly used for the magnetism application.

The catalytic performance of [Tb(TPP)(cyclen)]Cl can be explained by its structure energy level. Zhang and Xia [26] explained that the separation energy of the highest occupied molecular orbital (HOMO) and the lowest unoccupied molecular orbital (LUMO) could be used as a simple kinetic stability indicator. The low energy band gap of HOMO-LUMO indicated low kinetic stability and high chemical reactivity. The low HOMO-LUMO energetically was advantageous to increase the electron for high-lying LUMO and to extract electrons from low-lying HOMO. When comparing to the FePc

(Fe-phthalocyanine) from Ma et al. [27], it can be seen that FePc owed the lower HOMO-LUMO gap with better electrocatalytic performance compared to [Tb(TPP)(cyclen)]Cl (Fig. 13). The E<sub>onset</sub> and j<sub>k</sub> are shown in Table 8. The lower value of E<sub>onset</sub> and j<sub>k</sub> indicated that the electrocatalytic performance of [Tb(TPP)(cyclen)]Cl was not better than FePc.

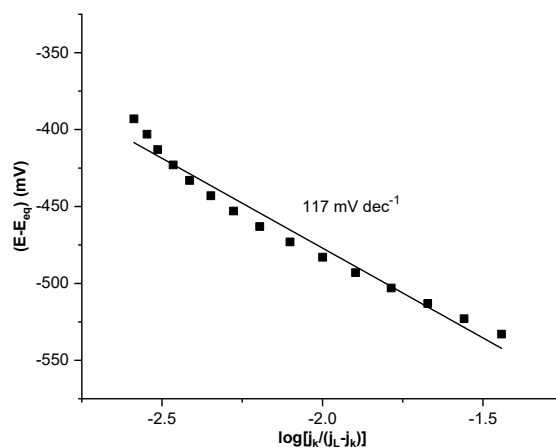


Fig 10. Relative Tafel plot for [Tb(TPP)(cyclen)]Cl in NaOH 0.1 M solution

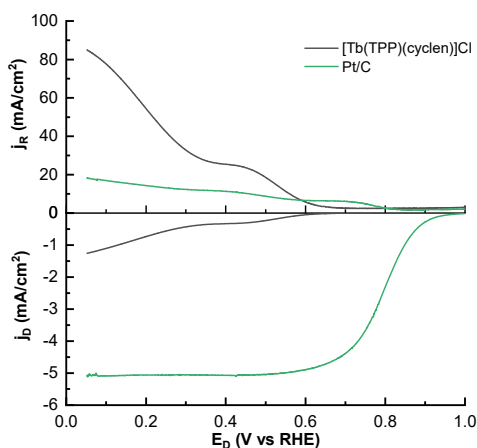


Fig 11. Polarization curve of RRDE for [Tb(TPP)(cyclen)]Cl and its comparison to Pt/C in the NaOH 0.1 M electrolyte at 2500 rpm

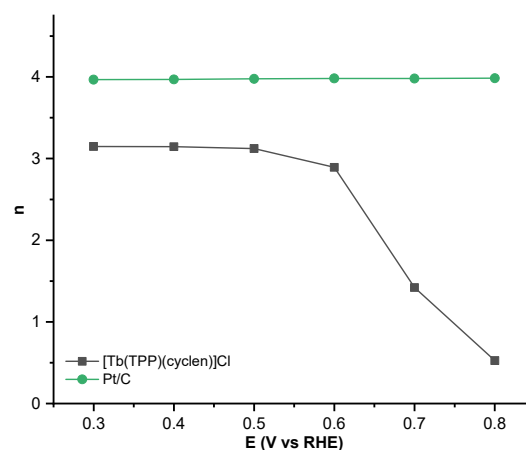
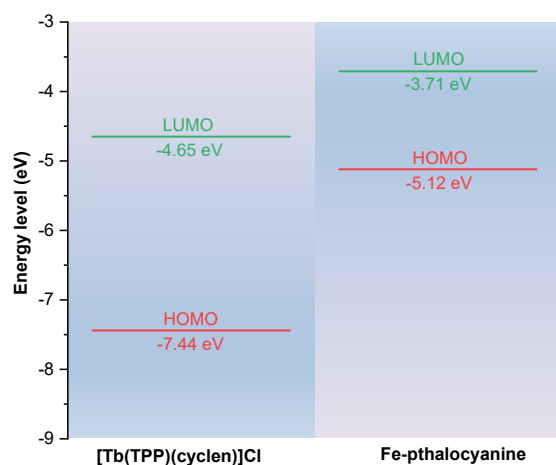


Fig 12. The n electron number of [Tb(TPP)(cyclen)]Cl and its comparison to Pt/C in NaOH 0.1 M solution at potential range of 0.8-0.3 V vs RHE

Table 7. Kinetic parameter of ORR of [Tb(TPP)(cyclen)]Cl and its comparison towards Pt/C

Electrocatalyst	n	j <sub>k</sub> (mA/cm <sup>2</sup> mg) at 0.8 V vs. RHE	j <sub>L</sub> (mA/cm <sup>2</sup> )	B (mV/dec)	j <sub>0</sub> (mA/cm <sup>2</sup> )
[Tb(TPP)(cylene)]Cl	2.38	0.06	0.52	117	4.30 × 10 <sup>-7</sup>
Pt/C 20%	3.98	132.79	32.03	134	4.92 × 10 <sup>-3</sup>



**Fig 13.** [Tb(TPP)(cyclen)]Cl and FePc energy level comparison

**Table 8.** Comparison of [Tb(TPP)(cyclen)]Cl and FePc

	[Tb(TPP)(cyclen)]Cl	FePc [27]
HOMO (eV)	-7.44	-5.12
LUMO (eV)	-4.65	-3.71
HOMO-LUMO gap (eV)	2.79	1.41
$E_{\text{onset}}$ (V vs RHE)	0.62	0.958
$j_k$ at 0.9 V ( $\text{mA}/\text{cm}^2$ )	$2.83 \times 10^{-4}$	1.417

## CONCLUSION

In the different electrolyte solutions, the Pt/C standard showed good results with an almost similar parameter value according to the literature ( $n$  close to 4). Meanwhile, the [Tb(TPP)(cyclen)]Cl sample was not a superior material for ORR electrocatalysis with an  $n$  electron transfer number of about 2.38. The result met the theoretical calculation of the HOMO-LUMO gap using DFT of about 2.79 eV, almost double to FePc (1.41 eV).

## ACKNOWLEDGMENTS

This work was partly achieved through the use of Supercomputer System SQUID at the Cybermedia Center, Osaka University.

## REFERENCES

- [1] Özgür, T., and Yakaryılmaz, A.C., 2018, A review: Exergy analysis of PEM and PEM fuel cell based CHP systems, *Int. J. Hydrogen Energy*, 43 (38), 17993–18000.
- [2] Park, K.Y., Sweers, M.E., Berner, U., Hirth, E., Downing, J.R., Hui, J., Mailoa, J., Johnston, C., Kim, S., Seitz, L.C., and Hersam, M.C., 2022, Mitigating Pt loss in polymer electrolyte membrane fuel cell cathode catalysts using graphene nanoplatelet pickering emulsion processing, *Adv. Funct. Mater.*, 32 (43), 2205216.
- [3] Gewirth, A.A., Varnell, J.A., and DiAscro, A.M., 2018, Nonprecious metal catalysts for oxygen reduction in heterogeneous aqueous systems, *Chem. Rev.*, 118 (5), 2313–2339.
- [4] Liu, M., Zhao, Z., Duan, X., and Huang, Y., 2019, Nanoscale structure design for high-performance Pt-based ORR catalysts, *Adv. Mater.*, 31 (6), 1802234.
- [5] Lv, H., Guo, H., Guo, K., Lei, H., Zhang, W., Zheng, H., Liang, Z., and Cao, R., 2021, Substituent position effect of Co porphyrin on oxygen electrocatalysis, *Chin. Chem. Lett.*, 32 (9), 2841–2845.
- [6] Liu, L., Ma, M., Xu, H., Yang, X., Lu, X., Yang, P., and Wang, H., 2022, S-doped M-N-C catalysts for the oxygen reduction reaction: Synthetic strategies, characterization, and mechanism, *J. Electroanal. Chem.*, 920, 116637.
- [7] Zhou, Y., Xing, Y.F., Wen, J., Ma, H.B., Wang, F.B., and Xia, X.H., 2019, Axial ligands tailoring the ORR activity of cobalt porphyrin, *Sci. Bull.*, 64 (16), 1158–1166.
- [8] Li, Y., Wang, N., Lei, H., Li, X., Zheng, H., Wang, H., Zhang, W., and Cao, R., 2021, Bioinspired  $N_4$ -metallomacrocycles for electrocatalytic oxygen reduction reaction, *Coord. Chem. Rev.*, 442, 213996.
- [9] Liang, Z., Wang, H.Y., Zheng, H., Zhang, W., and Cao, R., 2021, Porphyrin-based frameworks for oxygen electrocatalysis and catalytic reduction of carbon dioxide, *Chem. Soc. Rev.*, 50 (4), 2540–2581.
- [10] Santria, A., Fuyuhiko, A., Fukuda, T., and Ishikawa, N., 2017, Synthesis of a series of heavy lanthanide (III) monoporphyrinato complexes with tetragonal symmetry, *Inorg. Chem.*, 56 (17), 10625–10632.
- [11] Shao, M., Chang, Q., Dodelet, J.P., and Chenitz, R., 2016, Recent advances in electrocatalysts for oxygen reduction reaction, *Chem. Rev.*, 116 (6), 3594–3657.

- [12] Ruan, M., Liu, J., Song, P., and Xu, W., 2022, Meta-analysis of commercial Pt/C measurements for oxygen reduction reactions *via* data mining, *Chin. J. Catal.*, 43 (1), 116–121.
- [13] Dolg, M., Stoll, H., and Preuss, H., 1989, Energy-adjusted *ab initio* pseudopotentials for the rare earth elements, *J. Chem. Phys.*, 90 (3), 1730–1734.
- [14] Grimme, S., Antony, J., Ehrlich, S., and Krieg, H., 2010, A consistent and accurate *ab initio* parametrization of density functional dispersion correction (DFT-D) for the 94 elements H-Pu, *J. Chem. Phys.*, 132 (15), 154104.
- [15] Petersson, G.A., and Al-Laham, M.A., 1991, A complete basis set model chemistry. II. Open-shell systems and the total energies of the first-row atoms, *J. Chem. Phys.*, 94 (9), 6081–6090.
- [16] Wang, Q., Guesmi, H., Tingry, S., Cornu, D., Holade, Y., and Minteer, S.D., 2022, Unveiling the pitfalls of comparing oxygen reduction reaction kinetic data for Pd-based electrocatalysts without the experimental conditions of the current–potential curves, *ACS Energy Lett.*, 7 (3), 952–957.
- [17] Mukherjee, M., Samanta, M., Ghorai, U.K., Murmu, S., Das, G.P., and Chattopadhyay, K.K., 2018, One pot solvothermal synthesis of ZnPc nanotube and its composite with RGO: A high performance ORR catalyst in alkaline medium, *Appl. Surf. Sci.*, 449, 144–151.
- [18] Hebié, S., Bayo-Bangoura, M., Bayo, K., Servat, K., Morais, C., Napporn, T.W., and Boniface Kokoh, K., 2016, Electrocatalytic activity of carbon-supported metallophthalocyanine catalysts toward oxygen reduction reaction in alkaline solution, *J. Solid State Electrochem.*, 20 (4), 931–942.
- [19] Napporn, T.W., Holade, Y., Kokoh, B., Mitsushima, S., Mayer, K., Eichberger, B., and Hacker, V., 2018, "Electrochemical Measurement Methods and Characterization on the Cell Level" in *Fuel Cells and Hydrogen*, Eds. Hacker, V., and Mitsushima, S., Elsevier, Amsterdam, Netherlands, 175–214.
- [20] Garsany, Y., Baturina, O.A., Swider-Lyons, K.E., and Kocha, S.S., 2010, Experimental methods for quantifying the activity of platinum electrocatalysts for the oxygen reduction reaction, *Anal. Chem.*, 82 (15), 6321–6328.
- [21] Jin, W., Du, H., Zheng, S., Xu, H., and Zhang, Y., 2010, Comparison of the oxygen reduction reaction between NaOH and KOH solutions on a Pt electrode: The electrolyte-dependent effect, *J. Phys. Chem. B*, 114 (19), 6542–6548.
- [22] Wang, X., Li, Z., Qu, Y., Yuan, T., Wang, W., Wu, Y., and Li, Y., 2019, Review of metal catalysts for oxygen reduction reaction: From nanoscale engineering to atomic design, *Chem*, 5 (6), 1486–1511.
- [23] Sun, T., Wu, Q., Che, R., Bu, Y., Jiang, Y., Li, Y., Yang, L., Wang, X., and Hu, Z., 2015, Alloyed Co–Mo nitride as high-performance electrocatalyst for oxygen reduction in acidic medium, *ACS Catal.*, 5 (3), 1857–1862.
- [24] Wu, Z.S., Chen, L., Liu, J., Parvez, K., Liang, H., Shu, J., Sachdev, H., Graf, R., Feng, X., and Müllen, K., 2014, High-performance electrocatalysts for oxygen reduction derived from cobalt porphyrin-based conjugated mesoporous polymers, *Adv. Mater.*, 26 (9), 1450–1455.
- [25] Holade, Y., Servat, K., Napporn, T.W., and Kokoh, K.B., 2015, Electrocatalytic properties of nanomaterials synthesized from “bromide anion exchange” method - Investigations of glucose and glycerol oxidation, *Electrochim. Acta*, 162, 205–214.
- [26] Zhang, L., and Xia, Z., 2011, Mechanisms of oxygen reduction reaction on nitrogen-doped graphene for fuel cells, *J. Phys. Chem. C*, 115 (22), 11170–11176.
- [27] Ma, Y., Li, J., Liao, X., Luo, W., Huang, W., Meng, J., Chen, Q., Xi, S., Yu, R., Zhao, Y., Zhou, L., and Mai, L., 2020, Heterostructure design in bimetallic phthalocyanine boosts oxygen reduction reaction activity and durability, *Adv. Funct. Mater.*, 30 (50), 2005000.

## Copper-and-Nitrogen-Codoped Zirconium Titanate (Cu-N-ZrTiO<sub>4</sub>) as a Photocatalyst for Photo-Degradation of Methylene Blue under Visible-Light Irradiation

Lenny Rahmawati<sup>1</sup>, Rian Kurniawan<sup>2</sup>, Niko Prasetyo<sup>1</sup>, Sri Sudiono<sup>1</sup>, and Akhmad Syoufian<sup>1\*</sup>

<sup>1</sup>Department of Chemistry, Faculty of Mathematics and Natural Sciences, Universitas Gadjah Mada, Sekip Utara, Yogyakarta 55281, Indonesia

<sup>2</sup>Institute of Chemical Technology, Universität Leipzig, Linnéstr. 3, 04103 Leipzig, Germany

\* **Corresponding author:**

email: akhmadsyoufian@ugm.ac.id

Received: November 5, 2022

Accepted: December 29, 2022

DOI: 10.22146/ijc.78908

**Abstract:** Synthesis and characterization of copper-and-nitrogen-codoped zirconium titanate (Cu-N-ZrTiO<sub>4</sub>) as a photocatalyst for the degradation of methylene blue (MB) have been conducted. The main purpose of this research was to investigate the co-doping effect of copper and nitrogen dopants in ZrTiO<sub>4</sub> as a photocatalyst for the photodegradation of MB. Titanium-(IV) tetraisopropoxide (TTIP) was dissolved into ethanol and mixed with aqueous zirconia (ZrO<sub>2</sub>) suspension containing 10% nitrogen (N) (w/w to Ti) from urea and various amount of copper as dopants. The calcination was performed at temperatures of 500, 700, and 900 °C. The composites were characterized using Fourier transform infrared spectrophotometer (FTIR), X-ray diffractometer (XRD), scanning electron microscopy with energy dispersive X-ray (SEM-EDX) mapping, and specular reflectance UV-Visible spectrophotometer (SRUV-Vis). The degradation of 4 mg L<sup>-1</sup> MB solution was conducted for various irradiation times. Characterization shows a significant decrease of the ZrTiO<sub>4</sub> band gap from 3.09 to 2.65 eV, which was given by the composite with the addition of 4% Cu and calcination of 900 °C. Cu-N-ZrTiO<sub>4</sub> composite can degrade MB solution up to 83% after 120 min under the irradiation of visible light.

**Keywords:** band gap; degradation; methylene blue; Cu-N-codoped ZrTiO<sub>4</sub>

### ■ INTRODUCTION

Dyes are one of the larger groups of pollutants in wastewater from textiles and other industrial processes that can contaminate the environment. Most of the dyes have stable aromatic molecular structures, large molecular sizes, and are difficult to degrade in nature [1]. One of the dyes found in wastewater is methylene blue. Methylene blue (C<sub>16</sub>H<sub>18</sub>N<sub>3</sub>SCl) is a cationic heterocyclic aromatic compound that is used in the textile industry as a dye, but its waste has ecological toxicity and carcinogenicity [2]. Several waste decomposition methods have been developed, such as ozonation, chlorination, and biodegradation. However, these methods have several disadvantages, such as high operational costs and the use of chemical reagents [3]. Therefore, an alternative method is needed for wastewater treatment that can accelerate the decomposition of dye waste. The photo-degradation

method is effective for wastewater treatment because it is relatively inexpensive and easy to apply [4].

Degradation of dye waste has become a vital necessity to solve environmental problems and photocatalytic systems have received great attention for the removal of contamination [5]. In the photocatalytic process, light energy is required for the excitation of the photocatalyst. Photocatalyst is a photoactive material that uses photons to catalyze a reaction [6]. In heterogeneous photocatalysis, the photocatalyst is a metal oxide semiconductor with a corresponding band gap energy of about 1.7–3.2 eV [7]. Several semiconductor materials are currently being developed and investigated as photocatalysts, such as Fe<sub>2</sub>O<sub>3</sub> [8], CuO [9], ZnO [10], and ZrO<sub>2</sub>-TiO<sub>2</sub> [11]. The mechanism of photo-degradation of organic compounds by a photocatalyst is presented in Fig. 1.

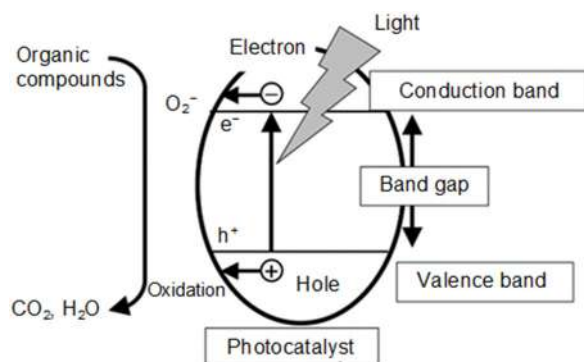
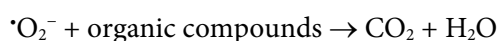
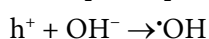
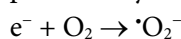
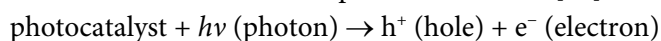


**Fig 1.** Mechanism of photocatalytic reactions of organic compounds [12]

The reaction can be explained as follows [13].



Titanium dioxide (TiO<sub>2</sub>) is widely used in photocatalytic reactions because it is non-toxic, stable, and has high efficiency in the degradation of organic pollutants [14]. The three phases of TiO<sub>2</sub> are rutile, anatase, and brookite. Rutile is the most stable phase of TiO<sub>2</sub>, anatase is metastable, and brookite will transform to rutile at temperatures above 600 °C [15]. The anatase phase of TiO<sub>2</sub> has a band gap energy of 3.20 eV, while the rutile has 3.02 eV. Although the band gap of anatase (3.20 eV) is slightly higher than rutile (3.02 eV), it exhibits superior photoactivity under UV light irradiation to that of rutile [16]. The degradation of methylene blue by several photocatalysts has been presented in Table 1. Synthesis of TiO<sub>2</sub>-S has been reported to degrade methylene blue up to 69.49% under visible light for 300 min of irradiation time [17]. The percentage of degradation of methylene blue by TiO<sub>2</sub> with dopants carbon (C) and nitrogen (N) reached 87% under visible light irradiation [18].

Zirconium dioxide (ZrO<sub>2</sub>) is a p-type semiconductor with a wide band gap in the range of 3.25–5.00 eV. ZrO<sub>2</sub> has low thermal conductivity, corrosive resistance, high mechanical, and stable photothermal properties [21]. ZrO<sub>2</sub> has good stability and easily produces holes in the valence band, leading to strong interactions with the active component. ZrO<sub>2</sub> has three

**Table 1.** Percent degradation of methylene blue by several photocatalysts

Photocatalysts	Percent degradation (%)
TiO <sub>2</sub> -S	69.49 [17]
N-codoped TiO <sub>2</sub>	87.00 [18]
N-doped TiO <sub>2</sub> /ZrO <sub>2</sub>	86.30 [19]
ZrO <sub>2</sub> -TiO <sub>2</sub>	81.20 [20]

polymorphic phases, including cubic (above 2370 °C), tetragonal (1170–2370 °C), and monoclinic (below 1170 °C) [22]. ZrO<sub>2</sub> is active under UV light; therefore, it needs to be modified to increase photocatalytic activity. The way to increase the photocatalytic activity of ZrO<sub>2</sub> is to combine it with a TiO<sub>2</sub> semiconductor. The addition of ZrO<sub>2</sub> to TiO<sub>2</sub> has been reported to increase the stability of anatase more than rutile [23]. ZrO<sub>2</sub> has been known as a support material for TiO<sub>2</sub>. The presence of Zr<sup>4+</sup> in TiO<sub>2</sub> will increase the stability of the anatase at high temperatures (900 °C) [24].

Coupling ZrO<sub>2</sub> with TiO<sub>2</sub> will give the advantages of a large surface area, thermal stability, and resistance to heat and corrosion [25]. Zirconium titanate (ZrTiO<sub>4</sub>) modified by the doping method will decrease the band gap to visible light. Several studies have reported that doping can be done with metals such as Fe [26], Mn [27], and Zn [28] and also non-metals such as N [29] and C [30]. In this study, copper (Cu) and nitrogen (N) were chosen as dopants because they have good charge-carrier separation efficiency. Nitrogen (N) is one of the elements that is effective in improving the mechanical properties and conductivity of metal oxide ions [31]. Several methods of preparing ZrTiO<sub>4</sub> codoped by Cu-N have been reported, such as the template-free hydrothermal method [32] and the polymer complex solution method [33]. Both methods still use toxic organic solvents, which are expensive and not environmentally friendly.

In this research, copper and nitrogen were codoped into ZrTiO<sub>4</sub> composite through the simple-and-environmentally-friendly sol-gel process. The goals of this study are to investigate the co-doping effects of metal-nonmetal (Cu and N) on ZrTiO<sub>4</sub> composite and its application as a photocatalyst to degrade methylene blue under visible light illumination. Various amounts of copper dopant (2, 4, 6, 8, and 10% (w/w to titanium))

were used to study their performance in shifting the bandgap of nitrogen-doped ZrTiO<sub>4</sub>. Variation of calcination temperatures (500, 700, and 900 °C) was carried out to study the stability of the crystal structure and its influence on the photocatalytic activity of the composite. Furthermore, photocatalytic evaluation was done by applying Cu-N-ZrTiO<sub>4</sub> as a photocatalyst to degrade methylene blue under visible light irradiation for 120 min.

## ■ EXPERIMENTAL SECTION

### Materials

Titanium(IV) tetraisopropoxide (TTIP, 97% purity, Sigma-Aldrich) was used as a TiO<sub>2</sub> precursor, and zirconia powder (ZrO<sub>2</sub>, Jiaozuo Huasu) was used as the coupling metal oxide. Copper(II) sulfate pentahydrate (CuSO<sub>4</sub>·5H<sub>2</sub>O, Merck) and urea (Merck) were used as dopant sources. Absolute ethanol (99.5% purity, Merck) and demineralized water (Jaya Sentosa) were used as solvents. Methylene blue (MB) (Thermo Fisher Scientific India Pvt. Ltd.) was used as a dye for the photocatalytic test.

### Instrumentation

Fourier transform infrared spectroscopy (FTIR) was done to observe absorption from the range of 400 to 4000 cm<sup>-1</sup> using the Thermo Nicolet iS10 (Thermo Fisher Scientific, USA). X-ray powder diffractometer (XRD) PANalytical X'Pert PRO MRD (Liaoning, China, Cu Kα radiation λ = 1.54 Å, 40 kV, 30 mA) was used to examine the crystalline structure of the materials. The crystal size (L) was calculated by the Scherrer equation [34],

$$L = \frac{0.9\lambda}{B \cos\theta}$$

where λ is the wavelength of the X-ray, θ is the Bragg angle, and B is half the full width of the maximum intensity of the peak in radians. The morphology of photocatalyst and the presence of copper-nitrogen were observed by scanning electron microscope equipped with an energy dispersive X-ray spectrometer (SEM-EDX) JSM-6510LA (Bridge Tronic Global, USA) and an accelerating voltage of 15 kV. The bandgap was determined from the absorption spectra obtained using specular reflectance UV-Vis spectrometer UV (SR-UV)

1700 Pharmaspec (Shimadzu, Japan). The band gap energy was calculated based on the absorption edge cross method of the absorbance spectra using the photon energy function [35],

$$E_g = \frac{hc}{\lambda}$$

where E<sub>g</sub> is the band gap energy (eV), h is Planck's constant (6.62607 × 10<sup>-34</sup> J/s), c is the speed of light (3 × 10<sup>8</sup> m), and λ is the edge wavelength (nm). Photocatalytic degradation of MB was tested using a LIFE MAX 30W/765 PHILIPS TLD lamp. The concentration of MB solution after degradation was determined by absorption at 664 nm using a Thermo Scientific Genesys 50 UV-Vis Spectrophotometer (Antylia Scientific, US).

### Procedure

#### Synthesis of Cu-N-ZrTiO<sub>4</sub>

Copper-and-nitrogen-codoped zirconium titanate were prepared by the sol-gel method. Initially, 2.5 mL of TTIP was dissolved in 25 mL of absolute ethanol and then stirred homogeneously. Amount of 1 g of ZrO<sub>2</sub> powder and 86.8 mg of urea (10% w/w to Ti) were dispersed into 10 mL of demineralized water along with 30.4, 63.5, 95.2, and 127 mg of CuSO<sub>4</sub>·5H<sub>2</sub>O. The copper concentration was varied with a ratio of 2, 4, 6, 8, and 10% (w/w to Ti). The mixture was stirred for 30 min. To separate the precipitate, the suspension was centrifuged at 2000 rpm for 1 h. The precipitate was aged in ambient condition for 24 h and then dried at 80 °C for 24 h. Finally, the composites were calcined at temperatures of 500, 700, and 900 °C for 4 h under atmospheric conditions. All composites were characterized using FTIR, XRD, SEM-EDX, and SRUV-Vis. N-doped ZrTiO<sub>4</sub> composite without Cu was also prepared as a reference.

#### Photocatalytic degradation of methylene blue

Firstly, 15 mg of Cu-N-ZrTiO<sub>4</sub> with various concentrations of Cu dopant was dispersed in 30 mL of 4 mg L<sup>-1</sup> aqueous MB. Under continuous stirring, the mixture was irradiated with a LIFE MAX 30W/765 PHILIPS TLD lamp for 15, 30, 45, 60, 75, 90, 105, and 120 min. The solution was centrifuged for 30 min at

3000 rpm to separate the photocatalyst. The concentration of MB after photocatalytic degradation was determined by absorption at 664 nm. Quantitative analysis of enhanced photocatalytic decomposition of MB was examined by employing a pseudo-first-order kinetic model [36]:

$$-\frac{dC}{dt} = k_{\text{obs}}C$$

in which,

$$\ln C = -k_{\text{obs}}t + \ln C_0$$

where  $C$  is the concentration of MB ( $\text{mg L}^{-1}$ ),  $t$  is irradiation time (min), and  $k_{\text{obs}}$  is the observed rate constant for the photocatalytic decomposition ( $\text{mg L}^{-1} \text{min}^{-1}$ ). Plots were given for irradiation time of 0 to 60 min as the highest photoactivity was observed in this time interval.

## RESULTS AND DISCUSSION

FTIR characterization was conducted to determine the functional groups in Cu-N-ZrTiO<sub>4</sub>. FTIR spectra of 4% Cu-N-ZrTiO<sub>4</sub> is shown in Fig. 2. ZrO<sub>2</sub> and N-doped ZrTiO<sub>4</sub> materials were used as references. The broad absorption band in the range of 500–600  $\text{cm}^{-1}$  can be attributed to the stretching vibrations of Ti–O and Cu–O [14]. The peaks at the wavenumber of 512 and 1635  $\text{cm}^{-1}$  are associated with the Zr–O and Zr–OH vibrational bands, respectively, which confirm the presence of ZrO<sub>2</sub> [21]. The absorption band at about 1120  $\text{cm}^{-1}$  increases up to 4% Cu co-doping, which could potentially be associated with Cu–O–Zr or Cu–O–Ti bonds, or both [18]. The peak intensity of ZrO<sub>2</sub> at 1600  $\text{cm}^{-1}$ , which is H–O–H bending [5], indicates a shift in vibration absorption to 1570  $\text{cm}^{-1}$  in N-doped ZrTiO<sub>4</sub> due to the formation of N–Ti–O.

The absorption band that appears around 3400  $\text{cm}^{-1}$  in all samples is recognized as the O–H stretching vibration of H<sub>2</sub>O [4]. It comes from the water molecules that are adsorbed during the synthesis process. FTIR spectra of 4% Cu-N-ZrTiO<sub>4</sub> calcined at 700 and 900 °C display a weak absorption of Zr–O at 500–600  $\text{cm}^{-1}$ . This is due to a phase transformation from anatase to rutile [17]. Absorption bands at 3300–3400 and 1600  $\text{cm}^{-1}$  decrease as the calcination temperature increases. The high

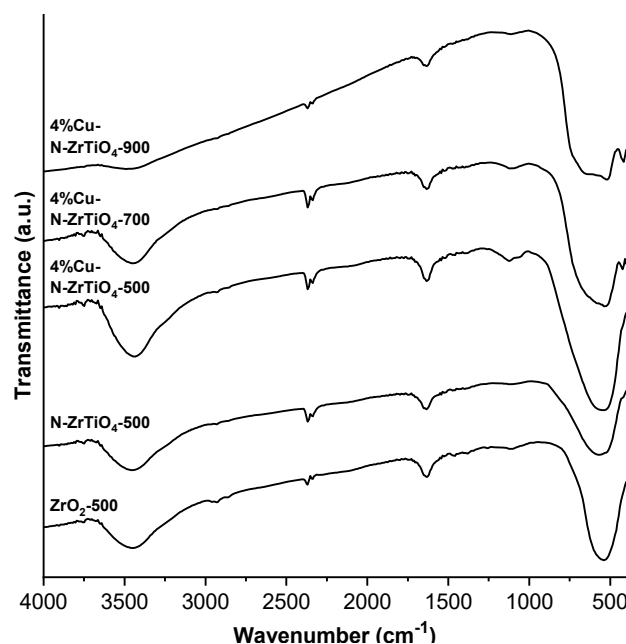


**Fig 2.** FTIR spectra of 4% Cu-N-ZrTiO<sub>4</sub> composites calcined at various temperatures with ZrO<sub>2</sub> and N-doped ZrTiO<sub>4</sub> as references

calcination temperature reduces the water content so that the O–H vibration frequency in the material decreases [6]. On the contrary, Ti–O–Cu vibration at 1120  $\text{cm}^{-1}$  decreases as calcination temperature increases up to 700 °C and disappears at 900 °C. The high calcination temperature causes the sintering of metal dopants [9].

Diffraction patterns of Cu-N-ZrTiO<sub>4</sub> with ZrO<sub>2</sub>, TiO<sub>2</sub>, ZrTiO<sub>4</sub>, and N-doped ZrTiO<sub>4</sub> as references are shown in Fig. 3. The diffraction patterns of ZrO<sub>2</sub> and TiO<sub>2</sub> calcined at 500 °C display the presence of tetragonal and anatase phases, respectively. The characteristic peaks of ZrO<sub>2</sub> tetragonal (JCPDS: 01-088-2390) appeared at  $2\theta = 31^\circ$  ( $d_{101}$ ) and  $51^\circ$  ( $d_{111}$ ). The characteristic peaks of TiO<sub>2</sub> anatase (JCPDS: 01-084-1286) appeared at  $2\theta = 25^\circ$  ( $d_{101}$ ) and  $48^\circ$  ( $d_{200}$ ). No Cu or CuO patterns were observed, even at 10% Cu-N-ZrTiO<sub>4</sub>.

The diffraction pattern of Cu-N-ZrTiO<sub>4</sub> calcined at 500 °C has a characteristic low-intensity anatase peak at  $25^\circ$  ( $d_{101}$ ). The presence of copper and nitrogen dopants inhibits the crystallization of anatase [13], while the presence of Zr<sup>4+</sup> in the TiO<sub>2</sub> system also inhibits the transformation of anatase to rutile [14]. The diffraction



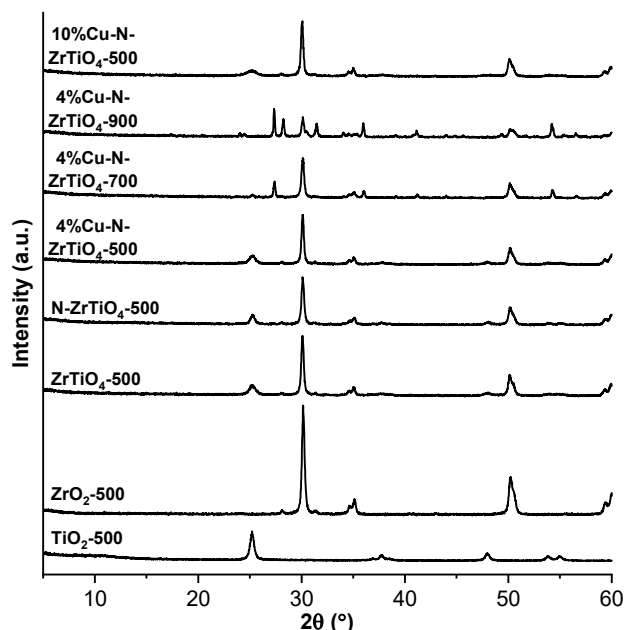


**Fig 3.** X-ray diffraction patterns of various Cu-N-ZrTiO<sub>4</sub> and references

pattern of ZrTiO<sub>4</sub> showed significant changes after calcination at higher temperatures. The diffraction pattern of 4% Cu-N-ZrTiO<sub>4</sub> composite after calcination at 700 °C showed rutile characteristics at  $2\theta = 27.5^\circ$  ( $d_{110}$ ) and  $36.1^\circ$  ( $d_{101}$ ), while the anatase peak at  $2\theta = 25^\circ$  ( $d_{101}$ ) disappeared. Moreover, the diffraction pattern of 4% Cu-N-ZrTiO<sub>4</sub> after calcination at 900 °C exhibits an intense rutile pattern (JCPDS: 01-076-1938) at  $2\theta = 27^\circ$  ( $d_{110}$ ),  $36^\circ$  ( $d_{101}$ ),  $41^\circ$  ( $d_{111}$ ) and  $54^\circ$  ( $d_{211}$ ), while the tetragonal phase transforms to monoclinic (JCPDS: 01-088-2390), displaying a pattern at  $2\theta = 28^\circ$  ( $d_{111}$ ),  $31^\circ$  ( $d_{111}$ ),  $34^\circ$  ( $d_{002}$ ) and  $51^\circ$  ( $d_{220}$ ).

The average crystallite size of Cu-N-ZrTiO<sub>4</sub>, particularly anatase and rutile, at various Cu concentrations and calcination temperatures has been shown in Table 2. The  $d_{101}$  reflex of the anatase phase and the  $d_{110}$  reflex of the rutile phase were chosen to calculate the crystallite size [15]. The crystallite size of the tetragonal phase shows no difference among Cu-N-ZrTiO<sub>4</sub>, except 4% Cu-N-ZrTiO<sub>4</sub> after calcination at 900 °C displays a monoclinic phase. The lower anatase crystallite size of all Cu-N-ZrTiO<sub>4</sub> compared to that of pristine TiO<sub>2</sub> indicates the inhibition of anatase crystallization by copper, which is doped properly in the structure of ZrTiO<sub>4</sub>.

SEM-EDX images of ZrO<sub>2</sub> and 4% Cu-N-ZrTiO<sub>4</sub> calcined at 500 °C are shown in Fig. 4. The morphology of 4% Cu-N-ZrTiO<sub>4</sub> appears slightly rougher than the ZrO<sub>2</sub> reference, while the particle size distribution of Cu-N-ZrTiO<sub>4</sub> is larger than ZrO<sub>2</sub>.

The surface elemental compositions of ZrO<sub>2</sub> and 4% Cu-N-ZrTiO<sub>4</sub> based on SEM images in Fig. 4 are presented in Table 3. The mass percentage of Zr is greater than Ti because Zr is a supporting material, so it will be more dominant [16]. The low amount of detected copper indicates that the Cu dopant was doped on the ZrTiO<sub>4</sub> surface [23].

SRUV-Vis spectra of Cu-N-ZrTiO<sub>4</sub> with various copper concentrations and calcination temperatures are shown in Fig. 5(a). The inflection point (absorption edge) of each synthesized photocatalyst is already at a wavelength of greater than 400 nm. This is due to the

**Table 2.** The average crystallite size of various Cu-N-ZrTiO<sub>4</sub>

Material	Crystal phase	L (nm)
TiO <sub>2</sub> 500 °C	Anatase	49
ZrTiO <sub>4</sub> 500 °C	Anatase	46
N-doped ZrTiO <sub>4</sub> 500 °C	Anatase	38
2% Cu-N-ZrTiO <sub>4</sub> 500 °C	Anatase	36
4% Cu-N-ZrTiO <sub>4</sub> 500 °C	Anatase	34
4% Cu-N-ZrTiO <sub>4</sub> 700 °C	Anatase	45
	Rutile	48
4% Cu-N-ZrTiO <sub>4</sub> 900 °C	Rutile	50
6% Cu-N-ZrTiO <sub>4</sub> 500 °C	Anatase	35
8% Cu-N-ZrTiO <sub>4</sub> 500 °C	Anatase	36
10% Cu-N-ZrTiO <sub>4</sub> 500 °C	Anatase	37

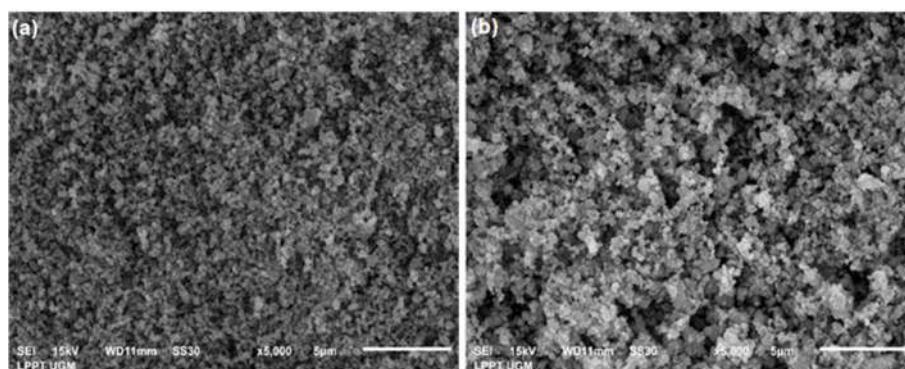


Fig 4. SEM images of (a)  $\text{ZrO}_2$  and (b) 4% Cu-N-ZrTiO<sub>4</sub> calcined at 500 °C

Table 3. EDX analysis of  $\text{ZrO}_2$  and 4% Cu-N-ZrTiO<sub>4</sub> calcined at 500 °C

Material	% Mass				
	Zr	O	Ti	N	Cu
$\text{ZrO}_2$	60.46	39.54	-	-	-
4% Cu-N-ZrTiO <sub>4</sub> 500 °C	30.76	38.92	23.96	3.93	2.43

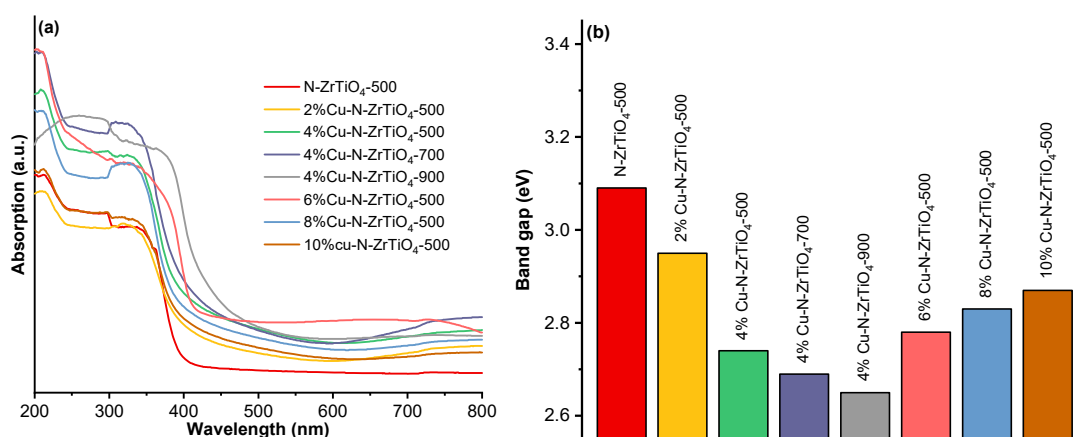
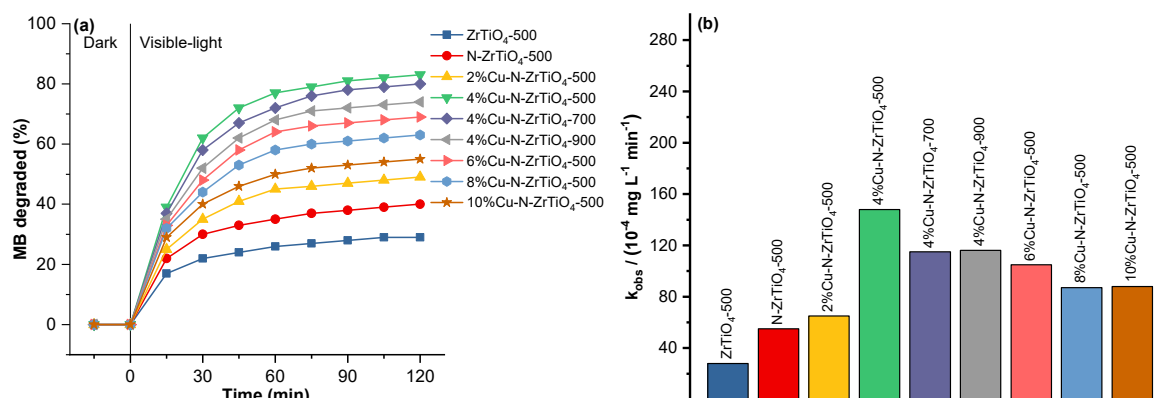


Fig 5. (a) UV-Vis absorption spectra and (b) calculated band gap of various Cu-N-ZrTiO<sub>4</sub>

heterojunction between the valence band and conduction band of  $\text{ZrO}_2$  with  $\text{TiO}_2$  [24]. The wide bandgap ( $E_g$ ) of  $\text{ZrO}_2$  mixes with the relatively small  $E_g$  of  $\text{TiO}_2$  until it reaches equilibrium, resulting in a  $\text{ZrTiO}_4$  band gap with a slightly smaller  $E_g$  [27]. Codoping of both nitrogen and copper shifts the absorption edge of the  $\text{ZrTiO}_4$  composite towards the visible light region until it reaches the saturation point [31]. If the injected dopants have reached the saturation point, the doping effect is reduced [28]. The addition of Cu and N dopants succeeded in shifting the absorption band towards a longer wavelength from 401.29 to 467.92 nm, which is in the visible-light region.

The  $E_g$  of the synthesized material is presented in Fig. 5(b). The addition of Cu and N dopants into  $\text{ZrTiO}_4$  material reduces the  $E_g$  from 3.09 to the lowest 2.65 eV. The band gap decreases until reaching 4% of Cu codoping, then increases with the increasing Cu concentration. Excess Cu concentrations above 4% can form aggregates and are not evenly distributed in the composite [29]. The absorption edges of 4% Cu-N-ZrTiO<sub>4</sub> calcined at 700 and 900 °C are shifted to the visible light region, thus resulting low  $E_g$  (2.69 and 2.65 eV, respectively). The calcination temperature above 500 °C causes the synthesized material to undergo



**Fig 6.** (a) Photo-degradation of MB over time and (b) observed rate constants of various Cu-N-ZrTiO<sub>4</sub> within 60 min irradiation

a phase transformation from anatase to rutile, which exhibits a lower  $E_g$  [14].

The photocatalytic activity of Cu-N-ZrTiO<sub>4</sub> was evaluated by applying the composite to the degradation of MB in the dark and visible light using a LIFE MAX 30W/765 PHILIPS TLD lamp. The percentage of MB degraded is shown in Fig. 6(a). In the dark, the percentage was very small (under 5%) because there was no photon to generate  $\bullet\text{OH}$  radicals [30]. Under the exposure of light, the degradation percentages increased because the photon stimulates the photocatalyst to generate  $\bullet\text{OH}$  radicals from water molecules [31]. When the photocatalyst is irradiated with high energy, it will produce holes ( $h^+$ ) that are strong oxidizing agents to form  $\bullet\text{OH}$  radicals, and these radicals degrade MB into simpler compounds [34].

Based on Fig. 6(a), there was a significant increase in the percentage of degradation at 15–60 min, while the increase in degradation at 75–120 min was less significant. Fig. 6(b) presents the observed rate constants of various Cu-N-ZrTiO<sub>4</sub> from a pseudo-first-order kinetics model [36]. The photocatalytic activity of all Cu-N-ZrTiO<sub>4</sub> is higher than references, i.e., pristine ZrTiO<sub>4</sub> and N-doped ZrTiO<sub>4</sub>. The co-doping of Cu improves the photocatalytic activity of N-doped ZrTiO<sub>4</sub> [23]. The 4% Cu-N-ZrTiO<sub>4</sub> composite calcined at 500 °C has the highest photocatalytic activity, while 2% Cu-N-ZrTiO<sub>4</sub> calcined at 500 °C has the lowest photocatalytic activity. The increasing amount of Cu above 4% decreases the photocatalytic activity of the composite due to diminishing doping effect by the saturation of Cu co-

doping. The increasing calcination temperature above 500 °C also decreases photocatalytic activity of the composite due to the formation of rutile phase.

## CONCLUSION

Copper-and-nitrogen-codoped ZrTiO<sub>4</sub> photocatalyst (Cu-N-ZrTiO<sub>4</sub>) has been successfully prepared through the sol-gel process. FTIR analysis shows that there is an absorption band at 1200  $\text{cm}^{-1}$  which relates to the Ti–O–Cu vibration as it intensifies at 4% of copper concentration. Co-doping with nitrogen and copper, as well as coupling with ZrO<sub>2</sub>, influence the crystallization of anatase and rutile at a higher temperature. The absorption band is also shifted towards a longer wavelength from 401.29 to 467.92 nm, which is responsive to visible light. Cu-N-ZrTiO<sub>4</sub> photocatalyst can degrade 4  $\text{mg L}^{-1}$  MB solution up to 83% at 120 min of irradiation time. Cu and N co-dopants give synergistic effects in improving the photocatalytic activity of ZrTiO<sub>4</sub>, and it is proven to have potential as a photocatalyst to decompose dyes under visible light irradiation. Further studies regarding the photocatalyst stability of the composite are necessary to be conducted.

## REFERENCES

- [1] Al-Mamun, M.R., Kader, S., Islam, M.S., and Khan, M.Z.H., 2019, Photocatalytic activity improvement and application of UV-TiO<sub>2</sub> photocatalysis in textile wastewater treatment: A review, *J. Environ. Chem. Eng.*, 7 (5), 103248.

- [2] Hamdy, M.S., Saputera, W.H., Groenen, E.J., and Mul, G., 2014, A novel TiO<sub>2</sub> composite for photocatalytic wastewater treatment, *J. Catal.*, 310, 75–83.
- [3] Zhang, T., Xiang, Y., Su, Y., Zhang, Y., Huang, X., and Qian, X., 2022, Anchoring of copper sulfide on cellulose fibers with polydopamine for efficient and recyclable photocatalytic degradation of organic dyes, *Ind. Crops Prod.*, 187, 115357.
- [4] Yan, K., Wu, G., Jarvis, C., Wen, J., and Chen, A., 2014, Facile synthesis of porous microspheres composed of TiO<sub>2</sub> nanorods with high photocatalytic activity for hydrogen production, *Appl. Catal. Environ.*, 148-149, 281–287.
- [5] Yaacob, N., Sean, G.P., Nazri, N.A.M., Ismail, A.F., Zainol Abidin, M.N., and Subramaniam, M.N., 2021, Simultaneous oily wastewater adsorption and photo-degradation by ZrO<sub>2</sub>-TiO<sub>2</sub> heterojunction photocatalysts, *J. Water Process Eng.*, 39, 101644.
- [6] El-Sharkawy, E., Soliman, A.Y., and Al-Amer, K.M., 2007, Comparative study for the removal of methylene blue via adsorption and photocatalytic degradation, *J. Colloid Interface Sci.*, 310 (2), 498–508.
- [7] Chen, D., Jiang, Z., Geng, J., Wang, Q., and Yang, D., 2017, Carbon and nitrogen co-doped TiO<sub>2</sub> with enhanced visible-light photocatalytic activity, *Ind. Eng. Chem. Res.*, 46 (9), 2741–2746.
- [8] Liu, W.J., Zeng, F.X., Jiang, H., Zhang, X.S., and Li, W.W., 2012, Composite Fe<sub>2</sub>O<sub>3</sub> and ZrO<sub>2</sub>/Al<sub>2</sub>O<sub>3</sub> photocatalyst: Preparation, characterization, and studies on the photocatalytic and chemical stability, *Chem. Eng. J.*, 180, 9–18.
- [9] Sharma, A., and Dutta, R.K., 2010, Studies on drastic improvement of photocatalytic degradation of acid orange-74 dye by TPPO capped CuO nanoparticles with suitable electron capturing agents, *RSC Adv.*, 5 (54), 43815–43823.
- [10] Jing, Y., Yin, H., Li, C., Chen, J., Wu, S., Liu, H., Xie, L., Lei, Q., Sun, M., and Yu, S., 2022, Fabrication of Pt doped TiO<sub>2</sub>-ZnO@ZIF-8 core@shell photocatalyst with enhanced activity for phenol degradation, *Environ. Res.*, 203, 111819.
- [11] Verma, S., Rani, S., Kumar, S., dan Khan, M.A.M., 2018, Rietveld refinement, micro-structural, optical and thermal parameters of zirconium titanate composites, *Ceram. Int.*, 44 (2), 1653–1661.
- [12] Liang, Q., Liu, X., Zeng, G., Liu, Z., Tang, L., Shao, B., Zeng, Z., Zhang, W., Liu, Y., Cheng, M., Tang, W., and Gong, S., 2019, Surfactant-assisted synthesis of photocatalysts: Mechanism, synthesis, *Chem. Eng. J.*, 372, 429–451.
- [13] Mogal, S.I., Mishra, M., Gandhi, V.G., and Tayade, R.J., 2012, Metal doped titanium dioxide: Synthesis and effect of metal ions on physico-chemical and photocatalytic properties, *Mater. Sci. Forum*, 734, 364–378.
- [14] Wang, J., Zhao, Y.F., Wang, T., Li, H., and Li, C., 2015, Photonic, and photocatalytic behavior of TiO<sub>2</sub> mediated by Fe, CO, Ni, N doping and co-doping, *Phys. B*, 478, 6–11.
- [15] Allen, N.S., Mahdjoub, N., Vishnyakov, V., Kelly, P.J., and Kriek, R.J., 2018, The effect of crystalline phase (anatase, brookite and rutile) and size on the photocatalytic activity of calcined polymorphic titanium dioxide (TiO<sub>2</sub>), *Polym. Degrad. Stab.*, 150, 31–36.
- [16] Zhang, J., Zhou, P., Liu, J., and Yu, J., 2014, New understanding of the difference of photocatalytic activity among anatase, rutile and brookite TiO<sub>2</sub>, *Phys. Chem. Chem. Phys.*, 16 (38), 20382–20386.
- [17] Gnanaprakasam, A., Sivakumar, V.M., and Thirumarimurugan, M., 2015, Influencing parameters in the photocatalytic degradation of organic effluent via nanometal oxide catalyst: A review, *Indian J. Mater. Sci.*, 2015, 601827.
- [18] Barkul, R.P., Koli, V.B., Shewale, V.B., Patil, M.K., and Delekar, S.D., 2016, Visible active nanocrystalline N-doped anatase TiO<sub>2</sub> particles for photocatalytic mineralization studies, *Mater. Chem. Phys.*, 173, 42–51.
- [19] Shao, G.N., Imran, S.M., Jeon, S.J., Engole, M., Abbas, N., Salman Haider, M., Kang, S.J., and Kim, H.T., 2014, Sol-gel synthesis of photoactive zirconia-titania from metal salts and investigation of their photocatalytic properties in the photo-degradation of methylene blue, *Powder Technol.*, 258, 99–109.

- [20] Zheng, J., Sun, L., Jiao, C., Shao, Q., Lin, J., Pan, D., Naik, N., and Guo, Z., 2021, Hydrothermally synthesized Ti/Zr bimetallic MOFs derived N self-doped TiO<sub>2</sub>/ZrO<sub>2</sub> composite catalysts with enhanced photocatalytic degradation of methylene blue, *Colloids Surf., A*, 623, 126629.
- [21] Sherly, E.D., Vijaya, J.J., Selvam, N.C.S., and Kennedy, L.J., 2014, Microwave assisted combustion synthesis of coupled ZnO-ZrO<sub>2</sub> nanoparticles and their role in the photocatalytic degradation of 2,4-dichlorophenol, *Ceram. Int.*, 40 (4), 5681–5691.
- [22] French, R.H., Glass, S.J., Ohuchi, F.S., Xu, Y.N., and Ching, W.Y., 1994, Experimental and theoretical determination of the electronic structure and optical properties of three phases of ZrO<sub>2</sub>, *Phys. Rev. B: Condens. Matter Mater. Phys.*, 49 (8), 5133–5142.
- [23] Piątkowska, A., Janus, M., Szymański, K., and Mozia, S., 2021, C-, N- and S-doped TiO<sub>2</sub> photocatalysts: A review, *Catalysts*, 11 (1), 144.
- [24] Kumaresan, L., Prabhu, A., Palanichamy, M., Arumugam, E., and Murugesan, V., 2014, Synthesis and characterization of Zr<sup>4+</sup>, La<sup>3+</sup> and Ce<sup>3+</sup> doped mesoporous TiO<sub>2</sub>: Evaluation of their photocatalytic activity, *J. Hazard. Mater.*, 186 (2-3), 1183–1192.
- [25] Dutta, H., Nandy, A., and Pradhan, S.K., 2016, Microstructure and optical characterizations of mechanosynthesized nanocrystalline semiconducting ZrTiO<sub>4</sub> compound, *J. Phys. Chem. Solids*, 95, 56–64.
- [26] Hayati, R., Kurniawan, R., Prasetyo, N., Sudiono, S., and Syoufian, A., 2022, Codoping effect of nitrogen (N) to iron (Fe) doped zirconium titanate (ZrTiO<sub>4</sub>) composite toward its visible light responsiveness as photocatalysts, *Indones. J. Chem.*, 22 (3), 692–702.
- [27] Muslim, M.I., Kurniawan, R., Pradipta, M.F., Trisunaryanti, W., and Syoufian, A., 2021, The effects of manganese dopant content and calcination temperature on properties of titania-zirconia composite, *Indones. J. Chem.*, 21 (4), 882–890.
- [28] Alifi, A., Kurniawan, R., and Syoufian, A., 2020, Zinc-doped titania embedded on the surface of Zirconia: A potential visible-responsive photocatalyst material, *Indones. J. Chem.*, 20 (6), 1374–1381.
- [29] Kim, J.Y., Kim, C.S., Chang, H.K., and Kim, T.O., 2011, Synthesis and characterization of N doped TiO<sub>2</sub>/ZrO<sub>2</sub> visible light photocatalysts, *Adv. Powder Technol.*, 22 (3), 443–448.
- [30] Venkatesan, A., Al-onazi, W.A., Elshikh, M.S., Pham, T.H., Suganya, S., Boobas, S., and Priyadharsan, A., 2022, Study of synergistic effect of cobalt and carbon codoped TiO<sub>2</sub> photocatalyst for visible light induced degradation of phenol, *Chemosphere*, 305, 135333.
- [31] Kim, C.S., Shin, J.W., Cho, Y.H., Jang, H.D., Byun, H.S., and Kim, T.O., 2013, Synthesis and characterization of Cu/N-doped mesoporous TiO<sub>2</sub> visible light photocatalysts, *Appl. Catal., A*, 455, 211–218.
- [32] Li, D., Qin, Q., Duan, X., Yang, J., Guo, W., and Zheng, W., 2013, General one-pot template-free hydrothermal method to metal oxide hollow spheres and their photocatalytic activities and lithium storage properties, *ACS Appl. Mater. Interfaces*, 5 (18), 9095–9100.
- [33] Khan, S., Kim, J., Sotto, A., and van der Bruggen, B., 2015, Humic acid fouling in a submerged photocatalytic membrane reactor with binary TiO<sub>2</sub>-ZrO<sub>2</sub> particles, *J. Ind. Eng. Chem.*, 21, 779–786.
- [34] Singh, H., Sunaina, S., Yadav, K.K., Bajpai, V.K., and Jha, M., 2020, Tuning the bandgap of *m*-ZrO<sub>2</sub> by incorporation of copper nanoparticles into visible region for the treatment of organic pollutants, *Mater. Res. Bull.*, 123, 110698.
- [35] Kurniawan, R., Sudiono, S., Trisunaryanti, W., and Syoufian, A., 2019, Synthesis of iron-doped zirconium titanate as a potential visible-light responsive photocatalyst, *Indones. J. Chem.*, 19 (2), 454–460.
- [36] Syoufian, A., and Nakashima, K., 2008, Degradation of methylene blue in aqueous dispersion of hollow titania photocatalyst: Study of reaction enhancement by various electron scavengers, *J. Colloid Interface Sci.*, 317 (2), 507–512.



## Polyvinylidene Fluoride (PVDF)/Modified Clay Hybrid Membrane for Humic Acid and Methylene Blue Filtration

Edi Pramono\*, Gadis Prihatin Wahyu Sejati, Sayekti Wahyuningsih, and Candra Purnawan

Department of Chemistry, Faculty of Mathematics and Natural Sciences, Universitas Sebelas Maret,  
Jl. Ir. Sutami 36A, Kentingan, Surakarta 57126, Indonesia

\* Corresponding author:

email: edi.pramono.uns@staff.uns.ac.id

Received: November 7, 2022

Accepted: March 11, 2023

DOI: 10.22146/ijc.78979

**Abstract:** This research studied the impact of silanized clay modification on performance and antifouling Poly(vinylidene fluoride) (PVDF) membrane toward humic acid and methylene blue filtration. Clay modification was carried out by using 3-aminopropyltriethoxysilane (APS) to produce modified clay (Clay-APS). Hybrid membranes were prepared by phase inversion for humic acid and methylene blue filtration. Hybrid membranes were characterized by measuring surface hydrophilicity, water flux, rejection, and antifouling properties. Clay and Clay-APS modification increased hybrid membrane surface hydrophilicity, as indicated by increasing the  $\beta$  fraction and decreasing the water contact angle. The PVDF/Clay and PVDF/Clay-APS hybrid membranes showed high permeability and selectivity with the highest water flux values of  $24.2 \text{ L m}^{-2} \text{ h}^{-1}$ . The rejections for humic acid and methylene blue were 98.8 and 99.3%, respectively. The highest antifouling property was obtained from the PVDF/Clay-APS hybrid membrane, with a flux recovery ratio was 96.0%. The PVDF/Clay hybrid membrane performance and antifouling properties showed that the membranes have the potential for water treatment.

**Keywords:** clay modification; dye filtration; hybrid membrane; polyvinylidene fluoride

### ■ INTRODUCTION

About 70% of the earth is water, but only 2.5% is a source of pure water and only 1% is fresh water accessible and used by 7.6 billion people [1]. Water sources in the tropics are mostly peat water, characterized by brownish-yellow water due to the high concentration of humic acid (HA) that cannot be consumed directly [2]. Therefore, peat water must be processed into clean water for daily needs, especially drinking water. In addition, clean water sources have also been significantly reduced with the development of industries that produce a lot of waste; as a result, more than 2 billion people have difficulty accessing clean water [3]. One produced waste is toxic dye waste, which can contaminate the soil, sediment, and surrounding surface water [4]. Wastewater treatment management is needed to balance water availability and demand at an affordable cost, which positively impacts the environment. Several technologies have been developed to address wastewater problems, such as

adsorption, sedimentation, coagulation, biological treatment, photodegradation, and membrane filtration [5-6]. Membrane technology is a promising technique for removing impurities in water where the filtration efficiency is influenced by hydrophilicity properties and the porosity of the membrane surface [7].

Polymer membranes have greater flexibility, good film-forming properties, mechanical strength, chemical stability, and high selectivity [8]. In water treatment technology, membranes based on hydrophobic polymers have been widely applied such as polysulfone, poly(vinylidene fluoride) (PVDF), and polytetrafluoroethylene [9-10]. Hydrophobic polymers, including PVDF, have a disadvantage because the high hydrophobic surface properties can interact with foulants, causing fouling and reducing membrane performance [11]. Fouling mitigation has been developed using additives, hydrodynamic optimization, and membrane surface modification [12]. One way to

increase membrane efficiency and reduce fouling is to add hydrophilic compounds to the membrane [13]. Antifouling properties are measured as flux recovery ratio (FRR). Several previous studies reported that the addition of hydrophilic fillers such as PVDF-*g*-PDMAEMA, MWCNTs-OH, and TiO<sub>2</sub> could increase membrane FRR [14-16]. Another material that has the potential to modify PVDF membranes is clay. Various types of clay can be found in Indonesia, including bentonite, cloisite, and kaolinite [17]. Clay modification of PVDF membranes has been reported, such as the use of cloisite and halloysite [18-19]. Cosmetic-graded clay has non-toxic properties, hydrophilic, is easily obtained, and is inexpensive compared to other clays. However, studies on cosmetic clay application to PVDF membranes have not been reported yet.

Direct application of inorganic materials such as clay has an effect called agglomeration. It is caused by differences in surface tension between the polymer and fillers [20], the resulting membrane that can be inhomogeneous and difficult to cast. Surface modification by organosilane modification, such as 3-aminopropyltriethoxysilane (APS) could increase interaction between polymer and clays [21]. Preliminary tests of PVDF modification with kaolin clay have been carried out and showed an increase in membrane hydrophilicity. In this study, organosilane-modified clay (Clay-APS) and a PVDF/Clay-APS hybrid membrane were developed. The membrane was made using PVDF with a different molecular mass from previous studies [22]. This research investigated the effect of various concentrations of Clay-APS on membrane performance toward HA and methylene blue (MB) filtration; and also discussed surface characteristics as well as antifouling properties.

## ■ EXPERIMENTAL SECTION

### Materials

The materials used in this study include PVDF (Mw 64.000 g/mol) was purchased from Jiangsu Freechem-China. *N,N*-dimethylformamide (DMF), polyethylene Glycol 400 (PEG400), hydrochloric Acid (HCl), and MB

(Mw 319.85 g/mol) were purchased from Merck. APS was obtained from Sigma-Aldrich. HA was prepared by Edulab Indonesia. Clay cosmetic-based (containing kaolinite) was purchased from Cipta Kimia.

### Instrumentation

The membranes were characterized using Attenuated Total Reflection Fourier Transform Infrared (ATR-FTIR Agilent 360) and Scanning Electron Microscopy (SEM, JEOL Benchtop JCM 7000). The dye solution concentration was analyzed using UV-Vis spectrophotometer (Hitachi UH5300).

### Procedure

#### **Modification of clay with APS**

Clay was ground and sieved to size 200 mesh. The 4 g clay was soaked in 100 mL, HCl 0.1 M for 24 h and then dried at room temperature for 24 h. Modification of clay with APS followed previous research [23-25]. About 4 g of clay was dispersed in 200 mL of ethanol, then 4 g of APS, which had been dispersed into 50 mL ethanol. The mixture was stirred for 24 h at a temperature of 70 °C. The mixture was filtered and dried at 60 °C for 12 h. The modification has been successfully carried out and confirmed by FTIR spectra peak at 1568 cm<sup>-1</sup>, which indicates the presence of an -NH group from APS, and at 2936 cm<sup>-1</sup> which corresponds to a CH<sub>2</sub> of organosilane [26].

#### **Membranes fabrication**

PVDF and hybrid membranes were fabricated using the phase inversion following the previous report [27]. The casting solution (Dope) was carried out by various concentrations shown in Table 1. Clay or Clay-APS, PEG, and PVDF were mixed into DMF with a total mass of 9 g. The solution was stirred at 60 °C for 24 h. The dope was cast on glass with a thickness regulator of 130 μm and immediately put into a water bath as a coagulant bath. The obtained membrane was stored in glycerin and washed before being analyzed.

#### **Characterization**

The membranes were characterized by morphology, functional groups, contact angles, and pore



**Table 1.** Composition of 12 g dope solution

PVDF (wt.%)	PEG (wt.%)	Clay (wt.%)	Clay-APS (wt.%)	Membrane code
18	4	0	0	PVDF
18	4	1	0	PVDF/ Ka1
18	4	3	0	PVDF/Ka3
18	4	5	0	PVDF/Ka5
18	4	7	0	PVDF/Ka7
18	4	9	0	PVDF/Ka9
18	4	0	1	PVDF/Ka-APS1
18	4	0	3	PVDF/ Ka-APS3
18	4	0	5	PVDF/Ka-APS5
18	4	0	7	PVDF/Ka-APS7
18	4	0	9	PVDF/Ka-APS9

measurement. Membrane surface and cross-section morphology was analyzed by SEM. Functional group analysis on PVDF/Clay-APS hybrid membranes was carried out using the ATR-FTIR. Membranes were scanned 48 times at a range of 400–4000  $\text{cm}^{-1}$  with a resolution of 4  $\text{cm}^{-1}$ . The membrane polymorphs were computed using Eq. (1) [28],

$$F(\beta) = \frac{A\beta}{A\beta + 1.26A\alpha} \quad (1)$$

where  $F(\beta)$  is the relative fraction of the  $\beta$  phase, while  $A\alpha$  and  $A\beta$  are the absorbances at the peaks of 769 and 840  $\text{cm}^{-1}$ , which correspond to the  $\alpha$  and  $\beta$  phases, respectively.

Surface hydrophilicity was determined by measuring the membrane's water contact angle (WCA). A flat membrane was prepared on the sample holder and the water was dropped on the membrane's surface. The water drop image was recorded and processed using ImageJ software with a contact angle plugin.

Membrane porosity was analyzed using the gravimetric method. The wet membrane ( $W_b$ ) was weighed and dried at 60 °C for 24 h. The dry membrane ( $W_k$ ) was weighed again, and the membrane porosity ( $\epsilon$ ) was determined through Eq. (2),

$$\epsilon(\%) = \left( \frac{W_b - W_k}{A \times l \times \rho} \right) \times 100 \quad (2)$$

where  $A$  is the area of the membrane,  $l$  is the thickness of the membrane, and  $\rho$  is the density of water.

### Membrane performance test

The measurements were carried out using a microfiltration device as a stirred cell with a dead-end system. A membrane with a 5 cm diameter was attached to the sample holder. The system was operated under a transmembrane pressure (TMP) of 2 bar using 200 mL water as the feed phase. The membrane was compacted for 15 min and calculated the time to obtain 2 mL of permeate. The water flux was computed using Eq. (3),

$$J = \frac{V}{A \times t} \quad (3)$$

where  $J$  is the permeate flux ( $\text{L}/\text{m}^2 \cdot \text{h}$ ),  $V$  is the volume of water permeate (L),  $A$  is the membrane surface area ( $\text{m}^2$ ), and  $t$  is the measurement time (h).

The average membrane pore size can be calculated using the Geurout–Elford–Ferry formula at Eq. (4) [29],

$$r_p = \sqrt{\frac{(2.9 - 1.75\epsilon) \times 8\rho \text{ lm } Jw}{\epsilon \times A \times \Delta P}} \quad (4)$$

where  $\epsilon$  is membrane porosity (%),  $\rho$  is the deionized water viscosity at 25 °C ( $8.9 \times 10^{-4}$  Pa s),  $\text{lm}$  is the wet membrane thickness,  $A$  is effective membranes surface,  $Jw$  is pure water flux, and  $\Delta P$  is operating pressure (0.2 MPa).

The membrane rejection was measured by replacing the feed phase with HA and MB with a concentration of 100  $\text{mg L}^{-1}$ . The structure of HA and MB are shown in Fig. 1 and 2 [30]. Permeate and retentate concentration was analyzed and the membrane rejection  $R(\%)$  was calculated using Eq. (5). The antifouling was analyzed by calculating the value of the FRR in the form of a presentation between the membrane flux that had been used for filtration and the initial water flux. The values obtained from each repetition were then averaged. The FRR value is determined using Eq. (6).

$$R(\%) = \left( 1 - \frac{C_p}{C_r} \right) \times 100\% \quad (5)$$

where  $C_p$  is the concentration of permeate and  $C_r$  is the retentate concentration.

$$\text{FRR} = \frac{J_n}{J_o} \times 100\% \quad (6)$$

where  $J_n$  is pure water flux after the rejection test and  $J_o$  is pure water flux before the rejection measurement.

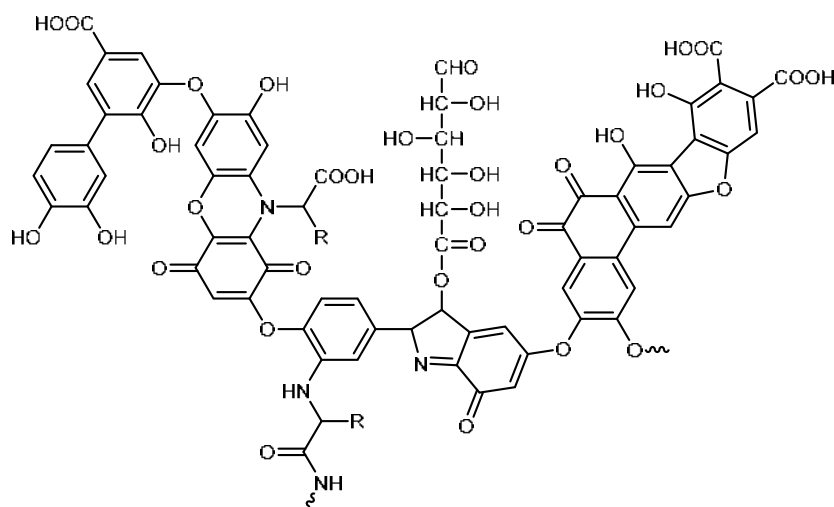


Fig 1. Hypothetic structure of humic acid [30]

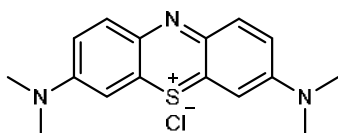


Fig 2. Chemical structure of methylene blue

## RESULTS AND DISCUSSION

### PVDF Membranes Polymorph

The polymorph of PVDF/Clay and PVDF/Clay-APS membranes were characterized by ATR-FTIR and presented in Fig. 3. The ATR-FTIR spectra in Fig. 3(a) obtained the peaks at 769 and 840  $\text{cm}^{-1}$ , corresponding to the vibration of C-H and C-F with different conformations. The peaks at 769 and 840  $\text{cm}^{-1}$  were related to the  $\alpha$  and  $\beta$  phases, respectively. The  $\alpha$  phase has

the non-polar TGTG' conformation and the  $\beta$  phase has the most polar nature with the TTTT' conformation. Fig. 3 also shows the change in the value of the  $\beta$  fraction on the membrane. Fig. 3(b) showed the  $\beta$  fraction of the pristine PVDF membrane of 0.47, and the addition of clay and Clay-APS to the PVDF membrane caused increasing in the  $\beta$  fraction. The increasing  $\beta$  phase of PVDF/Clay membranes is linear with the amount of clay added, indicating an increase in the hydrophilicity of the membrane because the  $\beta$  phase showed the polar nature of the PVDF [31]. The  $\beta$  fraction of PVDF/clay APS membranes is relatively constant in Clay-APS concentration up to 3%, and it is caused by the existence of a silane group from APS that tend to have hydrophobic property.

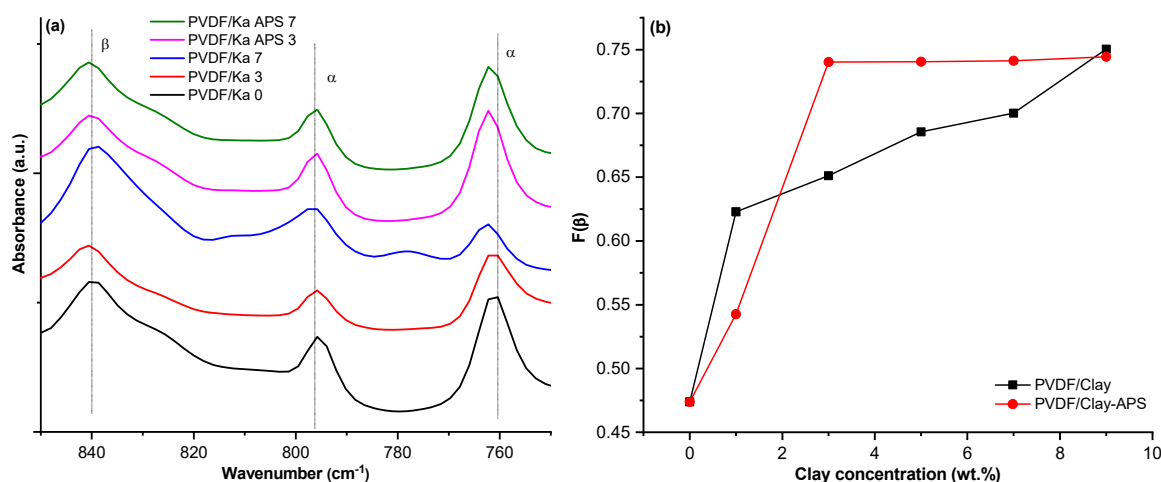


Fig 3. The (a) ATR-FTIR spectra and (b)  $\beta$  fraction of the hybrid membranes

### Membrane Surface Hydrophilicity

Membrane surface hydrophilicity was analyzed by WCA and given in Fig. 4. The pristine membrane obtained a WCA of 85.6°, which indicates that the membrane is relatively hydrophilic. Fig. 4 also showed decreasing WCA after PVDF/Clay and PVDF/Clay-APS modification. A considerable decrease in the contact angle occurs after the addition of clay with a concentration of 3 wt.% where the value is below 75 °C, and it reaches below 70 °C at the addition of 9 wt.% concentration. The clay and Clay-APS modified membranes are more hydrophilic due to the existence of Clay and the increasing of  $\beta$  fraction.

The image of water droplets on the membrane at various observation times is shown in Fig. 5. The water contact angle decreased with aging time, and the dimensions of the water droplets presented that there was no diameter widening. The dynamic contact angle reduction of PVDF/Clay 3% and PVDF/Clay-APS 7% in Fig. 6 were observed faster than the pristine membrane

and almost reached 20 °C for 12 min. The decrease in contact angle on the membrane surface can be influenced by surface hydrophilicity and pore properties. Decreasing the water droplet contact angle without a change of diameter indicated that it is dominantly caused

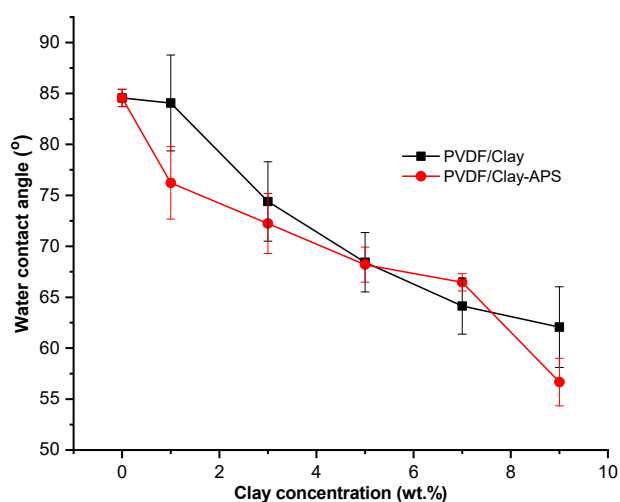
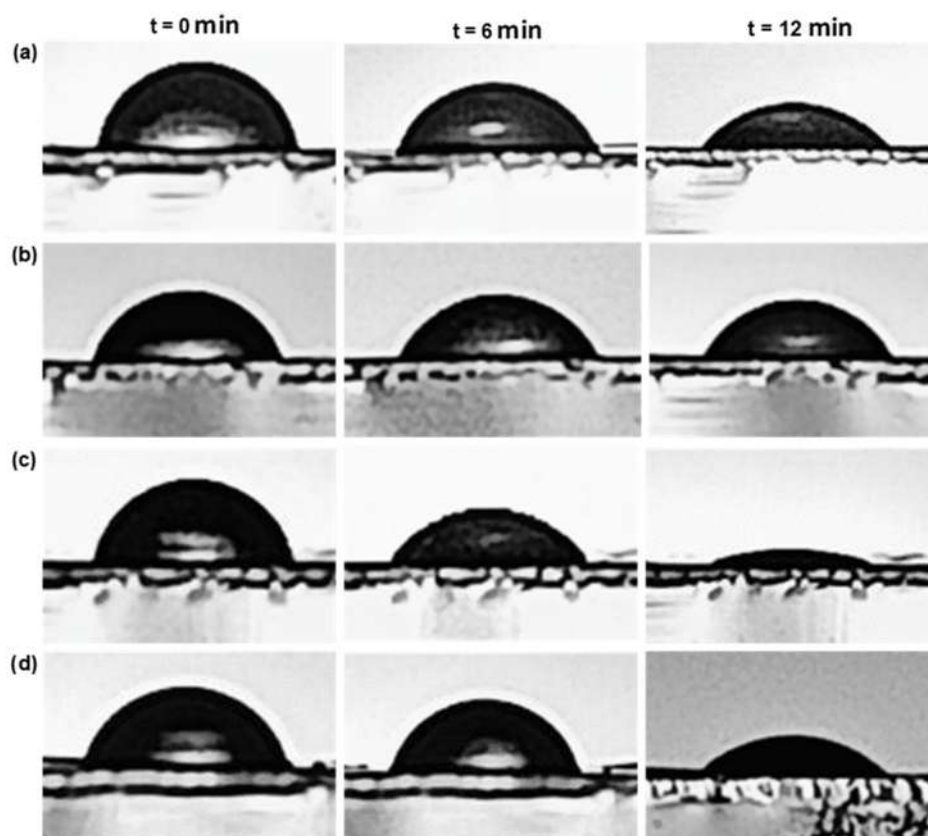
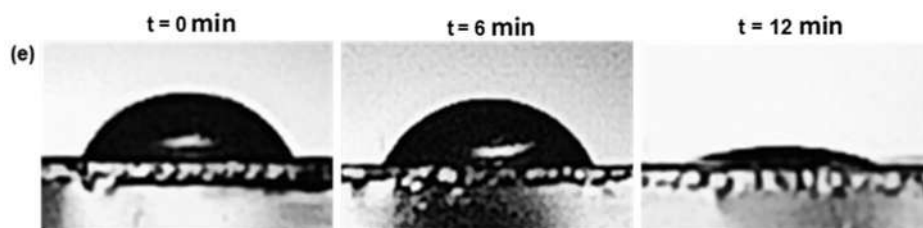
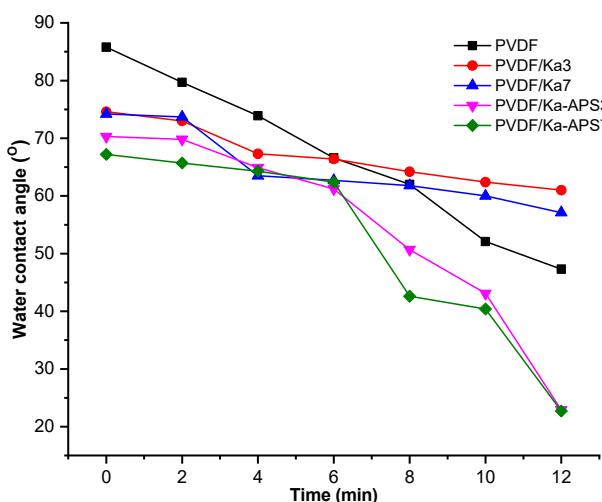


Fig 4. WCA of PVDF/Clay and PVDF/Clay-APS hybrid membranes





**Fig 5.** Water droplet aging on (a) PVDF;(b) PVDF/Ka 3%; (c) PVDF/Ka 7%; (d) PVDF/Ka-APS; (e) PVDF/Ka-APS 7 wt.% membrane surface



**Fig 6.** The dynamic water contact angle of hybrid membranes

by the pores in the membrane. The decline of water contact angle is in accordance with previous research [32] which shows that the pore factor can cause changes in contact angle.

### Membrane Porosity

Membrane porosity measurement was carried out using the gravimetric method and data presented in Fig. 7. The porosity of the pristine PVDF membrane has a high value of 80.2% and decreases with clay addition. On the other hand, the additional high concentration of clay APS increases membrane porosity. Membrane porosity is influenced by the presence of PEG as a porogen in dope. PEG can increase the number of pores and the pore area [33]. PEG, a hydrophilic substance, will be pulled out during the phase inversion due to the interaction with the water coagulant and leave pores in the membrane. The addition of clay can hinder water and PEG during the phase inversion [34], which impacts the exchange solvent-non-

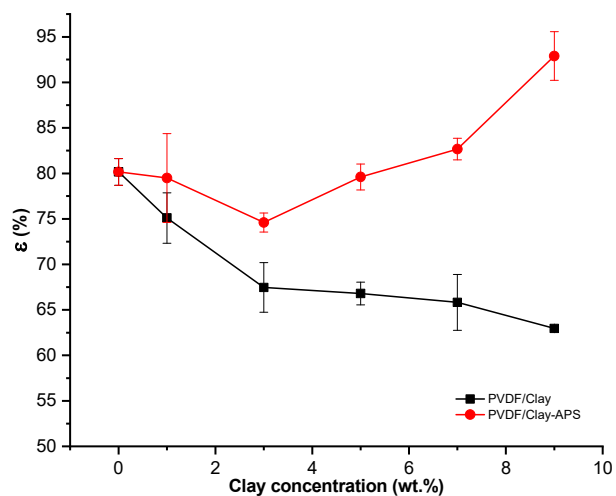


**Fig 7.** The porosity of PVDF/Clay and PVDF/Clay-APS hybrid membranes

solvent, resulting in lower porosity of the hybrid membrane. There is a probability that the presence of APS causes a different trend of porosity values in the PVDF/Clay-APS membrane. The existence of APS influences the membrane to be more hydrophobic; it affects the lower interaction with PEG and causes PEG to be easy to release during phase inversion.

### Membrane's Morphology

Membrane surface and cross-section morphology are shown in Fig. 8. Based on surface morphology, PVDF and hybrid membranes had relatively the same surface, i.e., dense and rough. The cross-section of the membrane showed an asymmetric structure and consisted of macro and micropores. As described in the previous section, these pores form when PEG is released from the polymer component during phase inversion, resulting in membrane pores [35]. Fig. 8 shows the micro and macropore dimensions differences between PVDF

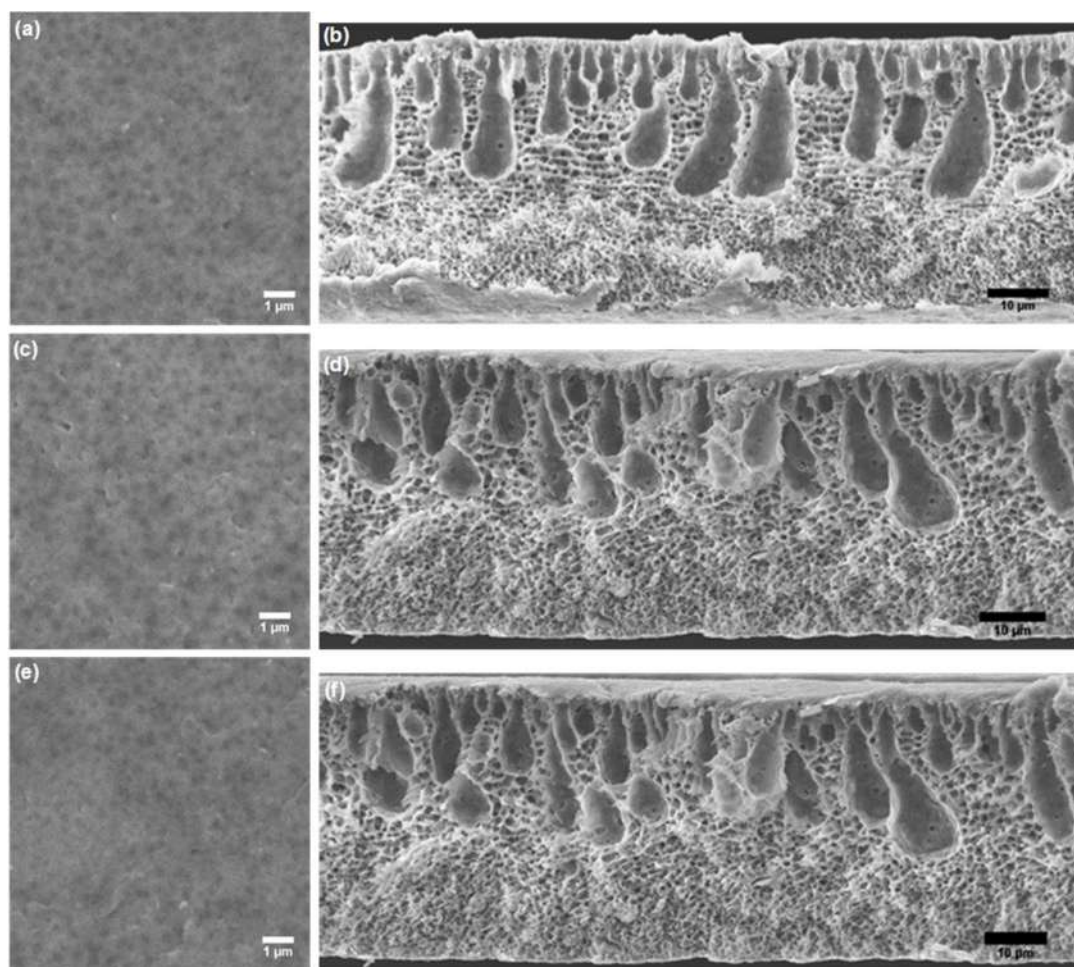


**Fig 8.** Surface and cross-section image of (a, b) PVDF; (c, d) PVDF/Clay 3%; (e, f) PVDF/Clay-APS 3 wt.%

and hybrid membranes. PVDF membrane produced a higher macropore but a smaller micropore on the bottom side. PVDF/Clay 3% and PVDF/Clay-APS 3% membranes showed a bigger micropore than the PVDF membrane. PVDF membrane had the lowest PWF because the micropore size was smaller, and PVDF/Clay 3% membrane had the highest flux due to the existence of macropore and high micropore.

#### Pure Water Flux and Pore Size of Membranes

Based on Fig. 9, the pure water flux (PWF) and pore size clay-modified membranes decreased with increasing clay concentration. This result was in line with the porosity data. The PWF increased by 1 and 3 wt.% Clay-APS addition. It could be due to the effect of APS as a modifier on the clay, which can increase the homogeneity of the membrane so that the obtained water flux can also

increase until it reaches a maximum concentration of 3 wt.%. PVDF/Clay 3% and PVDF/Clay-APS 3% have high PWF due to the existence of micropores. It was linear with morphology data. In contrast, higher concentration addition of Clay-APS decreased PWF. Higher clay concentration can induce agglomeration [36] and pore filling by clay substrate, making the membrane pores denser.

#### Performance of PVDF/Clay Membrane for HA Filtration

The membrane's performance on HA was analyzed by the water flux and its rejection. Fig. 10 shows that the water flux of the pristine PVDF membrane with HA as a feed obtained a lower value than pure water flux. The presence of HA results in interactions on the surface and closure of pores in the membrane, which results in a

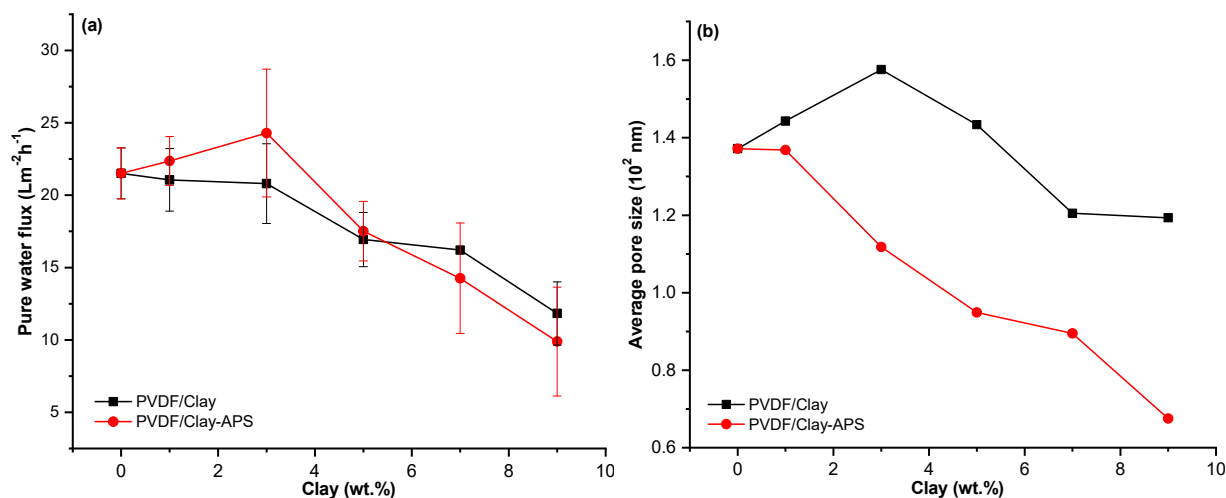


Fig 9. The (a) Pure water flux and (b) Average pore size of PVDF/Clay and PVDF/Clay-APS hybrid membranes

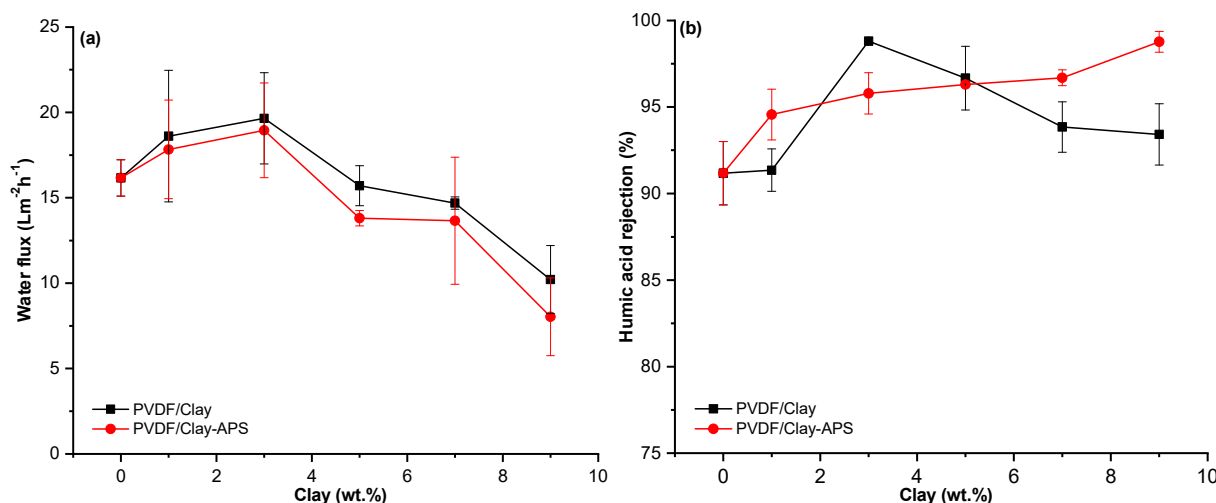


Fig 10. Performance of: (a) Water permeability and (b) Selectivity of PVDF/Clay and PVDF/Clay-APS membranes on HA filtration

decrease in membrane permeability. The PVDF/Ka3 and PVDF/KaAPS3 membranes showed the optimum water flux, where the flux value almost reaches  $20 \text{ L m}^{-2} \text{ h}^{-1}$ . On the other hand, adding a higher clay concentration causes the flux value to decrease considerably due to the possibility of agglomeration. These results are linear with the porosity and pore size of the membrane.

HA rejection was obtained above 90.0%, which indicates that PVDF and PVDF/clays hybrid membranes were acceptable for water treatment. The 3 wt.% addition increased the membrane rejection and water flux, where the %R was up to 98.8%. The membrane rejection

decreased at the clay addition of 5 to 9 wt.%, which could be caused by a larger pore size than the HA particle size. High clay content resulted in repulsion between the clay particles and the polymer and induced larger pores formation in the membrane cross-section. The PVDF/Clay-APS membrane showed an increase in the rejection value with the increase in filler concentration. The highest %R was reached at 9 wt.% Clay-APS addition of 98.0%. The linear enhancement of rejection percentage showed that the modification of Clay-APS in the membrane solution had a good effect on the membrane homogeneity.

### Performance of PVDF/Clay Membranes for MB Filtration

The membrane filtration performance was also carried out on the filtration of MB dye, and the results were presented in Fig. 11. The modification of clay and Clay-APS to the PVDF membrane demonstrated a high %R of more than 90.0% and increased until %R of 99.1% for 3 wt.% addition. The water flux of the PVDF/Clay membrane in MB filtration had almost the same pattern as the water flux in HA filtration, where the water flux decreased. The PVDF/Clay-APS membrane produced a lower flux than the PVDF/Clay membrane and obtained less than  $10 \text{ L m}^{-2} \text{ h}^{-1}$ . The overall %R value for MB was higher than HA. MB particles tend to interact with the clay-containing membrane surface so that it will be left in the feed phase.

The PVDF/Clay-APS membrane showed an increase in the rejection with increasing filler concentration up to 99.3% for PVDF/Clay-APS 3%. Membrane rejection PVDF/Clay-APS showed a value that tended to be constant at the addition of Clay-APS concentration above 3 wt.%, but the PVDF/Clay-APS 9% membrane had the highest rejection value of 99.5%. The water flux value of the PVDF/Ka-APS membrane was lower than clay-modified membranes, which results in a higher rejection value because the flux value is inversely proportional to the rejection value. The dye filtration was influenced by the pores' properties and the membrane's

interaction with the dye. MB particles in solution can form molecular aggregations [37], produce large molecular dimensions, and cannot pass through the membrane pores. The interaction of negative charge on clay and cationic dyes also causes MB to be retained longer on the membrane surface, resulting in a high %R.

### Membrane Antifouling Properties

Antifouling membrane properties were determined by calculating the FRR value for both HA and MB, and the results are given in Fig. 12. Pristine PVDF membrane obtained FRR of less than 80.0% toward HA filtration, indicating that water permeation decreased by about 20.0% after HA filtration. Decreasing water flux after feed filtration was related to fouling on the membrane surface [38-39]. The FRR value of the PVDF/clay membrane increased dramatically with the addition of 3 wt.%, where the value exceeded 90.0%. Membranes with the addition of clay and Clay-APS 3-7 wt.% had FRR relatively same, but there was an increase in FRR for Clay 9% and Clay-APS 9 wt.% contained membranes where the value exceeded 95.0% for HA and MB filtration.

Fig. 12 also revealed that the FRR value of the hybrid PVDF membrane for MB filtration was obtained lower than the FRR value for HA filtration. The FRR value on the membrane increased due to the increase in hydrophilicity, which is in accordance with the contact angle data. Membranes with hydrophilic surfaces will

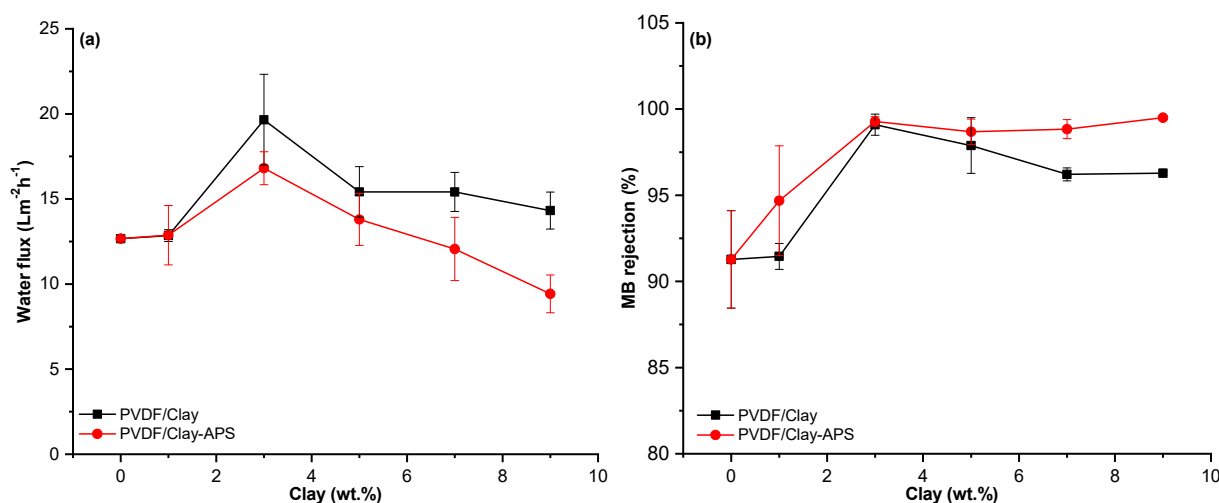


**Fig 11.** Performance of (a) water permeability and (b) selectivity of PVDF/Clay and PVDF/Clay-APS membranes on MB filtration

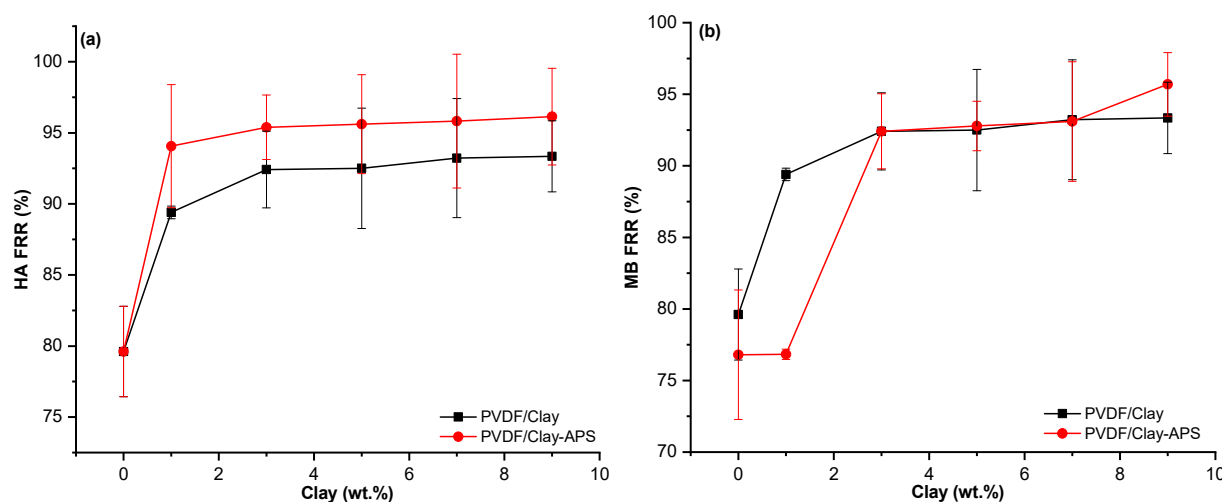


Fig 12. FRR of (a) HA and (b) MB filtration

Table 2. Comparative study of modified PVDF membranes for water treatment

Matrix	Type of membrane	Pure water flux (L m <sup>-2</sup> h <sup>-1</sup> )	Feed solution (Concentration)	Rejection (%)	FRR (%)	References
PVDF/Clay-APS	Micro filtration	24.3	MB (100 mg L <sup>-1</sup> )	99.3	92.4	This study
PVDF/Clay	Micro filtration	20.8	HA (100 mg L <sup>-1</sup> )	98.8	92.4	This study
PVDF/NZP	Ultra filtration	730.0	HA (20 mg L <sup>-1</sup> )	80.0	100.0	[43]
TP/PEI/PVDF	Ultra filtration	140.0	MB (20 mg L <sup>-1</sup> )	95.2	84.6	[44]
PVDF/Fe <sub>3</sub> O <sub>4</sub> - HNTs	Nano filtration	24.2	MB (100 mg L <sup>-1</sup> )	84.7	-	[45]
PVDF/GO-Ni	Ultra filtration	38.4	CR (50 mg L <sup>-1</sup> )	98.0	-	[46]

form a layer of pure water on the surface, which can prevent the adsorption and deposition of hydrophobic [40]. Antifouling properties were also supported by ATR-FTIR data which showed an increase in the  $\beta$  phase of the hybrid membrane. Based on the "Polar spreads on Polar" rule, the wettability of PVDF membranes could change according to the polarity of the crystalline phase, which affected membrane antifouling properties [41]. Conventional PVDF membranes generally contain a lot of non-polar phases and induced fouling due to high adhesive interactions between the foulant and the membrane surface. The presence of clay in the PVDF membrane influenced the strong interaction between the dye and membrane surface. Generally, clays particle were negatively charged and encouraged interactions with cationic molecules [42]. These resulted in a lower FRR of MB than HA for both PVDF and hybrid membranes.

PVDF/Clay and PVDF/Clay-APS membrane's performance shows the potential for water treatment

applications. The results of the water flux, rejection, and antifouling of membranes are quite high compared to several previous studies on modified PVDF membranes for water treatment, as shown in Table 2. The membrane flux value is not too high but produces a high rejection, which is more than 98.0% for HA. The rejection value of the PVDF/Clay-APS membrane on MB dye was 99.0%, also quite high compared to the rejection value of other modified PVDF membranes. The FRR value produced on PVDF/Clay and PVDF/Clay-APS membranes was > 90.0%, showing good antifouling properties compared with other modified PVDF membranes.

## CONCLUSION

PVDF and clay-modified hybrid membranes were successfully fabricated using phase inversion and produced asymmetric membranes with micro and macropore. Clay and Clay-APS addition could increase the membrane surface's hydrophilicity. The presence of



clay decreased membrane porosity and reversely for Clay-APS addition. The membrane's selectivity increased with the addition of Clay and Clay-APS. The most effective membrane for HA filtration is PVDF/Clay-APS 3% with water flux of  $18 \text{ L m}^{-2} \text{ h}^{-1}$ , rejection of 96.0%, and FRR above 95.0%. Meanwhile, the most effective membrane for MB filtration is PVDF/Clay 3% with a water flux of  $20 \text{ L m}^{-2} \text{ h}^{-1}$ , rejection of 99.1%, and FRR above 92.0%. These indicate that PVDF/Clay and PVDF/Clay-APS membranes can be applied in industrial applications, especially at HA and dye filtration.

### ■ ACKNOWLEDGMENTS

The author(s) would like to acknowledge LPPM UNS for providing financial support through a fundamental research grant No. 254/UN27.22/PT.01.03/2022.

### ■ AUTHOR CONTRIBUTIONS

Edi Pramono conducted data analysis, supervised the experiment, and wrote the manuscript. Gadis Prihatin Wahyu Sejati prepared a hybrid membrane and analyzed the membrane's performance. Sayekti Wahyuningsih and Candra Purnawan review the manuscript. All authors agreed to the final version of this manuscript.

### ■ REFERENCES

- [1] Yalcinkaya, F., Boyraz, E., Maryska, J., and Kucerova, K., 2020, A review on membrane technology and chemical surface modification for the oily wastewater treatment, *Materials*, 13 (2), 493.
- [2] Aryanti, P.T.P., Noviyani, A.M., Kurnia, M.F., Rahayu, D.A., and Nisa, A.Z., 2018, Modified polysulfone ultrafiltration membrane for humic acid removal during peat water treatment, *IOP Conf. Ser.: Mater. Sci. Eng.*, 288, 012118.
- [3] Lin, F., Zhang, S., Ma, G., Qiu, L., and Sun, H., 2018, Application of ceramic membrane in water and wastewater treatment, *E3S Web Conf.*, 53, 04032
- [4] Yaseen, D.A., and Scholz, M., 2019, Textile dye wastewater characteristics and constituents of synthetic effluents: A critical review, *Int. J. Environ. Sci. Technol.*, 16 (2), 1193–1226.
- [5] Muneeb, M., Ismail, B., Fazal, T., Khan, R.A., Khan, A.M., Bilal, M., Muhammad, B., and Khan, A.R., 2018, Water treatment by photodegradation on orthorhombic antimony sulfide powder and effect of key operational parameters using methyl orange as a model pollutant, *Arabian J. Chem.*, 11 (7), 1117–1125.
- [6] Xu, L., Shan, B., Gao, C., and Xu, J., 2020, Multifunctional thin-film nanocomposite membranes comprising covalent organic nanosheets with high crystallinity for efficient reverse osmosis desalination, *J. Membr. Sci.*, 593, 117398.
- [7] Gopakumar, D.A., Arumukhan, V., Gelamo, R., Pasquini, D., de Moraes, L.C., Rizal, S., Hermawan, D., Nzihou, A., and Khalil, H.P.S.A., 2019, Carbon dioxide plasma treated PVDF electrospun membrane for the removal of crystal violet dyes and iron oxide nanoparticles from water, *Nano-Struct. Nano-Objects*, 18, 100268.
- [8] Brunetti, A., Tocci, E., Cersosimo, M., Kim, J.S., Lee, W.H., Seong, J.G., Lee, Y.M., Drioli, E., and Barbieri, G., 2019, Mutual influence of mixed-gas permeation in thermally rearranged poly(benzoxazole-co-imide) polymer membranes, *J. Membr. Sci.*, 580, 202–213.
- [9] Shen, Z., Chen, W., Xu, H., Yang, W., Kong, Q., Wang, A., Ding, M., and Shang, J., 2019, Fabrication of a novel antifouling polysulfone membrane with in situ embedment of MXene nanosheets, *Int. J. Environ. Res. Public Health*, 16 (23), 4659.
- [10] Mat Nawi, N.I., Chean, H.M., Shamsuddin, N., Bilal, M.R., Narkkun, T., Faungnawakij, K., and Khan, A.L., 2020, Development of hydrophilic PVDF membrane using vapour induced phase separation method for produced water treatment, *Membranes*, 10 (6), 121.
- [11] Goh, P.S., Lau, W.J., Othman, M.H.D., and Ismail, A.F., 2018, Membrane fouling in desalination and its mitigation strategies, *Desalination*, 425, 130–155.
- [12] Arumugham, T., Kaleekkal, N.J., Rana, D., and Doraiswamy, M., 2016, Separation of oil/water emulsions using nano MgO anchored hybrid ultrafiltration membranes for environmental abatement, *J. Appl. Polym. Sci.*, 133 (1), 42848.

- [13] Kang, G., and Cao, Y., 2014, Application and modification of poly(vinylidene fluoride) (PVDF) membranes – A review, *J. Membr. Sci.*, 463, 145–165.
- [14] Liu, L., Huang, L., Shi, M., Li, W., and Xing, W., 2019, Amphiphilic PVDF-g-PDMPMA ultrafiltration membrane with enhanced hydrophilicity and antifouling properties, *J. Appl. Polym. Sci.*, 136 (42), 48049.
- [15] Wang, W., Xu, X., Zhang, Z., Zhang, P., Shi, Y., and Ding, P., 2021, Study on the improvement of PVDF flat ultrafiltration membrane with MWCNTs-OH as the additive and the influence of different MWCNTs-OH scales, *Colloid Interface Sci. Commun.*, 43, 100433.
- [16] Deng, W., Fan, T., and Li, Y., 2021, In situ biomineralization-constructed superhydrophilic and underwater superoleophobic PVDF-TiO<sub>2</sub> membranes for superior antifouling separation of oil-in-water emulsions, *J. Membr. Sci.*, 622, 119030.
- [17] Gonggo, S.T., Edyanti, F., and Suherman, S., 2013, Karakterisasi fisikokimia mineral lempung sebagai bahan dasar industri keramik di desa Lembah Bomban kecamatan Bolano Lambunu kabupaten Parigi Moutong, *JAK*, 2 (2), 105–113.
- [18] Wae AbdulKadir, W.A.F., Ahmad, A.L., and Ooi, B.S., 2021, A water-repellent PVDF-HNT membrane for high and low concentrations of oxytetracycline treatment via DCMD: An experimental investigation, *Chem. Eng. J.*, 422, 129644.
- [19] Farahani, M.H.D.A., and Vatanpour, V., 2018, A comprehensive study on the performance and antifouling enhancement of the PVDF mixed matrix membranes by embedding different nanoparticulates: Clay, functionalized carbon nanotube, SiO<sub>2</sub> and TiO<sub>2</sub>, *Sep. Purif. Technol.*, 197, 372–381.
- [20] Ravi, J., Othman, M.H.D., Matsuura, T., Ro'ıl Bilad, M., El-badawy, T.H., Aziz, F., Ismail, A.F., Rahman, M.A., and Jaafar, J., 2020, Polymeric membranes for desalination using membrane distillation: A review, *Desalination*, 490, 114530.
- [21] Ondrušová, D., Božeková, S., Buňová, L., Pajtašová, M., Labaj, I., Dubec, A., and Vrškova, J., 2018, Modification of alternative additives and their effect on the rubber properties, *MATEC Web Conf.*, 157, 07007.
- [22] Ismoyo, Y.A., Sejati, G.P.W., Pranoto, P., and Pramono, E., 2022, The potential of polyvinylidene fluoride (PVDF)-kaolin membrane for water treatment, *J. Phys.: Conf. Ser.*, 2190, 012022.
- [23] de Souza Lima, J., Costa, F.N., Bastistella, M.A., de Araújo, P.H.H., and de Oliveira, D., 2019, Functionalized kaolin as support for endoglucanase immobilization, *Bioprocess Biosyst. Eng.*, 42 (7), 1165–1173.
- [24] Mbaye, A., Diop, C.A.K., Mieke-Brendle, J., Senocq, F., and Maury, F., 2014, Characterization of natural and chemically modified kaolinite from Mako (Senegal) to remove lead from aqueous solutions, *Clay Miner.*, 49 (4), 527–539.
- [25] Tao, Q., Su, L., Frost, R.L., Zhang, D., Chen, M., Shen, W., and He, H., 2014, Silylation of mechanically ground kaolinite, *Clay Miner.*, 49 (4), 559–568.
- [26] Fatimah, I., 2018, Preparation, characterization and physicochemical study of 3-amino propyl trimethoxy silane-modified kaolinite for Pb(II) adsorption, *J. King Saud Univ., Sci.*, 30 (2), 250–257.
- [27] Pramono, E., Umam, K., Sagita, F., Saputra, O.A., Alfiansyah, R., Setyawati Dewi, R.S., Kadja, G.T.M., Ledyastuti, M., Wahyuningrum, D., and Radiman, C.L., 2023, The enhancement of dye filtration performance and antifouling properties in amino-functionalized bentonite/polyvinylidene fluoride mixed matrix membranes, *Heliyon*, 9 (1), e12823.
- [28] Yang, L., Qiu, J., Zhu, K., Ji, H., Zhao, Q., Shen, M., and Zeng, S., 2018, Effect of rolling temperature on the microstructure and electric properties of  $\beta$ -polyvinylidene fluoride films, *J. Mater. Sci.: Mater. Electron.*, 29 (18), 15957–15965.
- [29] Yuliwati, E., Ismail, A.F., Matsuura, T., Kassim, M.A., and Abdullah, M.S., 2011, Characterization of surface-modified porous PVDF hollow fibers for refinery wastewater treatment using microscopic observation, *Desalination*, 283, 206–213.
- [30] Stevenson, F.J., 1994, *Humus Chemistry: Genesis, Composition, Reactions*, 2<sup>nd</sup> Ed., John Wiley & Sons, New York.

- [31] Teoh, G.H., Ooi, B.S., Jawad, Z.A., and Low, S.C., 2021, Impacts of PVDF polymorphism and surface printing micro-roughness on superhydrophobic membrane to desalinate high saline water, *J. Environ. Chem. Eng.*, 9 (4), 105418.
- [32] Park, M.J., Wang, C., Seo, D.H., Gonzales, R.R., Matsuyama, H., and Shon, H.K., 2021, Inkjet printed single walled carbon nanotube as an interlayer for high performance thin film composite nanofiltration membrane, *J. Membr. Sci.*, 620, 118901.
- [33] Zahid, M., Rashid, A., Akram, S., Rehan, Z.A., and Razzaq, W., 2018, A comprehensive review on polymeric nano-composite membranes for water treatment, *J. Membr. Sci. Technol.*, 8 (1), 1000179.
- [34] Pramono, E., Alfiansyah, R., Ahdiat, M., Wahyuningrum, D., and Radiman, C.L., 2019, Hydrophilic poly(vinylidene fluoride)/bentonite hybrid membranes for microfiltration of dyes, *Mater. Res. Express*, 6, 105376.
- [35] Marino, T., Russo, F., and Figoli, A., 2018, The formation of polyvinylidene fluoride membranes with tailored properties via vapour/non-solvent induced phase separation, *Membranes*, 8 (3), 71.
- [36] Franco-Urquiza, E., Gamez Perez, J., Sánchez-Soto, M., Santana, O.O., and Maspocho, M.L., 2010, The effect of organo-modifier on the structure and properties of poly[ethylene-(vinyl alcohol)]/organo-modified montmorillonite composites, *Polym. Int.*, 59 (6), 778–786.
- [37] Golz, E.K., and Vander Griend, D.A., 2013, Modeling methylene blue aggregation in acidic solution to the limits of factor analysis, *Anal. Chem.*, 85 (2), 1240–1246.
- [38] Gayathri, S., and Govindaraju, K.M., 2019, Fabrication and characterization of Al/ZnO blended polyvinylidene fluoride (PVDF) membrane via electrospun method, *Res. J. Pharm. Technol.*, 12 (2), 787–790.
- [39] Woo, S.H., Kim, K.M., Park, J., and Min, B.R., 2015, Preparation and characterization of poly(vinylidene fluoride) (PVDF) membrane, *Chem. Lett.*, 44 (1), 85–87.
- [40] Fu, X., Zhu, L., Liang, S., Jin, Y., and Yang, S., 2020, Sulfonated poly( $\alpha,\beta,\beta$ -trifluorostyrene)-doped PVDF ultrafiltration membrane with enhanced hydrophilicity and antifouling property, *J. Membr. Sci.*, 603, 118046.
- [41] Zhang, Y., Ye, L., Zhao, W., Chen, L., Zhang, M., Yang, G., and Zhang, H., 2020, Antifouling mechanism of the additive-free  $\beta$ -PVDF membrane in water purification process: Relating the surface electron donor monopolarity to membrane-foulant interactions, *J. Membr. Sci.*, 601, 117873.
- [42] Mouri, E., Kajiwara, K., Kawasaki, S., Shimizu, Y., Bando, H., Sakai, H., and Nakato, T., 2022, Impacts of negatively charged colloidal clay particles on photoisomerization of both anionic and cationic azobenzene molecules, *RSC Adv.*, 12 (17), 10855–10861.
- [43] Zhang, R., Liu, Y., Li, Y., Han, Q., Zhang, T., Zeng, K., and Zhao, C., 2020, Polyvinylidene fluoride membrane modified by tea polyphenol for dye removal, *J. Mater. Sci.*, 55 (1), 389–403.
- [44] Liu, Y., Shen, L., Lin, H., Yu, W., Xu, Y., Li, R., Sun, T., and He, Y., 2020, A novel strategy based on magnetic field assisted preparation of magnetic and photocatalytic membranes with improved performance, *J. Membr. Sci.*, 612, 118378.
- [45] Liu, X., Chen, Y., Deng, Z., and Yang, Y., 2020, High-performance nanofiltration membrane for dyes removal: Blending  $\text{Fe}_3\text{O}_4$ -HNTs nanocomposites into poly(vinylidene fluoride) matrix, *J. Dispersion Sci. Technol.*, 42 (1), 93–102.
- [46] Zhao, Y., Yu, W., Li, R., Xu, Y., Liu, Y., Sun, T., Shen, L., and Lin, H., 2019, Electric field endowing the conductive polyvinylidene fluoride (PVDF)-graphene oxide (GO)-nickel (Ni) membrane with high-efficient performance for dye wastewater treatment, *Appl. Surf. Sci.*, 483, 1006–1016.

## Comparative Study of Soft Template on Gunningite Synthesis for Ibuprofen Adsorption Application

Maria Ulfa\* and Windi Apriliani

Study Program of Chemistry Education, Faculty of Teacher Training and Education, Sebelas Maret University, Jl. Ir. Sutami 36A, 57126 Surakarta, Central Java, Indonesia

\* Corresponding author:

email: mariaulfa@staff.uns.ac.id

Received: November 11, 2022

Accepted: February 18, 2023

DOI: 10.22146/ijc.79098

**Abstract:** This study aimed to investigate the effect of soft template variations on Zinc Sulfate Hydrate (Gunningite) synthesis and the maximum adsorption capacity of ibuprofen. This study employed the soft template method and hydrothermal at 100 °C, followed by calcination at 550 °C. Here, ZnSO<sub>4</sub> heptahydrate was used as the precursor for different templates. XRD analysis exhibited that the crystal sizes of Gunningite-F127G, Gunningite-F127, Gunningite-P123G, Gunningite-P123, and Gunningite-G were 18.35; 25.33; 25.67; 27.30; and 24.24 nm with crystallinity degrees of 36.89; 42.62; 46.83; 41.27; and 40.62%, respectively. FTIR examination indicated that the five samples contained functional groups of OH stretching at 3170 cm<sup>-1</sup>, Zn-O-Zn at 1637 cm<sup>-1</sup>, Zn-S=O symmetric and asymmetric at 900 and 1056 cm<sup>-1</sup>, and Zn-O at 521 cm<sup>-1</sup>. Furthermore, SEM-EDX investigation revealed that the morphology of all Gunningite samples was inhomogeneous due to agglomeration. Besides that, the elemental compositions in the samples were dominated by Zn and O elements. The maximum adsorption capacity obtained from each sample was 221.1 mg/g (Gunningite-F127G); 226.06 mg/g (Gunningite-F127); 234.23 mg/g (Gunningite-P123G); 229.76 mg/g (Gunningite-P123); and 222.85 mg/g (Gunningite-G). Moreover, the Gunningite kinetic model of ibuprofen adsorption followed Ho and McKay's pseudo-second-order kinetic model.

**Keywords:** Gunningite; ibuprofen; P123; F127; gelatin

### ■ INTRODUCTION

Pharmaceutical waste in waters derives from factory waste and the results of human body excretion. These wastes are in the form of beta blockers, non-steroidal anti-inflammatory drugs (NSAIDs), antibiotics, antiepileptic drugs, lipid regulators, and hormones [1]. One of the most commonly detected drugs in sewage treatment plants is Ibuprofen, with a concentration of 25 mg/L [2]. Ibuprofen is a type of drug that is extensively consumed in various parts of the world. For example, it has become one of the five most consumed drugs in the UK. Ibuprofen is a non-steroidal anti-inflammatory drug (NSAID), an analgesic, and an antipyretic drug used to treat rheumatism, relieve pain, and reduce fever. Ibuprofen is soluble in organic solvents but insoluble in water.

Toxicological studies have exposed different sensitivities of aquatic organisms to ibuprofen levels. In

small amounts, ibuprofen can inhibit the reproductive capacity of *Daphnia Magna*. Ibuprofen can inhibit lotus growth at levels of 0.4 g/m<sup>3</sup>, whereas, at 0.2 g/m<sup>3</sup> and 0.1 g/m<sup>3</sup>, it can affect the estrogen production of aquatic organisms and delay the hatching of Japanese yolk eggs, respectively [3]. Ibuprofen has been revealed to disrupt aquatic ecosystems. Among others, it affects the reproduction of invertebrates and vertebrates, fungi, and the growth of bacterial species; genetic and systemic damage to some shellfish fish species; and cytogenic properties in freshwater bivalves [4].

Several techniques have been conducted to overcome this pharmaceutical waste, one of which is the adsorption method. This technique can handle various levels of pollutants. In addition, it is also more efficient, easy to operate, not affected by toxins, suitable for continuous and partial processes, and the adsorbent can

be regenerated and used repeatedly [5]. One of the potential adsorbents is Gunningite which is a stable material containing zinc sulfate and monohydrate. Studies concerning Gunningite for ibuprofen adsorption are still very rare [6-7]. Materials previously used for the adsorption of ibuprofen include material-based carbon and silica. However, the stability and affinity of these materials were lacking [1,3,8]. The affinity of carbon or silica for ibuprofen was low. It can be compared from the electronegativities of C (2.5), Si (1.8), and Zn (1.6) [9] compared to O (3.5) in the O-H group, which has different electronegativities, respectively are 1.0, 1.7 and 1.9. With a high difference in electronegativity from Gunningite when interacting with Ibuprofen, it gives the advantage of attracting many ibuprofen molecules during the adsorption process.

Gunningite has been applied as an advanced material storage in the electrical field [10-11] and is a promising adsorbent for pollutant molecules [6-7]. Many technologies have been developed in synthesizing material particles, primarily to attain nanometer-sized particles, one of which is the dissolving process using either the sol-gel, hydrothermal, solvothermal, or self-assembly methods [12]. The sol-gel method is a promising way that needs a soft template as a structure directing agent for the main element of the material through intermolecular or intramolecular interaction forces. However, it generally only involves one template type and mainly uses synthetic templates such as Pluronic P123, Pluronic F127, or CTAB. On the one hand, the issue of environmentally friendly chemistry has occupied an important position in this century to cover various scopes of material synthesis, including replacing synthetic template materials with natural materials such as gelatin. Even though it is an important issue, research to observe differences in the effect of synthetic templates, natural templates, or a combination of both on materials is rarely carried out.

Types of synthetic soft templates often employed in synthesizing uniform materials include Pluronic F127 [13], Pluronic P123 [14], CTAB [15], and CTAC [16]. Pluronic F127 (MW 12500 g/mol) belongs to the biocompatible poloxamers group and is widely used in

clinics for various purposes. F127 is an amphiphilic polymer consisting of two PEO chains as the hydrophilic part and one PPO Poly(Propylene Oxide) chain as the hydrophobic part. F127 can be employed as a non-ionic emulsion surfactant due to its different polarity properties. Not only F127, Pluronic P123 or poly(ethylene oxide)-poly(propylene oxide)-poly(ethylene oxide) (PEO-PPO-PEO), having a molecular weight of 5750 g/mol, is also a dominant hydrophobic copolymer. Pluronic P123 has a relatively low critical micelle concentration (CMC) in water at about 0.313 M at 20 °C [17]. It is an excellent reason to select P123 as a sensitive surfactant to direct material structure in certain pore sizes at different temperatures. However, the high cost, low sustainability, time consumption, and complicated production are the arguments for minimizing or removing synthetic surfactants. Nevertheless, this matter can be solved by replacing the synthetic template with a natural template.

One of the natural templates is gelatin (MW close to 20000 g/mol) which can be obtained from the hydrolysis of animal skin, bone, and white fibrous tissue. The gelatin sources are sustainable and have an amine group as a high-affinity part to interact with other elements with lower electronegativity. As shown in previous research, the polar and non-polar groups in gelatin are an excellent reason to use them as a natural template. Based on the description, this work was conducted on the effects of soft template variations of F127, P123, and gelatin and their combinations to obtain Gunningite. After Gunningite had been successfully synthesized, further characterization was done to determine the crystallinity, morphology, functional groups, and adsorption capacity towards Ibuprofen.

## ■ EXPERIMENTAL SECTION

### Materials

The materials used in this study were Pluronic P123 (EO20PO70EO20) Amphiphilic Block Copolymer (MW 5790 g/mol), Pluronic F127 Poly(ethylene glycol)-*block*-poly(propylene glycol)-*block*-poly(ethylene glycol) diacrylate (MW 12,500 g/mol), gelatin (pure analysis, MW 400 KDa), ethanol, ibuprofen (2-[4-(2-methyl

propyl) phenyl]propanoic acid),  $\text{ZnSO}_4 \cdot 7\text{H}_2\text{O}$ , and *n*-hexane that were obtained from Sigma Aldrich and used without prior pretreatment.

### Instrumentation

The characterizations of the synthesized Gunningite samples involved several instruments, including X-Ray Diffraction (XRD) XRD/MAX-2550 HB/PC (Rigaku Co., Tokyo, Japan), Scanning Electron Microscopy (SEM) (JEOL JMS-700), and Fourier Transform Infrared (FTIR) with spectra recorded with a Bruker Vertex 70 spectroscope. The SEM-EDX test was performed at a voltage of 15.0 kV with a magnification of 10,000 $\times$ . Meanwhile, the FTIR analysis was done at a wavelength of 500–4000  $\text{cm}^{-1}$ .

### Procedure

#### Gunningite synthesis process

Ethanol (190 mL) was dropped with a flow rate of 3 mL/min into 3.6 g of F127/1.7 g of P123 with a burette at room temperature while it was stirred. The Erlenmeyer was kept from the air during the dripping process by covering it with plastic wrap. After the process was finished ( $\pm 4$ –5 d), 0.0346 g of 0.1% gelatin was added. Then, the mixture was stirred for 60 min. Next, 55.39 g of  $\text{ZnSO}_4$  heptahydrate were added and stirred for 24 h in a closed state with plastic wrap so that no air entered. Afterward, the sample was put into a hydrothermal reactor and heated at 100 °C for 24 h. Then, the sample was left to cool. The white solid was filtered through a Buchner filter and washed with distilled water until it obtained a pH of 7. The solid was heated in an oven at 100 °C for  $\pm 5$  h. Then, it was calcined in a furnace at 550 °C for 12 h. The synthesized sample in the form of a

white solid was stored in a closed, clear bottle (vial). The samples synthesized in this study were five types labeled in Table 1.

#### Characterization

Gunningite with various soft templates was characterized using Fourier transform infrared spectrophotometer (FTIR, Shimadzu 2100)- with a KBr pellet at a spectral resolution of 4  $\text{cm}^{-1}$ , operated from 400–4000  $\text{cm}^{-1}$  to analyze the functional group of the sample. Then, X-ray diffraction (XRD) (XRD-MAX-2550-Rigaku Co., Tokyo, Japan with 40 kV, 30 mA) at a range of  $2\theta = 5$  to 80° was performed to observe the crystallinity of the Gunningite. Scanning electron microscope (SEM, (JEOL JMS-700) coated by Pd/Au was employed to investigate the phase structure morphology of Gunningite.

#### Ibuprofen adsorption process

Ibuprofen was dissolved with hexane as a solvent to obtain 100 mL of ibuprofen with an initial concentration of 100 mg/L. Then, 50 mL of ibuprofen solution was taken and put in a beaker. Next, 0.02 g of gunningite was added to the beaker containing ibuprofen while it was stirred for 50 min at room temperature and closed. Afterward, 3 mL of the sample solution was taken every 5 min and analyzed by UV-Vis spectroscopy (model U-2000, Hitachi, Japan) at 272 nm wavelength.

## RESULTS AND DISCUSSION

XRD analysis was performed to gain information about the atomic size of crystalline and non-crystalline materials and determine the crystal structure and the orientation of the polycrystalline solid or powder sample.

**Table 1.** The type of samples synthesized in this study

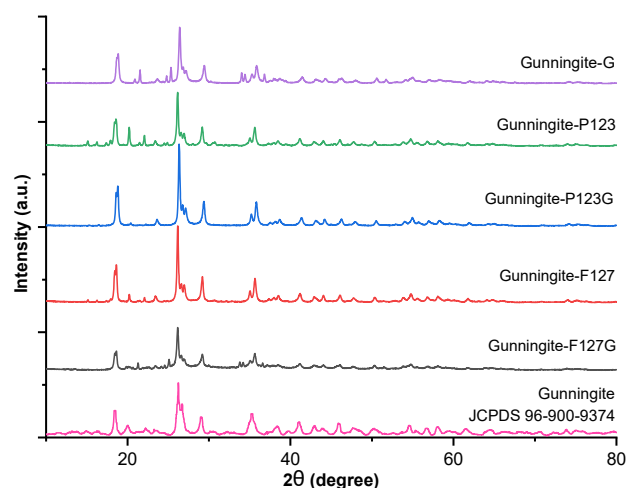
Sample	Template		
	Pluronic F127	Pluronic P123	Gelatin
Gunningite-F127G	√	-	√
Gunningite-F127	√	-	-
Gunningite-P123G	-	√	√
Gunningite-P123	-	√	-
Gunningite-G	-	-	√

Fig. 1 presents the diffraction patterns of Gunningite with variations of soft templates. It exhibits that all samples matched the Gunningite standard (JCPDS-96-900-9374). It indicated that all Gunningite samples had been successfully synthesized with  $ZnSO_4 \cdot H_2O$  as the ideal formula. It is in line with previous research [6,18]. Furthermore, the peaks of the diffractogram could be exploited to estimate the crystal size using the Debye-Scherrer equation. The results demonstrated that the crystal sizes of Gunningite-F127G, Gunningite-F127, Gunningite-P123G, Gunningite-P123, and Gunningite-G were 18.35; 25.33; 25.67; 27.30; and 24.24 nm with the crystallinity degrees of 36.89; 42.62; 46.83; 41.27; and 40.62%, respectively. The largest crystal size was achieved by Gunningite-P123. It was due to the high hydrophobic part compared to the other soft templates, which attains the large crystal size by intermolecular forces. An interesting result came from the combination of P123 and the gelatin soft template (Gunningite-P123G), which obtained the highest crystallinity at 46%. This is due to the synergy of the amine group from gelatin and the hydrophilic-hydrophobic parts or P123 to attain gunningite crystallinity degree during high-temperature treatment.

The effect of the different soft templates was also confirmed by SEM to determine the synthesized

compounds' morphology, crystal growth distribution, and physical changes in the preparation conditions. Observations were made with a magnification of 10,000 $\times$  and completed by EDX measurement to investigate elemental compositions.

Fig. 2 displays that the five samples had inhomogeneous particle shapes due to agglomeration. The morphology of the gunningite from P123, F127, gelatin, and their combination was a disordered hexagonal flake, disordered cuboid, disordered sphere, and the combination of sphere and flake. All Gunningite



**Fig 1.** Diffraction patterns of Gunningite with variations of soft templates

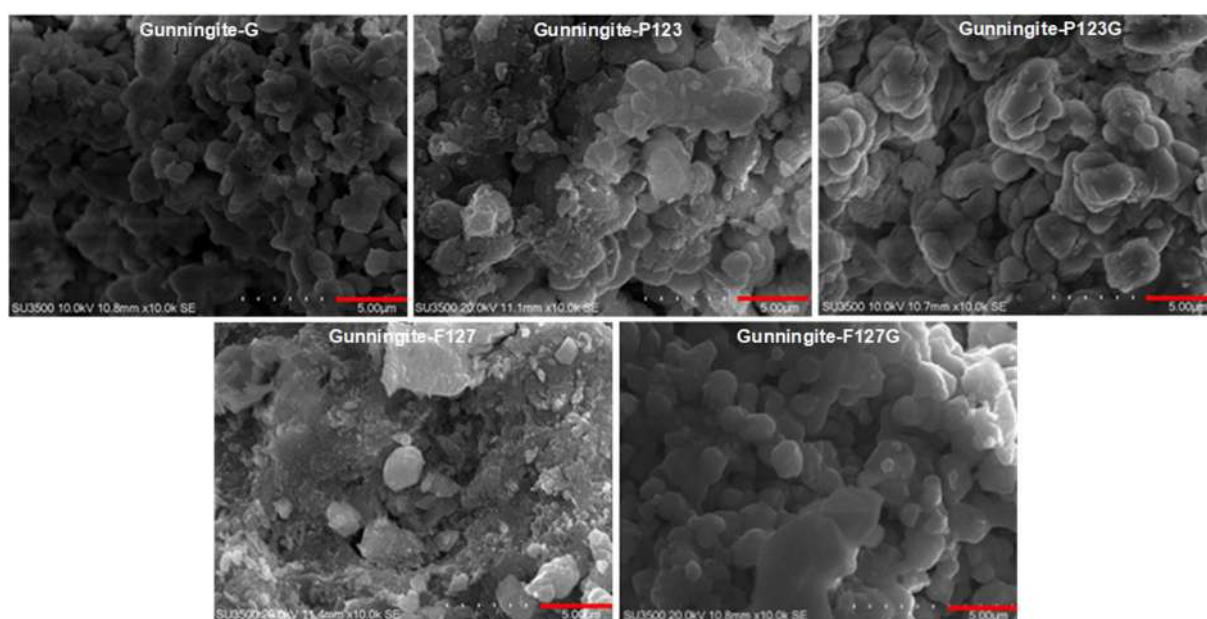


**Fig 2.** SEM images of Gunningite using the different templates

samples were agglomerated to obtain stable particle size and maintain the particle size distribution by direct hydrophobic-hydrophilic parts to interact with the precursor of Gunningite.

Fig. 3 shows the histogram of the particle size distribution from the SEM analysis. It shows that Gunningite reached the most uniform particle size distribution at P123 at  $0.67992 \mu\text{m}$  (Fig. 3(a)). It then decreased to  $0.65442 \mu\text{m}$  when combined with gelatin (Fig. 3(b)). However, the combination of F127-Gelatin

showed the largest particle distribution size at  $0.76316 \mu\text{m}$  (Fig. 3(e)). It was due to the interaction between the amine group in gelatin and the carbon chain of F127. These phenomena conclude that the domination of the hydrophobic part (PPO on P123) from the synthetic template and the amine group from the natural template decreases the particle size distribution due to the repulsive force between them. On the other hand, the domination of the hydrophilic part from the synthetic template (PEO in F127) with the hydrophobic part from

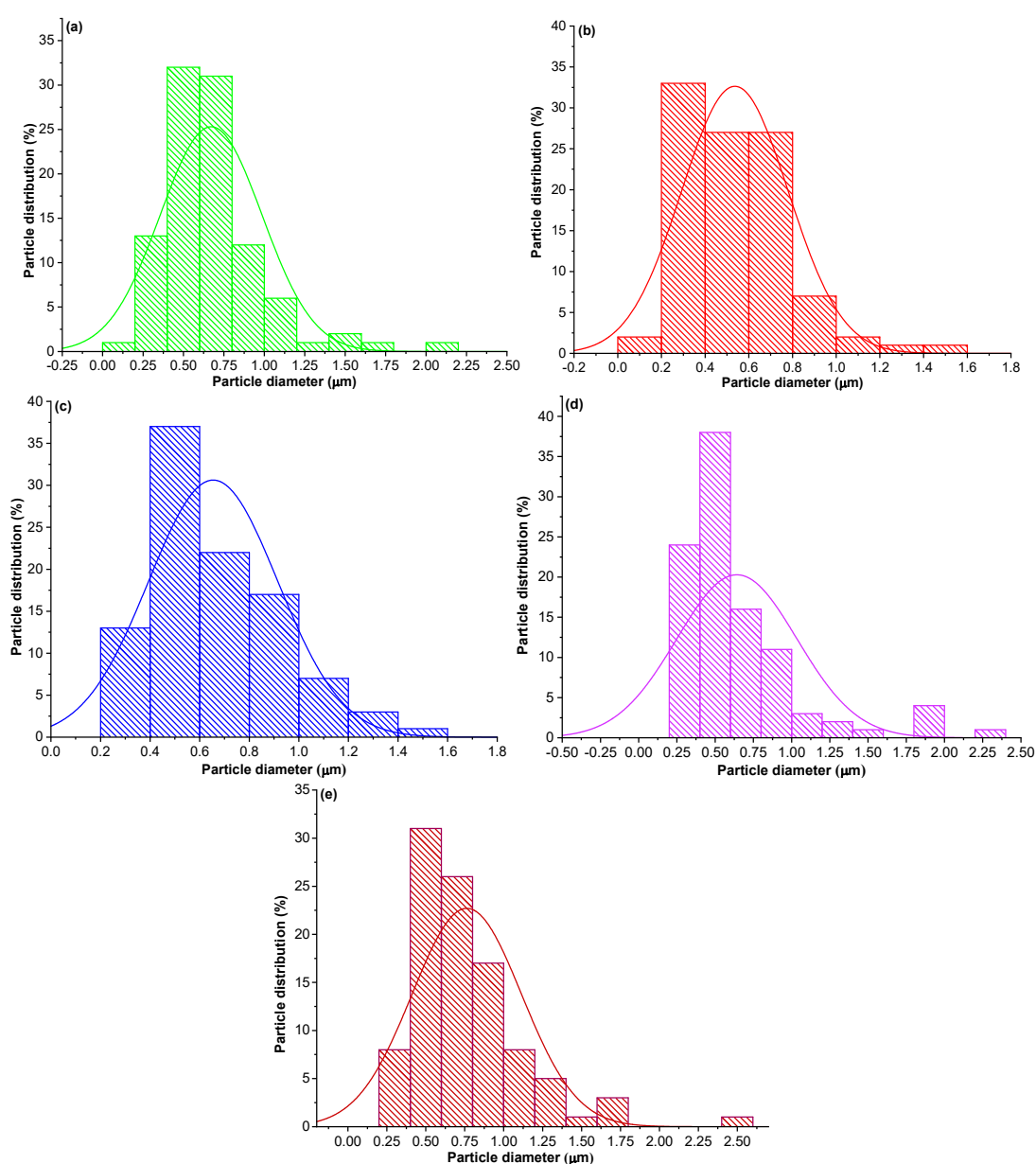


**Fig 3.** Particle size distribution of Gunningite using the templates of (a) Gelatin; (b) P123; (c) P123-Gelatin; (d) F127; and (e) F127-Gelatin



the natural template (amine group) increases the particle size distribution due to the high attraction between them due to intermolecular interaction, which is in line with previous studies [5,13,19-21].

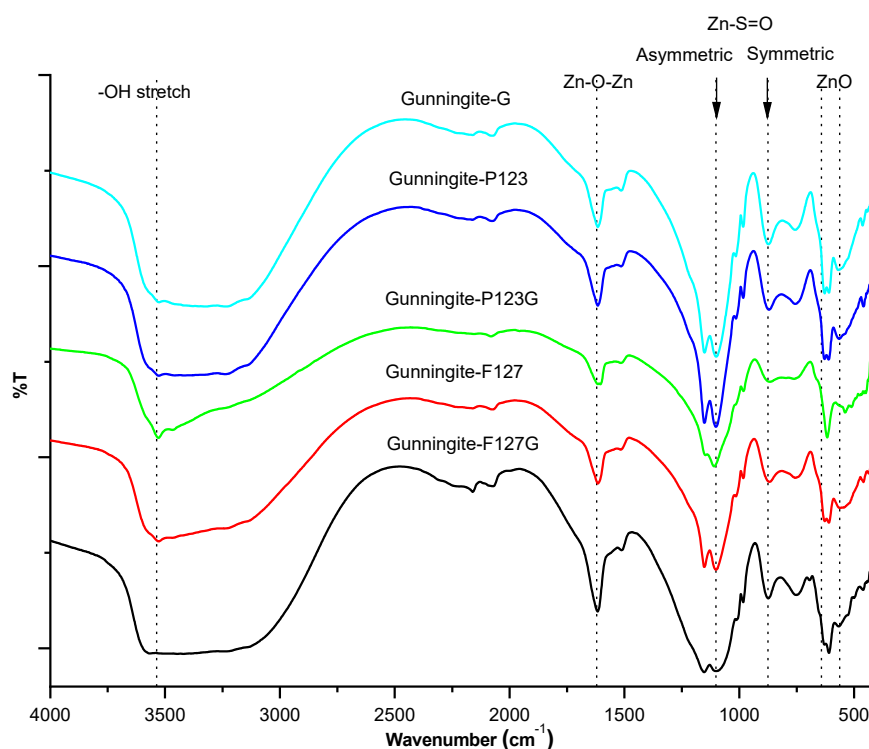
Table 2 presents the EDX results of all Gunningite samples containing Zn (67–75%), S (8.5–10%), and O (13.4–16.4%), implying the stable composition to obtain the formula of  $\text{ZnSO}_4 \cdot 1\text{H}_2\text{O}$ . The results revealed that gunningite synthesized with only P123 produced an impurity of carbon (Fig. 4(a)). It is because there is no high affinity in the functional group (such as the amine group from gelatin that pulls carbon out of the molecule during decomposition). However, Gunningite with only gelatin produced sodium as the impurity from gelatin extraction by NaOH (Fig. 4(b)). The good news was all Gunningite with only F127 (Fig. 4(d)), F127-gelatin (Fig. 4(e)), and P123-gelatin (Fig. 4(c)) exhibited high purities where P123-gelatin and F127 reached the highest composition of Zn. This is due to the synergy of the hydrophilic part and amine groups to maintain Gunningite's structure stability during decomposition.

Fig. 5 shows that the strong and broad absorption at about  $3170 \text{ cm}^{-1}$  was the stretching vibration of the

hydroxyl group of the water molecule originating from the monohydrate molecule in gunningite. Another air molecule could be found at the absorption of  $1637 \text{ cm}^{-1}$  as Zn-O-Zn bending vibrations. The strain vibrations at about  $900 \text{ cm}^{-1}$  were due to the presence of sulfate groups whose vibrations were symmetrical and asymmetrical S=O at  $1056 \text{ cm}^{-1}$ . This peak confirmed the presence of a S=O group on the sulfate group that occurred from the electrostatic interaction between hydrogen and zinc ions in the form of S=O-H-O-Zn. In contrast, the presence of Zn elements is indicated by the peak at  $521.81 \text{ cm}^{-1}$  as the Zn-O form. All of these results were in line with previous studies [6-7,10,18,22].

**Table 2.** EDX results of all Gunningite samples using various soft templates

Template	% W			
	Zn	S	O	C
Gelatin	71.2	10.1	16.4	-
P123	67.2	8.9	16.4	7.6
P123-Gelatin	76.9	8.5	14.6	-
F127	76.9	8.9	14.2	-
F127-Gelatin	75.9	8.9	13.4	-



**Fig 5.** FTIR spectra of all Gunningite from different template

Fig. 6 exhibits the maximum adsorption capacity of Gunningite on ibuprofen adsorption. Additionally, Table 1 presents the percentage of ibuprofen removal by Gunningite using templates of F127G, F127, P123G, P123, and G which was 86.9; 84.3; 93.8; 84.2; and 84.3%, respectively. Thus, the highest adsorption was found in the Gunningite-P123G sample. It was due to the highest Zn component among all samples. The Zn element, as the adsorption center, interacts with the OH group of ibuprofen through electrostatic forces. The highest elemental composition of Zn in the Gunningite-P123G sample was also observed from FTIR in the form of the sharpest/regular absorption compared to other samples, so the adsorption power of ibuprofen became greater as well.

Besides the amount of Zn in Gunningite, the low sulfur component indicated high adsorption removal performance. It was because Gunningite as the adsorbent and ibuprofen as the adsorbate also affected the adsorption capacity. The Gunningite compound acts as an adsorbent, and ibuprofen acts as an adsorbate interacting competitively between Zn-O-ibuprofen and S-O-ibuprofen. If the amount of sulfur is low, the interaction will occur on the hydroxyl group of ibuprofen with metal ions  $Zn^{2+}$ , allowing the formation of a stable

covalent coordination complex. Fig. 7 demonstrates the adsorption scheme of ibuprofen onto Gunningite.

The adsorption kinetics models performed in this study were pseudo-first-order and pseudo-second-order. The models were used to process data on the ibuprofen adsorption by Gunningite, determine the adsorption variables involved, and select the adsorption mechanism that occurs. The adsorption kinetics model can also predict the speed of adsorbate transferring from solution to adsorbent [23-24]. Table 3 presents the calculation results of the adsorption kinetics models of gunningite using pseudo-first-order and pseudo-second-order.

Fig. 8(a-b) presents the kinetic of gunningite with different templates by pseudo-first-order and pseudo-second-order models. The graphs reveal linear equations obtained by each sample. Based on Table 3 and Fig. 8(a),

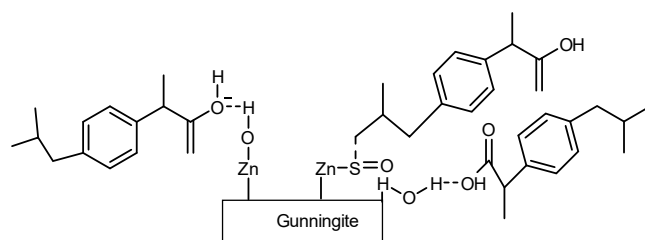


Fig 7. Adsorption scheme of ibuprofen onto Gunningite

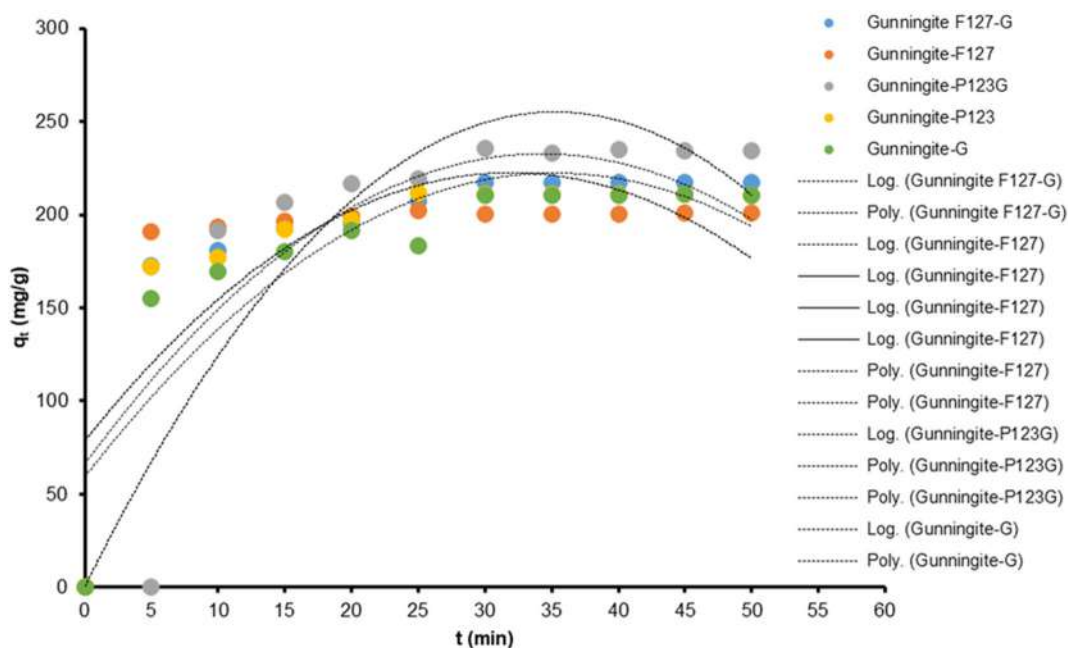
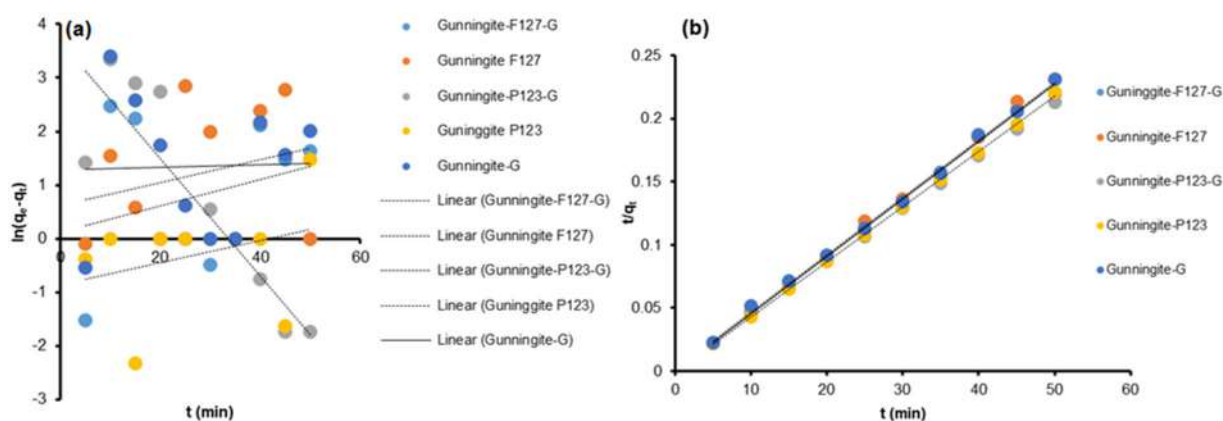


Fig 6. Adsorption performance of all sample of Gunningite

**Table 3.** Adsorption kinetics models of Gunningite using pseudo-first and pseudo-second-order

	Gunningite with various soft templates				
	F127-G	F127	F123-G	P123	G
Pseudo-first-order model: $\ln(q_e - q_t) = \ln q_e - k_1 t$					
$k_1$	0.0246	0.0214	0.1092	0.0205	0.0025
$q_{cal}$	0.1143	0.6149	3.6751	0.852	1.283
$R^2$	0.0748	0.0687	0.779	0.0905	0.0009
Pseudo-second-order model: $\left(\frac{t}{q_t} - \frac{1}{k_2 q_e q_e}\right) = kt$					
$k_2$	0.0047	0.0046	0.0048	0.0044	0.0045
$q_{cal}$	0.0024	0.0005	0.0029	0.0009	0.0014
$R^2$	0.9951	0.9949	0.9936	0.9996	0.9981
%Rem	86.9	84.3	93.8	84.2	80.3

**Fig 8.** Kinetic of Gunningite using different templates by (a) Pseudo-first-order and (b) Pseudo-second-order model

Gunningite-F127G possessed an equation of  $y = 0.0246x + 0.1143$  with  $R^2 = 0.0748$ . For the Gunningite-F127 sample, it was  $y = 0.0214x + 0.6149$  with  $R^2 = 0.0687$ . Gunningite-P123 sample had an equation of  $y = -0.1092x + 3.6751$  with  $R^2 = 0.779$ . The Gunningite-P123G sample exhibited  $y = 0.0205x - 0.8522$  with  $R^2 = 0.0905$ . Meanwhile, the Gunningite-G sample demonstrated an equation of  $y = 0.0025x + 1.283$  with  $R^2 = 0.0009$ . A good linear graph is a graph that has an  $R^2$  value close to or equal to 1. Of the five samples, four samples had  $R^2$  values that were far from 1, and only the Gunningite-P123G sample was close to 1. Besides the  $R^2$  of the graphic equation, the suitability of the adsorption kinetics model with the ibuprofen adsorption by Gunningite could also be seen from the  $q_e$  value (adsorption capacity). With this kinetic model, the  $q_e$  values attained differed from the  $q_e$  values of the experimental results. This indicated that

Lagergren's pseudo-first-order adsorption kinetics model was not suitable for the adsorption experiment of ibuprofen by gunningite. Next, the calculation was based on Ho and McKay's pseudo-second-order of adsorption kinetics model.

Based on Table 2 and Fig. 8(b), the linear equation for the Gunningite-F127G sample was  $y = 0.0046x - 0.0005$  with  $R^2 = 0.999$ . The Gunningite-F127 sample had a linear equation of  $y = 0.0046x - 0.0005$  with  $R^2 = 0.9949$ . Gunningite-P123G exhibited a linear equation of  $y = 0.0042x + 0.0047$  with  $R^2 = 0.9988$ . Gunningite-P123 revealed  $y = 0.0044x - 0.0009$  with  $R^2 = 0.9996$ . Gunningite-G presented  $y = 0.0045x + 0.0014$  with  $R^2 = 0.9981$ . The data showed that the linearity of each graph was appropriate, as indicated by their  $R^2$  values that were close to 1. In addition, the  $q_e$  values (adsorption capacity) based on this kinetic model were close to the  $q_e$  value of

the experimental results. This indicated that Ho and McKay's pseudo-second-order adsorption kinetics model was more suitable for the ibuprofen adsorption experiment by Gunningite. This was supported by the previous research [1-3,25-26] which demonstrated that the adsorption of ibuprofen with the pseudo-second-order adsorption kinetics model presented the best results compared to several other adsorption kinetics models, with the  $R^2$  value on the graph ranging from 0.95–0.99 for all samples and the  $q_e$  was close to the experimental  $q_e$  value.

## ■ CONCLUSION

Gunningite nanoparticles have been successfully synthesized through the soft template method, hydrothermal at 100 °C, and calcination at 550 °C using  $ZnSO_4$  heptahydrate as the precursor and various templates of F127, P123, and gelatin. The XRD results showed that the crystal sizes of the Gunningite in the template variations of Gunningite-F127G, Gunningite-F127, Gunningite-P123G, Gunningite-P123, and Gunningite-G were 18.35; 25.33; 25.67; 27.30; and 24.24 nm, respectively, while the crystallinity degrees were 36.89; 42.62; 46.83; 41.27; and 40.62%, respectively. The FTIR results exposed that the functional groups in gunningite were OH stretching, Zn-O-Zn, and gunningite. The SEM-EDX results demonstrated that the morphology of gunningite is inhomogeneous due to agglomeration, and the Zn and O elements dominated composition elements in the samples. The maximum adsorption capacity values of gunningite to adsorb ibuprofen on various templates of Gunningite-F127G, Gunningite-F127, Gunningite-P123G, Gunningite-P123, and Gunningite-G were 221.1; 226.06; 234.23; 229.76; and 222.85 mg/g, respectively. The gunningite kinetic model of ibuprofen adsorption followed Ho and McKay's pseudo-second-order kinetic model.

## ■ ACKNOWLEDGMENTS

The author would like to express special thanks to the Ministry of Research and Technology National Research and Innovation Agency (DIKTI) Indonesia for the funding grants on Fundamental research under No.

469.1/UN27.22/PT01.03/2022/2022 for Maria Ulfa from Sebelas Maret University.

## ■ AUTHOR CONTRIBUTIONS

Maria Ulfa, conceived and designed the experiments, concept, and method; analyzed, investigated, and interpreted the data analysis; contributed reagents and materials; wrote, revised, edited, reviewed, and supervised the manuscript. Windi Apriliani conducted the analysis tools or data, wrote the raw paper, and conducted the experiment and formal calculations. All authors agreed to the final version of this manuscript.

## ■ REFERENCES

- [1] Manzano, J.S., Singappuli-Arachchige, D., Parikh, B.L., and Slowing, I.I., 2018, Fine-tuning the release of molecular guests from mesoporous silicas by controlling the orientation and mobility of surface phenyl substituents, *Chem. Eng. J.*, 340, 73–80.
- [2] Das, S.K., Kahali, N., Bose, A., and Khanam, J., 2018, Physicochemical characterization and *in vitro* dissolution performance of ibuprofen-Captisol® (sulfobutylether sodium salt of  $\beta$ -CD) inclusion complexes, *J. Mol. Liq.*, 261, 239–249.
- [3] Wang, X., Liu, P., and Tian, Y., 2011, Preparation and drug release behavior of temperature-responsive mesoporous carbons, *J. Solid State Chem.*, 184 (6), 1571–1575.
- [4] Ulfa, M., Prasetyoko, D., Mahadi, A.H., and Bahruji, H., 2020, Size tunable mesoporous carbon microspheres using Pluronic F127 and gelatin as co-template for removal of ibuprofen, *Sci. Total Environ.*, 711, 135066.
- [5] Bouzidi, M., Sellaoui, L., Mohamed, M., Franco, D.S.P., Erto, A., and Badawi, M., 2023, A comprehensive study on paracetamol and ibuprofen adsorption onto biomass-derived activated carbon through experimental and theoretical assessments, *J. Mol. Liq.*, 376, 121457.
- [6] Ulfa, M., Ari, M., and Ali, P., 2022, Influence of calcination temperatures on gunningite-based gelatin template and its application as ibuprofen adsorption, *Indones. J. Chem.*, 22 (6), 1684–1692.

- [7] Prasetyoko, D., Sholeha, N.A., Subagyo, R., Ulfa, M., Bahruji, H., Holilah, H., Pradipta, M.F., and Jalil, A.A., 2023, Mesoporous ZnO nanoparticles using gelatin — Pluronic F127 as a double colloidal system for methylene blue photodegradation, *Korean J. Chem. Eng.*, 40 (1), 112–123.
- [8] Guedidi, H., Reinert, L., Soneda, Y., Bellakhal, N., and Duclaux, L., 2017, Adsorption of ibuprofen from aqueous solution on chemically surface-modified activated carbon cloths, *Arabian J. Chem.*, 10 (2), S3584–S3594.
- [9] Babikier, M., Wang, D., Wang, J., Li, Q., Sun, J., Yan, Y., Yu, Q., and Jiao, S., 2014, Fabrication and properties of sulfur (S)-doped ZnO nanorods, *J. Mater. Sci.: Mater. Electron.*, 25 (1), 157–162.
- [10] Ducher, M., Blanchard, M., and Balan, E., 2018, Equilibrium isotopic fractionation between aqueous Zn and minerals from first-principles calculations, *Chem. Geol.*, 483, 342–350.
- [11] Tilak, S., and Suresh Kumar, H.M., 2020, Optical, thermal, mechanical, dielectric and magnetic properties of zinc sulphate doped L-ascorbic acid NLO crystal, *Mater. Today: Proc.*, 27, 503–508.
- [12] Karakiliç, P., Toyoda, R., Kapteijn, F., Nijmeijer, A., and Winnubst, L., 2019, From amorphous to crystalline: Transformation of silica membranes into silicalite-1 (MFI) zeolite layers, *Microporous Mesoporous Mater.*, 276, 52–61.
- [13] Yan, Y., Wei, J., Zhang, F., Meng, Y., Tu, B., and Zhao, D., 2008, The pore structure evolution and stability of mesoporous carbon FDU-15 under CO<sub>2</sub>, O<sub>2</sub> or water vapor atmospheres, *Microporous Mesoporous Mater.*, 113 (1-3), 305–314.
- [14] Liu, T., Lai, D., Feng, X., Zhu, H., and Chen, J., 2013, Synthesis and characterization of a novel mesoporous bioactive glass/hydroxyapatite nanocomposite, *Mater. Lett.*, 92, 444–447.
- [15] Ulfa, M., Masykur, A., Nofitasari, A.F., Sholeha, N.A., Suprpto, S., Bahruji, H., and Prasetyoko, D., 2022, Controlling the size and porosity of sodalite nanoparticles from Indonesian kaolin for Pb<sup>2+</sup> removal, *Materials*, 15 (8), 2745.
- [16] Nagamine, S., Kurumada, K., Tanigaki, M., and Endo, A., 2001, Effects of catalytic acid and templating surfactant concentrations on mesostructure of submillimeter-thick mesoporous silica by solvent evaporation synthesis, *Microporous Mesoporous Mater.*, 49 (1-3), 57–64.
- [17] He, Z., and Alexandridis, P., 2018, Micellization thermodynamics of Pluronic P123 (EO<sub>20</sub>PO<sub>70</sub>EO<sub>20</sub>) amphiphilic block copolymer in aqueous ethylammonium nitrate (EAN) solutions, *Polymer*, 10 (1), 32.
- [18] Buzatu, A., Dill, H.G., Buzgar, N., Damian, G., Maftai, A.E., and Apopei, A.I., 2016, Efflorescent sulfates from Baia Sprie mining area (Romania) — Acid mine, *Sci. Total Environ.*, 542, 629–641.
- [19] Yang, J., Zhai, Y., Deng, Y., Gu, D., Li, Q., Wu, Q., Huang, Y., Tu, B., and Zhao, D., 2010, Direct triblock-copolymer-templating synthesis of ordered nitrogen-containing mesoporous polymers, *J. Colloid Interface Sci.*, 342 (2), 579–585.
- [20] Li, S., Jiang, M., Shi, X., Liu, Z., and Zhou, G., 2017, P123 assisted morphology-engineered and hierarchical TiO<sub>2</sub> microspheres for enhanced photocatalytic activity, *J. Porous Mater.*, 24 (6), 1425–1436.
- [21] Shi, F., Liu, J.X., Huang, X., Yu, L., Liu, S.H., Feng, X., Wang, X.K., Shao, G.L., Hu, S.C., Yang, B., and Fan, C.Y., 2015, Hydrothermal synthesis of mesoporous WO<sub>3</sub>-TiO<sub>2</sub> powders with enhanced photocatalytic activity, *Adv. Powder Technol.*, 26 (5), 1435–1441.
- [22] Wang, X., Wan, Y., Hu, W., Chou, I.M., Cao, J., Wang, X., Wang, M., and Li, Z., 2016, *In situ* observations of liquid–liquid phase separation in aqueous ZnSO<sub>4</sub> solutions at temperatures up to 400 °C: Implications for Zn<sup>2+</sup>-SO<sub>4</sub><sup>2-</sup> association and evolution of submarine hydrothermal fluids, *Geochim. Cosmochim. Acta*, 181, 126–143.
- [23] Ho, Y.S., and McKay, G., 1999, Pseudo-second order model for sorption processes, *Process Biochem.*, 34 (5), 451–465.
- [24] Ho, Y.S., 2004, Citation review of Lagergren kinetic

- rate equation on adsorption reactions, *Scientometrics*, 59 (1), 171–177.
- [25] Ulfa, M., Sari, A.Y., and Prasetyoko, D., 2018, Synthesis of unique natural silica (UNS) material via dual co-templating method using starch of waste rice-gelatin composite and their performance in drug delivery system, *AIP Conf. Proc.*, 2049, 020003.
- [26] Lei, X., Huang, L., Liu, K., Ouyang, L., Shuai, Q., and Hu, S., 2021, Facile one-pot synthesis of hierarchical N-doped porous carbon for efficient ibuprofen removal, *J. Colloid Interface Sci.*, 604, 823–831.

## Thermo- and pH-Responsive Behavior of Poly(*N*-isopropylacrylamide)-Block-Poly[(2-dimethylamino)ethyl Methacrylate]

Noverra Mardhatillah Nizado\*, Rida Hasna Fadhillah, and Ivandini Tribidasari Anggraningrum

Department of Chemistry, Faculty of Mathematics and Natural Sciences, Universitas Indonesia,  
Kampus UI, Depok 16424, Indonesia

\* **Corresponding author:**

tel: +62-21-7270027

email: noverra.mardhatillah@sci.ui.ac.id

Received: September 19, 2022

Accepted: January 23, 2023

DOI: 10.22146/ijc.79264

**Abstract:** The influence of poly(2-dimethylamino)ethyl methacrylate (PDMAEMA) block on the thermo- and pH-responsive behavior of poly(*N*-isopropyl acrylamide)-block-poly[(2-dimethylamino)ethyl methacrylate)] (PNIPAM-*b*-PDMAEMA) was studied. The block copolymers were synthesized using reversible addition-fragmentation chain transfer (RAFT) polymerization by varying the chain length of the second block (PDMAEMA). <sup>1</sup>H-NMR and FTIR spectra confirmed the formation of block copolymers PNIPAM<sub>21</sub>-*b*-PDMAEMA<sub>2</sub> and PNIPAM<sub>21</sub>-*b*-PDMAEMA<sub>7</sub> with the corresponding molar masses from the GPC data. Thermo- and pH-responsive behavior of block copolymers was investigated in phosphate buffer with various pHs. Interesting results showed that the hydrophilic carboxyl end group and the hydrophobic dodecyl end group of the RAFT agent affected the resulting phase transition temperature ( $T_c$ ), while the  $T_c$  was found to be low in the acidic environment. Moreover, larger particle sizes of PNIPAM<sub>21</sub>-*b*-PDMAEMA<sub>2</sub> were found with a pH of 9. It is noteworthy, that the resulted block copolymers might have the potential use in a drug delivery system.

**Keywords:** block copolymer; PNIPAM; PDMAEMA; thermo-responsive polymers; pH-responsive polymers

### ■ INTRODUCTION

Stimulus-responsive polymers can undergo reversible changes in properties in the solution when external stimuli are applied, such as pH, temperature, and chemical and biological agents. The combination of two or more different monomers that have a different response to a stimulus can result in multi-responsive copolymers [1]. In particular, temperature and pH are interesting stimuli that can be explored, including their applications [2-6] due to their availability in the environment.

Two types of thermo-responsive behavior for polymers are lower critical solution temperature (LCST) and upper critical solution temperature (UCST). In LCST-type polymers, the polymers are soluble at the temperature range below their phase transition temperature ( $T_c$ ), otherwise, a soluble-to-insoluble happens while heating. Vice-versa, UCST-type polymers are soluble above  $T_c$ . An example of a widely used LCST-type polymer is poly(*N*-isopropyl acrylamide) (PNIPAM)

with a  $T_c$  of 32 °C [7].

In addition to temperature, another external stimulus that is widely used in the field of responsive polymers is pH. There are two types of pH-responsive polymers, i.e., polymers with acidic groups (poly acids) and basic groups (poly bases) [1]. Deprotonation of acidic groups within the chain of poly acids results in a negative charge at high pH and causes the polymer to become more hydrophilic. Conversely, the basic group in polybasic is protonated at low pH and increases its solubility in water media as in the case of poly(2-(dimethylamino)ethyl methacrylate) (PDMAEMA) [7].

Research concerning thermo- and/ or pH-responsive block copolymers has been widely developed recently [8-9], especially in drug delivery systems due to the reversible solubility of thermo-responsive blocks [10] and reversible ionization of pH-responsive blocks [11]. The idea is to use both properties to promote self-assembly and form micelles because of the changes in

hydrophobic-hydrophilic properties, in which the hydrophobic drugs can be loaded in the core of the micelles and then released when the micelles deform to unimers.

Thermo- and pH-responsive block copolymers can be synthesized using one block that has thermo-responsive behavior, and the other block that consists of a pH-responsive polymer [1]. One possible way to synthesize such block copolymers is by using controlled radical polymerization, namely reversible addition-fragmentation chain transfer (RAFT). Several studies on the use of RAFT to synthesize multi-responsive block copolymers have been reported, not only for diblock [12] but also for triblock copolymers [13-15].

Herein we report our studies about the synthesis of block copolymers of PNIPAM-*b*-PDMAEMA via RAFT by varying the chain length of the second block of PDMAEMA and investigating their thermo- and pH-responsive behavior. 2-(Dodecylthiocarbonothioylthio)-2-methyl propionic acid (DDMAT) was used as a chain transfer agent, which hypothetically might also influence the pH-responsive behavior of the resulted block copolymers due to the presence of carboxyl groups [16-17]. The copolymers were constructed by forming PNIPAM as the macro-CTA first and followed by the addition of DMAEMA as the second block. To our knowledge, the thermo- and pH-responsive behavior of PNIPAM-*b*-PDMAEMA has not been studied yet.

## ■ EXPERIMENTAL SECTION

### Materials

The materials used in this study were N-isopropylacrylamide (NIPAM, 97% purity, Sigma-Aldrich), 2-(dimethylamino)ethyl methacrylate (DMAEMA, 98% purity, Sigma-Aldrich), 2-(dodecylthiocarbonothioylthio)-2-methylpropionic acid (DDMAT, 98% purity, Sigma-Aldrich). 1,4-dioxane was obtained from Smart-Lab. 2,2'-azobisisobutyronitrile (AIBN, 98% purity, Clariant), potassium dihydrogen phosphate (KH<sub>2</sub>PO<sub>4</sub>, 99% purity, Merck) and dipotassium hydrogen phosphate (K<sub>2</sub>HPO<sub>4</sub>, 99% purity, Merck). Sodium hydroxide (NaOH) and phosphoric acid (H<sub>3</sub>PO<sub>4</sub>) were obtained from Rofa Laboratorium Centre.

### Instrumentation

The instrumentations used in this study were Fourier transform infrared (Shimadzu-IR Prestige 21) and proton magnetic resonance (Bruker Advance 500 MHz) to characterize the chemical structure of the block copolymers. Gel permeation chromatography (Shimadzu LC-20 equipped with column LF 804) was used for molecular weight determination of the block copolymers. Thermo- and pH-responsive behavior was investigated using UV-Visible spectrophotometer (Thermo Scientific Multiscan Go UV-Visible spectrophotometer) and particle size analyzer (Horiba SZ 100z Nano Particle Size Analyzer).

### Procedure

#### Synthesis of PNIPAM macro-CTA

NIPAM monomer (2.8326 g, 25 mmol) and DDMAT (0.2572 g, 0.7 mmol) were dissolved in 5 mL 1,4-dioxane and put into a Schlenk flask equipped with a magnetic bar. The solution was degassed with nitrogen under stirring for 15 min, and the flask was placed in a preheated oil bath at 70 °C. After that, AIBN (0.02 g, 0.12 mmol), which was pre-dissolved in 2.5 mL 1,4-dioxane, was rapidly transferred into the Schlenk flask. Polymerization was carried out for 6 h at 70 °C under stirring. The polymerization reaction was quenched by placing the flask in an ice bath and exposing the solution to air. PNIPAM was isolated by three cycles of precipitation-decantation in cold *n*-hexane and then dried in an oven at 60 °C overnight to obtain yellow powder (2.1746 g, 69.92% yield). The synthesis procedure was adapted from the work of Giaouzi and Pispas [12].

#### Synthesis of PNIPAM-*b*-PDMAEMA block copolymers

PNIPAM was used as macro-CTA to produce PNIPAM-*b*-PDMAEMA block copolymers with the ratio that can be seen in Table 1. The synthesis procedure are as follows: DMAEMA (0.5830 g, 3.7 mmol), PNIPAM macro-CTA (0.4378 g, 0.16 mmol), and 5 mL 1,4-dioxane were added into a 25 mL Schlenk flask equipped with a magnetic bar. Oxygen was removed from the solution by bubbling with nitrogen for 15 min under stirring, and then the flask was placed in a preheated oil



**Table 1.** Recipe for the synthesis of PNIPAM-*b*-PDMAEMA

Product	NIPAM (g)	DMAEMA (g)	DDMAT (g)	Macro-CTA (g)	AIBN (g)
PNIPAM Macro-CTA	2.8326	-	0.2572	-	0.02
PNIPAM <sub>21</sub> - <i>b</i> -PDMAEMA <sub>2</sub>	-	0.5830	-	0.4378	0.0045
PNIPAM <sub>21</sub> - <i>b</i> -PDMAEMA <sub>7</sub>	-	0.7751	-	0.6077	0.0030

Note: Reaction occurred for 6 h at 70 °C

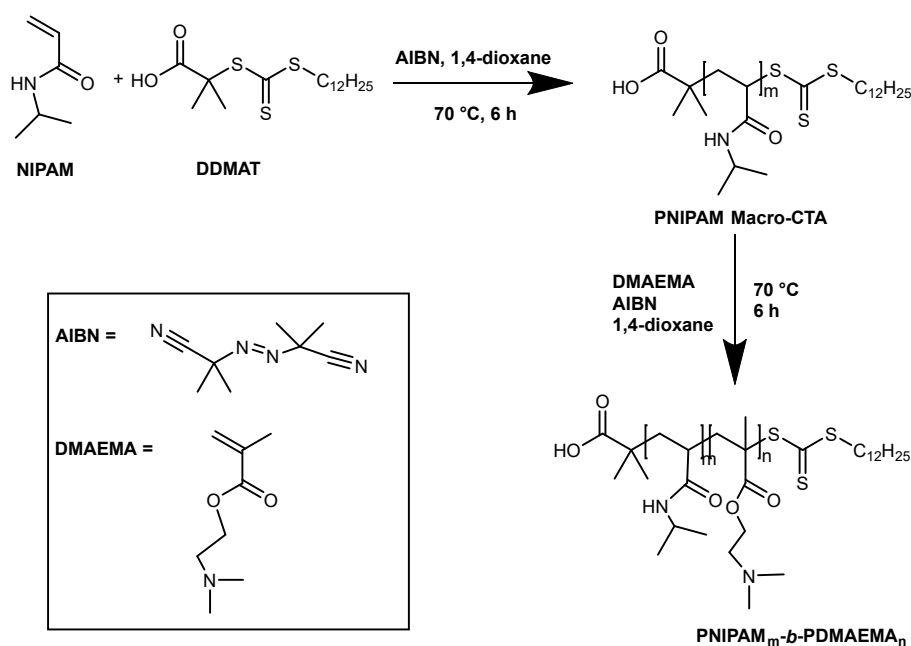
oil bath at 70 °C. Then, AIBN (0.0045 g, 0.03 mmol) in 2.5 mL 1,4-dioxane was added into a Schlenk flask. Polymerization was carried out at 70 °C with continuous stirring for 6 h and stopped by quenching it in an ice bath and exposing it to air. The polymerization product was obtained by three cycles of precipitation-decantation in cold *n*-hexane and then dried in an oven at 60 °C overnight. The synthesis method was adapted from the work of Giaouzi and Pispas and Tebaldi et al. with modifications [12,18].

## RESULTS AND DISCUSSION

### Synthesis and Characterization of PNIPAM-*b*-PDMAEMA Block Copolymers

PNIPAM<sub>21</sub> was used as the macro-chain transfer agent for the subsequent RAFT polymerization of DMAEMA to obtain PNIPAM-*b*-PDMAEMA block

copolymers. The PNIPAM-*b*-PDMAEMA was synthesized by varying different chain lengths of PDMAEMA, and each polymer was characterized by FTIR, <sup>1</sup>H-NMR, and GPC analysis. The synthetic route followed is depicted in Scheme 1. Fig. 1 shows the FTIR spectra of NIPAM, PNIPAM macro-CTA, and PNIPAM-*b*-PDMAEMA block copolymers. By comparing each of the spectra, some differences can be noticed, which indicate that a new compound has been formed. FTIR spectra of PNIPAM macro-CTA and PNIPAM-*b*-PDMAEMA showed no C=C peak at 1600–1650 cm<sup>-1</sup> [19], suggesting that polymerization has occurred [20]. Meanwhile, in the FTIR spectra of PNIPAM macro-CTA and PNIPAM-*b*-PDMAEMA, there were peaks at 3076 and 3075 cm<sup>-1</sup>, respectively, which could be attributed to the stretching vibration of C(sp<sup>2</sup>)-H group but the intensity of the peak was lower in



**Scheme 1.** Synthetic route of PNIPAM-*b*-PDMAEMA block copolymers

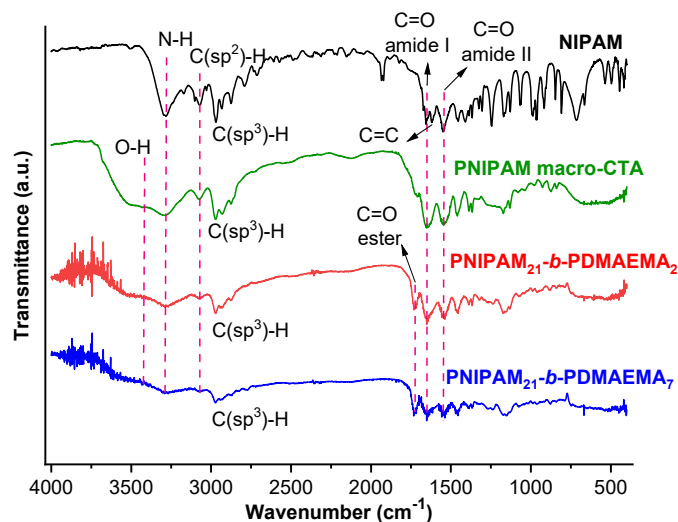


**Fig 1.** FTIR spectra of NIPAM, PNIPAM macro-CTA, and PNIPAM-*b*-PDMAEMA

comparison with NIPAM, confirming that some unreacted monomer still existed. Compared with the FTIR spectrum of PNIPAM macro-CTA, a peak at  $1728\text{ cm}^{-1}$  appeared in the FTIR spectra of PNIPAM-*b*-PDMAEMA after copolymerization, indicating the presence of C=O ester from the PDMAEMA block. Characteristic peaks of PNIPAM in FTIR spectra of PNIPAM-*b*-PDMAEMA can be observed, as evidenced by the presence of the peak at  $3288\text{ cm}^{-1}$  that was ascribed to N-H stretching vibration, while the peak at  $1647\text{ cm}^{-1}$

was ascribed to C=O amide I and the peak at  $1544\text{ cm}^{-1}$  was assigned to C=O amide II. The absorption peak at  $3436\text{ cm}^{-1}$  was a stretching vibration of O-H in the COOH end group.

$^1\text{H-NMR}$  spectra of PNIPAM macro-CTA and PNIPAM-*b*-PDMAEMA block copolymers in  $\text{CDCl}_3$  are shown in Fig. 2. Based on the resulting FTIR spectra, there was a peak of C(sp<sup>2</sup>)-H group in the products, which also occurred in the  $^1\text{H-NMR}$  spectra. In this study, one of the peaks of three protons from the vinyl group of PNIPAM was detected at 5.5 ppm, confirming that there were still some NIPAM monomer impurities remaining in the product (Fig. 2(a)). Fig. 2(b) and 2(c) show that peaks of DMAEMA monomer were still detected, which were attributed to peak o, p, and q. These results were similar to the results obtained by De Jesús-Télez et al. when characterizing the DMAEMA monomer [21], suggesting that there was still unreacted DMAEMA monomer in the copolymer product and the purification process has not been optimal. This happened most probably due to the non-polar properties of *n*-hexane that makes the immersion of the product in *n*-hexane needs to be longer before decantation to allow the monomers to be more soluble in *n*-hexane. Previous work from Göktaş in 2020 reported similar results of the existence of the vinyl peak

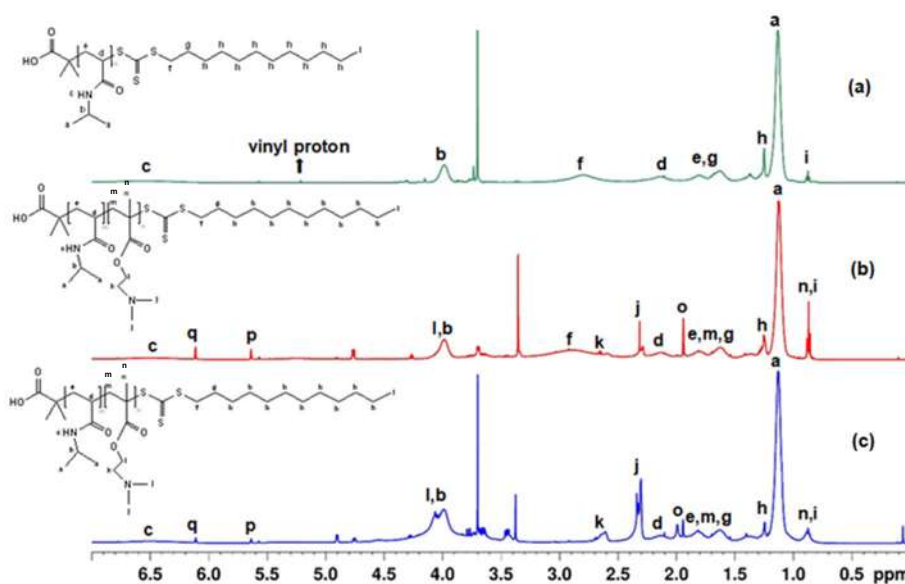


**Fig 2.**  $^1\text{H-NMR}$  spectra of PNIPAM macro-CTA (a), PNIPAM<sub>21</sub>-*b*-PDMAEMA<sub>2</sub> (b), and PNIPAM<sub>21</sub>-*b*-PDMAEMA<sub>7</sub> (c) in  $\text{CDCl}_3$

from the DMAEMA monomer when the purification was performed using methanol as the precipitation medium [22].

Based on Fig. 2(a), it is shown that PNIPAM macro-CTA was successfully synthesized, indicated by the presence of characteristic peaks a 1.12 ppm ( $-\text{CH}(\text{CH}_3)_2$ , 6H) and b 3.98 ppm ( $-\text{CH}(\text{CH}_3)_2$ , 1H) which were similar to the previous study [23]. By calculating the ratio of the integrated peak areas between peak b from PNIPAM and peak i from the dodecyl end group, the repeating unit of PNIPAM was found to be about 21 and the molecular weight ( $M_n$ ) was at 2728 g/mol.

As displayed in Fig. 2(b) and 2(c), some new peaks appeared in the  $^1\text{H-NMR}$  spectra of PNIPAM-*b*-PDMAEMA in comparison with the  $^1\text{H-NMR}$  spectrum of PNIPAM macro-CTA. Characteristic peaks of PDMAEMA were assigned to peak j, k, l, and n. Overlapping double peaks around 4 ppm were ascribed to the proton of  $-\text{CH}(\text{CH}_3)_2$  from the PNIPAM block (peak b) and the proton of  $-\text{CH}_2\text{CH}_2\text{N}(\text{CH}_3)_2$  from the PDMAEMA block (peak l). Peak f of the dodecyl end group did not always appear in every  $^1\text{H-NMR}$  spectrum of the PNIPAM-*b*-PDMAEMA block copolymers, as reported in a previous study [24].

The repeating unit of PDMAEMA in the copolymers was determined by comparing the integration of the protons j and a, which was found to be 2 with molecular weight ( $M_n$ ) at 3043 g/mol (Fig. 2(b)). Meanwhile, as seen in Fig. 2(c), the molecular weight ( $M_n$ ) at 3829 g/mol and degree polymerization (DP) at 7 were calculated from integral values of peak areas of the signals k and a.

The molecular weight characterization was performed by gel permeation chromatography (GPC) using THF as eluent and polystyrene as the standard

(Table 2). Analysis of PNIPAM macro-CTA using GPC resulted in narrow molecular weight distribution with tailing at the lower molecular weight side (Fig. 3). The presence of the tailing was probably due to the presence of residual impurities in the final product, such as chain transfer agent (CTA) [25].

Different from PNIPAM macro-CTA, GPC traces of block copolymers were relatively symmetric and showed no tailing at the lower molecular side (Fig. 3). Higher retention time was observed in the comparison of PNIPAM<sub>21</sub>-*b*-PDMAEMA<sub>2</sub> with PNIPAM<sub>21</sub>-*b*-PDMAEMA<sub>7</sub> suggesting that the resulting  $M_n$  were increased from 1860 to 1923 g/mol which was ascribed to PNIPAM<sub>21</sub>-*b*-PDMAEMA<sub>2</sub> and PNIPAM<sub>21</sub>-*b*-PDMAEMA<sub>7</sub>, respectively. Whereas the unexpected increase in retention time of both block copolymers in comparison with PNIPAM macro-CTA was observed, indicating that the molecular weight ( $M_n$ ) decreases in

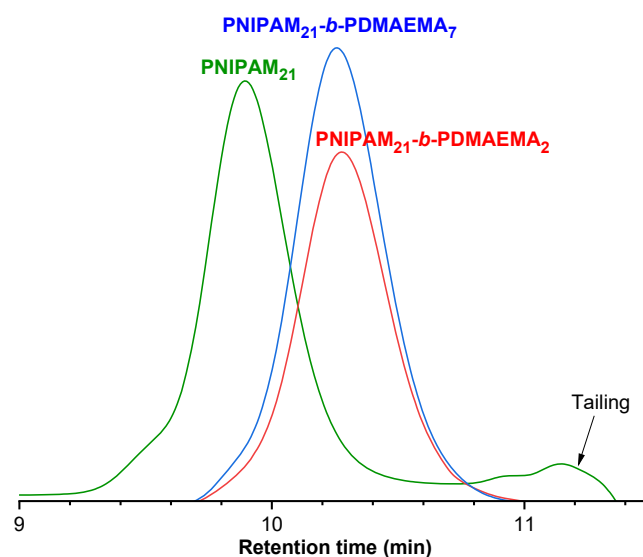


**Fig 3.** GPC traces of PNIPAM macro-CTA, PNIPAM<sub>21</sub>-*b*-PDMAEMA<sub>2</sub>, and PNIPAM<sub>21</sub>-*b*-PDMAEMA<sub>7</sub>

**Table 2.** Molecular characterization of block copolymers and macro-CTA

No	Sample	$M_n^a$ (g/mol)	$M_n^b$ (g/mol)	$M_w/M_n^c$
1	PNIPAM <sub>21</sub>	2728	3475	1.15
2	PNIPAM <sub>21</sub> - <i>b</i> -PDMAEMA <sub>2</sub>	3043	1860	1.10
3	PNIPAM <sub>21</sub> - <i>b</i> -PDMAEMA <sub>7</sub>	3829	1923	1.10

The degree of polymerization was estimated by  $^1\text{H-NMR}$  analysis. <sup>a</sup> The molecular weight by  $^1\text{H-NMR}$  analysis. <sup>b</sup> The molecular weight by GPC analysis. <sup>c</sup> The Polydispersity index (PDI) or  $M_w/M_n$  values determined by GPC analysis

contrast to the  $^1\text{H-NMR}$  result (Table 2). In GPC analysis, the sample must first dissolve in a solvent; once they have been dissolved, the molecules will change their conformation from long chains to coil conformation. These coiled-up polymers in the mobile phase would then flow into the GPC column. If polymer coils are larger than the pores, they do not enter the pores and need lower retention time, but small polymer coils can enter the pores and will take more time to pass the column. In other words, the retention time decreases when the hydrodynamic radius of the polymer is larger [26]. In this study, the interaction between PNIPAM and PDMAEMA block in polar THF, such as hydrophobic interaction and hydrogen bonding, might lead to reducing the size of hydrodynamic diameter and an increase in retention time. The previous study also reported unusual results on the retention time of PNIPAM-*b*-PPEGGA block copolymer, which was higher than the initial PNIPAM due to intense interaction between PNIPAM and PPEGGA via hydrogen bonding, indicating that the hydrodynamic volume of the block copolymer was smaller than the initial PNIPAM that could be attributed to higher retention time [27].

We also tried to synthesize PNIPAM-*b*-PDMAEMA block copolymers with a longer targeted PDMAEMA chain than PNIPAM, but it did not succeed, which might be due to the effect of the R group ( $\text{C}(\text{CH}_3)_2\text{COOH}$ ) from CTA on the DMAEMA monomer which caused the intermediate radical fragmentation to become a dormant chain and  $\text{R}\cdot$  took place slowly, where it was known that  $\text{R}\cdot$  plays a role in reinitiating the polymerization reaction [28].

### Thermo-Responsive Properties of PNIPAM-*b*-PDMAEMA Block Copolymers

PNIPAM is a thermo-responsive polymer with LCST-type behavior that undergoes a soluble-to-insoluble phase change upon heating. The phase transition temperature is the temperature at which the phase transition of the polymer solution at a specific concentration occurs from a soluble state to a collapsed state to form aggregates accompanied by the appearance of turbidity in the solution [29]. Meanwhile, LCST is the

minimum temperature at the binodal where the phase change occurs [30]. Above the LCST, there is a tendency for the microphase separation rather than the macro phase separation to produce nano aggregates from polymers. Therefore, the phase transition temperature ( $T_c$ ) is usually detected by an increase in the turbidity of the polymer solution [16]. It is widely known that PNIPAM has a  $T_c$  of  $32\text{ }^\circ\text{C}$  [7], independently of its molecular weight and concentration. The phase transition temperature of PNIPAM can be adjusted to a higher or lower temperature, one of which is by the addition of comonomers where water-soluble comonomers will increase the  $T_c$ , while hydrophobic comonomers will decrease  $T_c$ . In addition, the presence of the end group might also affect the shift in the  $T_c$  value of PNIPAM. A previous study reported that the end group derived from azo initiators such as AIBN is known to have minimal effect on  $T_c$ , whereas water-soluble end groups such as -OH and  $-\text{NH}_2$  tend to increase  $T_c$  and the hydrophobic end groups influence decreasing  $T_c$  [30]. It was expected that by adding comonomer of DMAEMA,  $T_c$  of PNIPAM-*b*-PDMAEMA would increase in comparison with its macro-CTA, PNIPAM itself.

As shown in Fig. 4, PNIPAM<sub>21</sub> does not show a significant change in transmittance at a temperature range of 15–45  $^\circ\text{C}$  and begins to experience a decrease in transmittance when the temperature is above 45  $^\circ\text{C}$ . This

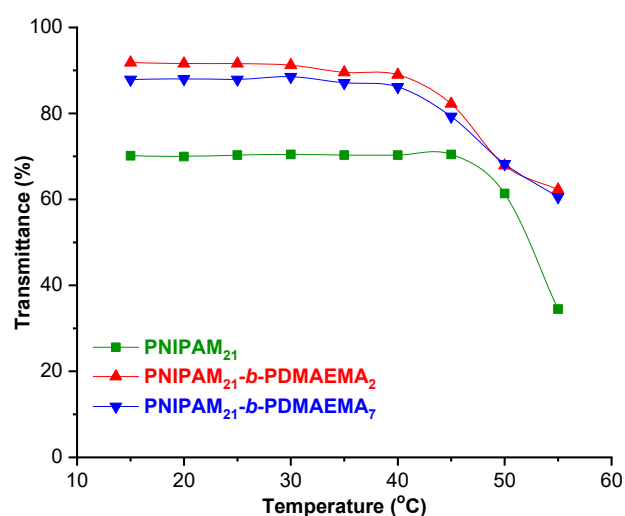


Fig 4. Thermo-responsive behavior of PNIPAM-*b*-PDMAEMA in pH 7.4 at a concentration of 1 g/L

behavior could be reasoned because at pH 7.4, the thermo-responsive behavior of PNIPAM<sub>21</sub> was influenced by the hydrophilic end group -COOH, which was ionized to -COO<sup>-</sup> at alkaline pH, and thus the  $T_c$  shifted to a higher temperature of 52 °C. Below the  $T_c$ , the amide group of PNIPAM can form hydrogen bonding with water molecules in the solution and become transparent. In the case of an increase in temperature above the  $T_c$ , the hydrogen bonds are weakened so that the hydrophobic interaction between the hydrophobic backbone and the isopropyl group of PNIPAM becomes dominant, in which the interactions lead to aggregation [31].

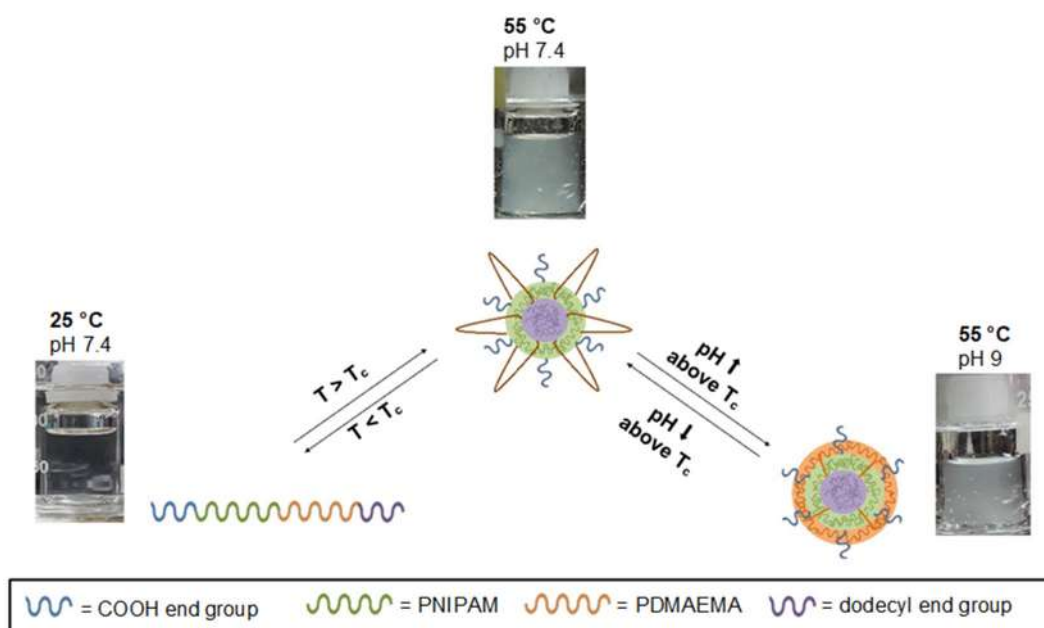
Furthermore, in block copolymers PNIPAM<sub>21</sub>-*b*-PDMAEMA<sub>2</sub> and PNIPAM<sub>21</sub>-*b*-PDMAEMA<sub>7</sub>, there was a significant decrease of transmittance at temperatures above 40 °C as displayed in Fig. 4, and the same values of  $T_c$  were obtained for each copolymer which was about 47 °C. The  $T_c$  of the PNIPAM-*b*-PDMAEMA block copolymers shifted to a lower temperature in comparison with the  $T_c$  of the PNIPAM<sub>21</sub> macro-CTA (52 °C). At first, it was predicted that there would be an increase in hydrophilicity of the block copolymers in the higher pH since PDMAEMA is partially protonated on its tertiary amino group at pH 7.4 and become positively charged. However, an opposite trend of decreased  $T_c$  was observed,

which might be due to the hydrophobic interaction from the dodecyl end group from the chain transfer agent and the carboxyl group in the protonated form.

As displayed in Scheme 2, above the  $T_c$ , hydrophobic interaction becomes dominant, and the solution appears cloudy, which shows that the block copolymers exhibit LCST behavior. These might also indicate the formation of a micelle with a PNIPAM block and dodecyl end group occupying the core of the micelle and a PDMAEMA block with a COOH end group constituting the hydrophilic shell of the micelle.

### pH-Responsive Properties of PNIPAM-*b*-PDMAEMA Block Copolymers

Fig. 5 shows the pH-responsiveness of PNIPAM macro-CTA and PNIPAM-*b*-PDMAEMA block copolymers in a phosphate buffer solution. In general, PNIPAM is not a pH-responsive polymer, but based on the observations using UV-Vis spectrophotometer in phosphate buffer at pH 5, 7.4, and 9, it was observed that there was a pH-responsive behavior from PNIPAM macro-CTA, indicated by the difference in the resulting  $T_c$ . At pH 5, PNIPAM<sub>21</sub> produces a  $T_c$  of 27 °C, lower than the  $T_c$  of PNIPAM in general, which is 32 °C. This is because of the dodecyl end group, which is closely attached to the PNIPAM block. The dodecyl group is



**Scheme 2.** Proposed illustration of self-assembly behavior of PNIPAM-*b*-PDMAEMA

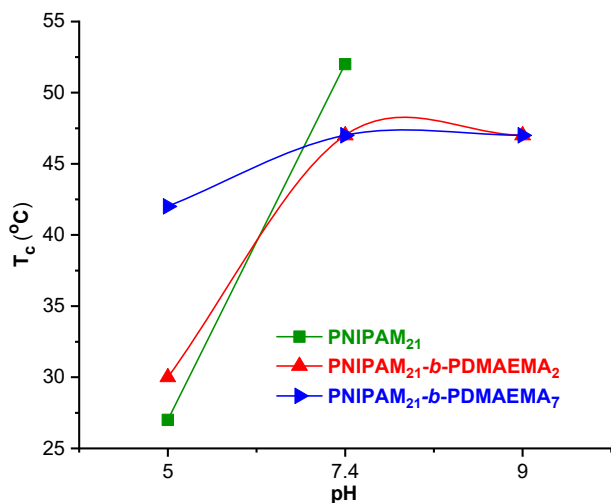


**Fig 5.** Effect of pH on the resulting  $T_c$  of 1 g/L PNIPAM-*b*-PDMAEMA and PNIPAM macro-CTA

known to be hydrophobic, which will increase the hydrophobic effect of the PNIPAM macro-CTA, resulting in a cloud point that can be achieved at a lower temperature. A similar phenomenon also occurred in the previous study [12].

Based on the graph in Fig. 5, it is shown that there was a drastic increase in the  $T_c$  of PNIPAM macro-CTA reaching 52 °C at pH 7.4, which was due to the increase in solubility of PNIPAM macro-CTA at pH 7.4, caused by the presence of the -COOH group in the macro-CTA PNIPAM. It was known that when -COOH was dissolved in an alkaline solution, deprotonation of COOH into COO<sup>-</sup> occurred, and thus, the solubility of PNIPAM macro-CTA increased. Meanwhile, increasing the pH to 9 showed that the  $T_c$  of macro-CTA PNIPAM was not observed at temperature measurement. This was probably due to the increase in hydrophilicity that also increased the  $T_c$ . A similar result was observed in the research conducted by FitzGerald et al. when observing surfactant PNIPAM, which had the same dodecyl and carboxyl end groups [17].

The effect of the PDMAEMA chain length on the PNIPAM-*b*-PDMAEMA block copolymer on pH was observed using a UV-Vis spectrophotometer. PDMAEMA is a pH-responsive polymer of the polybasic type which will be protonated at low pH (pH < pK<sub>a</sub> 7.5) [32]. Hence, the solubility of PDMAEMA in an acidic pH buffer solution increase, causing the hydrophilic effect of

PDMAEMA to be more dominant, accompanied by an increase in  $T_c$ . As shown in Fig. 5, at pH 5, PNIPAM<sub>21</sub>-*b*-PDMAEMA<sub>2</sub> and PNIPAM<sub>21</sub>-*b*-PDMAEMA<sub>7</sub> obtained  $T_c$  values of 30 and 42 °C, respectively, higher values in comparison to macro-CTA PNIPAM<sub>21</sub> (27 °C). The increase in  $T_c$  was due to the presence of PDMAEMA, which was protonated at pH 5, which attributed in affecting the changes in the hydrophilic-to-hydrophobic properties of its neighboring block PNIPAM due to weakening of the hydrophobic aggregation force in PNIPAM [14]. Above the  $T_c$ , PNIPAM-*b*-PDMAEMA self-assembled into nanostructures consisting of PNIPAM block and dodecyl end group as micelle core and PDMAEMA block with COOH end group as micelle shell (Scheme 2). Moreover, at pH 5,  $T_c$  increased the degree of polymerization of the PDMAEMA block due to the greater effect of the hydrophilicity of protonated PDMAEMA in the PNIPAM-*b*-PDMAEMA block copolymers.

When pH increased to 7.4, it was expected that increasing pH would cause the  $T_c$  of block copolymers to be reduced because the degree of protonation in PDMAEMA was much lower than that at pH 5. On the contrary, the  $T_c$  of PNIPAM<sub>21</sub>-*b*-PDMAEMA<sub>2</sub> and PNIPAM<sub>21</sub>-*b*-PDMAEMA<sub>7</sub> at pH 7.4 were increased from the previous pH, which could be reasoned by the existence of deprotonated COOH groups into COO<sup>-</sup>, leading to increased solubility of block copolymers in dispersing media and also increased  $T_c$ . Other than that, at pH 7.4, the  $T_c$  of block copolymers was lower than the  $T_c$  of PNIPAM macro-CTA (52 °C), in which the  $T_c$  values were similar for both block copolymers at approximately 47 °C (Fig. 5). The decrease in  $T_c$  in comparison with  $T_c$  PNIPAM macro-CTA might be contributed by the presence of PDMAEMA. At pH 7.4 it was known that PDMAEMA was in the protonated state, but the degree of protonation was lower than that at acidic pH. This resulted in the possibility of hydrophobic interactions between the PNIPAM block and the PDMAEMA block when the temperature increased.

PDMAEMA was deprotonated at pH 9. The resulting  $T_c$  of both block copolymers had the same

values with the values at pH 7.4; although the PDMAEMA might not be in the protonated state, the significant effect of deprotonated COOH still weakened the tendency of neighboring PNIPAM block to collapse, forming aggregates when temperature increased above the  $T_c$ . Moreover, the decrease in the  $T_c$  of the block copolymers in comparison with PNIPAM macro-CTA could be caused by the presence of a neutral form of PDMAEMA. This leads to PDMAEMA being dehydrated at a high temperature and producing changes in hydrophilic-to-hydrophobic properties. Notably, at pH 7.4 and pH 9, the same  $T_c$  values were produced for different chain lengths of the PDMAEMA block, which was due to the strong interaction between PNIPAM and PDMAEMA that might eliminate the effect of PDMAEMA degree polymerization on  $T_c$  [13].

PSA analysis was conducted to get information about the size distribution and Z-average diameter of the aggregates. The trend of the Z-average diameter of the PNIPAM<sub>21</sub>-*b*-PDMAEMA<sub>2</sub> at pH 5 is shown in Fig. 6(a). It was observed that the resulting Z-average diameter exhibited a similar trend compared to transmittance from UV-Vis spectroscopy. The result had shown that the size of micelles became bigger when temperature increased, as evidenced by the decrease in transmittance and an increase in the Z-average diameter (Fig. 6(a)). As displayed in Fig. 6(b), the particle diameter distribution shifted towards a larger diameter side as increasing

temperature. This might indicate that the block copolymer experienced self-assembly behavior to form micelles to minimize the contact from the hydrophobic groups with water in its surrounding environment. Increasing the temperature further may lead micelles to form clusters, and thus, large particle sizes were obtained.

It was also observed that there was a big difference between the resulting Z-average diameter of PNIPAM<sub>21</sub>-*b*-PDMAEMA<sub>2</sub> at pH 5 and 9, in which the diameter of the Z-average at pH 9 was 846 nm while at pH 5 it was about 293 nm (Table 3). The possible reason was due to the differences in the shape of the micelles formed. It was known that at pH 5, the amine group in the PDMAEMA block was protonated, resulting in the positive charge that caused PDMAEMA to become more hydrophilic. Therefore when temperature increased, PDMAEMA tended to occupy the hydrophilic part as the shell of the micelles. The presence of PDMAEMA, which were positively charged on the shell of the micelles, caused an electric repulsion phenomenon that caused the particle to move apart from each other, and the micelles tended

**Table 3.** Z-average diameter of PNIPAM<sub>21</sub>-*b*-PDMAEMA<sub>2</sub> at different pH

pH	Z-average diameter at 45 °C
5	293 nm
9	846 nm

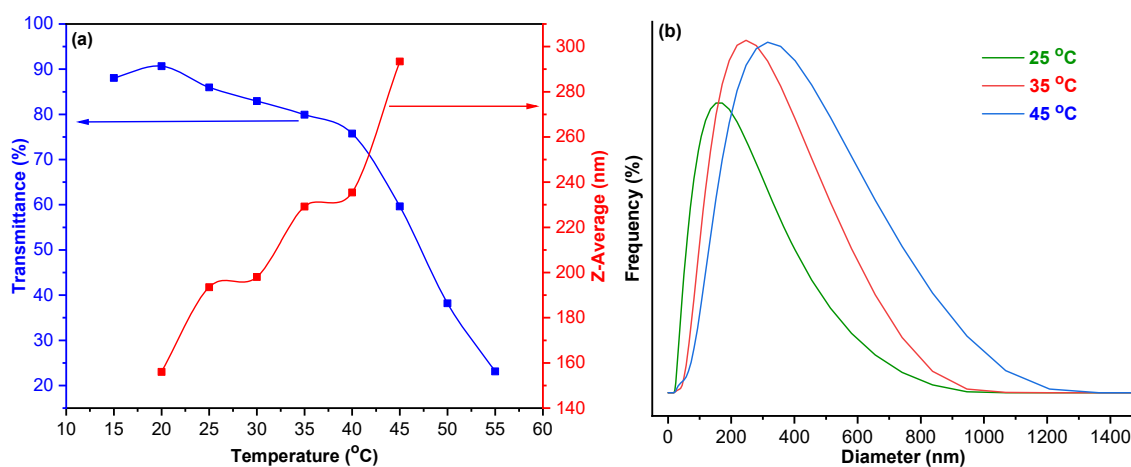


**Fig 6.** Thermo-responsive behavior and changes in Z-average of PNIPAM<sub>21</sub>-*b*-PDMAEMA<sub>2</sub> at pH 5 (a). Distribution of diameter of the PNIPAM<sub>21</sub>-*b*-PDMAEMA<sub>2</sub> at pH 5 (b)

to be stabilized from forming larger aggregate clusters. On the contrary, at pH 9 the PNIPAM block and PDMAEMA block would transform from hydrophilic to more hydrophobic when the temperature increased, and thus, they would occupy the core of the micelles since the shell of the micelles also preferred the hydrophobic interaction (Scheme 2). This could make the micelles unstable and form a cluster of micelles [33].

## ■ CONCLUSION

Block copolymers PNIPAM-*b*-PDMAEMA containing thermo- and pH-responsive properties have been synthesized via RAFT polymerization. FTIR and <sup>1</sup>H-NMR revealed the successful formation of PNIPAM-*b*-PDMAEMA. GPC confirmed the successful synthesis of block copolymers with well-controlled molecular weight as evidenced by narrow symmetrical molecular weight distribution with low polydispersity. The block copolymers showed micellization properties which were assigned to thermo- and pH-responsive behavior by exhibiting phase transition and increase of Z-average diameter upon heating. At pH 5, the longer the PDMAEMA chain would increase the T<sub>c</sub> of the PNIPAM-*b*-PDMAEMA block copolymer, while at pH 7.4 and 9, T<sub>c</sub> was not affected by the PDMAEMA chain length. Moreover, the synthesized block copolymers are open for new potential material in drug delivery systems.

## ■ ACKNOWLEDGMENTS

The author would like to thank the Faculty of Mathematics and Natural Sciences Universitas Indonesia (FMIPA UI), for the research funding of *Hibah Riset Penugasan* FMIPA UI with contract number: 023/UN2.F3.D/PPM.00.02/2022. The authors acknowledge the NMR and DLS (particle size analyzer) facilities of the Integrated Laboratory and Research Center (ILRC) Universitas Indonesia. Noteworthy, the authors thank Dody Andi Winarto, B.Eng., M.Eng. from *Badan Riset Inovasi Nasional* (BRIN) for his support in facilitating the Gel Permeation Chromatography analysis in BRIN.

## ■ AUTHOR CONTRIBUTIONS

Noverra Mardhatillah Nizardo designed the experiment, wrote, and revised the manuscript, Rida

Hasna Fadhilah conducted the experiment and wrote the manuscript, Ivandini Tribidasari Anggraningrum wrote and revised the manuscript. All authors agreed to the final version of this manuscript.

## ■ REFERENCES

- [1] Kocak, G., Tuncer, C., and Bütün, V., 2017, pH-Responsive polymers, *Polym. Chem.*, 8 (1), 144–176.
- [2] Madhusudana Rao, K., Mallikarjuna, B., Krishna Rao, K.S.V., Siraj, S., Chowdoji Rao, K., and Subha, M.C.S., 2013, Novel thermo/pH sensitive nanogels composed from poly(*N*-vinylcaprolactam) for controlled release of an anticancer drug, *Colloids Surf., B*, 102, 891–897.
- [3] Suka, I.G., and Simanjuntak, W., 2011, Preparation of temperature-responsive polymer by grafting of *N*-isopropylacrylamide (NIPAAm) onto solid waste cassava, *Indones. J. Chem.*, 11 (1), 9–15.
- [4] Ningrum, E.O., Purwanto, A., Rosita, G.C., and Bagus, A., 2020, The properties of thermosensitive zwitterionic sulfobetaine NIPAM-*co*-DMAAPS polymer and the hydrogels: The effects of monomer concentration on the transition temperature and its correlation with the adsorption behavior, *Indones. J. Chem.*, 20 (2), 324–335.
- [5] Jha, A., Rama, A., Ladani, B., Verma, N., Kannan, S., and Naha, A., 2021, Temperature and pH-responsive nanogels as intelligent drug delivery systems: A comprehensive review, *J. Appl. Pharm. Sci.*, 11 (12), 001–016.
- [6] Nizardo, N.M., Alimin, D.F., and Lestari, M.L.A.D., 2022, Synthesis and characterization of dual-responsive poly(*N*-vinylcaprolactam-*co*-*N*-methylolacrylamide) nanogels, *Des. Monomers Polym.*, 25 (1), 155–164.
- [7] Ward, M.A., and Georgiou, T.K., 2011, Thermoresponsive polymers for biomedical applications, *Polymers*, 3 (3), 1215–1242.
- [8] Göktaş, M., and Deng, G., 2018, Synthesis of poly(methyl methacrylate)-*b*-poly(*N*-isopropylacrylamide) block copolymer by redox polymerization and atom transfer radical polymerization, *Indones. J. Chem.*, 18 (3), 537–543.



- [9] Nizardo, N.M., and Tania, T.P., 2021, The effect of poly(*N*-hydroxymethyl acrylamide) chain length in poly(*N*-vinyl pyrrolidone)-block-poly(*N*-hydroxymethyl acrylamide) on its sensitivity to pH, *Rasayan J. Chem.*, 14 (4), 2671–2676.
- [10] Kotsuchibashi, Y., Ebara, M., Aoyagi, T., and Narain, R., 2016, Recent advances in dual temperature responsive block copolymers and their potential as biomedical applications, *Polymers*, 8 (11), 380.
- [11] Reyes-Ortega, F., 2014, "pH-Responsive Polymers: Properties, Synthesis and Applications" in *Smart Polymers and their Applications*, Eds. Aguilar, M.R., and San Román, J., Woodhead Publishing Limited, Sawston, Cambridge, 45–92.
- [12] Giaouzi, D., and Pispas, S., 2020, PNIPAM-*b*-PDMAEA double stimuli responsive copolymers: Effects of composition, end groups and chemical modification on solution self-assembly, *Eur. Polym. J.*, 135, 109867.
- [13] Li, Q., Gao, C., Li, S., Huo, F., and Zhang, W., 2014, Doubly thermo-responsive ABC triblock copolymer nanoparticles prepared through dispersion RAFT polymerization, *Polym. Chem.*, 5 (8), 2961–2972.
- [14] Huang, Y., Yong, P., Chen, Y., Gao, Y., Xu, W., Lv, Y., Yang, L., Reis, R.L., Pirraco, R.P., and Chen, J., 2017, Micellization and gelatinization in aqueous media of pH- and thermo-responsive amphiphilic ABC (PMMA<sub>82</sub>-*b*-PDMAEMA<sub>150</sub>-*b*-PNIPAM<sub>65</sub>) triblock copolymer synthesized by consecutive RAFT polymerization, *RSC Adv.*, 7 (46), 28711–28722.
- [15] Giaouzi, D., and Pispas, S., 2020, Effects of chemical modifications on the thermoresponsive behavior of a PDMAEA-*b*-PNIPAM-*b*-POEGA triblock terpolymer, *Polymers*, 12 (6), 1382.
- [16] Škvarla, J., Raya, R.K., Uchman, M., Zedník, J., Procházka, K., Garamus, V.M., Meristoudi, A., Pispas, S., and Štěpánek, M., 2017, Thermoresponsive behavior of poly(*N*-isopropylacrylamide)s with dodecyl and carboxyl terminal groups in aqueous solution: pH-dependent cloud point temperature, *Colloid. Polym. Sci.*, 295 (8), 1343–1349.
- [17] FitzGerald, P.A., Gupta, S., Wood, K., Perrier, S., and Warr, G.G., 2014, Temperature- and pH-responsive micelles with collapsible poly(*N*-isopropylacrylamide) headgroups, *Langmuir*, 30 (27), 7986–7992.
- [18] Tebaldi, M.L., Leal, D.A., Montoro, S.R., and Petzhold, C., 2014, Synthesis of stimuli-sensitive copolymers by RAFT polymerization: Potential candidates as drug delivery systems, *Mater. Res.*, 17 (Suppl. 1), 191–196.
- [19] Farooqi, Z.H., Butt, Z., Begum, R., Khan, S.R., Sharif, A., and Ahmed, E., 2015, Poly(*N*-isopropylacrylamide-*co*-methacrylic acid) microgel stabilized copper nanoparticles for catalytic reduction of nitrobenzene, *Mater. Sci.-Pol.*, 33 (3), 627–634.
- [20] Ilić-Stojanović, S., Nikolić, L., Nikolić, V., Petrović, S., Oro, V., Mitić, Ž., and Najman, S., 2021, Semi-crystalline copolymer hydrogels as smart drug carriers: *In vitro* thermo-responsive naproxen release study, *Pharmaceutics*, 13 (2), 158.
- [21] De Jesús-Téllez, M.A., Sánchez-Cerrillo, D.M., Quintana-Owen, P., Schubert, U.S., Contreras-López, D., and Guerrero-Sánchez, C., 2020, Kinetic Investigations of quaternization reactions of poly[2-(dimethylamino)ethyl methacrylate] with diverse alkyl halides, *Macromol. Chem. Phys.*, 221 (9), 1900543.
- [22] Gökteş, M., 2020, Synthesis and characterization of temperature-responsive block copolymers using macromonomeric initiator, *Chem. Pap.*, 74 (7), 2297–2307.
- [23] Song, T., Zhu, Y., Liang, S., Zou, G., and Zhang, Q., 2018, Coordinate bond breaking induced by collapse of poly(*N*-isopropyl acrylamide) as ligands of a rare earth complex, *Chin. J. Chem. Phys.*, 31 (5), 677–683.
- [24] Kwon, Y., Choi, Y., Jang, J., Yoon, S., and Choi, J., 2020, NIR laser-responsive PNIPAM and gold nanorod composites for the engineering of thermally reactive drug delivery nanomedicine, *Pharmaceutics*, 12 (3), 204.
- [25] Chen, J., Liu, M., Gao, C., Lü, S., Zhang, X., and Liu, Z., 2013, Self-assembly behavior of pH- and thermo-responsive hydrophilic ABCBA-type

- pentablock copolymers synthesized by consecutive RAFT polymerization, *RSC Adv.*, 3 (35), 15085–15093.
- [26] Philipps, K., Junkers, T., and Michels, J.J., 2021, The block copolymer shuffle in size exclusion chromatography: The intrinsic problem with using elugrams to determine chain extension success, *Polym. Chem.*, 12 (17), 2522–2531.
- [27] St Thomas, C., Maldonado-Textle, H., Cabello-Romero, J.N., Macossay, J., Zhang, X., Esturau-Escofet, N., and Guerrero-Santos, R., 2014, New dialkoxamine-trithiocarbonate for the synthesis of multiblock copolymers through in tandem RAFT/NMP, *Polym. Chem.*, 5 (8), 3089–3097.
- [28] Moad, G., Rizzardo, E., and Thang, S.H., 2008, Radical addition-fragmentation chemistry in polymer synthesis, *Polymer*, 49 (5), 1079–1131.
- [29] Zhang, Q., Weber, C., Schubert, U.S., and Hoogenboom, R., 2017, Thermoresponsive polymers with lower critical solution temperature: From fundamental aspects and measuring techniques to recommended turbidimetry conditions, *Mater. Horiz.*, 4 (2), 109–116.
- [30] Pasparakis, G., and Tsitsilianis, C., 2020, LCST polymers: Thermoresponsive nanostructured assemblies towards bioapplications, *Polymer*, 211, 123146.
- [31] Jain, K., Vedarajan, R., Watanabe, M., Ishikiriya, M., and Matsumi, N., 2015, Tunable LCST behavior of poly(*N*-isopropylacrylamide/ionic liquid) copolymers, *Polym. Chem.*, 6 (38), 6819–6825.
- [32] Samsonova, O., Pfeiffer, C., Hellmund, M., Merkel, O.M., and Kissel, T., 2011, Low molecular weight pDMAEMA-*block*-pHEMA block-copolymers synthesized via RAFT-polymerization: Potential non-viral gene delivery agents, *Polymers*, 3 (2), 693–718.
- [33] Zhou, J., Wang, L., Zha, X., and Wang, H., 2020, Synthesis of pH-responsive block copolymer micelles via RAFT polymerization induced self-assembly and its application in emulsifier-free emulsion polymerization, *Phosphorus, Sulfur Silicon Relat. Elem.*, 195 (2), 131–141.

## Effect of Activated Carbon Particle Size on Methylene Blue Adsorption Process in Textile Wastewater

Akhmad Masykur Hadi Musthofa<sup>1\*</sup>, Mindriany Syafila<sup>2</sup>, and Qomarudin Helmy<sup>2</sup>

<sup>1</sup>Department of Environmental Engineering, Institut Teknologi Bandung, Jl. Ganesha No. 10, Bandung 40132, West Java, Indonesia

<sup>2</sup>Water and Wastewater Engineering Research Group, Faculty of Civil and Environmental Engineering, Institut Teknologi Bandung, Jl. Ganesha No. 10, Bandung 40132, West Java, Indonesia

\* **Corresponding author:**

email: 25320307@mahasiswa.itb.ac.id

Received: December 7, 2022

Accepted: February 20, 2023

DOI: 10.22146/ijc.79784

**Abstract:** Up to 60–70% of the total textile dyes produced are azo dyes. An example of azo dye is methylene blue, which is commonly used in dyeing wool, silk, and cotton. This substance possessed harmful effects on the environment. Therefore, the removal process is mandatory. The adsorption process is a common method for dye removal in wastewater. One innovation to increase adsorption efficiency even further is by reducing adsorbent particle size. To understand the effect of adsorbent particle size on the adsorption process, in this study, granular activated carbon (GAC) was pulverized into powder (PAC) and superfine powder (SPAC). Adsorbent characterizations, isotherm, kinetics, and thermodynamics tests were conducted. Based on this study, surface area, pore volume, and adsorption capacity were increased for smaller adsorbent particle sizes. Isotherm and kinetic analysis showed that there was no difference in the isotherm and kinetic models that applied to each activated carbon, but there was an increase in the isotherm and kinetic coefficient values at smaller particle sizes. Meanwhile, based on the thermodynamic test, there were differences in the dominant adsorption mechanism for each activated carbon. In GAC and SPAC, the dominant adsorption mechanism was electrostatic interactions, while in PAC was van der Waals forces.

**Keywords:** activated carbon; adsorption; methylene blue; superfine powdered activated carbon

### ■ INTRODUCTION

A textile company with an 8000 kg/day production capacity requires 1.6 million liters of water, with the dyeing process using about 16% of that amount. The wastewater from the dyeing process contributes around 10–15% of the total textile industry wastewater discharge [1]. The wastewater from the dyeing process contains high concentrations of dyes because some of the dyes do not bind to the textile fibers. The percentage of unbound dye concentrations varies from 1–50% depending on the type of dye used [2]. Because of this, the textile industry is considered to be the largest producer of dye effluents in the world, with a percentage of 54% of the total dye effluents produced [3].

It is estimated that there are 10,000 different types of

textile dyes based on the color index. Among these various kinds of dyes, azo dyes are the most widely used dyes in the textile industry, reaching 60–70% of the total dyes produced [4]. An example of azo dye is methylene blue, which is commonly used in dyeing wool, silk, and cotton fabrics [5-6]. The release of wastewater containing azo dyes into the environment can reduce dissolved oxygen concentrations and degrade water quality. In addition, azo dyes also have acute toxicity, carcinogenic, and mutagenic effects on living things [7]. The dye concentration in the textile industry effluent varies from 10 to 250 mg/L [2].

Adsorption with activated carbon is a widely used dye-removal process. This process is considered to be fast, affordable, simple, does not produce sludge, has

high efficiency, is stable, and can be recycled [8-10]. To increase adsorption efficiency even further, reducing the particle size of activated carbon is one of the efforts which has been done [11]. Superfine powdered activated carbon (SPAC) is a result of reducing particle size to improve the adsorption process. SPAC is produced from the further reduction of powdered activated carbon (PAC) by a pulverization process using a bead mill, ball mill, or micro grinding to a size of  $< 1 \mu\text{m}$ . SPAC is considered to have advantages over PAC in terms of adsorption capacity and high rate of absorption kinetics [12-14].

The study about the effects of activated carbon particle size was limited because previously, it was believed that adsorption occurred in the internal pores of activated carbon, which does not depend on particle size [15]. This belief was later contradicted by some newer studies, which showed a significant effect of activated carbon particle size on adsorption capacities, especially in the adsorption of large molecular organic matters [16]. Although SPAC not always have higher adsorption capacity (depending on the adsorbate molecules), the kinetic rate of SPAC was always found to be superior compared to PAC [15,17-19]. Based on these findings, SPAC has a big potential to be used in the water/wastewater treatment process. Therefore, to understand the effect of particle size of activated carbon even further, this research not only analyzes the adsorption capacity and kinetics but also analyzes the thermodynamics of the adsorption process. In this study, the analysis was carried out on three types of activated carbon with different sizes, namely granular, powder, and superfine powdered.

## ■ EXPERIMENTAL SECTION

### Materials

The materials used in this study were deionized water, methylene blue dye (99% purity, Merck 115943 C.I.52015), and Jacobi-activated carbon AquaSorb 1000.

### Instrumentation

Several instruments used in the experimental phase of this study include mortar and pestle, laboratory glassware (beaker glass, Erlenmeyer flask, volumetric

flask), high energy ball mill (Retsch planetary ball mill PM 400), Scanning Electron Microscope test instrumentation (SEM-EDX JEOL JSM-6510LA), Brunauer-Emmett-Teller test instrumentation (BET, Quantachrome Autosorb iQ ASiQwin-Automated Gas Sorption), Fourier transform Infrared Spectroscopy test instrumentation (Shimadzu FTIR Prestige 21), nanoparticle size analyzer (Horiba SZ-100), mechanical sieve shaker (Gilson SS-8R), jartest (VELP Scientifica JLT6), pH meter (ATC Pen Type PH-009), centrifuge (Hettich Rotofix 32 A 35° angle rotor 12-place), Visible light spectrophotometer (Thermo Scientific Genesys 30), heating and magnetic stirrer (Thermo Scientific Cimarec 2), and analytical scale (OHAUS PA224).

### Procedure

#### **Size reduction and activated carbon characterization**

The activated carbon used in this study was Jacobi Aquasorb 1000 which is a commercial granular activated carbon (GAC). The 20 g of Jacobi Aquasorb 1000 was mashed using a mortar and pestle for 20 min to become powder (PAC). Some of the PAC was further pulverized to become superfine powdered activated carbon (SPAC) using a high energy ball mill with a rotational speed of 350 rpm for 8 h. All activated carbons were then characterized physically and chemically. Physical characterizations consist of an analysis of particle size distribution (mechanical sieving and PSA), SEM, and BET tests. The particle size distribution of GAC and PAC was carried out using a mechanical sieving device, and the test for SPAC was carried out using a nanoparticle size analyzer at a scattering angle of 90°. The SEM test for GAC was performed at magnifications of 500, 1000, 2000, and 5000 times while the magnifications used for PAC and SPAC were 2000, 5000, 10000, and 20000 times. Meanwhile, the chemical characterizations of activated carbon were carried out by FTIR test at the wavelength of 400–4000  $\text{cm}^{-1}$  and point of zero charge test conducted according to Khalil et al. [20].

#### **Preliminary test of particle size effect on equilibrium and adsorption capacity**

This test was carried out by contacting different types of activated carbon (GAC, PAC, and SPAC) with

methylene blue artificial wastewater. Activated carbon as much as 1 g was contacted with 500 mL of methylene blue artificial wastewater at a concentration of 250 mg/L. The mixture was then stirred at a speed of 120 rpm to ensure there was sufficient contact between the adsorbent and the adsorbate [21]. Samples of PAC and SPAC mixture were then taken at a time range of 10, 20, 30, 60, 90, and 120 min to measure the concentration of dyes and COD [22]. Whereas in the GAC mixture, the sampling time was extended to 150, 180, 210, and 240 min to ensure equilibrium was reached.

After the test, PAC and SPAC were separated from the wastewater by centrifugation process with a force of 4.146 G for 5 and 20 min. The determination of color concentration was carried out by converting the color absorbance values using a visible spectrophotometer at a wavelength of 664 nm with a calibration curve [22-23]. Meanwhile, the determination of COD concentration was carried out using a method based on SNI 6989.2: 2019 about Spectrophotometric Closed Reflux COD Analysis.

#### **Particle size effect on adsorption isotherms test**

Identification of activated carbon particle size effect on adsorption isotherms was carried out by contacting 1 g of GAC or PAC with 500 mL of methylene blue artificial wastewater at various dye concentrations 100, 125, 150, 175, and 200 mg/L. At the same time, the variations in dye concentration used in the identification of SPAC adsorption isotherms were 300, 350, 400, 450, and 500 mg/L. This mixture was then stirred with a stirring speed of 120 rpm for 120 min (PAC and SPAC) and 240 min (GAC). The determination of dye concentration variation and length of contact time was based on preliminary tests. The experimental data were then analyzed with non-linear equations of the isotherm model to find out the isotherm coefficient values using OriginPro2022b. Non-linear equations were used to minimize bias due to data transformation into linear equations. The obtained data then matched with Giles isotherm classification to determine the most suitable isotherm model and the adsorption mechanism for each activated carbon [24-26].

#### **Particle size effect on adsorption kinetics test**

The adsorption kinetics test was carried out by contacting 1 g of activated carbon with 500 mL of methylene blue artificial wastewater at a dye concentration of 250 mg/L. The determination of duration for the adsorption kinetics test was based on preliminary test results. In the SPAC experiment, samples were taken every 4 min for 20 min; in the PAC experiment, samples were taken every 12 min for 60 min; and in the GAC experiment, samples were taken every 42 min for 210 min. Analysis of the kinetic coefficient values was carried out by matching the experimental data with the non-linear equations of the kinetic model using OriginPro2022b. If based on the isotherm analysis, the adsorption process dominated by chemisorption, the kinetic test data will be matched with pseudo-second-order model. Meanwhile, if the dominant mechanism in adsorption process is physisorption, the kinetics test data will be matched with pseudo-first-order and intraparticle diffusion model. To determine which model is more suitable, error analysis between the value of adsorption capacity at certain time ( $q_t$ ) based on model and  $q_t$  value based on experiment will be conducted. The error analysis consists of sum of square error (SSE), average relative error (ARE), hybrid fractional error function (HYBRID), and The Marquardt's percent standard deviation (MPSED). The equations for each error analysis can be seen in Eq. (1) through Eq. (4) as follows [24-26].

$$SSE = \sum (q_{t,cal} - q_{t,exp})^2 \quad (1)$$

$$ARE = \frac{1}{N} \sum \left| \frac{q_{t,cal} - q_{t,exp}}{q_{t,exp}} \right| \times 100 \quad (2)$$

$$HYBRID = \frac{1}{N - P} \sum \frac{(q_{t,cal} - q_{t,exp})^2}{q_{t,exp}} \times 100 \quad (3)$$

$$MPSED = \sqrt{\frac{\sum ((q_{t,exp} - q_{t,cal}) / q_{t,exp})^2}{N - P}} \times 100 \quad (4)$$

where  $q_{t,cal}$  is the adsorption capacity at certain time (t) based on calculation from each model (mg/g),  $q_{t,exp}$  is the adsorption capacity at certain time (t) based on the

experiment (mg/g),  $N$  is the number of data, and  $P$  is the degree of freedom.

#### Particle size effect on adsorption thermodynamics test

The thermodynamic analysis was carried out by varying the temperature of the adsorption system to 25, 35, 45, and 55 °C. From the obtained data, the maximum adsorption capacity was determined to calculate the value of  $K_e$  (adsorption thermodynamic constant) with Eq. (5) as follows:

$$K_e = \frac{q_e/q_m}{(1 - q_e/q_m)C_e/C_0} \quad (5)$$

where  $q_e$  is the adsorption capacity at equilibrium (mol/g),  $q_m$  is the maximum adsorption capacity (mol/g),  $C_e$  is the adsorbate concentration at equilibrium (mol/L), and  $C_0$  is the molar concentration of the standard reference solution (assumed to be 1 mol/L).

After that, a Van't Hoff curve can be constructed, which is a plot of  $\ln(K_e)$  to  $1/T$ . The values of  $\Delta H^\circ$  (standard enthalpy change) and  $\Delta S^\circ$  (standard entropy change) can be identified based on the slope and intercept of the Van't Hoff curve [25,27].

## ■ RESULTS AND DISCUSSION

FTIR test was performed on PAC and SPAC. The

results of the GAC FTIR test were considered to be the same as PAC because they came from the same material source, namely Jacobi Aquasorb 1000. Meanwhile, the SPAC test was carried out to determine whether the pulverization process with a high-energy ball mill caused changes in functional groups on the surface of the activated carbon. The FTIR test results, as shown in Fig. 1 indicated that SPAC and PAC produced the same peak at wavelengths of 3429.43 and 1568.13  $\text{cm}^{-1}$ , which indicated the presence of a functional group in the form of a hydroxyl group (-OH) and an aromatic bond in the form of C=C. However, the SPAC FTIR test showed a lower transmission value (%T) at a wavelength of 3429.43  $\text{cm}^{-1}$ . A lower %T value indicates a greater number of functional groups on the activated carbon surface. Therefore, it can be concluded that the pulverization process with a ball mill did not cause a change in the type of functional groups but increased the number of functional groups available on the activated carbon surface. Apart from these two wavelengths, the peak also occurs at a wavelength of 460.99; 796.60; 1091.71  $\text{cm}^{-1}$ , which probably indicates the presence of functional groups of C-O and C-C, C-H, and C-O-C, which are commonly found in ether, ester or phenol groups [20,28].

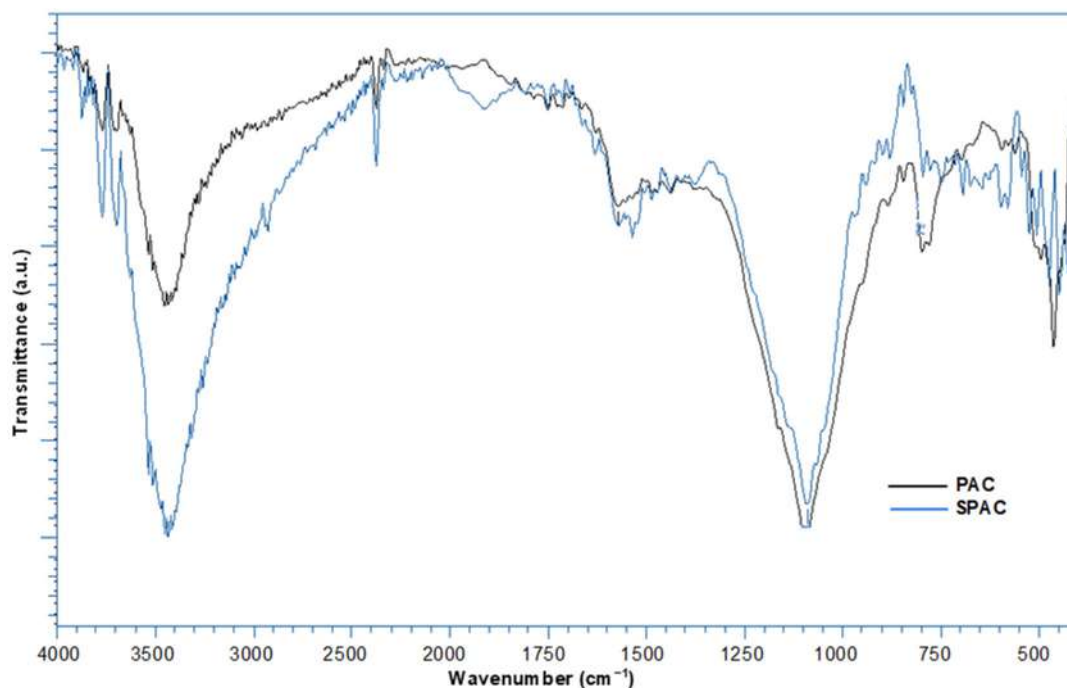


Fig 1. FTIR test results of PAC and SPAC

Another chemical characterization test of adsorbent, which was zero point of discharge, showed different results on each activated carbon. The  $\text{pH}_{\text{PZC}}$  value of GAC was 6.65, while the  $\text{pH}_{\text{PZC}}$  values of PAC and SPAC were 6.75 and 7.00, as shown in Fig. 2. This finding showed that activated carbon was more alkaline at smaller particle sizes. These results are different from previous research [17,29]. In those studies, the  $\text{pH}_{\text{PZC}}$  values decreased at smaller particle sizes, indicating a more acidic nature. This difference can possibly be caused by a different source of activated carbon used. In the previous study, activated carbon was made from wood, coconut shell, and lignite coal. Meanwhile, the activated carbon used in this study was made from bituminous coal.

Based on the mechanical sieving test, GAC particle size ranged from 0.42–2.00 mm with a  $d_{50}$  of 0.58 mm. The dominant GAC particle size was 1.18 and 2.00 mm, with occurrence frequencies reaching 71.02 and 22.40%. The particle size of PAC ranges from 0.053–0.42 mm with a  $d_{50}$  of 0.108 mm. The dominant PAC particle size was 0.42 and 0.149 mm, with occurrence frequencies of 28.68 and 36.13%. Meanwhile, based on the nanoparticle size analysis test, the particle size of SPAC ranged from 246.98–4622.81 nm with a  $d_{50}$  of 550 nm and an average diameter size of 704.93 nm. The dominant particle size was in the range of 315.27–513.71 nm with occurrence frequencies ranging from 4 to 13% and 1541.04–2511.05 nm with occurrence frequencies ranging from 5 to 6%. The average size of the SPAC in this study complied with the applicable requirement which is smaller than 1  $\mu\text{m}$ . The detailed results of mechanical sieving tests and particle size analysis can be seen in Fig. 3, 4, and 5.

The SEM test results on GAC with the magnification of 500, 1000, 2000, and 5000 times are shown in Fig. 6. Based on that figure, the GAC surface was corrugated and porous. However, the pores formed were not uniform, and some of the pore openings were covered with smaller particles. Porous surfaces were also identified in the PAC SEM test results with magnifications of 2000, 5000, 10000, and 20000 times as seen in Fig. 7. Pores on the PAC surface were seen more clearly than on the GAC surface. This can be caused by the opening of small diameter pores

to become larger due to the pulverization process [30]. Meanwhile, the SEM test results on SPAC with the magnification of 2000, 5000, 10000, and 20000 $\times$ , which can be seen in Fig. 8, showed that the particle size of the adsorbent was smaller than the previous two types of adsorbents. This is in accordance with the results of the particle size analysis test that has been described previously.

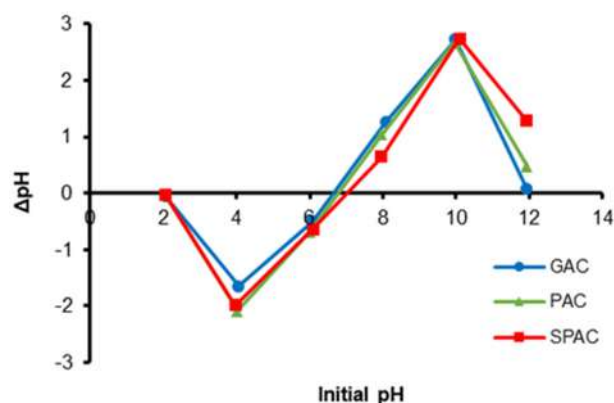


Fig 2. Point of zero charge test result

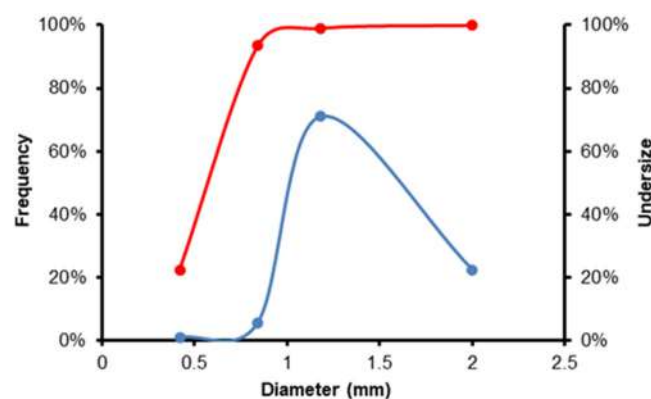


Fig 3. Particle size distribution of GAC

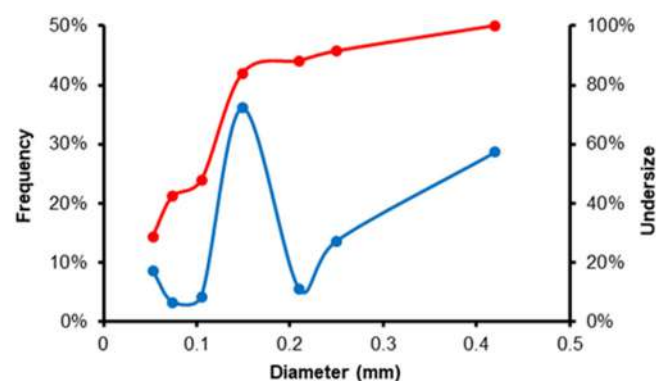


Fig 4. Particle size distribution of PAC

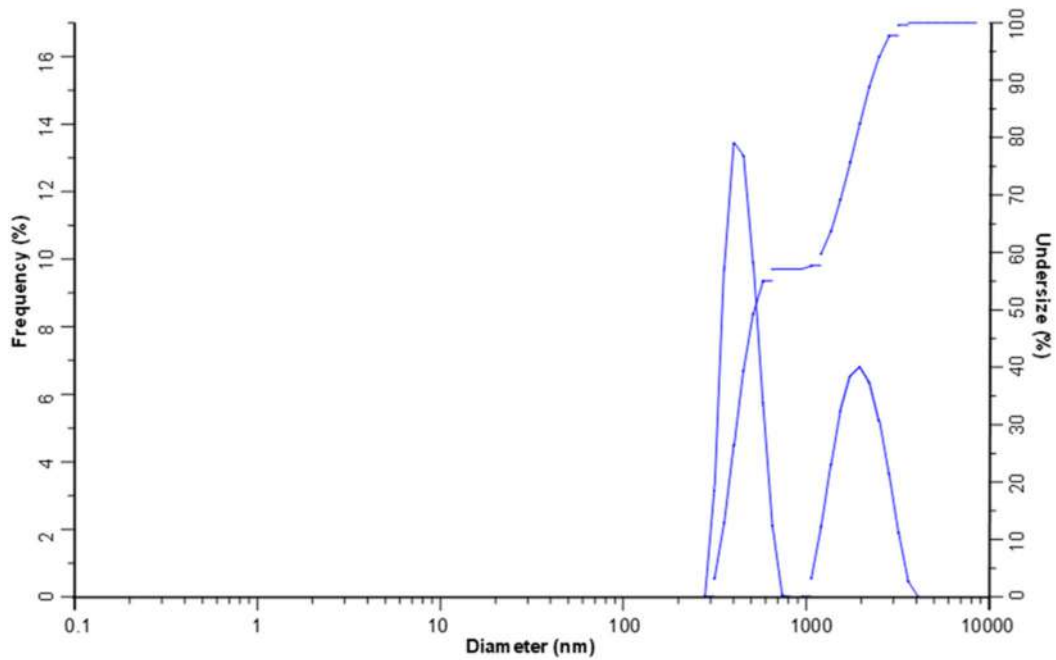


Fig 5. Particle size distribution of SPAC

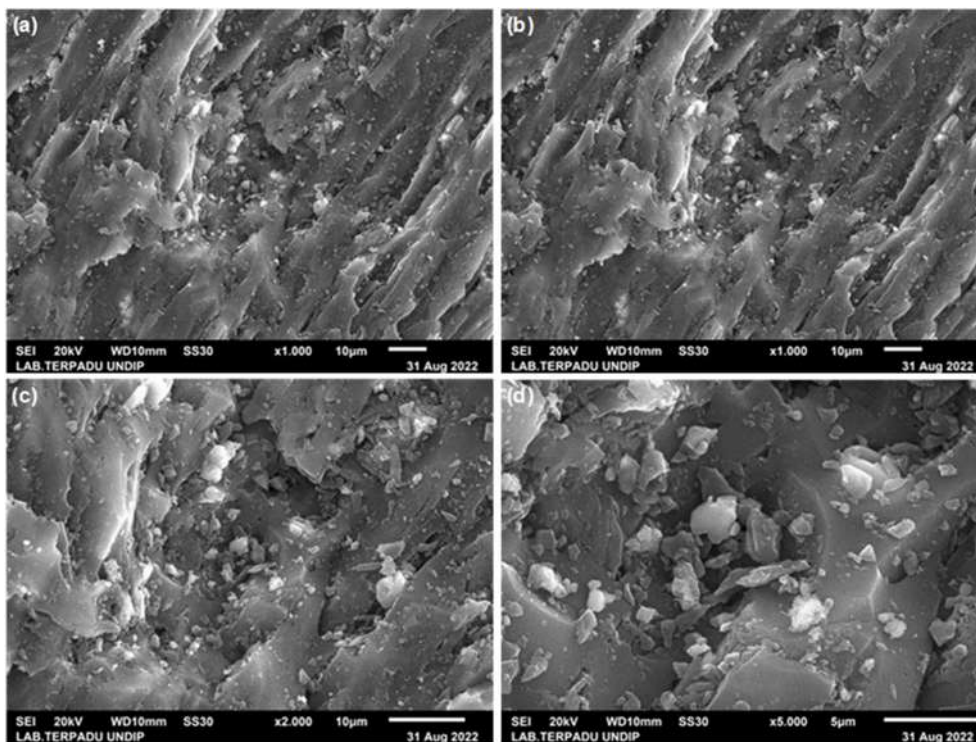


Fig 6. SEM test results of GAC with magnification of (a) 500 $\times$ , (b) 1000 $\times$ , (c) 2000 $\times$ , and (d) 5000 $\times$

Based on BET tests, size reduction of activated carbon from GAC to PAC and SPAC caused an increase in total pore volume and surface area of activated carbon. The total pore volume increased from 0.4576 cm<sup>3</sup>/g

(GAC) to 0.4618 cm<sup>3</sup>/g (PAC) and 0.4743 cm<sup>3</sup>/g (SPAC). This increase in pore volume can be caused by the formation of spaces between particles due to the pulverizing process, which is then measured as pores [29].



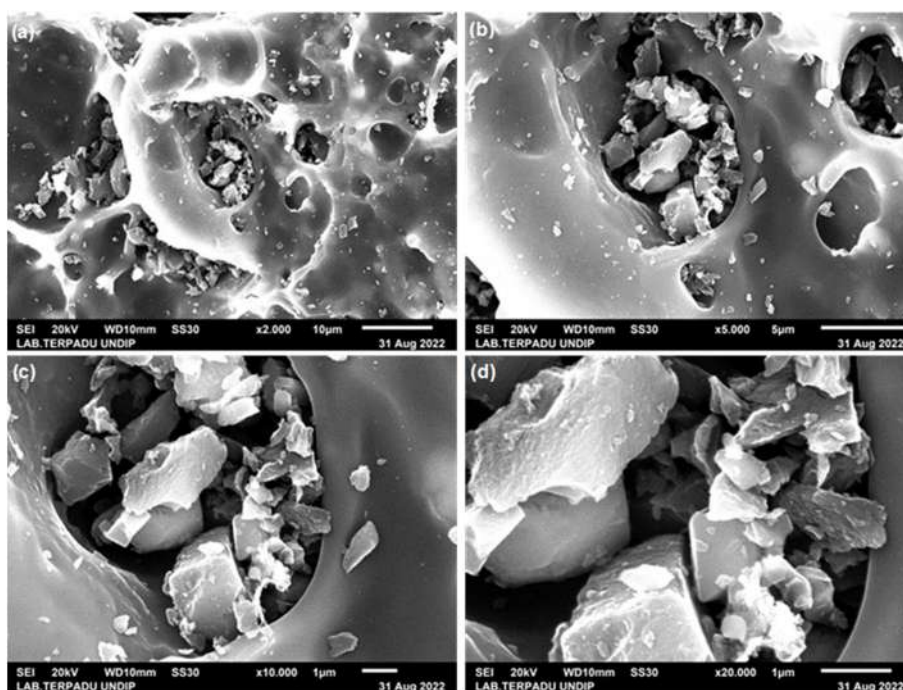


Fig 7. SEM test results of PAC with magnification of (a) 2000 $\times$ , (b) 5000 $\times$ , (c) 10000 $\times$ , and (d) 20000 $\times$

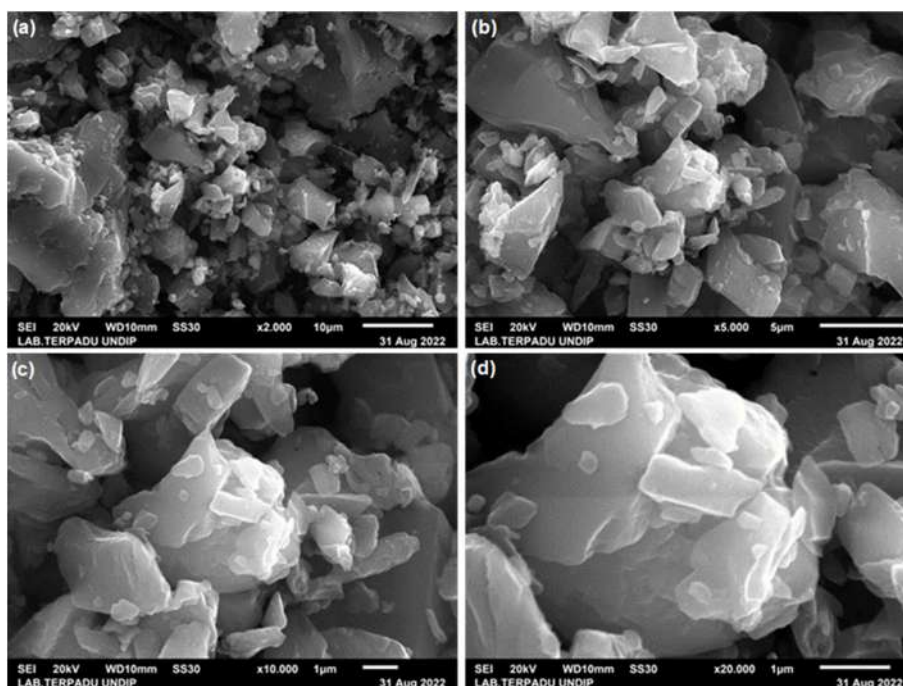


Fig 8. SEM test results of SPAC with magnification of (a) 2000 $\times$ , (b) 5000 $\times$ , (c) 10000 $\times$ , and (d) 20000 $\times$

These results were in accordance with previous research, which stated that the activated carbon particle size change did not cause a substantial change in pore structure [12,31]. Meanwhile, the surface area of activated carbon increased from 776.439 m<sup>2</sup>/g (GAC) to 787.443 m<sup>2</sup>/g

(PAC) and 790.478 m<sup>2</sup>/g (SPAC). This increase was due to a reduction of particle size and pore widening of activated carbon. But the escalation of surface area in smaller particle size was not as significantly different as particle size. This can be caused by the disappearance of

some surface area available in the parent material, such as pore channels, due to the pulverization process [29-30].

### Preliminary Tests

Preliminary test results showed that activated carbon was effective at removing the dye in methylene blue artificial wastewater. SPAC had the highest dye adsorption capacity compared to PAC and GAC. The dye adsorption capacities of SPAC ranged from 112.57–122.21 mg/g, while the dye adsorption capacities of PAC and GAC ranged from 34.67–60.96 mg/g and 4.34–16.66 mg/g. Reduction in dye concentration was also followed by a decrease in COD concentration. The COD adsorption capacities of SPAC ranged from 158.97–171.32 mg/g, while the COD adsorption capacities of PAC and GAC ranged from 39.64–55.61 mg/g and 9.91–22.99 mg/g. The escalation in adsorption capacity was mostly due to the increase of activated carbon's surface area rather than the increase in pores volume [18]. Structural pore changes due to the pulverizations process were not large. The increase in pore volume was only 0.0042 (GAC to PAC) and 0.0167 cm<sup>3</sup>/g (GAC to SPAC). But the increase in adsorption capacity can be explained based on the shell adsorption model (SAM). Based on SAM, more adsorbate is adsorbed on the outside (shell) of a particle if the radius of the activated carbon particle is smaller than the diffusion penetration depth of a particle whose value depends on the type of adsorbent and adsorbate. Because the outer surface area of the particles increases as the particle size decreases, the adsorption

capacity increases [14].

### Particle Size Effect on Adsorption Isotherms Test

The isotherm test results on each activated carbon can be seen in Fig. 9. Based on the Giles isotherm classification, the methylene blue adsorption process on each activated carbon followed the "High-Affinity Isotherm". This is because the  $q_e$  value is always greater than zero, even though the adsorbate concentration is close to zero. This type of isotherm generally occurs in adsorbates with large molecular sizes, such as polymers. This isotherm indicates the adsorption process occurs chemically (chemisorption) or adsorption by electrostatic forces [25].

Although each adsorption process followed a high-affinity isotherm, the adsorption process for each activated carbon was in a different subclass. The methylene blue adsorption process using GAC followed the mx subclass, while PAC and SPAC followed subclasses 4 and 2. The mx subclass was characterized by a decrease in adsorption capacity when the adsorbate concentration was increased. This decrease in adsorption capacity occurs because the interaction between the adsorbate molecules is stronger than the interaction between the adsorbate and the adsorbent. Subclass 4 is characterized by the presence of two lines with a gentle slope connected by a line with a steeper slope. This indicates the formation of a new active surface which can be caused by the reorientation of the adsorbed molecules from horizontal to vertical, which

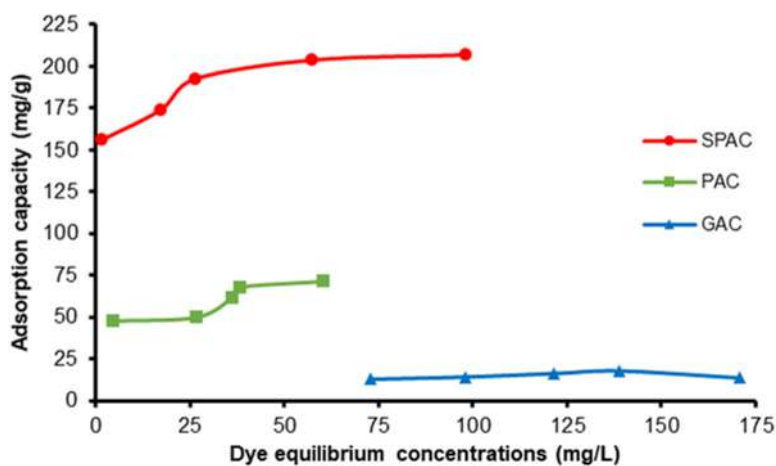


Fig 9. Isotherm graph

allows more adsorbate particles to be adsorbed. While subclass 2 is characterized by the appearance of longitudinal horizontal lines caused by the absence of intramolecular interactions of the adsorbate. Since there is no intramolecular interaction of the adsorbate, the adsorption process is monolayer [25]. All of these isotherm subclasses indicate a monolayer adsorption process. Therefore, the data obtained from the experiment were matched with the Langmuir isotherm to determine the value of the coefficient ( $K_L$ ) and maximum adsorption capacity ( $q_m$ ) using OriginPro2022b.  $q_m$  and  $K_L$  values can be seen in Table 1.

The maximum adsorption capacity and Langmuir coefficient ( $K_L$ ) increased in the adsorbent with the smaller particle size. An increase in  $K_L$  value indicates a stronger interaction between the adsorbent and the adsorbate on the smaller activated carbon particles [32]. The increase in maximum adsorption capacity for adsorbents with smaller particle sizes also occurred in previous research [15,29]. According to Ando et al. [31] adsorption capacity of activated carbon for certain adsorbate depends on adsorbent particle size. The dependence of adsorption capacity on activated carbon particle size might be associated with high-molecular mass of adsorbate and adsorbate characteristics. Moreover, the properties of activated carbon can also affect the adsorption capacity in smaller particle sizes.

### Particle Size Effect on Adsorption Kinetics Test

Based on isotherm analysis, the adsorption process of methylene blue on all activated carbon was caused by electrostatic forces. This will be further proven in thermodynamic tests to determine the enthalpy value of the adsorption process. Because the adsorption process was caused by electrostatic forces, the adsorption process was considered physisorption. Several kinetic models that can be used to describe the kinetics of the physisorption process are pseudo-first order and intraparticle diffusion models [33-34]. Therefore, the experimental data were analyzed with both models using OriginPro 2022b. From these two models, one model was then selected based on the lowest sum of square error (SSE), average relative error (ARE), hybrid fractional error function (HYBRID), and The Marquardt's percent standard deviation (MPSED) [24,35]. Analysis of the kinetic parameters using OriginPro2022b produced kinetic parameters of the pseudo-first-order and intraparticle diffusion models as seen in Table 2 and 3.

Error analysis to compare the suitability of each model to the experimental data can be seen in Table 4. Based on Table 4, the pseudo-first-order kinetic model had smaller error values for all types of activated carbon compared to the intraparticle diffusion model. This indicates that the first-order pseudo model was more

**Table 1.** Langmuir Isotherm Coefficients

Adsorbent types	$q_m$ (mg/g)	$K_L$ (L/mg)
GAC	$27.72505 \pm 3.49558$	$0.01156 \pm 0.00329$
PAC	$66.46779 \pm 5.81396$	$0.51107 \pm 0.38549$
SPAC	$197.70408 \pm 7.1626$	$2.28743 \pm 1.00784$

**Table 2.** Pseudo-first-order kinetic parameters

Adsorbent types	$K_1$ ( $\text{min}^{-1}$ )	$q_e$ (mg/g)
GAC	$0.01472 \pm 0.00129$	$24.15746 \pm 0.74313$
PAC	$0.11407 \pm 0.04308$	$41.66993 \pm 2.97193$
SPAC	$1.13446 \pm 0.03338$	$119.82991 \pm 0.07587$

**Table 3.** Intraparticle diffusion kinetic parameters

Adsorbent types	$K_i$ ( $\text{mg/g}\cdot\text{min}^{-0.5}$ )	$C_i$ (mg/g)
GAC	$1.47001 \pm 0.11054$	$2.85518 \pm 1.23684$
PAC	$2.59757 \pm 1.26843$	$35.53882 \pm 7.6106$
SPAC	$0.53902 \pm 0.15386$	$117.76349 \pm 0.53299$

**Table 4.** Error values of kinetic models

Adsorbent types	Time (min)	$q_{t,exp}$ (mg/g)	Pseudo-first-order				Intraparticle diffusion					
			$q_t$ (mg/g)	SSE	ARE	HYBRID	MPSED	$q_t$ (mg/g)	SSE	ARE	HYBRID	MPSED
GAC	42	11.84	11.14					12.38				
	84	16.63	17.14					16.33				
	126	20.19	20.38	1.148	2.709	2.492	4.178	19.36	1.435	2.607	2.657	3.982
	164	21.68	22.00					21.68				
	210	23.56	23.06					24.16				
PAC	12	33.42	31.07					44.54				
	24	35.83	38.97					48.26				
	36	36.60	40.98	70.661	8.307	57.459	11.961	51.12	710.742	31.017	632.012	41.245
	48	41.01	41.50					53.54				
	60	47.61	41.63					55.66				
SPAC	4	118.55	118.55					118.84				
	8	119.60	119.82					119.29				
	12	119.84	119.83	0.068	0.071	0.019	0.126	119.63	0.269	0.176	0.075	0.251
	16	119.89	119.83					119.92				
	20	119.97	119.83					120.17				

**Table 5.** Adsorption thermodynamics parameters

Temp (K)	$C_e$ (mol/L)	$q_e$ (mol/g)	$q_m$ (mg/g)	$K_e$	$\Delta G^\circ$ (KJ/mol)	$\Delta H^\circ$ (KJ/mol)	$\Delta S^\circ$ (J/mol.K)
GAC							
298	0.000228	0.000041	27.73	3886.50	-20.48		
308	0.000169	0.000064	28.77	14965.52	-24.62	59.92	272.35
318	0.000128	0.000092	35.52	38167.25	-27.89		
328	0.000123	0.000097	38.87	32221.93	-28.31		
PAC							
298	0.000014	0.000149	66.47	187063.39	-30.08		
308	0.000007	0.000150	72.91	288742.62	-32.20	14.68	150.94
318	0.000006	0.000151	74.63	294613.25	-33.30		
328	0.000006	0.000160	77.67	337172.66	-34.71		
SPAC							
298	0.000005	0.000488	197.70	780186.08	-33.61		
308	0.000002	0.000445	201.94	1571975.09	-36.54	58.92	309.46
318	0.000001	0.000463	205.83	1798797.87	-38.08		
328	0.000000	0.000468	207.92	8525412.86	-43.52		

suitable for describing the adsorption mechanism that occurred. In addition, based on Table 2, the value of the adsorption kinetics coefficient increased on activated carbon with a smaller particle size. This indicates a faster adsorption process on SPAC compared to PAC or GAC. An increase in the adsorption rate on the smaller activated carbon particles also occurred in previous research [17,19].

#### Particle Size Effect on Adsorption Thermodynamics Test

The results of the thermodynamic test on each activated carbon can be seen in Table 5. Based on Table 5, the change in Gibbs free energy ( $\Delta G^\circ$ ) was negative. This indicates that the methylene blue adsorption process using activated carbon was spontaneous and favorable. The increasingly negative  $\Delta G^\circ$  value indicates

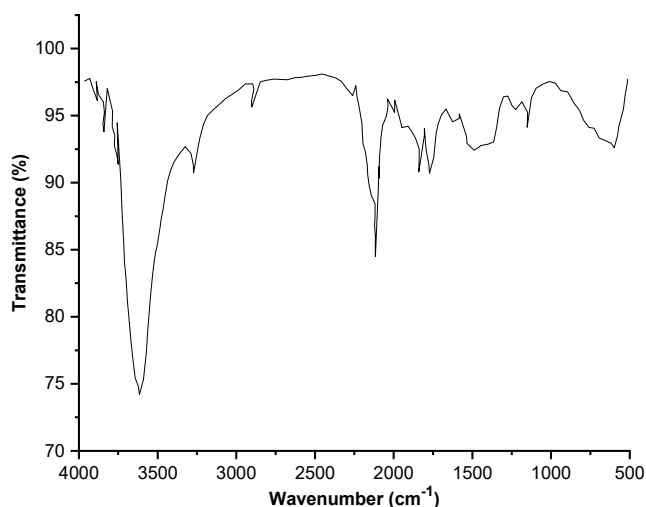


**Fig 10.** FTIR test results of MB solution before adsorption process

that the adsorption process was better and more spontaneous on the smaller activated carbon particle size and at higher temperatures [25].

Unlike the  $\Delta G^\circ$  values, the  $\Delta H^\circ$ , and  $\Delta S^\circ$  values were positive for all activated carbons. A positive  $\Delta H^\circ$  value indicates the adsorption process was endothermic. This is proven by the increased adsorption capacity at higher temperatures. Meanwhile, a positive  $\Delta S^\circ$  value indicates increased randomness at the interface of adsorbent-adsorbate and a good affinity of adsorbent to adsorbate [25]. The value of  $\Delta H^\circ$  can also be used to determine the adsorption mechanism that occurred. The value of  $\Delta H^\circ$  at PAC, which was less than 20 KJ/mol indicates physisorption was dominated by van der Waals forces interactions. Meanwhile, the  $\Delta H^\circ$  values of GAC and SPAC which were in the range of 20–80 KJ/mol indicate physisorption was dominated by electrostatic interactions.

These adsorption mechanisms were supported by FTIR test results on methylene blue artificial wastewater before and after the adsorption process (Fig. 10 and 11). Before the adsorption process, methylene blue artificial wastewater showed peaks in the functional group region ( $\lambda > 1500 \text{ cm}^{-1}$ ) at the wavelength of 3429.43; 2924.09; 2856.58; and 1602.85  $\text{cm}^{-1}$ . These peaks indicated the presence of hydroxyl (OH-), methylene (CH<sub>2</sub>), methyl

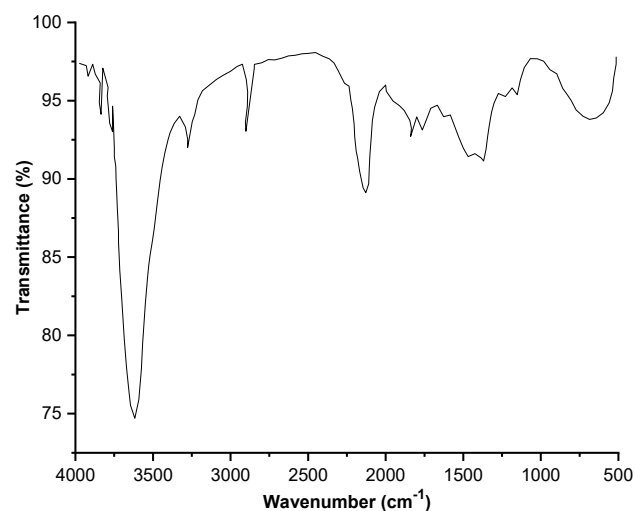


**Fig 11.** FTIR test results of MB solution after adsorption process

ether (O-CH<sub>3</sub>), and C=C functional groups. Meanwhile in fingerprint region ( $\lambda < 1500 \text{ cm}^{-1}$ ) peaks were formed at wavelength of 1492.90; 1442.75; 1396.46; 1350.17; 1247.94; 1176.58; 1141.86; and 1041.56  $\text{cm}^{-1}$ . These peaks could be formed because of the presence of aromatic bonds of (C=C-C), methyl (CH<sub>3</sub>), tri-methyl, methine (=CH-), aromatic ether, secondary amine (C-N), cyclic ether, and cyclohexane ring [36]. After the adsorption process, peaks in the functional group region remain unchanged. But, in the fingerprint region, some peaks disappeared at wavelength 1492.90; 1442.75; 1247.94; and 1176.58  $\text{cm}^{-1}$ .

The disappearance of some functional groups could be caused by several interactions: 1)  $\pi$ - $\pi$  interactions between the aromatic functional groups on the surface of the adsorbent and aromatic bonds (C=C-C), aromatic ethers, and other benzenic rings of methylene blue, 2) Electrostatic interactions between the negatively charged functional groups on the surface of the adsorbent and the positively charged methylene blue molecules (cations), 3) The hydrogen bond between the nitrogen (N) on the methylene blue molecule and functional groups containing oxygen, such as hydroxyl (OH-) on the surface of activated carbon [6,20,37].

The schematic mechanisms of the methylene blue adsorption process can be seen in Fig. 12.

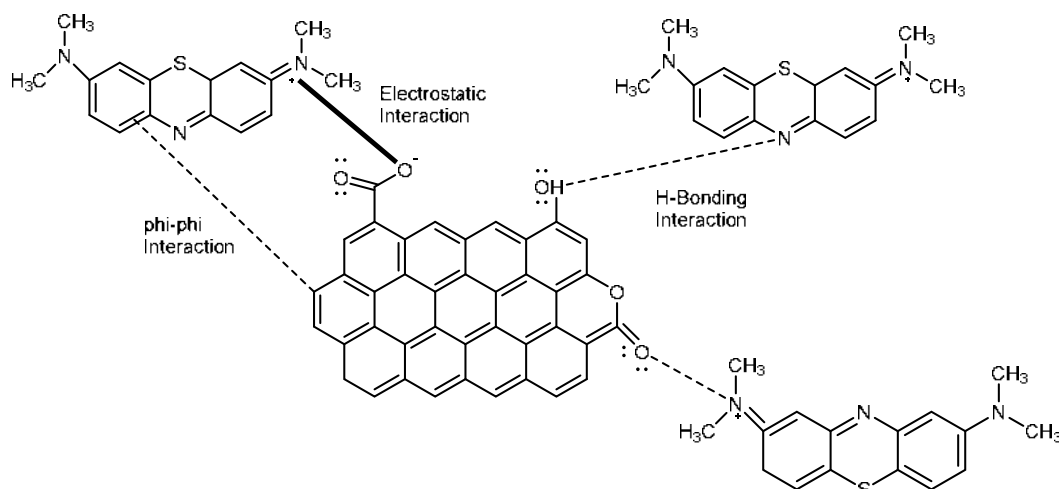


Fig 12. Scheme of adsorption interactions of MB and activated carbon

## ■ CONCLUSION

The chemical characterization of activated carbon showed that the pulverization process could change the  $pH_{pzc}$  to be more alkaline and increase the number of functional groups present on the surface of the activated carbon but did not change the type of functional groups available. At the same time, the physical characterization showed that there were differences in particle size distribution in GAC, PAC, and SPAC. The pulverization process also caused an increase in the surface area and pore volume of activated carbon. Based on isotherm and kinetic analysis, particle size variations did not change the type of isotherm and kinetics model that applied to the adsorption process, but it caused an increase in maximum adsorption capacity, Langmuir coefficient, and kinetics coefficient in smaller particle sizes. The thermodynamic test showed that the adsorption process took place more spontaneously and more favorably at the smaller particle size, and there was a difference in the dominant mechanism that caused the adsorption process in different particle sizes of activated carbon based on  $\Delta H^\circ$  values. The dominant adsorption mechanism on GAC and SPAC was electrostatic interaction, while on PAC was van der Waals forces. Based on these results, SPAC has good potential to be used in the water/wastewater treatment process, especially in the tertiary process, to remove recalcitrant pollutants such as hydrocarbons, pesticides, and textile dyes.

## ■ AUTHOR CONTRIBUTIONS

Akhmad Masykur Hadi Musthofa conducted the experiments, calculations, and wrote the manuscript. Mindriany Syafila and Qomarudin Helmy reviewed the methodology and manuscript. All authors agreed to the final version of this manuscript.

## ■ REFERENCES

- [1] Kant, R., 2012, Textile dyeing industry an environmental hazard, *Nat. Sci.*, 4 (1), 22–26.
- [2] Ghaly, A.E., Ananthashankar, R., Alhattab, M., and Ramakrishna, V.V., 2013, Production, characterization and treatment of textile effluents: A critical review, *J. Chem. Eng. Process Technol.*, 5 (1), 1000182.
- [3] Velusamy, S., Roy, A., Sundaram, S., and Kumar Mallick, T., 2021, A review on heavy metal ions and containing dyes removal through graphene oxide-based adsorption strategies for textile wastewater treatment, *Chem. Rec.*, 21 (7), 1570–1610.
- [4] Balapure, K., Bhatt, N., and Madamwar, D., 2015, Mineralization of reactive azo dyes present in simulated textile waste water using down flow microaerophilic fixed film bioreactor, *Bioresour. Technol.*, 175, 1–7.
- [5] Fatkhasari, Y., Rouf, N.A., Ermadayanti, W.A., Kurniawan, R.Y., and Bagastyo, A.Y., 2019, Synthesis of  $TiO_2$ /zeolite-A composite for the

- removal of methylene blue on direct sunlight, *Jurnal Teknik ITS*, 8 (2), 115–120.
- [6] Giraldo, S., Robles, I., Godínez, L.A., Acelas, N., and Flórez, E., 2021, Experimental and theoretical insights on methylene blue removal from wastewater using an adsorbent obtained from the residues of the orange industry, *Molecules*, 26 (15), 4555.
- [7] Saratale, R.G., Saratale, G.D., Chang, J.S., and Govindwar, S.P., 2011, Bacterial decolorization and degradation of azo dyes: A review, *J. Taiwan Inst. Chem. Eng.*, 42 (1), 138–157.
- [8] Dutta, S., Gupta, B., Srivastava, S.K., and Gupta, A.K., 2021, Recent advances on the removal of dyes from wastewater using various adsorbents: A critical review, *Mater. Adv.*, 2 (14), 4497–4531.
- [9] Sultana, M., Rownok, M.H., Sabrin, M., Rahaman, M.H., and Alam, S.M.N., 2022, A review on experimental chemically modified activated carbon to enhance dye and heavy metals adsorption, *Cleaner Eng. Technol.*, 6, 100382.
- [10] Zhang, Z., Xu, L., Liu, Y., Feng, R., Zou, T., Zhang, Y., Kang, Y., and Zhou, P., 2021, Efficient removal of methylene blue using the mesoporous activated carbon obtained from mangosteen peel wastes: Kinetic, equilibrium, and thermodynamic studies, *Microporous Mesoporous Mater.*, 315, 110904.
- [11] Sun, X., Ma, L., Ye, G., Wu, L., Li, J., Xu, H., and Huang, G., 2021, Phenol adsorption kinetics and isotherms on coal: Effect of particle size, *Energy Sources, Part A*, 43 (4), 461–474.
- [12] Partlan, E., 2017, Superfine Powdered Activated Carbon (S-PAC) Coupled with Microfiltration for the Removal of Trace Organics in Drinking Water Treatment, *Dissertation*, Clemson University, South Carolina.
- [13] Takaesu, H., Matsui, Y., Nishimura, Y., Matsushita, T., and Shirasaki, N., 2019, Micro-milling super-fine powdered activated carbon decreases adsorption capacity by introducing oxygen/hydrogen-containing functional groups on carbon surface from water, *Water Res.*, 155, 66–75.
- [14] Pan, L., Nishimura, Y., Takaesu, H., Matsui, Y., Matsushita, T., and Shirasaki, N., 2017, Effects of decreasing activated carbon particle diameter from 30  $\mu\text{m}$  to 140 nm on equilibrium adsorption capacity, *Water Res.*, 124, 425–434.
- [15] Matsui, Y., Nakao, S., Sakamoto, A., Taniguchi, T., Pan, L., Matsushita, T., and Shirasaki, N., 2015, Adsorption capacities of activated carbons for geosmin and 2-methylisoborneol vary with activated carbon particle size: Effects of adsorbent and adsorbate characteristics, *Water Res.*, 85, 95–102.
- [16] Shi, B., Fang, L., Li, Z., and Wang, D., 2014, Adsorption behavior of DOM by PACs with different particle sizes, *CLEAN – Soil, Air, Water*, 42 (10), 1363–1369.
- [17] Partlan, E., Ren, Y., Apul, O.G., Ladner, D.A., and Karanfil, T., 2020, Adsorption kinetics of synthetic organic contaminants onto superfine powdered activated carbon, *Chemosphere*, 253, 126628.
- [18] Matsui, Y., Ando, N., Yoshida, T., Kurotobi, R., Matsushita, T., and Ohno, K., 2011, Modeling high adsorption capacity and kinetics of organic macromolecules on super-powdered activated carbon, *Water Res.*, 45 (4), 1720–1728.
- [19] Bonvin, F., Jost, L., Randin, L., Bonvin, E., and Kohn, T., 2016, Super-fine powdered activated carbon (SPAC) for efficient removal of micropollutants from wastewater treatment plant effluent, *Water Res.*, 90, 90–99.
- [20] Khalil, K.M.S., Elhamdy, W.A., Mohammed, K.M.H., and Said, A.E.A.A., 2022, Nanostructured P-doped activated carbon with improved mesoporous texture derived from biomass for enhanced adsorption of industrial cationic dye contaminants, *Mater. Chem. Phys.*, 282, 125881.
- [21] Aljeboree, A.M., Alshirifi, A.N., and Alkaim, A.F., 2017, Kinetics and equilibrium study for the adsorption of textile dyes on coconut shell activated carbon, *Arabian J. Chem.*, 10, S3381–S3393.
- [22] Medhat, A., El-Maghrabi, H.H., Abdelghany, A., Abdel Menem, N.M., Raynaud, P., Moustafa, Y.M., Elsayed, M.A., and Nada, A.A., 2021, Efficiently activated carbons from corn cob for methylene blue adsorption, *Appl. Surf. Sci. Adv.*, 3, 100037.

- [23] Hajjaligol, S., and Masoum, S., 2019, Optimization of biosorption potential of nano biomass derived from walnut shell for the removal of Malachite Green from liquids solution: Experimental design approaches, *J. Mol. Liq.*, 286, 110904.
- [24] Subramanyam, B., and Das, A., 2014, Linearised and non-linearised isotherm models optimization analysis by error functions and statistical means, *J. Environ. Health Sci. Eng.*, 12 (1), 92.
- [25] Bonilla-Petriciolet, A., Mendoza-Castillo, D.I., and Reynel-Ávila, H.E., 2017, *Adsorption Processes for Water Treatment and Purification*, Springer Cham, Switzerland.
- [26] Prasad, A.L., Santhi, T., and Manonmani, S., 2015, Recent developments in preparation of activated carbons by microwave: Study of residual errors, *Arabian J. Chem.*, 8 (3), 343–354.
- [27] Soldatkina, L., and Yanar, M., 2021, Equilibrium, kinetic, and thermodynamic studies of cationic dyes adsorption on corn stalks modified by citric acid, *Colloids Interfaces*, 5 (4), 52.
- [28] Hien Tran, T., Le, A.H., Pham, T.H., Duong, L.D., Nguyen, X.C., Nadda, A.K., Chang, S.W., Chung, W.J., Nguyen, D.D., and Nguyen, D.T., 2022, A sustainable, low-cost carbonaceous hydrochar adsorbent for methylene blue adsorption derived from corncobs, *Environ. Res.*, 212, 113178.
- [29] Ellerie, J.R., Apul, O.G., Karanfil, T., and Ladner, D.A., 2013, Comparing graphene, carbon nanotubes, and superfine powdered activated carbon as adsorptive coating materials for microfiltration membranes, *J. Hazard. Mater.*, 261, 91–98.
- [30] Partlan, E., Davis, K., Ren, Y., Apul, O.G., Mefford, O.T., Karanfil, T., and Ladner, D.A., 2016, Effect of bead milling on chemical and physical characteristics of activated carbons pulverized to superfine sizes, *Water Res.*, 89, 161–170.
- [31] Ando, N., Matsui, Y., Kurotobi, R., Nakano, Y., Matsushita, T., and Ohno, K., 2010, Comparison of natural organic matter adsorption capacities of super-powdered activated carbon and powdered activated carbon, *Water Res.*, 44 (14), 4127–4136.
- [32] Ragadhita, R., and Nandiyanto, A.B.D., 2021, How to calculate adsorption isotherms of particles using two-parameter monolayer adsorption models and equations, *Indones. J. Sci. Technol.*, 6 (1), 205–234.
- [33] Agbovi, H.K., and Wilson, L.D., 2021, “Adsorption Processes in Biopolymer Systems: Fundamentals to Practical Applications” in *Natural Polymers-Based Green Adsorbents for Water Treatment*, Eds. Kalia, S., Elsevier, Cambridge, US, 1–51.
- [34] Yao, C., and Chen, T., 2017, A film-diffusion-based adsorption kinetic equation and its application, *Chem. Eng. Res. Des.*, 119, 87–92.
- [35] Sreńscek-Nazzal, J., Narkiewicz, U., Morawski, A.W., Wróbel, R.J., and Michalkiewicz, B., 2015, Comparison of optimized isotherm models and error functions for carbon dioxide adsorption on activated carbon, *J. Chem. Eng. Data*, 60 (11), 3148–3158.
- [36] Nandiyanto, A.B.D., Oktiani, R., and Ragadhita, R., 2019, How to read and interpret FTIR spectroscopy of organic material, *Indones. J. Sci. Technol.*, 4 (1), 97–118.
- [37] Jawad, A.H., Saud Abdulhameed, A., Wilson, L.D., Syed-Hassan, S.S.A., AlOthman, Z.A., and Rizwan Khan, M., 2021, High surface area and mesoporous activated carbon from KOH-activated dragon fruit peels for methylene blue dye adsorption: Optimization and mechanism study, *Chin. J. Chem. Eng.*, 32, 281–290.



## Indonesian Purple Rice Ferulic Acid as a Candidate for Anti-aging through the Inhibition of Collagenase and Tyrosinase Activities

Ernanin Dyah Wijayanti<sup>1,2,3</sup>, Anna Safitri<sup>2,4</sup>, Dian Siswanto<sup>1</sup>, and Fatchiyah Fatchiyah<sup>1,2\*</sup>

<sup>1</sup>Department of Biology, Faculty of Mathematics and Natural Sciences, Brawijaya University, Jl. Veteran, Malang 65145, East Java, Indonesia

<sup>2</sup>Research Center of Smart Molecule of Natural Genetics Resource, Brawijaya University, Jl. Veteran, Malang 65145, East Java, Indonesia

<sup>3</sup>Health Polytechnique of Putra Indonesia Malang, Jl. Barito 5, Malang 65123, East Java, Indonesia

<sup>4</sup>Department of Chemistry, Faculty of Mathematics and Natural Sciences, Brawijaya University, Jl. Veteran, Malang 65145, East Java, Indonesia

\* **Corresponding author:**

email: fatchiya@ub.ac.id

Received: December 6, 2022

Accepted: February 20, 2023

DOI: 10.22146/ijc.79819

**Abstract:** Skin aging is associated with decreased skin firmness and excessive pigmentation, which is caused by the activity of aging enzymes. This process can be prevented with powerful antioxidants from nature, such as ferulic acid which is abundant in rice. This study examines the nutritional content and phytochemicals of Indonesian purple rice and evaluates the bioactivity of ferulic acid as an anti-aging agent. Indonesian purple rice has less fat than black and white rice, more amino acids involved in aging regulation, and a similar phytochemical profile to black and white rice. Indonesian purple rice has a lower concentration of ferulic acid ( $4.114 \pm 0.013$  mg/L) than black rice but shows strong reducing power ( $IC_{50} 9.35 \pm 1.95$   $\mu$ g/mL), high anti-tyrosinase ( $IC_{50} 59.57 \pm 3.60$   $\mu$ g/mL), and moderate anti-collagenase activities ( $IC_{50} 74.18 \pm 3.11$   $\mu$ g/mL). This study supports the use of Indonesian purple rice as a promising active ingredient in natural anti-aging cosmetics.

**Keywords:** anti-aging; collagenase; ferulic acid; purple rice; tyrosinase

### ■ INTRODUCTION

Skin aging refers to the process of the skin losing its structural integrity and physiological function as a result of both internal and external influences. Genetics is an intrinsic component that is altered by time. The environment, particularly ultraviolet (UV) radiation, is an external influence [1-2]. Smoking, pollution, poor diet, lack of sleep, stress, and severe temperatures are a few more environmental factors that affect or may influence skin aging [3].

Exposure to UV radiation promotes the production of excess free radicals or reactive oxygen species (ROS), which activates collagenase and tyrosinase via the mitogen-activated protein kinase (MAPK) pathway [4-5]. Collagenase breaks down collagen and generates wrinkle

formation, and tyrosinase catalyzes melanin synthesis from tyrosine, and causes hyperpigmentation [6-9].

Wrinkle formation and hyperpigmentation are signs of aging that can be prevented with an anti-aging strategy [7,9-10]. The anti-aging mechanism includes the ability to scavenge free radicals, protect the skin from UV exposure, increase skin moisture, and increase collagen production or prevent collagen degradation [3]. Collagenase and tyrosinase inhibitors have been widely used in cosmetic or pharmaceutical products as anti-aging agents [8,11].

Recently, there has been a surge of interest in naturally occurring active ingredients for anti-aging products. One potent antioxidant found in nature is ferulic acid, also known as 4-hydroxy-3-methoxycinnamic acid [12-13]. Ferulic acid can be

found in rice, oats, wheat, pineapple, seeds of coffee, beans, nuts, artichoke, and peanuts [14]. However, rice is the most common source of ferulic acid [15].

Among the rice varieties, pigmented rice is richer in nutrients than non-pigmented rice because it is produced without a grinding and polishing process [16]. There is Indonesian purple rice (IPR) produced by crossbreeding between *Mentik Wangi* black rice (BR-MW) and *Mentik Susu* white rice (WR-MS) [17]. Up to this point, there has never been an exploration of the potential for ferulic acid from rice in Indonesia, particularly the IPR. Ferulic acid levels commonly were found to correlate positively with rice pigmentation [18], but rice with a light purple color (variety YF67) obtained from a crossbreeding between black rice and white rice from China, produced higher levels of ferulic acid than black rice parental [19]. The higher concentration of ferulic acid in variety YF67 makes us wonder if the IPR is a potential source of ferulic acid, and further research into its ferulic acid content is required.

Previous research demonstrating the antimicrobial and anti-inflammatory properties of IPR ferulic acid supports its anti-aging potential [20-21]. Nevertheless, the ability to scavenge free radicals and inhibit aging enzymes needs further investigation. Moreover, the nutritional and phytochemical content, which may support anti-aging properties, is also important to explore. Therefore, this study aims to analyze the nutritional value and phytochemical profile of IPR and evaluate the potential of its ferulic acid content as an anti-aging.

## ■ EXPERIMENTAL SECTION

### Materials

The research material used were ferulic acid ( $\leq 100\%$ , Sigma-Aldrich, PHR1791), Folin-Ciocalteu (Merck, 1.09001.0500), collagenase from *Clostridium histolyticum* ( $\geq 125$  units per mg, Type 2, Worthington), tyrosinase from *Agaricus bisporus* (1240 units per mg, Worthington), kojic acid ( $> 98\%$ , TCI, KD010), L-ascorbic acid ( $> 99\%$ , TCI, A0537), tricine ( $> 99.0\%$ , TCI, T0682), L-tyrosine ( $> 98.5\%$ , TCI, T0550), *N*-[3-(2-furyl)acryloyl]-*l*-tyr-gly-pro-ala]/FALGPA (95.2%, HPLC

grade, Sigma, F5135), potassium ferricyanide, and trichloroacetic acid.

Four cultivars of rice were used in this research. Indonesian purple rice (IPR), *Mentik Wangi* black rice (BR-MW), and *Mentik Susu* white rice (WR-MS) were obtained from a local farmer in the Ngawi region, East Java, Indonesia. The *Jeliteng* black rice (BR-J), the national standard black rice, was used as the positive control for rice. This rice was obtained from The Indonesian Agency for Agricultural Research and Development, Ministry of Agriculture, Republic of Indonesia.

### Instrumentation

The instruments used were a shaker water bath (Memmert), rotary evaporator (IKA HB 10), Fourier Transform Infrared spectrophotometer (FTIR, Shimadzu, IR Type Prestige 21), High-Performance Liquid Chromatography (HPLC, Prominence-I, LC-2030C 3D Plus, serial no. L214556, Shimadzu) with shim-pack GIST C18 column (5  $\mu\text{m}$ ,  $4.6 \times 150$ , Shimadzu), Ultra Performance Liquid Chromatography (UPLC), Liquid Chromatography-Tandem Mass Spectrometry (LC-MS/MS), and UV-Vis spectrophotometer (SmartSpec Plus™, BioRad Laboratories Inc., Hercules, CA, USA).

### Procedure

#### *Proximate analysis*

Proximate analysis was carried out in the Central Laboratory of Life Sciences, Brawijaya University. The analysis consists of carbohydrate, protein, lipid, ash, and water contents according to Indonesian National Standard (SNI 01-2891-1992) method.

#### *Determination of amino acids*

Determination of amino acid content was conducted in PT. Saraswanti Indo Genetech, Bogor, West Java, Indonesia. The UPLC was used to analyze L-histidine, L-isoleucine, L-leucine, L-lysine, L-phenylalanine, L-threonine, L-valine, L-alanine, L-arginine, L-aspartic acid, L-glutamic acid, glycine, L-proline, L-serine, and L-tyrosine, according to the 18-5-17/MU/SMM-SIG protocol. L-methionine and L-cysteine were analyzed using LC-MS/MS according to

18-12-38/MU/SMM-SIG protocol, while L-tryptophan was analyzed using HPLC according to 18-5-63/MU/SMM-SIG. The UPLC was performed using AccQ.Tag Ultra C18 1.7  $\mu\text{m}$  column (2.1  $\times$  100 mm). The mobile phase consisted of A: Eluent A concentrate Amino Acid Analysis AccQ.Tag Ultra; B: Eluent B Amino Acid Analysis AccQ.Tag Ultra 10% in water; C: Aquabidest; D: Eluent B Amino Acid Analysis AccQ.Tag Ultra. The rate of flow was fixed at 0.5 mL/min. A photometric diode array (PDA) at the wavelength of 260 nm was used as the detector [22].

### Phytochemical screening

As much as 4 g of rice powder were macerated in 96% ethanol at room temperature for 24 h and then filtrated using Whatman paper No. 1. The filtrates were screened for phytochemical content including phenolic, flavonoid, tannin, anthocyanin, leucoanthocyanidin, glycoside, and anthraquinone using the standard methods [23-24].

### Extraction of ferulic acid

Rice was extracted to obtain ferulic acid using the modified method [25]. Alkaline hydrolysis was applied by adding 300 mL of 0.5 M sodium hydroxide to 50 g of rice powder, followed by constant shaking for 4 h at 60 °C. A total amount of 600 mL of 96% ethanol was added to dissolve ferulic acid then the pH was neutralized by adding 37% hydrochloric acid. The mixture was filtered with Whatman filter paper No 41 attached to a vacuum Buchner funnel and evaporated for about 30 min to obtain the concentrated extract. The brown extract indicated the existence of ferulic acid.

### Determination of total phenolic content

The Folin-Ciocalteu method was used to determine the total phenolic content. Briefly, 200  $\mu\text{L}$  of rice extract (1 mg/mL) was added with distilled water up to 3 mL and mixed with 0.5 mL of Folin-Ciocalteu reagent for 3 min. The mixture was added with 2 mL of 20% sodium carbonate and then incubated in dark conditions for 60 min. The absorbance was measured at 650 nm by a UV-Vis spectrophotometer [26]. Ferulic acid (0–10 ppm) was used as the standard calibration curve. The total phenolic content was calculated by the following formula:

$$\text{Total phenolic content} = \frac{C \times V \times DF}{m}$$

where C represents the concentration of the sample calculated using the standard calibration curve equation (ppm), V represents the volume of the sample (mL), DF represents the dilution factor of the sample, and m represents the mass of the extract (g). The total phenolic content was expressed as mg ferulic acid equivalent per gram (mg FAE/g) [27].

### Identification and determination of ferulic acid content

The ferulic acid functional group was identified using FTIR based on standard methods in the Analysis and Measurement Units of the Chemistry Department, Faculty of Mathematics and Natural Sciences, Brawijaya University. To confirm the presence of ferulic acid, we conducted HPLC. The concentrated extracts were dissolved in methanol and passed through 0.45  $\mu\text{m}$  nylon filters. A 10  $\mu\text{L}$  of the filtrate was then injected into an HPLC system with a shim-pack GIST C18 column. The mobile phase consisted of methanol and water (1% HAc) (65:35, v/v). The flow rate was 1 mL/min, the oven temperature was 35 °C, and the detector was set at 320 nm. Quantification of ferulic acid was performed via a calibration curve of standard (six different concentration levels range 1.17–35.1 mg/L) [25].

### Reducing power assay

Reducing power was determined using Ferric Reducing Antioxidant Potential (FRAP) method modified from [28]. Briefly, 100  $\mu\text{L}$  of the sample (0–10 ppm) were mixed with 2.5 mL of phosphate buffer (pH 6.6) and 2.5 mL of 1% of potassium ferricyanide, then incubated in a dark condition at 50 °C for 20 min. The mixture was added with 2.5 mL of 10% of TCA. Then 5 mL of each mixture was added with 5 mL of distilled water and 1 mL of 0.1% of  $\text{FeCl}_3$ . The absorbance was measured at 700 nm by a UV-Vis spectrophotometer. Ascorbic acid was used as the positive control. The antioxidant activity was calculated using the following equation:

$$\% \text{ Reducing power} = \frac{A_s - A_c}{A_s} \times 100\%$$

where  $A_s$  represents the absorbance of the sample and  $A_c$  represents the absorbance of control. The reducing power was expressed in terms of  $IC_{50}$  values, which determined the concentration of sample required to inhibit 50% of free radicals. The higher the reducing power, the lower the  $IC_{50}$  value.

### Anti-aging activity assay

The anti-aging activity of purple rice ferulic acid extract was determined by inhibiting collagenase and tyrosinase activity. The collagenase inhibitory activity assay was performed based on [29]. A mixture of 10  $\mu$ L of collagenase, 60  $\mu$ L of Tricine buffer, and 30  $\mu$ L of the sample (0–100 ppm) was incubated at 37 °C for 20 min. The mixture was added with 20  $\mu$ L of *N*-[3-(2-furyl)acryloyl]-*l*-*g*-*l*-*g*-*l*-*p*-*a* (1 mM in Tricine buffer) then incubated at 37 °C for 10 min. The absorbance was measured at 335 nm. Ascorbic acid was used as the positive control [11].

The tyrosinase inhibitory activity assay was performed using the modified method [30]. The mixed solution included 1.7 mM L-tyrosine, 10 mM phosphate buffer (pH 6.8), 100  $\mu$ L of sample (0–100 ppm) and 125 U/mL tyrosinase was incubated at 37 °C for 10 min. The absorbance was measured at 475 nm by a UV-Vis spectrophotometer. Kojic acid was used as the positive control. The collagenase and tyrosinase inhibitory activity was calculated using the following equation [31]:

$$\% \text{ Inhibitory activity} = \frac{A_c - A_s}{A_c} \times 100\%$$

where  $A_c$  represents the absorbance of the control, and  $A_s$  represents the absorbance of the sample. The anti-aging activity was also expressed as  $IC_{50}$  values as in antioxidant activity.

### Data analysis

Statistical analysis was performed using GraphPad Prism 8 software. The one-way analysis of variance (ANOVA) followed by Tukey's HSD test was used to determine the significant differences between TPC and  $IC_{50}$  values. We also measured the linear relationship between sample concentration and antioxidant activity, anti-aging, and the relationship between TPC and ferulic acid concentrations by Pearson correlation. Differences

or correlations were considered significant when  $p < 0.05$  [32].

## RESULTS AND DISCUSSION

### Nutritional Content

The nutritional content of IPR is presented in Table 1. The IPR contained lower carbohydrate and higher protein contents than BR-MW. The IPR had a lower level of fat and ash than BR-MW and BR-J. In contrast, the water level of IPR was higher than BR-MW and BR-J. In previous studies, proximate analysis of WR-MS showed carbohydrate content of 74.62%, protein 10.62%, fat 2.92%, water 11.08%, and ash 1.26% [22]. The IPR has lower fat content than both parental and BR-J, which prevents age-related diseases [33-35].

Table 1 also shows the amino acid content of IPR, including essential and non-essential amino acids. We found that IPR had a higher concentration of L-histidine, L-phenylalanine, L-threonine, L-arginine, L-serine, and L-tyrosine than BR-J and BR-MW. The concentration of amino acids is also higher when compared to the concentration of the amino acid WR-MS determined in previous studies [22]. Amino acids play a crucial role in aging regulation and help maintain healthy skin. Aspartic acid and glutamate build the DNA of skin cells, arginine restores skin damage and is a precursor to nitrogen oxides which are essential regulators for blood circulation in the dermis. Arginine is also a component of creatine that stimulates collagen and elastin production and skin function. Histidine protects against UV and smooths the skin. Tyrosine acts as an anti-melanogenic [36-38]. Phenylalanine and tyrosine are precursors of ferulic acid biosynthesis by shikimate or phenylpropanoid pathways [13].

### Phytochemical Profile

The overview of the general phytochemical profile of IPR ethanol extract was performed using a color reactions test. Table 2 shows that IPR contains phenolic compounds, flavonoids, tannins, anthocyanins, leucoanthocyanidins, and glycosides. The level of these compounds varied in BR-J and BR-MW. Previously, the screening was done on an ethanol extract of WR-MS,

**Table 1.** The nutritional content of IPR (a) proximate analysis, (b) amino acid content

a. Component	Concentration (%)		
	BR-J	BR-MW	IPR
Carbohydrate	76.67	78.20*	77.75
Protein	8.26*	7.32	7.82
Lipid	1.98*	1.94*	0.64
Water	11.91	11.58	13.24*
Ash	1.18*	0.96	0.55
b. Amino Acid	Concentration (ppm)		
	BR-J	BR-MW	IPR
Essential			
L-Histidine	1940.76	1996.26*	2004.15*
L-Isoleucine	2946.15*	2828.51	2769.24
L-Leucine	6643.06*	6489.40	6197.65
L-Lysine	2872.76*	2858.04*	2639.26
L-Methionine	740.85*	712.54	691.16
L-Phenylalanine	4293.06	4271.29	4593.89*
L-Threonine	3294.73	3501.47	3594.92*
L-Tryptophan	856.48*	783.87	800.27
L-Valine	4413.15*	4401.53*	4254.92
Non-essential			
L-Alanine	3379.15	3436.69*	3187.78
L-Arginine	6751.55	6750.51	6942.86*
L-Aspartic acid	5840.53	5849.29*	5742.45
L-Cysteine	2036.69*	1806.50	729.72
L-Glutamic acid	12832.30*	12242.01	12298.76
Glycine	3627.65	3784.39*	3546.90
L-Proline	3372.86*	3359.61*	3260.84
L-Serine	4706.81	4701.81	4729.39
L-Tyrosine	2685.67	2762.49	2896.75*

Note: An asterisk notation (\*) indicates the highest significant value (Tukey's HSD;  $P < 0.05$ ). BR-J: *Jeliteng* black rice, BR-MW: *Mentik wangi* black rice, IPR: Indonesian purple rice

**Table 2.** Phytochemical screening by color reactions

Compounds	BR-J	BR-MW	IPR
Phenolics	+++	++	++
Flavonoids	++	++	+
Tannins	+	+	+
Anthocyanins	+++	+++	+
Leucoanthocyanidins	++	++	+
Glycosides	++	++	+
Anthraquinones	-	-	-

Note: (-) absence of targeted compound, (+) low intensity of targeted compound, (++) moderate intensity of targeted compound, (+++) high intensity of targeted compound. BR-J: *Jeliteng* black rice, BR-MW: *Mentik wangi* black rice, IPR: Indonesian purple rice

which revealed the presence of phenolic compounds and tannins. At the same time, no leucoanthocyanidins or glycosides were found [22]. Furthermore, IPR showed the total phenolic content (Fig. 1) at the same level as the parents, BR-MW and WR-MS.

### Identification of Ferulic Acid

The FTIR analysis was performed to identify ferulic acid functional groups in IPR. The transmittance percentage of IPR was compared to ferulic acid and plotted on the graph (Fig. 2). The FTIR spectra of IPR showed the same pattern as BR-J, BR-MW, and WR-MS.

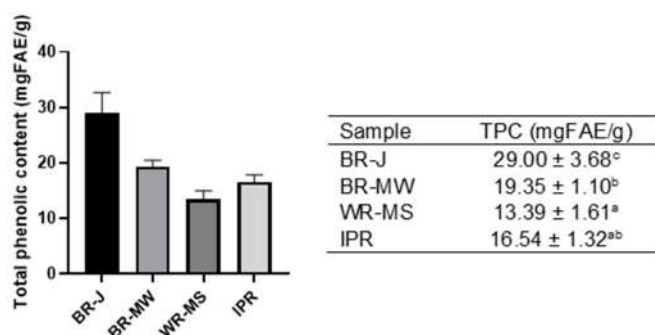


**Fig 1.** Total phenolic content by the Folin-Ciocalteu method, the different letters indicated significant differences (Tukey's HSD;  $P < 0.05$ ). BR-J: *Jeliteng* black rice, BR-MW: *Mentik wangi* black rice, WR-MS: *Mentik susu* white rice, IPR: Indonesian purple rice

The maximum absorption differed from ferulic acid spectra which could be influenced by the presence of

other compounds in the extract. However, the bands were in the same wavenumber zone as ferulic acid. Those similarities showed that several ferulic acid functional groups are present in the IPR, indicating that IPR contains ferulic acid.

The OH, C-H, C-O, and C=C are the functional groups in the structure of ferulic acid [39]. The OH functional group is the fundamental part of most phenolic compounds. The OH and the double bond in the benzene ring contribute to the antioxidant activity. In phenolic acids, the number and position of the OH group are associated with the ability to scavenge free radicals [40-42].

The HPLC analysis confirmed ferulic acid in IPR. The chromatogram (Fig. 3) showed an intense peak at retention time (RT) = 2.144 min, similar to standard

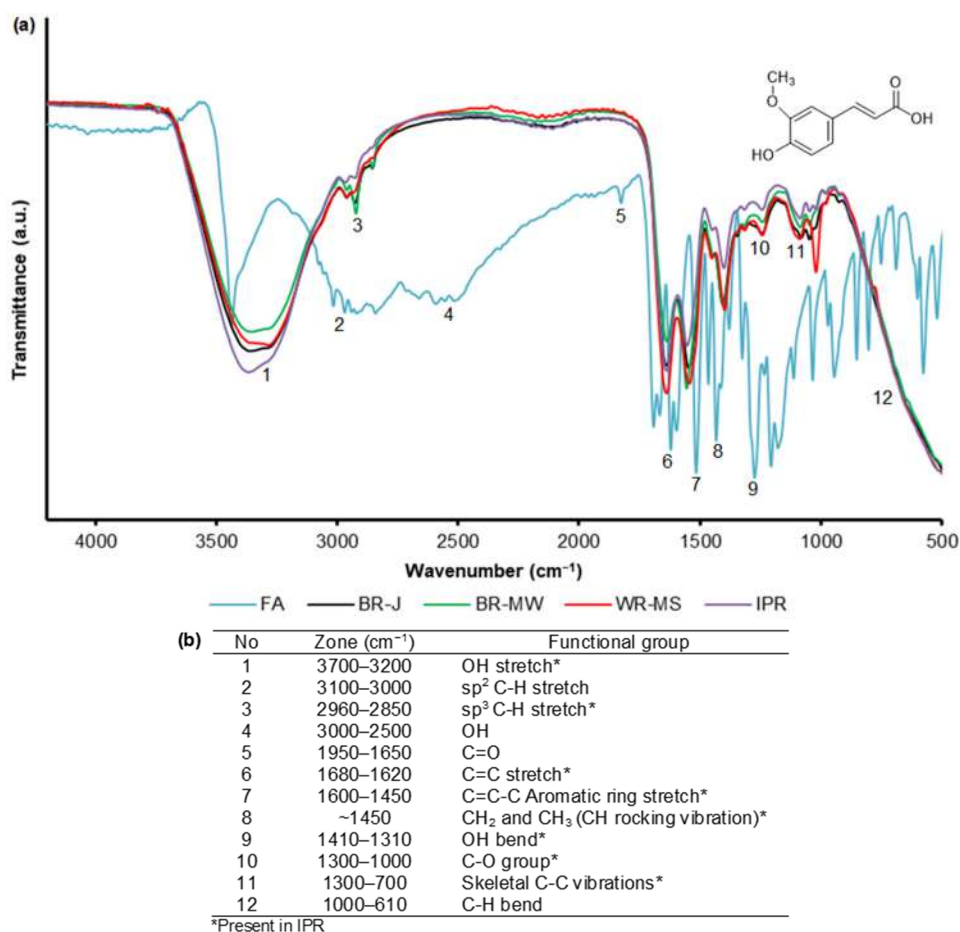


**Fig 2.** Functional group identification by FTIR. (a) FTIR spectra, (b) Table of functional group prediction. FA: Ferulic acid, BR-J: *Jeliteng* black rice, BR-MW: *Mentik wangi* black rice, WR-MS: *Mentik susu* white rice, IPR: Indonesian purple rice

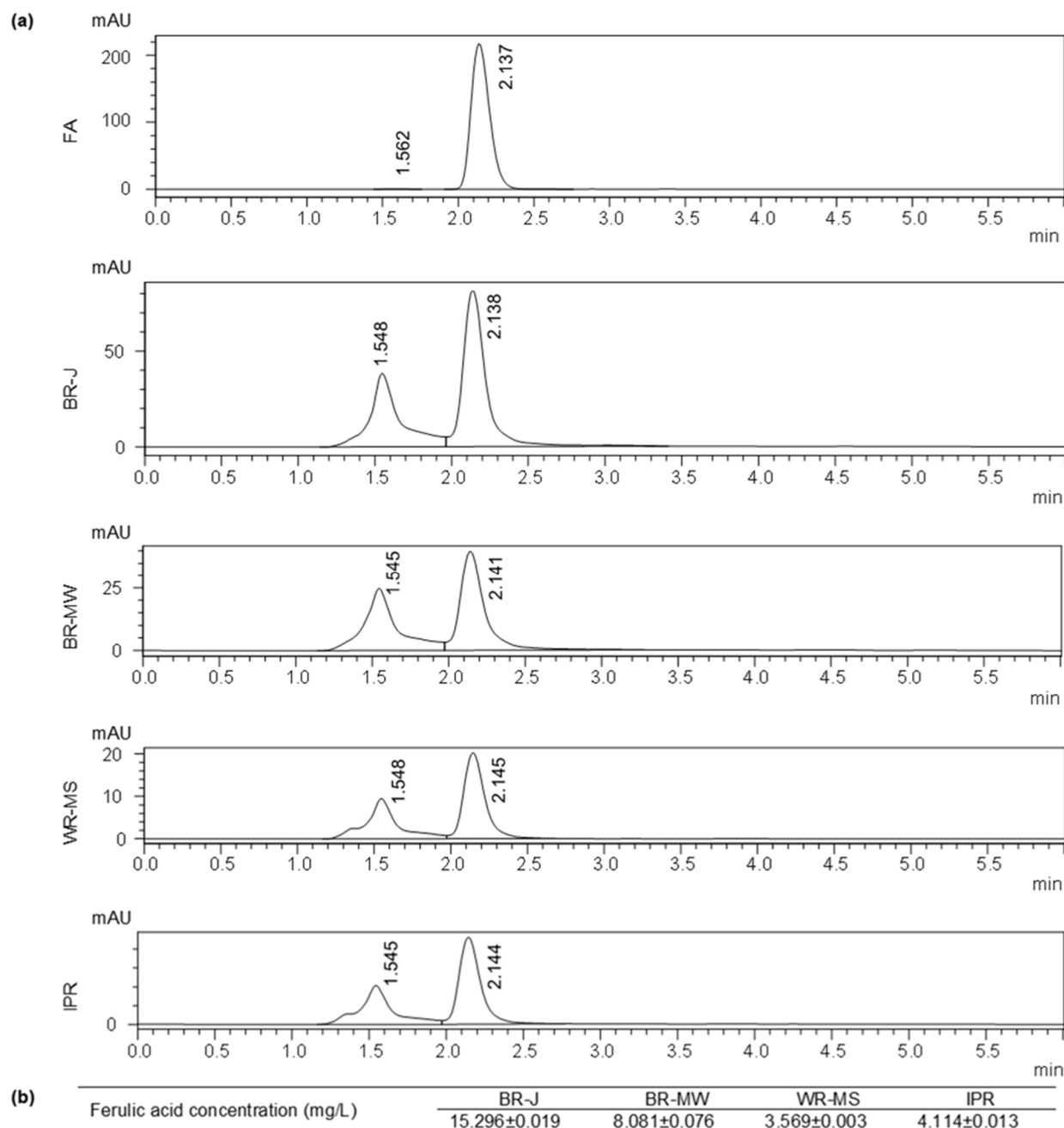


**Fig 3.** Identification and determination of ferulic acid concentration in IPR. (a) HPLC chromatogram. (b) Table of ferulic acid concentration. FA: Ferulic acid, BR-J: *Jeliteng* black rice, BR-MW: *Mentik wangi* black rice, WR-MS: *Mentik susu* white rice, IPR: Indonesian purple rice

ferulic acid (RT = 2.137 min). Therefore, it revealed the presence of ferulic acid in IPR. Other rice samples also showed the presence of ferulic acid with similar RT. In the chromatogram, we found another peak that appears before the RT of ferulic acid, indicating the presence of another compound in the extract. Because the extract was

not purified, thus there are still other phenolic acids. The peak is predicted to be *p*-coumaric acid, the second major phenolic acid after ferulic acid in rice, Fig. 4.

Ferulic acid is found at 56–77% of the total phenolic acid in rice, followed by *p*-coumaric acid at 8–24% [42]. Some studies reported similar chromatogram

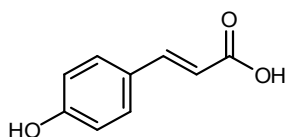


Fig 4. The structure of *p*-coumaric acid

results, in which *p*-coumaric acid appears first and adjacent to the ferulic acid peak. Among these are phenolic acid separations in potatoes, coffee, thymus, and podded bean [43-46].

The concentration of ferulic acid in IPR was determined based on a standard calibration curve. The level of ferulic acid in IPR was higher than WR-MS but lower than BR-J and BR-MW. Ferulic acid concentration positively correlated with total phenolic content (Pearson correlation;  $P < 0.05$ ).

### Reducing Power

Reducing power of IPR by the FRAP method used potassium ferricyanide as an oxidant. Potassium ferricyanide ( $K_3[Fe(CN)_6]$ ) is a ferric salt containing the octahedrally coordinated ion  $[Fe(CN)_6]^{3-}$ , which is frequently used as an oxidant in electron chain reactions [47-48]. The antioxidant compounds react with potassium ferricyanide to form potassium ferrocyanide [49]. The presence of reductants, which exert antioxidant action by breaking free radical chains by donating a hydrogen atom, is commonly associated with the presence of reducing power [50].

Fig. 5 shows the graph of correlation between the sample concentrations (0–10  $\mu\text{g/mL}$ ) and reducing

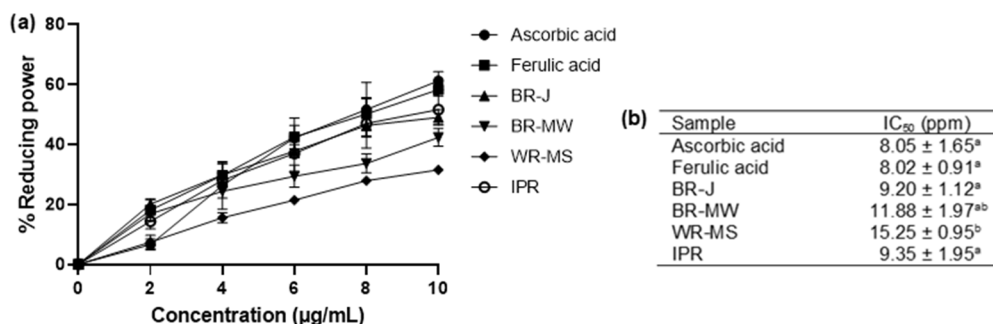


Fig 5. Reducing power of IPR. (a) Percentage of reducing power, (b)  $IC_{50}$  value, the different letters indicated significant differences (Tukey's HSD;  $P < 0.05$ ). BR-J: *Jeliteng* black rice, BR-MW: *Mentik wangi* black rice, WR-MS: *Mentik susu* white rice, IPR: Indonesian purple rice

power, and table of  $IC_{50}$  values. The higher the sample concentration, the greater the increase in reducing power (Pearson correlation;  $P < 0.05$ ). According to the  $IC_{50}$  values, IPR had the same reducing power as BR-J. The reducing power of IPR was comparable to ascorbic and ferulic acid.

The reducing power of IPR is classified as potent because the  $IC_{50}$  value is less than 50 ppm [51]. The activity level is equal to ascorbic acid and standard ferulic acid, which are powerful antioxidants [52-54]. By the FRAP method, the mechanism of IPR ferulic acid in scavenging free radicals is predicted by reducing  $Fe^{3+}$  ions to  $Fe^{2+}$ , as seen in Fig. 6. Ferulic acid acts as a chelating of metal ions such as  $Cu^{2+}$  or  $Fe^{2+}$  [55]. The phenolic rings also support strong antioxidant properties, which stabilize and delocalize unpaired electrons [15,42].

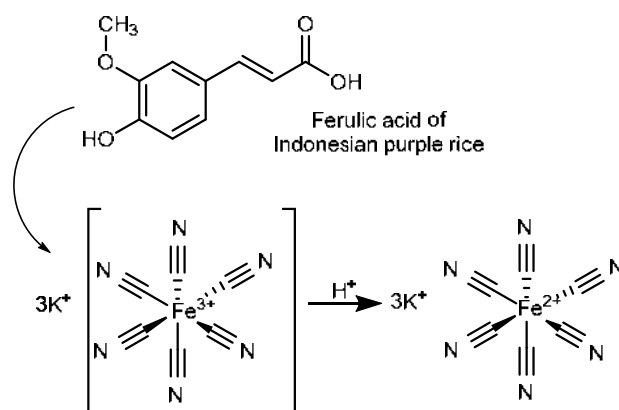


Fig 6. The prediction of IPR ferulic acid mechanism in scavenging free radicals by reducing  $Fe^{3+}$  to  $Fe^{2+}$



## Anti-aging Activity

The ability to inhibit collagenase and tyrosinase was used to assess anti-aging activity. The activities were compared to positive controls, ascorbic acid and kojic acid as the collagenase and tyrosinase inhibitors, respectively [8,11,56]. The activity was also compared to ferulic acid. Fig. 7 shows that the concentrations of samples (0–100  $\mu\text{g/mL}$ ) positively correlated with the anti-collagenase and anti-tyrosinase activity (Pearson correlation;  $P < 0.05$ ). The IPR demonstrated the same level of collagenase inhibition as BR-J. The inhibitory power was also the same as ferulic acid but lower than ascorbic acid. In the tyrosinase inhibition, IPR was equal to BR-J. The strength was also the same as kojic acid but lower than ferulic acid. This demonstrates that IPR has a more efficient inhibitory activity than BR-J due to its lower FA concentration while producing the same activity. The IPR is more potent as a tyrosinase inhibitor than collagenase, as indicated by activity that is comparable to the positive control of the tyrosinase inhibitor, kojic acid, but lower than the positive control of the collagenase inhibitor, ascorbic acid.

For enzyme inhibitor screening, the  $\text{IC}_{50}$  value could be compared to a positive control [56]. According to the  $\text{IC}_{50}$  value, IPR showed a weaker inhibition of collagenase than ascorbic acid but the same as ferulic acid, while the tyrosinase inhibition by IPR was as strong as kojic acid. This finding indicated that IPR has high anti-tyrosinase and moderate anti-collagenase activities. The tyrosinase inhibition was supported by ferulic acid in IPR with metal ions chelating properties. Generally, copper-chelating aromatic compounds inhibit tyrosinase by mimicking the substrate of tyrosinase [56]. The interaction of hydroxyl groups and benzene rings in ferulic acid with collagenase may cause a conformational change that inhibits collagenase [11].

Compounds with antioxidant activity could prevent aging by inhibiting the activities of ROS and aging enzymes [31]. The ROS activates the MAPK pathway, which increases microphthalmia-associated transcription factor (MITF) expression and thus tyrosinase-regulated melanogenesis [5]. The MAPK activation also induces activator protein 1 (AP-1) and nuclear factor kappa-B (NF- $\kappa$ B), which upregulate matrix

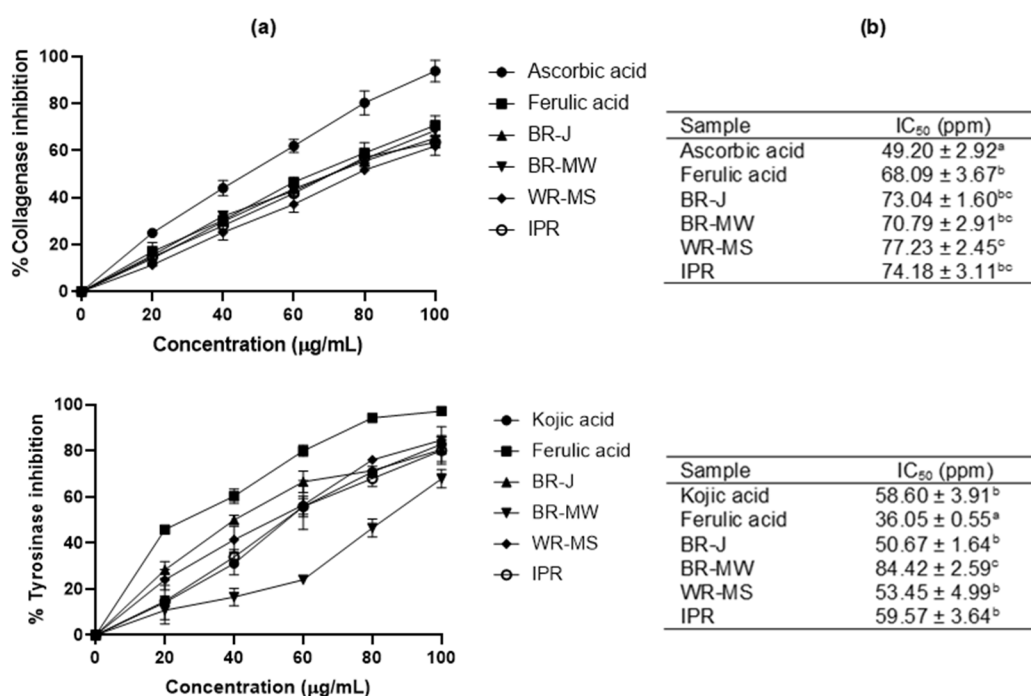


**Fig 7.** The anti-aging activity of IPR. (a) Percentage of inhibition. (b)  $\text{IC}_{50}$  value. The difference letter in the table indicated significant differences among samples (Tukey's HSD;  $P < 0.05$ ). BR-J: *Jeliteng* black rice, BR-MW: *Mentik wangi* black rice, WR-MS: *Mentik susu* white rice, IPR: Indonesian purple rice

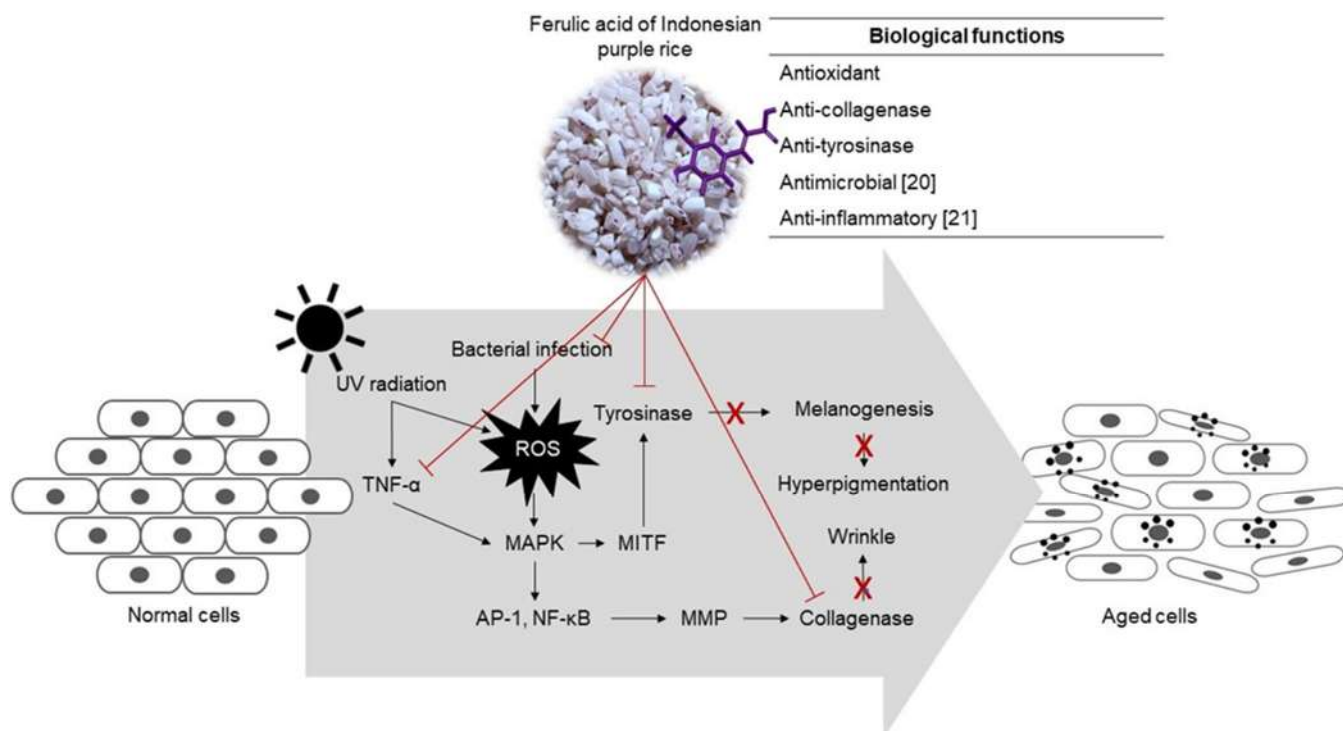


**Fig 8.** The anti-aging mechanism of IPR ferulic acid via the MAPK pathway. ROS: reactive oxygen species, MAPK: mitogen-activated protein kinase, AP-1: activator protein 1, NF- $\kappa$ B: nuclear factor kappa-B, MMP: matrix metalloproteinase, MIF: microphthalmia-associated transcription factor, TNF- $\alpha$ : tumor necrosis factor-alpha.  $\rightarrow$ : stimulate,  $\dashv$ : inhibit,  $\times$ : not stimulate

metalloproteinases (MMPs), one of which is collagenase, which degrades collagen fibers and causes wrinkles [2].

Ferulic acid of IPR demonstrates an anti-aging mechanism through the MAPK pathway by inhibiting collagenase and tyrosinase activity, as seen in Fig. 8. In the previous study, ferulic acid of IPR acts as an antimicrobial on *Salmonella typhimurium* and *Listeria monocytogenes* [20]. Bacterial infection induces ROS production [57]. Moreover, ferulic acid also acts as an anti-inflammatory by inhibiting tumor necrosis factor-alpha (TNF- $\alpha$ ) signaling [21]. The TNF- $\alpha$  stimulates MAPK pathway activation [58]. By controlling the MAPK pathway, the aging process can be suppressed [59]. In this study, we found that ferulic acid of IPR inhibited collagenase and tyrosinase activity; thus, wrinkle formation and hyperpigmentation could be prevented.

The IPR has a lower ferulic acid concentration than BR-J and BR-MW. Interestingly, IPR could provide excellent biological activity, which could be a unique

characteristic of IPR, in which synergistic activity between ferulic acid and other compounds results in high activity. The synergistic effects of plant compounds increase their activity [60]. The IPR has higher reducing power than both parentals, higher anti-tyrosinase activity than BR-MW, and higher anti-collagenase activity than WR-MS. These results suggest that IPR has improved properties, resulting in higher bioactivity than its parentals. However, the IPR activity is not as great as ferulic acid, a pure compound. Ferulic acid is still present in IPR as extracts; thus, the presence of other compounds contributes to the resulting activity.

To the best of our knowledge, the exploration of ferulic acid in IPR and its biological function as anti-aging is reported here for the first time. The IPR offers excellent antioxidant and anti-aging activities with high nutritional content. These findings supported the potential of IPR as a promising active compound of nature-based skin anti-aging products.

## ■ CONCLUSION

The current study revealed the IPR nutritional value, phytochemical profile, and anti-aging potential of ferulic acid content. The IPR has a low lipid content, a high level of some amino acids including L-histidine, L-phenylalanine, L-threonine, L-arginine, and L-tyrosine, and some phytochemicals such as phenolics, flavonoids, tannins, anthocyanins, leucoanthocyanidins, and glycosides. The total phenolics content of IPR is related to its ferulic acid level, which is lower than black rice. Nevertheless, IPR demonstrated potent reducing power, anti-collagenase, and anti-tyrosinase activity. The combination of IPR's nutritional content and ferulic acid properties as an antioxidant, anti-collagenase, and anti-tyrosinase showed the potential of IPR as an anti-aging. Further research using an *in vivo* approach is required to confirm the findings of this study, and then IPR can be developed as a natural ingredient in skin care formulations.

## ■ ACKNOWLEDGMENTS

We acknowledge The Indonesia Endowment Fund for Education (*Lembaga Pengelola Dana Pendidikan*, LPDP), Ministry of Finance, the Republic of Indonesia for funding this research, RISPRO-PRN-LPDP-PAJALE research for the laboratory facilities, and members of the SMONAGENES Research Center, Brawijaya University, for the discussions.

## ■ AUTHOR CONTRIBUTIONS

Ernanin Dyah Wijayanti contributes to conceptualization, methodology, data collection, sample analysis, validation, data curation, writing – the initial draft. Anna Safitri contributes to methodology, student supervision, writing – revisions, project management. Dian Siswanto contributes to methodology, student supervision, writing – revisions. Fatchiyah contributes to conceptualization, methodology, student supervision, project leadership; project management; and funding acquisition.

## ■ REFERENCES

- [1] Girsang, E., Ginting, C.N., Lister, I.N.E., Widowati, W., Wibowo, S.H.B., Perdana, F.S., and Rizal, R., 2019, *In silico* analysis of phytochemical compound found in snake fruit (*Salacca zalacca*) peel as anti-aging agent, *Thai J. Pharm. Sci.*, 43 (2), 105–109.
- [2] Kim, M., and Park, H.J., 2016, "Molecular Mechanisms of Skin Aging and Rejuvenation" in *Molecular Mechanisms of the Aging Process and Rejuvenation*, Eds. Shiomi, N., IntechOpen, Rijeka, 57–76.
- [3] Campa, M., and Baron, E., 2018, Anti-aging effects of select botanicals: Scientific evidence and current trends, *Cosmetics*, 5 (3), 54.
- [4] Mukherjee, P.K., Maity, N., Nema, N.K., and Sarkar, B.K., 2011, Bioactive compounds from natural resources against skin aging, *Phytomedicine*, 19 (1), 64–73.
- [5] Shin, S.Y., Ko, J.Y., Kim, M.J., Song, N., and Park, K.M., 2021, Morin induces melanogenesis via activation of MAPK signaling pathways in B16F10 mouse melanoma cells, *Molecules*, 26 (8), 2150.
- [6] Apraj, V.D., and Pandita, N.S., 2016, Evaluation of skin anti-aging potential of *Citrus reticulata* Blanco peel, *Pharmacogn. Res.*, 8 (3), 160–168.
- [7] El-Nashar, H.A.S., El-labbad, E.M., Al-Azzawi, M.A., and Ashmawy, N.S., 2022, A new xanthone glycoside from *Mangifera indica* L.: Physicochemical properties and *in vitro* anti-skin aging activities, *Molecules*, 27 (9), 2609.
- [8] Hashemi, S.M., and Emami, S., 2015, Kojic acid-derived tyrosinase inhibitors: Synthesis and bioactivity, *Pharm. Biomed. Res.*, 1 (1), 1–17.
- [9] Tu, P.T.B., and Tawata, S., 2015, Anti-oxidant, anti-aging, and anti-melanogenic properties of the essential oils from two varieties of *Alpinia zerumbet*, *Molecules*, 20 (9), 16723–16740.
- [10] Ganceviciene, R., Liakou, A.I., Theodoridis, A., Makrantonaki, E., and Zouboulis, C.C., 2012, Skin anti-aging strategies, *Derm.-Endocrinol.*, 4 (3), 308–319.
- [11] Vijayakumar, R., Abd Gani, S.S., and Mokhtar, N.F., 2017, Anti-elastase, anti-collagenase and antimicrobial activities of the underutilized red pitaya peel: An *in vitro* study for anti-aging

- applications, *Asian J. Pharm. Clin. Res.*, 10 (8), 251–255.
- [12] Das, S., and Wong, A.B.H., 2020, Stabilization of ferulic acid in topical gel formulation via nanoencapsulation and pH optimization, *Sci. Rep.*, 10 (1), 12288.
- [13] de Paiva, L.B., Goldbeck, R., dos Santos, W.D., and Squina, F.M., 2013, Ferulic acid and derivatives: Molecules with potential application in the pharmaceutical field, *Braz. J. Pharm. Sci.*, 49 (3), 395–411.
- [14] Kumar, N., and Pruthi, V., 2014, Potential applications of ferulic acid from natural sources, *Biotechnol. Rep.*, 4, 86–93.
- [15] Alam, M.A., 2019, Anti-hypertensive effect of cereal antioxidant ferulic acid and its mechanism of action, *Front. Nutr.*, 6, 121.
- [16] Saha, S., 2016, Black rice: The new age super food (An extensive review), *AJRFANS*, 16 (1), 51–55.
- [17] Wijayanti, E.D., Safitri, A., Siswanto, D., and Fatchiyah, F., 2022, Genomic profile of OsCOMT in Indonesian purple rice, *Biotropika*, 10 (3), 185–190.
- [18] Sing, S.X., Lee, H.H., Wong, S.C., Bong, C.F.J., and Yiu, P.H., 2015, Ferulic acid, gamma oryzanol and GABA content in whole grain rice and their variation with bran colour, *Emir. J. Food Agric.*, 27 (9), 706–711.
- [19] Zhang, H., Shao, Y., Bao, J., and Beta, T., 2015, Phenolic compounds and antioxidant properties of breeding lines between the white and black rice, *Food Chem.*, 172, 630–639.
- [20] Wijayanti, E.D., Safitri, A., Siswanto, D., Triprisila, L.F., and Fatchiyah, F., 2021, Antimicrobial activity of ferulic acid in Indonesian purple rice through toll-like receptor signaling, *Makara J. Sci.*, 25 (4), 247–257.
- [21] Wijayanti, E.D., Safitri, A., Siswanto, D., and Fatchiyah, F., 2022, Virtual prediction of purple rice ferulic acid as anti-inflammatory of TNF- $\alpha$  signaling, *Berkala Penelitian Hayati*, 27 (2), 59–66.
- [22] Fatchiyah, F., Sari, D.R.T., Safitri, A., and Cairns, J.R.K., 2020, Phytochemical compound and nutritional value in black rice from Java Island, Indonesia, *Syst. Rev. Pharm.*, 11 (7), 414–421.
- [23] Godghate, A., Sawant, R., and Sutar, A., 2012, Phytochemical analysis of ethanolic extract of roots of *Carrisa carandus* Linn, *Rasayan J. Chem.*, 5 (4), 456–459.
- [24] Maimulyanti, A., Prihadi, A.R., and Safrudin, I., 2016, Chemical composition, phytochemical screening and antioxidant activity of *Acmella uliginosa* (Sw.) Cass leaves, *Indones. J. Chem.*, 16 (2), 162–174.
- [25] Stavova, E., Porizka, J., Stursa, V., Enev, V., and Divis, P., 2017, Extraction of ferulic acid from wheat bran through alkaline hydrolysis, *MendelNet*, 24, 574–579.
- [26] Baba, S.A., and Malik, S.A., 2015, Determination of total phenolic and flavonoid content, antimicrobial and antioxidant activity of a root extract of *Arisaema jacquemontii* Blume, *J. Taibah Univ. Sci.*, 9 (4), 449–454.
- [27] Hapsari, A.M., Masfria, M., and Dalimunthe, A., 2018, Pengujian kandungan total fenol ekstrak etanol tempuyung (*Shoncus arvensis* L.), *Talenta Conf. Ser.: Trop. Med.*, 1 (1), 284–290.
- [28] Agustin, A.T., Safitri, A., and Fatchiyah, F., 2021, Java red rice (*Oryza sativa* L.) nutritional value and anthocyanin profiles and its potential role as antioxidant and anti-diabetic, *Indones. J. Chem.*, 21 (4), 968–978.
- [29] Widowati, W., Fauziah, N., Herdiman, H., Afni, M., Afifah, E., Kusuma, H.S.W., Nufus, H., Arumwardana, S., and Rihibiha, D.D., 2016, Antioxidant and anti aging assays of *Oryza sativa* extracts, vanillin and coumaric acid, *J. Nat. Rem.*, 16 (3), 88–99.
- [30] Kim, K.Y., Lee, E.J., Whang, W.K., and Park, C.H., 2019, *In vitro* and *in vivo* anti-aging effects of compounds isolated from *Artemisia iwayomogi*, *J. Anal. Sci. Technol.*, 10 (1), 35.
- [31] Girsang, E., Lister, I.N.E., Ginting, C.N., Bethasari, M., Amalia, A., and Widowati, W., 2020, Comparison of antiaging and antioxidant activities

- of protocatechuic and ferulic acids, *MCBS*, 4 (2), 68–75.
- [32] Dwiwibangga, Y., Safitri, A., and Fatchiyah, F., 2022, Profiling of phytochemical compounds of East Java red rice bran has the high-value biological activities as antioxidant and antidiabetic, *Indones. J. Chem.*, 22 (5), 1304–1320.
- [33] Spencer, S.J., D'Angelo, H., Soch, A., Watkins, L.R., Maier, S.F., and Barrientos, R.M., 2017, High-fat diet and aging interact to produce neuroinflammation and impair hippocampal- and amygdalar-dependent memory, *Neurobiol. Aging*, 58, 88–101.
- [34] Tucker, L.A., 2019, Milk fat intake and telomere length in U.S. women and men: The role of the milk fat fraction, *Oxid. Med. Cell. Longevity*, 2019, 1574021.
- [35] Yin, Z., Raj, D.D., Schaafsma, W., van der Heijden, R.A., Kooistra, S.M., Reijne, A.C., Zhang, X., Moser, J., Brouwer, N., Heeringa, P., Yi, C.X., van Dijk, G., Laman, J.D., Boddeke, E.W.G.M., and Eggen, B.J.L., 2018, Low-fat diet with caloric restriction reduces white matter microglia activation during aging, *Front. Mol. Neurosci.*, 11, 65.
- [36] Bojarska, J., 2020, Amino acids and short peptides as anti-aging "superfood", *Int. J. Nutr. Sci.*, 5 (1), 1039.
- [37] Jana, B.R., and Idris, M., 2018, Anti-aging amino acids in *Euryale ferox* (Salisb.): A review, *Adv. Plants Agric. Res.*, 8 (1), 39–43.
- [38] Park, J., Jung, H., Jang, B., Song, H., Han, I., and Oh, E., 2020, D-tyrosine adds an anti-melanogenic effect to cosmetic peptides, *Sci. Rep.*, 10 (1), 262.
- [39] Sibhatu, H.K., Jabasingh, S.A., Yimam, A., and Ahmed, S., 2021, Ferulic acid production from brewery spent grains, an agro-industrial waste, *LWT-Food Sci. Technol.*, 135, 110009.
- [40] Adeyemo, O.A., Osibote, E., Adedugba, A., Bhadmus, O.A., Adeosun, A.A., and Allison, M.O., 2018, Antioxidant activity, total phenolic contents and functional group identification of leaf extracts among lemongrass (*Cymbopogon citratus*) accessions, *NISEB J.*, 18 (2), 83–91.
- [41] Chen, J., Yang, J., Ma, L., Li, J., Shahzad, N., and Kim, C.K., 2020, Structure-antioxidant activity relationship of methoxy, phenolic hydroxyl, and carboxylic acid groups of phenolic acids, *Sci. Rep.*, 10 (1), 2611.
- [42] Goufo, P., and Trindade, H., 2014, Rice antioxidants: Phenolic acids, flavonoids, anthocyanins, proanthocyanidins, tocopherols, tocotrienols,  $\gamma$ -oryzanol, and phytic acid, *Food Sci. Nutr.*, 2 (2), 75–104.
- [43] Doncea, S.M., Stoica, R., Ion, M.R., Trandafir, I., and Pavel, V., 2010, An HPLC method for identification and separation of some phenolic acids in the coffee, *Petroleum - Gas University of Ploiesti Bulletin, Technical Series*, 62 (3A), 143–148.
- [44] Jabri-Karoui, I., Bettaieb, I., Msaada, K., Hammami, M., and Marzouk, B., 2012, Research on the phenolic compounds and antioxidant activities of Tunisian *Thymus capitatus*, *J. Funct. Foods*, 4 (3), 661–669.
- [45] Jin, C.Y., Liu, H., Xu, D., Zeng, F.K., Zhao, Y.C., Zhang, H., and Liu, G., 2018, Glycoalkaloids and phenolic compounds in three commercial potato cultivars grown in Hebei, China, *Food Sci. Hum. Wellness*, 7 (2), 156–162.
- [46] Weidner, S., Król, A., Karamać, M., and Amarowicz, R., 2018, Phenolic compounds and the antioxidant properties in seeds of green- and yellow-podded bean (*Phaseolus vulgaris* L.) varieties, *CyTA-J. Food*, 16 (1), 373–380.
- [47] Sadeer, N.B., Montesano, D., Albrizio, S., Zengin, G., and Mahomoodally, M.F., 2020, The versatility of antioxidant assays in food science and safety-chemistry, applications, strengths, and limitations, *Antioxidants*, 9 (8), 709.
- [48] Kose, L.P., Bingol, Z., Kaya, R., Goren, A.C., Akincioglu, H., Durmaz, L., Koksall, E., Alwasel, S.H., and Gülçin, I., 2020, Anticholinergic and antioxidant activities of avocado (*Folium perseae*) leaves – phytochemical content by LC-MS/MS analysis, *Int. J. Food Prop.*, 23 (1), 878–893.
- [49] Xiao, F., Xu, T., Lu, B., and Liu, R., 2020, Guidelines for antioxidant assays for food components, *Food Front.*, 1 (1), 60–69.
- [50] Rahman, M., Islam, B., Biswas, M., and Khurshid Alam, A.H.M., 2015, *In vitro* antioxidant and free

- radical scavenging activity of different parts of *Tabebuia pallida* growing in Bangladesh, *BMC Res. Notes*, 8 (1), 621.
- [51] Syakri, S., Syahrana, N.A., Ismail, A., Tahir, K.A., and Masri, A., 2021, A review: Testing antioxidant activity on kawista plants (*Limonia acidissima* L.) in Indonesia, *Open Access Maced. J. Med. Sci.*, 9 (F), 281–287.
- [52] Bilska, K., Wojciechowska, N., Alipour, S., and Kalemba, E.M., 2019, Ascorbic acid: The little-known antioxidant in woody plants, *Antioxidants*, 8 (12), 645.
- [53] de Oliveira Silva, E., and Batista, R., 2017, Ferulic acid and naturally occurring compounds bearing a feruloyl moiety: A review on their structures, occurrence, and potential health benefits, *Compr. Rev. Food Sci. Food Saf.*, 16 (4), 580–616.
- [54] Zayova, E., Stancheva, I., Geneva, M., Petrova, M., and Dimitrova, L., 2013, Antioxidant activity of *in vitro* propagated *Stevia rebaudiana* Bertoni plants of different origins, *Turk. J. Biol.*, 37 (1), 106–113.
- [55] Zduńska, K., Dana, A., Kolodziejczak, A., and Rotsztejn, H., 2018, Antioxidant properties of ferulic acid and its possible application, *Skin Pharmacol. Physiol.*, 31 (6), 332–336.
- [56] Zolghadri, S., Bahrami, A., Hassan Khan, M.T., Munoz-Munoz, J., Garcia-Molina, F., Garcia-Canovas, F., and Saboury, A.A., 2019, A comprehensive review on tyrosinase inhibitors, *J. Enzyme Inhib. Med. Chem.*, 34 (1), 279–309.
- [57] Strickertsson, J.A.B., Desler, C., and Rasmussen, L.J., 2014, Impact of bacterial infections on aging and cancer: Impairment of DNA repair and mitochondrial function of host cells, *Exp. Gerontol.*, 56, 164–174.
- [58] Pokharel, S.M., Chiok, K., Shil, N.K., Mohanty, I., and Bose, S., 2021, Tumor necrosis factor-alpha utilizes MAPK/NFκB pathways to induce cholesterol-25 hydroxylase for amplifying pro-inflammatory response via 25-hydroxycholesterol-integrin-FAK pathway, *PLoS One*, 16 (9), e0257576.
- [59] Lei, L., Zeng, Q., Lu, J., Ding, S., Xia, F., Kang, J., Tan, L., Gao, L., Kang, L., Cao, K., Zhou, J., Xiao, R., Chen, J., and Huang, J., 2017, MALAT1 participates in ultraviolet B-induced photo-aging via regulation of the ERK/MAPK signaling pathway, *Mol. Med. Rep.*, 15 (6), 3977–3982.
- [60] Metsämuuronen, S., and Sirén, H., 2019, Bioactive phenolic compounds, metabolism, and properties: A review on valuable chemical compounds in Scots pine and Norway spruce, *Phytochem. Rev.*, 18 (3), 623–664.

## Kinetics Study of Yttrium Leaching from Zircon Tailings Using Sulfuric Acid

Harry Supriadi<sup>1</sup>, Iga Trisnawati<sup>2</sup>, Tri Handini<sup>1</sup>, Sri Rinanti Susilowati<sup>1</sup>,  
Vincent Sutresno Hadi Sujoto<sup>3,4</sup>, Panut Mulyono<sup>3,4</sup>, and Himawan Tri Bayu Murti Petrus<sup>3,4\*</sup>

<sup>1</sup>Research Center for Mining Technology, National Research and Innovation Agency, Co-Working Space Babarsari, Babarsari St., Mailbox 6101 ykbb, Yogyakarta 55281, Indonesia

<sup>2</sup>Polytechnic Institute of Nuclear Technology, National Research and Innovation Agency, Babarsari St., Mailbox 6101 ykbb, Yogyakarta 55281, Indonesia

<sup>3</sup>Department of Chemical Engineering, Faculty of Engineering, Universitas Gadjah Mada, Grafika St. No. 2, Yogyakarta 55281, Indonesia

<sup>4</sup>Unconventional Georesources Research Center, Faculty of Engineering, Universitas Gadjah Mada, Grafika St. No. 2, Yogyakarta 55281, Indonesia

\* **Corresponding author:**

email: bayupetrus@ugm.ac.id

Received: December 9, 2022

Accepted: February 10, 2023

DOI: 10.22146/ijc.79966

**Abstract:** From the analysis of zircon tailings using X-Ray Fluorescence (XRF), Yttrium is a rare earth element (REE) with the highest concentration compared to other REEs. The purpose of this study is to determine the best kinetic model for describing how sulfuric acid extracts Yttrium from zircon tailings. Leaching temperatures of 200, 250, and 300 °C were used to determine the kinetics. Samples were obtained at 0, 20, 40, 60, 80, 100, and 120 min for each temperature. This study discovered that the chemical reaction model's kinetics are the most closely related to those of the leaching process. The evaluation of the model utilizing the coefficient of determination ( $R^2$ ) on the relationship between each model and time lends support to this conclusion. The activation energy ( $E_a$ ) of the leaching process is determined by the Arrhenius plot between  $\ln k$  and  $1/T$ . In the Yttrium leaching procedure, the  $E_a$  value is 14.42 kJ/mol. The chemical reaction model was in charge of the leaching process, according to the  $E_a$  value. The premise of the chemical reaction model is that chemical reactions regulate the rate of the reaction.

**Keywords:** zircon tailings; leaching; rare earth elements; kinetics; Yttrium

### ■ INTRODUCTION

Rare earth elements (REEs) are strategic materials that are hard to come by and have a wide range of applications. The usage of REE, either singly or in combination, is on the rise at the moment. This is due to the fact that REE has strong mechanical properties, a high melting point, and a sizable cross-section for neutron absorption. Because of this, REE is widely used in many technological domains [1]. Fifteen elements with atomic numbers ranging from 57 to 71 are referred to be REEs or lanthanides. Due to their comparable chemical and physical characteristics, two more elements, scandium and yttrium, are also regarded as belonging to the same group [2]. REEs are derived from monazite and xenotime,

which are found in zircon tailings. Consequently, processing the tailings is necessary to increase their economic value [3].

As "essential" minerals for contemporary industrial uses, REE is currently in the limelight for raw materials policy. Numerous combinations of REEs are utilized in a variety of sectors, including phosphorus (Eu, Y, Nd, Tb, Er, Gd), metal alloys (La, Ce, Pr, Nd, Y), catalysts (La, Ce), and magnets, which all have a high demand (Nd, Pr, Dy, Sm). Prior to production, REE-containing minerals must undergo downstream processing and chemical separation. High-purity REE oxides can be purchased through this technique and sold to the manufacturing sector [4].

Known as industrial vitamins, REEs are a unique non-renewable resource. Some of its physicochemical characteristics have significant strategic implications and are widely applicable in the sectors of permanent magnet materials, petroleum, chemical, metallurgy, textile, and ceramics. The demand for REE is rising yearly in a number of nations due to the rapid development of numerous advanced and novel technologies [5]. The Department of Energy (DOE) has classified some of them as essential components for the clean energy economy. From 2015 to 2025, Ce and La were discovered to be near-critical, while five REEs, i.e., Dy, Tb, Eu, Nd, and Y, were revealed to be critical. China currently controls 95% of the global REE production market, making up the majority of the REE market globally. In 2017, there was no mining of REE in the United States, and from 2013 to 2016, China supplied 78% of imports. The Chinese government's export policies have a significant impact on the price volatility of REEs traded internationally [6]. Rare earth markets have recently been migrating away from older, primarily Light REE-using applications, like catalysts, and toward newer, Heavy REE-using applications, including permanent magnets used in wind turbines and hybrid/electric vehicles [7].

Yttrium is one of the most important REEs, used in a wide range of items like fluorescent lighting, cubic zirconia jewelry, fighter jet engines, industrial, medical, and graphic technology, as well as electronic parts for missile defense systems. The cathode ray tubes (CRTs) from televisions and computers are one of the most important secondary sources of yttrium. Even though LCD and LED panels have completely replaced outmoded equipment, there is still a tremendous amount of human waste that needs to be dealt with [8].

Yttrium is used extensively in a variety of fields, including metallurgy, electronics, ceramics, laser technology, and fluorescent materials. Yttrium (Y) and lanthanides always coexist in rare earth minerals due to their similar chemical characteristics, especially in the ion-adsorption type rare earth deposits [9]. One of the most significant REEs, Y, is also the second most common REE in the crust of the earth after cerium. Because it has the highest thermodynamic affinity for oxygen, Y has

been employed in phosphors, ceramics, and metallurgy. Many nations and regions, including the United States, China, Japan, and the European Union, have designated Y as a critical metal [10].

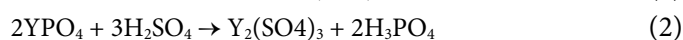
Chemistry's field of "reaction kinetics" is concerned with the rate of reactions and the variables that influence that speed. The change in the concentration of the reactants or reaction products over a given period of time is used to express the reaction rate. An essential component of a chemical process that helps explain how the process works are the study of reaction kinetics. The method of managing the reaction rate, kinetic parameters (reaction rate constants or diffusion coefficients), activation energies, and equations or kinetic models can all be known from the findings of the study of reaction kinetics. The process scale-up steps can be carried out on an industrial scale based on the findings of kinetic studies. For constructing both chemical process but also for leaching processes, kinetic examinations of the reactions are crucial. The majority of leaching procedures include interactions between liquid and solid phases [11].

The pyrometallurgical and hydrometallurgical approaches are the two basic techniques for recycling REE. The hydrometallurgical techniques now employed to recover REE include dense medium centrifugation, flotation recovery, precipitation, selective Y dissolution by strong acidic and basic solutions, and solvent extraction. Because so many different metals are present, the pyro-metallurgical approach frequently takes a lot of energy, and it is difficult to isolate and recover specific metals. The pyrometallurgical recovery of Y includes feed preparation, blending and pelletizing, reduction, incineration, melting, and casting. In addition to oxidized REEs, volatile organic compounds (VOCs), furan gasses, and dioxins, which all complicate cleanup and have adverse effects on the environment, this multi-step process needs a lot of energy and necessitates a high temperature. In comparison to pyrometallurgical methods, hydrometallurgy operations are significantly more profitable because of their low operating costs, potential for leachate recovery, and decreased air pollution levels [12].



Leaching is one of the most effective methods in extractive metallurgy for removing REE from their ores by dissolving them in an appropriate leaching agent and then further processing them using both conventional and cutting-edge methods [13]. Leaching is frequently utilized in a variety of sectors, particularly the mining sector. The pretreatment of the solid particles to be extracted depends on the characteristics of the solvent used, the distribution of the solvent in the solid, and the nature of the solid particles [14]. The process of separating REE by the acid method can be carried out with sulfuric acid, nitric acid, and perchloric acid. However, sulfuric acid is commonly used because the price is relatively low, and the process is simpler than using nitric acid or perchloric acid [15].

Recovery of REE like Y from actual wastes has already been accomplished using hydrometallurgical techniques like acid leaching. For leaching agents, including sulfuric acid, nitric acid (HNO<sub>3</sub>), and hydrochloric acid (HCl), different extraction efficiencies have been recorded (H<sub>2</sub>SO<sub>4</sub>). Hydrogen peroxide, cyanide, iodine, thiourea, halides, thiosulphate, and other substances are examples of additional leaching agents [16]. It was determined that the process of relocating Y into the solution was more effective in H<sub>2</sub>SO<sub>4</sub> based on the data reported by authors in different media (HNO<sub>3</sub>, HCl), so this leaching medium was chosen as the right one for this investigation [17]. Chemical reactions that occur during leaching using sulfuric acid [18]:



The sulfuric acid-based separation of monazite has a long history. The separation of REE and thorium from coastal sand monazite was first developed in the early to mid-1900s. In this study, the monazite in the reactor was stirred at a temperature of 200–245 °C, using a weight ratio of acid and concentrate varying from 1.5:1 to 3:1. From this study, it was concluded that a minimum temperature of about 200 °C is required for almost complete decomposition of monazite. While the minimum acid and concentrate ratio required is 1.6:1 [19].

Similar studies have been carried out in the research on the processing of Bangka monazite with the acid

method by digestion using sulfuric acid. The dimensions of the monazite ore, the amount of sulfuric acid used, the temperature, the length of time, and the amount of water used for washing are among the factors considered. The results showed that the optimum digestion conditions were monazite ore size ~ 58 μm, the weight ratio of ore:sulfuric acid is 1:2.5, digestion temperature 190 °C, digestion time 3 h and washing consumption 8 times the weight of monazite feed with digested recovery U = 99.90%, Th = 99.44%, REE = 99.54% and PO<sub>4</sub> = 99.88% [18].

Research related to sulfuric acid digestion is research on the effect of digestion temperature. In this study, temperature variations were carried out between 200–800 °C. From this research, it can be concluded that digestion at 300 °C produced amorphous phosphate deposits, while the dissolved REEs increased to 99% [15]. Research on the separation of REEs from zircon tailings has also been carried out. The initial stage of the research was the alkaline fusion process; the feed ratio of NaOH: zircon tailings is 1:1. The result of the alkaline fusion process is used as leaching feed using HCl. From these results, the optimum conditions for the alkaline fusion zircon tailings leaching process were obtained at a temperature of 60 °C, HCl concentration of 1 M, and a ratio of yield of the alkaline fusion: HCl is 1:10 for 7.5 min. Y recovery reached 87%, and the activation energy value (E<sub>a</sub>) was 20.21 kJ/mol [20].

The solvent used in this study was sulfuric acid. Meanwhile, the reactor used in this study was an autoclave without an agitator, and this study was conducted without pretreatment. From the results of the study of reaction kinetics, the process of controlling the reaction rate, kinetic parameters, activation energies, and equations or kinetic models can be known. From the results of kinetic studies, the process scale-up stages can be carried out on an industrial scale.

## ■ EXPERIMENTAL SECTION

### Materials

The materials used in this study include zircon tailings from PT. Monokem Surya, H<sub>2</sub>SO<sub>4</sub> (95–97%) produced by Merck & Co., Inc., distilled water produced

by PSTA-BATAN kernel fabrication laboratory and filter paper.

### Instrumentation

The instruments used in this study were a ball mill (planetary ball mill type, Changsha Tianchuang Powder Technology Co. Ltd.), furnace (vertical lift door type, produced by PT. Suhaterm), autoclave, laboratory glassware (Thermo scientific Heraeus), sieve, analytical balance, and X-Ray Fluorescence (NEX QC RIGAKU, S/N QC 1202).

### Procedure

#### Determination of leaching kinetics

The determination of leaching kinetics was carried out by varying the leaching temperature with the variation of 200, 250, and 300 °C. At each temperature, samples were taken at a leaching process of 0, 20, 40, 60, 80, 100, and 120 min. The solvent used in the zircon tailings leaching process was sulfuric acid.

#### Analysis of leaching result

The leaching residue was analyzed using X-Ray Fluorescence to determine the levels of each element. Determining the percentage of recovery is carried out using the following equation:

$$\text{Recovery} = \frac{X_0 - X_i}{X_0} \times 100\% \quad (3)$$

with,  $X_0$  = mass of leaching feed x concentration of element, % and  $X_i$  = mass of leaching residue x concentration of element, %.

#### Data interpretation

Determination of the fitting of the kinetic model to the experimental results (trend line) is done by comparing each kinetic model with the experimental data. The kinetic data will be plotted in the form of a graph of the relationship between the kinetic model and time to get the most appropriate model. The kinetic model obtained is then used to calculate the value of the constant  $k$ , as well as plots of  $\ln k$  and  $1/T$ , to get the  $E_a$  value.

Each kinetic model was compared with experimental data. After obtaining the constant value  $k$ , the value of time ( $t$ ) is calculated again by dividing the value obtained from various models by the value of  $k$ . The

equation for finding  $t$  values for various models is presented in Table 1.

Furthermore, the calculated  $t$  value is compared with the  $t$  value at various recovery fractions ( $x$ ) in the experimental results.

## RESULTS AND DISCUSSION

### Characterization of Zircon Tailings Composition

The raw material used in this research is zircon tailings from PT. Monokem Surya. The initial stage of this research is the drying process of zircon tailings which will later be used as research feed. Drying was carried out at 110 °C for 3 h. After the drying process, a filtering process is carried out to remove impurities. In the early stages of the study, analysis was also carried out using X-Ray Fluorescence (XRF). The concentration of each REE per total REEs concentration is presented in Fig. 1.

As shown in Fig. 1, it can be seen that the levels of each REE per total REEs level are presented; it can be seen that the highest concentration of metal is Y at 35%, followed by Ce metal at 27%, La metal at 12%, and Nd at 10%.

Based on the results of the characterization of zircon tailings using X-Ray Diffraction (XRD) can be seen that the xenotime content is 42.6%, where xenotime

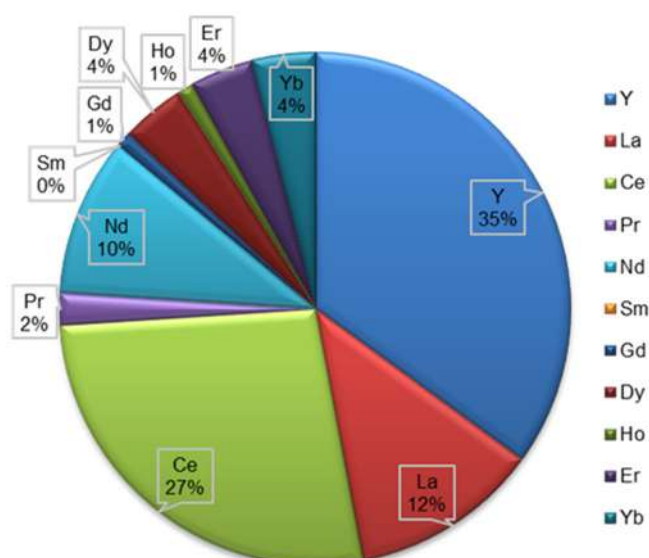


Fig 1. The concentration of each REE per total REEs concentration

**Table 1.** The equation for finding the t value for various models [21]

Model	Time, t
Chemical reaction control	$t = \frac{1 - (1 - x)^{\frac{1}{3}}}{k_s}$
Ash diffusion control	$t = \frac{1 - 3(1 - x)^{\frac{2}{3}} + 2(1 - x)}{k_a}$
Zhuravlev, Lesokhin, and Templeman	$t = \frac{\left(\frac{1}{(1-x)^{\frac{1}{3}}} - 1\right)^2}{k_{sa}}$
Jander cylindrical	$t = \frac{\left(1 - (1 - x)^{\frac{1}{2}}\right)^2}{k_{aj}}$
Jander 3D	$t = \frac{\left(1 - (1 - x)^{\frac{1}{3}}\right)^2}{k_{ab}}$
Dickinson	$t = \frac{\left(\frac{1}{(1-x)^{\frac{1}{3}}} - 1\right)}{k_{ad}}$

Where t is time (min), x is the recovery fraction,  $k_s$  is the apparent rate constant for the chemical reaction control ( $\text{min}^{-1}$ ),  $k_a$  is the apparent rate constant for the ash diffusion control ( $\text{min}^{-1}$ ),  $k_{sa}$  is the apparent rate constant for the Zhuravlev-Lesokhin-Templeman control ( $\text{min}^{-1}$ ),  $k_{aj}$  is the apparent rate constant for the Jander cylindrical control ( $\text{min}^{-1}$ ),  $k_{ab}$  is the apparent rate constant for the Jander 3D control ( $\text{min}^{-1}$ ), and  $k_{ad}$  is the apparent rate constant for the Dickinson control ( $\text{min}^{-1}$ )

is a mineral that contains Y, and it was another mineral with the highest composition in the zircon tailings followed by monazite-Ce (34.2%), zircon (17%), anatase (4.3%), rutile (1.2%), and cerianite (0.7%) [20].

### Leaching Kinetics of Yttrium from Zircon Tailings Using Sulfuric Acid

Determining the leaching kinetics was carried out by varying the leaching time to 0, 20, 40, 60, 80, 100, and 120 min. At each leaching time, the processes were carried out at 200, 250, and 300 °C. Leaching was carried out with a grain size of zircon tailings of 119  $\mu\text{m}$  and a liquid/solid ratio of 1 mL/g for each temperature variation (grain size of zircon tailings and liquid/solid ratio obtained from the optimization results in previous studies). The results of the leaching of REEs at each temperature can be seen in Fig. 2.

As shown in Fig. 2, it can be seen that for temperatures of 300 °C, the recovery trend obtained increased drastically from 0 to 60 min, then after reaching 60 min the recovery slowly increased. For temperatures of 250 and 200 °C, the recovery trend obtained increased

drastically from 80 to 100 min. From the recovery trend of the three temperatures, it can be seen that temperature greatly influences the time needed to achieve a significant increase in recovery. Increasing temperature, the value of the reaction rate constant will increase, and the reaction rate will be faster because the reaction rate constant is very dependent on temperature. The data obtained from the study were then used for kinetics evaluation.

In this study, an evaluation of the leaching kinetics of REEs was carried out using the developed model to predict the leaching process of rare earth elements from zircon tailings. Several models were used to evaluate the leaching process are Chemical reaction model, the Ash diffusion model, the Zhuravlev-Lesokhin-Templeman model (Z-L-T), the Jander Cylindrical model, the Dickinson model, and the Jander 3D models. The leaching kinetics models are often used to describe the leaching process in the extraction of elements from ores.

Each kinetic model was compared with experimental data. After obtaining the constant value k,

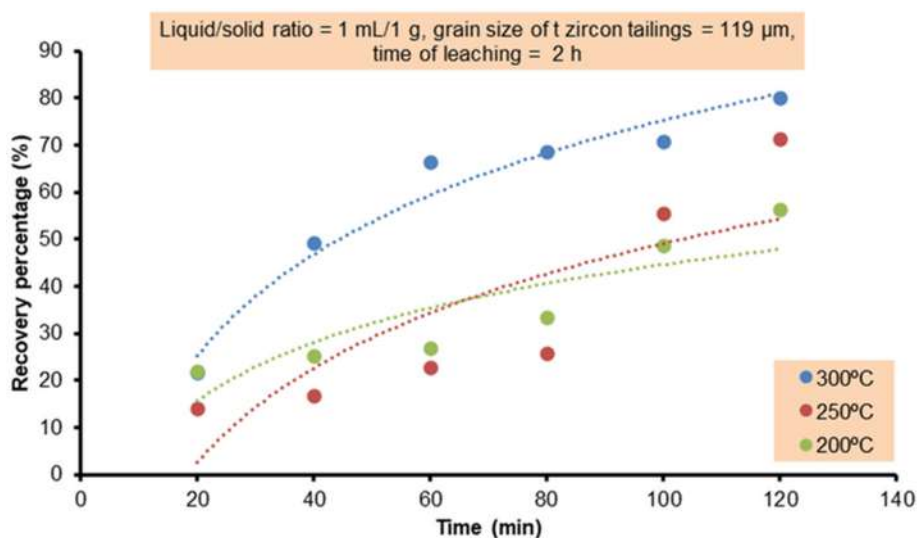
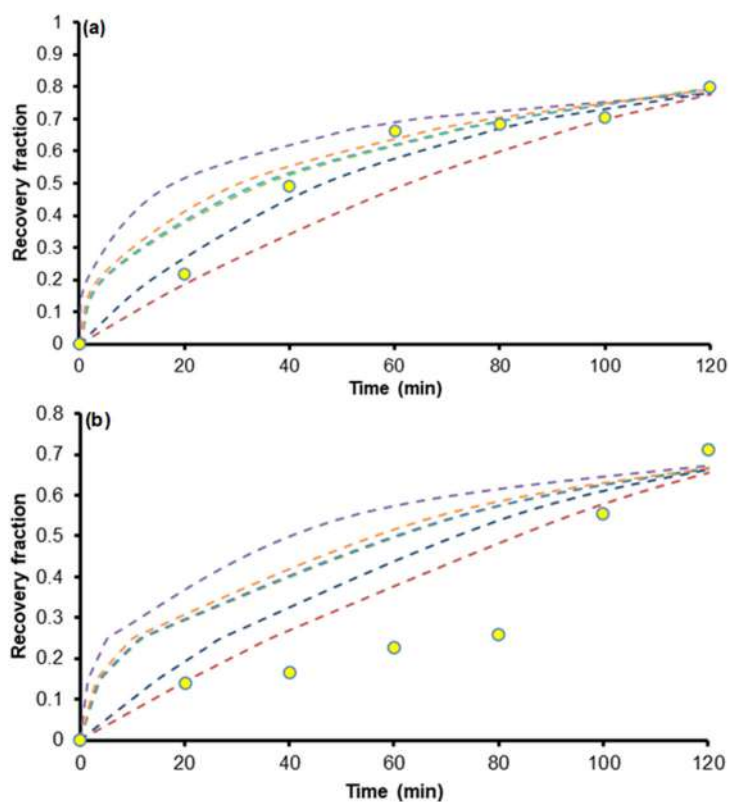


Fig 2. Percent recovery plot with time at 300, 250, and 200 °C for Yttrium

the value of time ( $t$ ) is calculated again by dividing the value obtained from various models by the value of  $k$ . Furthermore, the calculated  $t$  value is compared with the  $t$  value at various  $x$  in the experimental results. A comparison of the accuracy of the use of the model in this study can be seen in Fig. 3.

This study discovered that the chemical reaction model is the kinetic model that comes the closest to the kinetics of the leaching process, as illustrated in Fig. 3. The examination of the model utilizing the  $R^2$  value on the relationship between each model over time lends support to this. The  $R^2$  value for each kinetic model



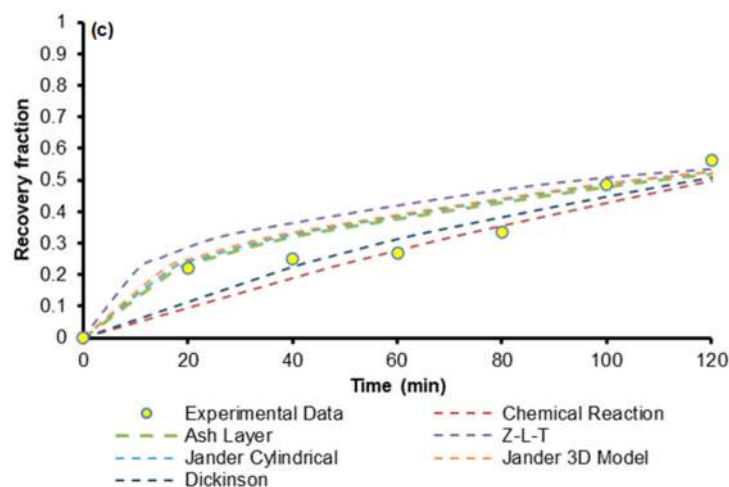


Fig 3. Recovery fraction plot with time for fitting the kinetic model at (a) 300, (b) 250, and (c) 200 °C for Yttrium

Table 2. R<sup>2</sup> value of various research models

Kinetic Model	Temperature (°C)	R <sup>2</sup>
Chemical Reaction	300	0.9412
	250	0.8234
	200	0.7964
Ash Layer Diffusion	300	0.9352
	250	0.6814
	200	0.6939
Zhuravlev, Lesokhin, and Templeman	300	0.8638
	250	0.5952
	200	0.6155
Jander 3D	300	0.9298
	250	0.6599
	200	0.6745
Jander Cylindrical	300	0.9345
	250	0.6756
	200	0.6887
Dickinson	300	0.9157
	250	0.7655
	200	0.7731

employed in the study is shown in Table 2.

As shown in Table 2, it can be seen that the appropriate kinetic model is the chemical reaction model because it has the highest coefficient of determination (R<sup>2</sup>) when compared to other kinetic models. The chemical reaction model assumes that chemical reactions control the rate of the reaction.

Based on the results of the leaching process approach with the models used, the most suitable model can be used to calculate E<sub>a</sub> value. The plot between models

$(1 - (1 - x)^{1/3})$  and time in Fig. 4 was used to find the value of the apparent rate constant for the chemical reaction control ( $k_s$ ), as the slope from the curve of model and time. From the calculation results obtained, the value of  $k_s$  at each temperature of 0.0038 (300 °C), 0.0022 (250 °C), and 0.0019 (200 °C). The equations are as follows:

Chemical reaction control:

$$k_s \cdot t = 1 - (1 - x)^{1/3} \quad (4)$$

where  $t$  is time (min),  $x$  is the recovery fraction, and  $k_s$  is the apparent rate constant for the chemical reaction control ( $\text{min}^{-1}$ ).

The  $E_a$  was determined by using Arrhenius plots:

$$k_s = A \exp\left(\frac{-E_a}{RT}\right) \quad (5)$$

$$k_s = \ln A - \frac{E_a}{RT} \quad (6)$$

$$E_a = -R * \left(\text{slope from the curve of } \ln k_s \text{ vs } \frac{1}{T}\right) \quad (7)$$

where  $E_a$  is the activation energy (J/mol),  $R = 8.314462$  (J/(mol.K)),  $k_s$  is the apparent rate constant for the chemical reaction control ( $\text{min}^{-1}$ ),  $A$  is the frequency factor, and  $T$  is the leaching temperature (K).

The Arrhenius plot in Fig. 5 was used to find the  $E_a$  of the leaching process. The  $E_a$  value for the leaching of

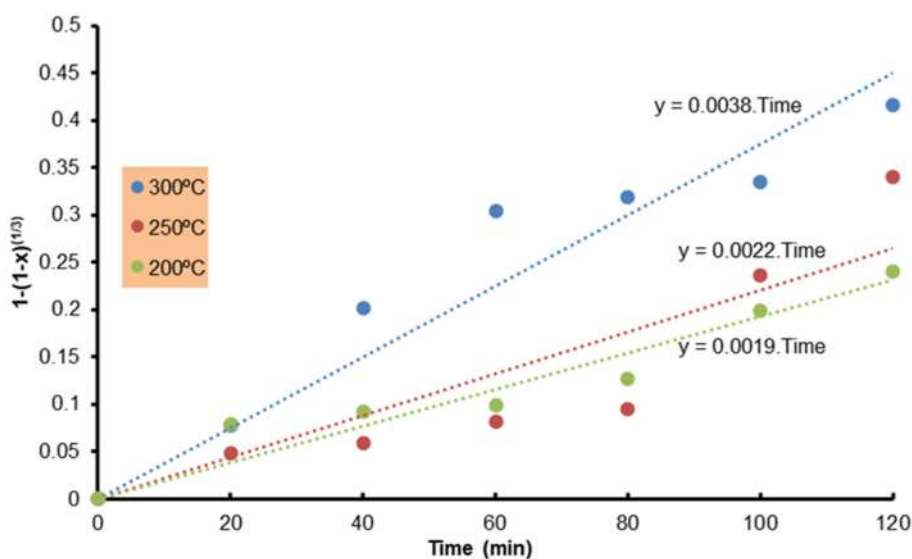


Fig 4. Recovery fraction of suitable model plot with time at 300, 250, and 200 °C for Yttrium

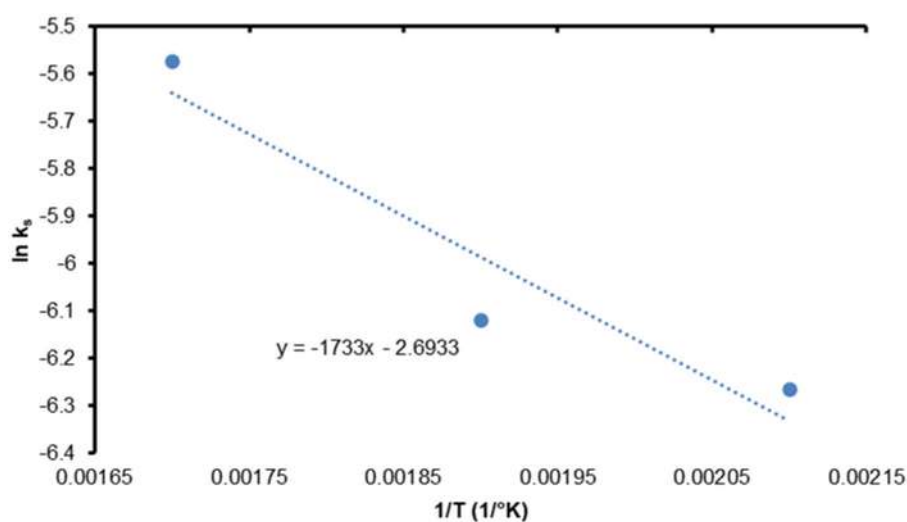


Fig 5. Arrhenius plot

Table 3. The value of  $E_a$  from previous research

Researcher	$E_a$ , kJ/mol	Sample
[2]	26.95	Concentrate after roasting treatment
[20]	20.21	Alkaline fusion treatment results

REEs from zircon tailings using sulfuric acid was 14.42 kJ/mol. The value of  $E_a$  from previous research is presented in Table 3.

The chemical reaction will govern the leaching process if the  $E_a$  value is less than 20 kJ/mol, whereas diffusion through the ash layer will control it if the  $E_a$  value is greater than 40 kJ/mol [22]. From the results of the study, if it is seen from the obtained  $E_a$  value, the model that is suitable for the leaching process of Yttrium from zircon tailings using sulfuric acid is the chemical reaction model.

## ■ CONCLUSION

According to the results of fitting the kinetic model, the chemical reaction model that governs is comparable to the sulfuric acid-assisted Yttrium leaching process from zircon tailings. The evaluation of the model based on the value of the coefficient of determination ( $R^2$ ) on the correlation between each model and time also supports this. Sulfuric acid's  $E_a$  value was 14.42 kJ/mol for the leaching of Yttrium from zircon tailings. The  $E_a$  value demonstrated that the leaching process was within the control of the chemical reaction model.

## ■ ACKNOWLEDGMENTS

The author would like to thank the employees of building 02 National Research and Innovation Agency Yogyakarta, especially the 2<sup>nd</sup> floor of the chemistry field, and colleagues who have helped in this research.

## ■ REFERENCES

- [1] Biyantoro, D., Subagiono, R., and Basuki, K.T., 2005, Ekstraksi Larutan Senotim Menggunakan DEHP (Diester) dan DEHP (Mono & Diester) Pada Pemisahan Y, La, Ce, Gd, dan Eu, *Prosiding PPI - PDIPTN*, Puslitbang Teknologi Maju, 152–158.
- [2] Talan, D., and Huang, Q., 2022, A review of environmental aspect of rare earth element extraction processes and solution purification techniques, *Miner. Eng.*, 179, 107430.
- [3] Trisnawati, I., Yulandra, A., Prameswara, G., Pusparini, W.R., Mulyono, P., Prasetya, A., and Petrus, H.T.B.M., 2021, Optimization of multistage precipitation processes for rare earth element purification from Indonesian zircon tailings, *J. Sustainable Metall.*, 7 (2), 537–546.
- [4] Paulick, H., and Machacek, E., 2017, The global rare earth element exploration boom: An analysis of resources outside of China and discussion of development perspectives, *Resour. Policy*, 52, 134–153.
- [5] Li, M., Li, J., Zhang, D., Gao, K., Wang, H., Xu, W., Geng, J., Zhang, X., and Ma, X., 2020, Decomposition of mixed rare earth concentrate by NaOH roasting and kinetics of hydrochloric acid leaching process, *J. Rare Earths*, 38 (9), 1019–1029.
- [6] Liu, J., Martin, P.F., and Peter McGrail, B., 2021, Rare-earth element extraction from geothermal brine using magnetic core-shell nanoparticles-techno-economic analysis, *Geothermics*, 89, 101938.
- [7] Laudal, D.A., Benson, S.A., Addleman, R.S., and Palo, D., 2018, Leaching behavior of rare earth elements in Fort Union lignite coals of North America, *Int. J. Coal Geol.*, 191, 112–124.
- [8] Innocenzi, V., De Michelis, I., Ferella, F., and Vegliò, F., 2017, Leaching of yttrium from cathode ray tube fluorescent powder: Kinetic study and empirical models, *Int. J. Miner. Process.*, 168, 76–86.
- [9] Wu, G., Zhang, Z., Li, Y., and Liao, W., 2022, Extraction and separation of yttrium from other rare earths in chloride medium by phosphorylcarboxylic acids, *J. Rare Earths*, 40 (6), 958–964.
- [10] Xiao, S., Geng, Y., Rui, X., Su, C., and Yao, T., 2022, Behind of the criticality for rare earth elements: Surplus of China's yttrium, *Resour. Policy*, 76, 102624.
- [11] Çetintaş, S., and Bingöl, D., 2016, Response surface methodology approach to leaching of nickel laterite and evaluation of different analytical techniques used for the analysis of leached solutions, *Anal. Methods*, 8 (15), 3075–3087.
- [12] Saratale, R.G., Kim, H.Y., Park, Y., Shin, H.S., Ghodake, G., Bharagava, R.N., Mulla, S.I., Kim, D.S., and Saratale, G.D., 2020, Hydrometallurgical process for the recovery of yttrium from spent

- fluorescent lamp: Leaching and crystallization experiments, *J. Cleaner Prod.*, 261, 121009.
- [13] Shahbaz, A., 2022, A systematic review on leaching of rare earth metals from primary and secondary sources, *Miner. Eng.*, 184, 107632.
- [14] Fernández, L., Ortega, J., and Wisniak, J., 2017, New computational tool to evaluate experimental VLE and VLLE data of multicomponent systems, *Comput. Chem. Eng.*, 106, 437–463.
- [15] Demol, J., Ho, E., and Senanayake, G., 2018, Sulfuric acid baking and leaching of rare earth elements, thorium and phosphate from a monazite concentrate: Effect of bake temperature from 200 to 800 °C, *Hydrometallurgy*, 179, 254–267.
- [16] Pinto, J., Colónia, J., Viana, T., Ferreira, N., Tavares, D., Jacinto, J., Abdolvasei, A., Monteiro, F.L., Henriques, B., and Pereira, E., 2022, Potential of the macroalga *Ulva* sp. for the recovery of yttrium obtained from fluorescent lamp waste, *J. Cleaner Prod.*, 369, 133299.
- [17] Miskufova, A., Kochmanova, A., Havlik, T., Horvathova, H., and Kuruc, P., 2018, Leaching of yttrium, europium and accompanying elements from phosphor coatings, *Hydrometallurgy*, 176, 216–228.
- [18] Prassanti, R., 2013, Digesti monasit Bangka dengan asam sulfat, *Eksplorium*, 33 (1), 41–54.
- [19] Zhang, Z., Jia, Q., and W. Liao, 2015, 'Progress, in the Separation Processes for Rare Earth Resources' in *Handbook on the Physics and Chemistry of Rare Earths*, Eds. Bünzli, J.C., and Pecharsky, V.K., Volume 48, Amsterdam, Netherlands, 287–376.
- [20] Prameswara, G., Trisnawati, I., Poernomo, H., Mulyono, P., Prasetya, A., and Petrus, H.T.B.M., 2020, Kinetics of yttrium dissolution from alkaline fusion on zircon tailings, *Min. Metall. Explor.*, 37 (4), 1297–1305.
- [21] Prameswara, G., Tyassena, F.Y.P., Pasaribu, M., Trisnawati, I., and Petrus, H.T.B.M., 2023, Nickel recovery optimization and kinetic study of Morowali laterite ore, *Trans. Indian Inst. Met.*, 2023, s12666-022-02858-1.
- [22] Sililo, B., 2016, Modelling Uranium Leaching Kinetics, *Thesis*, Faculty of Engineering, Built Environment and Information Technology, University of Pretoria, South Africa.



## Calcium Phosphate Cement Composed of Hydroxyapatite Modified Silica and Polyuegenol as a Bone Filler Material

Tri Windarti<sup>1\*</sup>, Nor Basid Adiwibawa Prasetya<sup>1</sup>, Ngadiwiyana Ngadiwiyana<sup>1</sup>, and Limpat Nulandaya<sup>2,3</sup>

<sup>1</sup>Department of Chemistry, Faculty of Science and Mathematics, Universitas Diponegoro, Jl. Prof. Soedharto SH, Tembalang, Semarang 50275, Indonesia

<sup>2</sup>Center for Progressive Materials-Technology and Innovation Park, University of Pavol Jozef Šafárik, 04001 Košice, Slovakia

<sup>3</sup>Institute of Experimental Physics, Slovak Academy of Sciences, Watsonova 47, 04001 Košice, Slovakia

\* Corresponding author:

email: tri.windarti@lecturer.undip.ac.id

Received: December 16, 2022

Accepted: March 10, 2023

DOI: 10.22146/ijc.80298

**Abstract:** A composite of hydroxyapatite modified silica (HAsiO<sub>2</sub>) and 10% (w/w) polyuegenol (PE) was synthesized to produce a calcium phosphate cement with antibacterial activity. The compatibility of the composite (HAsiO<sub>2</sub>\_PE) with bone filler requirements was determined due to its crystal, surface, antibacterial, and cytocompatibility properties. The results showed that compositing HAsiO<sub>2</sub> and PE did not affect HA's chemical and crystal properties. The presence of PE changed HAsiO<sub>2</sub> morphology to be coarser and denser than before composited. PE tends to agglomerate but does not affect the hydrophilicity of HAsiO<sub>2</sub>. The presence of PE increased the surface area and total pore volume but lowered the average pore size. Different from pure PE, the composite of HAsiO<sub>2</sub>\_PE that contains of 10% PE has higher antibacterial activity toward *Escherichia coli* than *Staphylococcus aureus*. The composite is biocompatible because the cytotoxicity test toward pre-osteoblast cells resulted in an IC<sub>50</sub> of 2092 µg/mL. Thus, due to its chemical, surface, antibacterial, and cytocompatibility properties, the HAsiO<sub>2</sub>\_PE composite can be recommended as a bone filler material.

**Keywords:** antibacterial; bone; calcium phosphate cement; hydroxyapatite; polyuegenol

### ■ INTRODUCTION

The material used in orthopedic surgery affects its susceptibility to infection. Implants provide a significant risk of infection since they are regarded as foreign bodies in the body [1-2]. On the other hand, tissue opening during surgery is susceptible to bacterial infection [3]. Osteomyelitis is an inflammation of the bone that is often caused by a bacterial infection. More than 50% of these infections are caused by *Staphylococcus aureus* bacteria, where 28% of them are resistant to methicillin [4]. *Staphylococcus* species made up approximately 36.88% of hip joint surgeries [5]. The problem of infection caused by the rejection of implants can be overcome by using materials that are biocompatible and have strong bioactivity. Hydroxyapatite (HA, Ca<sub>10</sub>(PO<sub>4</sub>)<sub>6</sub>(OH)<sub>2</sub>) is a calcium phosphate that fulfills these criteria. Moreover, HA can be produced into a paste to be used as an

injectable calcium phosphate cement (CPC) [6]. The surface morphology and mechanical strength of HA are the determining factors for successful implantation. HA must be combined with other materials, such as silica (SiO<sub>2</sub>), to increase its mechanical strength because of its fragility [7-10]. HA, which is composited with SiO<sub>2</sub> from rice husk, shows that HA covers the surface of the composite. Therefore, the biocompatibility and bioactivity properties of HA can be preserved [11].

There have been several attempts to add antibacterial properties to HA, including by compositing with a polymer. The polymers already used are chitosan [12], carboxylated chitosan [13], and  $\gamma$ -polyglutamic acid [14]. As is the basis for selecting the main material for CPC, the selection of an antibacterial agent must also consider its biocompatibility properties. For this reason, polyuegenol (PE) is an alternative polymer that meets

these criteria. PE is the result of the polymerization of eugenol monomers. Eugenol has so far been applied as an antibacterial agent in dental treatment. Eugenol can be isolated from clove oil, nutmeg oil, and cinnamon bark. Eugenol's antibacterial activity was included in the "moderate-strong" level, where eugenol inhibited the growth of the tested pathogens, such as *Escherichia coli* and *S. aureus* [15-16]. Eugenol polymerization into PE is expected to produce antibacterial properties that can last long term. The antibacterial activity appears due to the release of eugenol as a result of the depolymerization of PE in a physiological environment. Several studies have shown that eugenol and its derivatives still exhibit antibacterial activity when encapsulated or combined with polymers such as poly(lactic acid)/gelatin [17], poly( $\epsilon$ -caprolactone)/gelatin [15], resorcinol diglycidyl ether [16], dopamine methacrylamide [18], poly(3-hydroxybutyrate-co-3-hydroxyvalerate) [19] and poly(eugenol-co-methylmethacrylate)/polypropylene [20]. A composite of HA-modified SiO<sub>2</sub> (HASiO<sub>2</sub>) and PE (HASiO<sub>2</sub>\_PE) is expected to produce CPC with good antibacterial properties that can last a long time in the bone.

In this study, the HASiO<sub>2</sub> was synthesized in situ by the sol-gel method using cetyltrimethylammonium bromide (CTAB) surfactant as a morphology-directing agent [21-22]. PE was synthesized by polymerization of eugenol using BF<sub>3</sub> catalyst [10-12]. Both were used to make CPC by mixing with 2.5% Na<sub>2</sub>HPO<sub>4</sub> solution in a ratio of 1:1 (w/v). The final cement was then characterized to ascertain its crystal parameters, surface characteristics, antibacterial activity, and cytotoxicity. CPC is expected to maintain the superior properties of HA as a bone implant so that, at the end, the transformation of the implant into living tissue can occur. In other words, the addition of antibacterial properties to CPC must be capable to accommodate the process of implant deformation and bone tissue formation by the activity of osteoclasts and osteoblasts cells [23].

## ■ EXPERIMENTAL SECTION

### Materials

The Chemicals used for the synthesis of HASiO<sub>2</sub> were Ca(NO<sub>3</sub>)<sub>2</sub>·4H<sub>2</sub>O (Merck), KH<sub>2</sub>PO<sub>4</sub> (Merck), NH<sub>4</sub>OH

(Merck), SiO<sub>2</sub> (Merck), and CTAB (Sigma Aldrich). For the synthesis of PE, eugenol (Merck), chloroform (Merck), anhydrous Na<sub>2</sub>SO<sub>4</sub> (Merck), and BF<sub>3</sub> in diethyl ether were used. Materials for the production of CPC are synthesized HASiO<sub>2</sub> and PE as the powder component and Na<sub>2</sub>HPO<sub>4</sub> (Merck). For the antibacterial test, DMSO (Merck), *E. coli* (gram-negative), and *S. aureus* (gram-positive) bacteria were used. While for the cytotoxicity test, pre-osteoblast MC3T3E1 cells, MEM- $\alpha$  media (Gibco), 10% FBS (Sigma Aldrich), 2% Pen-Strep (Gibco), Fungizone 0.5% (Gibco), 0.5 mg/mL MTT (Biobasic), DMSO (Merck) were used.

### Procedure

#### Preparation of HASiO<sub>2</sub>

The synthesis of hydroxyapatite-modified silica was conducted according to the previous work [11]. A 50 mL of a solution that contained Ca(NO<sub>3</sub>)<sub>2</sub>·4H<sub>2</sub>O 1.2 M, SiO<sub>2</sub> 0.048 M, and CTAB (0.045 mmol) was slowly added by 50 mL of a solution that contained KH<sub>2</sub>PO<sub>4</sub> 1 M and CTAB (0.045 mmol). The mixture was then added 15 mL of 32% NH<sub>4</sub>OH to obtain a pH higher than 9 and stirred for 1 h. The mixture was then aged for 24 h at room temperature. The precipitate formed was washed with aquabidest until neutral and then dried in an electric oven at 50 °C for 48 h. The result was then calcined at 600 °C for 2 h in the air atmosphere. Then the product was ground and sieved by 200 mesh sieve. The obtained powder was called HASiO<sub>2</sub> sample.

#### Synthesis of PE

PE was obtained by adding chloroform solution to a three-neck flask containing eugenol (5.8 g, 35 mmol). During the polymerization process, the system was fed with nitrogen gas at room temperature while adding BF<sub>3</sub> in diethyl ether (1 mL) dropwise. Polymerization was carried out overnight, and the reaction was stopped by adding 1 mL of methanol. The polymerization results were dissolved in diethyl ether and then washed using distilled water until a neutral pH was reached. The organic layer was then dried by adding anhydrous Na<sub>2</sub>SO<sub>4</sub>. The solvent was evaporated with a rotary evaporator, and the PE residue was dried in a desiccator before being used.

### Synthesis of HASiO<sub>2</sub>\_PE Composite

HASiO<sub>2</sub> and PE powder with a ratio of 9:1 (w/w) are used as the powder component, and 2.5% Na<sub>2</sub>HPO<sub>4</sub> solution as a liquid component. CPC was made with a liquid:powder ratio of 1:1 (w/v). The mixture of the two components was stirred with a spatula until a homogeneous paste was formed. The paste was then left to harden at room temperature. The result is called the HASiO<sub>2</sub>\_PE composite or CPC.

### Characterizations

The Fourier Transform-Infrared spectrophotometer (FTIR, Shimadzu Prestige 21) was used to identify functional groups through a KBr pellets method. The X-Ray Diffractometer (XRD, Shimadzu type XRD-6000) equipped with monochromatic Cu K $\alpha$  radiation operated at 40 kW ( $\lambda = 1.54 \text{ \AA}$ ) was used to characterize the crystal structure. The X-ray scanned in the range of  $3^\circ \leq 2\theta \leq 80^\circ$  with a scan step degree of  $0.02^\circ$ . The XRD data was analyzed through Rietveld refinement by MAUD 2.933 software. The standard Crystallography Information File (CIF) for HA (COD-1011242) was obtained from the Crystallography Open Database (COD) website. Surface morphology and element distribution were observed using Scanning Electron Microscope-Energy Dispersive Spectroscopy (SEM-EDS, Hitachi type SU3500) and JEOL (type JED-2300) for HASiO<sub>2</sub> and HASiO<sub>2</sub>\_PE, respectively. Hitachi MC1000 sputter ion was used for sample coating with gold in a thickness of 1 nm. Surface area analysis was conducted by BET method using Quantachrome Instruments version 11.03.

Antibacterial activity was tested by using the diffuse method using *E. coli* (gram-negative) and *S. aureus* (gram-positive) bacteria. The concentrations of *E. coli* and *S. aureus* were  $2.6 \times 10^6$  and  $1.8 \times 10^6$  CFU/mL, respectively. The sample concentration was produced by dissolving 0.5 g HASiO<sub>2</sub>\_PE in 5 mL DMSO. The test was carried out on a Nutrient Agar medium, with a petri dish size of 12 cm, and incubation at 37 °C.

Cytotoxicity test was conducted using pre-osteoblast MC3T3E1 cells grown in MEM- $\alpha$  media, supplemented with 10% FBS, 2% Pen-Strep, and Fungizone 0.5%. Cells were cultivated in 96-well plates. In each well, 100  $\mu$ L of cell suspension (contain  $2 \times 10^4$  cells)

was incubated for 24 h. Then it was treated with HASiO<sub>2</sub>\_PE according to the serial concentration and incubated for 24 h. The MTT assay was performed by injecting 100  $\mu$ L of 0.5 mg/mL MTT into each well, incubated for 4 h, and stopped with DMSO 100  $\mu$ L/well. The absorbance was measured using Tecan Spark® (Tecan Trading AG, Switzerland) at 570 nm. Calculation of IC<sub>50</sub> values was done by non-linear regression using GraphPad Prism 7 software. The average value of cell viability with HASiO<sub>2</sub>\_PE treatment was calculated by Microsoft Excel and One Way ANOVA with GraphPad Prism 7 software (GraphPad Software, CA, USA). The cell viability was calculated by:

$$\% \text{Viability} = \frac{\text{OD treatment} - \text{OD media control}}{\text{OD cell control} - \text{OD media control}} \times 100\%$$

## RESULTS AND DISCUSSION

Mixing the powder and liquid components using a spatula produced a homogeneous CPC paste. The time needed to form the paste was about 2 min, and the time needed for the paste to harden into cement was about 3 h (Fig. 1). The characterization with FTIR for HASiO<sub>2</sub>, PE, and the HASiO<sub>2</sub>\_PE composite is shown in Fig. 2. In the PE spectra, it can be seen that the specific peaks have the aromatic C=C functional group ( $1600 \text{ cm}^{-1}$ ), the -OH phenolic functional group ( $3450 \text{ cm}^{-1}$ ) and the C-O-C ether functional group ( $1166 \text{ cm}^{-1}$ ). The HASiO<sub>2</sub> spectra identified functional groups that are identical to HA. The presence of PO<sub>4</sub><sup>3-</sup> group is identified by asymmetric stretching ( $\nu_3$ ) that appears as sharp peaks at  $1088$  and  $1043 \text{ cm}^{-1}$ , and asymmetric deformation ( $\nu_4$ ) at  $568$  and  $604 \text{ cm}^{-1}$  [24-25]. The O-H group of HA and the adsorbed H<sub>2</sub>O appear as broad peaks around  $3500 \text{ cm}^{-1}$ .



**Fig 1.** Paste (left) and cement (right) of HASiO<sub>2</sub>\_PE composite

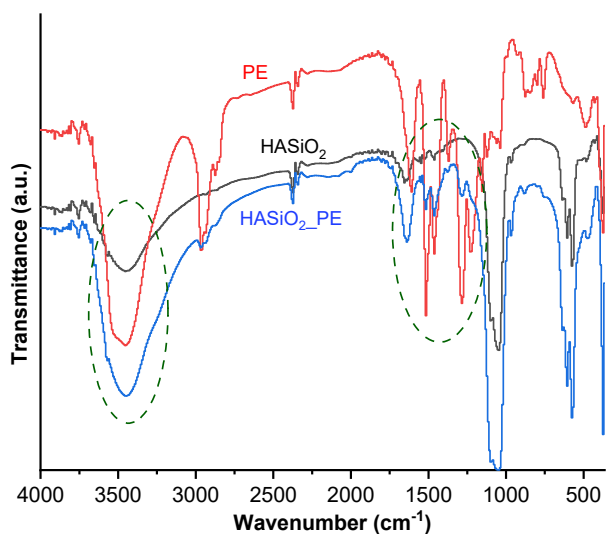


Fig 2. FTIR spectra of HASiO<sub>2</sub>, PE, and HASiO<sub>2</sub>\_PE

A peak at 1637 cm<sup>-1</sup> ensures the presence of adsorbed H<sub>2</sub>O. Some of PO<sub>4</sub><sup>3-</sup> in the HA structure were substituted by CO<sub>3</sub><sup>2-</sup> groups due to the presence of a peak at 1489 cm<sup>-1</sup>. The Si–O–Si asymmetric stretching vibration coincides with the PO<sub>4</sub><sup>3-</sup> asymmetric stretching vibration peak at 1088 cm<sup>-1</sup> [11]. The HASiO<sub>2</sub> and PE spectral patterns were found in the HASiO<sub>2</sub>\_PE spectra, but the peak intensity of PE in HASiO<sub>2</sub>\_PE is lower than HASiO<sub>2</sub> due to its low concentration (10%).

The XRD diffractogram (Fig. 3) shows that PE is amorphous due to the wide peak at 2θ = 5–30°. The diffraction patterns of HASiO<sub>2</sub> and HASiO<sub>2</sub>\_PE composites are very similar, except for 2θ = 5–25°, in which HASiO<sub>2</sub>\_PE composite has a higher intensity. HA lattice crystal is known as hexagonal with a space group P63/m. The Rietveld refinement using MAUD 2.993 software showed no change in the lattice parameters of HA due to the composite formation (Fig. 4). Lattice parameters of HA in HASiO<sub>2</sub> and HASiO<sub>2</sub>\_PE are a = b = 9.47 Å, c = 6.92 Å, and lattice volume = 537.4 Å<sup>3</sup>. The crystallite sizes of HA in HASiO<sub>2</sub> and HASiO<sub>2</sub>\_PE are 14.56 and 14.49 nm, respectively (Table 1). These results

are similar to previous studies and COD-1011242 as the standard [26-27]. The same lattice parameters of HA and the same crystallite size of HASiO<sub>2</sub> and HASiO<sub>2</sub>\_PE are highly expected because HA's bioactivity depends on its lattice parameters. The bioactivity of HA is determined by its solubility properties, where the solubility of solids is determined by its crystal parameters. The similarity of HASiO<sub>2</sub>\_PE crystallite size with bone mineral size (> 40 nm) supports its compatibility with bone tissue [6].

The BET method determined surface area, pore volume, and pore average. Fig. 5 shows the isotherm graphs for HASiO<sub>2</sub> and HASiO<sub>2</sub>\_PE. Both samples demonstrated a type III adsorption-desorption isotherm curve, where the adsorbent quantity rose as the relative pressure increased. The adsorbate-adsorbate interaction is stronger than the adsorbent-adsorbent. Type III has an unlimited number of layers on the surface of the adsorbent (multilayer). The decrease in the vertical axis is caused by the fact that the amount of N<sub>2</sub> absorbed by the composite reduces by decreasing pressure. A standard BET multi-point was used to calculate the

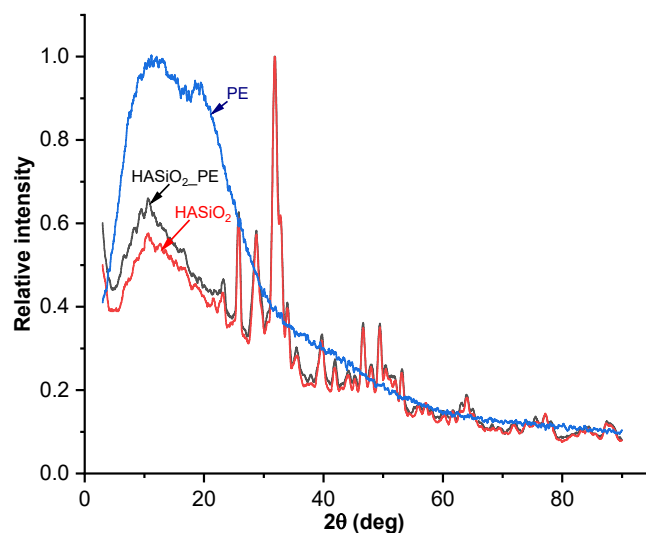


Fig 3. XRD diffractogram

Table 1. Crystal lattice parameters

Sample	a (Å)	c (Å)	Volume (Å <sup>3</sup> )	Crystallite size (nm)	Rietveld agreement factors	
					χ <sup>2</sup>	Rw (%)
HASiO <sub>2</sub>	9.47	6.92	537.4	14.56	1.31	10.56
HASiO <sub>2</sub> _PE	9.47	6.92	537.4	14.49	1.30	10.27

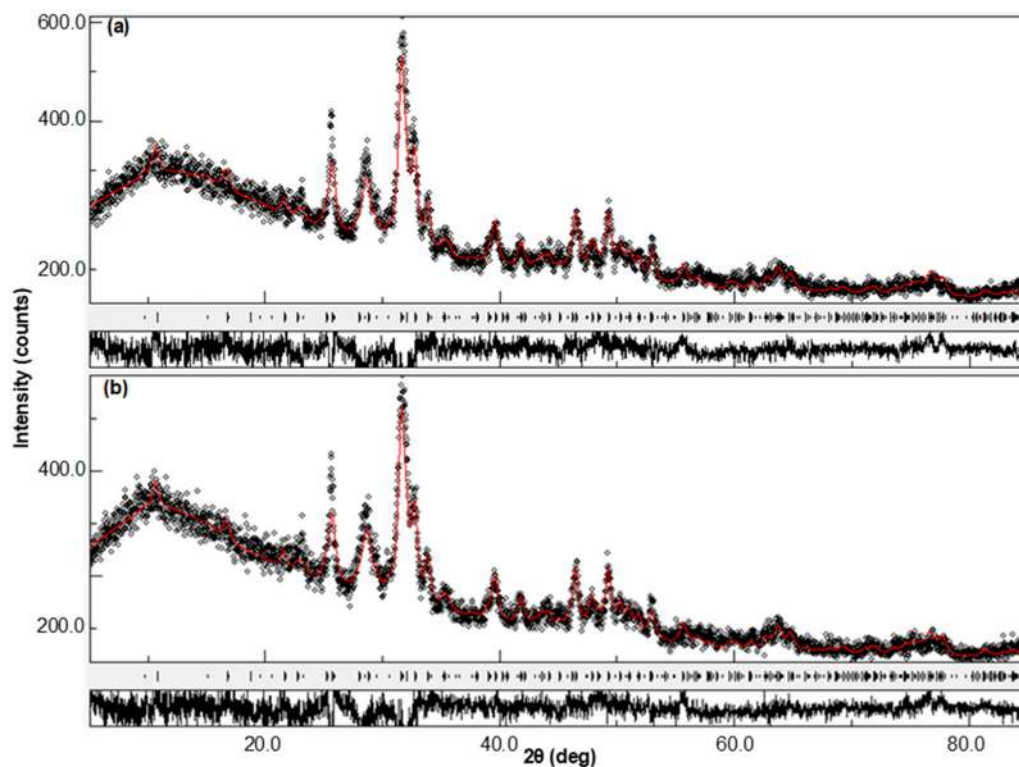


Fig 4. Results of refinement for (a) HASiO<sub>2</sub> and (b) HASiO<sub>2</sub>\_PE

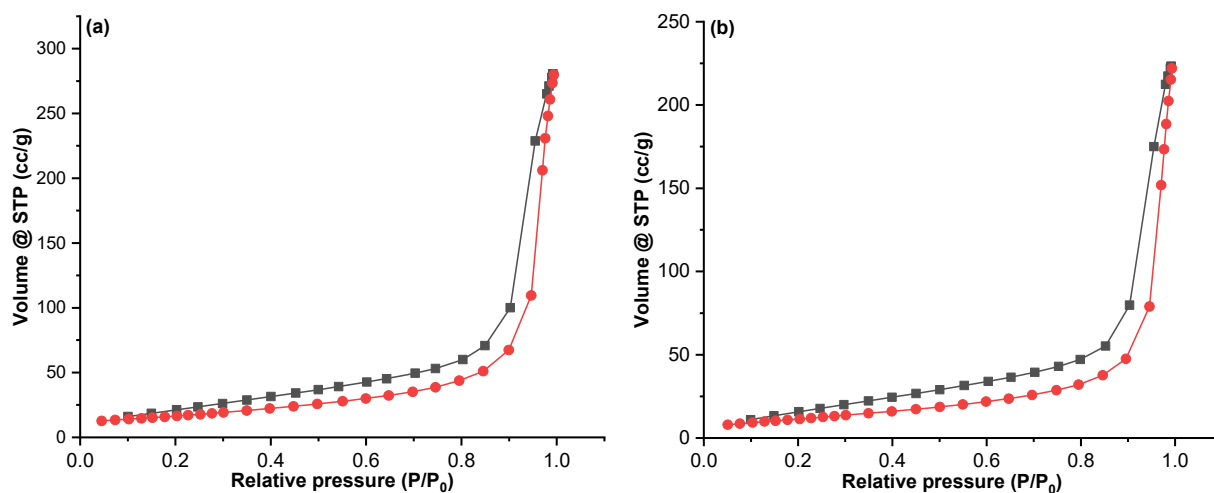


Fig 5. Graph of (a) HASiO<sub>2</sub> and (b) HASiO<sub>2</sub>\_PE isotherms

specific surface area of the two materials.

HA structure modification usually affects the adsorption-desorption behavior, surface area, total pore volume, and average pore size [28–30]. Table 2 shows that HASiO<sub>2</sub> and HASiO<sub>2</sub>\_PE have a specific surface area of 59.295 and 43.350 m<sup>2</sup>/g, respectively. HASiO<sub>2</sub> has a larger surface area than the HASiO<sub>2</sub>\_PE sample, or making composites reduces the surface area by 26.89%. The total

pore volume also decreased from 0.433 to 0.343 (cm<sup>3</sup>/g). However, the HASiO<sub>2</sub>\_PE composite has an average pore size larger than HASiO<sub>2</sub>, which is 15.844 and 14.606 nm, respectively. The pore size is included in the mesoporous category (range of pore size 2–50 nm). Thus, both HASiO<sub>2</sub> and HASiO<sub>2</sub>\_PE have surface properties that support bone cell attachment and proliferation.

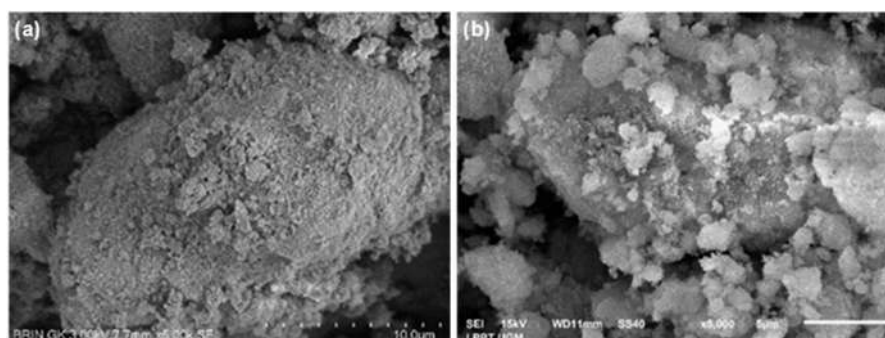
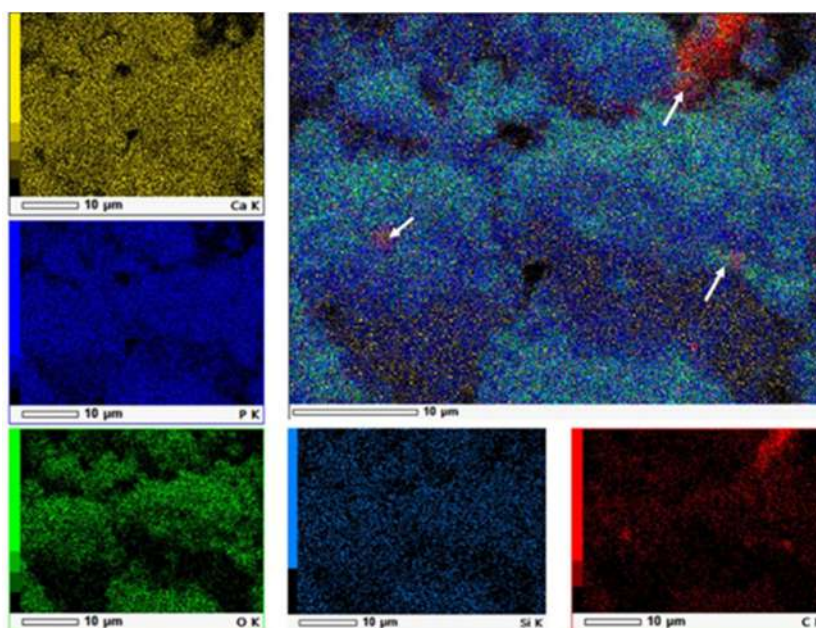
**Table 2.** Comparison of surface area, pore volume and pore average

Sample	Surface area ( $S_{\text{BET}}$ ) ( $\text{m}^2/\text{g}$ )	Total pore volume ( $V_{\text{TOT}}$ ) ( $\text{cm}^3/\text{g}$ )	Average pore size (nm)
HASiO <sub>2</sub>	59.295	0.433	14.606
HASiO <sub>2</sub> _PE 10%	43.350	0.343	15.844

The analysis results with SEM at 5000 times magnification showed that the surface morphology of HASiO<sub>2</sub> is uneven (Fig. 6). The agglomeration of nano-sized particles leads to the formation of a variety of particle sizes. The large particles showed a consistent shape, a capsule-like shape, with dimensions on a micron scale. In the HASiO<sub>2</sub>\_PE composite, the particle shape is irregular, and the morphology is uneven. The agglomeration behavior of the two samples was different, despite the fact that the XRD data did not show any

difference in the HA lattice parameters and the crystallite size. The surface of the HASiO<sub>2</sub>\_PE composite is rougher and denser than HASiO<sub>2</sub>. Synthesis of HA-modified silica without using CTAB surfactants produced a flat surface, unlike in this study [11].

Element mapping on the surface of the HASiO<sub>2</sub>\_PE composite has shown how the composite surface is covered by Ca, P, O, Si, and C elements (Fig. 7). The presence of Ca, P, O, and Si elements indicate the presence of HASiO<sub>2</sub>, while C and O indicate the presence

**Fig 6.** Surface profiles of (a) HASiO<sub>2</sub> and (b) HASiO<sub>2</sub>\_PE**Fig 7.** Results of elemental mapping on the HASiO<sub>2</sub>\_PE surface

of PE. On individual mapping, Ca dominates the composite surface and is evenly distributed. There are several dark areas that are confirmed as C elements (from PE). The same distribution pattern occurs for the P element mapping. The P elements belong to HA, where  $\text{Ca}^{2+}$  binds to  $\text{PO}_4^{3-}$  through Ca-O-P bonds. The O element shows a slightly different pattern, in which O forms a contour that can be compared with the combined element mapping results. It can be concluded that O tends to be found on the composite surface or is exposed on the surface. This is highly desirable because the presence of O, mainly in the form of phosphate, carbonate, or hydroxyl groups, supports the biocompatibility and bioactivity of the composite in physiological environments [28]. The distribution of Si elements has the same pattern as Ca and P elements. Confirming the results of earlier research that the silica-modified HA composite had silica within and HA on the surface [11]. C Element appears to be partially distributed and agglomerated in some areas, filling in the dark areas on the mapping of Ca and P elements. This confirmed that the hydrophobicity of PE is high so that PE is not soluble in the  $\text{Na}_2\text{HPO}_4$  solution. The combined mapping showed that the composite surface is uneven and that the PE (arrows) agglomerates on some of the surface's area. Such a surface supports the attachment of cells and ions when the composite is in a physiological environment [29].

The elemental composition on the surface was measured by EDX and the results could be seen in Table 3. Compositing  $\text{HASiO}_2$  and PE caused the amount of Ca to decrease significantly from 33.00 to 13.00%. This is because C, which represents the presence of PE, covers the surface in a large amount, namely 20%. This also causes a decrease in the P element from 11.40 to 9.00%. On the other hand, the amount of O element experienced a slight increase from 54.80 to 57.70%, which was a contribution from PE. The same with Ca and P, the amount of Si decreases from 0.80 to 0.30%. This condition caused the Ca/P ratio to decrease from 2.89 to 1.44, indicating that Ca no longer dominates the surface compared to P. This also causes the Ca/O ratio to decrease, in addition to the increase in the amount of O element on the surface. The presence of PE on the surface is expected

**Table 3.** Elemental composition on the surface of  $\text{HASiO}_2$  and  $\text{HASiO}_2\text{-PE}$

Element	Atomic (%)	
	$\text{HASiO}_2$	$\text{HASiO}_2\text{-PE}$
Ca	33.00	13.00
P	11.40	9.00
O	54.80	57.70
Si	0.80	0.30
C	-	20.00
Ca/P	2.89	1.44
Ca/O	0.60	0.23

**Table 4.** Antibacterial test results

Sample	<i>E. coli</i>		<i>S. aureus</i>	
	Inhibition zone (mm)	Average (mm)	Inhibition zone (mm)	Average (mm)
PE	1.60	1.80	2.00	2.30
	1.90		2.60	
	1.90		2.30	
$\text{HASiO}_2\text{-PE}$	3.10	2.83	1.50	1.43
	2.50		1.40	
	2.90		1.40	
Chloramphenicol	11.00	11.50	13.20	14.00
	12.00		14.90	
	11.50		13.90	
Erythromycin	5.40	5.97	5.40	5.07
	6.30		5.30	
	6.20		4.50	

because PE will interact directly with the physiological environment, and the degradation of PE from the cement will bring about the antibacterial activity. The presence of PE on the surface did not reduce the hydrophilicity of HASiO<sub>2</sub> according to the surface wetting test. As a result, the HASiO<sub>2</sub>\_PE composite retains the superior properties of HA.

The antibacterial test was carried out using *E. coli* and *S. aureus* bacteria. The inhibition zone of PE and HASiO<sub>2</sub>\_PE compared to chloramphenicol and erythromycin is shown in Table 4. PE has better antibacterial activity against *S. aureus* than *E. coli*. This result is different from the previous research that found PE to have the same activity against both bacteria [31]. In contrast, the HASiO<sub>2</sub>\_PE composite revealed better antibacterial activity on *E. coli* than *S. aureus*. This could

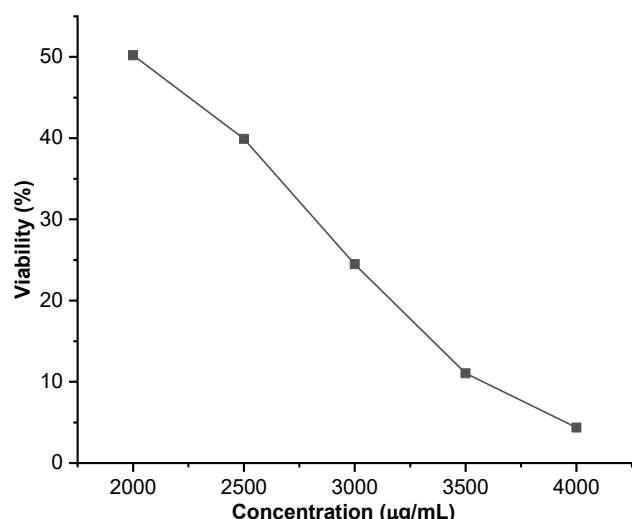


**Fig 8.** Graph of pre-osteoblast cell viability at various concentrations of the HASiO<sub>2</sub>\_PE composite

be due to the synergy of HASiO<sub>2</sub> and PE has produced a higher antibacterial activity toward a gram-negative than a gram-positive bacterium. It may also be due to the small amount of PE (10%) compared to HASiO<sub>2</sub>. The antibacterial activity toward *S. aureus* can be increased by increasing the PE content in the composite.

The cytotoxicity test of HASiO<sub>2</sub>\_PE composite was conducted by MTT assays with an incubation time of 24 h using *pre-osteoblast* cells. Percent viability decreased non-linearly with the concentration of HASiO<sub>2</sub>\_PE (Fig. 8). The calculation obtained the IC<sub>50</sub> value = 2092 µg/mL with R<sup>2</sup> = 0.9446. These data indicate that the HASiO<sub>2</sub>\_PE composite is non-toxic or biocompatible and can be accepted by bone cells [32-33]. A comparison of the cells' state in control and in the 2000 µg/mL of HASiO<sub>2</sub>\_PE resulted in the different numbers of cells or cell population (Fig. 9). Some cells seem to change in shape and size, the shape changes to round, and the size becomes smaller. Based on the IC<sub>50</sub> value and the cell morphology profile, it is feasible to conclude that the CPC made from the HASiO<sub>2</sub>\_PE composite is biocompatible [12]. The composite will promote osteoblast proliferation and is predicted to play positive roles in osteoblast differentiation and next to the mineralized bone matrix formation [34-35].

## CONCLUSION

Compositing 10% (w/w) PE and HASiO<sub>2</sub> did not affect the HA crystal structure in which the lattice parameters are counted as a = b = 9.47 Å, c = 6.92 Å, and lattice volume = 5374 Å<sup>3</sup>. The HA crystallite size is close to bone mineral size (> 40 nm). The composite has a

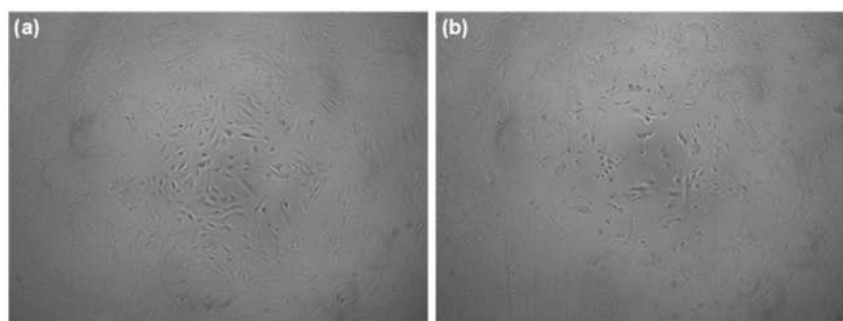


**Fig 9.** Morphological differences between (a) control cells and (b) HASiO<sub>2</sub>\_PE 2000 µg/mL in the cytotoxicity test with the MTT assay



morphology that is coarser and denser than HASiO<sub>2</sub>. PE that contributes antibacterial activity can be found on the composite's surface. Both HASiO<sub>2</sub> and the composite have a relatively similar surface area, total pore volume, and average pore size. Compositing PE with HASiO<sub>2</sub> decreased its antibacterial activity toward *S. aureus* but increased its antibacterial activity against *E. coli*. The composite is non-toxic due to the IC<sub>50</sub> of 2092 µg/mL when tested with pre-osteoblast cells. As long as the non-toxic property can be maintained, increasing the PE content in the composite is recommended to boost the antibacterial activity toward *S. aureus*.

### ■ ACKNOWLEDGMENTS

The authors gratefully acknowledge Faculty of Mathematics and Sciences, Universitas Diponegoro, Semarang, Indonesia for the financial support through the research grant "Riset Madya" with the contract number: 1263J/UN7.5.8/PP/2022.

### ■ AUTHOR CONTRIBUTIONS

Tri Windarti, Nor Basid Adiwibawa Prasetya, and Ngadiwiyana carried out the experiment, Limpat Nulandaya carried out the refinement of XRD data, all authors analyzed data and wrote the manuscript.

### ■ REFERENCES

- [1] Flurin, L., Greenwood-Quaintance, K.E., and Patel, R., 2019, Microbiology of polymicrobial prosthetic joint infection, *Diagn. Microbiol. Infect. Dis.*, 94 (3), 255–259.
- [2] Tubb, C.C., Polkowksi, G.G., and Krause, B., 2020, Diagnosis and prevention of periprosthetic joint infections, *J. Am. Acad. Orthop. Surg.*, 28 (8), e340–e348.
- [3] Izakovicova, P., Borens, O., and Trampuz, A., 2019, Periprosthetic joint infection: Current concepts and outlook, *EFORT Open Rev.*, 4 (7), 482–494.
- [4] Lipsky, B.A., Weigelt, J.A., Gupta, V., Killian, A., and Peng, M.M., 2007, Skin, soft tissue, bone, and joint infections in hospitalized patients: Epidemiology and microbiological, clinical, and economic outcomes, *Infect. Control Hosp. Epidemiol.*, 28 (11), 1290–1298.
- [5] Maaloum, Y., Meybeck, A., Olive, D., Boussekey, N., Delannoy, P.Y., Chiche, A., Georges, H., Beltrand, E., Senneville, E., d'Escrivan, T., and Leroy, O., 2013, Clinical spectrum and outcome of critically ill patients suffering from prosthetic joint infections, *Infection*, 41 (2), 493–501.
- [6] Ginebra, M.P., Espanol, M., Montufar, E.B., Perez, R.A., and Mestres, G., 2010, New processing approaches in calcium phosphate cements and their applications in regenerative medicine, *Acta Biomater.*, 6 (8), 2863–2873.
- [7] Akao, M., Aoki, H., and Kato, K., 1981, Mechanical properties of sintered hydroxyapatite for prosthetic applications, *J. Mater. Sci.*, 16 (3), 809–812.
- [8] Moheet, I.A., Luddin, N., Ab Rahman, I., Masudi, M., Kannan, T.P., and Nik Abd Ghani, N.R., 2018, Evaluation of mechanical properties and bond strength of nano-hydroxyapatite-silica added glass ionomer cement, *Ceram. Int.*, 44 (8), 9899–9906.
- [9] Villacampa, A.I., and García-Ruiz, J.M., 2000, Synthesis of a new hydroxyapatite-silica composite material, *J. Cryst. Growth*, 211 (1), 111–115.
- [10] Lei, C., Cao, Y., Hosseinpour, S., Gao, F., Liu, J., Fu, J., Staples, R., Ivanovski, S., and Xu, C., 2021, Hierarchical dual-porous hydroxyapatite doped dendritic mesoporous silica nanoparticles based scaffolds promote osteogenesis *in vitro* and *in vivo*, *Nano Res.*, 14 (3), 770–777.
- [11] Windarti, T., Widjijono, W., and Nuryono, N., 2021, Deposition of hydroxyapatite on silica made from rice husk ash to produce powder component of calcium phosphate cement, *Indones. J. Chem.*, 21 (3), 588–597.
- [12] Qiao, Y., Zhai, Z., Chen, L., and Liu, H., 2015, Cytocompatible 3D chitosan/hydroxyapatite composites endowed with antibacterial properties: toward a self-sterilized bone tissue engineering scaffold, *Sci. Bull.*, 60 (13), 1193–1202.
- [13] Yang, Y., Campbell Ritchie, N., and Everitt, N.M., 2021, Recombinant human collagen/chitosan-based soft hydrogels as biomaterials for soft tissue engineering, *Mater. Sci. Eng., C*, 121, 111846.

- [14] Shu, X., Liao, J., Wang, L., Shi, Q., and Xie, X., 2020, Osteogenic, angiogenic, and antibacterial bioactive nano-hydroxyapatite co-synthesized using  $\gamma$ -polyglutamic acid and copper, *ACS Biomater. Sci. Eng.*, 6 (4), 1920–1930.
- [15] Li, Z., Zhou, P., Zhou, F., Zhao, Y., Ren, L., and Yuan, X., 2018, Antimicrobial eugenol-loaded electrospun membranes of poly( $\epsilon$ -caprolactone)/gelatin incorporated with REDV for vascular graft applications, *Colloids Surf., B*, 162, 335–344.
- [16] Modjinou, T., Versace, D.L., Abbad-Andaloussi, S., Langlois, V., and Renard, E., 2017, Antibacterial and antioxidant photoinitiated epoxy co-networks of resorcinol and eugenol derivatives, *Mater. Today Commun.*, 12, 19–28.
- [17] Li, M., Yu, H., Xie, Y., Guo, Y., Cheng, Y., Qian, H., and Yao, W., 2021, Fabrication of eugenol loaded gelatin nanofibers by electrospinning technique as active packaging material, *LWT*, 139, 110800.
- [18] Xu, H., Zhang, D., and Li, J., 2019, Antibacterial nanoparticles with universal adhesion function based on dopamine and eugenol, *J. Bioresour. Bioprod.*, 4 (3), 177–182.
- [19] Melendez-Rodriguez, B., Figueroa-Lopez, K.J., Bernardos, A., Martínez-Máñez, R., Cabedo, L., Torres-Giner, S., and Lagaron, J.M., 2019, Electrospun antimicrobial films of poly(3-hydroxybutyrate-co-3-hydroxyvalerate) containing eugenol essential oil encapsulated in mesoporous silica nanoparticles, *Nanomaterials*, 9 (2), 227.
- [20] Saltan, F., 2021, Preparation of poly(eugenol-co-methyl methacrylate)/polypropylene blend by creative route approach: Structural and thermal characterization, *Iran. Polym. J.*, 30 (11), 1227–1236.
- [21] Predoi, S.A., Ciobanu, C.S., Motelica-Heino, M., Chifiriuc, M.C., Badea, M.L., and Iconaru, S.L., 2021, Preparation of porous hydroxyapatite using cetyl trimethyl ammonium bromide as surfactant for the removal of lead ions from aquatic solutions, *Polymers*, 13 (10), 1617.
- [22] Li, Y., Tjandra, W., and Tam, K.C., 2008, Synthesis and characterization of nanoporous hydroxyapatite using cationic surfactants as templates, *Mater. Res. Bull.*, 43 (8-9), 2318–2326.
- [23] Larsson, S., Stadelmann, V.A., Arnoldi, J., Behrens, M., Hess, B., Procter, P., Murphy, M., and Pioletti, D.P., 2012, Injectable calcium phosphate cement for augmentation around cancellous bone screws. In vivo biomechanical studies, *J. Biomech.*, 45 (7), 1156–1160.
- [24] Fahami, A., Beall, G.W., and Betancourt, T., 2016, Synthesis, bioactivity and zeta potential investigations of chlorine and fluorine substituted hydroxyapatite, *Mater. Sci. Eng., C*, 59, 78–85.
- [25] Malakauskaite-Petruleviciene, M., Stankeviciute, Z., Niaura, G., Prichodko, A., and Kareiva, V., 2015, Synthesis and characterization of sol-gel derived calcium hydroxyapatite thin films spin-coated on silicon substrate, *Ceram. Int.*, 41 (6), 7421–7428.
- [26] da Silva Brum, I., de Carvalho, I.I., da Silva Pires, J.L., de Carvalho, M.A.A., dos Santos, L.B.F., and Elias, C.N., 2019, Nanosized hydroxyapatite and  $\beta$ -tricalcium phosphate composite: Physico-chemical, cytotoxicity, morphological properties and *in vivo* trial, *Sci. Rep.*, 9 (1), 19602.
- [27] Singh, G., Jolly, S.S., and Singh, R.P., 2020, Cerium substituted hydroxyapatite mesoporous nanorods: Synthesis and characterization for drug delivery applications, *Mater. Today: Proc.*, 28, 1460–1466.
- [28] Wilson, O.C., and Hull, J.R., 2008, Surface modification of nanophase hydroxyapatite with chitosan, *Mater. Sci. Eng., C*, 28, 434–437.
- [29] Fuh, L.J., Huang, Y.J., Chen, W.C., and Lin, D.J., 2017, Preparation of micro-porous bioceramic containing silicon-substituted hydroxyapatite and beta-tricalcium phosphate, *Mater. Sci. Eng., C*, 75, 798–806.
- [30] Hajimirzaee, S., Chansai, S., Hardacre, C., Banks, C.E., and Doyle, A.M., 2019, Effects of surfactant on morphology, chemical properties and catalytic activity of hydroxyapatite, *J. Solid State Chem.*, 276, 345–351.
- [31] Prasetya, N.B.A., Asiyah, A., Sarjono, P.R., Ngadiwiyana, N., and Ismiyanto, I., 2021, Synthesis

- of sulfonated poly-(eugenol divinylbenzene) nanosilver composite and its application as antibacterial compound of cotton fabric, *J. Phys.: Conf. Ser.*, 1943, 012183.
- [32] Baharum, Z., Akim, A.M., Taufiq-Yap, Y.H., Hamid, R.A., and Kasran, R., 2014, *In vitro* antioxidant and antiproliferative activities of methanolic plant part extracts of *Theobroma cacao*, *Molecules*, 19 (11), 18317–18331.
- [33] Atjanasuppat, K., Wongkham, W., Meepowpan, P., Kittakooop, P., Sobhon, P., Bartlett, A., and Whitfield, P.J., 2009, *In vitro* screening for anthelmintic and antitumour activity of ethnomedicinal plants from Thailand, *J. Ethnopharmacol.*, 123 (3), 475–482.
- [34] Noor, M., Al Mamun, M.A., Atique Ullah, A.K.M., Matsuda, A., Kawamura, G., Hakim, M.A., Islam, M.F., and Matin, M.A., 2021, Physics of  $Ce^{3+} \leftrightarrow Ce^{4+}$  electronic transition in phytosynthesized  $CeO_2/CePO_4$  nanocomposites and its antibacterial activities, *J. Phys. Chem. Solids*, 148, 109751.
- [35] Liu, J.L., Zhang, B., Song, S.J., Ma, M., Si, S.Y., Wang, Y.H., Xu, B.X., Feng, K., Wu, J.G., and Guo, Y.C., 2014, Bovine collagen peptides compounds promote the proliferation and differentiation of MC3T3-E1 pre-osteoblasts, *PLoS One*, 9 (6), e99920.

## Anticancer Activity of Venom Protein Hydrolysis Fraction of Equatorial Spitting Cobra (*Naja sumatrana*)

Naseer Ahmed<sup>1</sup>, Garnis Putri Erlista<sup>1</sup>, Tri Joko Raharjo<sup>1\*</sup>,  
Respati Tri Swasono<sup>1</sup>, and Slamet Raharjo<sup>2</sup>

<sup>1</sup>Department of Chemistry, Faculty of Mathematics and Natural Sciences, Universitas Gadjah Mada, Sekip Utara, Yogyakarta 55281, Indonesia

<sup>2</sup>Department Internal Medicine, Faculty of Veterinary Medicine, Universitas Gadjah Mada, Sekip Utara, Yogyakarta 55281, Indonesia

\* **Corresponding author:**

email: trijr\_mipa@ugm.ac.id

Received: December 28, 2022

Accepted: January 30, 2023

DOI: 10.22146/ijc.80720

**Abstract:** Bioactive peptides play an important role in targeting cancer cells. Venom protein from *Naja sumatrana* can be explored as a source of bioactive peptides. This research aims to identify and study the molecular docking of bioactive peptides (BPs) from trypsin hydrolysate of *N. sumatrana* venom protein which was fractionated using an SPE C<sub>18</sub> column. The venom of *N. sumatrana* was hydrolyzed with trypsin enzyme. The protein hydrolysate was then fractionated using an RP-SPE HyperSep Retain PEP column, and the peptide fractions were tested for their anticancer activity against MCF-7 breast cancer cells using the (3-(4,5-dimethylthiazol-2-yl)-2,5-diphenyltetrazolium bromide (MTT) method. Identification of peptides in the active fraction was carried out through high-resolution mass spectrometry. The identified peptides were molecularly docked with the EGFR receptor using AutoDock Vina. The results showed that the degree of hydrolysis was 74.7%. The 75% methanol fraction is the active fraction against MCF-7 cells, with an IC<sub>50</sub> value of 4.80 µg/mL and a selectivity index of 5.00. Peptide-active anticancer fractions with the sequence of NSLLVK, SLLVK and TVPVKR were successfully identified and exhibited high binding affinity values, good RMSD values, and the most suitable model for the epidermal growth factor receptor.

**Keywords:** bioactive peptides; trypsin; venom; *N. sumatrana*; molecular docking

### ■ INTRODUCTION

Globally, cancer is regarded as a major health problem. Based on the Global Cancer Statistics published in 2015, there were around 32.6 million cancer patients worldwide in 2012 [1]. Furthermore, the WHO reported that in 2019 cancer was the leading cause of death before the age of 70 [2]. Breast cancer is the second leading cause of death due to conventional drug resistance [3]. The use of chemotherapy, surgery and radiation therapy using anticancer drugs can cause side effects. This treatment cannot differentiate between normal cells and cancer cells, resulting in systemic toxicity [4]. Thus, the discovery of new drugs with high selectivity and specificity is needed for overcoming cancer.

Bioactive peptides (BPs) derived from animals are able to target cancer cells so that they can function as anticancer agents and are less toxic to normal cells. BPs consist of 2–50 amino acid residues (10<sup>2</sup>–10<sup>3</sup> Da), so they easily disrupt cell membranes and result in apoptosis or necrosis [5]. Consequently, BPs become promising alternative candidates for the development of a new generation of anticancer therapies [6]. One source of bioactive peptides can be obtained from snake venom. The therapeutic use of snake venom has been widely carried out by scientists. Protein components, peptides, and chemical compounds in snake venom have a high potential for toxicity. Snake venom contains a complex mixture of peptides, proteins, enzymes, carbohydrates, and minerals with low molecular masses and certain

biological activities [7]. L-amino acid oxidases (LAAOs), phospholipase A<sub>2</sub> (PLA<sub>2</sub>), three-finger toxins (3FTxs), the snake venom metalloprotease family (SVMP), cobra venom factor (CVF), and cysteine-rich secretory protein (CRISP) are some of the components that have been isolated from various snake venoms which can be used as anticancer agents [8].

Research [9] reported that croptamine, a short 42-amino acid polypeptide stabilized by cysteine, has shown *in vitro* and *in vivo* toxicity to cancer cells in a melanoma mouse model with concentrations of 5 µg/mL, which was lethal to B16-F10 (murine melanoma cells), SK-Mel-28 (human melanoma cells), and Mia PaCa-2 (human pancreatic carcinoma cells) but not in normal cells. Studies revealed that snake venom contains specific molecules that can slow down cancer cells [10]. The svPLA<sub>2</sub> component of the *Bothrops jararacussu* venom shows anticancer activity against MDA-MB-231 triple-negative breast cancer cells [11]. Bioactive peptides from snake venom can contribute significantly to medical treatment and specifically target cancer cell membranes [12]. Bioactive peptides can be encoded in snake venom proteins, and after cleavage, they have more active biological activity as an anticancer [13]. Among several methods of producing bioactive peptides from protein precursors, the most commonly used is enzymatic hydrolysis [14-15].

The enzymatic hydrolysis method uses controlled pH and temperature conditions to reduce the formation of unwanted products [16]. The trypsin enzyme has been widely utilized for the identification of bioactive peptides, which usually cleaves the peptide bond at the C-terminal end of amino acids (R or K), but not when they are next to the P amino acid. Eel protein hydrolysate (EPH) with a molecular weight of 3 kDa showed the highest inhibition of MCF-7 breast cancer cells with an IC<sub>50</sub> value of 6.50 µg/mL [17]. Studies on protein hydrolysate of oyster (*Saccosrea cucullata*) reported that the peptide sequence Leu-Ala-Asn-Ala-Lys exhibited anticancer activity against human colon carcinoma (HT-29) cell lines [18]. The different structural sequences of the bioactive peptides are unique so that they can interact with the active sites of the substrates. Unique peptide sequences can be used to determine the mechanism of anticancer

action, such as being able to destroy cancer cells through apoptosis and necrosis by membrane lysis or pore formation [19]. The mechanism of action of anticancer peptides can be ascertained by the interaction of peptides with inhibitors through molecular docking. Docking is a computational technique capable of predicting the conformation and interaction of a ligand with a particular protein. Molecular docking is an approach utilized to more easily identify the mechanism of peptide action [20].

Based on previous research, this study aims to identify BPs from *N. Sumatrana* venom protein hydrolysate fractionated using an SPE C<sub>18</sub> column. The anticancer activity of the fractions was tested against MCF-7 breast cancer cells. High-resolution mass spectrometry was then used to identify BPs in the active fraction. After identifying the BPs, a docking study was carried out to examine the interaction of the peptide with the active site of the receptor, which determines the mechanism of action.

## ■ EXPERIMENTAL SECTION

### Materials

Materials and chemicals included in this research were *N. Sumatrana* venom, trypsin USP (G-Bioscience), trypsin sequence grade enzyme (Merck), SPE C<sub>18</sub> column (HyperSep Retain PEP, Supelco, Thermo Scientific), ammonium bicarbonate 0.05 M (Sigma-Aldrich®), and methanol (Merck). Meanwhile, anticancer activities were carried out by using Dulbecco's Modified Eagle Medium (DMEM) media, MTT solution, 0.05% trypsin, amphotericin B (fungizone), phosphate buffer saline (PBS) solution, penicillin-streptomycin 2%, fetal bovine serum (FBS) from Sigma-Aldrich, a breast cancer cell line (MCF-7), a normal cell line (Vero), and doxorubicin (Kalbe).

### Instrumentation

The Instrumentations used in this study were Amicon® ultra-15 (3000 Da MWCO centrifugal filter, Merck), UV-Vis Spectrophotometer (Shimadzu UV 1800), Centrifuge (Biofuge Primo R Centrifuge 7590, Thermo Scientific), Inverted Microscope (Olympus

CKX41), Elisa Reader (Bio-Rad 680 XR), High-Resolution Mass Spectrometry (HRMS, Q-Exactive Hybrid Quadrupole-Orbitrap Mass Spectrometer Thermo Scientific), and Proteome Discoverer Ver. 2.5 software (Thermo Scientific).

## Procedure

### **Sample collection of venom and protein extraction**

*N. sumatrana* venom ( $\pm 150$  mg) was collected from Bhumi Merapi, Yogyakarta, by experienced veterinarians specializing in exotic animals at the Faculty of Veterinary Medicine, UGM. Venom collection was carried out by following the protocol that has been ethically approved according to the letter number 0052/EC-FKH/Ex./2020. The venom was lyophilized and stored in a refrigerator at  $-20$  °C until use. The lyophilized venom (20 mg) was dissolved in 0.05 M ammonium bicarbonate. Venom protein and small molecules were separated with Amicon® ultra-15 with 3000 Da MWCO. The concentration of protein was determined with a UV-Vis spectrophotometer.

### **Proteomic analysis of *N. sumatrana***

A trypsin sequence grade enzyme solution was added to the protein venom solution with a ratio of 1:20 (w/w), and then the solution was incubated at 37 °C overnight. After 24 h of incubation, the sample was put into an oven at 80 °C to stop the hydrolysis process, then centrifuged at  $5000\times g$  for 45 min. Supernatants were filtered with a 0.22  $\mu\text{m}$  filter membrane, and a total of 5  $\mu\text{L}$  of the sample was transferred into injection vials for analysis using LC-HRMS. Proteome Discoverer software version 2.5 was used to process the raw MS chromatogram data. The database uses *N. naja* because the *N. sumatrana* database is not yet available. The *N. naja* database was downloaded from UniProt.org.

### **Hydrolysis of venom protein**

*N. sumatrana* protein hydrolysate is produced by hydrolysis of venom protein using the same method as the proteome analysis procedure, but the quantities and grades of the trypsin enzyme are different for preparative purposes. Then the absorbance of the protein hydrolysate obtained was measured with a UV-Vis spectrophotometer at a wavelength of 280 nm to determine the degree of hydrolysis.

### **Fractionation of venom hydrolysate using reversed-phase SPE column**

Fractionation was carried out with a 1 mL column of HyperSep Retain PEP Cartridge in an SPE chamber equipped with a manifold vacuum pump.  $2 \times 0.5$  mL of methanol was used to condition the column, and  $2 \times 0.5$  mL of distilled water was used to balance it. The procedure was terminated when the sample level was just above the adsorbent by progressively pushing the sample into the column using a pump. After washing the column with  $2 \times 0.5$  mL of 5% methanol, methanol at various concentrations of 25, 50, 75, and 100% was used to elute the column. Each obtained fraction's absorbance was measured at a wavelength of 280 nm using the UV-Vis spectrophotometer to calculate the protein concentration in each fraction [21].

### **Anticancer activity test**

A total of 100  $\mu\text{L}$  of cell culture medium was added into 96-well plates where three wells were kept specific for media control and three other wells for control cells. The cell's plate was incubated at 37 °C for 24 h in a 5%  $\text{CO}_2$  flow to recover cell conditions after culturing. The media in the test well was emptied, and 100  $\mu\text{L}$  of the solution was added in a series created by diluting the media. Each series of concentrations, whether cancer cells or normal cells, was repeated three times. The test was also conducted on doxorubicin as a positive control and then incubated for 24 h in an incubator with a 5%  $\text{CO}_2$  flow at 37 °C. After incubation, the media sample was removed and 0.5 mg/mL of MTT solution was prepared in a 10 ml media culture with 100  $\mu\text{L}$  added to each well, including control media (without cells). They were incubated again for 4 h until a formazan (purple) color appeared. It was then observed under an inverted microscope at  $20\times$  magnification, and a 100  $\mu\text{L}$  stopper SDS 10% was added. The 96-well plates were wrapped in paper and incubated in the dark at room temperature overnight. After that, those plates were put into the Elisa Reader to be measured by the absorbance at 595 nm and the half-maximal inhibitory concentration ( $\text{IC}_{50}$ ) value was calculated. The percentage of cell inhibition obtained from each sample concentration was calculated using the following Eq. (1):

$$\% \text{ inhibition} = \frac{\text{Absorbance control} - \text{Absorbance sample}}{\text{Absorbance control}} \quad (1)$$

The selectivity index was obtained from the IC<sub>50</sub> ratio of Vero cells compared to the IC<sub>50</sub> of MCF-7 cancer cells. The selectivity index was calculated using the following Eq. (2):

$$\text{Selectivity index} = \frac{\text{IC}_{50} \text{ Vero cell}}{\text{IC}_{50} \text{ MCF-7 cell}} \quad (2)$$

### Identification of anticancer peptides

An Acclaim® PepMap RSLC column was used for HRMS analysis of the active anticancer fraction (C<sub>18</sub>, 75 m × 150 cm). The mobile phase was divided into two categories: mobile phase A containing water and 0.05% trifluoroacetic acid (TFA), and mobile phase B containing water, acetonitrile 20:80, and 0.1% TFA. Then, a gradient was applied using both mobile phases at a flow rate of 0.1 mL/min. By using full MS/ddMS<sup>2</sup> mode and *m/z* range of 150–2250, peptides were examined by MS/MS. Split power was set to 140,000 (FWHM) for the complete MS parameter, and the resolution was set to 17,500 for the ddMS<sup>2</sup> parameter (FWHM). The MS data were examined by utilizing Proteome Discoverer Software ver. 2.5 using the *N. naja* genome downloaded from UniProt.org.

### The peptide's molecular docking with EGFR

Peptides from the active fraction were docked with the EGFR receptor to examine the interaction of bioactive peptides with the EGFR receptor. The EGFR receptor was downloaded from the RCSB Protein Data Bank (PDB ID: 1M17). Peptide structures were drawn in a Gaussian view and semiempirically optimized with Gaussian. AutoDock Vina was employed to simulate docking, and Discovery Studio was used to visualize the results. AutoDock Vina has up to twice the speed compared to AutoDock 4. In addition to increased speed, AutoDock Vina has increased accuracy and significantly more predictable binding modes than AutoDock 4. Then, the value with the lowest binding affinity was chosen.

## RESULTS AND DISCUSSION

### Proteomic of *N. sumatrana* Venom

Analyses of proteomics were performed using HRMS. The results showed that there were 14 identified proteins, consisting of enzymatic and non-enzymatic proteins, in *N. sumatrana* venom originating from Sumatra, which is presented in Table 1. The main protein

**Table 1.** *N. sumatrana* enzymatic and non-enzymatic protein identified in proteome analysis

No.	Accession number	Protein	Length (Amino acid residues)	MW (kDa)	Calc. pI
Enzymatic protein					
1	Q9PVK7	Zinc metalloproteinase-disintegrin-like cobrin	600	67.6	6.3
2	A4FS04	Acidic phospholipase A2 natratoxin	119	13.2	5.1
3	D3TTC2	Zinc metalloproteinase disintegrin-like atragin	613	69.1	6.4
4	V8P395	Glutathione peroxidase (Fragment)	264	29.6	8.1
5	A0A2I4HXH5	Snake venom 5'-nucleotidase (Fragment)	529	58.2	7.3
6	A8QL58	L-amino-acid oxidase (Fragment)	507	57.9	8.5
7	Q10749	Snake venom metalloproteinase-disintegrin-like mocarhagin	609	68.1	6.7
8	A0A2D0TC04	Venom phosphodiesterase	830	94.6	7.8
Non-enzymatic protein					
9	P60309	Cytotoxin SP15d	60	6.6	9.4
10	P60308	Cytotoxin SP15c	60	6.8	9.1
11	P82885	Thaicobrin	108	12.0	9.1
12	P60306	Cytotoxin SP13b	60	6.8	9.2
13	P01140	Venom nerve growth factor	116	13.0	6.1
14	Q91132	Cobra venom factor	1642	184.4	6.4

families of *N. sumatrana* were detected, such as phospholipase A<sub>2</sub> (PLA<sub>2</sub>) and three-finger toxins (3FTxs). Previous studies also reported that the two main categories of *N. sumatrana* proteins identified by LC-MS were phospholipase A<sub>2</sub> and three-finger toxins (5 neurotoxins and 9 cardiotoxins, or cytotoxins). In addition, proteins such as thaicobrin, aminopeptidase, zinc metalloproteinase-disintegrin (cobrin), CRISP, cobra venom factor, cobra serum albumin, and natriuretic peptide were also identified [21]. *N. sumatrana* venom from four different regions, namely Penang, Negeri Sembilan, Southern Thailand, and Sumatra, showed that the three-finger toxins (3FTxs) components followed by phospholipase A<sub>2</sub> (PLA<sub>2</sub>) were the main proteins present in all *N. sumatrana* venoms. Seven protein families were consistently identified from the four regions, including three-finger toxins (3FTX), phospholipase A<sub>2</sub> (PLA<sub>2</sub>), phosphodiesterase (PDE), L-amino acid oxidase (LAAO), venom nerve growth factor (vNGF), snake venom metalloproteinase (SVMP), and cobra venom factor (CVF) [22].

Components of snake venom, such as PLA<sub>2</sub>, are enzymatic proteins that have various pharmacological activities and are usually present in snake venom [23]. The PLA<sub>2</sub> enzymatic protein detected in *N. sumatrana* venom is diverse and contains acidic PLA<sub>2</sub> in almost every cobra [24]. Cytotoxin SP15d, cytotoxin SP15c, and cytotoxin SP13b consist of 60 amino acids with molecular weights of 6.6, 6.8 and 6.8 kDa, respectively, and isoelectric points of 9.45, 9.14 and 9.29, respectively. Cytotoxin SP15d mostly shows cytolytic activity in various cells and functions to bind heparin with high affinity and create pores in the lipid membrane of organisms [25]. Cytotoxin SP13b and SP15c have their isoelectric points in the hydrophobic zone. Cytotoxin SP13b is an S-type cytotoxin that exhibits a high isoelectric point so that this protein can penetrate the membrane [26]. Cobra cytotoxins (CTX) can also be known as cardiotoxins, which are generally present in the cobra venom of *Naja* spp. [27]. This type of venom is involved in the pathogenesis of cytotoxicity and tissue necrosis [28]. Thaibobrin consists of 108 amino acids, has a molecular weight of 12 kDa, and an isoelectric point of 9.11. Venom

phosphodiesterase consists of 830 amino acids with a molecular weight of 94.6 kDa and an isoelectric point value of 7.8. L-amino oxidase consists of 507 amino acids with a molecular weight of 57.9 kDa, has a relatively high isoelectric point of 8.5, and exhibits hydrophobic properties. The minor protein components identified in the *N. sumatrana* venom, such as SVMP, CVF, vNGF, PDE, and SVSP, generally have high molecular weights. These components play a role in the inflammatory response as well as facilitate the spread of venom during venomous snake bites [29].

### Hydrolysis of Venom Protein

Bioactive peptides are obtained by hydrolyzing them from protein sources. The enzymatic hydrolysis method is easy to carry out, controllable and can maintain the amino acid structure. In this study, *N. sumatrana* venom protein was hydrolyzed with the trypsin enzyme to obtain bioactive peptides. The enzyme hydrolyzes the peptide bonds on the carboxylic side of lysine and arginine [30]. In the trypsin enzyme, there is a negatively charged aspartic acid catalytic bag that is responsible for binding the basic amino acids with a positive charge [31]. This enzyme works optimally in the pH range of 7.5–8.5 and at a temperature of 37 °C. Combinations such as temperature conditions, type of enzyme, pH, and concentration of protein substrates are needed for enzyme activity to maximize the degree of hydrolysis [32]. The degree of hydrolysis is the ratio of the number of peptides cleaved during hydrolysis to the total number of peptide bonds in the protein mass [33]. In the current study, the degree of hydrolysis was 74.7%. In previous research [34], trypsin was utilized to hydrolyze *Jatropha* seed protein and achieved a degree of hydrolysis of 82.1%. Protein hydrolysis with trypsin can hydrolyze up to 65.9% of proteins [35]. Protein from epiphytic bacteria associated with the brown algae *Sargassum* sp. was successfully hydrolyzed with the trypsin enzyme, resulting in a degree of hydrolysis of 27% in 9 h [36]. Soy protein was hydrolyzed using trypsin, resulting in a degree of hydrolysis of 20.4% [37]. The high percentage of hydrolysis value indicates that the hydrolysis is going well.



### Anticancer Activity

A cytotoxicity test of venom protein, protein hydrolysate, and anticancer peptide fraction was performed on MCF-7 breast cancer cells and normal cells (Vero) with  $IC_{50}$  as a parameter. The smaller the  $IC_{50}$  value, the higher the potential of the test compound. Tests on Vero cells were conducted to determine the selectivity index value of the samples tested. The anticancer activity was tested using the MTT assay, where the reduction of tetrazolium salt to formazan produced a purple color. The more purple formazan crystals formed indicate that the cells are alive. The  $IC_{50}$  values of venom protein, protein hydrolysate, and peptide fractions are presented in Table 2. The venom protein produced a smaller  $IC_{50}$  value for MCF-7 cells or Vero cells compared to that of protein hydrolysate and had a selectivity index of 9.12. The selectivity index was calculated by dividing the  $IC_{50}$  value of normal cells by the  $IC_{50}$  value of MCF-7 cancer cells. If the selectivity index is higher than 2, this sample can be used as an anticancer agent [38]. The greater selectivity index, the higher the selectivity. Samples with high selectivity can kill cancer cells but are safe for normal cells.

Based on the results of the four fractions, the 75% methanol fraction produced a relatively smaller  $IC_{50}$  value with a selectivity index of 5.00 compared to the other fractions Table 2. This proves that the 75% methanol fraction has high selectivity. BPs can inhibit the active site of the MCF-7 cancer cell line and cause anticancer activity

[39]. Crude venom of *N. sumatrana* showed concentration-dependent cytotoxic activity against lung cancer cells (A549), prostate cancer cells (PC-3), and MCF-7 cancer cells with an  $IC_{50}$  value of  $0.88 \pm 0.06$ ,  $3.13 \pm 0.58$ , and  $9.10 \pm 0.56$   $\mu\text{g/mL}$ , respectively. The highest selectivity was produced by lung cancer cells (A549), which was 2.17 [28]. Even though the anticancer activity of *N. sumatrana* venom has not been widely reported, proteomics of *N. sumatrana* venom has identified anticancer proteins such as  $PLA_2$ , neurotoxin, and cardiotoxin. A previous study has found that phospholipase  $A_2$  ( $PLA_2$ ) purified from *Daboia russelii siamensis* venom contains anticancer activity [40]. However, peptides derived from the hydrolysis of *N. sumatrana* trypsin venom as anticancer agents have never been studied before. The current study is the first to conduct this topic.

The appearance of purple formazan crystals could be seen after the addition of MTT to control MCF-7 cells (Fig. 1(a)) and control Vero cells (Fig. 1(c)). Both control cells formed a lot of formazan crystals, which indicates that many cells were alive. The concentration determines the amount of purple formazan crystals formed. This study used a variety of concentrations: 7.8125; 15.625; 31.25; 62.5; 125; 250; and 500  $\mu\text{g/mL}$ . The greater the concentration is given, the smaller of cell viability percentage and the more cells die (no purple formazan is formed). Meanwhile, adding 75% methanol

**Table 2.** Anticancer activity of venom, hydrolyzed venom protein, and the peptide fractions

Sample	Toxicity		Selectivity index
	Cell line	$IC_{50}$ ( $\mu\text{g/mL}$ )	
Venom protein	MCF-7	6.16	9.12
	Vero	56.23	
Protein hydrolysate	MCF-7	398.10	2.29
	Vero	912.01	
Fraction of 25% methanol	MCF-7	20.42	2.60
	Vero	52.50	
Fraction of 50% methanol	MCF-7	16.10	1.16
	Vero	18.60	
Fraction of 75% methanol	MCF-7	4.80	5.00
	Vero	24.00	
Fraction of 100% methanol	MCF-7	12.02	0.46
	Vero	5.50	

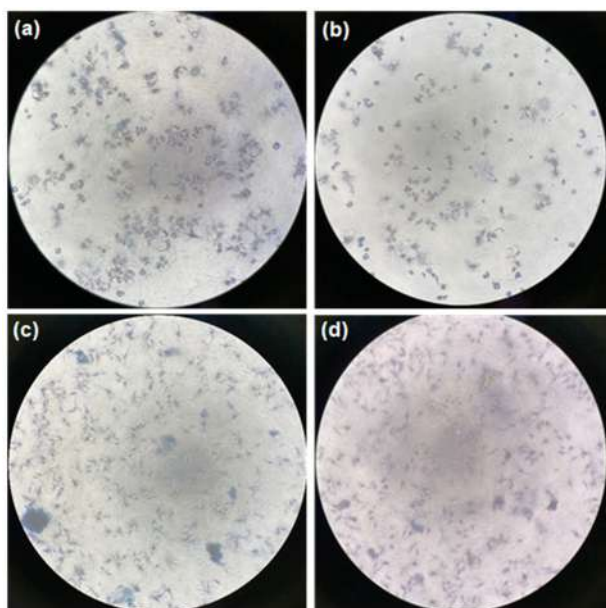


**Fig 1.** Microscopic images of untreated MCF-7 cell (a), MCF-7 cell treated with 75% methanol fraction (b), untreated Vero cell (c) and Vero cell treated with 75% methanol fraction (d)

fraction to MCF-7 cells (Fig. 1(b)) caused fewer purple-colored formazan crystals to form, implying that many cells died when treated with the active fraction. When 75% methanol fraction was added to Vero cells (Fig. 1(d)), the number of purple formazan crystals was not much different from that of the control Vero cells. Thus, it can be said that the administration of the active fraction did not kill all the Vero cells.

### Identification of Anticancer Peptides

HRMS was employed to identify the peptide

sequence of the active fraction as an anticancer. Using HRMS for peptide identification has been successful in determining the active fraction of peptides [34-35,41]. The *N. sumatrana* database is not yet available in the transcriptome database with Proteome Discover version 2.5, which includes the Sequest and Mascot search algorithms. The peptide sequence of the active fraction consisting of four peptides is presented in Table 3.

According to the database of peptides based on the genome of *Ophiophagus hannah*, the NSLLVK peptide was identified, and it was eluted at a retention time of 7.0383 min. The result obtained  $[M-H]^+ = 673.42290$  Da, with a  $z = +2$ , MS<sup>2</sup> fragmentation with mono  $m/z = 337.21509$  Da. Its GRAVY Score was 0.600, and the pI was 8.75. It was lysed from protein-tyrosine-phosphatase, EC 3.1.3.48, at a location of 562–567 amino acids. The mass spectra of the NSLLVK are displayed in Fig. 2(a).

Ion  $y_1^+ = 147.11237$  confirmed the presence of K amino acids at the end of the C-terminal peptide. The mass difference between the  $y_2^+$  ion (246.18051) and the  $y_1^+$  ion confirmed the presence of V (99.06814), leading to a sequence of VK at the C-terminus. Sequentially, the difference in mass between  $y_3^+$  (359.26419) and  $y_2^+$  ions was 113.08368 (L), and between  $y_4^+$  (472.34811) and  $y_3^+$  ions was 113.08392 (L). In addition,  $y_4^{2+}$  ions = 236.67761 was also confirmed. Meanwhile, the difference in mass between  $y_5^+$  (559.37933) and ions  $y_4^+$  was 87.03122 (S), thereby confirming the SLLVLK amino acid sequence. The mass of the  $b_1^+$  ion was 115.05013, confirming the presence of N amino acids. The mass difference between

**Table 3.** Peptide sequence identified from anticancer active peptide fractions

No.	Peptide sequences	$[M-H]^+$ Da	The protein of the peptides origin*	Amino acid position in the protein	GRAVY	Predicted pI
1	NSLLVK	673.42229	Protein tyrosine phosphatase, EC 3.1.3.48, putative	562–567	0.600	8.75
2	SLLVK	646.41240	Methyl cytosine dioxygenase TET, EC 1.14.11.n2, putative	1229–1234	1.050	8.47
3	TVPVKR	699.45096	Cytotoxin 2, CX2 (Toxin CM-7A), putative	31–36	–0.383	11.00
4	MFMVSNK	872.39893	Cytotoxin 3, CX3 (Toxin CM-7), putative	24–30	0.371	8.50

\*) based on *Ophiophagus hannah* and *Naja siamensis* protein database

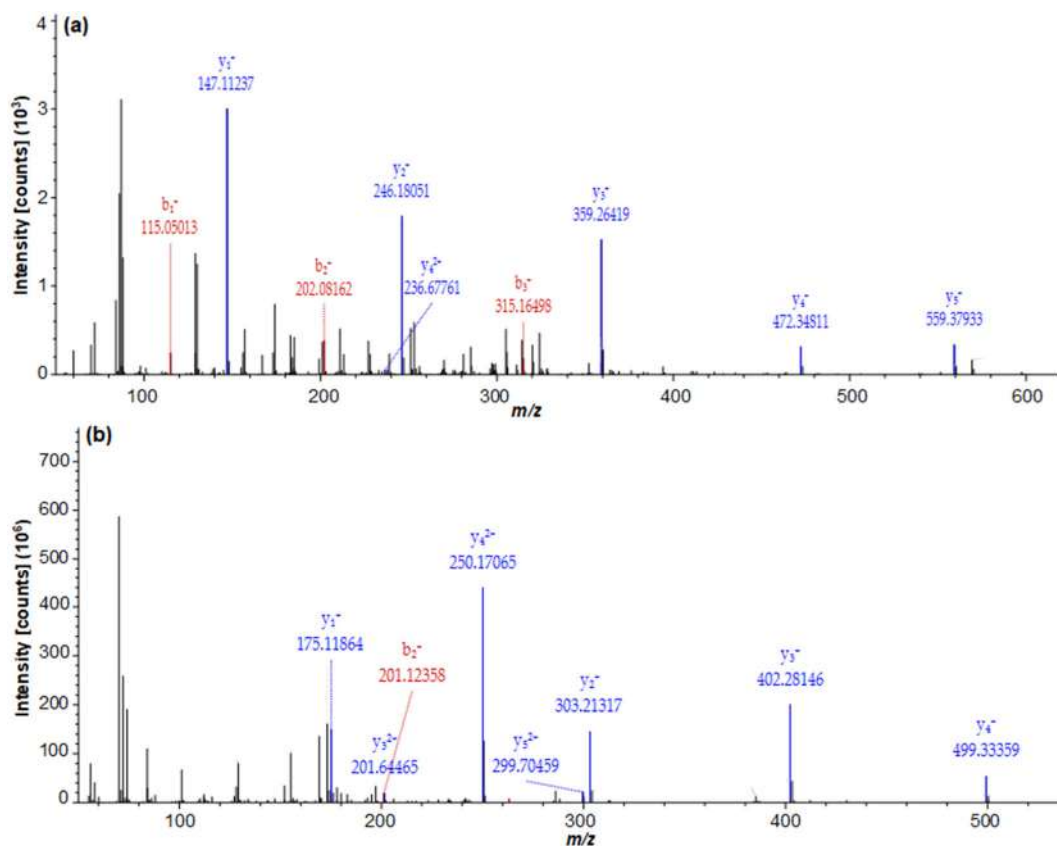


**Fig 2.** The MS/MS spectra of NSLLVK peptide (a) and TVPVKR peptide (b)

the  $b_2^+$  (202.08162) and  $b_1^+$  ions confirmed the presence of S (87.03149), and the mass difference between the  $b_3^+$  (315.16498) and  $b_2^+$  ions confirmed the presence of L (113.08336).

The TVPVKR was eluted at a retention time of 1.4765 min and this peptide was identified from the peptide database based on the genome of *Naja siamensis*. MS<sup>2</sup> fragmentation of TVPVKR was detected with  $m/z$  value of 233.82184 Da. It obtained  $[M-H]^+ = 699.45096$  Da and  $z = +3$ . Its GRAVY score was  $-0.383$ , while the pI value recorded was 11.00. It was isolated from one of the *N. sumatrana* venom proteins Cytotoxin 2, CX2 (Toxin CM-7A), at the location of 31-36 amino acids. The mass spectra of the TVPVKR are displayed in Fig. 2(b). The  $y_1^+$  ion was formed due to the cleavage of the C-N bond between lysine (K) at the N-terminus with the arginine (R). The mass difference between the  $y_2^+$  (303.21317) and  $y_1^+$  ions confirmed the presence of K (128.09453), which leads to a KR sequence at the C-terminus. Sequentially, the difference in mass between  $y_3^+$  (402.28146) and  $y_2^+$

ions was 99.06829 (V), and between  $y_4^+$  (499.33359) and  $y_3^+$  ions was 97.05213 (P). Moreover,  $y_3^{2+}$  ions (201.64465),  $y_4^{2+}$  ions (250.17065), and  $y_5^{2+}$  ions (299.70459) were also confirmed, thereby confirming the PVKR amino acid sequence. In addition, Ion  $b_2^+$  (201.12358) confirmed the presence of amino acid V.

### Study of Molecular Docking

Molecular docking studies are useful for drug discovery and development. Similar significant advances have been made in the field of peptide therapy [42]. Molecular docking was used to determine the interaction between peptides and receptors in breast cancer anticancer peptides produced from the active fraction. The receptor used as EGFR, which was overexpressed in nearly half of triple-negative and inflammatory breast cancer patients. The EGFR protein was overexpressed by 16–36% in breast cancer [43]. The binding affinity and interactions of amino acid residues (hydrogen bonds and hydrophobic interactions) with

the ligand and the active site are important parameters in determining the stability of the protein-ligand. Both parameters have a significant impact on predicting the mode of protein-ligand interaction. The initial step was redocking between the native ligand (erlotinib) and the EGFR receptor to avoid blind docking and study the receptor interaction of the original ligand. Thus, data concerning the active site and RMSD value will be obtained. The original ligand interactions can be seen in Fig. 3.

The native ligand (erlotinib) formed conventional hydrogen bonds, namely the Cys773 amino acid residue. In addition, three cations consisting of Met742, Lys721, and Asp831 formed hydrophobic interactions, similar to the three alkyl interactions at the amino acid residues of Leu821, Leu764, and Val702. Some of the electrostatic interactions found were Glu738, Thr830, Phe699, Asp776, Phe771, Gly772, Leu694, Thr766, Met769, Leu768, Ala719, and Gln767. After redocking, the peptide was docked to the EGFR receptor. The interactions of the peptide with the EGFR receptor are shown in Fig. 4. NSSLVK peptides produced a good bonding affinity of  $-6.7$  kcal/mol with an RMSD value of 1.953. NSSLVK demonstrated the best-matched model to the EGFR-receptor breast cancer cell line. NSSLVK peptides exhibited conventional hydrogen bonding consisting of Cys773, Lys721, Glu738, and Cys751 amino acid residues. These hydrogen interactions were more numerous than those of the original ligand (erlotinib) when the redocking process made the NSSLVK peptide's interaction with the receptor more stable. The peptide has the same position as the original ligand, which was located on the Cys773 amino acid residue. This proves that NSSLVK interacts with the active site of the EGFR receptor. There were also several electrostatic bonds consisting of Arg17, Leu820, Met769, Leu694, Thr830, Ala719, Ile720, Thr766, Ile765, Leu764, Phe832, Val702, Asp827, Phe699, Gly695, Asn818, Phe771, and Gly772. Moreover, one hydrophobic interaction was also found, which was the pi-ionic Asp776 bond presented in Fig. 4.

The SSSLVK peptide formed hydrogen bonds with Cys773, Asp831, Asp776, and Arg817 amino acid residues, including the same Cys773 amino acid residues

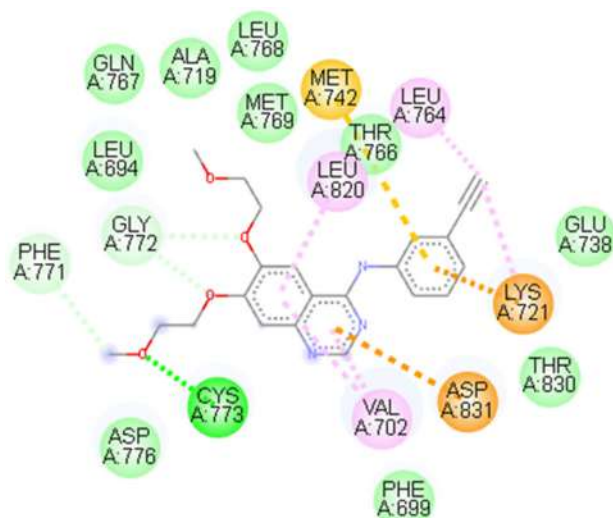


**Fig 3.** Interaction of the erlotinib (native ligand) to the EGFR

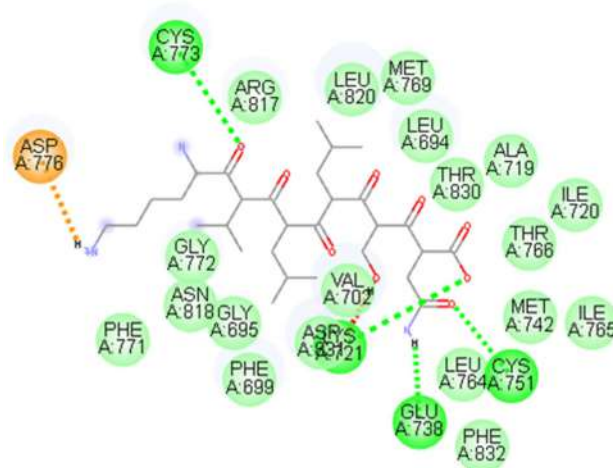


**Fig 4.** Interaction of NSSLVK peptide to the EGFR

as the original ligand. These hydrogen bonds were more numerous than those of the docking ligands. Therefore, they had a higher negative bond affinity value because more hydrogen bonds were formed with the receptor. The binding affinity value obtained was  $-6.65$  kcal/mol, and the RMSD showed a value of  $1.890 \text{ \AA}$ , confirming that the SSSLVK peptide has a stable interaction with the active site and is the most suitable model with the EGFR receptor. In addition, SSSLVK also had electrostatic interactions on the amino acid residues of Leu694, Leu820, Met769, Thr830, Asn818, Gly772, Gly695, Phe699, and Tyr766. Several other interactions were also present, i.e., the hydrophobic alkyl interactions at the

amino acid residue Ala719, Lys721 and Val702, which is shown in Fig. 5.

The affinity value of the TVPVKR peptide bond was  $-6.70$  kcal/mol, and the RMSD score was  $1.900$  Å. The TVPVKR peptide exhibited hydrogen bonding with the receptor consisting of Cys773, Met769, and Gln767 amino acid residues, which were more than the redocking of the native ligand. Cys773 amino acid residues were similar to the native ligand, which proves that TVPVKR interacts with the same active site as the original ligand (erlotinib). In addition to hydrogen bonds, several electrostatic interactions were also shown by TVPVKR peptides, namely Phe699, Glu738, Thr766, Val702, Ala719, Leu768, Leu820, Asn818, Leu694, Gly772, Arg817, Asp776, and Glu780, which were fewer in number than those of the original ligands. Several hydrophobic interactions were also shown by the TVPVKR peptide, and there were three pi-ionic interactions found at Lys721, Asp831, and Asp813 residues. In addition, three alkyl interactions were present, including Tyr777, Phe771, and His781 (Fig. 6). Previous studies on the docking of peptides with AutoDock Vina from black soybean showed that the purified Leu/Ile-Val-Pro-Lys (L/I-VPK) peptide effectively binds to four proteins (XIAP, caspase-3, caspase-7, and Bcl-2) via hydrophobic effect and hydrogen bonding [44]. Peptides from the sea cucumber (*Cucumaria frondose*) were docked with four proteins (EGFR, PI3K, AKT1, and CDK4) using AutoDock Vina, indicating that the twelve peptides bind to the active sites

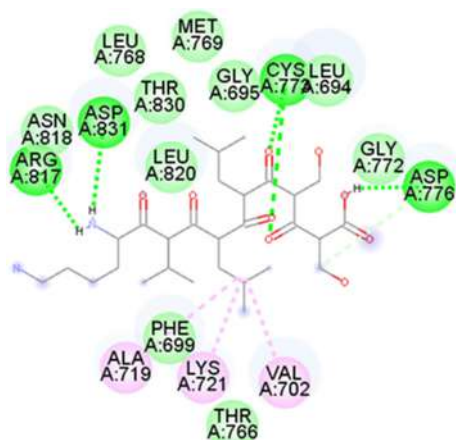


Fig 5. Interaction of SSSLVK peptide to the EGFR

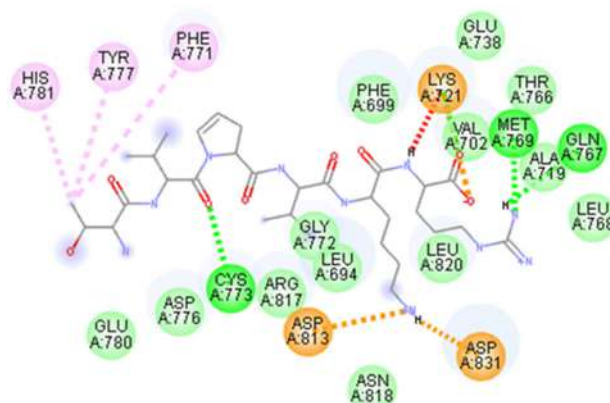


Fig 6. Interaction of TVPVKR peptide to the EGFR

of the four proteins. WPPNYQW and YDWRF peptides bind to proteins with lower binding affinity values than inhibitors (positive control) [45].

## CONCLUSION

The trypsin enzyme successfully hydrolyzed *N. sumatrana* venom, resulting in a relatively high degree of hydrolysis. Hydrolysis of trypsin from venom followed by fractionation using an SPE  $C_{18}$  column showed that the 75% methanol fraction had anticancer activity against breast cancer (MCF-7) with a selectivity index of 5.00. The peptides identified by HRMS from the active fraction produced four peptide sequences, namely MFMVSNK, NSLLVK, SSSLVK, and TVPVKR. According to the docking study, the NSLLVK, SSSLVK, and TVPVK peptides possessed high binding affinity values and good RMSD values, making them the most suitable models for 1M17, the breast cancer EGFR receptor.

## ACKNOWLEDGMENTS

The researcher would like to thank Mr. Tri Wahyudi for his assistance in HRMS analysis.

## REFERENCES

- [1] Torre, L.A., Bray, F., Siegel, R.L., Ferlay, J., Lortet-Tieulent, J., and Jemal, A., 2015, Global cancer statistics, 2012, *Ca-Cancer J. Clin.*, 65 (2), 87–108.
- [2] Fadelu, T., and Rebeck, T.R., 2021, The rising burden of cancer in low- and middle-Human Development Index countries, *Cancer*, 127 (16), 2864–2866.

- [3] Pérez-Peinado, C., Defaus, S., and Andreu, D., 2020, Hitchhiking with nature: Snake venom peptides to fight cancer and superbugs, *Toxins*, 12 (4), 255.
- [4] Nikolaou, M., Pavlopoulou, A., Georgakilas, A.G., and Kyrodimos, E., 2018, The challenge of drug resistance in cancer treatment: A current overview, *Clin. Exp. Metastasis*, 35 (4), 309–318.
- [5] Wang, S.H., and Yu, J., 2018, Structure-based design for binding peptides in anti-cancer therapy, *Biomaterials*, 156, 1–15.
- [6] dos Santos-Silva, C.A., Zupin, L., Oliveira-Lima, M., Vilela, L.M.B., Bezerra-Neto, J.P., Ferreira-Neto, J.R., Ferreira, J.D.C., de Oliveira-Silva, R.L., de Jesús Pires, C., Aburjaile, F.F., de Oliveira, M.F., Kido, E.A., Crovella, S., and Benko-Iseppon, A.M., 2020, Plant antimicrobial peptides: state of the art, in silico prediction and perspectives in the omics era, *Bioinf. Biol. Insights*, 14, 1177932220952739.
- [7] Calderon, L.A., Sobrinho, J.C., Zaqueo, K.D., de Moura, A.A., Grabner, A.N., Mazzi, M.V., Marcussi, S., Nomizo, A., Fernandes, C.F.C., Zuliani, J.P., Carvalho, B.M.A., da Silva, S.L., Stábeli, R.G., and Soares, A.M., 2014, Antitumoral activity of snake venom proteins: New trends in cancer therapy, *Biomed Res. Int.*, 2014, 203639.
- [8] Aziz, M.M., Abdel-Rahman, M.A., Abbas, O.A., Mohammed, E.A., and Hassan, M.K., 2022, Snake venoms-based compounds as potential anticancer prodrug: sand viper cerastes as a model, *Egypt. J. Chem.*, 65 (8), 43–55.
- [9] Pereira, A., Kerkis, A., Hayashi, M.A.F., Pereira, A.S.P., Silva, F.S., Oliveira, E.B., Prieto da Silva, A.R.B., Yamane, T., Rádis-Baptista, G., and Kerkis, I., 2011, Crotonamine toxicity and efficacy in mouse models of melanoma, *Expert Opin. Invest. Drugs*, 20 (9), 1189–1200.
- [10] Nunes, E.S., Souza, M.A.A., Vaz, A.F.M., Silva, T.G., Aguiar, J.S., Batista, A.M., Guerra, M.M.P., Guarnieri, M.C., Coelho, L.C.B.B., and Correia, M.T.S., 2012, Cytotoxic effect and apoptosis induction by *Bothrops leucurus* venom lectin on tumor cell lines, *Toxicon*, 59 (7-8), 667–671.
- [11] de Vasconcelos Azevedo, F.V.P., Zóia, M.A.P., Lopes, D.S., Gimenes, S.N., Vecchi, L., Alves P.T., Rodrigues, R.S., Silva, A.C.A., Yoneyama, K.A.G., Goulart, L.R., and de Melo Rodrigues, V., 2019, Antitumor and antimetastatic effects of PLA<sub>2</sub>-BthTX-II from *Bothrops jararacussu* venom on human breast cancer cells, *Int. J. Biol. Macromol.*, 135, 261–273.
- [12] Kerkis, I., Hayashi, M.A.F., Prieto Da Silva, A.R.B., Pereira, A., De Sá Júnior, P.L., Zaharenko, A.J., Rádis-Baptista, G., Kerkis, A., and Yamane, T., 2014, State of the art in the studies on crotonamine, a cell penetrating peptide from South American rattlesnake, *Biomed Res. Int.*, 2014, 675985.
- [13] Rizzello, C.G., Lorusso, A., Russo, V., Pinto, D., Marzani, B., and Gobetti, M., 2017, Improving the antioxidant properties of quinoa flour through fermentation with selected autochthonous lactic acid bacteria, *Int. J. Food Microbiol.*, 241, 252–261.
- [14] Bhat, Z.F., Kumar, S., and Bhat, H.F., 2015, Bioactive peptides from egg: A review, *Nutr. Food Sci.*, 45 (2), 190–212.
- [15] Baharuddin, N.A., Halim, N.R.A., and Sarbon, N.M., 2016, Effect of degree of hydrolysis (DH) on the functional properties and angiotensin I-converting enzyme (ACE) inhibitory activity of eel (*Monopterus* sp.) protein hydrolysate, *Int. Food Res. J.*, 23 (4), 1424–1431.
- [16] Halim, N.R.A., Yusof, H.M., and Sarbon, N.M., 2016, Functional and bioactive properties of fish protein hydrolysates and peptides: A comprehensive review, *Trends Food Sci. Technol.*, 51, 24–33.
- [17] Halim, N.R.A., Azlan, A., Yusof, H.M., and Sarbon, N.M., 2018, Antioxidant and anticancer activities of enzymatic eel (*Monopterus* sp.) protein hydrolysate as influenced by different molecular weight, *Biocatal. Agric. Biotechnol.*, 16, 10–16.
- [18] Umayaparvathi, S., Meenakshi, S., Vimalraj, V., Arumugam, M., Sivagami, G., and Balasubramanian, T., 2014, Antioxidant activity and anticancer effect of bioactive peptide from enzymatic hydrolysate of oyster (*Saccostrea cucullata*), *Biomed. Prev. Nutr.*, 4 (3), 343–353.

- [19] Hoskin, D.W., and Ramamoorthy, A., 2008, Studies on anticancer activities of antimicrobial peptides, *Biochim. Biophys. Acta, Biomembr.*, 1778 (2), 357–375.
- [20] Kaur, K., Kaur, P., Mittal, A., Nayak, S.K., and Khatik, G.L., 2017, Design and molecular docking studies of novel antimicrobial peptides using AutoDock molecular docking software, *Asian J. Pharm. Clin. Res.*, 10 (16), 28–31.
- [21] Yap, M.K.K., Fung, S.Y., Tan, K.Y., and Tan, N.H., 2014, Proteomic characterization of venom of the medically important Southeast Asian *Naja sumatrana* (Equatorial spitting cobra), *Acta Trop.*, 133, 15–25.
- [22] Tan, C.H., Tan, K.Y., Wong, K.Y., Tan, N.H., and Chong, H.P., 2022, Equatorial spitting cobra (*Naja sumatrana*) from Malaysia (Negeri Sembilan and Penang), Southern Thailand, and Sumatra: Comparative venom proteomics, immunoreactivity and cross-neutralization by antivenom, *Toxins*, 14 (8), 522.
- [23] Gutiérrez, J.M., and Lomonte, B., 2013, Phospholipases A<sub>2</sub>: Unveiling the secrets of a functionally versatile group of snake venom toxins, *Toxicon*, 62, 27–39.
- [24] Wong, K.Y., Tan, C.H., and Tan, N.H., 2016, Venom and purified toxins of the spectacled cobra (*Naja naja*) from Pakistan: Insights into toxicity and antivenom neutralization, *Am. J. Trop. Med. Hyg.*, 94 (6), 1392–1399.
- [25] Chang, L.S., Huang, H.B., and Lin, S.R., 2000, The multiplicity of cardiotoxins from *Naja naja atra* (Taiwan cobra) venom, *Toxicon*, 38 (8), 1065–1076.
- [26] Katali, O., Shipingana, L., Nyaragó, P., Pääkkönen, M., Haindongo, E., Rennie, T., James, P., Eriksson, J., and Hunter, C.J., 2020, Protein identification of venoms of the African spitting cobras, *Naja mossambica* and *Naja nigricincta nigricincta*, *Toxins*, 12 (8), 520.
- [27] Wong, K.Y., Tan, K.Y., Tan, N.H., and Tan, C.H., 2021, A neurotoxic snake venom without phospholipase A<sub>2</sub>: Proteomics and cross-neutralization of the venom from Senegalese cobra, *Naja senegalensis* (Subgenus: *Uraeus*), *Toxins*, 13 (1), 60.
- [28] Chong, H.P., Tan, K.Y., and Tan, C.H., 2020, Cytotoxicity of snake venoms and cytotoxins from two Southeast Asian cobras (*Naja sumatrana*, *Naja kaouthia*): Exploration of anticancer potential, selectivity, and cell death mechanism, *Front. Mol. Biosci.*, 7, 583587.
- [29] Silva-de-França, F., Villas-Boas, I.M., de Toledo Serrano, S.M., Cogliati, B., de Andrade Chudzinski, S.A., Lopes, P.H., Kitano, E.S., Okamoto, C.K., and Tambourgi, D.V., 2019, *Naja annulifera* snake: New insights into the venom components and pathogenesis of envenomation, *PLoS Neglected Trop. Dis.*, 13 (1), e0007017.
- [30] Deng, Y., Gruppen, H., and Wierenga, P.A., 2018, Comparison of protein hydrolysis catalyzed by bovine, porcine, and human trypsins, *J. Agric. Food Chem.*, 66 (16), 4219–4232.
- [31] Olsen, J.V., Ong, S.E., and Mann, M., 2004, Trypsin cleaves exclusively C-terminal to arginine and lysine residues, *Mol. Cell. Proteomics*, 3 (6), 608–614.
- [32] Butré, C.I., Sforza, S., Gruppen, H., and Wierenga, P.A., 2014, Determination of the influence of substrate concentration on enzyme selectivity using whey protein isolate and *Bacillus licheniformis* protease, *J. Agric. Food Chem.*, 62 (42), 10230–10239.
- [33] Nasri, R., Younes, I., Jridi, M., Trigui, M., Bougateg, A., Nedjar-Arroume, N., Dhulster, P., Nasri, M., and Karra-Châabouni, M., 2013, ACE inhibitory and antioxidative activities of Goby (*Zosterisessor ophiocephalus*) fish protein hydrolysates: Effect on meat lipid oxidation, *Food Res. Int.*, 54 (1), 552–561.
- [34] Raharjo, T.J., Utami, W.M., Fajr, A., Haryadi, W., and Swasono, R.T., 2021, Antibacterial peptides from tryptic hydrolysate of *Ricinus communis* seed protein fractionated using cation exchange chromatography, *Indones. J. Pharm.*, 32 (1), 74–85.
- [35] Atmawati, D.R., Andriana, Z., Swasono, R.T., and Raharjo, T.J., 2022, Antibacterial peptide from solid phase extraction (SPE) fractionation on trypsin hydrolysis of jatropha (*Ricinus communis*) seed protein acid extract, *Rasayan J. Chem.*, 15 (2), 1288–1295.

- [36] Asmi, N., Ahmad, A., Massi, M.N., and Natsir, H., 2019, The potency of protein hydrolysate from epiphytic bacteria associated with brown algae *Sargassum* sp. as anticancer agents, *J. Phys.: Conf. Ser.*, 1341, 032013.
- [37] Rostammiry, L., Saeidiasl, M.R., Safari, R., and Javadian, R., 2017, Optimization of the enzymatic hydrolysis of soy protein isolate by alcalase and trypsin, *Biosci., Biotechnol. Res. Asia*, 14 (1), 193–200.
- [38] Demirgan, R., Karagöz, A., Pekmez, M., Öney-Uçar, E., Artun, F.T., Gürer, Ç., and Mat, A., 2016, *In vitro* anticancer activity and cytotoxicity of some papaver alkaloids on cancer and normal cell lines, *Afr. J. Tradit., Complementary Altern. Med.*, 13 (3), 22–26.
- [39] Cheng, C.Y., and Su, C.C., 2010, Tanshinone IIA may inhibit the growth of small cell lung cancer H146 cells by up-regulating the Bax/Bcl-2 ratio and decreasing mitochondrial membrane potential, *Mol. Med. Rep.*, 3 (4), 645–650.
- [40] Khunsap, S., Pakmanee, N., Khaw, O., Chanhom, L., Sitprija, V., Suntravat, M., Lucena, S.E., Perez, J.C., and Sanchez, E.E., 2011, Purification of a phospholipase A<sub>2</sub> from *Daboia russelii siamensis* venom with anticancer effects, *J. Venom Res.*, 2, 42–51.
- [41] Ahmed, N., Raharjo, S., Swasono, R.T., and Raharjo, T.J., 2022, The antibacterial peptides (AMPS) originated from tryptic hydrolysis of *Naja sumatrana* venom fractionated using cation exchange chromatography, *Rasayan J. Chem.*, 15 (4), 2642–2653.
- [42] Kumar, P.K., and Piramanayagam, S., 2021, Molecular docking analysis of antimicrobial peptides with the CXCL1 protein target for colorectal cancer, *Bioinformation*, 17 (3), 369–376.
- [43] Tsutsui, S., Kataoka, A., Ohno, S., Murakami, S., Kinoshita, J., and Hachitanda, Y., 2002, Prognostic and predictive value of epidermal growth factor receptor in recurrent breast cancer, *Clin. Cancer Res.*, 8 (11), 3454–3460.
- [44] Chen, Z., Li, W., Santhanam, R.K., Wang, C., Gao, X., Chen, Y., Wang, C., Xu, L., and Chen, H., 2019, Bioactive peptide with antioxidant and anticancer activities from black soybean [*Glycine max* (L.) Merr.] byproduct: Isolation, identification and molecular docking study, *Eur. Food Res. Technol.*, 245 (3), 677–689.
- [45] Wargasetia, T.L., Ratnawati, H., Widodo, N., and Widyananda, M.H., 2021, Bioinformatics study of sea cucumber peptides as antibreast cancer through inhibiting the activity of overexpressed protein (EGFR, PI3K, AKT1, and CDK4), *Cancer Inf.*, 20, 11769351211031864.



## Advanced Oxidation Processes of Amoxicillin Based on Visible Light Active Nitrogen-Doped TiO<sub>2</sub> Photocatalyst

Kusuma Putri Suwondo, Nurul Hidayat Aprilita, and Endang Tri Wahyuni\*

Department of Chemistry, Faculty of Mathematics and Natural Sciences, Universitas Gadjah Mada, Sekip Utara, Yogyakarta 55281, Indonesia

\* Corresponding author:

email: endang\_triw@ugm.ac.id

Received: January 17, 2023

Accepted: March 16, 2023

DOI: 10.22146/ijc.81387

**Abstract:** Environmental consequences during the COVID-19 pandemic have attracted attention due to the excessive use of antibiotics which lead to the release of the drug's residue, such as amoxicillin (AMX), into the environment. In this work, an advanced oxidation process based on a visible, active N-doped TiO<sub>2</sub> photocatalyst was carried out to eliminate AMX. Nitrogen with different initial doping concentrations (15, 30, 45% w/w) was doped into TiO<sub>2</sub> by the sol-gel method. The characterization technique such as XRD, FTIR, UV-SRS, and SEM-EDX revealed that nitrogen with 30% doping concentration improved the TiO<sub>2</sub> response in the visible region, attributed to the lower band gap energy (2.97 eV). In the photodegradation processes, the TiO<sub>2</sub>-N (30%) photocatalyst possessed higher AMX degradation than undoped TiO<sub>2</sub> for both UV and visible light irradiation. In an aqueous solution, the degradation percentage of AMX by TiO<sub>2</sub>-N (30%) was 68.5 and 84.12%, while the degradation percentage of AMX by TiO<sub>2</sub> was 38.7 and 78.01% under visible and UV light, respectively.

**Keywords:** antibiotic resistance; visible light active; N-doped TiO<sub>2</sub>; amoxicillin

### ■ INTRODUCTION

The Coronavirus disease 2019 (COVID-19) has become an outbreak pandemic since 2020. Up to now, 600 million cases worldwide have been reported, causing more than 6 million deaths [1]. The pandemic brought not only a global health crisis but also environmental damage.

The use of pharmaceutical compounds, especially antibiotics, has dramatically increased during the pandemic. Around 75% of COVID-19 patients were prescribed antibiotics to cure or prevent secondary bacterial infection [2]. The ingested antibiotic is mostly excreted through feces and urine because it is poorly metabolized. Hence, their continuous overuse or misuse led to abundant environmental drug residue. The most crucial problem is that antibiotics increase antimicrobial resistance (AMR). The World Health Organization (WHO) declared AMR as a global health crisis problem [3-4]. As a result, removing antibiotics attracts a particular point of view on pollutant remediation.

Among the antibiotics, amoxicillin (AMX) is the second-line antibiotic for COVID-19 patients after

doxycycline, suggested by National Institute for Health and Care Excellence (NICE) COVID-19 guidance [5]. Besides, AMX is also used to treat other diseases and in veterinary medicine. Due to the highly used and poorly metabolized (80–90% excreted by the body), AMX could be detected in the environment. AMX has been detected in the Eastern Mediterranean Sea up to 127.8 ng/L, the highest among other detected pharmaceuticals [6]. In addition, the Predicted Environmental Concentration (PEC) of AMX in the UK emergency hospital at Harrogate is 30 ng/L in the baseline river and 400 ng/L in the case of 95% of the patient prescribed antibiotics [5]. Conventional water treatment, such as filtration, cannot remove the AMX residue [3]. Therefore, the development of remediation techniques is urgently needed to treat antibiotic pollutants.

In recent years, advanced oxidation processes (AOPs) have been recognized as one of the promising techniques for antibiotic removal. AOPs use the in situ-generated strong oxidative species (H<sub>2</sub>O<sub>2</sub>, OH<sup>•</sup>, and <sup>•</sup>O<sub>2</sub><sup>-</sup>) to degrade antibiotic compounds into harmless

substances [7–9]. Heterogeneous photocatalysis is the most popular AOPs method because of its effectiveness and environmentally friendly. The semiconductor is used for photocatalysis processes, and the photon induces the oxidation reaction [10].

The semiconductor that has been studied for photodegradation of AMX such as NiO [11], ZnO [12-13], and TiO<sub>2</sub> [14-15]. TiO<sub>2</sub> is one of the most used in AOPs owing to its photo and chemical stability, non-toxicity, and excellent photoactivity. However, the major drawback of TiO<sub>2</sub> is the wide band gap of 3.2 eV. Consequently, the photoactivity of TiO<sub>2</sub> is only possessed in the presence of UV light. The doping method has been studied to improve the TiO<sub>2</sub> activity under visible light irradiation by narrowing the band gap and shifting the absorption regions [16-17]. Doping with metal or non-metal to improve TiO<sub>2</sub> activity in visible or solar light for AMX degradation has been studied extensively [3,18-21].

Doping TiO<sub>2</sub> with metal could enhance the photocatalytic activity due to the lower band gap energy, and metal could act as an electron trapper that inhibits electron and hole recombination. However, metal doping could leach during the photocatalytic process; consequently, the catalyst would deactivate, and a second source of pollutants formed [22]. Meanwhile, non-metal doping is more environmentally friendly and lower cost compared to metal doping. The non-metal elements, such as nitrogen, carbon, and sulfur, could substitute oxygen in the TiO<sub>2</sub> lattice which leads to narrower band gap energy. Among other non-metal dopants, nitrogen-doped TiO<sub>2</sub> shows outstanding photocatalytic activity under visible light for organic compound degradation [23-24]. That is due to the 2p states of the nitrogen atom could be mixed with the 2p states of the oxygen atom, allowing the band gap to narrow; as a result, a red shift of the absorption band edge to the visible region [22,24-25].

Therefore, in this work, the nitrogen element was selected as the dopant element to improve the TiO<sub>2</sub> activity for AMX degradation under visible light radiation. The nitrogen was doped into TiO<sub>2</sub> by the sol-gel method. The effect of nitrogen initial doping concentration was also studied. Different characterization methods XRD, FTIR, UV-SRS, and SEM-EDX, were

carried out to examine the optimum doping level. Importantly, the photodegradation process of AMX was conducted under commercially visible LED-light irradiation. To the best of our knowledge, the AMX degradation by N-doped TiO<sub>2</sub> compared to undoped TiO<sub>2</sub> under commercially LED-light irradiation without an additional oxidative agent has not been conducted.

## ■ EXPERIMENTAL SECTION

### Materials

Titanium tetraisopropoxide (TTIP) (C<sub>12</sub>H<sub>28</sub>O<sub>4</sub>Ti; 98%) was purchased from Shanghai Chemical Industry. Ethanol (C<sub>2</sub>H<sub>6</sub>O, 99.99%), nitric acid (HNO<sub>3</sub>, 65%), and urea (CH<sub>2</sub>N<sub>2</sub>O) were supplied by Merck company. All the chemicals used in this work were analytical grade. Amoxicillin trihydrate (C<sub>16</sub>H<sub>25</sub>N<sub>3</sub>O<sub>8</sub>S) was provided by the National Agency of Drug and Food Control, Republic of Indonesia.

### Instrumentation

The N-doped TiO<sub>2</sub> properties were studied using different characterization techniques. Fourier Transform Infra-Red (FTIR) spectrum of undoped and N-doped TiO<sub>2</sub> was obtained on Shimadzu Prestige21. The crystal structure of the photocatalysts was investigated using an X-ray diffractometer (Shimadzu 6000D) with Cu K $\alpha$  radiation in the range of = 10–80° with a scan speed of 3°/min. The UV-Visible specular reflectance spectroscopy (UV-SRS) UV1700 Pharmaspec was used to obtain the absorption spectra. The surface morphology and element composition of the photocatalysts were observed by scanning electron microscope (SEM) (JSM-6510LA) and energy dispersive spectroscopy (EDS).

### Procedure

#### Synthesis of N-doped TiO<sub>2</sub>

N-doped TiO<sub>2</sub> (TiO<sub>2</sub>-N) with different nitrogen amounts was synthesized by sol-gel method using TTIP 98% and urea as TiO<sub>2</sub> and nitrogen precursor. In a typical sol-gel synthesis, 2 mL of TTIP was dissolved in 10 mL of ethanol under continuous stirring for 30 min to prepare solution A. In a beaker, urea was dissolved in water and mixed with ethanol to form solution B. The

pH of the solution was adjusted to 3 with the addition of  $\text{HNO}_3$ . The weight of urea was controlled to get the N/ $\text{TiO}_2$  mass ratio of 15, 30, and 45% (w/w). Later, solution B was added dropwise into solution A under continuous stirring for 1 h. The obtained white solution was left overnight at room temperature to complete the gel formation. After that, the gel was dried for 5 h at  $80^\circ\text{C}$  to remove the excess solution. The dried gel was ground to form a fine powder. Lastly, the powder was calcined in a muffle furnace for 2 h at  $500^\circ\text{C}$ . A yellowish powder was obtained after the calcination process. The undoped  $\text{TiO}_2$  was also synthesized in a similar procedure without adding urea.

### Photocatalytic degradation of amoxicillin

The AMX photodegradation process was conducted in a batch photoreactor under visible light irradiation using LED lamps ( $4 \times 18\text{ W}$ , 400–700 nm). The photocatalytic process under UV light was also evaluated using a UVA lamp ( $4 \times 18\text{ W}$ , 320–400 nm). Firstly, a specific amoxicillin weight was diluted to get a 20 mg/L solution concentration. The N-doped  $\text{TiO}_2$  (catalyst dosage 1 g/L) was dispersed into AMX solution followed by 1 h stirring in the dark to reach the adsorption equilibrium between the drug and the catalyst. Later, the solution was irradiated at specific time intervals. After each irradiation time, the AMX solution was separated from the catalyst by centrifugation. The remaining AMX in solution was analyzed at maximum wavelength

absorption (227 nm) [26] using a UV-Visible spectrophotometer. The absorption spectrum of AMX is shown in Fig. 1. The percentage of AMX degradation was calculated using Eq. (1):

$$\% \text{ Dye degradation} = \frac{A_0 - A_t}{A_0} \times 100\% \quad (1)$$

where  $A_0$  and  $A_t$  denote the AMX concentration before and after the degradation, respectively.

## RESULTS AND DISCUSSION

### X-ray Diffraction Analysis

The crystal structure of the photocatalyst was characterized by the X-ray diffraction method and presented in Fig. 2. The diffraction pattern for both

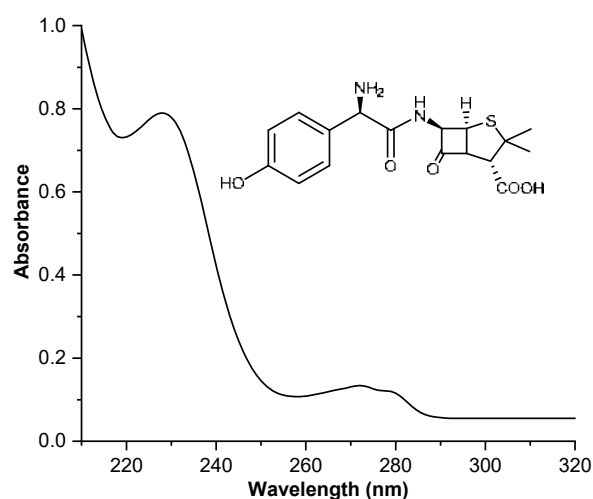


Fig 1. The UV absorption spectrum of amoxicillin

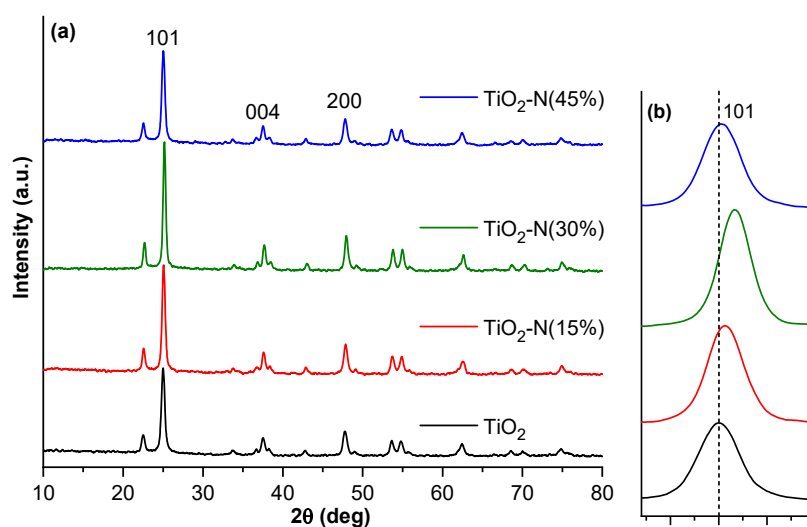


Fig 2. The X-ray diffraction patterns of N-doped and undoped  $\text{TiO}_2$  in the range of  $10\text{--}80^\circ$  (a) and  $24.25\text{--}26^\circ$  (b)

undoped and N-doped TiO<sub>2</sub> are well-matched with the TiO<sub>2</sub> anatase (JCPDS card no. 21-1272). The anatase phase performs better photocatalytic activity compared to the rutile or brookite phase due to the larger surface area and better charge-carrier mobility [27-28]. Therefore, confirming the TiO<sub>2</sub> crystal structure for photocatalysis application is necessary. The peak of undoped TiO<sub>2</sub> observed at 2θ values of 25.00°, 37.57°, 47.79°, 53.65°, and 54.80° correspond to 101, 004, 200, 105, and 211 planes of the anatase phase. No new diffraction peaks were introduced in the N-doped TiO<sub>2</sub> diffractogram, which indicates that the N doping has not triggered the formation of any secondary and impurity phases of TiO<sub>2</sub> [23,29]. However, a positive shift of 101 peaks was observed for N-doped samples (Fig. 2(b)). The peak shift indicates the nitrogen has successfully doped into the TiO<sub>2</sub> lattice, engendered oxygen vacancies [30].

Moreover, the crystallinity of TiO<sub>2</sub> improved for the N-doped sample (15% and 30% doping levels), which may be the result of the doping nitrogen species. By applying Scherrer's equation, the average crystallite size was obtained. The increase in initial nitrogen concentration up to 30% leads to an increase in average crystallite size from 10.159 to 13.189 nm, as listed in Table 1. The incorporation of nitrogen into the TiO<sub>2</sub> lattice promotes the TiO<sub>2</sub> crystal growth [31-32]. On the other hand, at higher nitrogen doping levels (45%), the average crystallite size has slightly decreased, indicating enormous amounts of dopant had an inhibition effect on the crystal growth [33]. The N-doping on TiO<sub>2</sub> was well discovered by XRD analysis. FTIR analysis was performed to ensure nitrogen had successfully doped into the TiO<sub>2</sub>.

### FTIR Analysis

FTIR spectra displayed in Fig. 3 elucidate the surface functional group of undoped TiO<sub>2</sub> and N-doped TiO<sub>2</sub> at different amounts of nitrogen loading. All the samples present almost the same spectra at around 400–900, 1631, and broadband at 3449 cm<sup>-1</sup>, which corresponds to the TiO<sub>2</sub> anatase phase. The absorption band at 400–900 cm<sup>-1</sup> is assigned to the Ti–O–Ti stretching vibration, while the 1631 and 3449 cm<sup>-1</sup> bands are attributed to O–H bending and O–H stretching vibration from Ti–O–H [34-35]. The

**Table 1.** The average crystallite size and band gap energy of N-doped and undoped TiO<sub>2</sub>

Sample	Average crystallite size (nm)	Band gap (eV)
TiO <sub>2</sub>	10.159	3.18
TiO <sub>2</sub> -N (15%)	10.716	3.04
TiO <sub>2</sub> -N (30%)	13.189	2.97
TiO <sub>2</sub> -N (45%)	10.054	3.03

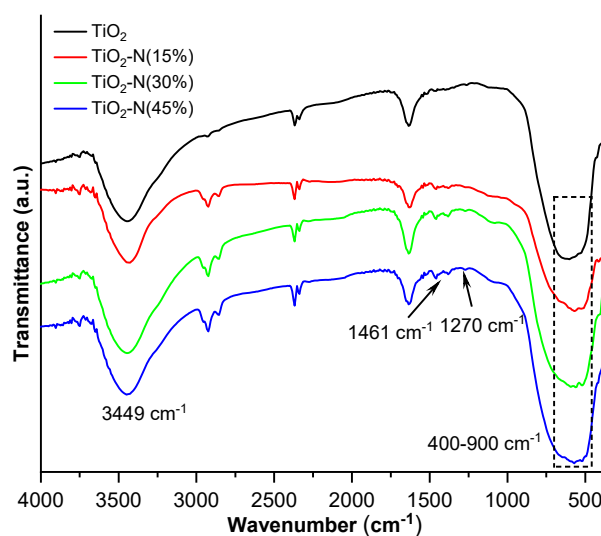


**Fig 3.** FTIR spectra of N-doped and undoped TiO<sub>2</sub>

doped samples show notable bands at around 1461 and 1270 cm<sup>-1</sup> correspond to the vibration of the N–Ti bond, which are the typical bands of N in the TiO<sub>2</sub> lattice [22,30,36-37]. The findings are in good agreement with the XRD analysis as discussed above.

### UV-SRS Analysis

Incorporating nitrogen in TiO<sub>2</sub> could narrow the gap between the valance and conduction bands, and then improve the photocatalytic activity [23]. Those optical properties were investigated by UV-SRS, as shown in Fig. 4. It was observed that nitrogen doping contributed to the redshift because of the narrowing of the band gap. The edge of absorption spectra slightly shifts to the longer wavelength. Additionally, after doping with nitrogen, the absorption of the N-doped sample in the visible region rises. At a 30% doping level, the highest absorption was achieved. As predicted, this sample would give the lowest band gap energy of 2.97 eV. The narrowing of band gap energy could be

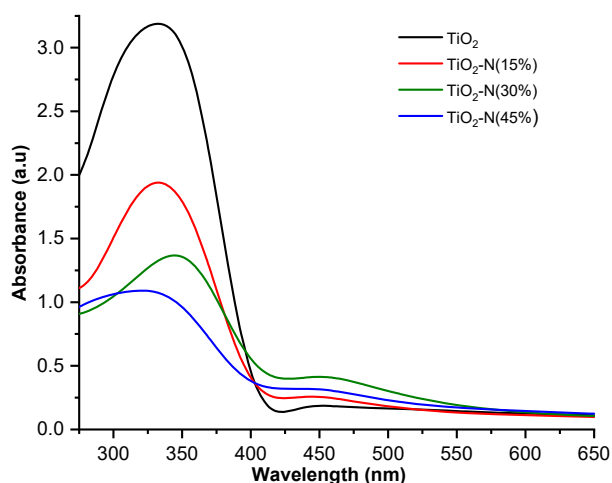


**Fig 4.** UV-SRS absorbance spectra of N-doped and undoped  $\text{TiO}_2$

attributed to the substitution of N instead of O in the  $\text{TiO}_2$  lattice, creating a new energy level [22-24], which leads to the absorption of visible light and initiates photocatalysis as proposed in Fig. 9.

The band gap energy was determined using the Tauc plot and displayed in Fig. 5. The amount of nitrogen doping influences the redshift of light adsorption region and band gap energy. The higher nitrogen loading, the higher the absorption in the visible region and the lower the band gap. On the other hand, the incorporation of nitrogen into the  $\text{TiO}_2$  lattice becomes ineffective at massive nitrogen levels, and crystal growth is inhibited. Hence, at a 45% doping level, the band gap was obviously higher than the 30% nitrogen doping level. This result was in accordance with the XRD analysis.

### SEM-EDX Analysis

Fig. 6(a) and b present the morphology and surface

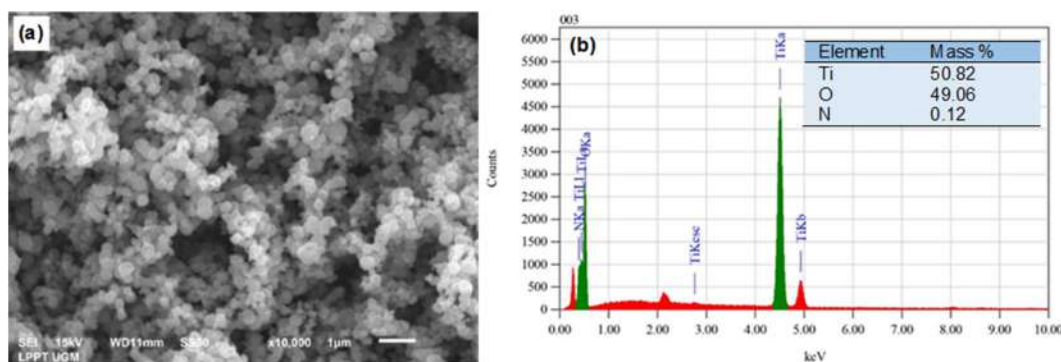


**Fig 6.** SEM image (a) and energy-dispersive spectra (b) of  $\text{TiO}_2\text{-N}(30\%)$

composition of  $\text{TiO}_2\text{-N}(30\%)$  by SEM-EDX. The N-doped  $\text{TiO}_2$  particles were spherically shaped in nano size. No observations of particle agglomeration in the sample, which would be advantageous for the photocatalytic process. The EDX analysis verified the presence of nitrogen in the sample. The nitrogen content present in  $\text{TiO}_2$  (0.12%) was drastically dropped compared to initial nitrogen concentrations (30%). The result agrees with the previous report that only a small amount of nitrogen is deposited into the  $\text{TiO}_2$  lattice. Meanwhile, the particular nitrogen element presents as amine absorbed in  $\text{TiO}_2$  and then decomposed during the heat treatment at  $500^\circ\text{C}$  [25,30].

### Photocatalytic Degradation of Amoxicillin

To confirm the photocatalytic activity of the N-doped and undoped  $\text{TiO}_2$ , the degradation processes of AMX have been conducted in both UV and visible light.

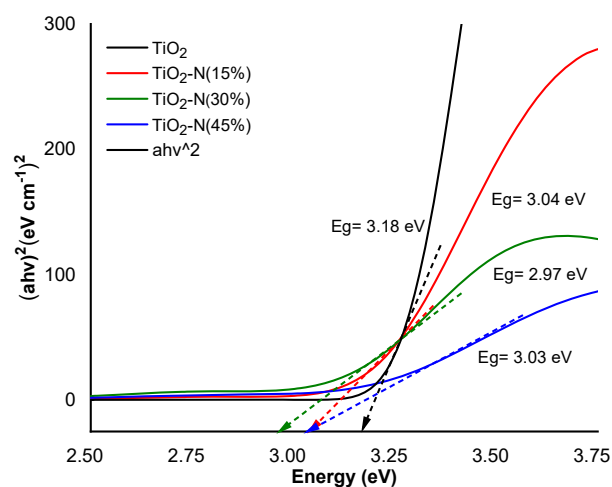


**Fig 5.** Tauc plot obtained from UV-SRS spectra of N-doped and undoped  $\text{TiO}_2$

The result is exhibited in Fig. 7. The direct photolysis of AMX by visible light resulting 12.4% degradation after 300 min. Thus, confirming that the contribution of direct photolysis is quite low, even at longer light exposure. The finding was in accordance with the previous report. AMX is stable through photolysis by irradiation of light above the wavelength of 300 nm [38-40].

As predicted, the AMX degradation percentage by N-doped  $\text{TiO}_2$  was higher than undoped  $\text{TiO}_2$ . The N-doped and undoped  $\text{TiO}_2$  degradation percentages were 68.5 and 38.7%, respectively. The result has a good agreement with the characterization as discussed above, that the nitrogen doping at 30% initial dopant concentration has successfully incorporated in  $\text{TiO}_2$ , increased the absorption in the visible region, and narrowed the band gap energy (2.97 eV). Therefore, it is reasonable that N-doped  $\text{TiO}_2$  exhibits higher photocatalytic activity under visible light irradiation compared to bare  $\text{TiO}_2$ . Moreover, the N-doped increased the degradation percentage to 84.12% compared to pure  $\text{TiO}_2$  (78.01%) in UV irradiation.  $\text{TiO}_2$  itself has good photocatalytic activity under UV irradiation, while the nitrogen dopant allows to a lower electron-hole recombination rate that enhances the  $\text{TiO}_2$  activity [21,23].

The result is in accordance with the previous report [26,41-42] that the AMX could not completely degrade by  $\text{TiO}_2$  or doped  $\text{TiO}_2$ . The removal of AMX at the first stage was due to the adsorption of AMX on the active site of the catalyst. While the radiation starts, the AMX starts to decompose by the oxidative species produced by the catalyst. However, at the longer time of light exposure, the degradation rate decreases and the AMX could not completely degrade. This can be caused by the saturated active site of the catalyst. Additionally, at the late stage, the oxidative species have been consumed to oxidize the AMX and hence the amount of oxidative species was not sufficient to degrade all the AMX molecules [41]. Despite that, nitrogen doping successfully increased the degradation of AMX by  $\text{TiO}_2$  under visible light irradiation, which is more environmentally benign. Further study is required to increase the catalyst's active

site and increase the number of oxidative species, so the pharmaceutical pollutant can completely decompose.

The progressive degradation of AMX by N-doped  $\text{TiO}_2$  under visible light illumination is displayed in Fig. 8. The maximum wavelength of AMX solution is 227 nm. The maximum peak gradually decreased as the irradiation time increased and almost vanished after 300 min irradiation. No new absorption peak was observed during the degradation, indicating that other compounds

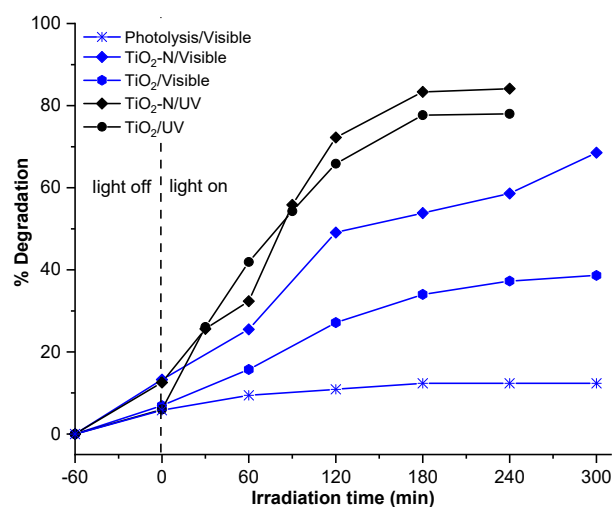


**Fig 7.** The AMX degradation by  $\text{TiO}_2$  compared to  $\text{TiO}_2$ -N (30%) under UV and visible light irradiation ( $[\text{AMX}]_0 = 20 \text{ mg/L}$ , catalyst dosage = 1 g/L)

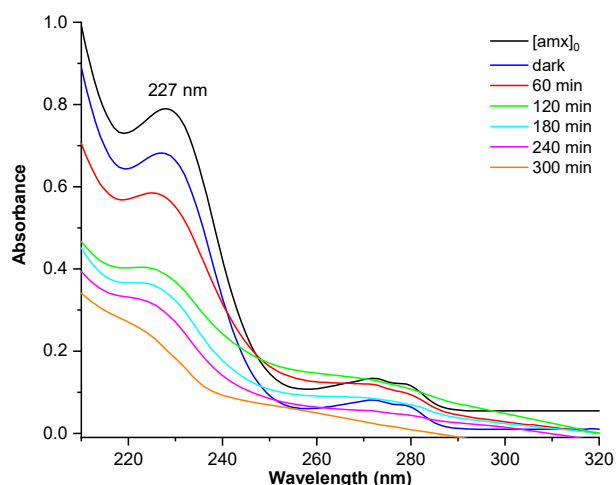


**Fig 8.** The changeover UV-Visible spectra of AMX before and after photodegradation by N-doped  $\text{TiO}_2$  under visible light irradiation ( $[\text{AMX}]_0 = 20 \text{ mg/L}$ , catalyst dosage = 1 g/L, irradiation time = 60–300 min)

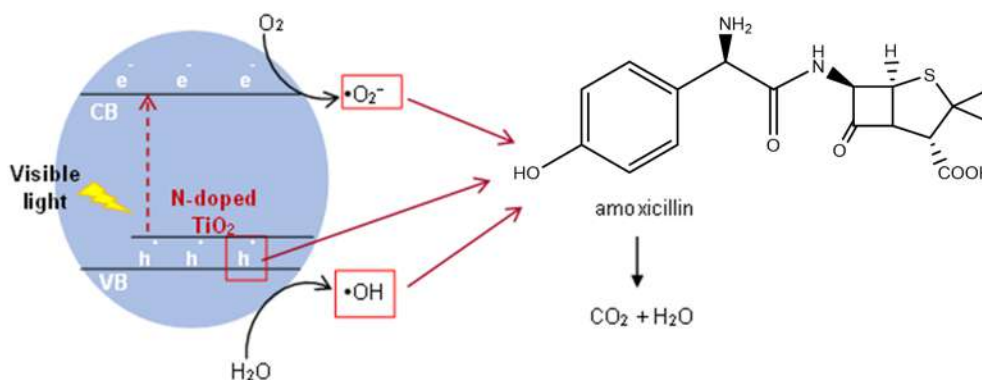


**Fig 9.** Proposed degradation mechanism of AMX by using N-doped TiO<sub>2</sub>

or intermediates were not detected in this degradation process. The AMX degraded up to 68.5%, resulting in small molecules such as H<sub>2</sub>O and CO<sub>2</sub>. The proposed degradation mechanism of AMX by advanced oxidation process using N-doped TiO<sub>2</sub> is presented in Fig. 9. The nitrogen doping forms a new energy level between the valence and conduction band of TiO<sub>2</sub> and narrows the band gap [24-25]. Therefore, visible light irradiation is adequate to excite an electron from the valence band into the conduction band. The formation pairs of electrons (e<sup>-</sup>) and holes (h<sup>+</sup>) will initiate the production of oxidative species: OH<sup>•</sup> and O<sub>2</sub><sup>-•</sup>. The oxidative species (h<sup>+</sup>, OH<sup>•</sup>, and O<sub>2</sub><sup>-•</sup>) played an essential role in the degradation of AMX, then decomposed the compound into CO<sub>2</sub> and H<sub>2</sub>O [3,19]. The proposed mechanism was adopted from the previous study [9,20,43-44].

## ■ CONCLUSION

The result of our study showed that initial nitrogen concentration affects the resulting N-doped TiO<sub>2</sub> catalyst. Nitrogen with an initial concentration of 30% (w/w) was successfully doped onto TiO<sub>2</sub> and had the lowest band gap energy of 2.97 eV. The presence of nitrogen increases the photodegradation of AMX for both UV and visible light irradiation. Nitrogen has narrowed the TiO<sub>2</sub> band gap energy that enhanced the TiO<sub>2</sub> activity under visible light for AMX degradation. AMX degraded 68.5% under visible light radiation, higher than bare TiO<sub>2</sub> (38.7%). Therefore, N-doped TiO<sub>2</sub> had good potential as a photocatalyst for the degradation of pharmaceutical pollutant under visible light irradiation in a natural aqueous solution without an additional oxidative agent.

## ■ ACKNOWLEDGMENTS

The authors acknowledge the financial support from the PMDSU scholarship by the Ministry of Research, Technology and Higher Education, Republic of Indonesia (Contract No. 3139/UN1.DITLIT/DITLIT/PT/2020).

## ■ AUTHOR CONTRIBUTIONS

Kusuma Putri Suwondo performed the experiment, analyzed the data, and wrote the article. Nurul Hidayat Aprilita contributed to supervise the data interpretation and revised the manuscript, and Endang Tri Wahyuni contributed to conceive the idea of this research, supervised the data interpretation, and revised the manuscript.

## ■ REFERENCES

- [1] Center for Systems Science and Engineering (CSSE) at Johns Hopkins University, 2023, *COVID-19 Dashboard* [Updated 2023 January], <https://coronavirus.jhu.edu/>, accessed on January 10, 2023.
- [2] Langford, B.J., So, M., Raybardhan, S., Leung, V., Soucy, J.P.R., Westwood, D., Daneman, N., and MacFadden, D.R., 2021, Antibiotic prescribing in patients with COVID-19: Rapid review and meta-analysis, *Clin. Microbiol. Infect.*, 27 (4), 520–531.
- [3] Salimi, M., Behbahani, M., Sobhi, H.R., Gholami, M., Jonidi Jafari, A., Rezaei Kalantary, R., Farzadkia, M., and Esrafil, A., 2019, A new nanophotocatalyst based on Pt and Bi co-doped TiO<sub>2</sub> for

- efficient visible-light photo degradation of amoxicillin, *New J. Chem.*, 43 (3), 1562–1568.
- [4] Munguia, J., and Nizet, V., 2018, Pharmacological targeting of the host-pathogen interaction: Alternatives to classical antibiotics to combat drug-resistant superbugs, *Trends Pharmacol. Sci.*, 38 (5), 473–488.
- [5] Comber, S.D.W., Upton, M., Lewin, S., Powell, N., and Hutchinson, T.H., 2020, COVID-19, antibiotics and one health: A UK environmental risk assessment, *J. Antimicrob. Chemother.*, 75 (11), 3411–3412.
- [6] Alygizakis, N.A., Gago-Ferrero, P., Borova, V.L., Pavlidou, A., Hatzianestis, I., and Thomaidis, N.S., 2016, Occurrence and spatial distribution of 158 pharmaceuticals, drugs of abuse and related metabolites in offshore seawater, *Sci. Total Environ.*, 541, 1097–1105.
- [7] Khan, A.H., Khan, N.A., Ahmed, S., Dhingra, A., Singh, C.P., Khan, S.U., Mohammadi, A.A., Changani, F., Yousefi, M., Alam, S., Vambol, S., Vambol, V., Khursheed, A., and Ali, I., 2020, Application of advanced oxidation processes followed by different treatment technologies for hospital wastewater treatment, *J. Cleaner Prod.*, 269, 122411.
- [8] Cuerda-Correa, E.M., Alexandre-Franco, M.F., and Fernández-González, C., 2020, Advanced oxidation processes for the removal of antibiotics from water. An overview, *Water*, 12 (1), 102.
- [9] Wang, J., and Zhuan, R., 2020, Degradation of antibiotics by advanced oxidation processes: An overview, *Sci. Total Environ.*, 701, 135023.
- [10] Byrne, C., Subramanian, G., and Pillai, S.C., 2018, Recent advances in photocatalysis for environmental applications, *J. Environ. Chem. Eng.*, 6 (3), 3531–3555.
- [11] Balarak, D., and Mostafapour, F.K., 2019, Photocatalytic degradation of amoxicillin using UV/Synthesized NiO from pharmaceutical wastewater, *Indones. J. Chem.*, 19 (1), 211–218.
- [12] Elmolla, E.S., and Chaudhuri, M., 2010, Photocatalytic degradation of amoxicillin, ampicillin and cloxacillin antibiotics in aqueous solution using UV/TiO<sub>2</sub> and UV/H<sub>2</sub>O<sub>2</sub>/TiO<sub>2</sub> photocatalysis, *Desalination*, 252 (1-3), 46–52.
- [13] Moradi, M., Hasanvandian, F., Isari, A.A., Hayati, F., Kakavandi, B., and Setayesh, S.R., 2021, CuO and ZnO co-anchored on g-C<sub>3</sub>N<sub>4</sub> nanosheets as an affordable double Z-scheme nanocomposite for photocatalytic decontamination of amoxicillin, *Appl. Catal., B*, 285, 119838.
- [14] Chinnaiyan, P., Thampi, S.G., Kumar, M., and Balachandran, M., 2019, Photocatalytic degradation of metformin and amoxicillin in synthetic hospital wastewater: Effect of classical parameters, *Int. J. Environ. Sci. Technol.*, 16 (10), 5463–5474.
- [15] Dimitrakopoulou, D., Rethemiotaki, I., Frontistis, Z., Xekoukoulotakis, N.P., Venieri, D., and Mantzavinos, D., 2012, Degradation, mineralization and antibiotic inactivation of amoxicillin by UV-A/TiO<sub>2</sub> photocatalysis, *J. Environ. Manage.*, 98, 168–174.
- [16] Xing, X., Du, Z., Zhuang, J., and Wang, D., 2018, Removal of ciprofloxacin from water by nitrogen doped TiO<sub>2</sub> immobilized on glass spheres: Rapid screening of degradation products, *J. Photochem. Photobiol., A*, 359, 23–32.
- [17] Wetchakun, K., Wetchakun, N., and Sakulsermsuk, S., 2019, An overview of solar/visible light-driven heterogeneous photocatalysis for water purification: TiO<sub>2</sub>- and ZnO-based photocatalysts used in suspension photoreactors, *J. Ind. Eng. Chem.*, 71, 19–49.
- [18] Bergamonti, L., Graiff, C., Bergonzi, C., Potenza, M., Reverberi, C., Ossiprandi, M.C., Lottici, P.P., Bettini, R., and Elviri, L., 2022, Photodegradation of pharmaceutical pollutants: New photocatalytic systems based on 3D printed scaffold-supported Ag/TiO<sub>2</sub> nanocomposite, *Catalysts*, 12 (6), 580.
- [19] Lalliansanga, L., Tiwari, D., Lee, S.M., and Kim, D.J., 2022, Photocatalytic degradation of amoxicillin and tetracycline by template synthesized nano-structured Ce<sup>3+</sup>@TiO<sub>2</sub> thin film catalyst, *Environ. Res.*, 210, 112914.
- [20] Çağlar Yılmaz, H., Akgeyik, E., Bougarrani, S., El Azzouzi, M., and Erdemoğlu, S., 2020, Photocatalytic degradation of amoxicillin using Co-doped TiO<sub>2</sub> synthesized by reflux method and



- monitoring of degradation products by LC-MS/MS, *J. Dispersion Sci. Technol.*, 41 (3), 414–425.
- [21] Mhemid, R.K.S., Salman, M.S., and Mohammed, N.A., 2022, Comparing the efficiency of N-doped TiO<sub>2</sub> and commercial TiO<sub>2</sub> as photo catalysts for amoxicillin and ciprofloxacin photodegradation under solar irradiation, *J. Environ. Sci. Health, Part A: Toxic/Hazard. Subst. Environ. Eng.*, 57 (9), 813–829.
- [22] Gomes, J., Lincho, J., Domingues, E., Quinta-Ferreira, R.M., and Martins, R.C., 2019, N-TiO<sub>2</sub> photocatalysts: A review of their characteristics and capacity for emerging contaminants removal, *Water*, 11 (2), 373.
- [23] Zhao, W., Liu, S., Zhang, S., Wang, R., and Wang, K., 2019, Preparation and visible-light photocatalytic activity of N-doped TiO<sub>2</sub> by plasma-assisted sol-gel method, *Catal. Today*, 337, 37–43.
- [24] Asahi, R., Morikawa, T., Irie, H., and Ohwaki, T., 2014, Nitrogen-doped titanium dioxide as visible-light-sensitive photocatalyst: Designs, developments, and prospects, *Chem. Rev.*, 114 (19), 9824–9852.
- [25] Nolan, N.T., Synnott, D.W., Seery, M.K., Hinder, S.J., Van Wassenhoven, A., and Pillai, S.C., 2012, Effect of N-doping on the photocatalytic activity of sol-gel TiO<sub>2</sub>, *J. Hazard. Mater.*, 211-212, 88–94.
- [26] Verma, M., and Haritash, A.K., 2020, Photocatalytic degradation of Amoxicillin in pharmaceutical wastewater: A potential tool to manage residual antibiotics, *Environ. Technol. Innovation*, 20, 101072.
- [27] Hanaor, D.A.H., and Sorrell, C.C., 2011, Review of the anatase to rutile phase transformation, *J. Mater. Sci.*, 46 (4), 855–874.
- [28] Odling, G., and Robertson, N., 2015, Why is anatase a better photocatalyst than rutile? The importance of free hydroxyl radicals, *ChemSusChem*, 8 (11), 1838–1840.
- [29] Zhao, Z., Omer, A.A., Qin, Z., Osman, S., Xia, L., and Singh, R.P., 2019, Cu/N-codoped TiO<sub>2</sub> prepared by the sol-gel method for phenanthrene removal under visible light irradiation, *Environ. Sci. Pollut. Res.*, 27 (15), 17530–17540.
- [30] Li, H., Hao, Y., Lu, H., Liang, L., Wang, Y., Qiu, J., Shi, X., Wang, Y., and Yao, J., 2015, A systematic study on visible-light N-doped TiO<sub>2</sub> photocatalyst obtained from ethylenediamine by sol-gel method, *Appl. Surf. Sci.*, 344, 112–118.
- [31] Yang, G., Jiang, Z., Shi, H., Xiao, T., and Yan, Z., 2010, Preparation of highly visible-light active N-doped TiO<sub>2</sub> photocatalyst, *J. Mater. Chem.*, 20 (25), 5301–5309.
- [32] Huo, Y., Jin, Y., Zhu, J., and Li, H., 2009, Highly active TiO<sub>2-x-y</sub>N<sub>x</sub>F<sub>y</sub> visible photocatalyst prepared under supercritical conditions in NH<sub>4</sub>F/EtOH fluid, *Appl. Catal., B*, 89 (3-4), 543–550.
- [33] Cheng, X., Yu, X., and Xing, Z., 2012, Characterization and mechanism analysis of N doped TiO<sub>2</sub> with visible light response and its enhanced visible activity, *Appl. Surf. Sci.*, 258 (7), 3244–3248.
- [34] Liu, C., Yu, T., Tan, X., and Huang, X., 2017, Comparison N-Cu-codoped nanotitania and N-doped nanotitania in photocatalytic reduction of CO<sub>2</sub> under UV light, *Inorg. Nano-Met. Chem.*, 47 (1), 9–14.
- [35] Reda, S.M., Khairy, M., and Mousa, M.A., 2020, Photocatalytic activity of nitrogen and copper doped TiO<sub>2</sub> nanoparticles prepared by microwave-assisted sol-gel process, *Arabian J. Chem.*, 13 (1), 86–95.
- [36] Wang, H., Yang, X., Xiong, W., and Zhang, Z., 2015, Photocatalytic reduction of nitroarenes to azo compounds over N-doped TiO<sub>2</sub>: Relationship between catalysts and chemical reactivity, *Res. Chem. Intermed.*, 41 (6), 3981–3997.
- [37] Etacheri, V., Seery, M.K., Hinder, S.J., and Pillai, S.C., 2010, Highly visible light active TiO<sub>2-x</sub>N<sub>x</sub> heterojunction photocatalysts, *Chem. Mater.*, 22 (13), 3843–3853.
- [38] Bergamonti, L., Bergonzi, C., Graiff, C., Lottici, P.P., Bettini, R., and Elviri, L., 2019, 3D printed chitosan scaffolds: A new TiO<sub>2</sub> support for the photocatalytic degradation of amoxicillin in water, *Water Res.*, 163, 114841.
- [39] Kanakaraju, D., Kockler, J., Motti, C.A., Glass, B.D., and Oelgemöller, M., 2015, Titanium dioxide/zeolite integrated photocatalytic

- adsorbents for the degradation of amoxicillin, *Appl. Catal., B*, 166-167, 45–55.
- [40] Moreira, N.F.F., Orge, C.A., Ribeiro, A.R., Faria, J.L., Nunes, O.C., Pereira, M.F.R., and Silva, A.M.T., 2015, Fast mineralization and detoxification of amoxicillin and diclofenac by photocatalytic ozonation and application to an urban wastewater, *Water Res.*, 87, 87–96.
- [41] Gar Alalm, M., Tawfik, A., and Ookawara, S., 2016, Enhancement of photocatalytic activity of TiO<sub>2</sub> by immobilization on activated carbon for degradation of pharmaceuticals, *J. Environ. Chem. Eng.*, 4 (2), 1929–1937.
- [42] Klauson, D., Babkina, J., Stepanova, K., Krichevskaya, M., and Preis, S., 2010, Aqueous photocatalytic oxidation of amoxicillin, *Catal. Today*, 151 (1-2), 39–45.
- [43] Wahyuni, E.T., Yulikayani, P.Y., and Aprilita, N.H., 2020, Enhancement of visible-light photocatalytic activity of Cu-doped TiO<sub>2</sub> for photodegradation of amoxicillin in water, *J. Mater. Environ. Sci.*, 11 (4), 670–683.
- [44] Nguyen, T.L., Pham, T.H., Viet, N.M., Thang, P.Q., Rajagopal, R., Sathya, R., Jung, S.H., and Kim, T., 2022, Improved photodegradation of antibiotics pollutants in wastewaters by advanced oxidation process based on Ni-doped TiO<sub>2</sub>, *Chemosphere*, 302, 134837.

**Short Communication:****Adsorption of Methyl Orange Dyes on Oriented Co/Fe-MOF Bimetallic Organic Framework in Wastewater Treatment****Kim Ngan Thi Tran<sup>1,2\*</sup>, Cao Phuong Khanh Phan<sup>3</sup>, Vuong Thinh Ho<sup>3</sup>, Hung Dung Chau<sup>1</sup>, and Thi Nhu Dung Nguyen<sup>2,4</sup>**<sup>1</sup>*Institute of Applied Technology and Sustainable Development, Nguyen Tat Thanh University, Ho Chi Minh City 70000, Vietnam*<sup>2</sup>*Faculty of Environmental and Food Engineering, Nguyen Tat Thanh University, Ho Chi Minh City 70000, Vietnam*<sup>3</sup>*Faculty of Chemical Engineering, Ho Chi Minh City University of Technology, Ho Chi Minh City 70000, Vietnam*<sup>4</sup>*Ho Chi Minh City University of Natural Resources and Environment (HCMUNRE), Ho Chi Minh City 70000, Vietnam***\* Corresponding author:**

tel: +84-765712086

email: nganttk@ntt.edu.vn

Received: June 21, 2022

Accepted: August 23, 2022

DOI: 10.22146/ijc.75636

**Abstract:** The production of highly efficient and reusable adsorbents that can be used in pigment treatment has been of great scientific interest. Metallic organic frameworks (MOFs) are considered a new type of material with extremely diverse structures and can be used as adsorbents to remove environmental pollutants. The selected Co/Fe-MOF material was synthesized in this study by using the solvent-thermal method. Then, the effects of several influencing factors such as adsorbent dosage, pH, initial concentration of MO, and exposure time on the adsorption capacity of methyl orange (MO) dyes by Co/Fe-MOF were evaluated. Under acidic conditions (pH 4), the effective removal of MO from aqueous solution reached equilibrium after 60 min upon exposure to MO at the concentration of 200 mg/L, and the adsorption capacity was 137.6 mg/g. The two models of adsorption isotherms, Freundlich and Langmuir, showed good compatibility with the experimental data, and the calculated correlation coefficients ( $R^2$ ) were both greater than 0.96. The MO adsorption efficiency was proposed to fit the pseudo-quadratic and pseudo-first-order kinetic models. Therefore, MOF materials can be considered as a potential agent for wastewater treatment, thereby providing a possible solution to solve water pollution.

**Keywords:** bimetallic-organic framework; adsorption; methylene orange; kinetic model; isotherms model

**■ INTRODUCTION**

In recent years, rapid industrialization development has been associated with the disposal of a large amount of wastewater and environmental pollution. One of the leading causes of environmental pollution has been widely known as textile dyes [1]. Previous studies have shown that direct disposal of untreated wastewater that contains toxic organic substances would significantly harm human health and destroy the natural environment [2-3]. Methyl orange (MO) is an anionic dye that is commonly used in the textile industry, with varied colors depending on the pH values. MO is recognized as a highly

toxic substance and is associated with many health hazards [4].

Several methods have been used to remove chromogenic organic substances from aqueous media, such as precipitation, filtration, reverse osmosis, and adsorption. With the goal of achieving high efficiency at a reduced cost while reducing wastewater volume and improving the treatment quality, adsorption has been considered an effective method with numerous outstanding advantages [5-7]. Recently, the bimetallic organic framework (M/MOFs) containing the second metal (e.g., Ni, Co, Mn, and Cu) has much better adsorption capacity as compared with monometallic

materials [8-12]. The structure and properties of MOFs can vary depending on different ligands and metal ions, resulting in materials with high pore structure, large surface area, and multifunctional surface [13-14]. Therefore, MOFs have high applicability in the field of catalysis, gas storage, gas separation, adsorbent or electrode materials in sensors.

Recent studies have shown that the methylene blue removal efficiency of mixed MOFs was 2.8 times higher than that of Fe-MOF [15]. The Ni/Fe-MOFs became more porous, and the surface area was increased due to the formation of mixed metal clusters, as compared to the single-metal Fe-MOFs [16]. Wang et al. [17] successfully synthesized Ti-doped Fe-MOFs bimetallic materials to increase the yield and shorten the decomposition time of Orange II. In another study, MM-MOF was synthesized by replacing  $\text{Fe}^{3+}$  in Fe-BDC with  $\text{Cu}^{2+}$  to obtain FeCu-BDC. Significantly, the synergistic effect of Fe and Cu on the material surface as a heterogeneous catalyst was evaluated for the antimicrobial activity of sulfamethoxazole (SMX) [12].

Therefore, in order to promote the attractive properties and increase the adsorption capacity of MOF materials, the present study has combined Fe-MOF with  $\text{Co}^{2+}$  metal ions to prepare Co/Fe-MOF material based on the solvothermal method in *N,N*-dimethylformamide solvent with the combination of metal salts and 1,4-benzenedicarboxylic acid ligand. The MO dyes were used in this study to evaluate the adsorption capacity of the material.

## ■ EXPERIMENTAL SECTION

### Materials

Chemicals and reagents used in this study were  $\text{FeCl}_3 \cdot 6\text{H}_2\text{O}$  (99%),  $\text{Co}(\text{NO}_3)_2 \cdot 6\text{H}_2\text{O}$  (99%), and 1,4-benzenedicarboxylic acid (99.8%) from Xilong-China. Meanwhile, *N,N*-dimethylformamide (DMF) was purchased from Macron-Fisher and methyl orange dye was obtained from Sigma-Aldrich.

### Instrumentation

Equipment used in this study included a Memmert UN110 oven (108 L, 300 °C), a thermostatic shaker

Jeotech IST-4075 (20 erlen, 250–300 mL), a Teflon-lined solvothermal synthesis autoclave reactor (100 mL), 8D Advance Bruker (Germany) for XRD, Nicolet 6700 device-Thermo Fisher Scientific (USA) for FTIR, S4800-JEOL Japan for SEM, Micromeritics 2020 (USA) for BET, and UV-Vis spectrophotometer (Thermo, USA).

### Procedure

#### **Synthesis of Co/Fe-MOF sample**

The Co-doped Fe-MOF material was synthesized through the solvent-thermal method, following the previous protocol by Ding et al. [18] with slight modifications. At first,  $\text{FeCl}_3 \cdot 6\text{H}_2\text{O}$  (99%) and  $\text{Co}(\text{NO}_3)_2 \cdot 6\text{H}_2\text{O}$  were mixed at a mass ratio of  $\text{Co}^{2+}:\text{Fe}^{3+}$  of 0.267 and 2.482 g. Subsequently, 0.83 g of 1,4-benzenedicarboxylic acid was dissolved in 60 mL of DMF under constant stirring for 30 min. The solution was allowed to react at 150 °C for 20 h in a 100 mL Teflon tube with a stainless steel-based protective case. The mixture was then allowed to cool reaching room temperature, centrifuged to separate the solids, and washed with DMF and ethanol. The synthesized material was then vacuum dried at 120 °C for 24 h.

#### **Characterization of the synthesized materials**

The physical properties and structural composition of the were analyzed by several methods. X-Ray Diffraction (XRD) was measured by using  $\text{Cu-K}\alpha$  radiation at  $2\theta$  scanning angle from 10 to 35°. The characteristic functional groups on the surface of materials through FTIR spectroscopy. The structure and crystal morphology of the materials were analyzed by SEM images. The surface area and porosity of the adsorbent were determined by  $\text{N}_2$  adsorption-desorption isotherm (BET). The MO adsorption capacity of the materials was determined using a UV-Vis spectrophotometer.

#### **Methyl orange (MO) adsorption experiments**

The adsorption capacity of the MO-removing materials was evaluated based on several influencing factors such as contact time, pH, adsorbent dosage, and initial MO concentration. The adsorption was carried out in a 250 mL conical flask and placed on a heat shaker at 200 rpm. In each experiment, adsorbent at various concentrations of 0.002–0.030 g/L was accurately

weighed and mixed with 50 mL of MO solution (concentrations ranged from 30 to 300 ppm). The pH factor of the medium was also adjusted within the range of 2–12. After 10 to 240 min, 4 mL of sample solution was removed and centrifuged at 6000 rpm for 5 min to separate the adsorbent. The concentration of MO dye was determined at  $\lambda_{\max} = 465$  nm on a UV-Vis instrument.

## ■ RESULTS AND DISCUSSION

The structural characteristics and crystalline phase composition of the synthesized materials were determined based on the results of the XRD analysis. Fig. 1(a) has shown that Fe-MOF and CoFe-MOF samples have characteristic diffraction peaks appearing at  $2\theta$  angle  $< 30^\circ$ , which are the characteristic diffraction peaks for Fe-MOF. It is significant to be noted that the positions of XRD diffraction peaks of these CoFe-MOF materials have a slight shift towards the smaller  $2\theta$  angle than that of the synthesized Fe-MOF under the same conditions, indicating that Co has been phased doped into the Fe-MOF lattice. Blake et al. [19] firstly explained that the partial replacement of  $\text{Fe}^{3+}$  ions with other divalent metal ions ( $\text{M}^{2+}$ ) would lead to a slight decrease in the Fe–O bond length and a slight increase in the Fe–O–Fe angle. The process of doping Co in Fe-MOF causes the diffraction intensity to decrease but still maintains the Fe-MOF structure. In addition, the ionic charge significantly affects the material modification efficiency. Competition for electron affinity between two metal ions with the same

charge leads to distortion of the original material structure [20].

The FTIR spectra of Fe-MOF and CoFe-MOF samples show that the sample has a full range of material-specific oscillations at the absorption bands at 532, 751, 1390, 1589 and 3600–3000  $\text{cm}^{-1}$ , respectively (Fig. 1(b)). The symmetric and asymmetrical elongation of O–C–O is shown by oscillations in the region 1600–1400  $\text{cm}^{-1}$ . Fe–O oscillations and C–H bending vibrations of benzene are located at the maximum peaks of 532 and 751  $\text{cm}^{-1}$ , respectively. In addition, the formation of bimetallic centers of CoFe-MOF was determined based on the clear appearance of the peak at 622  $\text{cm}^{-1}$ , corresponding to the Co–O oscillations. This result is in high agreement with the previous study by Liang et al. [21].

The surface morphology of the material was determined by SEM images, and the results are presented in Fig. 2. The results show a clear change in the shape and size of the material in the presence of  $\text{Co}^{2+}$ . In the Fe-MOF sample, the surface morphology is uneven, the particle size is large, the grain boundary is not clear, and there is a clump of particles. When doping  $\text{Co}^{2+}$  ions into the Fe-MOF lattice framework occurs, the particles are uniform in size and shape. The grain size is more obvious, and the catch shape tends to have sharp peaks. The ratio difference in the reaction between  $\text{Fe}^{3+}$  and  $\text{Co}^{2+}$  with  $\text{H}_2\text{BDC}$  facilitates the growth of bimetallic MOFs.

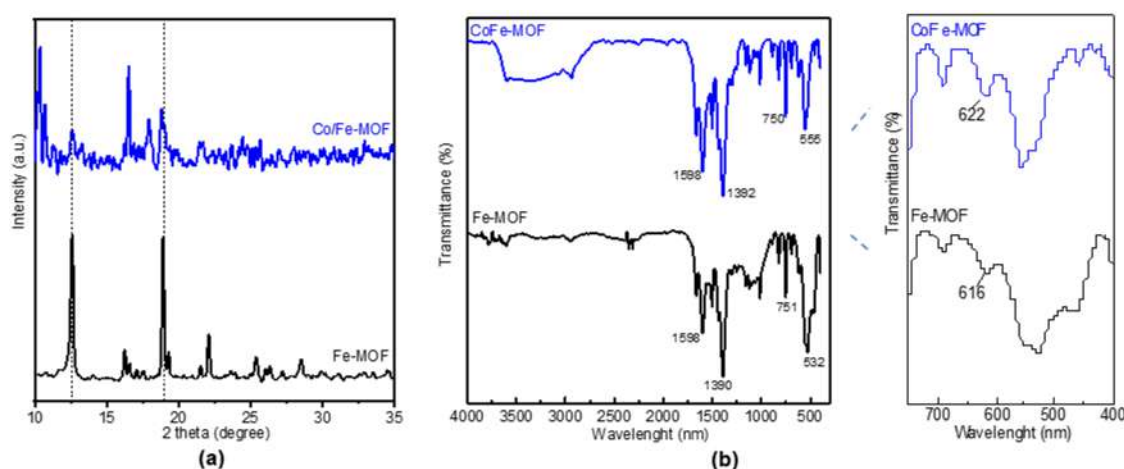


Fig 1. XRD patterns (a) and FTIR spectra (b) of Fe-MOF, CoFe-MOF

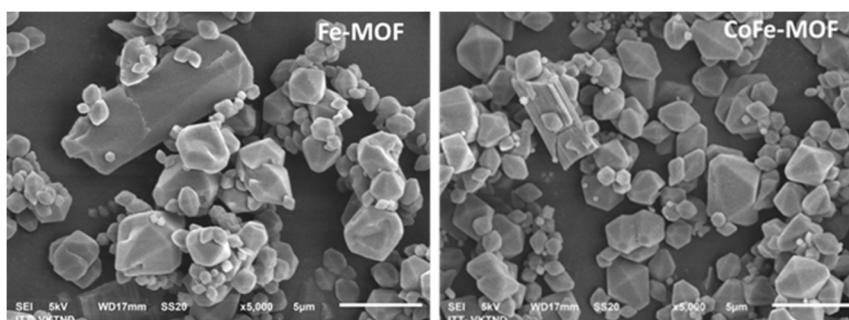


Fig 2. SEM image of the as-synthesized MOF

The  $N_2$  adsorption and desorption isotherms of the composites are shown in Fig. 3. The results show that the isotherm curve belongs to type II, according to the IUPAC classification. The synthesized Fe-MOF and CoFe-MOF materials have a BET surface area of 32.8 and 52.6  $m^2 \cdot g^{-1}$  and pore volumes of 0.06 and 0.09  $cm^3/g$ , respectively. The presence of Co metal in the Fe-MOF framework increases the specific surface area and porous volume, thus increasing the accessibility of the active sites and molecular diffusion to facilitate the high adsorption efficiency of water pollutants [22]. The inclusion of the second metal in the Fe-MOF framework is beneficial to promoting complete contact of the active sites of the resulting bimetallic M/Fe-MOF. The modification of metal ions into the original structure will contribute to the release of charges, making the material more porous and increasing the surface area. Recent research by Wang et al.

[23] showed an increase in specific surface area in the presence of the second metal Co at different ratios with Fe-MOF ( $32.8 m^2 \cdot g^{-1}$ ) and FeCo-MOF-1/3 ( $466.3 m^2 \cdot g^{-1}$ ). The presence of Co metal in the Fe-MOF framework increases the specific surface area and porous volume because the Co radius (65 nm) is slightly larger than that of Fe (64 nm), and the carboxyl groups react simultaneously with two metal ions.

One of the important parameters that directly affect the adsorption process is pH. Fig. 4(a) shows that the MO adsorption capacity of CoFe-MOF is higher than that of Fe-MOF in the pH range from 2 to 12. The MO adsorption capacity of the materials increases continuously from pH 2 to 4, yet sharply decreases when pH continues to increase to 12. The highest MO adsorption capacity of CoFe-MOF (104 mg/g) was achieved in an acid medium at pH 4. Therefore, it can be seen that the adsorption

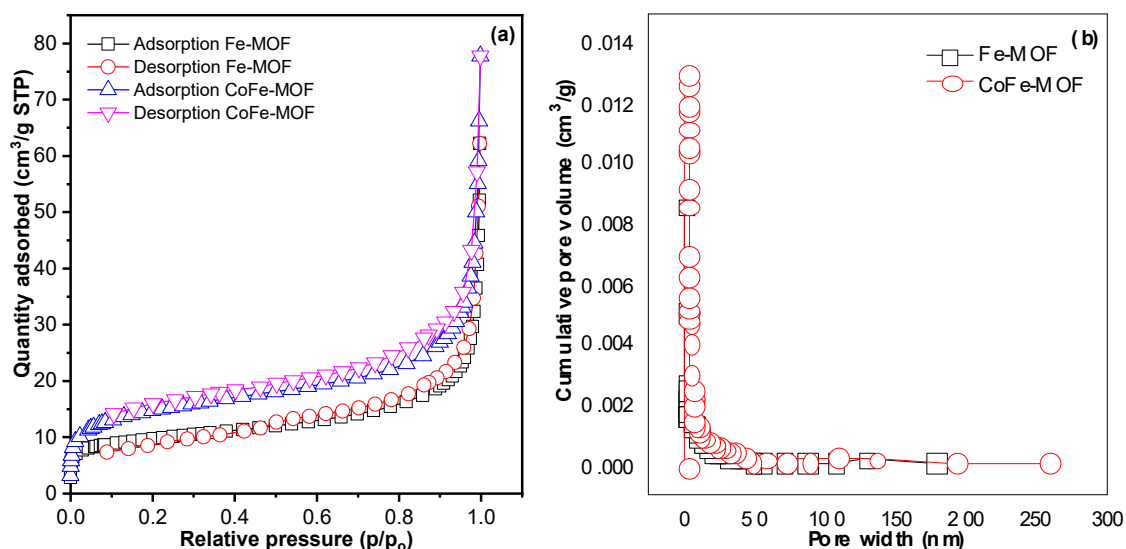


Fig 3.  $N_2$  adsorption-desorption isotherms (a) and pore size distributions (b) of Fe-MOF and CoFe-MOF samples

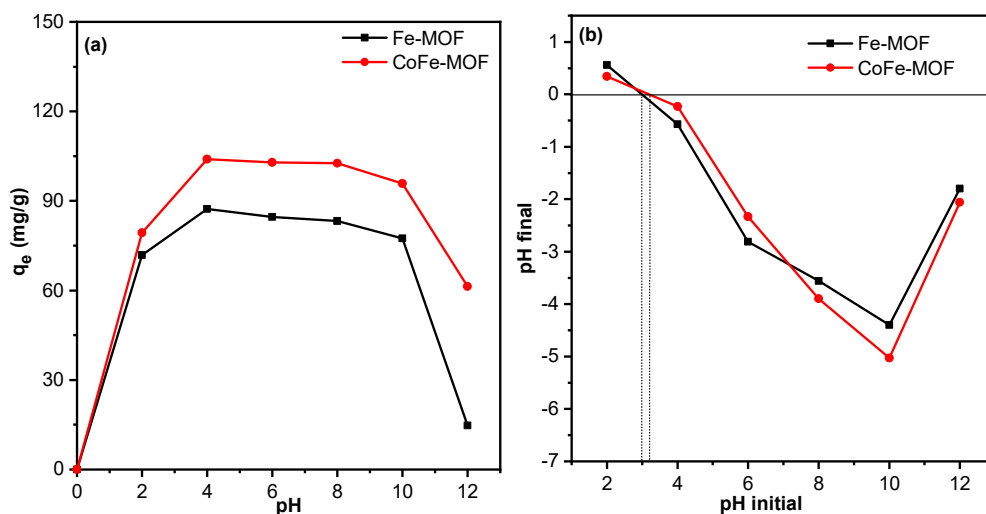


Fig 4. Effect of initial pH MO (a) and zero charge point (b) of Fe-MOF and CoFe-MOF

capacity of both materials strongly depends on the pH value. Furthermore, the surface charge of the adsorbent is also an important factor that requires attention. The surface charge of the material is evaluated based on the  $\text{pH}_{\text{pzc}}$  parameter when the pH variation reaches zero. Fig. 4(b) shows that the  $\text{pH}_{\text{pzc}}$  values of Fe-MOF and CoFe-MOF are 3.0 and 3.2, respectively. With the value of  $\text{pH}_{\text{pzc}} < \text{pH}$ , it is possible to determine the surface of the material exhibits a negative charge, which corresponds to the previous study [24]. The doped metals reduce the specific surface area of Fe-MOF, and the changes in the crystal structure and appearance morphology mainly produce the enhancement of adsorption capacity, which is due to competitive coordination between metal ions doped with

saturated iron ions to bind carboxylic groups in the BDC and thus an increasing number of active Fe sites are generated.

Subsequently, the effect of time, the dose of adsorbent, and the initial concentration of MO on the removal of MO colorant in an aqueous solution by Fe-MOF and CoFe-MOF samples were then investigated. For the effect of time, the adsorption reached equilibrium within 240 min under the conditions of fixed pH, adsorbent dosage, and initial MO concentration (Fig. 5(a)). The MO adsorption capacity of CoFe-MOF took place quickly within 60 min with an adsorption capacity of 105.2 mg/g. In contrast, the adsorption capacity of Fe-MOF material only reached

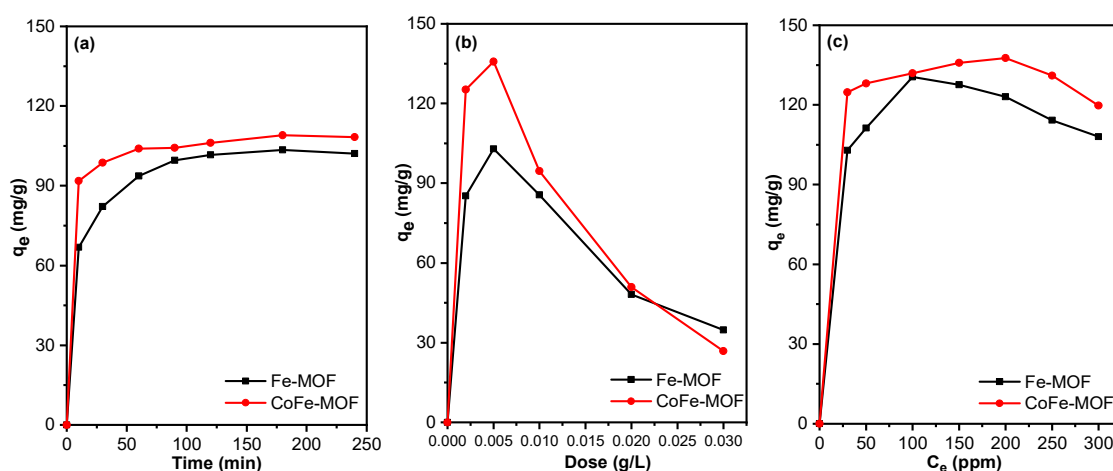


Fig 5. Effect of time (a), dose (b) and MO concentration initial (c) on the adsorption capacity of Fe-MOF and CoFe-MOF

95.7 mg/g after 60 min, and it took another 30 min to achieve the adsorption capacity of 100.6 mg/g. To increase the MO processing capacity, the amount of investigated material was in the range of 0.002–0.030 g/L, with other conditions being fixed. The results of Fig. 5(b) show that the adsorption capacity of both materials tends to sharply decrease when increasing the adsorbent dosage. Typically, CoFe-MOF at the concentration of 0.005 g/L has a much higher MO removal capacity (125.7 mg/g) than Fe-MOF at the concentration of 102.9 mg/g. Such an increase in MO removal efficiency may be dependent on increasing the adsorbent dosage, yet using a high dosage can reduce the diffusion capacity of the solution to the surface or change the physical properties of the material. The effect of the initial MO concentration (30–300 ppm) on the adsorption capacity was also evaluated in Fig. 5(c). The results have shown that the adsorption capacity strongly depends on the initial concentration of MO, with the highest MO removal capacity of Fe-MOF being 130.5 mg/g at the concentration of 100 ppm, while that of CoFe-MOF being 137.6 mg/g at the concentration of 200 ppm. When continuing to increase the MO concentration, the adsorption capacity decreased markedly since once the adsorption process have reached an equilibrium state, the MO residue was still high, thus filling the surface of the material. The influence of the pH factor is considered essential in the adsorption process, suggesting that the interaction between the surface of the adsorbent and the charge of the dye is an electrostatic interaction necessary for the adsorption mechanism. In addition, the size of the dye molecules (MO) is also considered a key factor in the adsorption process. The strong interaction can cause the migration of the dyes closer to the adsorbent and cause

the dyes to be adsorbed rapidly. Besides, the  $\pi$ - $\pi$  interaction of materials and aromatic rings of MO also facilitated the adsorption process [25].

In this study, the MO adsorption kinetics was evaluated based on four models of pseudo-first order and pseudo-second order. The results of the kinetic constants of both models are listed in Table 1 and Fig. 6(a). The influence of the contact time of the MO adsorption on CoFe-MOF was investigated from 0 to 240 min. According to Fig. 6(a), the equilibrium adsorption time was obtained at 60 min. Results have shown that the MO adsorption kinetics is suitable for both pseudo-first-order and pseudo-second-order models with correlation coefficients  $R^2$  of 0.993 and 0.998, respectively. Therefore, the adsorption of MO on CoFe-MOF materials was chemisorption through the electrostatic interaction between the adsorbents.

To describe the adsorption behavior of CoFe-MOF materials, Langmuir and Freundlich's models are used to assume that the adsorption mechanism occurs on the surface of the material. Fig. 6(b) shows the effect of different concentrations (30 to 300 mg/L) on the equilibrium adsorption capacity of MO. From the study of Langmuir and Freundlich adsorption isotherm models, it can be seen that the experimental data are more consistent with the Langmuir isotherm model (Table 2). The Langmuir correlation coefficient  $R^2$  is 0.982, which is larger than the Freundlich correlation coefficient  $R^2$  (0.969). According to calculations from the Langmuir adsorption heat transfer equation, the maximum adsorption capacity ( $Q_m$ ) is 136.19 mg/g. The results confirm that the Langmuir isotherm can be used to study the adsorption process.

**Table 1.** The adsorption kinetic constants

Kinetic models	Equation	Parameters	Value
Pseudo-first-order	$Q_t = Q_1 (1 - \exp(-k_1 t))$	$k_1$ ( $\text{min}^{-1}/(\text{mg/L})^{1/n}$ )	0.21
		$Q_1$ (mg/g)	104.34
		$R^2$	0.993
Pseudo-second-order	$Q_t = \frac{t}{\frac{1}{k_2 Q_2^2} + \frac{t}{Q_2}}$	$k_2 \cdot 10^4$ ( $\text{g}/(\text{mg} \cdot \text{min})$ )	0.0054
		$Q_2$ (mg/g)	106.79
		$R^2$	0.998



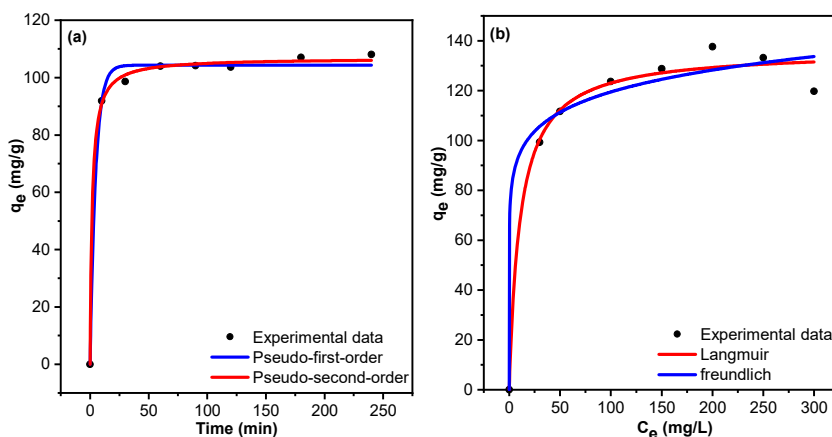


Fig 6. Kinetic and isothermal model of MO adsorption onto CoFe-MOF

Table 2. The adsorption isotherm constants

Kinetic models	Equation	Parameters	Value
Langmuir	$Q_e = \frac{Q_m K_L C_e}{1 + K_L C_e}$	$K_L$ (L/mg)	0.093
		$Q_m$ (mg/g)	136.19
	$R_L = \frac{1}{1 + K_L C_0}$	$R^2$	0.982
	Freundlich	$Q_e = K_F C_e^{1/n}$	$K_F$ (mg/g)/(mg/L) <sup>1/n</sup>
1/n			1/0.1024
$R^2$			0.969

## CONCLUSION

Fe-MOF and CoFe-MOF adsorbents were successfully synthesized at 150 °C by using the solvothermal method and DMF as the solvent. The results have shown that the CoFe-MOF material sample has a higher adsorption capacity than Fe-MOF in terms of MO removal. In acidic media (pH 4), the adsorption capacity reached 137.6 mg/g at the MO concentration of 200 ppm, the adsorbent dosage was 0.005 g/L, and the time to reach equilibrium after 60 min. The interaction between MO and CoFe-MOF dyes has been demonstrated through two kinetic models, i.e., pseudo-first order and pseudo-second order, and adsorption equilibrium data which is consistent with Langmuir isotherm with a maximum adsorption capacity of 136.19 mg/g.

## ACKNOWLEDGMENTS

The study was supported by The Youth Incubator for Science and Technology Program, managed by Youth Development Science and Technology Center – Ho Chi Minh Communist Youth Union and Department of

Science and Technology of Ho Chi Minh City with a contract number No. 10/2021/HĐ-KHCNT-VU.

## AUTHOR CONTRIBUTIONS

Cao Phuong Khanh Phan and Vuong Thinh Ho conducted the experiment, Kim Ngan Thi Tran and Thi Nhu Dung Nguyen wrote and revised the manuscript. All authors agreed to the final version of this manuscript.

## REFERENCES

- [1] Benkhaya, S., M'rabet, S., and El Harfi, A., 2020, A review on classifications, recent synthesis and applications of textile dyes, *Inorg. Chem. Commun.*, 115, 107891.
- [2] Khan, M.S., Khalid, M., and Shahid, M., 2020, What triggers dye adsorption by metal organic frameworks? The current perspectives, *Mater. Adv.*, 1 (6), 1575–1601.
- [3] Khan, I., Saeed, K., Zekker, I., Zhang, B., Hendi, A.H., Ahmad, A., Ahmad, S., Zada, N., Ahmad, H., Shah, L.A., Shah, T., and Khan, I., 2022, Review on

- methylene blue: Its properties, uses, toxicity and photodegradation, *Water*, 14 (2), 242.
- [4] Salama, R.S., Abd El-Hakam, S., Samra, S.E., El-dafrawy, S.M., El-Hakam, S.A., Samra, S.E., El-Dafrawy, S.M., and Ahmed, A.I., 2018, Adsorption, equilibrium and kinetic studies on the removal of methyl orange dye from aqueous solution by the use of copper metal organic framework (Cu-BDC), *Int. J. Mod. Chem.*, 10 (2), 195–207.
- [5] Fajriati, I., Mudasir, M., and Wahyuni, E.T., 2019, Adsorption and photodegradation of cationic and anionic dyes by TiO<sub>2</sub>-chitosan nanocomposite, *Indones. J. Chem.*, 19 (2), 441–453.
- [6] Iryani, A., Nur, H., Santoso, M., and Hartanto, D., 2020, Adsorption study of rhodamine B and methylene blue dyes with ZSM-5 directly synthesized from Bangka kaolin without organic template, *Indones. J. Chem.*, 20 (1), 130–140.
- [7] Hami, H.K., Abbas, R.F., Azeez, S.A., and Mahdi, N.I., 2021, Azo dye adsorption onto cobalt oxide: Isotherm, kinetics, and error analysis studies, *Indones. J. Chem.*, 21 (5), 1148–1157.
- [8] Abednatanzi, S., Gohari Derakhshandeh, P., Depauw, H., Coudert, F.X., Vrielinck, H., Van Der Voort, P., and Leus, K., 2019, Mixed-metal metal-organic frameworks, *Chem. Soc. Rev.*, 48 (9), 2535–2565.
- [9] Sun, Q., Liu, M., Li, K., Han, Y., Zuo, Y., Chai, F., Song, C., Zhang, G., and Guo, X., 2017, Synthesis of Fe/M (M = Mn, Co, Ni) bimetallic metal organic frameworks and their catalytic activity for phenol degradation under mild conditions, *Inorg. Chem. Front.*, 4 (1), 144–153.
- [10] Nguyen, V.H., Nguyen, T.D., Bach, L.G., Hoang, T., Bui, Q.T.P., Tran, L.D., Nguyen, C.V., Vo, D.V.N., and Do, S.T., 2018, Effective photocatalytic activity of mixed Ni/Fe-base metal-organic framework under a compact fluorescent daylight lamp, *Catalysts*, 8 (11), 487.
- [11] Nguyen, H.T.T., Dinh, V.P., Phan, Q.A.N., Tran, V.A., Doan, V.D., Lee, T., and Nguyen, T.D., 2020, Bimetallic Al/Fe Metal-Organic Framework for highly efficient photo-Fenton degradation of rhodamine B under visible light irradiation, *Mater. Lett.*, 279, 128482.
- [12] Tang, J., and Wang, J., 2020, Iron-copper bimetallic metal-organic frameworks for efficient Fenton-like degradation of sulfamethoxazole under mild conditions, *Chemosphere*, 241, 125002.
- [13] Choi, S., Cha, W., Ji, H., Kim, D., Lee, H.J., and Oh, M., 2016, Synthesis of hybrid metal-organic frameworks of {Fe<sub>x</sub>M<sub>y</sub>M'<sub>1-x-y</sub>}–MIL-88B and the use of anions to control their structural features, *Nanoscale*, 8 (37), 16743–16751.
- [14] Dey, C., Kundu, T., Biswal, B.P., Mallick, A., and Banerjee, R., 2014, Crystalline metal-Organic frameworks (MOFs): Synthesis, structure and function, *Acta Crystallogr., Sect. B: Struct. Sci., Cryst. Eng. Mater.*, 70 (1), 3–10.
- [15] Soni, S., Bajpai, P.K., Mittal, J., and Arora, C., 2020, Utilisation of cobalt doped Iron based MOF for enhanced removal and recovery of methylene blue dye from waste water, *J. Mol. Liq.*, 314, 113642.
- [16] Nguyen, H.T.T., Tran, K.N.T., Van Tan, L., Tran, V.A., Doan, V.D., Lee, T., and Nguyen, T.D., 2021, Microwave-assisted solvothermal synthesis of bimetallic metal-organic framework for efficient photodegradation of organic dyes, *Mater. Chem. Phys.*, 272, 125040.
- [17] Wang, M., Yang, L., Guo, C., Liu, X., He, L., Song, Y., Zhang, Q., Qu, X., Zhang, H., Zhang, Z., and Fang, S., 2018, Bimetallic Fe/Ti-based metal-organic framework for persulfate-assisted visible light photocatalytic degradation of Orange II, *ChemistrySelect*, 3 (13), 3664–3674.
- [18] Ding, L., Zeng, M., Wang, H., and Jiang, X.B., 2021, Synthesis of MIL-101-derived bimetal-organic framework and applications for lithium-ion batteries, *J. Mater. Sci.: Mater. Electron.*, 32 (2), 1778–1786.
- [19] Blake, A.B., Yavari, A., Hatfield, W.E., and Sethulekshmi, C.N., 1985, Magnetic and spectroscopic properties of some heterotrinary basic acetates of chromium(III), iron(III), and divalent metal ions, *J. Chem. Soc., Dalton Trans.*, 12, 2509–2520.
- [20] Cheng, X., Zhang, A., Hou, K., Liu, M., Wang, Y., Song, C., Zhang, G., and Guo, X., 2013, Size- and morphology-controlled NH<sub>2</sub>-MIL-53(Al) prepared

- in DMF–water mixed solvents, *Dalton Trans.*, 42 (37), 13698–13705.
- [21] Liang, H., Liu, R., Hu, C., An, X., Zhang, X., Liu, H., and Qu, J., 2021, Synergistic effect of dual sites on bimetal-organic frameworks for highly efficient peroxide activation, *J. Hazard. Mater.*, 406, 124692.
- [22] Wu, Q., Siddique, M.S., and Yu, W., 2021, Iron-nickel bimetallic metal-organic frameworks as bifunctional Fenton-like catalysts for enhanced adsorption and degradation of organic contaminants under visible light: Kinetics and mechanistic studies, *J. Hazard. Mater.*, 401, 123261.
- [23] Wang, Z., Wu, C., Zhang, Z., Chen, Y., Deng, W., and Chen, W., 2021, Bimetallic Fe/Co-MOFs for tetracycline elimination, *J. Mater. Sci.*, 56 (28), 15684–15697.
- [24] Shakly, M., Saad, L., Seliem, M.K., Bonilla-Petriciolet, A., and Shehata, N., 2022, New insights into the selective adsorption mechanism of cationic and anionic dyes using MIL-101(Fe) metal-organic framework: Modeling and interpretation of physicochemical parameters, *J. Contam. Hydrol.*, 247, 103977.
- [25] Valadi, F.M., Ekramipooya, A., and Gholami, M.R., 2020, Selective separation of Congo Red from a mixture of anionic and cationic dyes using magnetic-MOF: Experimental and DFT study, *J. Mol. Liq.*, 318, 114051.

**Review:****Chemometrics-Assisted UV-Vis Spectrophotometry for Quality Control of Pharmaceuticals: A Review**

Laela Hayu Nurani<sup>1</sup>, Citra Ariani Edityaningrum<sup>1</sup>, Irnawati Irnawati<sup>2</sup>, Anggita Rosiana Putri<sup>3</sup>, Anjar Windarsih<sup>4</sup>, Any Guntarti<sup>1</sup>, and Abdul Rohman<sup>5,6\*</sup>

<sup>1</sup>Faculty of Pharmacy, Universitas Ahmad Dahlan, Jl. Prof Soepomo, Janturan, Yogyakarta 55164, Indonesia

<sup>2</sup>Faculty of Pharmacy, Universitas Halu Oleo, Kendari 93232, Indonesia

<sup>3</sup>Department of Pharmacy, Faculty of Medicine, Universitas Brawijaya, Jl. Veteran, Malang 65145, Indonesia

<sup>4</sup>Research Center for Food Technology and Processing (PRTTP), National Research and Innovation Agency (BRIN), Gunungkidul, Yogyakarta 55861, Indonesia

<sup>5</sup>Center of Excellence Institute of Halal Industry and Systems, Universitas Gadjah Mada, Yogyakarta 55281, Indonesia

<sup>6</sup>Department of Pharmaceutical Chemistry, Faculty of Pharmacy, Universitas Gadjah Mada, Yogyakarta 55281, Indonesia

**\* Corresponding author:**

email: [abdul\\_kimfar@ugm.ac.id](mailto:abdul_kimfar@ugm.ac.id)

Received: April 25, 2022

Accepted: February 7, 2023

DOI: 10.22146/ijc.74329

**Abstract:** Spectroscopic method in the UV-Vis region is considered the most molecular spectrometric method for content determination of a single component. However, a lot of pharmaceutical dosage forms comprise two or more components which lead to peak overlapping. Moreover, in the chemical stability test, active pharmaceutical ingredient (API) was also found along with the degradation products, impurities, and adulterant compounds. UV-Vis spectroscopy is one of the methods of choice for the determination or quantification of a single component in pharmaceutical preparations. The pharmaceutical products typically contain two or more APIs having chromophoric agents capable of absorbing UV-Vis beams and the absorbance values are summative from the absorption of each UV-Vis active compound according to the additive nature of Lambert-Beer law. The main problem for the simultaneous determination of API along with impurities and the degradation products in pharmaceutical preparations is the presence of overlapping peaks of UV-Vis spectra. The chemometrics-assisted spectroscopy is one of the analytical efforts to solve these problems. This review highlighted the application of chemometrics in combination with UV-Vis spectroscopy for the assay of API, impurities, adulteration issues and degradation products present in pharmaceutical dosage forms.

**Keywords:** UV-Vis spectroscopy; chemometrics; API; degradation products; pharmaceutical dosage forms

**List of Abbreviations**

AC	= Acephylline piperazine	AP	= 4-Aminophenol
ACA	= 4-Chloroacetanilide	API	= Active pharmaceutical ingredients
ACH	= Acetophenone	ASP	= Aspirin
AKN	= Alkaline degradation products	ATN	= Atenolol
ALP	= Allopurinol	ATV	= Atorvastatin calcium
AM	= 1-Methyl-3-phenylpropylamine	B <sub>1</sub>	= Thiamine
AME	= Absolute mean error	B <sub>6</sub>	= Pyridoxin
AML	= Amlodipin	BET	= Betamethasone
ANN	= Artificial neural networks	BX	= Bromhexine hydrochloride
		BZ	= Benazepril hydrochloride

BZA	= <i>p</i> -Hydroxybenzoic acid	LS-SVM	= Least squares support vector machine
CAFF	= Caffeine	LV	= Latent variable
CAR	= Carbidopa	MCR	= Mean centering ratio spectra
CBM	= Carbamazepine	MET	= Metformin hydrochloride
CBME	= Carbamazepine epoxide	MF	= Mometazone furoate
CBS	= Cobicistat	MNZ	= 2-Methyl-5-nitro-1 <i>H</i> -imidazole
CBT	= Carbetocin	MP	= Methylparaben
CEF	= Cefixime	MTZ	= Metamizole
CEL	= Celecoxib	NAP	= Naproxen
CFS	= Cefoxitin sodium	NAPH	= Naphazoline hydrochloride
CLS	= Classical least square	NEO	= Neomycin
CP	= 4-Chlorophenol	NF	= Norfloxacin
CPX	= Ciprofloxacin	NIF	= Nifuroxazide
CRA	= Concentration residual augmented	NLP	= Nalbuphine
CS	= Cromolyn sodium	NMR	= Nuclear magnetic spectroscopy
CTM	= Chlorpheniramine maleate	NP	= 4-Nitrophenol
CZX	= Chlorzoxazone	ONZ	= Ornidazole
DAP	= 2,6-Diaminopyridine	OXI	= Oxidative degradation products
DIA	= Diacerein	PC	= Principal component
DOX	= Doxycycline hyclate	PCR	= Principal component regression
DP	= Diprophyline	PCT	= Paracetamol
DPF	= Dapagliflozin	PH	= Phenobarbitone
DPH	= Diphenhydramine hydrochloride	PHE	= Phenylephrine
DRV	= Darunavir ethanolate	PHEN	= Phenylephrine hydrochloride
EBV	= Elbasvir	PHZ	= Phenazopyridine hydrochloride
EMP	= Empagliflozin	PIM	= Pimozide
ENM	= Enalapril maleate	PIO	= Pioglitazone
ENT	= Entacapone	PLSR	= Partial least square regression
ERD	= Erdosteine	PP	= Papaverine hydrochloride
ET	= Etodolac	PROPI	= Propyphenazone
ETB	= Emtricitabine	PrP	= Propylparaben
EZT	= Ezetimibe	PZ	= Prazosin
FA	= Fenofibric acid	RAM	= Ramipril
FEN	= Fenofibrate	RIS	= Risperidone
GAANN	= Genetic algorithm artificial neural networks	ROS	= Rosuvastatin Calcium
GA-PLS	= Genetic algorithm partial least square	RMSEC	= Root mean square error of calibration
GLM	= Glimepiride	RMSECV	= Root mean square error of cross-validation
GLZ	= Gliclazide	RMSEP	= Root mean square error of prediction
GMI	= Gemifloxacin	RSE	= Relative standard error
GRV	= Grazoprevir	SAX	= Saxagliptin
GUA	= Guaifenesin	SFB	= Sofosbuvir
HB	= <i>p</i> -Hydroxybenzaldehyde	SL	= Salbutamol sulfate
HCT	= Hydrochlorothiazide	SMLR	= Stepwise multiple linear regression
HP	= Haloperidol	SMT	= Simvastatin
HPLC	= High-performance liquid chromatography	SOF	= Sofosbuvir
IBU	= Ibuprofen	SPR	= Spironolactone
IMB	= Imatinib	SRA	= Spectral residual augmented
IMD	= Imidapril hydrochloride	STA	= Stavudine
ISX	= Isoxsuprine	STG	= Sitagliptin
LAM	= Lamivudine	SVR	= Support vector regression
LDV	= Ledipasvir	TAF	= Tenofovir alafenamide fumarate
LES	= Lesinurad	TC	= Thiocolchicoside
LEV	= Levodopa	THEO	= Theophylline

TMP	= Trimethoprim
TRM	= Tramadol
TZ	= Tinidazole
VAL	= Valsartan

VDG	= Vildagliptin
VEP	= Velpatasvir
VNC	= Vancomycin
GLZ	= Gliclazide

## ■ INTRODUCTION

Spectroscopy is a discipline concerned with the interaction between electromagnetic radiation in certain wavelengths and samples. Ultraviolet-Visible (UV-Vis) spectrophotometry is a common analytical method used in the routine analytical laboratory and pharmaceutical industry due to its simplicity and rapidity. The versatility of instruments, the simplicity of analytical procedures, and the method performance make UV-Vis spectroscopic method widely used for content determination of pharmaceutical dosage forms. This spectroscopic technique is also more economical compared to other spectroscopic techniques like infrared and NMR and other instrumental methods like chromatography and electrophoresis [1-2]. In UV-Vis spectroscopy, electrons in analytes absorbing UV radiation (200–400 nm) and visible radiation (400–800 nm) are excited from the ground state into excited states. UV-Vis spectroscopy is quantized, in which only electromagnetic radiation with a precise energy level can make electronic transitions [3].

UV-Vis spectroscopy is a method of choice for the determination of a single component in pharmaceutical preparations. Unfortunately, pharmaceutical products typically contain two or more active pharmaceutical products having chromophoric agents capable of absorbing UV-Vis beams [4], causing signal overlapping that challenges the analysis. Quantitative analysis of spectroscopic methods is based on Lambert-Beer's law, which relates to the absorbance and concentration of analytes, as depicted in Eq. (1).

$$A = abc \quad (1)$$

in which A is the absorbance value, a is the specific absorptivity of analytes which depends on wavelength and solvents used, b is the cuvette thickness, and c expresses the concentration of analytes.

The main challenge of UV-Vis spectroscopy for simultaneous quantitative analysis of more than one active chromophoric compound in the same mixtures is

the presence of overlapping UV spectra. Consequently, the absorbance value in a certain wavelength is added from each chromophoric compound in the mixture. Under computer-controlled spectrophotometers, some efforts have been made to resolve the overlapping UV-Vis spectra coming from the mixtures of compounds, including derivative spectrophotometry or its combination with chemometrics [5-6], Vierordt's method and its modified method [7], H-point standard addition method [8], and chemometrics of multivariate calibration such as CLS, SMLR, PCR, PLSR, GA-PLS and ANNs [9].

## ■ METHOD

Reputable databases including Scopus (<http://www.scopus.com/>), Web of Science (<http://webofknowledge.com/>), DOAJ ([doaj.org](http://doaj.org/)), ScienceDirect (<http://www.sciencedirect.com/>), PubMed (<http://www.ncbi.nlm.nih.gov/pubmed/>), Springer Link (<http://link.springer.com/>), American Chemical Society (<https://pubs.acs.org/>), Wiley Online Library (<http://onlinelibrary.wiley.com/>), recognized books, abstracts and non-indexed journals were explored while searching the literature. The keywords used were "UV-Vis spectroscopy", "Chemometrics", "UV-Vis spectroscopy for assay for Active Pharmaceutical Ingredients", "UV-Vis spectroscopy for assay for Pharmaceutical Products". This procedure was adopted by Hosssain et al. [10].

## ■ DISCUSSION

### Chemometrics

Chemometric methods are powerful tools used in analytical chemistry to extract chemical data into more understandable information. The application of chemometrics in the quality control of pharmaceutical products is continuously increasing due to the advanced development in statistical software and instrumentation that allow the exploration of new issues in analytical

chemistry [10]. The term chemometrics originated from the word *kemometri* (*kemo* refers to chemistry and *metri* refers to measure) and was first introduced by Svante Wold in 1972. Chemometrics is considered an interdisciplinary study combining mathematical and statistical methods with chemistry to extract chemical information from chemical data. Chemometrics is a science related to the measurements of responses, including from UV-Vis spectra, to be extracted into more understandable information [11]. In spectroscopic applications, the chemometric techniques widely used in pharmaceutical analysis are UV-Vis spectral processing, pattern recognition or classification methods, and regression methods using multivariate data [12], as shown in Fig. 1.

Among chemometrics techniques, multivariate calibrations such as CLS, SMLR, PCR, PLSR, GA-PLS,

and ANNs [9] are typically used. PCR and PLSR methods are considered inverse calibration methods in which the concentrations in y-axes are modeled using absorbance values in x-axes [13]. The inverse calibration of PLS and PCR in which the concentration (y-axis) is modeled with UV-Vis spectra (x-axis) is the most widely multivariate calibration applied for the quantitative analysis of API, degradation products, and impurities with overlapping UV-Vis spectra. Multivariate calibrations offered reliable prediction models of analytes because they used some absorbances in large wavenumber ranges, thus enhancing the model's accuracy. In PCR and PLSR, the original variables were converted to LVs, and then LVs used as variables to be modeled with analyte concentrations. The phenomena of under-fitting and over-fitting must be considered by comparing the model performances in calibration and validation models [14].

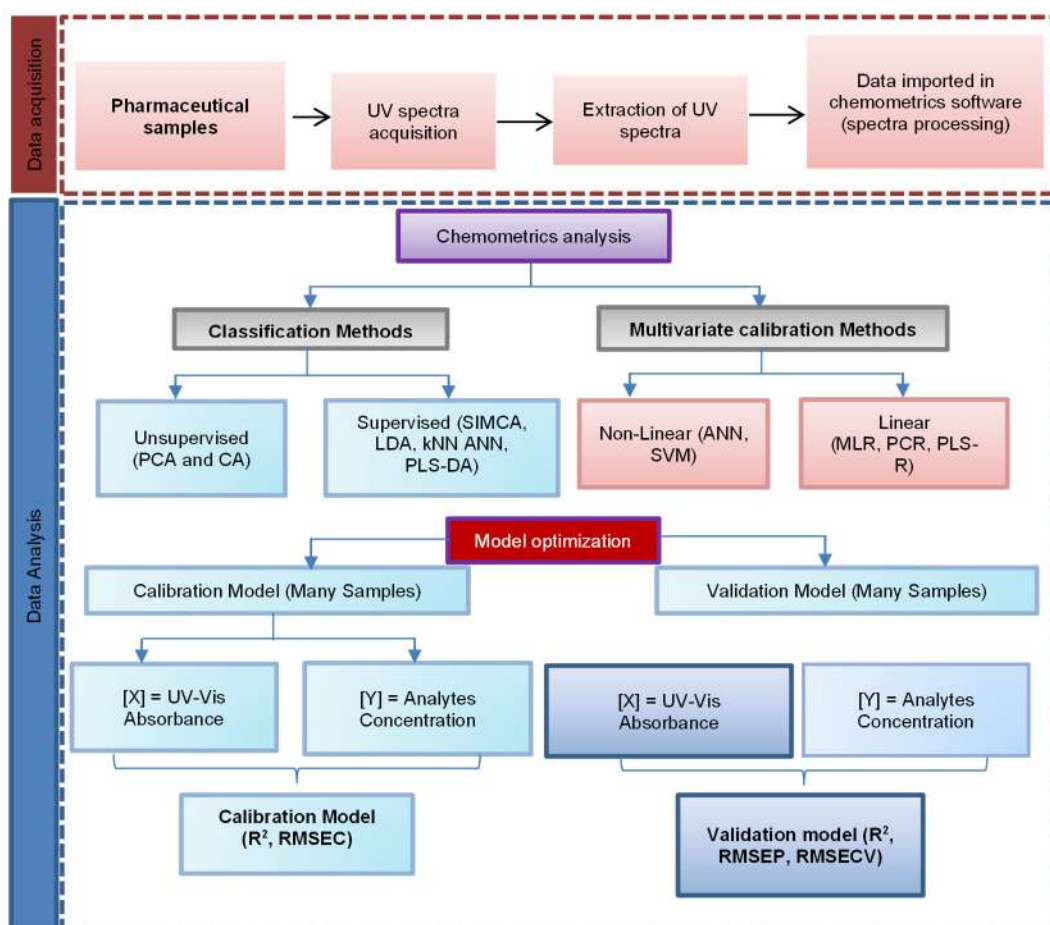


**Fig 1.** The Schematic representation regarding the chemometrics technique application using UV-Vis spectral absorbances variables. See list of abbreviation

### Application of UV-Vis Spectroscopy and Chemometrics for Determination of Active Pharmaceutical Ingredients

The combination of chemometrics with UV-Vis spectroscopy as a non-destructive analytical method has been widely employed to: (1) determine the levels of API in pharmaceutical preparations, (2) quantify APIs and their metabolites in the biological fluids, (3) determine the degradation products of APIs occurring during process and storage, (4) perform the quantitative analysis of impurities in APIs, and (5) identify the counterfeits in pharmaceutical products [15-17].

UV-Vis spectra contain a lot of data that can be used for multivariate analysis. The absorbance values could be extracted for the analytical assay of the targeted compounds. To analyze multiple compounds, chemometrics is required to obtain more selective and sensitive results. The spectra pre-processing treatments could be applied prior to data extraction, such as spectra normalization, baseline correction, and spectra derivatization, to improve the analysis results. Hundreds of variables resulting from data extraction are used for chemometrics analysis. Several data pre-processing could also be applied before chemometrics analysis, such as data scaling and mean-centering to obtain good data variation. For quantitative analysis, multivariate calibrations of PLS and PCR could predict the concentration of compounds with high accuracy and high precision using the optimized variables. PLSR searches the latent variables which have essential roles in concentration prediction. Meanwhile, PCR builds a regression model using factors from principal components generated from variables. The optimization of variables was evaluated using the coefficient of determination ( $R^2$ ) both in the calibration and validation model to measure good fitness and error values demonstrated by RMSEC, RMSEP, and RMSECV. High  $R^2$  values and low error values are required to be categorized as good models. Chemometrics offers advantages for the simultaneous analysis of analytes. However, the calibration model used for certain pharmaceutical products could not be extended to other formulations with different compositions. Therefore, the

different formulas of pharmaceutical products need new model optimization of the multivariate calibrations [18].

### Assay of Active Pharmaceutical Ingredients in Pharmaceutical Dosage Form

Table 1 compiled the reported publications regarding the use of UV-Vis spectroscopic methods in combination with multivariate calibrations for the determination of API in raw materials and in pharmaceutical preparations. Multivariate calibration-assisted UV spectroscopy was developed for the simultaneous analysis of four APIs, namely PCT, DPH, CAFF, and PHEN in the tablet. Seventeen samples mixture of these ingredients prepared in different ratios were used for PCR and PLSR analysis. UV measurement was performed at 240–320 nm with an interval of 1 nm. The UV spectra were then extracted for PCR and PLSR analysis. Additionally, HPLC analysis was performed coupled with chemometrics for the assay of PCT, DPH, CAFF, and PHEN. HPLC was carried out in isocratic mode using the mobile phase of MeOH-KH<sub>2</sub>PO<sub>4</sub> buffer (pH 3, 10 mM) (50:50 v/v) delivered isocratically at 0.81 mL/min. Compound separation was performed using a Phenomenex ODS column and the detection of analytes was carried out at 220 nm. The HPLC method was validated by determining the performance characteristics, including linearity, selectivity, accuracy, precision, and robustness. The results obtained from UV spectroscopy measurement were compared statistically with the results obtained using the HPLC method. The initial step in UV measurement was wavelength optimization providing the best calibration models providing the best predictive capability between actual and predicted values of analytes using PCR and PLSR, as indicated by the highest  $R^2$  and low RMSEC, RMSEP and RMSECV. Finally, the absorbance values at 240–320 nm applying an interval of 1 nm were selected. The calibration and validation samples were prepared in the concentration ranges of 2–16, 80–400, 4–14, and 20–120 µg/mL for PCT, DPH, CAFF and PHEN, respectively. The results showed that PCR and PLSR showed good accuracy and precision at the selected variables (PCs and LVs) with low values of RMSEC and



**Table 1.** The use of spectroscopy UV-Vis in combination with chemometrics for determination of active pharmaceutical ingredients in pharmaceutical dosage forms\*

Drugs	Chemometrics	Wavelength	Pharmaceutical dosage form	Sample preparation	Results	Ref.
PCT and CAFF	PLSR and ANN	205–300 nm with an interval of 1 nm	Tablet	The calibration and validation samples were prepared in concentration levels of 8.0–40.0 µg/mL (PCT) and 5.0–36.0 µg/mL (CAFF). The powdered tablet was dissolved in methanol.	ANN revealed a better prediction model than PLSR. Using ANN, the R <sup>2</sup> -values were 99.28% (PCT) and 99.13% (CAFF). The recovery percentages of PCT and CAFF were 75–86% and 77–92% from labeled claims for PCT and CAFF, respectively.	[34]
PCT, ENM and HCT	MLR, CLS, and TLRC	200–320 nm with an interval of 1 nm	Invozide® tablet containing 325 mg PCT, 25 mg HCT 10 mg ENM	The standard solutions in the range of 5–35 µg/mL (PCT), 1.5–40 µg/mL (HCT) and 5–40 µg/mL (ENM) were prepared. Tablet was powdered, added with methanol 0.1 M in HCl and filtered.	TLRC, MLRC and CLS were accurate and valid for the prediction of these drugs. ANOVA-test revealed that the recoveries obtained using these three methods and HPLC did not differ significantly ( $p > 0.05$ ).	[35]
ET and TC	PLS, PCR, and CLS	Absorbance was measured in 240–440 nm with an interval of 1 nm.	Tablet containing of 400 mg ET and 8 mg TC.	Calibration samples (25 sets) and validation samples (8 sets) in the binary mixture consisting of ET in the range of 15–75 µg/mL and TC in the range of 1–10 µg/mL through factorial design. Methanol is used as extracting solvent. The mixture was sonicated for 15 min.	All multivariate calibrations (PLSR, PCR, and CLS) yielded acceptable validation parameters. PLSR and PCR offered better calibration and validation models. The recovery percentages obtained in tablet using PLS, PCR, and CLS were 98.26, 98.16, and 98.17% for ET as well as 99.14, 98.26, and 98.15% for TC.	[36]
CPX and ONZ.	PLS and PCR	267–330 nm with interval $\lambda$ of 0.5 nm	Tablet, containing CPX 500 mg and ONZ 500 mg	The calibration and validation sample sets (36 mixtures) with concentration ranges of 2.0–12.0 µg/mL. The powder is dissolved in methanol and sonicated for 15 min.	Both PLS and PCR methods resulted in R <sup>2</sup> of 0.9893–0.9949 either in calibration or validation models. The percentages of recovery were 101.6–102.0%. RMSEP and RMSEC values were 0.26–0.35.	[37]
CPX and DOX	PLSR and PCR	200–400 nm with intervals 2 nm	CPX tablets labeled to contain 500 mg and DOX capsule labeled to contain 100 mg	Calibration and validation samples were prepared in the concentration ranges of 1–10 µg/mL for CPX and 5–25 µg/mL for DOX. The powdered tablets or capsules were added with	PLSR and PCR models previously optimized were accurate and precise for the prediction of CPX and DOX in the samples with recovery percentages of 97.50–101.87% and RSD values < 2%. RMSEP and RMSEC	[38]

				aquades, ultrasonicated for 15 min, filtrated, and subjected to UV spectra measurement.	values were 0.142–0.208 and 0.278–0.824. High recoveries and low values of RSD, RMSEC and RMSECV indicated that the developed method was acceptable for predicting unknown samples containing CPX and DOX.	
ATV and EZT	PLSR and PCR	230–260 nm with an interval of 0.5 nm	Tablet, containing ATV 10 mg and EZT 10 mg	Twenty-eight (28) calibration sample sets and eight (8) validation sample set at the level of 5.0–30.0 µg/mL were prepared. The powder was dissolved in methanol.	Both PLSR and PCR resulted in recovery percentages of about 100% (for accuracy studies) with RSD values < 2% (for precision studies). The LoD and LoQ values using PLS or PCR were 0.53 and 1.61 µg/mL (ATV) and 0.18 and 0.57 µg/mL (EZT).	[39]
MET and GLZ	PLSR and CLS	220–278 nm with an interval of 3 nm	Tablet Fixed Dose Combination (FDC) containing 500 mg MET and GLZ 30–80 mg	The concentration ranges were 8–20 µg/mL (MET) and 1–5 µg/mL (GLZ). FDC Tablet was powdered, added with MeOH and sonicated for 10 min, filtered, and scanned.	PLSR offered a better accuracy model than CLS. The values of LOD using PLSR were 0.0965 µg/mL (MET) and 0.0441 µg/mL (GLZ).	[40]
PCT, PROPI, and CAFF	PLSR	220–313 nm with an interval of 3 nm	Tablet containing 250 mg PCT, 150 mg PROPI, and 50 mg CAFF	Tablet was powdered, dissolved with methanol, sonicated for 10 min, filtered, and scanned.	The R <sup>2</sup> values for the relationship between actual and calculated values were 0.9994, 0.9878, and 0.9919 for PCT, PROPI, and CAFF, respectively. RMSEC values were 0.027–0.082%. The recovery percentages obtained were 90.70, 90.49, 103.38% for PCT, PROPI, and CAFF from the labeled claim.	[41]
BET and NEO)	PLSR	200–400 nm	Cream containing BET 1 mg and NEO 5 mg	Crems were added with 96% EtOH and homogenized. The mixture was subjected to sonication for 15 min. The standard addition method was used by spiking samples with standard solutions.	The recovery percentages of BET and NEO were 91.35% and 97.56% from labeled claimed. RSD values for BET and NEO were 0.93% and 1.73%. RMSEC values were 0.0230 and 0.3553, with RMSEP values of 0.1558 and 0.0820. The predictive ability of the developed method meets the requirement for cream dosage form according to USP XXX.	[42]
VEP and SOF	CLS, PCR, PLSR and GAPLS	230–400 nm with an interval 1 nm	Tablet consisted of VEP 100 mg and SOF 400 mg.	VEP and SOF were prepared in the levels of 5–9 µg/mL and 24–	The recovery percentages and RSD values of VEP and SOF using CLS, PCR, PLS, and	[43]

				32 µg/mL. The powdered tablet was dissolved in methanol.	GAPLS are acceptable. One-way ANOVA indicated that there is no significant difference ( $p > 0.05$ ) for four recoveries.	
EBV and GRV	ANN and GAANN models	230–400 nm with 1 nm interval	Tablets containing of EBV 50 mg and GRV 100 mg.	13 calibration samples and 12 validation samples at levels of 1–9 µg/mL EBV and 6–14 µg/mL GRV. The powdered tablet was dissolved in methanol.	The recovery percentages were in the range of 99.76–100.27%. RMSEC and RMSEP values were 0.1247–0.2968 and 0.2065–0.3018. The results obtained using UV spectroscopy combined with ANN and GAANN do not differ statistically from HPLC method based on ANOVA test.	[44]
LES and ALP	PLSR, PCR, and GAPLS	240–280 nm with an interval of 1 nm	172, Tablets containing 200 mg LES and 300 mg ALP	Thirteen sample mixtures were applied in the calibration set, and twelve samples were used in the validation set at levels of 4–12 µg/mL LES and 6–18 µg/mL ALP. The powdered tablet was dissolved in methanol.	All multivariate calibrations were acceptable, as indicated by $R^2$ and low values. The mean recoveries for LES and ALP were 99.56 and 99.85 (PCR), 100.63 and 100.73 (PLSR), 100.37 and 100.01 (GAPLS). There is no significant difference ( $p > 0.05$ ) between UV spectroscopy combined with PLSR, PCR, and GAPLS with HPLC method.	[45]
PHEN and CTM	CLS and PCR	200–400 nm with an interval of 3 nm	Sine Up syrup labeled to contain 100 mg% PHEN and 50% CTM	10 calibration solutions and 10 validation solutions with concentrations range 10–60 µg/mL (PHEN) and 4–30 µg/mL (CTM).	Determination of PHEN and CTM in authentic, laboratory-made samples and syrup dosage form using CLS and PCR resulted in acceptable values of recoveries (98.1–100.7%). UV spectroscopy is comparable with HPLC ( $P > 0.05$ ).	[46]
DRV and CBS	CLS and PLSR	UV spectra at 235–285 nm with an interval of 1 nm	Binary mixture and tablets. Tablet consisted of DRV 800 mg and CBS 150 mg.	Twenty-five and eight samples for calibration and validation datasets were designed using the experimental design of a multilevel multifactor with concentration ranges of 5–30 µg/mL either in DRV or CBS.	Both PLSR and CLS methods provide high $R^2$ (0.996–0.999) for DRV and CBS. PLSR provided better sensitivity and accuracy than CLS. The recoveries of DRV and CBS in tablets using PLS were $99.71 \pm 0.13$ and $99.27 \pm 0.54$ . ANOVA test informed that there is no significant difference ( $p > 0.05$ ) between UV spectroscopy-multivariate calibrations and HPLC method.	[47]

GLM and PIO	Residual augmented CLS (ARCLS), PCR, and PLSR	215–235 nm in the intervals of $\Delta\lambda$ of 0.4 nm	Amaglust® tablets containing 4 mg GLM and 30 mg PIO	Set calibration and validation mixtures were prepared with concentration ranges of 24–60 $\mu\text{g}/\text{mL}$ for PIO and 3.2–8 $\mu\text{g}/\text{mL}$ for GLM. The powder equivalent to PIO 30 mg and GLM 4 mg was dissolved with ACN, sonicated for 15 min and filtered using filter paper 0.45 $\mu\text{m}$ .	PLSR and PCR were selected because the statistical performances were acceptable, as indicated by high $R^2$ and low values of RMSEC, RMSEP, and RMSECV. There is no significant difference for mean recovery between the HPLC and UV spectroscopy-PLSR, UV-PCR and UV-ARCLS.	[48]
AML and VAL related	ANN and LS-SVM	200–500 nm with an interval of 1 nm	Tablet dosage forms containing 10 mg AML and 160 mg VAL	The standard solutions used as calibration and validation samples were prepared with levels of 5–25 $\mu\text{g}/\text{mL}$ AML and 9–5 $\mu\text{g}/\text{mL}$ VAL. Ethanol was used as the solvent.	LS-SVM is the preferred method offering recovery percentages of 100.22% (RSD of 2.719%) for AML and 100.37% (RSD of 0.7342%) for VAL. No significant differences were observed ( $p > 0.05$ ) between HPLC and the proposed method.	[49]
ATN, RAM, HCT, SMT and ASP	PLSR and Genetic algorithms-PLS	210–330 nm with interval of 1 nm	Polycap™ capsules containing ATN 50 mg, HCT 12.5 mg, RAM 5 mg, SMT 20 mg and ASP 100 mg.	The calibration and validation solutions were prepared in methanol with levels of 6–22, 4–16, 10–30, 10–30 and 2–8 $\mu\text{g}/\text{mL}$ for ASP, SMT, ATN, RAM, and HCT, respectively.	The recovery percentages obtained using PLSR, GA-PLS and HPLC methods are not significantly different ( $p > 0.05$ ) using ANOVA test. The recovery percentages of all drugs were in the range of 98.06–100.07%.	[50]
Sulphonamides and TMP	CLS, PCR and PLSR	200–350 nm with an interval of 1 nm	Tablets of Sulphonamides (sulfadiazine, sulfamethoxazole, sulfadimidine and sulphanilamide)	The synthetic mixtures containing these compounds were used in calibration (16 mixtures) and validation (16 samples) models spanning the concentration ranges of 2–6 $\mu\text{g}/\text{mL}$ .	PLSR and PCR provide better prediction models than CLS. The percentages of relative errors were 2–10%. The recovery percentages were close to 100% indicating that UV spectra combined with PLS and PCR were accurate and precise for sulphonamides drugs analysis.	[51]
VEP and SOF	ANN and GAANN	UV spectra at 200–380 nm with an interval of 1 nm	Tablets (VEP 100 mg and SOF 400 mg)	Tablet was powdered, added with methanol, filtered, and subjected to UV spectral measurement. The calibration and validation sets were prepared with levels of 5–9 $\mu\text{g}/\text{mL}$ VEP and 24–30 $\mu\text{g}/\text{mL}$ SOF.	Both methods offered acceptable accuracy and precision with recovery percentages of 99.48–100.75% (VEP and SOF). RSD values were $< 2\%$ . No significant difference between the student t-test and the F-test.	[52]
LEV and CAR	PLSR	UV spectra at 200–300 nm and	Five laboratory samples were made	LEV was prepared at 15.4–57.1 $\mu\text{g}/\text{mL}$ and	LEV and CAR can be simultaneously analyzed	[53]

		at 300–600 nm after reaction with KIO <sub>4</sub>	by mixing LEV and CAR and tablet formulation	CAR at 3.4–17.1 µg/mL. The powder was added with 0.1 M HCl, sonicated for 30 min, centrifugation at 3500 rpm for 15 min and filtered.	using PLSR without sample pre-treatment. No significant difference between the proposed and HPLC methods (p > 0.05).
Quaternary mixture of IMB, GMI, NLP and NAP	PLSR using normal and derivative spectra	200–400 nm with 0.2 nm intervals	Tablets containing 100 mg IMB per tablet, 320 mg GMI per tablet, 500 mg NAP per tablet and ampule containing 20 mg NLP per mL	Concentration of IMB, GMI, NLP and NAP in the calibration and validation sets were 4–8, 3–11, 10–18, and 1–3 µg/mL, respectively. For tablet: the powder was added with MeOH, sonicated for 30 min, filtered, and scanned.	PLSR using original (normal) and first derivative spectra provide a close correlation between predicted values and labeled claims with recovery percentages of 98.5–102.4%. [54]
EMP and MET	PLS-2	200–300 nm with 0.1 nm intervals	Tablets containing 12.5 mg EMP and 500 mg MET per tablet	Both EMP and MET in calibration and validation sets were prepared in the concentration ranges of 2–10 µg/mL. The powdered tablet was dissolved with methanol.	The levels of EMP and MET in the tablet yielded the mean of the recovery percentages and SD was 95.57% ± 0.49 and 102.16% ± 0.35, respectively using PLS-2 method. T-test of recovery percentages showed no significant difference between UV-PLS-2 and UPLC. [55]
DP, PH, and PP	PLSR and PCR	200–380 nm with 1 nm intervals	Tablet containing DP150 mg, PH 20 mg, and PP 30 mg.	Calibration and validation sets were prepared using 23 sample mixtures at ranges of 10–25 µg/mL for DP and 1.5–5 µg/mL for PH and PP. Powdered tablet was dissolved with methanol.	Both multivariate calibration methods were reliable for simultaneous quantification of DP, PH and PP as indicated by high R <sup>2</sup> and low values of RMSEC and RMSECV. Student's t-test and the F-ratio showed no significant differences observed (p > 0.05) between HPLC and the proposed methods. [56]
THEO	PLSR	210–350 nm with an interval of 1 nm	Syrup containing 8.0 mg/mL THEO	Syrups containing THEO were subjected to dilution with NaOH 0.1 M.	PLS could accurately predict the levels of THEO in syrup. There is no significant difference for THEO levels using UV spectroscopy-PLS and HPLC methods. [57]
GUA, SL, with the presence of preservatives of MP and PrP	PLSR and PCR	232–300 nm with intervals of 0.8 nm	Syrup (5 mL) containing GUA 50 mg, SL 2 mg, MP 3 mg and PrP 1.5 mg	A training set of 25 mixtures in calibration and validation sets in 0.1 M NaOH with a concentration range of 20–60, 1–3, 1–5, and 0.6–1.8 µg/mL for GUA, SL, MP, and PrP,	Both methods could provide accurate and precise results with recovery percentages (± SD) of 100.0–100.1% (± 0.15–0.48). One-way ANOVA indicated that both methods were not significantly [58]

				respectively. Syrup was diluted with NaOH 0.1 M.	different to HPLC method with a P-value of > 0.05.	
AC and BX with the presence of preservatives of MP and PP.	PLSR and PCR	235–275 nm with an interval of 0.4 nm	Each 5 mL Syrup contains AC 100 mg, BX 4 mg, MP 4.5 mg, and PP 0.5 mg.	A training set of 25 mixtures in calibration and validation sets 0.1M HCl in the concentration range of 20–80, 1–5, 1–5, and 0.2–1.8 µg/mL for AC, BX, MP and PP, respectively. Syrup was diluted with HCl 0.1 M.	Both methods could provide reliable results with recovery percentages ( $\pm$ SD) of 99.8–100.1% ( $\pm$ 0.13-2.10). One-way ANOVA indicated that both methods were not significantly different to HPLC method with a P-value of > 0.05.	[58]
LAM and STA	CLS and PCR	200–310 nm with an interval of 1 nm	Tablet containing 150 mg LAM and 30 mg STA	Standard solutions were prepared for calibration and validation sets at levels of 2–12 and 3–15 µg/mL for LAM and STA. The powdered tablet was diluted with 0.1 M HCl, sonicated, and filtered.	The methods were accurate, with acceptable recoveries in most cases. The deviation ranges of LAM and STA between actual and predicted were 0.28% and 1.57% (CLS), 0.03% and 1.77% (PCR), respectively.	[59]
PCT and TRM	PLSR and GA-PLS	200–320 nm with interval 1 nm	Tablets containing PCT 325 mg and Tramadol 37.5 mg.	The working solution was in the range of 15–37 µg/mL for PCT and 1.7–4.3 µg/mL for TMD. A-25 standard mixtures were used in the calibration and validation dataset.	The reliable model was achieved using PLSR method for PCT with a mean recovery of 99.5% and RSE of 0.89%. GA-PLS was the preferred method for TRM with a mean recovery of 99.4% and RSE 1.69%.	[60]
MTZ, B <sub>1</sub> , and B <sub>6</sub>	Multivariate calibration of PLSR	200–400 nm with a 2 nm interval	The tablet dosage form containing 500 mg of MET, 50 mg of B <sub>1</sub> , 100 mg of B <sub>6</sub> , and 100 µg of B <sub>12</sub>	The stock solutions were prepared freshly in HCl 0.1 M and used for preparing 20 calibration samples and 10 validation samples at levels of 9–48, 0.01–0.19, and 2–19 µg/mL for MET, B <sub>12</sub> , B <sub>1</sub> and B <sub>6</sub> .	The methods have good accuracy with R <sup>2</sup> (RMSEP) values were 0.999 (0.3993%); 0.999 (0.1926%); 0.999 (0.1434%) for MET, B <sub>1</sub> and B <sub>6</sub> , respectively.	[61]
SFB and LDV	PLS, CWT, and DS	200 to 400 nm with a 1 nm interval	Commercial tablets containing SFB 400 mg and LDV 90 mg.	The calibration and validation datasets were made at ranges of 24–64 and 6–16 µg/mL in ACN for SFB and LDV, respectively.	Each method has a good correlation coefficient with a value of R <sup>2</sup> > 0.99. The method was compared with HPLC. ANOVA reveals there are no significant differences among methods (p > 0.05).	[62]
RIS and HP	LS-SVM, FIS, ANFIS	200–300 nm	Tablets containing RIS and HP	The standard solutions in calibration and validation datasets were prepared in MeOH at 6–75 µg/mL for RIS and HP.	RMSE values using FIS and ANFIS models were 0.878, 2.124, and 0.285, 0.206 for RIS and HP. ANOVA test exhibited no significant differences between the	[63]

					proposed and HPLC methods.	
VDG, SAX and STG	PLSR, GA-PLS, ANN, and GA-ANN	190–400 nm with 0.5 nm intervals	Januvia® tablets (100 mg STG), Onglyza® tablets (5 mg SAX), Galvus® tablets (50 mg VDG)	Training sets in calibration and validation datasets were prepared at ranges of 10–22, 24–40, and 82–130 µg/mL for VDG, SAX, and STG, respectively.	PLSR, GA-PLS, ANN, and GA-ANN were successfully developed for the prediction of analytes. No different results ( $p > 0.05$ ) between the proposed method and HPLC. RMSEC values were low, indicating a precise method.	[64]
PIM	CLS, PCR, and PLSR	240–370 nm	Orape forte® containing 4 mg of PIM per tablet	The samples was prepared in a concentration range of 30–60 µg/mL PIM in methanol, 20–60 µg/mL in alkaline, and 20–60 µg/mL in Acidic solution.	The proposed method was successful for PIM quantification in tablets without interference. No significant difference ( $p > 0.05$ ) between the proposed and HPLC methods. RMSEP values were 0.0030, 0.0028, and 0.0072 for CLS, PCR, and PLSR.	[65]
PCT, IBU and CAFF	PLSR, GA-PLS, and PC-ANN	200–400 nm with interval of 1 nm	Tablet containing PCT 325 mg, IBU 200 mg and CAFF 40 mg.	Standard solutions were prepared in MeOH -0.1 M HCl (3:1). Two sets of calibration and validation samples were prepared in 25 and 20 mixtures.	UV spectra combined with these multivariate calibrations are accurate and precise methods as indicated by acceptable recoveries and RSD-values.	[66]
AML, VAL and HCT	PLS-1, GA-PLS, ANN, GA-ANN and PCA-ANN	200–400 nm	EXFORGE HCT® tablets containing AML5 mg, Val160 mg, and HCT 12.5 mg.	Training sets used in calibration and validation data sets were prepared in methanol.	The combination of UV spectra and five multivariate calibrations provide an accurate and precise quantitative analysis.	[67]
CEL and DIA	CLS, ILS, PCR, and PLSR	200–400 nm	Capsule OSTEGARD®, Containing 100 mg and 200 mg.	Twenty-five training sets in calibration and validation datasets were prepared in the range of 5–25 µg/mL (CEL) and 3–15 µg/mL (DIA).	The proposed methods provide comparable results, and there are no significant differences among methods ( $p > 0.05$ ).	[68]
HCT and BZ	PLSR and SVR	220–350 nm	Cibadrex® tablets containing 20 mg of BZ and 25 mg of HCT	The stock solutions were made to obtain 100 µg/mL of HCT and BZ and 30 µg/mL of HCT and DSA working solutions. The samples were dissolved in methanol, filtered, and diluted to obtain 100 µg/mL working solution.	UV spectra-multivariate calibrations provide accurate analysis of HCT and BZ in the presence of HCT impurities as indicated by acceptable mean percentage recoveries of 100.01–101.01%, which are comparable to HPLC method.	[69]
SMT and EZT	polynomial least squares based on	200–400 nm	Tablets (40 mg of SMT and 10 mg of EZT), Tablets (20 mg SMT and 10	Stock solutions were made at a concentration of 1 mg/mL of SMT and EZT, respectively.	The proposed method is reliable for the simultaneous determination of drugs in mixtures with acceptable	[70]

	Savitzky-Golay (SG) filters.		mg of EZT), Zocozet tablets (10 mg SMT and EZT)	Working solutions of SMT were made at a concentration of 100 µg/mL of SMT and EZT.	accuracy and precision. The method is successful in the analysis of raw materials and pharmaceutical preparations.	
PAR, GUA, and PHE	CRACLS, MCR-ALS, PCA-ANN	200-400 nm with 2 nm intervals	Panadol® COLD + FLU All in One Tablet (containing 250 mg of PAR, 100 mg GUA, and 5 mg PHE)	The standard solutions were made at 100 mg/mL in MeOH. The calibration and validation samples were made at ranges of 40–50, 16–20, and 1–9 µg/mL for PAR, GUA, and PHE.	The proposed method was valid for the simultaneous determination of PAR, GUA, and PHE in tablets without any separation step.	[71]
ENT, LEV and CAR	Multivariate calibration of PLSR	UV-Vis spectra at 200–600 nm with an interval at 2 nm	Stalevo® tablets (market sample) nominally containing 200 mg ENT, 150 mg LEV and 37.5 mg of CAR per tablet	The standard solutions of ENT, LEV and CAR at 100, 300, and 300 µg/mL were dissolved in methanol-water (7:3).	The developed method was reliable for simultaneous quantitative analysis of drugs in tablets without any separation step.	[72]
DPF and SAX	FZM, FDM, and FRM	200-400 nm	Onglyza® tablets contain 5 mg SAX and Forxiga® tablets contain 10 mg DPF per tablet.	The stock solutions were made at a concentration of 1 mg/mL of each DPF and SAX, and each working solution were made at a concentration 0.1 mg/mL.	The methods provide good accuracy and precision for the simultaneous determination of drugs over the concentration ranges of 2.5–50.0 (DPX) and 2.5–60.0 µg/mL (SAX).	[73]
CEF and ERD	CLS and PLSR	200-400 nm	Suprax® 200 capsules labeled to contain 223.8 mg CEF/capsule and Mucotec® contain 300 mg ERD/capsule	The standard solutions of CEF and ERD were prepared in 1 mg/mL concentration. The working solutions were made at concentration ranges of 20–30 (CEF) and 15–45 µg/mL (ERD).	The developed method was reliable for the simultaneous determination of drugs in dosage form with acceptable recoveries. The accuracy and precision of the proposed method were comparable with the HPLC reference method.	[74]
AML, CEL, and RAM	ACM	210–400 nm	Cardace® AM tablets containing AML 10 mg and RAM 10 mg.	The standard stock solutions were made in 100 µg/mL concentration for AML and CEL. The sample solutions were prepared at 5–60, 5–30 and 5–110 µg/mL for AML, CEL and RAM.	The LoD is 0.5781–0.7132, 0.6497–1.0450, and 0.0001–0.0003 µg/mL for AML, CEL, and RAM. No significant difference between the proposed method and the reference method ( $p > 0.05$ ).	[75]
VNC and CPX	PLSR and ANN	190-400 nm	Vancomycin with 99.80% purity and Ciprofloxacin with 99.30%	The stock solutions were made in 100 µg/mL concentration. The working solutions were prepared in the concentration range 3–30 and 1–10 µg/mL for VNC and CPX.	The methods have high %recovery, 98.79 and 98.23% for VNC and CPX. There are no significant differences between the proposed and reference methods. The RMSEP values for PLS-1 were 0.07 and 0.06% for VNC and CPX and	[76]



AML and MET	Isosbestic point and dual-wavelength methods	200–400 nm	Amlodipine besylate (99.40%) and metoprolol succinate (99.20%)	The standard solutions were made in 100 µg/mL concentration. The sample solutions were made at 2–25 and 2–30 µg/mL for AML and MET.	the RMSEP values of ANN were 0.12 and 0.11% for VNC and CPX. The developed method (UV spectra-chemometrics) was reliable for the simultaneous determination of AML and MET.	[77]
-------------	--	------------	--	---	--	------

\*See list of abbreviation

RMSECV. The  $R^2$  values obtained were 0.9991–0.9999 either in calibration or validation models using PLSR and PCR. An assay of pharmaceutical drugs revealed that the recoveries of drugs were 101.076–103.603% (PCR) and 100.943–103.814% (PLSR), respectively. On the other hand, validation analysis using HPLC also revealed good linearity ( $> 0.999$ ), good precision showed by the RSD value of less than 2%, as well as good accuracy demonstrated by the recovery values ( $100.85 \pm 0.59$  for PCT;  $101.72 \pm 0.31$  for DPH;  $101.93 \pm 0.43$  for CAFF;  $102.91 \pm 0.65$  for PHEN). Statistical analysis using One-way ANOVA ( $p = 0.05$ ) revealed that recoveries obtained using UV spectroscopy-PLSR, UV spectroscopy-PCR, and HPLC methods were not significantly different ( $p > 0.05$ ). It can be concluded that the combination of UV spectroscopy and chemometrics (PLSR and PCR) can be used as an alternative method to HPLC with the main advantages of simple, rapid, inexpensive and not requiring a sophisticated instrument [14].

### Analysis of APIs in Biological Fluids

The combination of UV-Vis spectroscopy with chemometrics of PLSR has been used for quantitative analysis not only in pharmaceuticals but also in biological fluids. Analysis of CBM in the presence of the main metabolite of CBME in human serum was successfully performed using absorbance values of second derivative spectra at the wavelength range of 280–350 nm with interval 1 nm. The use of the second derivative could eliminate the shift baseline effect present in the original UV spectra. The extraction of CBM and CBM-EP was done using benzene. Recovery percentages obtained in spiked plasma samples with 4 different levels of CBM

using the proposed method were in the range of 98.0–101.7% with low relative percentage difference, indicating acceptable accuracy and precision. Statistical evaluations using Student's t-test and F-test revealed that both methods did not reveal a significant difference at a confidence interval of 95% ( $p > 0.05$ ). From this result, UV spectroscopy combined with PLS could be an alternative method for the determination of API in biological fluids with the presence of API's metabolite [63]. PLS using the variable of absorbance values at 190–350 nm with an interval 1 nm was also successful for the determination of CBM along with its metabolite (CBME). The mean recovery percentages for the determination of CBM and CBME were also performed using reference HPLC methods as a comparison to the proposed method (PLSR-UV spectra). The results showed that the recovery percentages of CBM and CBME in synthetic mixtures were 102.57 and 103.00% (for PLS) and 99.40% and 102.20% (HPLC), respectively. Based on the statistical test, there are no significant differences between CBM and CBME using PLSR-UV and HPLC methods ( $p > 0.05$ ) [19]. UV-spectroscopy and PLSR were also successful in the analysis of amoxicillin and its metabolites in human urines with acceptable validation performance [20].

### Analysis of API and Its Degradation Products

UV spectroscopy using MCR and multivariate calibrations of PLSR and PCR was successfully applied for simultaneous analysis of CS and its alkaline degradation products identified as Deg-1 and Deg-2 as shown in Fig. 2. UV spectra revealed the extensive overlapping, therefore the chemometrics was applied to

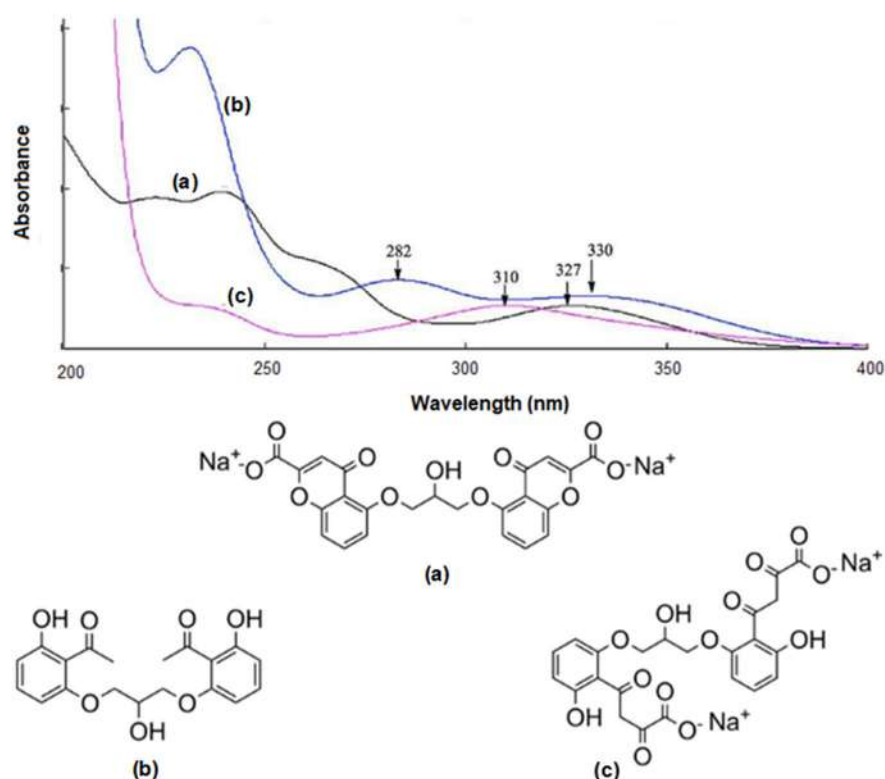


**Fig 2.** UV spectra and chemical structures of Cromolyn Sodium (a) and its degradation products identified as Deg-1 (b) and Deg-2 (c) scanned at 200–400 nm. Taken with CC-BY license

facilitate the quantification of analytes. The absorbance values after MCR at 367.8, 373.8, and 310.6 nm were used within linear concentration ranges of 2–40, 5–40, and 10–100  $\mu\text{g/mL}$  for CS, Deg-1, and Deg-2, respectively. Using MCR method, the recovery percentages  $\pm$  SD obtained were  $99.91 \pm 1.33$ ,  $100.28 \pm 1.44$ , and  $100.61\% \pm 1.55$  for CS, Deg-1, and Deg-2, respectively indicating that MCR is an accurate and precise method for stability-indicating assay of CS, Deg-1 and Deg-2. PCR and PLS-2 models using variables of absorbance values at wavelength 230–400 nm with 0.2 nm intervals (851 data points) at concentration ranges of 5–13 (CS), 8–16 (Deg-1), and 10–30  $\mu\text{g/mL}$  (Deg-2). The developed method has been successfully used for quantitative analysis of CS and its degradation products in eye drops dosage form. The levels of CS in eye drops dosage form (labeled to contain 40 mg of CS/mL) were  $102.40 \pm 0.83$  and  $101.75\% \pm 0.69$  from the claimed label [21].

The UV-Vis spectroscopy and chemometrics method were performed for the determination of MF in the presence of its degradation product. The study was

conducted in a forced degradation study of MF performed in basic conditions. Samples were scanned at the range of 220–350 nm. The UV spectra of mixtures of MF with its degradants were used for the quantification of MF. Chemometrics of PLS regression was carried out for the determination of MF concentration. The calibration model demonstrated a good mean recovery of 100.2% with low error indicated by the low value of RMSEC (0.002%). Meanwhile, the mean recovery of the validation model was 97.24%, with RMSEP of 0.04%. The recoveries obtained from sample measurement ranged from 98.47–102.66% indicating no interference from the MF degradation products [22].

UV-Vis spectrophotometry and chemometrics have also been used for the analysis of paracetamol in the presence of its degradants resulting from the basic condition. PCA was performed to differentiate compounds obtained from UV-Vis measurement. The results of PCA suggested the presence of four compounds, namely a reactant (PCT), a degradant, and two intermediate compounds. Chemometrics of MCR-

ALS was further used to confirm the results from PCA. MCR-ALS was aimed at the constraint of non-negativity, either spectral or concentration profiles. Besides, it was also used for the unimodality of the concentration profiles. Results demonstrated that chemometrics of MCR-ALS had a similar result to PCA, recognizing the presence of four compounds. The study was compared using HPLC measurement and it proved the presence of two intermediates. The concentration profiles obtained from UV-Vis and MCR-ALS were in agreement with those obtained from HPLC measurement [23].

UV-Vis spectrophotometry method combined with MCR-ALS has been used to analyze tamoxifen and its degradation products. The acquisition of the UV-Vis spectra was conducted from 0 to 160 min using an irradiation power 400 W/m<sup>2</sup> and from 0 to 120 min at irradiation power of 765 W/m<sup>2</sup>. The degradation process could be observed by UV-Vis spectra indicated by the changing of spectra profiles. The use of chemometrics MCR-ALS using variables of absorbance extracted from UV-Vis spectra demonstrated four species of degradation products of tamoxifen as the impurities. It suggested that UV-Vis spectrophotometry method combined with chemometrics of MCR-ALS could be used for the analysis of tamoxifen and its degradation products [24]. Table 2 demonstrates the summary of some analysis of API and its degradation products in pharmaceutical dosage form using a combination of spectroscopy UV-Vis and chemometrics.

### Analysis of API and Its Impurity

Combination of UV spectroscopy and multivariate calibration is applied for simultaneous analysis of NF, TZ and impurity of TZ, namely MNZ. Three multivariate calibrations, namely CLS, PLSR and SVR were used for making calibration and validation models for three compounds. The 16 calibration samples and 18 validation 8 samples sets were prepared in the concentration ranges of 4.0–6.5 (NF), 6.0–10.0 (TZ), and 0.10–0.17 (MNZ) µg/mL. The variables used were absorbance values at 220–360 nm using a 1 nm interval. PLSR and SVR revealed better prediction models; therefore, both multivariate calibrations were used for the prediction of NF, TZ and

MNZ in tablets. The analytical results using PLSR and SVR on commercial tablets (Tinidol Plus®) exhibited acceptable recoveries (97.84–101.33%) with RSD values less than 2%. Statistical tests of mean recoveries using the independent-t test for both multivariate calibrations did not differ significantly ( $p > 0.05$ ), while ANOVA test for mean recoveries of UV spectroscopy-PLSR, UV spectroscopy SVR and HPLC method was not different significantly with P-value of 5.050 ( $p > 0.05$ ). This indicated that the combination of UV spectroscopy and PLSR/SVR could be an alternative method over HPLC for simultaneous analysis of API and its impurity [25].

The chemometrics models of PLSR and ANN models were optimized and developed for the simultaneous determination of PCT and CZX along with their related impurities namely AP, ACA, NP, CP and ACP. PLS and ANN were compared using all UV spectra at the wavelength range of 200–400 nm and using wavelength of 220–360 nm based on wavelength selection using GA. Therefore, four models were compared namely PLSR, GA-PLS, ANN and GA-ANN. All analyzed compounds and capsules containing PAR and CZX were dissolved in methanol. Fifteen calibration models and 9 validation models were constructed consisting of 8–16 (PAR), 6–22 (CZX), 2–6 (AP, CA, NP and CP), and 5–13 (ACP) µg/mL. The four chemometrics models were successfully used for quantitative analysis of PAR and CZX either in raw materials or in the pharmaceutical dosage form. The recovery percentages for the accuracy study were in the range of 98.62–102.7% for PAR, CZX, AP, CA, NP, ACP, and CP, with RSD values of < 3.00%. The statistical test using one-way ANOVA revealed that the mean recoveries of the developed methods and HPLC method for PAR and CZX are not significantly different ( $p > 0.05$ ). It can be concluded that the proposed method can be easily applied for the simultaneous determination of PAR and CZX without any separation [26].

UV-Vis spectrophotometry method combined with chemometrics has been used for determining NIF and impurities. Spectra acquisition was carried out using a double-beam UV-Vis spectrophotometer with a spectral band of 2 nm employing a scanning speed of

**Table 2.** The use of spectroscopy UV-Vis in combination with chemometrics for the determination of active pharmaceutical ingredients and its degradation products in pharmaceutical preparations\*

Drugs and degradation products	Chemo-metrics	Wave-length	Pharmaceutical dosage form	Sample preparation	Results	Ref.
CFS and Deg-CFS	PCR, PLS, GA-PLSR, ANNs, GA-ANNs, and CLS	200 to 400 nm, with an interval of 1 nm	IV injection and IV infusion containing 1 g CEF per vial.	Alkali degradation product of CFS was prepared by refluxing CFS with 0.1 M NaOH for 10 min. The calibration and validation solutions were in the range of 16–24 µg/mL CFS and CFS-Deg.	All chemometrics techniques provide acceptable accuracy and precision. The percentage recoveries for CFS using PCR, PLS, GA-PLS, ANNs, GA-ANNs, and CLS were 100.98, 100.31, 100.54, 99.53, 100.36, and 100.98%, respectively.	[78]
ISX and its photodegradation products, namely ACH, AM, BZA and HB	PLSR, GA-PLS, ANN and GA-ANN	200 to 400 nm with interval of 0.1 nm	Tablets comprising 20 mg ISX	The standard solutions for calibration and validation sets were prepared in the ranges of concentration ranges of 10–20 (ISX), 1–3 (ACH and HB), 100–140 (AM) and 1–5 (BZA) µg/mL. The powdered tablet was added with methanol, sonicated for 10 min, centrifuged at 4000 rpm, and clear supernatant was subjected to UV spectral measurement.	The chemometric methods have been successfully applied for the evaluation of stability, indicating methods for the simultaneous quantitative determination of ISX and its photothermal degradation products either in bulk materials and/or in tablets. One-way ANOVA test indicated that the proposed methods did not differ significantly ( $p > 0.05$ )	[79]
NAPH, CTM, and NAPH-Deg	PLSR and PCR	200 to 400 nm with an interval of 2 nm	Eye/nose drops labeled to contain 0.5 mg/mL NAPH and 0.5 mg/mL CTM	25 synthetic mixtures for calibration and validation sets were prepared in 5–25, 5–25 and 5–13 µg/mL for NAPH, CLO, and NAPH-Deg. Eye drop samples were diluted with methanol	Three methods (HPTLC, PLS and PCR using normal and derivative spectra) were successfully applied for simultaneous analysis of NAPH, CTM, and NAPH-Deg with acceptable accuracy and precision. Based on the t-test and F-test, mean recoveries and SD of three methods revealed no significant difference ( $p > 0.05$ )	[80]
IMD in the presence of AKN and OXI	PLSR and PCR	205–305 nm with an interval of 1 nm	Tablets containing 10 mg IMD	25 synthetic mixtures for calibration and validation sets were prepared in 12–18 µg/mL for IMD, 2.4–3.6 µg/mL for AKN and OKI	Both multivariate calibrations offered acceptable accuracy and precision as indicated by recovery percentages of 99.96–100.09% and RMSEP value of 0.004–0.012. There is no significant difference between PLS-UV, PCR-UV and HPLC methods ( $p > 0.05$ ).	[81]
ROS and FEN along with ROS-Deg and FA	PLS and PCR	200–400 nm with	Tablets containing 5 mg	The concentration ranges of mixtures used in calibration and validation	PLSR and PCR-assisted UV spectroscopy was successfully applied for the determination	[82]

		wavelength interval 1 nm	ROS and 160 mg FEN	sets were 2.00–18.00 (ROS), 5.00–17.00 (FEN), 2.00–4.00 (FA) and 2.00–10.00 µg/mL (ROS-Deg). The powdered tablet was dissolved in methanol	of drugs with recovery percentages of 99.30–100.45% with SD values of 0.547–1.591. No significant differences among PLSR-UV, PCR-UV, and HPLC methods ( $P > 0.05$ )
ETB and TAF	ANN, PLSR, and PCR	200–400 nm with a wavelength interval of 2 nm	Tablet containing ETB 200 mg and TAF 25 mg per tablet	30 synthetic mixtures were produced randomly in different concentrations. 19 and 11 synthetic mixtures for calibration and validation set were prepared in the concentration range of 5–18 (EMT) and 5–40 µg/mL (TAF). Stock solutions dissolved with distilled water.	Based on LM and GDG algorithms layer = 5 with neuron 3 and layer = 7 with neuron 7 were considered as the best layers of FM for ETM and TAF, respectively. The best number of components of ETB is 7 and 11 for PLS and PCR methods, with RMSE 0.0160 and 0.0158, respectively. The best number of components for TAF is 5 and 6 in PLS and PCR techniques with RMSE 0.2432 and 0.2815. [83]
PCT, GUA and CTM	PLS	200–400 nm with a wavelength interval of 2 nm	Twenty different tablets containing PCT, GUA, and CTM	30 mixtures for calibration and validation were prepared to contain 2–15 (PCT), 3–19 (GUA), and 2–20 (CTM) µg/mL in methanol: hydrochloric acid 0.1 M (3:1). The solution is shaken vigorously for 30 min and filtered for UV measurements.	UV spectrophotometry combined with PLS can be used for quantitative analysis of PCT, GUA, and CTM with $R^2$ for the relationship between actual values and predicted values was 0.999972, 0.999826, 0.999725 and the RMSEC values of 0.022019, 0.067889, 0.083875, respectively. [84]
HCT and SPR	PLSR and GA-PLSR	216–300 nm with wavelength interval 0.4 nm	Tablet containing 25 mg of HCT and SPR	30 concentration mixtures for calibration and validation were prepared to contain 2.00–6.00 (HCT), 3.00–7.00 (SPR), and 1.00–5.00 (CT, DSA, and SPR deg) µg/mL.	The developed method provides reliable results for the simultaneous determination of HCT, SPR, and its degradation products and its impurities with $R^2$ of 0.9994 and 0.9987 for HCT and SPR. [85]
HCT and SPR	CLS, ILS, PCR and PLS	220–290 with wavelength interval 2 nm	Tablets containing 25 mg SPR and 25 mg HTC per tablet	25 standard synthetic mixture for calibration and validation sets containing SPR and HCT was prepared at level of 2–20 µg/mL.	Four chemometrics methods applied to UV spectra were successful for the simultaneous determination of drugs in mixtures and tablets with $R^2$ for calibration and validation of $> 0.99$ and the lowest error. ANOVA test exhibited no significant difference among the methods ( $p > 0.05$ ). [86]
CBT and MET	PCA and PLSR	190–600 nm with wavelength	Injection solution containing	The central composite design was used for optimization of the	The combination of UV-Vis spectra and chemometrics was reliable for determining the [87]

interval 0.5 nm	0.100 mg CBT and 1 mg MET	developed method. 90 and 12 samples for calibration and validation were prepared. The tablets were dissolved in a buffer solution.	content of CBT and MET in injection solution with R <sup>2</sup> and RMSE of 0.991 (1.2), 0.989 (1.34) for calibration, and 0.993 (1.21), 0.989 (1.11) for validation, respectively.
-----------------	---------------------------	--	--

\*See list of abbreviation

2800 nm/min. Chemometrics of CRACLS and SRACLS were used for the analysis of NIF and its four carcinogenic impurities. The impurities are named as (S[4-hydroxy benzohydrazide(*p*-hydroxybenzohydrazide)], [methyl 4-hydroxybenzoate], [(5-nitrofuran-2-yl)methylidene diacetate], and [(*E,E*)-*N,N*-bis[(5-nitrofuran-2-yl)methylidene]hydrazine(5-nitrofurfuralazine)] and they are coded as A, B, C, and D, respectively. Chemometrics of PLSR was also performed for comparative study purposes. The concentration range of NIF from 10.00 to 50.00 µg/mL was used for creating regression models. Meanwhile, the concentration range of impurities A and B was 0.05 to 0.45 µg/mL and for impurities, C and D was 0.10 to 0.90 µg/mL. Result revealed that chemometrics of CRACLS, SRACLS, and PLSR was successfully used to determine NIF and its four impurities either in the pharmaceutical formulation or in the prepared mixtures [27].

Simultaneous determination of PHZ and TMP in the presence of phenazopyridine HCl impurity, namely DAP has been performed using spectroscopy UV-Vis combined with univariate and multivariate analysis. The univariate method was performed for the determination of phenazopyridine at the wavelength of 412 nm in the concentration range of 1.00–10.00 µg/mL. Univariate method was also successfully used for determination of PHZ, TMP, and DAP. For multivariate analysis, chemometrics multivariate calibration of PLS and PCR was applied for the determination of PHZ and TMP in the presence of DAP. Result demonstrated that PLS and PCR could be used for simultaneous determination of PHZ and TMP in the presence of DAP at the concentration range of 24.00–56.00 µg/mL of TMP. The proposed method was successfully applied to determine the concentration of PHZ and TMP in the pharmaceutical formulation [28].

## Detection of Counterfeit Pharmaceutical Products

The presence of Counterfeit pharmaceutical products is a global problem, not only in developing countries but also in developed countries. The United States Food and Drug Administration (FDA) estimates that counterfeits make up more than 10% of the global medicines market [29]. The counterfeits include drugs without sufficient active ingredients, without any active ingredients, or fake packaging [30].

The use of UV-Vis spectroscopy method has been applied for the analysis of counterfeit in acetaminophen. Samples were prepared by mixing binary mixtures of pure acetaminophen with other compounds as adulterants, namely cement, rice flour, vitamin C, and lactose in several concentration levels. The mixtures were dissolved in three different solvents; H<sub>2</sub>O (neutral), 0.1 M HCl (acid), and 0.1 M NaOH (alkaline). The samples were scanned using UV-Vis spectrophotometer at a wavelength of 240–500 nm. The concentration used was ranging from 0.01–0.04 mg/mL. Results revealed that the presence of adulterants decreased the absorption of acetaminophen at 254 nm while other parts showed a slight increase in the spectrum. This method here could be used for the quality control of API from counterfeit adulterants [31].

UV-Vis spectroscopy method has been used for the analysis of PCT tablets to determine the concentration of PCT compared to its label. The tablet samples were obtained from several countries on several continents, including Africa, Asia, Europe and Caribbean Island. Sample preparation was performed to extract PCT from tablets. Samples were then analyzed using UV-Vis spectrophotometer method at a wavenumber of 244 nm. It was found that in some samples from different countries, PCT tablets contained an insufficient level of PCT. The actual concentration obtained from the

measurement did not match the label claim. It suggested that UV-Vis spectrophotometry method is the potential to be used for analysis of counterfeit drugs in quality control of API concentration. Another drug successfully studied using UV-Vis spectrometry has been carried out on Tylenol. UV-Vis spectrophotometry could separate peaks of Tylenol and its ingredients, and the concentration of Tylenol could be determined accurately [32].

Determination of TZ in the presence of PZ as a counterfeit drug has been performed using UV-Vis spectrophotometry and chemometrics of machine learning. Spectra acquisition was carried out in absorbance mode at intervals of 0.1 nm. The region used for measurement was 200–400 nm. Machine learning was performed for the determination of PZ and TZ at five concentration levels. The variables used for creating a machine learning model were absorbance values selected using a variable selection algorithm to obtain the most important variables. Machine learning method was evaluated using RMSE,  $R^2$ , and AME. Result showed that the linear model provided the best prediction model among other models. The obtained RMSE,  $R^2$ , and AME for the training dataset or calibration model were 0.159, 0.997, and 0.131, respectively, whereas for the prediction model or test dataset, the RMSE,  $R^2$ , and AME were 0.196, 0.99, and 0.161, respectively. The model could be applied for the determination of PZ in the presence of TZ in all the pharmaceutical formulation samples [33].

## ■ CONCLUSION

The development of analytical methods for quality control of pharmaceutical products has grown rapidly. UV-Vis spectrophotometry method has become a method of choice for the analysis of API in pharmaceutical products. It offers rapid analysis as well as easy sample preparation and it can be applied for wide range of API analysis. Moreover, it has been used for routine analysis for quality control purposes of pharmaceutical products. Combined with chemometrics of multivariate analysis including pattern recognition such as PCA, LDA, and PLS-DA as well as multivariate calibration such as PLS, PCR, and MCR-ALS, UV-Vis

spectrophotometry method could be an ideal technique for quality control of pharmaceutical products. Some spectra pre-treatment techniques in chemometrics, such as baseline correction, normalization, and derivatization, could be used to improve the simultaneous analysis of compounds. The data treatment on chemometrics such as scaling, is widely used to obtain a good variety of multivariate data. Chemometrics model evaluation could be performed using  $R^2$  of calibration and validation to evaluate model fitting. Meanwhile, RMSEC, RMSECV, and RMSEP were used for the evaluation of model error and precision. This technique can be applied to analysis of API in pharmaceutical products and analysis of API in biological fluids. Moreover, it can be used for analysis of API in the presence of degradation products, impurities, and detection of counterfeit pharmaceutical products. Therefore, it suggested that a combination of UV-Vis spectrophotometry and chemometrics method has been proved as a good analytical technique for quality control of pharmaceutical products.

## ■ ACKNOWLEDGMENTS

The authors thank anonymous reviewers for their valuable comments to improve this manuscript.

## ■ REFERENCES

- [1] Bosch Ojeda, C., and Sanchez Rojas, F., 2004, Recent developments in derivative ultraviolet/visible absorption spectrophotometry, *Anal. Chim. Acta*, 518 (1-2), 1–24.
- [2] Sánchez Rojas, F., and Bosch Ojeda, C., 2009, Recent development in derivative ultraviolet/visible absorption spectrophotometry: 2004-2008: A review, *Anal. Chim. Acta*, 635 (1), 22–44.
- [3] Atole, D.M., and Rajput, H.H., 2018, Ultraviolet spectroscopy and its pharmaceutical applications- A brief review, *Asian J. Pharm. Clin. Res.*, 11 (2), 59–66.
- [4] Siddiqui, M.R., AlOthman, Z.A., and Rahman, N., 2017, Analytical techniques in pharmaceutical analysis: A review, *Arabian J. Chem.*, 10, S1409–S1421.

- [5] Korany, M.A., Mahgoub, H., Haggag, R.S., Ragab, M.A.A., and Elmallah, O.A., 2018, Chemometrics-assisted spectrophotometric green method for correcting interferences in biowaiver studies: Application to assay and dissolution profiling study of donepezil hydrochloride tablets, *Spectrochim. Acta, Part A*, 199, 328–339.
- [6] Hajian, R., and Soltaninezhad, A., 2013, The spectrophotometric multicomponent analysis of a ternary mixture of paracetamol, aspirin, and caffeine by the double divisor-ratio spectra derivative method, *J. Spectrosc.*, 2013, 405210.
- [7] Patel, H., and Solanki, S., 2012, Development and validation of spectrophotometric methods for simultaneous estimation of furosemide and spironolactone in combined tablet dosage form, *Int. J. Pharm. Pharm. Sci.*, 4 (4), 383–386.
- [8] Hajian, R., Shams, N., and Rad, A., 2009, Application of H-point standard addition method for simultaneous spectrophotometric determination of hydrochlorothiazide and propranolol, *J. Braz. Chem. Soc.*, 20 (5), 860–865.
- [9] Prajapati, P.R., Rathod, D.N., Modi, V.S., and Basuri, T., 2016, Chemometrics and its applications in UV spectrophotometry, *Int. J. Pharm. Chem. Anal.*, 3 (1), 43–50.
- [10] Peris-Díaz, M.D., and Krężel, A., 2021, A guide to good practice in chemometric methods for vibrational spectroscopy, electrochemistry, and hyphenated mass spectrometry, *TrAC, Trends Anal. Chem.*, 135, 116157.
- [11] Gad, H.A., El-Ahmady, S.H., Abou-Shoer, M.I., and Al-Azizi, M.M., 2013, Application of chemometrics in authentication of herbal medicines: A review, *Phytochem. Anal.*, 24 (1), 1–24.
- [12] Jamwal, R., Amit, A., Kumari, S., Sharma, S., Kelly, S., Cannavan, A., and Singh, D.K., 2021, Recent trends in the use of FTIR spectroscopy integrated with chemometrics for the detection of edible oil adulteration, *Vib. Spectrosc.*, 113, 103222.
- [13] Rohman, A., and Putri, A.R., 2019, The chemometrics techniques in combination with instrumental analytical methods applied in Halal authentication analysis, *Indones. J. Chem.*, 19 (1), 262–272.
- [14] Palur, K., Archakam, S.C., and Koganti, B., 2020, Chemometric assisted UV spectrophotometric and RP-HPLC methods for simultaneous determination of paracetamol, diphenhydramine, caffeine and phenylephrine in tablet dosage form, *Spectrochim. Acta, Part A*, 243, 118801.
- [15] Vignaduzzo, S.E., Maggio, R.M., and Olivieri, A.C., 2020, Why should the pharmaceutical industry claim for the implementation of second-order chemometric models—A critical review, *J. Pharm. Biomed. Anal.*, 179, 112965.
- [16] Mazivila, S.J., and Olivieri, A.C., 2018, Chemometrics coupled to vibrational spectroscopy and spectroscopic imaging for the analysis of solid-phase pharmaceutical products: A brief review on non-destructive analytical methods, *TrAC, Trends Anal. Chem.*, 108, 74–87.
- [17] El-Gindy, A., Emara, S., and Mostafa, A., 2006, Application and validation of chemometrics-assisted spectrophotometry and liquid chromatography for the simultaneous determination of six-component pharmaceuticals, *J. Pharm. Biomed. Anal.*, 41 (2), 421–430.
- [18] Cámara, M.S., Mastandrea, C., and Goicoechea, H.C., 2005, Chemometrics-assisted simple UV-spectroscopic determination of carbamazepine in human serum and comparison with reference methods, *J. Biochem. Biophys. Methods*, 64 (3), 153–166.
- [19] Hemmateenejad, B., Rezaei, Z., Khabnadideh, S., and Saffari, M., 2007, A PLS-based extractive spectrophotometric method for simultaneous determination of carbamazepine and carbamazepine-10,11-epoxide in plasma and comparison with HPLC, *Spectrochim. Acta, Part A*, 68 (3), 718–724.
- [20] García-Reiriz, A., Damiani, P.C., and Olivieri, A.C., 2007, Different strategies for the direct determination of amoxicillin in human urine by second-order multivariate analysis of kinetic-spectrophotometric data, *Talanta*, 71 (2), 806–815.



- [21] El Zahar, N.M., Tadros, M.M., and Ayoub, B.M., 2020, Development of advanced chemometric-assisted spectrophotometric methods for the determination of cromolyn sodium and its alkaline degradation products, *Molecules*, 25 (24), 24551.
- [22] Sayed, R.A., El-Masri, M.M., Hassan, W.S., El-Mammi, M.Y., and Shalaby, A., 2018, Validated stability-indicating methods for determination of mometasone furoate in presence of its alkaline degradation product, *J. Chromatogr. Sci.*, 56 (3), 254–261.
- [23] Feng, X., Zhang, Q., Cong, P., and Zhu, Z., 2013, Determination of the paracetamol degradation process with online UV spectroscopic and multivariate curve resolution-alternating least squares methods: Comparative validation by HPLC, *Anal. Methods*, 5 (19), 5286–5293.
- [24] Marín-García, M., Ioele, G., Franquet-Griell, H., Lacorte, S., Ragno, G., and Tauler, R., 2018, Investigation of the photodegradation profile of tamoxifen using spectroscopic and chromatographic analysis and multivariate curve resolution, *Chemom. Intell. Lab. Syst.*, 174, 128–141.
- [25] Naguib, I.A., Abdelaleem, E.A., Hassan, E.S., Ali, N.W., and Gamal, M., 2020, Partial least squares and linear support vector regression chemometric models for analysis of Norfloxacin and Tinidazole with Tinidazole impurity, *Spectrochim. Acta, Part A*, 239, 118513.
- [26] Saad, A.S., AlAlamein, A.M.A., Galal, M.M., and Zaazaa, H.E., 2018, Traditional versus advanced chemometric models for the impurity profiling of paracetamol and chlorzoxazone: Application to pure and pharmaceutical dosage forms, *Spectrochim. Acta, Part A*, 205, 376–380.
- [27] Hegazy, M.A., Abdelwahab, N.S., Ali, N.W., Sharkawi, M.M.Z., Abdelkawy, M.M., and El-Saadi, M.T., 2019, Comparison of two augmented classical least squares algorithms and PLS for determining nifuroxazide and its genotoxic impurities using UV spectroscopy, *J. Chemom.*, 33 (12), 15–22.
- [28] Soudi, A.T., Hussein, O.G., Elzanfaly, E.S., Zaazaa, H.E., and Abdelkawy, M., 2020, Simultaneous determination of phenazopyridine HCl and trimethoprim in presence of phenazopyridine HCl impurity by univariate and multivariate spectrophotometric methods - Quantification of phenazopyridine HCl impurity by univariate methods, *Spectrochim. Acta, Part A*, 239, 118516.
- [29] Nafie, L.A., 2020, Recent advances in linear and nonlinear Raman spectroscopy, *J. Raman Spectrosc.*, 51 (12), 2354–2376.
- [30] Nuhu, A.A., 2011, Recent analytical approaches to counterfeit drug detection, *J. Appl. Pharm. Sci.*, 1 (5), 6–13.
- [31] Figueroa, G., Palacio, L.A., Ray, B.D., Petrache, H.I., and Lopez-Yunez, A., 2015, Detecting counterfeit pharmaceuticals through UV spectrophotometry, *Biophys. J.*, 108 (2), 622a.
- [32] Bolla, A.S., Patel, A.R., and Priefer, R., 2020, The silent development of counterfeit medications in developing countries – A systematic review of detection technologies, *Int. J. Pharm.*, 587, 119702.
- [33] Ibrahim, A.M., Hendawy, H.A.M., Hassan, W.S., Shalaby, A., and ElMasry, M.S., 2020, Determination of terazosin in the presence of prazosin: Different state-of-the-art machine learning algorithms with UV spectroscopy, *Spectrochim. Acta, Part A*, 236, 118349.
- [34] Uddin, M.N., Mondol, A., Karim, M.M., Jahan, R.A., and Rana, A.A., 2019, Chemometrics assisted spectrophotometric method for simultaneous determination of paracetamol and caffeine in pharmaceutical formulations, *Bangladesh J. Sci. Ind. Res.*, 54 (3), 215–222.
- [35] Singh, V.D., and Daharwal, S.J., 2017, Development and validation of multivariate calibration methods for simultaneous estimation of Paracetamol, Enalapril maleate and hydrochlorothiazide in pharmaceutical dosage form, *Spectrochim. Acta, Part A*, 171, 369–375.
- [36] Albayrak, M., Demirkaya-Miloglu, F., Senol, O., and Polatdemir, E., 2019, Design, optimization, and validation of chemometrics-assisted spectrophotometric methods for simultaneous determination of etodolac and thiocolchicoside in

- pharmaceuticals, *J. Anal. Sci. Technol.*, 10 (1), 16.
- [37] Gandhi, S.V., Waghmare, A.D., Nandwani, Y.S., Mutha, A.S., College, A., and Road, K., 2017, Chemometrics-assisted UV spectrophotometric method for determination of ciprofloxacin and ornidazole in pharmaceutical formulation, *ARC J. Pharm. Sci.*, 3 (1), 19–25.
- [38] Eticha, T., Kahsay, G., Asefa, F., Hailu, T., Gebretsadik, H., Gebretsadikan, T., and Thangabalan, B., 2018, Chemometric-assisted spectrophotometric method for the simultaneous determination of ciprofloxacin and doxycycline hyclate in pharmaceutical formulations, *J. Anal. Methods Chem.*, 2018, 9538435.
- [39] Gandhi, S.V., and Mutha, A.S., 2017, Chemometric-assisted UV spectrophotometric method for determination of antihyperlipidemic agents in pharmaceutical formulation, *J. Appl. Pharm. Res.*, 5 (2), 27–33.
- [40] Bhaskar, R., Bhaskar, R., Sagar, M. K., Saini, V., and Bhat, K.M., 2012, UV-spectrophotometric-assisted chemometric methods for the simultaneous determination of metformin hydrochloride and gliclazide in pharmaceutical formulations, *Pharm. Anal. Acta*, 3 (4), 1000158.
- [41] Rohman, A., Dzulfianto, A., and Riswanto, F.D.O., 2017, The employment of UV-spectroscopy combined with multivariate calibration for analysis of paracetamol, propyphenazone and caffeine, *Indones. J. Pharm.*, 28 (4), 191–197.
- [42] Bachri, M., Reveny, J., Permata, Y.M., and Panjaitan, D.N., 2019, Chemometric calculation for determination of betamethasone and neomycin mixture in cream supply by ultraviolet spectrophotometry, *Open Access Maced. J. Med. Sci.*, 7 (22), 3911–3916.
- [43] Abdelazim, A.H., Shahin, M., and Abu-khadra, A.S., 2021, Application of different chemometric assisted models for spectrophotometric quantitative analysis of velpatasvir and sofosbuvir, *Spectrochim. Acta, Part A*, 252, 119540.
- [44] Zeid, A.M., Abdelazim, A.H., and Shahin, M., 2021, Simultaneous spectrophotometric quantitative analysis of elbasvir and grazoprevir using assisted chemometric models, *Spectrochim. Acta, Part A*, 252, 119505.
- [45] Abdelazim, A.H., and Shahin, M., 2021, Different chemometric assisted approaches for spectrophotometric quantitative analysis of lesinurad and allopurinol, *Spectrochim. Acta, Part A*, 251, 119421.
- [46] Al-Shaalan, N.H., 2010, Determination of phenylephrine hydrochloride and chlorpheniramine maleate in binary mixture using chemometric-assisted spectrophotometric and high-performance liquid chromatographic-UV methods, *J. Saudi Chem. Soc.*, 14 (1), 15–21.
- [47] Devi Singh, V., and Kumar Singh, V., 2021, Chemometric assisted UV-spectrophotometric methods for simultaneous estimation of Darunavir ethanolate and Cobicistat in binary mixture and their tablet formulation, *Spectrochim. Acta, Part A*, 250, 119383.
- [48] El-Zaher, A.A., Elkady, E.F., Elwy, H.M., and Saleh, M.A.E.M., 2017, Simultaneous spectrophotometric determination of glimepiride and pioglitazone in binary mixture and combined dosage form using chemometric-assisted techniques, *Spectrochim. Acta, Part A*, 182, 175–182.
- [49] Darbandi, A., Sohrabi, M.R., and Bahmaei, M., 2020, Development of a chemometric-assisted spectrophotometric method for quantitative simultaneous determination of Amlodipine and Valsartan in commercial tablet, *Optik*, 218, 165110.
- [50] Elsonbaty, A., Serag, A., Abdulwahab, S., Hassan, W.S., and Eissa, M.S., 2020, Analysis of quinary therapy targeting multiple cardiovascular diseases using UV spectrophotometry and chemometric tools, *Spectrochim. Acta, Part A*, 238, 118415.
- [51] Ni, Y., Qi, Z., and Kokot, S., 2006, Simultaneous ultraviolet-spectrophotometric determination of sulfonamides by multivariate calibration approaches, *Chemom. Intell. Lab. Syst.*, 82 (1-2), 241–247.
- [52] Attia, K.A.M., El-Abasawi, N.M., El-Olemy, A., Abdelazim, A.H., Goda, A.I., Shahin, M., and Zeid, A.M., 2021, Simultaneous spectrophotometric

- quantitative analysis of velpatasvir and sofosbuvir in recently approved FDA pharmaceutical preparation using artificial neural networks and genetic algorithm artificial neural networks, *Spectrochim. Acta, Part A*, 251, 119465.
- [53] Damiani, P.C., Moschetti, A.C., Rovetto, A.J., Benavente, F., and Olivieri, A.C., 2005, Design and optimization of a chemometrics-assisted spectrophotometric method for the simultaneous determination of levodopa and carbidopa in pharmaceutical products, *Anal. Chim. Acta*, 543 (1-2), 192–198.
- [54] Belal, F., Ibrahim, F., Sheribah, Z.A., and Alaa, H., 2018, New spectrophotometric/chemometric assisted methods for the simultaneous determination of imatinib, gemifloxacin, nalbuphine and naproxen in pharmaceutical formulations and human urine, *Spectrochim. Acta, Part A*, 198, 51–60.
- [55] Ayoub, B.M., 2016, Development and validation of simple spectrophotometric and chemometric methods for simultaneous determination of empagliflozin and metformin: Applied to recently approved pharmaceutical formulation, *Spectrochim. Acta, Part A*, 168, 118–122.
- [56] El-Gindy, A., 2005, HPLC and chemometric assisted spectrophotometric methods for simultaneous determination of diprophylline, phenobarbitone and papaverine hydrochloride, *Farmaco*, 60 (9), 745–753.
- [57] Culzoni, M.J., De Zan, M.M., Robles, J.C., Mantovani, V.E., and Goicoechea, H.C., 2005, Chemometrics-assisted UV-spectroscopic strategies for the determination of theophylline in syrups, *J. Pharm. Biomed. Anal.*, 39 (5), 1068–1074.
- [58] El-Gindy, A., Emara, S., and Shaaban, H., 2007, Development and validation of chemometrics-assisted spectrophotometric and liquid chromatographic methods for the simultaneous determination of two multicomponent mixtures containing bronchodilator drugs, *J. Pharm. Biomed. Anal.*, 43 (3), 973–982.
- [59] Mohamed, A.E.M.I., and Mikre, W., 2009, Determination of lamivudine and stavudine in pharmaceutical preparations using chemometrics-assisted spectrophotometry, *Saudi Pharm. J.*, 17 (4), 275–281.
- [60] Glavanović, S., Glavanović, M., and Tomišić, V., 2016, Simultaneous quantitative determination of paracetamol and tramadol in tablet formulation using UV spectrophotometry and chemometric methods, *Spectrochim. Acta, Part A*, 157, 258–264.
- [61] Chotimah, C., Sudjadi, S., Riyanto, S., and Rohman, A., 2015, Simultaneous determination of metamizole, thiamin and pyridoxin using UV-spectroscopy in combination with multivariate calibration, *Adv. Pharm. Bull.*, 5 (4), 593–598.
- [62] Khalili, M., Sohrabi, M.R., Mirzabeygi, V., and Torabi Ziaratgahi, N., 2018, Chemometric simultaneous determination of Sofosbuvir and Ledipasvir in pharmaceutical dosage form, *Spectrochim. Acta, Part A*, 194, 141–151.
- [63] Alibakhshi, M., Sohrabi, M.R., and Davallo, M., 2021, Application of adaptive Neuro-fuzzy interference system, fuzzy interference system and least squares support vector machine for rapid simultaneous spectrophotometric determination of antipsychotic drugs in binary mixtures and biological fluid, *Optik*, 232, 166569.
- [64] Belal, F., El-Shabrawy, Y., Barseem, A., and Ahmed, H., 2020, The use of green spectroscopy with multivariate calibration models for simultaneous analysis of ternary drug mixture in combined oral antidiabetic pill, *Spectrochim. Acta, Part A*, 241, 118638.
- [65] Abou Al Alamein, A.M., Hussien, L.A.E.A., and Mohamed, E.H., 2015, Univariate spectrophotometry and multivariate calibration: Stability-indicating analytical tools for the quantification of pimozide in bulk and pharmaceutical dosage form, *Bull. Fac. Pharm. Cairo Univ.*, 53 (2), 173–183.
- [66] Khoshayand, M.R., Abdollahi, H., Shariatpanahi, M., Saadatfard, A., and Mohammadi, A., 2008, Simultaneous spectrophotometric determination of paracetamol, ibuprofen and caffeine in pharmaceuticals by chemometric methods, *Spectrochim. Acta, Part A*, 70 (3), 491–499.

- [67] Darwish, H.W., Hassan, S.A., Salem, M.Y., and El-Zeany, B.A., 2014, Different approaches in Partial Least Squares and Artificial Neural Network models applied for the analysis of a ternary mixture of Amlodipine, Valsartan and Hydrochlorothiazide, *Spectrochim. Acta, Part A*, 122, 744–750.
- [68] Patel, N.S., Nandurbarkar, V.P., Patel, A.J., and Patel, S.G., 2014, Simultaneous spectrophotometric determination of Celecoxib and Diacerein in bulk and capsule by absorption correction method and chemometric methods, *Spectrochim. Acta, Part A*, 125, 46–52.
- [69] Naguib, I.A., Abdelaleem, E.A., Draz, M.E., and Zaazaa, H.E., 2014, Linear support vector regression and partial least squares chemometric models for determination of Hydrochlorothiazide and Benazepril hydrochloride in presence of related impurities: A comparative study, *Spectrochim. Acta, Part A*, 130, 350–356.
- [70] Magdy, N., and Ayad, M.F., 2015, Two smart spectrophotometric methods for the simultaneous estimation of Simvastatin and Ezetimibe in combined dosage form, *Spectrochim. Acta, Part A*, 137, 685–691.
- [71] Yehia, A.M., and Mohamed, H.M., 2016, Chemometrics resolution and quantification power evaluation: Application on pharmaceutical quaternary mixture of Paracetamol, Guaifenesin, Phenylephrine and p-aminophenol, *Spectrochim. Acta, Part A*, 152, 491–500.
- [72] Abdel-Ghany, M.F., Hussein, L.A., Ayad, M.F., and Youssef, M.M., 2017, Investigation of different spectrophotometric and chemometric methods for determination of entacapone, levodopa and carbidopa in ternary mixture, *Spectrochim. Acta, Part A*, 171, 236–245.
- [73] Lotfy, H.M., Mohamed, D., and Elshahed, M.S., 2019, Novel univariate spectrophotometric determination of the recently released solid dosage form comprising dapagliflozin and saxagliptin via factorized response spectra: Assessment of the average content and dosage unit uniformity of tablets, *Spectrochim. Acta, Part A*, 222, 117120.
- [74] Mahrouse, M.A., Elwy, H.M., and Salem, E.M., 2020, Simultaneous determination of cefixime and erdosteine in combined dosage form using validated spectrophotometric methods, *Spectrochim. Acta, Part A*, 241, 118647.
- [75] Attala, K., and Elsonbaty, A., 2021, Smart UV spectrophotometric methods based on simple mathematical filtration for the simultaneous determination of celecoxib and ramipril in their pharmaceutical mixtures with amlodipine: A comparative statistical study, *Spectrochim. Acta, Part A*, 244, 118853.
- [76] Abd-El-Aziz, H., Fathy, M.E., El-Enany, N., Aly, F.A., and Tolba, M.M., 2021, Investigation of some univariate and multivariate spectrophotometric methods for concurrent estimation of vancomycin and ciprofloxacin in their laboratory prepared mixture and application to biological fluids, *Spectrochim. Acta, Part A*, 253, 119570.
- [77] Kamal, A.H., Hammad, S.F., and Kamel, D.N., 2021, Chemometric spectrophotometric methods for simultaneous estimation of metoprolol succinate and amlodipine besylate in their tablet formulation, *Spectrochim. Acta, Part A*, 254, 119641.
- [78] Attia, K.A.S.M., Abdel-Aziz, O., Magdy, N., and Mohamed, G.F., 2018, Development and validation of different chemometric-assisted spectrophotometric methods for determination of cefoxitin-sodium in presence of its alkali-induced degradation product, *Future J. Pharm. Sci.*, 4 (2), 241–247.
- [79] Saad, A.S., Elzanfaly, E.S., Halim, M.K., and Kelani, K.M., 2019, Comparing the predictability of different chemometric models over UV-spectral data of isoxsuprine and its toxic photothermal degradation products, *Spectrochim. Acta, Part A*, 219, 444–449.
- [80] el deen Sayed, N., Hegazy, M., Abdelkawy, M., and Abdelfatah, R., 2013, Spectrophotometric, chemometric and chromatographic determination of naphazoline hydrochloride and chlorpheniramine maleate in the presence of naphazoline hydrochloride alkaline degradation product, *Bull. Fac. Pharm. Cairo Univ.*, 51 (1), 57–68.

- [81] Hegazy, M.A.M., Eissa, M.S., Abd El-Sattar, O.I., and Abd-El-Kawy, M.M., 2014, Determination of a novel ACE inhibitor in the presence of alkaline and oxidative degradation products using smart spectrophotometric and chemometric methods, *J. Pharm. Anal.*, 4 (2), 132–143.
- [82] Hegazy, M.A., Bakr, M.A., Badawey, A.M., and Abbas, S.S., 2021, Univariate and multivariate assisted spectrophotometric methods for determination of rosuvastatin calcium and fenofibrate in bulk powders and tablets along with their degradation products, *Spectrochim. Acta, Part A*, 248, 119163.
- [83] Arabzadeh, V., Sohrabi, M.R., Goudarzi, N., and Davallo, M., 2019, Using artificial neural network and multivariate calibration methods for simultaneous spectrophotometric analysis of Emtricitabine and Tenofovir alafenamide fumarate in pharmaceutical formulation of HIV drug, *Spectrochim. Acta, Part A*, 215, 266–275.
- [84] Rohman, A., Ardiyanti, Y., Sudjadi, S., and Riyanto, S., 2015, Simultaneous determination of paracetamol, guaiphenesin and chlorpheniramine maleate using ultraviolet spectroscopy in combination with multivariate calibration, *J. Med. Sci.*, 15 (5), 221–228.
- [85] Hegazy, M.A., Metwaly, F.H., Abdelkawy, M., and Abdelwahab, N.S., 2010, Spectrophotometric and chemometric determination of hydrochlorothiazide and spironolactone in binary mixture in the presence of their impurities and degradants, *Drug Test. Anal.*, 2 (5), 243–251.
- [86] Dinç, E., and Üstündağ, Ö., 2003, Spectrophotometric quantitative resolution of hydrochlorothiazide and spironolactone in tablets by chemometric analysis methods, *Farmaco*, 58 (11), 1151–1161.
- [87] Angheluta, A., Guizani, S., Saunier, J., and Rönnback, R., 2020, Application of chemometric modelling to UV-Vis spectroscopy: development of simultaneous API and critical excipient assay in a liquid solution continuous flow, *Pharm. Dev. Technol.*, 25 (8), 919–929.

## Supplementary Data

This supplementary data is a part of a paper entitled “Pancreatic Lipase Inhibition Activity in Lipid Absorption Using Traditional Plants: A Systematic Review and Meta-Analysis”.

Table S1. Data collection for Metaanalysis

Study ID	Subgroup*	Research place	Year	Solvent	Phytochemical constituent	Nc	Xc	SDc	Ne	Xe	SDe
1	<i>Cassia siamea</i>	India	2012	Ethanol	Cassiamin A	3	0.012	0.02	3	41.8	2.078461
2	<i>Murdannia loriformis</i>	Thailand	2012	Aqueous	Phenolic	3	1.34	0.225167	3	110	0.017321
3	<i>Stevia rebaudiana</i>	Thailand	2012	Aqueous	Phenolic	3	1.34	0.225167	3	530	0.034641
4	<i>Centella asiatica</i>	Thailand	2012	Aqueous	Phenolic	3	1.34	0.225167	3	120	0.017321
5	<i>Carthamus tinctorius</i>	Thailand	2012	Aqueous	Phenolic	3	1.34	0.225167	3	560	0.069282
6	<i>Ginkgo biloba</i>	Thailand	2012	Aqueous	Phenolic	3	1.34	0.225167	3	500	0.069282
7	<i>Orthosipon aristatus</i>	Thailand	2012	Aqueous	Phenolic	3	1.34	0.225167	3	130	0.017321
8	<i>Cassia angustifolia</i>	Thailand	2012	Aqueous	Phenolic	3	1.34	0.225167	3	810	0.051962
9	<i>Gynostemma penthaphyllum</i>	Thailand	2012	Aqueous	Phenolic	3	1.34	0.225167	3	580	0.086603
10	<i>Morus alba</i>	Thailand	2012	Aqueous	Phenolic	3	1.34	0.225167	3	100	0.017321
11	<i>C. Fenestratum</i>	Thailand	2012	Hexane:Dichloromethane: Ethanol (1:1:1)	Flavonoid	3	9.25	1.25	3	160	0.02
12	<i>Cassia auriculata</i>	UK	2012	Methanol	Flavonoid	4	0.72	0.14	4	6.0	2
13	<i>Achillea santolina</i>	Algeria	2013	Ethyl acetate fraction	Phenolic	3	0.2	0.00	3	370	0.00
14	<i>Achillea santolina</i>	Algeria	2013	Butanol fraction	Phenolic	3	0.2	0.00	3	50	0.00
15	<i>Achillea santolina</i>	Algeria	2013	Butanol fraction	Saponin	3	0.2	0.00	3	1190	0.03
16	<i>Zizyphus lotus</i>	Algeria	2013	Ethyl acetate fraction	Phenolic	3	0.2	0.00	3	450	0.00
17	<i>Zizyphus lotus</i>	Algeria	2013	Butanol fraction	Phenolic	3	0.2	0.00	3	60	0.00
18	<i>Zizyphus lotus</i>	Algeria	2013	Butanol fraction	Saponin	3	0.2	0.00	3	1153	0.46
19	<i>Passiflora nitida</i>	Japan	2013	20% Ethanol + 80% water	Flavonoid	3	0.8	0.173205	3	21.2	1.385641
20	<i>Garcinia vilersiana</i>	Thailand	2015	Ethanol	Flavonoid, Alkaloid	3	0.08	0.20	3	0.11	1.10
21	<i>P. Chamaepeuce</i>	Thailand	2015	Ethanol	Flavonoid, Alkaloid	3	0.08	0.20	3	0.45	2.40
22	<i>Hibiscus sabdariffa</i>	Germany	2015	Methanol	Polyphenol	3	0.0019	0.03	3	36	0.001
23	<i>Hibiscus sabdariffa</i>	Germany	2015	Aqueous	Polyphenol	3	0.0019	0.03	3	41	0.006
24	<i>Mentha aquatica</i>	Germany	2015	Methanol	N/A	3	0.0019	0.03	3	76	0.002
25	<i>Mentha aquatica</i>	Germany	2015	Aqueous	N/A	3	0.0019	0.03	3	9940	0.081
26	<i>Punica granatum</i>	Germany	2015	Methanol	N/A	3	0.0019	0.03	3	109	0.012
27	<i>Punica granatum</i>	Germany	2015	Aqueous	N/A	3	0.0019	0.03	3	2261	0.372
28	<i>Tamarindus Indica</i>	Germany	2015	Methanol	N/A	3	0.0019	0.03	3	152	0.007
29	<i>Tamarindus Indica</i>	Germany	2015	Aqueous	Oleanolic acid	3	0.0019	0.03	3	212	0.002
30	<i>Olea europaea</i>	Germany	2015	Methanol	Oleanolic acid	3	0.0019	0.03	3	186	0.012
31	<i>Olea europaea</i>	Germany	2015	Aqueous	N/A	3	0.0019	0.03	3	6772	0.479
32	<i>Punica granatum</i>	Germany	2015	Methanol	N/A	3	0.0019	0.03	3	186	0.009
33	<i>Punica granatum</i>	Germany	2015	Aqueous	N/A	3	0.0019	0.03	3	188	0.014
34	<i>Rosmarinus officianalis</i>	Germany	2015	Methanol	N/A	3	0.0019	0.03	3	196	0.017
35	<i>Rosmarinus officianalis</i>	Germany	2015	Aqueous	N/A	3	0.0019	0.03	3	4598	0.645
36	<i>Peumus boldus Molina</i>	Germany	2015	Methanol	N/A	3	0.0019	0.03	3	217	0.015
37	<i>Peumus boldus Molina</i>	Germany	2015	Aqueous	N/A	3	0.0019	0.03	3	2268	0.171

38	<i>Ocimum gratissimum</i>	Nigeria	2016	Methanol then by separatory funnel with hexane, aqueous phase extracted by ethyl acetate	Phenolic, Flavonoid	3	3.48	0.13	3	20.69	2.14
39	<i>Ocimum basilicum</i>	Nigeria	2016	Methanol then by separatory funnel with hexane, aqueous phase extracted by ethyl acetate	Phenolic, Flavonoid	3	3.48	0.13	3	52.14	3.96
40	<i>Moringa oleifera</i>	Indonesia	2016	Methanol	Niazirin	3	0.02126	0.00536	3	17.05	3.87
41	<i>Moringa oleifera</i>	Indonesia	2016	Methanol	Niazirin	3	0.02126	0.00536	3	42.31	16.39
42	<i>Dendrobium formasum Roxb</i>	Thailand	2017	Methanol (FII2 of Fraction Ethyl acetate, hexane gradient chromatography column)	Confusarin	3	0.013	0.004	3	154.61	8.58
43	<i>Dendrobium formasum Roxb</i>	Thailand	2017	Methanol (GIII2 of fraction CH2-Cl2-Hexane gradient chromatography column)	5-Methoxy-7-hydroxy-9,10-dihydro-1,4-phenanthrenequinone	3	0.013	0.004	3	69.45	10.14
44	<i>Adiantum capillus-veneris</i>	Jordan	2017	Water	Ferulic Acid	3	0.114	0.00693	3	1600	173.21
45	<i>Ficus carica</i>	South Africa	2018	Hexane	Malic acid	3	1894	0.017	3	26885.5	550.9
46	<i>Ficus carica</i>	South Africa	2018	Ethyl acetate	Malic acid	3	1894	0.017	3	2492.36	234.77
47	<i>Ficus carica</i>	South Africa	2018	Ethanol	Malic acid	3	1894	0.017	3	230475	96521
48	<i>Ficus carica</i>	South Africa	2018	Aqueous	Malic acid	3	1894	0.017	3	310.16	13216
49	<i>Ficus carica</i>	South Africa	2018	Hexane	Malic acid	3	1894	0.017	3	113019.5	317.3
50	<i>Ficus carica</i>	South Africa	2018	Ethyl acetate	Malic acid	3	1894	0.017	3	2943.07	220.90
51	<i>Ficus carica</i>	South Africa	2018	Ethanol	Malic acid	3	1894	0.017	3	364.96	2176
52	<i>Ficus carica</i>	South Africa	2018	Aqueous	Malic acid	3	1894	0.017	3	442.8	129.14
53	<i>Ficus carica</i>	South Africa	2018	Hexane	Malic acid	3	1894	0.017	3	276085.1	1403.4
54	<i>Ficus carica</i>	South Africa	2018	Ethyl acetate	Malic acid	3	1894	0.017	3	41574.56	20.25
55	<i>Ficus carica</i>	South Africa	2018	Ethanol	Malic acid	3	1894	0.017	3	688.56	69.9
56	<i>Ficus carica</i>	South Africa	2018	Aqueous	Malic acid	3	1894	0.017	3	842.70	151.34
57	Grapefruit	China	2018	70% Ethanol	Phenolic, Flavonoid	3	0.103	0.004	3	216.7	3.87
58	Pomelo	China	2018	70% Ethanol	Phenolic, Flavonoid	3	0.103	0.004	3	248.91	11.35
59	Kumquat	China	2018	70% Ethanol	Phenolic, Flavonoid	3	0.103	0.004	3	292.11	1.60
60	Citrus Mandarin, Owari unshu	China	2018	70% Ethanol	Phenolic, Flavonoid	3	0.103	0.004	3	129.40	7.96
61	Ponkan	China	2018	70% Ethanol	Phenolic, Flavonoid	3	0.103	0.004	3	126.62	7.46
62	Tingerine	China	2018	70% Ethanol	Phenolic, Flavonoid	3	0.103	0.004	3	109.44	5.51
63	Lemon	China	2018	70% Ethanol	Phenolic, Flavonoid	3	0.103	0.004	3	164.82	1.41
64	Sweet orange	China	2018	70% Ethanol	Phenolic, Flavonoid	3	0.103	0.004	3	87.25	7.15
65	<i>Solenostemma argel</i>	Egypt	2019	Methanol (ultrasonic)	Flavonoid	3	35.34	0.21	3	36.31	1.63
66	<i>Solenostemma argel</i>	Egypt	2019	Aqueous (ultrasonic)	Flavonoid	3	35.34	0.21	3	40.11	0.00
67	<i>Solenostemma argel</i>	Egypt	2019	50% Ethanol (Ultrasonic)	Flavonoid	3	35.34	0.21	3	62.65	3.93
68	<i>Solenostemma argel</i>	Egypt	2019	70% Ethanol (ultrasonic)	Flavonoid	3	35.34	0.21	3	29.04	0.08
69	<i>Solenostemma argel</i>	Egypt	2019	90% Ethanol (ultrasonic)	Flavonoid	3	35.34	0.21	3	31.22	0.004
70	<i>Rumex maderensis</i>	Portugal	2019	Methanol	Flavonol, Catechin	3	0.47	0.02	3	6.59	0.32

71	<i>Rumex maderensis</i>	Portugal	2019	Methanol	Flavononol, Catechin	3	0.47	0.02	3	5.17	0.25
72	<i>Rumex maderensis</i>	Portugal	2019	Methanol	Flavonol, Catechin	3	0.47	0.02	3	4.27	0.18
73	<i>J. Communis</i>	India	2020	Toluene	Tanin, Phenolic	3	68.75	0.14	3	102.93	0.44
74	<i>J. Communis</i>	India	2020	Cloroform	Tanin, Phenolic	3	68.75	0.14	3	112.12	1.05
75	<i>J. Communis</i>	India	2020	Methanol	Tanin, Phenolic, Flavonoid	3	68.75	0.14	3	69.93	1067
76	<i>J. Communis</i>	India	2020	Ethyl acetate	Tanin, Phenolic, Flavonoid	3	68.75	0.14	3	82.31	2.01
77	<i>J. Communis</i>	India	2020	aqueous	Tanin, Phenolic, Flavonoid	3	68.75	0.14	3	116.19	0.86
78	<i>Echium angustifolium</i>	Palestine 1	2020	Hexane	Saponin	3	12.3	0.35	3	29.1	0.62
79	<i>Echium angustifolium</i>	Palestine 1	2020	Acetone	Saponin	3	12.3	0.35	3	26.3	0.23
80	<i>Echium angustifolium</i>	Palestine 1	2020	Methanol	Flavonoid	3	12.3	0.35	3	34.67	0.46
81	<i>Echium angustifolium</i>	Palestine 1	2020	Aqueous	Flavonoid	3	12.3	0.35	3	24.54	0.66
82	<i>Anchusa ovata</i>	Palestine 2	2020	Hexane fraction	Saponin	3	12.3	0.35	3	501.18	0.65
83	<i>Anchusa ovata</i>	Palestine 2	2020	Acetone fraction	Tannin, Phenolic	3	12.3	0.35	3	331.1	0.47
84	<i>Anchusa ovata</i>	Palestine 2	2020	Methanol fraction	Phenolic, Tannin, Terpenoid	3	12.3	0.35	3	53.7	0.41
85	<i>Anchusa ovata</i>	Palestine 2	2020	Aqueous fraction	Phenolic, Tannin, Alkaloid	3	12.3	0.35	3	75.85	0.62
86	<i>P. mildbraedii</i>	Nigeria	2021	Ethanol	Flavonoid, Saponin	3	0.089	0.001732	3	19.87	0.467654
87	<i>P. mildbraedii</i>	Nigeria	2021	Hexane fraction	Flavonoid, Saponin	3	0.089	0.001732	3	9.74	1.316359
88	<i>M. flagellipes</i>	Nigeria	2021	Ethanol	Flavonoid, Saponin	3	0.089	0.001732	3	15.88	1.195115
89	<i>M. flagellipes</i>	Nigeria	2021	Hexane Fraction	Flavonoid, Saponin	3	0.089	0.001732	3	10.67	0.779423
90	<i>M. flagellipes</i>	Nigeria	2021	Butanol fraction	Flavonoid, Saponin	3	0.089	0.001732	3	8.25	0.398372
91	<i>Elettaria cardamomum L</i>	Saudi Arabia	2021	Aqueous	Phenolic, Flavonoid	3	23.8	1.4	3	288.75	1.3

\*References of Subgroup 1-91 = [28-46]. Abbreviation: Nc = Sample size of control (Orlistat); Xc = Average of IC<sub>50</sub> Pancreas Lipase; SDc = Standard deviation of control; Ne = Sample size of experiment (plant); Xe = Average of IC<sub>50</sub> Pancreas lipase of experiment; SDe = Standard deviation of control; N/A= Not Available.







**Review:****Pancreatic Lipase Inhibition Activity in Lipid Absorption Using Traditional Plants: A Systematic Review and Meta-Analysis**Hasim Hasim<sup>1\*</sup>, Didah Nur Faridah<sup>2,3</sup>, Eka Nurul Qomaliyah<sup>4</sup>, and Frendy Ahmad Afandi<sup>5</sup><sup>1</sup>Department of Biochemistry, IPB University, Jl. Tanjung, Kampus IPB Dramaga, Bogor 16680, Indonesia<sup>2</sup>Department of Food Science and Technology, Faculty of Agricultural Technology, IPB University, Jl. Tanjung, Kampus IPB Dramaga, Bogor 16680, Indonesia<sup>3</sup>Southeast Asian Food and Agricultural Science and Technology (SEAFAST) Center, IPB University, Jl. Tanjung, Kampus IPB Dramaga, Bogor 16680, Indonesia<sup>4</sup>Department of Pharmacy, Bumigora University, Jl. Ismail Marzuki No.22, Mataram 83127, Indonesia<sup>5</sup>Deputy Ministry for Food and Agribusiness, Coordinating Ministry for Economic Affairs, Republic of Indonesia, Jakarta 10710, Indonesia**\* Corresponding author:**

email: hasim@apps.ipb.ac.id

Received: August 5, 2022

Accepted: January 22, 2023

DOI: 10.22146/ijc.76873

**Abstract:** Obesity is a complex and multifactorial disease resulting from excessive accumulation of fat. With a significant annual increase, it has become a health concern across the globe in the last decades. To tackle this problem, an exploration of traditional medicinal plants (TMP) functioning as anti-obesity drugs using an ethnopharmacology approach has been carried out. Research on the drug development of obesity treatment was directed at how to inhibit pancreatic lipase as the enzyme accounted for lipid absorption. Using a systematic review and meta-analysis, this current study investigated TMP anti-obesity from the articles published in 6 scientific databases, i.e., Scopus, Science Direct, Proquest, Cengage Library, Ebsco, and Emerald, using particular keywords. The review resulted in 19 articles containing 91 eligible data based on inclusive and exclusive criteria. Meta-analysis extracted data as follows:  $IC_{50}$ , number of replications, and standard error, regarding the anti-obesity effects of medicinal plants and orlistat as a positive control. The results showed 8 medicinal plants showing anti-obesity via inhibition of pancreatic lipase, including *Solenostemma argel*, *Garcinia vilsianiana*, *Phyllanthus chamaepeuce*, *Cassia auriculata*, *Moringa oleifera*, *Ficus carica*, *Ocimum gratissimum*, and *Adiantum capillus-veneris*.

**Keywords:** anti-obesity; ethnopharmacology; medicinal plants; meta-analysis; lipase inhibition

**■ INTRODUCTION**

The obesity problem has been on the rise worldwide, with a dramatic increase [1]. Obesity refers to a multifactorial state that harms health due to excessive fat accumulation in adipose. The disparity results from a chronic imbalance between food intake and energy expenditure. Energy excess is restored as triglycerides in adipose, and it continues to expand, which can lead to an increment of fat storage and then impair health [2-3].

Obesity is often defined using a body mass index (BMI) of  $\geq 30 \text{ kg/m}^2$  [1].

Obesity as a complex disease relies on the combination of several factors, including genetics, environment, behavior, social, and economic [4-5]. Besides genetic factors, the current human lifestyle, which is characterized by limited physical activities and dysregulation of the meal, is deemed able to stimulate the pathogenicity of obesity [6-7]. In addition, obesity is

the cause of comorbidities, including the development of type 2 diabetes mellitus, coronary disease, cardiovascular disease, various cancers and other health problems which can lead to further morbidity and mortality [8-9]. Specifically, some diseases, including hypertension, diabetes, insulin resistance, atherosclerosis, and sleep apnea, are associated with obesity [10]. With the increase of obesity-related diseases and becoming a global health concern, there is a crucial demand for how to develop attempts in the prevention, treatment, and management of obesity [11].

Orlistat, an anti-obesity drug, inhibits the activity of pancreatic lipase, thus reducing fat absorption into cells [12]. European Medicines Agency (EMA) and the US still recommend orlistat as an anti-obesity drug which is considered a safe alternative compared with other drugs [12]. Therefore, research discussing obesity management without producing side effects have been increased incredibly. In this regard, ethnopharmacology becomes the foremost approach for future drug development [13-14].

The most common active compounds exhibiting anti-obesity effects, involved in weight loss, fat mass, and plasma triglycerides/cholesterol both *in vitro* and *in vivo* are flavonoids [15-17]. Sub-class of flavonoid compounds commonly found in plants (fruits, stems, roots) that have anti-obesity effects are tiliroside (kaempferol 3-*O*-glucoside-6''-*E*-coumaroyl or [(2R,3S, 4S,5R,6S)-6-[5,7-dihydroxy-2-(4-hydroxyphenyl)-4-oxo-chromen-3-yl]oxy-3,4,5-trihydroxyoxan-2-yl]methyl(*E*)-3-(4-hydroxyphenyl)-prop-2-enoate) [15]. Trans-tiliroside in doses of 0.1, 1, and 10 mg/kg bw strongly inhibited weight gain, especially visceral fat weight, and increased plasma glucose levels after glucose loading in rats [15]. It was also found that tiliroside can inhibit triglyceride accumulation and glycerol-3-phosphate dehydrogenase activity in 3T3-L1 cells [18]. Tiliroside shows the ability to be an anti-obesity which is better than orlistat [19].

Next, flavonoid compounds commonly found in plants with great bioactivity potential are quercetin [20-21]. In addition to flavonoids, pancreatic lipase inhibitory phytochemicals contained in plants or isolated from plants have been reported to be saponins, polyphenols,

alkaloids, carotenoids, and terpenes [22-23]. Phenolic derivatives such as chlorogenic acid, catechin, and caffeic acid have a positive correlation with pancreatic lipase inhibition [24].

Some countries have their own empiric evidence on how diseases, primarily obesity, are treated by using herbs and medicinal plants [25]. There are 5 groups of herbal-based treatments for obesity, i.e., reduction of energy intake, increment of energy expenditure, reduction of lipogenesis and enhancement of lipolysis, attenuation of differentiation and proliferation of pre-adipose, as well as reduction of fat absorption [14]. The mechanism of fat absorption reduction via inhibition of pancreatic lipase can be noted as an important base in the exploration of herb-based treatment, with the mode of similar action to orlistat [14].

Although sample evidence on pancreatic lipase inhibition by traditional medicinal plants (TMP) has been reported, there is no systematic review and meta-analysis focusing on the topic, especially aiming to compare the efficacy of such plants compared with orlistat as standard. This present work aimed to screen medicinal plants able to function as anti-obesity agents recognized globally via inhibition of pancreatic lipase. The main data used in the meta-analysis referred to the ability of lipase inhibition based on inhibition of pancreatic lipase at 50% (expressed as  $IC_{50}$ ) while also compared with orlistat.

## ■ MATERIALS AND METHODS

### Literature Search

The present systematic review and meta-analysis complied with Preferred Reporting Items for Systematic Reviews and Meta-analyses (PRISMA) according to the guideline handbook [26-27]. During the study, we did a checklist based on the PRISMA statement table. Numerous kinds of literature discussing anti-obesity were collected through various article databases such as Science Direct, Proquest, Ebsco, Emerald and Cengage Library (up to May 2021). A total of 19 research articles selected were able to be accessed through PubMed and Embase databases. The search of articles employed the following keywords: "anti-obesity", "medicinal plants",

and “lipase inhibition”. We screened the titles and abstract, then excluded irrelevant research articles by using Collandrapp. Subsequently, we examined the full text of all remaining articles to determine eligibility. The discrepancies were verified by discussion and consensus. We also reviewed the identified trials and reviewed articles in reference lists to find any other potential proper articles.

### Eligibility Criteria

Studies were eligible for the present systematic review and meta-analysis according to the following criteria: (1) design: lipase inhibition experiment; (2) population: all research articles carried out using *in vitro* protocols for anti-obesity treatment published in the last 10 years; (3) intervention: comparison between lipase inhibition  $IC_{50}$  properties selected medicinal plants and orlistat; and (4) data: adequate information (data) for calculating the standardized mean difference (SMD) and the corresponding 95% confidence interval (CI). Further, all published papers were written in English.

### Data Extraction

Extraction and integration of data collected from the selected articles were performed by using Collandrapp. The following information was extracted using a predefined form, i.e., first author name, year of publication, country of origin, number of experiments, intervention, control, solvent, method, and outcomes data ( $IC_{50}$  lipase inhibition). The discrepancies were verified by discussion and consensus.

### Statistical Analysis

Meta-analysis was conducted in qualified research papers according to certain criteria. The papers shall contain the following information: averaged concentration of compounds in traditional medicinal plants and orlistat for  $IC_{50}$ , number of replications, and standard deviation. Since all the observation indexes are continuous and the measurement time of outcome is inconsistent across studies, we pooled the SMD with a corresponding 95% CI using the random-effects model.

## ■ RESULT

### Trial Selection and Risk of Bias Assessment

The initial search from 6 scientific databases successfully collected and identified 810 articles, of which 326 articles were chosen for full-text review, resulting in 19 articles [28-46] that met the inclusion criteria. Meanwhile, the rest (484 articles) was rejected due to incompatible substance from the title and abstract. Nine additional articles from reference lists of the identified trials were included in the study because they met the inclusion criteria. Following a full review, a total of 331 articles were excluded (8 review articles, 291 not having data compatible with analysis). Totally the meta-analysis involved 19 articles. The stage of article selection is exhibited in Fig. 1.

### Characteristics of Articles

Nineteen selected articles contained 91 experimental data published between 2011 and 2021. The PICO of this research is defined as Participants, Interventions, Comparisons, Outcomes, and Study Design. Participants in the *in vitro* experiment were  $IC_{50}$  pancreatic lipase inhibition. Interventions used were medicinal plants. Comparisons were orlistat as an anti-obesity drug. The outcome of this research was the best potential lipase inhibition activity by medicinal plants. The study design used in this research was randomized control.

### The Most Promising Anti-Obesity Plants

#### *Inhibition of pancreatic lipase*

In this work, our systematic review and meta-analysis used  $IC_{50}$  of pancreatic lipase inhibition as the criteria for screening studies. Summary table of meta-analysis (Table 1) and additional table about data collection for meta-analysis (Table S1), meta-analysis modeling indicated an overall standardized mean difference (SMD) of 12.75 (95% CI 10.144-15.362) with  $I^2 = 89.83\%$  and  $P < 0.001$ . There were 8 medicinal plants from all studied countries that showed smaller effect size than the average, i.e., *Solenostemma argel* (Hargel)

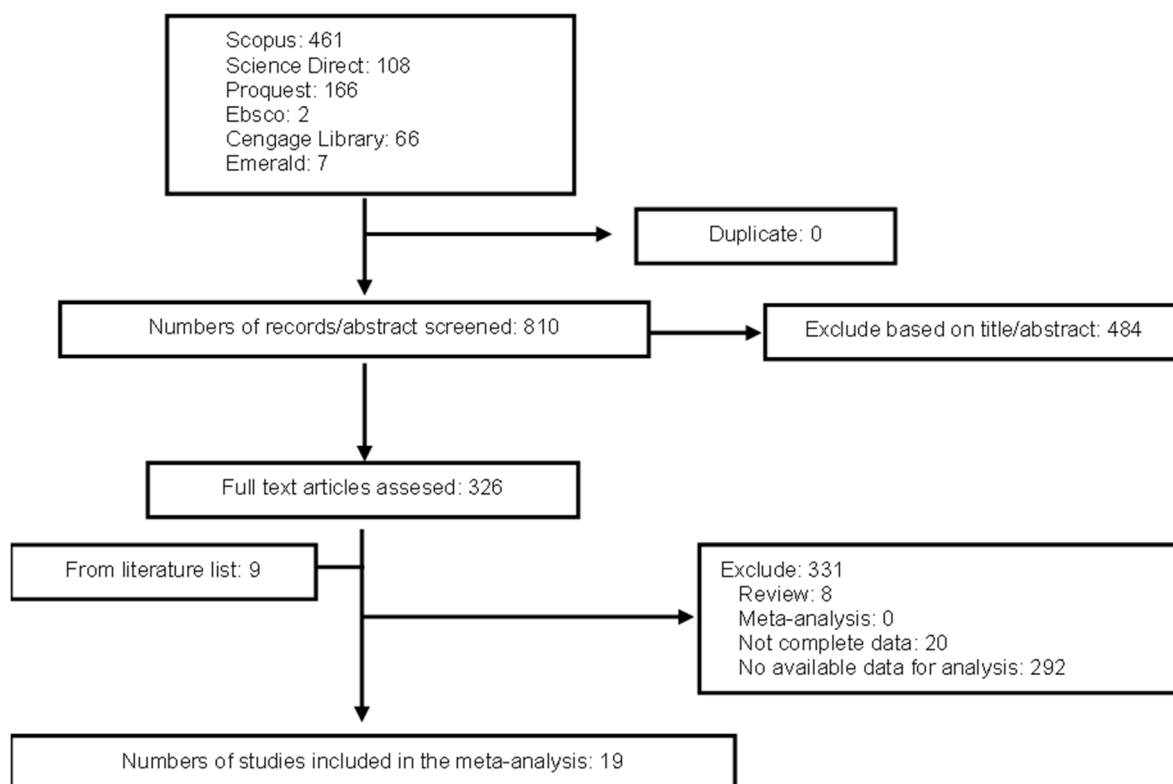


Fig 1. The Prisma flow diagram of the systematic review process

-2.166 (95% CI -12.211-7.875), *Garcinia vilersiana* 0.030 (95% CI -1.570-1.777), *Phyllanthus chamaepeuce* 0.173 (95% CI -1.430-1.777), *Cassia auriculata* (Tanner's Cassia) 3.235 (95% CI -12.211-7.875), *Moringa oleifera* (Drumstick tree) 3.610 (95% CI 3.689-14.467), *Ficus carica* 6.178 (95% CI 1.703-5.517), *Ocimum gratissium* (African basil) 9.058 (95% CI 3.689-14.467), and *Adiantum capillus-veneris* (southern maidenhair fern) 10.422 (95% CI 4.312-16.533).

#### Bioactive compounds contributing to anti-obesity

Medicinal plants with anti-obesity effects were screened in the previous stage according to their inhibitory activity against pancreatic lipase (expressed as  $IC_{50}$ ). The further stage focused on the selection of bioactive compounds most contributing to anti-obesity via inhibition of pancreatic lipase. The results indicated different scores of SMD between compounds, i.e., flavonoid-alkaloid 0.102 (95% CI -1.031-1.234], niazirin 3.610 (95% CI 1.703-5.517), mallic acid 6.178 (95% CI 2.645-9.711), flavonoid 6.316 (95% CI 0.507-12.126], 5-Methoxy-7-hidroxy-9,10-dihydro-1,4-phenanthrenequinone 7.727 (95% CI 3.071-12.382), combination of tannin, phenolic and flavonoid

7.977 (95% CI -2.379-18.333), and ferulic acid 10.422 (95% CI 4.312-16.533); those compounds are lower than the average 12.753 (95% CI 10.144-15.362). Niazirin belongs to a group of phenolic glycosides [47]. Based on the forest plot, herbal plants with flavonoids and alkaloids exerted a powerful inhibitory activity towards pancreatic lipase compared with those with flavonoids or phenolics alone. The inhibition rate of plants containing flavonoids and alkaloids reached 60, higher than those containing flavonoids.

#### Solvents used to isolate the bioactive compounds

The most proper solvent to extract bioactive compounds for anti-obesity was ordered as follows: ethanol 70% with a homogenizer, ultrasonication, ethanol 90% with ultrasonication, methanol with ultrasonication, ethanol 50% with ultrasonication, methanol, water, and ethyl acetate. From Table 1 comparison of solvent to  $IC_{50}$  indicated that ultrasonication-assisted extraction would improve the inhibition of pancreatic lipase in comparison with maceration. Ethanol 70% is the best solvent. Compared to methanol, extraction of the anti-obesity

Table 1. Summary table of the Metaanalysis

Subgroup*	Country	Solvent	Bioactive molecule	N	Effect size (random effect model)			SE	p-value	Heterogeneity		Egger's test
					SMD	C.L (Lower to Upper)				I <sup>2</sup>	Q	
<i>Cassia Siamea</i>	India	Ethanol	Cassiamin A	3	22.69	9.75	35.62	43.55	NA	NA	NA	NA
<i>Miurdannia ioriformis</i>	Thailand	Aqueous	Phenolic	3	543.38	235.93	860.83	24564.61	NA	NA	NA	NA
<i>Stevia rebaudiana</i>	Thailand	Aqueous	Phenolic	3	2619.73	1137.50	4101.96	571366.70	NA	NA	NA	NA
<i>Centella asiatica</i>	Thailand	Aqueous	Phenolic	3	593.39	257.65	929.13	29293.91	NA	NA	NA	NA
<i>Carthamus tinctorius</i>	Thailand	Aqueous	Phenolic	3	2678.56	1163.05	4194.08	596666.30	NA	NA	NA	NA
<i>Ginkgo biloba</i>	Thailand	Aqueous	Phenolic	3	2390.89	1038.14	3743.63	475385.10	NA	NA	NA	NA
<i>Orthosipon aristatus</i>	Thailand	Aqueous	Phenolic	3	643.39	279.36	1007.43	34439.29	NA	NA	NA	NA
<i>Cassia angustifolia</i>	Thailand	Aqueous	Phenolic	3	3951.29	1715.67	6186.91	1299331	NA	NA	NA	NA
<i>Gynostemma penthaphyllum</i>	Thailand	Aqueous	Phenolic	3	2706.69	1175.26	4238.12	610454.50	NA	NA	NA	NA
<i>Morus alba</i>	Thailand	Aqueous	Phenolic	3	493.38	214.22	772.53	20251.41	NA	NA	NA	NA
<i>C. fenestratum</i>	Thailand	Hexane:Dichloro methane:Ethanol (1:1:1)	Flavonoid	3	136.06	59.06	213.06	1543.48	NA	NA	NA	NA
<i>Cassia auriculata</i>	UK	Methanol	Flavonoid	4	3.24	1.13	5.34	1154	NA	NA	NA	NA
<i>Achillea santolina</i>	Algeria	Ethyl acetate fraction	Phenolic	3	575508.82	-118268.27	1269285.91	693777.09	<0.01	90.84	NA	0.410
		Butanol fraction	Phenolic	3	4172746.16	1011836.15	6533656.17	1.45 × 10 <sup>12</sup>	-	-	-	-
		Butanol fraction	Saponin	3	561932.83	243995.27	879870.41	2.63 × 10 <sup>10</sup>	-	-	-	-
<i>Zizyphus lotus</i>	Algeria	Butanol fraction	Phenolic	3	44751.52	19431.43	70071.61	1.67 × 10 <sup>8</sup>	-	-	-	-
		Ethyl acetate fraction	Phenolic	3	689657.39	-179526.11	1556640.91	2.15 × 10 <sup>12</sup>	<0.01	91.63%	NA	0.412
		Butanol fraction	Phenolic	3	5075449.49	220379.37	7947102.61	3.79 × 10 <sup>10</sup>	-	-	-	-
		Butanol fraction	Saponin	3	674770.742	292990.27	1056551.21	5 666379.40	-	-	-	-
<i>Passiflora nitida</i>	Japan	20% Ethanol + 80% water	Flavonoid	3	1556640.91	-179526.12	4427.78	23.31	NA	NA	NA	NA
<i>Garcinia vilersiana</i>	Thailand	Ethanol	Flavonoid, Alkaloid	3	14.49	7.02	25.94	0.67	NA	NA	NA	NA
<i>P. chamaepeuce</i>	Thailand	Ethanol	Flavonoid, Alkaloid	3	0.03	-1.57	1.63	0.67	NA	NA	NA	NA
<i>Hibiscus sabdariffa</i>	Germany	Methanol	Polyphenol	3	0.17	-1.43	1.78	0.67	NA	NA	NA	NA
		Aqueous	Polyphenol	3	1423.98	853.34	1994.42	152603.70	0.78	0%	NA	NA
<i>Mentha aquatica</i>	Germany	Methanol	NA	3	1353.23	567.58	2116.80	190538.20	<0.01	91.28%	NA	NA
		Aqueous	NA	3	1512.10	656.56	2367.63	677901.10	-	-	-	-
<i>Punica granatum</i>	Germany	Methanol	NA	3	129859.26	56381.91	203310.62	1.41 × 10 <sup>9</sup>	-	-	-	-
		Aqueous	NA	3	5312.83	3668.78	6957.48	3421569	0.34	9.74	NA	<0.001
		Methanol:s (1:1)	NA	3	3806.40	1652.80	5960.16	1207443	-	-	-	-
		Methanol:s (2:1)	NA	3	4836.04	2969.25	10703.92	3894288	-	-	-	-
<i>Tamarindus Indica</i>	Germany	Methanol	NA	3	6700.83	2909.55	10492.12	3741769	-	-	-	-
		Aqueous	NA	3	6407.71	2792.27	10033.15	3421569	-	-	-	-
		Methanol	NA	3	6352.69	3771.78	8933.58	5275024	0.39	0%	NA	NA
		Aqueous	NA	3	5567.49	2417.44	8717.62	2583087	-	-	-	-
		Methanol	NA	3	7956.14	3454.61	12457.67	5275024	-	-	-	-

<i>Olea europaea</i>	Germany				10274.50	1220.34	19328.65		0.06	72.27%	NA	NA
		Methanol	NA	3	4495.51	2820.39	10170.62	3515973	-	-	-	-
		Aqueous	NA	3	15921.58	6913.26	24929.90	21124736	-	-	-	-
<i>Rosmarinus officianalis</i>	Germany				7044.81	4208.66	9880.96		0.59	0%	NA	NA
		Methanol	NA	3	6413.81	2784.92	1604.69	3428079	-	-	-	-
		Aqueous	NA	3	8035.16	3409.93	12591.40	5380326	-	-	-	-
<i>Peumus boldus Molina</i>	Germany				10102.09	3036.16	17168.01		0.12	59.27%	NA	NA
		Methanol	NA	3	7300.20	3169.79	11430.60	4441077	-	-	-	-
		Aqueous	NA	3	1474.73	6400.53	2300.93	18107421	-	-	-	-
<i>Ocimum gratissimum</i>	Nigeria	Methanol then by Phenolic, separatory funnel with hexane, aqueous phase extracted by ethyl acetate	Flavonoid	3	9.06	3.69	14.43	7.50	NA	NA	NA	NA
<i>Ocimum basilicum</i>	Nigeria	Methanol then by Phenolic, separatory funnel with hexane, aqueous phase extracted by ethyl acetate	Flavonoid	3	13.85	5.85	21.86	16.67	NA	NA	NA	NA
<i>Moringa oleifera</i>	India				3.61	1.70	5.51		0.31	2.93%	NA	NA
		Methanol	Niazirin	3	4.97	1.73	8.19	2.72	-	-	-	-
		Methanol	Niazirin	3	2.91	0.61	5.21	1.37	-	-	-	-
<i>Dendrobium formosum Roxb</i>	Thailand				12.86	0.72	24.99		0.05	74.35	NA	NA
		Methanol (FII2 of Fraction acetate, hexane gradient chromatography column)	Confusarin	3	20.33	8.71	31.94	35.11	-	-	-	-
		Methanol (GIII2 of fraction CH2-Cl2-Hexane gradient chromatography column)	5-Methoxy-7-hydroxy-9,10-dihydro-1,4-phenanthren equinone	3	7.73	3.07	5.21	5.64	-	-	-	-
<i>Adiantum capillus-veneris</i>	Jordan	water	Ferulic acid	3	10.42	4.31	16.53	9.72	NA	NA	NA	NA
<i>Ficus carica</i>	South Africa				3	55.06	23.87	86.26	<0.01	87.56%	NA	0.03
		Hexane	Malic acid	3	11.97	5.01	18.93	253.34	-	-	-	-
		Ethyl acetate	Malic acid	3	2.69	0.46	4.90	12.61	-	-	-	-
		Ethanol	Malic acid	3	0.03	-1.57	1.63	1.27	-	-	-	-
		Aqueous	Malic acid	3	0.02	-1.57	1.63	0.67	-	-	-	-
		Hexane	Malic acid	3	401.91	174.50	629.31	13461.78	-	-	-	-
		Ethyl acetate	Malic acid	3	15.02	6.37	23.67	19.48	-	-	-	-
		Ethanol	Malic acid	3	0.188	-1.41	1.79	0.67	-	-	-	-
		Aqueous	Malic acid	3	3.85	1.15	6.56	1.90	-	-	-	-
		Hexane	Malic acid	3	221.98	96.37	347.58	4106.92	-	-	-	-
		Ethyl acetate	Malic acid	3	2316.53	1005.85	3627.20	447192.90	-	-	-	-
		Ethanol	Malic acid	3	11.01	4.61	17.55	10.91	-	-	-	-
		Aqueous	Malic acid	3	6.27	2.38	10.16	3.94	-	-	-	-
Grapefruit	China	70% Ethanol	Phenolic, Flavonoid	3	63.15	27.38	98.92	333.03	NA	NA	NA	NA
Pomelo	China	70% Ethanol	Phenolic, Flavonoid	3	24.74	10.65	38.82	51.65	NA	NA	NA	NA
Kumquat	China	70% Ethanol	Phenolic, Flavonoid	3	205.93	89.40	322.46	3534.72	NA	NA	NA	NA



Citrus Mandarin, Owari unshu Ponkan	China	70% Ethanol	Phenolic, Flavonoid	3	10.33	7.83	38.82	28.66	NA	NA	NA	NA
Tingerine	China	70% Ethanol	Phenolic, Flavonoid	3	19.14	0.19	30.08	31.18	NA	NA	NA	NA
Lemon	China	70% Ethanol	Phenolic, Flavonoid	3	22.40	9.66	35.16	42.45	NA	NA	NA	NA
Sweet orange	China	70% Ethanol	Phenolic, Flavonoid	3	131.82	57.22	206.41	1448.65	NA	NA	NA	NA
<i>Solenostemma argel</i>	Egypt											
		Methanol (ultrasonic)	Flavonoid	3	-2.17	-12.21	7.87		<0.01	91.06%	NA	0.74
		Aqueous (ultrasonic)	Flavonoid	3	0.66	-0.98	2.31	0.70	-	-	-	-
		50% Ethanol (ultrasonic)	Flavonoid	3	25.63	11.04	40.22	55.41	-	-	-	-
		70% Ethanol (ultrasonic)	Flavonoid	3	7.83	3.12	12.54	5.78	-	-	-	-
		90% Ethanol (ultrasonic)	Flavonoid	3	-31.63	-49.60	-13.66	84.06	-	-	-	-
<i>Rumex maderensis</i>	Portugal											
		Methanol	Flavonoid	3	22.01	14.75	29.27		0.96	0%	NA	0.08
		Methanol	Flavonol, Catechin	3	21.54	9.25	33.83	39.33	-	-	-	-
		Methanol	Flavonol, Catechin	3	21.14	9.07	33.22	37.93	-	-	-	-
		Methanol	Flavonol, Catechin	3	23.67	10.11	37.16	47.38	-	-	-	-
<i>J. communis</i>	India											
		Toluene	Tanin, Phenolic	3	20.13	7.45	32.81		<0.01	90.93%	NA	0.23
		Chloroform	Tanin, Phenolic	3	46.19	20.01	72.38	582.08	-	-	-	-
		Methanol	Tanin, Phenolic, Flavonoid	3	46.19	20.01	72.38	178.53	-	-	-	-
		Methanol	Tanin, Phenolic, Flavonoid	3	0.001	-1.59	1.60	0.67	-	-	-	-
		Ethyl acetate	Tanin, Phenoluc, Flavonoid	3	7.59	3.00	12.18	5.472	-	-	-	-
		Aqueous	Tanin, Phenolic, Flavonoid	3	61.43	7.90	29.06	315.20	-	-	-	-
<i>Echium angustifolium</i>	Palestine											
		Hexane	Saponin	3	27.94	17.13	38.74		0.17	40.34%	NA	0.01
		Acetone	Saponin	3	26.62	11.47	41.77	59.75	-	-	-	-
		Methanol	Flavonoid	3	37.72	16.31	59.12	119.23	-	-	-	-
		Aqueous	Flavonoid	3	43.67	18.91	69.43	159.59	-	-	-	-
<i>Anchusa ovata</i>	Palestine											
		Hexane fraction	Saponin	3	16.40	7.90	29.06	29.15	<0.01	87.35%	NA	0.08
		Acetone fraction	Tannin, Phenolic	3	200.59	69.81	331.37		-	-	-	-
		Methanol fraction	Phenolic, Tannin, Terpenoid	3	747.23	324.45	1170.02	46531.08	-	-	-	-
		Aqueous fraction	Phenolic, Tannin, Alkaloid	3	613.86	266.54	961.19	31403.24	-	-	-	-
		Methanol fraction	Phenolic, Tannin, Terpenoid	3	96.65	37.60	135.71	626.46	-	-	-	-
		Aqueous fraction	Phenolic, Tannin, Alkaloid	3	109.72	43.71	157.73	846.02	-	-	-	-

<i>P. mildbraedii</i>	Nigeria			25.66	-12.72	64.06		0.01	87.35%	NA	NA	
		Ethanol	Flavonoid, Saponin	3	47.72	20.67	74.78	190.50	-	-	-	-
		Hexane fraction	Flavonoid, Saponin	3	9.27	3.32	13.22	6.37	-	-	-	-
<i>M. flagellipes</i>	Nigeria			16.54	10.96	22.11		0.56	0%	NA	0.01	
		Ethanol	Flavonoid, Saponin	3	14.90	6.32	23.49	19.19	-	-	-	-
		Hexane Fraction	Flavonoid, Saponin	3	15.31	6.50	24.13	20.22	-	-	-	-
		Butanol fraction	Flavonoid, Saponin	3	23.11	9.93	36.29	45.19	-	-	-	-
<i>Eletaria cardamomium</i>	Saudi Arabia	Aqueous	Phenolic, flavonoid	3	156.48	67.93	245.04	156.49	NA	NA	NA	NA
<b>Overall</b>				12.75	10.14	15.36		<0.01	89.93%	NA	<0.01	

\*References of Subgroup 1-91 = [28-46]. Abbreviation: N = Sample size of study; SMD = Standardized Mean Difference; SE = Standard Error; Q = homogeneity test; I<sup>2</sup> = Index 95%; CI = Confidence Interval around I<sup>2</sup>; NA = Not available

compound by ethanol produced a much higher amount of yield, reaching up to 2.5 times higher than methanol.

### Countries with the most appreciable anti-obesity effect

From the screening of articles published in 6 databases, there was no research paper from Indonesia that meets the criteria of meta-analysis. The absence of Indonesian research articles could relate to a scarcity of research publications on herbal plants promoting anti-obesity activities. In addition, the published articles did not fit the criteria. Meta-analysis indicated some potential countries that are associated with plants containing an inhibitor of pancreatic lipase, i.e., Egypt, the UK, South Africa, India, Thailand, and Jordan, respectively. The effect size of these countries was better than the overall score.

### Research mapping related to anti-obesity

In this work, we portrayed research focusing on anti-obesity. Analysis of bibliometric data accessed from 6 databases suggested 4 research clusters of obesity, each displayed in different colors. Green cluster represented *in vivo* anti-obesity experiments using experimental animals such as a rat. The experiment applied various methods and evaluated the lipid profile of the animals. Meanwhile, the yellow cluster delineated studies on the mode of action of anti-obesity drugs, covering the investigation of PPAR $\gamma$  gene expression, adipose alteration, lipogenesis, and lipid accumulation. However, this group of research was scarcely conducted, as presented in pale-yellow color. In addition, the red cluster displayed studies on other

bioactivities, such as anti-diabetic activity via  $\alpha$ -glucosidase and  $\alpha$ -amylase test, and their relationship with bioactive compounds in drugs such as flavonoids. The blue cluster depicted pharmacotherapy experiments, disease diagnosing, and evaluation of potential plants for medicines. However, the pale blue color indicated that the studies on this cluster were scant (Supplementary File).

Based on bibliometric data from 6 databases within the last 10 years analyzed using VoS viewer, we noted current anti-obesity research discussing phytochemical profiles and obesity management directly on obese individuals. From this bibliometric, a considerable rise in anti-obesity studies started in 2015. As illustrated in the graph, research topics on light colors indicated that they were intensively carried out; on the contrary, topics on dark color were rarely studied. We also found that TCM became massively published topics, while research on the mechanism of anti-obesity effect by lipase inhibition and phytochemicals was rarely investigated (Fig. S1 and S2).

## DISCUSSION

In this meta-analysis, we present 91 experimental data regarding the use of medicinal plants from numerous countries, in which these plants provide anti-obesity effects via inhibition of pancreatic lipase under *in vitro* experiments. The data used are eligible, following verification based on inclusion criteria, including the presence of IC<sub>50</sub> value, number of replications, and standard deviation. As one of the key

criteria, we define  $IC_{50}$  as a minimum concentration required to inhibit the activity of pancreatic lipase by 50%. It is well-known that pancreatic lipase constitutes a pivotal enzyme that dictates fat absorption [14]. Hence, a drug or a compound showing lower  $IC_{50}$  is more powerful as an inhibitor. Actually, the mechanism of anti-obesity through pancreatic lipase inhibition is applied by a conventional drug, i.e., orlistat [48]. Furthermore, the inhibition of such enzymes has been massively studied. This condition provokes exploration of medicinal plants highlighting their ability to retard pancreatic lipase as an attempt in search of anti-obesity drugs.

Among 91 plants studied, we show 8 TMP exhibiting the most appreciable source of anti-obesity according to effect size compared with orlistat. These plants include *Solenostemma argel*, *Garcinia vilersiana*, *P. chamaepeuce*, *Cassia auriculata*, *Moringa oleifera*, *Ficus carica*, *Ocimum gratissimum* and *Adiantum capillus-veneris*. These plants are applied in different parts of the plant, such as the leaf, fruit, and root. Meanwhile, there are 5 bioactive compounds functioning as a pancreatic lipase inhibitor, i.e., phenolic, flavonoid, saponin, alkaloid, and terpenoid [36,48]. Other studies reported some potential bioactive compounds for inhibiting pancreatic lipase, i.e., flavonoid, phenol, and alkaloid [48-50]. Consistent with former studies, this meta-analysis also demonstrates that secondary metabolites suitable for anti-obesity include a combination of flavonoid-alkaloid, niazirin, malic acid, flavonoid, 5-methoxy-7-hydroxy-9,10-dihydro-1,4-phenanthrenequinone, a combination of tannin, phenolic, and flavonoid, as well as ferulic acid.

Regarding the relationship between solvent and pancreatic lipase inhibition, extraction of bioactive compounds using ethanol and methanol with an ultrasonication system is associated with higher inhibitory activity. Ultrasonication-assisted extraction enables the enhancement of efficiency, selectivity of the process, high reproducibility, less amount of solvent used, shorter time, and higher production content yield [51]. Hence, these advantages are reasons for the popularity of ultrasonic in plant-source extraction for drug development [52]. Solvents are often selected for their polarity. A polar solvent is highly effective in isolating and

dissolving polar and semi-polar compounds, and vice versa [53]. Solvent classification according to a degree of polarity can be sequenced (non-polar to polar) as follows: hexane < chloroform < ethyl acetate < acetone < ethanol < methanol < water [53]. Ethanol is the ideal solvent for the extraction of polyphenols, including flavonoids. In addition, concerning safety, ethanolic extract appears to be safer for humans. Meanwhile, methanol is proper for the extraction of flavonols with a higher molecular weight and alkaloid is best extracted by ethanol rather than methanol and water [54-55].

*Solenostemma argel* is a traditional perennial herb widely distributed in some regions such as Egypt, Africa, and Arabian Peninsula [56]. Besides providing inhibition towards pancreatic lipase, the anti-obesity mechanism by the argel is based on its stimulatory effect on the expression of  $\beta$ -oxidation, modulation of adipokine activity, regulation of satiation hormone, control of body weight, and improvement of lipid profile [57]. The flavonoid in the argel is reported as a main contributor to anti-obesity [31]. Another potential plant for anti-obesity management is *Garcinia vilersiana*, popular as yellow mangosteen. Several species of *Garcinia* can be found in tropical regions of Asia, Africa, and Polynesia, and they are included in ayurvedic medicine [58]. In this meta-analysis, *Garcinia vilersiana* originates from Thailand. Flavonoids and alkaloids in yellow mangosteen are two bioactive compounds responsible for anti-obesity activity [29]. *Phyllanthus chamaepeuce*, a member of *Phyllanthus*, mostly occurs in tropical and sub-tropical areas in Asia, Africa, America, and Oceania, and for *Phyllanthus chamaepeucea*, it is distributed in Asia countries such as Malaysia and Thailand [59-60]. In addition, we also observed *P. chamaepeuce* from Thailand as one of the anti-obesity agents, in which flavonoids and alkaloids are also key bioactive compounds for curing obesity [29].

Moreover, *Cassia auriculata*, widely recognized as avartaki in India, is an annual or biennial shrub found throughout the country and in this work, Indian avartaki is one of the ayurvedic plants [61]. Avartaki exerts anti-obesity properties regarding its ability to reduce the action of pancreatic lipase as well as diminishing

adiposity differentiation which leads to body weight loss [62]. Flavonoid is a bioactive compound responsible for the anti-obesity effect of avertaki [34]. *Moringa oleifera*, also known as the drumstick tree, is a popular plant throughout the world and spread in most parts of the globe, including India, Asia, and Africa [63]. With its stunning bioactivity, moringa leaf is listed in the top 50 future plants [64]. Anti-obesity activity by moringa leaf relates to its action on inhibition of pancreatic lipase as well as regulation of fat storage through the down-regulating expression of adipogenesis-associated proteins peroxisome proliferator-activated receptor gamma (PPAR $\gamma$ ) and fatty acid synthase (FAS), up-regulating the expression of the lipolysis-related protein, i.e. adipose triglyceride lipase (ATGL), suppressing content of leptin, retarding expression of lipogenesis, and adipogenesis-related proteins [65-66]. In addition, moringa leaf is reported to be able to improve lipid profile by reducing the content of total cholesterol, triglyceride, low-density lipoprotein (LDL), and very low-density lipoprotein (VLDL), but at the same time, increasing high-density lipoprotein (HDL) [65]. The experiment in animal subjects indicates that moringa enables to decline in body weight of obese rats significantly [67]. The incredible activity of moringa as an anti-obesity agent is associated with the presence of niazirin [46], which belongs to a member of phenolic glycoside [68].

*Ficus carica*, also known as fig, originates from Southwest Asia and East Mediterranean; and the plant is believed as one the first cultivated plants in human history [69]. In this meta-analysis, *Ficus carica* is from South Africa. *Ficus carica* often relates to management of diabetes; hence its activity as an anti-obesity agent is linked to the ability of the plant to regulation of glucose, lipid metabolism, and oxidative stress [70]. The malic acid in *Ficus carica* is the main actor in its anti-obesity effect [30]. In addition, *Ocimum gratissimum* can be found in tropical regions of Asia and Africa, such as Nigeria, which is widely applied in folkloric medicine [71-72]. In this work, *Ocimum gratissimum* studied originates from Nigeria, emphasizing the performance of anti-obesity by phenolic and flavonoids in the plant [73]. Some fern species, *Adiantum capillus-veneris* is popularly applied in

traditional medicine in many parts of the world, including China, India, and the United States Pharmacopoeia [74]. Ferulic acid isolated from the plant is revealed to provide an anti-obesity effect [45]. Regarding the mode of action, the anti-obesity effect of bioactive compounds in fern species depends on how they regulate the activity of gastrointestinal enzymes, especially those that account for the digestion and absorption of carbohydrates and lipids. This suggests that bioactive compounds in fern plants can perform dual targets in the regulation of glycemia, which is associated with obesity and diabetes [73].

### **Brief Description of the Mechanism of Pancreatic Lipase Inhibition by Bioactive Compounds**

Pancreatic lipase is an important enzyme of pancreatic juice responsible for the digestion of dietary triglycerides in the small intestine into free fatty acids and diacylglycerol [49]. The way of inhibiting pancreatic lipase enzymes by orlistat or tetrahydrolipstatin itself is to form a covalent bond with the active serine moiety site of lipases and then inactivate them to hydrolyze dietary fat [75]. The bioactive molecules that have potential as pancreatic lipase inhibitors are also the same, which will bind to the active site of the lipase enzyme located in the stomach and small intestine, changing the conformation of the enzyme, thereby inhibiting catalytic activity, thereby reducing digestion and absorption of fat and accumulation in tissues. Adipose tissue to achieve obesity control [76-77]. The advantage of lipase inhibitors acting on peripheral elements in the development of new drugs is that they do not enter the human blood vessels and nervous system and do not affect the balance between the body's minerals and bone circulation lipase inhibition [77-78]. The lipase inhibitor has proven to be relatively safe [49].

### **Limitations and Strengths of This Study**

This present systematic review and meta-analysis possess several limitations that are worth nothing. First, although the search strategy of this study was comprehensive, it is possible that pertinent unpublished reports or studies published in languages other than English are not included in this study. Future studies

should consider gray literature apart from easily accessible international databases and include publications with no language limitation, unpublished resources, including books, dissertations, and non-English publications. Second, the trials involved in this work include studies published in the last 10 years (2010–2021) considered as recent research reporting pancreatic lipase inhibition by anti-obesity plants. Future works covering previous years' research should be envisaged. Third, there are several articles in which the procedure fits our criteria for pancreatic lipase inhibition. However, the description of the intervention is inadequate to explain the number of repetitions of samples and orlistat, and the value of the standard deviation or standard error is not shown. Therefore, some articles are excluded after full-text reading because they only show % inhibition without providing the  $IC_{50}$  value of pancreatic lipase inhibition.

The strength of the current meta-analysis is the coverage of traditional plant medicines from many parts of the world as anti-obesity with specific mechanisms as an inhibitor of pancreatic lipase. Moreover, we perform subgroup analysis to identify the main sources of heterogeneity and introduce the influence of secondary metabolites in each intervention, as well as specific solvents used in the extraction procedure. Ultimately, using VoS viewer, this study is enriched with a review of how far studies pertaining to obesity are carried out.

## ■ CONCLUSION

The electronic search collected 810 research articles from 6 scientific databases, and 91 of them contained eligible data reporting the use of TMP for treating anti-obesity via inhibition of pancreatic lipase. Among these plants, we found some plants showing the best anti-obesity activity, i.e., *Solenostemma argel*, *Garcinia vilersiana*, *P. chamaepeuce*, *Cassia auriculata*, *Moringa oleifera*, *Ficus carica*, *Ocimum gratissimum*, and *Adiantum capillus-veneris*, respectively. Their anti-obesity effects were evaluated according to the inhibition of pancreatic lipase expressed as  $IC_{50}$ . One explanation of their bioactivity is related to the content of bioactive compounds such as flavonoid, alkaloid, phenolic, malic acid, and ferulic acid. To isolate specific compounds

acting as pancreatic lipase inhibitors, the use of solvents, i.e., 70% ethanol, 90% ethanol, and methanol, combined with ultrasonication, were reported to show the best outcome.

## ■ AUTHOR CONTRIBUTIONS

Designed the subject and revised the article: Hasim and Didah Nur Faridah. Developed inclusion and exclusion criteria, developed and performed the search strategy, conducted the statistical analysis, and wrote the article: Frendy Ahmad Afandi, Eka Nurul Qomaliyah, Hasim, and Didah Nur Faridah. Screened relevant literature, and made decisions according to inclusion and exclusion criteria: Frendy Ahmad Afandi and Eka Nurul Qomaliyah.

## ■ REFERENCES

- [1] World Health Organization, 2018, *Noncommunicable Disease Country Profiles 2018*, World Health Organization, Geneva.
- [2] Chooi, Y.C., Ding, C., and Magkos, F., 2018, The epidemiology of obesity, *Metabolism*, 92 (1), 6–10.
- [3] Müller, M., and Geisler, C., 2017, Defining obesity as a disease, *Eur. J. Clin. Nutr.*, 71 (11), 1256–1258.
- [4] Hu, F.B., 2013, Resolved: There is sufficient scientific evidence that decreasing sugar-sweetened beverage consumption will reduce the prevalence of obesity and obesity-related diseases, *Obes. Rev.*, 14 (8), 606–619.
- [5] Williams, E.P., Mesidor, M., Winters, K., Dubbert, P.M., and Wyatt, S.B., 2015, Overweight and obesity: Prevalence, consequences, and causes of a growing public health problem, *Curr. Obes. Rep.*, 4 (3), 363–370.
- [6] Ernst, B., Wilms, B., Thurnheer, M., and Schultes, B., 2015, Eating behaviour in treatment-seeking obese subjects – Influence of sex and BMI classes, *Appetite*, 95, 96–100.
- [7] Nicolaidis, S., 2019, Environment and obesity, *Metabolism*, 100, 153942.
- [8] Koliaki, C., Liatis, S., and Kokkinos, A., 2018, Obesity and cardiovascular disease: Revisiting an old relationship, *Metabolism*, 92, 98–107.

- [9] Ginsberg, H.N., and MacCallum, P.R., 2009, The obesity, metabolic syndrome, and type 2 diabetes mellitus pandemic: Part I. Increased cardiovascular disease risk and the importance of atherogenic dyslipidemia in persons with the metabolic syndrome and type 2 diabetes mellitus, *J. CardioMetab. Syndr.*, 4 (2), 113–119.
- [10] Csige, I., Ujvárosy, D., Szabó, Z., Lőrincz, I., Paragh, G., Harangi, M., and Somodi, S., 2018, The impact of obesity on the cardiovascular system, *J. Diabetes Res.*, 2018, 3407306.
- [11] Hasani-Ranjbar, S., Jouyandeh, Z., and Abdollahi, M., 2013, A systematic review of anti-obesity medicinal plants - An update, *J. Diabetes Metab. Disord.*, 12 (1), 28.
- [12] Mahmoud, R.H., and Elnour, W.A., 2013, Comparative evaluation of the efficacy of ginger and orlistat on obesity management, pancreatic lipase and liver peroxisomal catalase enzyme in male albino rats, *Eur. Rev. Med. Pharmacol. Sci.*, 17, 75–83.
- [13] Bujjirao, G., and Ratna Kumar, K.P., 2013, Anti-obese therapeutics from medicinal plants-A review, *Int. J. Bioassays*, 2 (10), 1399–1406.
- [14] Yun, J.W., 2018, Possible anti-obesity therapeutics from nature – A review, *Phytochemistry*, 7 (14-15), 1625–1641.
- [15] Rufino, A.T., Costa, V.M., Carvalho, F., and Fernandes, E., 2020, Flavonoids as antiobesity agents: A review, *Med. Res. Rev.*, 41 (1), 556–585.
- [16] Hossain, M.K., Dayem, A.A., Han, J., Yin, Y., Kim, K., Saha, S.K., Yang, G.M., Choi, H.Y., and Cho, S.G., 2016, Molecular mechanisms of the anti-obesity and anti-diabetic properties of flavonoids, *Int. J. Mol. Sci.*, 17 (4), 569.
- [17] Song, D., Cheng, L., Zhang, X., Wu, Z., and Zheng, X., 2019, The modulatory effect and the mechanism of flavonoids on obesity, *J. Food Biochem.*, 43 (8), e12954.
- [18] Nagatomo, A., Nishida, N., Matsuura, Y., and Shibata, N., 2013, Rosehip extract inhibits lipid accumulation in white adipose tissue by suppressing the expression of peroxisome proliferator-activated receptor gamma, *Prev. Nutr. Food Sci.*, 18 (2), 85–91.
- [19] Ninomiya, K., Matsuda, H., Kubo, M., Morikawa, T., Nishida, N., and Yoshikawa, M., 2007, Potent anti-obese principle from *Rosa canina*: Structural requirements and mode of action of *trans*-tiliroside, *Bioorg. Med. Chem. Lett.*, 17 (11), 3059–3064.
- [20] Lesjak, M., Beara, I., Simin, N., Pintač, D., Majkić, T., Bekvalac, K., Orčić, D., and Mimica-Dukić, N., 2018, Antioxidant and anti-inflammatory activities of quercetin and its derivatives, *J. Funct. Foods*, 40, 68–75.
- [21] Batiha, G.E., Beshbishy, A.M., Ikram, M., Mulla, Z.S., Abd El-Hack, M.E., Taha, A.E., Algammal, A.M., and Elewa, Y.H., 2020, The pharmacological activity, biochemical properties, and pharmacokinetics of the major natural polyphenolic flavonoid: Quercetin, *Foods*, 9 (3), 374.
- [22] Bajes, H.R., Almasri, I., and Bustanji, Y., 2020, Plant products and their inhibitory activity against pancreatic lipase, *Rev. Bras. Farmacogn.*, 30 (3), 321–330.
- [23] Mohamed, G.A., Ibrahim, S.R.M., Elkhayat, E.S., and El Dine, R.S., 2014, Natural anti-obesity agents, *Bull. Fac. Pharm. Cairo Univ.*, 52 (2), 269–284.
- [24] Marrelli, M., Loizzo, M.R., Nicoletti, M., Menichini, F., and Conforti, F., 2013, Inhibition of key enzymes linked to obesity by preparations from Mediterranean dietary plants: Effects on  $\alpha$ -amylase and pancreatic lipase activities, *Plant Foods Hum. Nutr.*, 68 (4), 340–346.
- [25] de Freitas Junior, L.M., and de Almeida, E.B., 2017, Medicinal plants for the treatment of obesity: Ethnopharmacological approach and chemical and biological studies, *Am. J. Transl. Res.*, 9 (5), 2050–2064.
- [26] Liberati, A., Altman, D.G., Tetzlaff, J., Mulrow, C., Gøtzsche, P.C., Ioannidis, J.P.A., Clarke, M., Devereaux, P.J., Kleijnen, J., and Moher, D., 2009, The PRISMA statement for reporting systematic reviews and meta-analyses of studies that evaluate health care interventions: Explanation and elaboration, *J. Clin. Epidemiol.*, 62 (10), e1-e34.
- [27] Afandi, F.A., 2020, Meta-analisis faktor-faktor penentu nilai indeks glikemik bahan pangan pati-

- patian dan verifikasinya dengan menggunakan model pangan, *Dissertation*, IPB University.
- [28] El-Shiekh, R.A., Al-Mahdy, D.A., Mouneir, S.M., Hifnawy, M.S., and Abdel-Sattar, E.A., 2019, Anti-obesity effect of argel (*Solenostemma argel*) on obese rats fed a high fat diet, *J. Ethnopharmacol.*, 238, 111893.
- [29] Dechakhamphu, A., and Wongchum, N., 2015, Screening for anti-pancreatic lipase properties of 28 traditional Thai medicinal herbs, *Asian Pac. J. Trop. Biomed.*, 5 (12), 1042–1045.
- [30] Mopuri, R., Ganjari, M., Meriga, B., Koorbanally, N.A., and Islam, M.S., 2018, The effects of *Ficus carica* on the activity of enzymes related to metabolic syndrome, *J. Food Drug Anal.*, 26 (1), 201–210.
- [31] Inthongkaew, P., Chatsumpun, N., Supasuteekul, C., Kitisripanya, T., Putalun, W., Likhitwitayawuid, K., and Sritularak, B., 2017,  $\alpha$ -Glucosidase and pancreatic lipase inhibitory activities and glucose uptake stimulatory effect of phenolic compounds from *Dendrobium formosum*, *Rev. Bras. Farmacogn.*, 27 (4), 480–487.
- [32] Kumar, D., Karmase, A., Jagtap, S., Shekhar, R., and Bhutani, K.K., 2013, Pancreatic lipase inhibitory activity of cassiamin A, a bianthraquinone from *Cassia siamea*, *Nat. Prod. Commun.*, 8 (2), 195–198.
- [33] Adisakwattana, S., Intrawangso, J., Hemrid, A., Chanathong, B., and Mäkynen, K., 2012, Extracts of edible plants inhibit pancreatic lipase, cholesterol esterase and cholesterol micellization, and bind bile acid, *Food Technol. Biotechnol.*, 50 (1), 11–16.
- [34] Habtemariam, S., 2012, Identification of the antidiabetic and antihyperlipidemic principles of *Cassia auriculata*, *Planta Med.*, 78 (11), PD51.
- [35] Kaewpiboon, C., Lirdpramongkol, K., Srisomsap, C., Winayanuwattikun, P., Yongvanich, T., Puwaprisirisan, P., Svasti, J., and Assavalapsakul, W., 2012, Studies of the *in vitro* cytotoxic, antioxidant, lipase inhibitory and antimicrobial activities of selected Thai medicinal plants, *BMC Complementary Altern. Med.*, 12, 217.
- [36] Teixeira, L.S., Lima, A.S., Boleti, A.P.A., Lima, A.A.N., Libório, S.T., de Paula, L., Oliveira, M.I.B., Lima, E.F., Costa, G.M., Reginatto, F.H., and Lima, E.S., 2013, Effects of *Passiflora nitida* Kunth leaf extract on digestive enzymes and high caloric diet in rats, *J. Nat. Med.*, 68 (2), 316–325.
- [37] Buchholz, T., and Melzig, M.F., 2015, Medicinal plants traditionally used for treatment of obesity and diabetes mellitus - Screening for pancreatic lipase and  $\alpha$ -amylase inhibition, *Phytother. Res.*, 30 (2), 260–266.
- [38] Huang, R., Zhang, Y., Shen, S., Zhi, Z., Cheng, H., Chen, S., and Ye, X., 2020, Antioxidant and pancreatic lipase inhibitory effects of flavonoids from different citrus peel extracts: An *in vitro* study, *Food Chem.*, 326, 126785.
- [39] Bais, S., and Patel, N.J., 2012, In vitro anti diabetic and anti obesity effect of *J. communis* extract on 3T3L1 mouse adipocytes: A possible role of MAPK/ERK activation, *Obes. Med.*, 18, 100219.
- [40] Al-Rimawi, F., Jaradat, N., Qneibi, M., Hawash, M., and Emwas, N., 2020, Free radicals and enzymes inhibitory potentials of the traditional medicinal plant *Echium angustifolium*, *Eur. J. Integr. Med.*, 38, 101196.
- [41] Spínola, V., Llorent-Martínez, E.J., and Castilho, P.C., 2019, Inhibition of  $\alpha$ -amylase,  $\alpha$ -glucosidase and pancreatic lipase by phenolic compounds of *Rumex maderensis* (Madeira sorrel). Influence of simulated gastrointestinal digestion on hyperglycaemia-related damage linked with aldose reductase activity and protein glycation, *LWT*, 118, 108727.
- [42] Anyanwu, G.O., Anzaku, D., Donwell, C.C., Usunobun, U., Adegbeji, A.J., Ofoha, P.C., and Rauf, K., 2021, Chemical composition and *in vitro* antiobesity and *in vivo* anti-hyperlipidemic effects of *Ceratotherca sesamoides*, *Jatropha tanjorensis*, *Mucuna flagellipes*, *Pterocarpus mildbraedii* and *Piper guineense*, *Phytomed. Plus*, 1 (3), 10042.
- [43] Al-Yousef, H.M., Alqahtani, A.S., Hassan, W.H., Alzoubi, A., and Sahar, A.A., 2021, Chemical profile, *in vitro* antioxidant, pancreatic lipase, and alpha-amylase inhibition assays of the aqueous extract of *Elettaria cardamomum* L. fruits, *J. Chem.*, 2021, 5583001.

- [44] Jaradat, N., Qadi, M., Abualhasan, M.N., Al-lahham, S., Al-Rimawi, F., Hattab, S., Hussein, F., Zakarneh, D., Hamad, I., Sulayman, I., Issa, L., and Mousa, A., 2020, Carbohydrates and lipids metabolic enzymes inhibitory, antioxidant, antimicrobial and cytotoxic potentials of *Anchusa ovata* Lehm. from Palestine, *Eur. J. Integr. Med.*, 34, 101066.
- [45] Kasabri, V., Al-Hallaq, E.K., Bustanji, Y.K., Abdul-Razzak, K.K., Abaza, I.F., and Afifi, F.U., 2017, Antiobesity and antihyperglycaemic effects of *Adiantum capillus-veneris* extracts: *In vitro* and *in vivo* evaluations, *Pharm. Biol.*, 55 (1), 164–172.
- [46] Gururaja, G.M., Mundkinajeddu, D., Kumar, S., Allan, J., Dethe, S.M., and Agarwal, A., 2016, Cholesterol lowering potentials of a blend of standardized methanol extracts of *Moringa oleifera* leaves and fruits in albino wistar rats, *Int. J. Pharm. Pharm. Sci.*, 8 (11), 262–268.
- [47] Wang, F., Bao, Y., Shen, X., Zengin, G., Lyu, Y., Xiao, J., and Weng, Z., 2019, Niazirin from *Moringa oleifera* Lam. attenuates high glucose-induced oxidative stress through PKC $\zeta$ /Nox4 pathway, *Phytomedicine*, 86, 153066.
- [48] Rajan, L., Palaniswamy, D., and Mohankumar, S.K., 2020, Targeting obesity with plant-derived pancreatic lipase inhibitors: A comprehensive review, *Pharmacol. Res.*, 155, 104681.
- [49] Lee, E.M., Lee, S.S., Chung, B.Y., Cho, J.Y., Lee, I.C., Ahn, S.R., Jang, S.J., and Kim, T.H., 2010, Pancreatic lipase inhibition by C-glycosidic flavones isolated from *Eremochloa ophiuroides*, *Molecules*, 15 (11), 8251–8259.
- [50] Lunagariya, N.A., Patel, N.K., Jagtap, S.C., and Bhutani, K.H., 2014, Inhibitors of pancreatic lipase: State of the art and clinical perspectives, *EXLI J.*, 13, 897–921.
- [51] Chemat, F., Rombaut, N., Sicaire, A.G., Meullemiestre, A., Fabiano-Tixier, A.S., and Abert-Vian, M., 2016, Ultrasound assisted extraction of food and natural products. Mechanisms, techniques, combinations, protocols and applications. A review, *Ultrason. Sonochem.*, 34, 540–560.
- [52] Azmir, J., Zaidul, I.S.M., Rahman, M.M., Sharif, K.M., Mohamed, A., Sahena, F., Jahurul, M.H.A., Ghafoor, K., Norulaini, N.A.N., and Omar, A.K.M., 2013, Techniques for extraction of bioactive compounds from plant materials: A review, *J Food Eng.*, 117 (4), 426–436.
- [53] Altemimi, A., Lakhssassi, N., Baharlouei, A., Watson, D.G., and Lightfoot, D.A., 2017, Phytochemicals: Extraction, isolation, and identification of bioactive compounds from plant extracts, *Plants*, 6 (4), 42.
- [54] Dai, J., and Mumper, R.J., 2010, Plant phenolics: Extraction, analysis and their antioxidant and anticancer properties, *Molecules*, 15 (10), 7313–7352.
- [55] Iswantini, D., Darusman, L.K., and Fitriyani, A., 2010, Uji *in vitro* ekstrak air dan etanol dari buah asam gelugur, rimpang lengkuas, dan kencur sebagai inhibitor aktivitas lipase pancreas, *JSTI*, 12 (1), 15–20.
- [56] Hassan, H.A., Hamed, A.I., El-Emary, N.A., Springuel, I.V., Mitome, H., and Miyaoka, H., 2001, Pregnene derivatives from *Solenostemma argel* leaves, *Phytochemistry*, 57 (4), 507–511.
- [57] El-shiekh, R.A., Al-Mahdy, D.A., Hifnawy, M.S., and Abdel-Sattar, E., 2019, *In-vitro* screening of selected traditional medicinal plants for their anti-obesity and anti-oxidant activities, *S. Afr. J. Bot.*, 123, 43–50.
- [58] Angami, T., Wangchu, L., Debnath, P., Sarma, P., Singh, B., Singh, A.K., Singh, S., Singh, M.C., Aochen, C., and Lungmuana, L., 2021, *Garcinia* L.: A gold mine of future therapeutics, *Genet. Resour. Crop Evol.*, 68 (1), 11–24.
- [59] Hoffmann, P., Kathriarachchi, H., and Wurdack, K.J., 2006, A phylogenetic classification of *Phyllanthaceae* (*Malpighiales*; *Euphorbiaceae sensu lato*), *Kew Bull.*, 61 (1), 37–53.
- [60] Jantan, I., Haque, M.A., Ilangkovan, M., and Arshad, L., 2019, An insight into the modulatory effects and mechanisms of action of *Phyllanthus* species and their bioactive metabolites on the immune system, *Front. Pharmacol.*, 10, 878.



- [61] Meena, V., Baruah, H., and Parveen, R., 2019, *Cassia auriculata*: A healing herb for all remedy, *J. Pharmacogn. Phytochem.*, 8 (3), 4093–4097.
- [62] Garg, A., and Singh, R., 2015, Antiobesity activity of ethanolic extract of *Cassia auriculata* in high fat diet induced obese rats, *Int. J. Pharm. Pharm. Sci.*, 7 (4), 237–243.
- [63] Singh, M., Singh, S., and Verma, D., 2020, Morphological and pharmacognostical evaluation of *Moringa oleifera* Lam. (Moringaceae): A plant with high medicinal value in tropical and subtropical parts of the world, *Pharmacogn. Rev.*, 14 (28), 138–145.
- [64] WWF and Knorr, 2019, *Future 50 Food: A Report*, [https://www.wwf.org.uk/sites/default/files/2019-02/Knorr\\_Future\\_50\\_Report\\_FINAL\\_Online.pdf](https://www.wwf.org.uk/sites/default/files/2019-02/Knorr_Future_50_Report_FINAL_Online.pdf), accessed on July 30, 2021.
- [65] Redha, A.A., Perna, S., Riva, A., Petrangolini, G., Peroni, G., Nichetti, M., Iannello, G., Naso, M., Faliva, M.A., and Rondanelli, M., 2021, Novel insights on anti-obesity potential of the miracle tree, *Moringa oleifera*: A systematic review, *J. Funct. Foods*, 84, 104600.
- [66] Nahar, S., Faisal, F.M., Iqbal, J., Rahman, M.M., and Yusuf, M.A., 2016, Antiobesity activity of *Moringa oleifera* leaves against high fat diet-induced obesity in rats, *Int. J. Basic Clin. Pharmacol.*, 5 (4), 1263–1268.
- [67] Kim, K.B., and Shin, Y.A. 2020, Males with obesity and overweight, *J. Obes. Metab. Syndr.*, 29 (1), 18–25.
- [68] Bao, Y., Xiao, J., Weng, Z., Lu, X., Shen, X., and Wang, F., 2020, A phenolic glycoside from *Moringa oleifera* Lam. improves the carbohydrate and lipid metabolisms through AMPK in db/db mice, *Food Chem.*, 311, 125948.
- [69] Mawa, S., Husain, K., and Jantan, I., 2013, *Ficus carica* L. (Moraceae): Phytochemistry, traditional uses and biological activities, *Evidence-Based Complementary Altern. Med.*, 2013, 974256.
- [70] Arafa, E.S.A., Hassan, W., Murtaza, G., Buabeid, M.A., 2020, *Ficus carica* and *Sizigium cumini* regulate glucose and lipid parameters in high-fat diet and streptozocin-induced rats, *J Diabetes Res.*, 2020, 6745873.
- [71] Mahajan, N., Rawal, S., Verma, M., Poddar, M., and Alok, S., 2013, A phytopharmacological overview on *Ocimum* species with special emphasis on *Ocimum sanctum*, *Biomed. Prev. Nutr.*, 3 (2), 185–192.
- [72] Mann, A., 2012, Phytochemical constituents and antimicrobial and grain protectant activities of clove basil (*Ocimum gratissimum* L.) grown in Nigeria, *Int. J. Plant Res.*, 2 (1), 51–58.
- [73] Irondi, E., Agboola, S., Oboh, G., and Boligon, A., 2016, Inhibitory effect of leaves extracts of *Ocimum basilicum* and *Ocimum gratissimum* on two key enzymes involved in obesity and hypertension *in vitro*, *J. Intercult. Ethnopharmacol.*, 5(4), 396–402.
- [74] Yumkham, S.D., Elangbam, M., Nongmaithem, R., Naorem, P.D., and Singh, P.K., 2018, Maiden hair ferns (*Adiantum* L., Pteridaceae–Vittarioideae) of North East India: Diversity, phytochemistry and utilization, *Genet. Resour. Crop Evol.*, 65 (4), 1269–1280.
- [75] Jawed, A., Singh, G., Kohli, S., Sumera, A., Haque, S., Prasad, R., and Paul, D., 2018, Therapeutic role of lipases and lipase inhibitors derived from natural resources for remedies against metabolic disorders and lifestyle diseases, *S. Afr. J. Bot.*, 120, 25–32.
- [76] Sánchez, J., Priego, T., Palou, M., Tobaruela, A., Palao, A., and Picó, C., 2008, Oral supplementation with physiological doses of leptin during lactation in rats improves insulin sensitivity and affects food preferences later in life, *Endocrinology*, 149 (2), 733–740.
- [77] Liu, T.T., Liu, X.T., Chen, Q.X., and Shi, Y., 2020, Lipase inhibitors for obesity: A review, *Biomed. Pharmacother.*, 128, 110314.
- [78] Olędzka, A., Cichocka, K., Woliński, K., Melzig, M.F., and Czerwińska, M.E., 2022, Potentially bio-accessible metabolites from an extract of *Cornus mas* fruit after gastrointestinal digestion *in vitro* and gut microbiota *ex vivo* treatment, *Nutrients*, 14 (11), 2287.